Wetting & Capillarity: From Thin Film Mediated Processes to Droplet-Surface Interactions

by

Sirshendu Misra

A thesis
presented to the University of Waterloo
in fulfillment of the
thesis requirement for the degree of
Doctor of Philosophy
in
Mechanical and Mechatronics Engineering

Waterloo, Ontario, Canada, 2023

Examining Committee Membership

The following served on the Examining Committee for this thesis. The decision of the Examining Committee is by majority vote.

External Examiner:	David Sinton Professor, Dept. of Mechanical & Industrial Engineering, University of Toronto
Supervisor(s):	Sushanta K. Mitra Professor, Dept. of Mechanical & Mechatronics Engineering, University of Waterloo
Internal Member:	Carolyn Ren Professor, Dept. of Mechanical & Mechatronics Engineering, University of Waterloo
Internal Member:	Kevin Musselman Associate Professor, Dept. of Mechanical & Mechatronics Engineering, University of Waterloo

Internal-External Member: Boxin Zhao
Professor,
Dept. of Chemical Engineering,
University of Waterloo

Author's Declaration

This thesis consists of material, all of which I authored or co-authored: see Statement of Contributions included in the thesis. This is a true copy of the thesis, including any required final revisions, as accepted by my examiners.

I understand that my thesis may be made electronically available to the public.

Statement of Contributions

Contents from 10 journal articles (8 published/accepted and 2 currently under review) are used in preparing this thesis. I was an author in all these works with major contributions to the conceptualization, design of experiments, data acquisition, analysis, and writing of the papers' material. 7 of these journal articles are my first author/equally contributing first author works and the remaining 3 are my co-authored contribution where I worked with Postdoctoral fellows or visiting researchers. Below I provide a chapter-wise summary of the contributions and link the chapters to the respective journal articles, wherever applicable.

Chapter 1 is solely authored by me with inputs from my supervisor Prof. Sushanta K. Mitra.

Chapter 2 is adapted with permission from **S. Misra**, K. Trinavee, N. S. K. Gunda, S.K. Mitra, "Encapsulation with an interfacial liquid layer: Robust and efficient liquid-liquid wrapping." *Journal of Colloid and Interface Science*, 558C (2020) pp. 334-344. As the first author, I was primarily responsible for conceptualization, setup design, methodology, data acquisition, validation, analysis, writing the original draft, and executing revisions suggested by the peer reviewers.

Chapter 3 is adapted from **S. Misra***, U. Banerjee*, S. K. Mitra, "Liquid-liquid encapsulation: Penetration vs. trapping at a liquid interfacial layer." just accepted (acceptance date: April 20, 2023) for publication in *ACS Applied Materials & Interfaces* (manuscript id: am-2023-021773), *: Equally contributing first author. As an equally contributing first author, I worked with a Postdoctoral fellow in our lab on the development of research concepts, design of methodology, data acquisition, validation, analysis, writing the original draft, and executing revisions suggested by the peer reviewers.

Chapter 4 is adapted from M. R. Gunjan*, U. Banerjee*, **S. Misra***, S. K. Mitra, "Manipulation of ferrofluid wrapped drops: Translation, coalescence and release." Under review in *Advanced Materials Interfaces* (manuscript id: admi.202300144), *: Equally contributing first author. As an equally contributing first author, I worked with two Postdoctoral fellows on the conceptualization of research, development of methodology, data acquisition, validation, analysis, writing the original draft, and executing revisions suggested by the peer reviewers.

Chapter 5 is adapted with permission from U. Banerjee*, **S. Misra***, S. K. Mitra, "Liquid–Liquid Encapsulation of Ferrofluid Using Magnetic Field." *Advanced Materials Interfaces*, 2022, 2200288. *: Equally contributing first author. As an equally contributing first author, I worked with a Postdoctoral fellow in our lab on the conceptualization, methodology, data acquisition, validation, analysis, writing the original draft, and executing revisions suggested by the peer reviewers.

Note that the works presented in **Chapters 3, 4 and 5** are built upon the foundational concepts developed and described in **Chapter 2**.

Chapter 6 is adapted with permission from **S. Misra**, H. Teshima, K. Takahashi, S. K. Mitra, "Reflected Laser Interferometry: A Versatile Tool to Probe Condensation of Low-Surface-Tension Droplets.", *Langmuir*, 2021, 37, 27, 8073-8082. As the first author, I was primarily responsible for conceptualization, methodology, data acquisition, development of custom software for the interpretation of data, formal analysis, writing the original draft, and executing revisions suggested by the peer reviewers.

Chapter 7 is adapted with permission from H. Teshima, **S. Misra**, K. Takahashi, S. K. Mitra, "Precursor-Film-Mediated Thermocapillary Motion of Low-Surface-Tension Microdroplets." *Langmuir*, 2020, 36, 19, 5096–5105. As a co-author, I worked with a visiting researcher on the development of the research concept, and methodology, building the software program for data analysis, and writing – review & editing.

Note that the framework developed in **Chapter 6** was used to perform the analysis presented in this work.

Chapter 8 is adapted from **S. Misra**, M. Tenjimbayashi, W. Weng, S. K. Mitra, M. Naito, "Bioinspired slippery coatings with excellent long-term durability." Under review in *ACS Applied Materials & Interfaces* (manuscript id: am-2023-031282). As the first author, I was primarily responsible for research design, methodology, data acquisition, data analysis, writing the original draft, and executing revisions suggested by the peer reviewers.

Chapter 9 is adapted with permission from K. Raj M, **S. Misra**, S. K. Mitra, "Friction and adhesion of microparticle suspension on repellent surfaces." *Langmuir*, 2020, 36, 45, 13689–13697. As a co-author, I worked with a Postdoctoral fellow on research design, methodology, and writing – review & editing.

Chapter 10 is adapted with permission from S. Shyam*, **S. Misra***, S. K. Mitra, "A universal capillary-deflection based adhesion measurement technique." *Journal of Colloid and Interface Science*, 2023, 630, 322-333. *: Equally contributing first author. As an equally contributing first author, I worked with a Postdoctoral fellow in our lab on the conceptualization of research, development of methodology, data acquisition, validation, analysis, writing the original draft, and executing revisions suggested by the peer reviewers.

Chapter 11 is adapted with permission from K. Raj M, **S. Misra**, S. K. Mitra, "Microparticle suspensions and bacteria laden droplets: Are they the same in terms of wetting signature?", *Langmuir*, 2021, 37, 4, 1588–1595. As a co-author, I worked with a Postdoctoral fellow on research design, methodology, data acquisition (in part), and writing – review & editing.

Chapter 12 is solely authored by me with inputs from my supervisor Prof. Sushanta K. Mitra.

Abstract

Wetting and capillarity remain ubiquitous in both daily lives and industrial applications. The present thesis explores several fundamentally interesting problems of practical relevance in wetting and capillarity. Two primary thematic directions are adopted in developing this thesis, namely, thin film-mediated wetting and direct quantification of droplet-substrate interfacial interaction.

Under thin film-mediated wetting, we first demonstrate the development of a robust liquid-liquid encapsulation framework where a liquid core analyte is stably wrapped by a thin layer of another shell-forming liquid. Two approaches to achieve encapsulation are discussed - impact-driven and magnet-assisted. The underlying mechanism leading to encapsulation are explored in detail for both approaches. We show that successful encapsulation by either approach provides efficient protection to the core analyte even in aggressive surroundings. Multiple practical use cases, including ultrafast encapsulation, shell-hardening, and subsequent extraction/handling of the wrapped cargo, the formation of encapsulated Janus droplets with similar/dissimilar core compositions, are reported. Further, impact-driven encapsulation with a magnetoresponsive (ferrofluid) shell layer is also illustrated, which allows magnet-assisted efficient, non-contact manipulation of the encapsulated cargo, including translation, controlled coalescence, and the release of the inner core. Although we can confirm successful wrapping via indirect evidence (e.g., alteration in wetting signature/physical appearance & efficient protection in aggressive surrounding upon encapsulation) in our liquid-liquid encapsulation framework, direct visualization of the thin wrapping film remains extremely challenging via standard optical means. To this effect, a complete interferometric framework is developed to detect and reconstruct the spatiotemporal dynamics of such ultrathin ($\sim$ nm - μm) liquid films. The framework is tested by investigating the dynamics of dropwise condensation of volatile, low-surface-tension test liquids. In doing so, a previously unknown spontaneous motion of the condensed microdroplets on high-surface energy test substrates is unraveled. The nucleated smaller microdroplets spontaneously migrate towards a bigger microdroplet in the vicinity. With rational experimentation and theoretical arguments, we attribute this motion to the combined effect of the formation of an ultrathin precursor film underneath the nucleated microdroplets and thermocapillary action. Finally, a direct practical application of

thin film-mediated wetting in functional materials research, the development of a robust lubricant-infused surface, is reported. The fundamental concept of capillarity transport is leveraged to develop a lubricant-depletion tolerant, long-term stable, large-scale slippery surface with exceptional outdoor durability. If depleted, the thin surface lubricant layer, responsible for the slippery functionality of the material, can be self-replenished via unassisted capillary transport even after multiple lubricant loss-recovery cycles.

A key performance indicator of the liquid-liquid encapsulation protocol is the practical stability of the encapsulated cargo, which is primarily dictated by its interaction with the solid surfaces it encounters. The second thematic direction of the present thesis stems from the requirement of quantifying this droplet-substrate interfacial interaction. Contact angle goniometry was the standard method for characterizing such liquid-solid wetting interactions. However, as already established in the literature, optical goniometry suffers from significant imaging challenges due to optical noise caused by scattering and diffraction near the triple contact line. We show that the cantilever deflection approach, where a microdroplet attached to the tip of a flexible polymeric cantilever is used to probe the adhesion and frictional characteristics of test substrates, is a simple and more accurate alternative in this regard. However, in the conventional approach, the characteristic adhesion between a probe droplet and a target substrate is calculated at the instance of maximum deflection of the cantilever, which is assumed to coincide with the detachment of the probe droplet from the test substrate. This restricts the approach to low-energy (super)repellent surfaces only as the probe droplet cannot completely detach from the test substrate and instead gets split in two if the substrate has a higher surface energy. We critically revisit the conventional framework and establish that complete detachment of the probe droplet is not a strict prerequisite for the applicability of the framework as the sole physical criterion that has a direct correspondence with characteristic adhesion is the depinning of the triple contact line. It allows us to generalize the cantilever-based framework to higher energy surfaces. Further, with a detailed mechanistic analysis of the cantilever's motion, we establish that the instance of zero acceleration of the cantilever corresponds to the depinning of the triple contact line and, thus, to the characteristic adhesion. The developed methodology is general and straightforward. Simple tracking of the motion of the cantilever and subsequent computation of its acceleration, which can be automated,

enable the user to characterize the ensuing adhesion interaction between the probe droplet and the test substrate even on higher energy surfaces which was a significant bottleneck in literature. Finally, we use the cantilever deflection method to study how bacteria-laden droplets interact with (super)repellent surfaces and, in the process, uncover an anomalous adhesion behavior when live bacteria are used as dopants inside the probe droplet where increasing the concentration of live bacteria in the probe droplet leads to a reduction in adhesion force. The anomalous behavior is attributed to the motility of the live bacteria.

Acknowledgements

First and foremost, I would like to thank my supervisor Prof. Sushanta Mitra for giving me this opportunity to pursue doctoral studies under his supervision and for his continuous guidance, enthusiasm, and encouragement. Prof. Mitra, I have learned so much from working with you in the past 4.5 years. You did not only guide me in my pursuit of interface science but also taught me how to be a balanced researcher. Honestly speaking, every single interaction with you to date has been a learning opportunity for me. The way you look at every problem & situation is truly inspiring. Your clarity of thought amazes me to date. For every problem, both scientific and practical, you always have a unique take. You recognized and acknowledged my strengths and gave me ample scope to arrange my work style accordingly. You gave me unparalleled flexibility to freely explore multiple research directions in interface science while keeping a close check that I am always on track. I believe it has helped me a lot to realize my potential and broaden my horizon. Most importantly, you taught me how to prioritize tasks and when to stop being overly pedantic and let go. I won't say I have mastered it, but I am trying. Looking back today, I believe joining your group was one of the best decisions in my career thus far. It has been an absolute privilege to grow under your tutelage.

I would also like to thank the external examiner, Dr. David Sinton, and members of my supervisory committee, Dr. Carolyn Ren, Dr. Kevin Musselman & Dr. Boxin Zhao, for their valuable suggestions during my thesis evaluation and Ph.D. defense. I would like to thank Dr. Mahla Poudineh, Dr. Shirley Tang, Dr. Boxin Zhao, Dr. Juewen Liu, and Dr. Kam Tong Leung of the University of Waterloo community for allowing me to use the instruments available in their lab at different stages of my Ph.D.

I would like to thank National Institute for Material Science (NIMS), Japan, for giving me an opportunity to pursue a collaborative research internship there, where I learned a lot regarding functional material synthesis for wetting applications. Special thanks to Dr. Masanobu Naito and Dr. Mizuki Tenjimbayashi for all their support during my internship. It was truly a great learning experience. In fact, Chapter 8 of this thesis is based on the work carried out during this research internship. I thank Mitacs, Canada, for supporting this research visit via a Mitacs Globalink Research Award - Abroad. I would also like to

thank Waterloo Institute for Nanotechnology (WIN) for making this internship possible. Tenjimbayashi san - thank you so much for your general scientific mentorship, I learned a lot about improving the presentation quality of data and general research directions from you.

I also thank Waterloo Institute for Nanotechnology (WIN) for the funding support via Nanofellowship 2018 & 2020 awards and for providing a healthy lab & office environment during my Ph.D. tenure. Special Thanks to Chris Kleven for all his assistance with general infrastructure.

I am thankful to all past and present members (Kumari, Dr. Naga, Dr. Badu, Enrique, Hideaki, Kiran, Surjyasish, Utsab, Madhu, Sudip, Priyam, Soumyadeep, Jon, A-Reum, Iris) of Micro & Nano-scale Transport Laboratory (MNT Lab) for their constant co-operation, support, and friendship. In addition to excellent academic collaborations, I am fortunate to have developed strong friendships with most of you. You made life both inside and outside the lab fun & interesting. Dr. Snehasish Mondal & Antara Mondal - you were my family away from family. You know what you mean to me. I wish you all the very best in whatever you do in life.

I would like to thank my family for all their support and belief in me. No word is enough to express my gratitude to you. You gave me so much freedom to pursue my dreams so far away from home, even when you were in dire need of my presence at home. Maa (Mom) - you are probably the strongest person I have ever met. I have faced some serious personal hurdles (health challenges, etc.) in recent years. Your support always kept me going. Thank you, Baba (Dad) - you don't know how much your anecdotes helped me in difficult times. I haven't seen you in the last 3.5 years, and I can't wait to see you. Whatever I am today is because of you. This thesis is dedicated to you. I would also like to thank my Dida (grandmother), who passed away during the COVID-19 pandemic, for all the love since my childhood. I miss you so much. Finally, I thank the divine spirit for keeping the hope alive in me in tough times.

To mom & dad

Table of Contents

List of Figures

List of Tables

Chapter 1

Introduction

1.1 Motivation

Capillarity is defined [1] as the study of the interfaces between two immiscible liquids or between a liquid and air. The interfaces are inherently deformable and continuously evolve in a complex manner to minimize the overall surface energy of the system.

Beginning of formal explorations [2–9] into capillarity and wetting can be traced back to late seventeenth century AD. However, much before the beginning of formal explorations, the implications of wetting & capillarity were felt. As per a recent study [10] by Bonn *et al.*, ancient Egyptians might have used the capillary bridges in $\sim$ 1800 BC to transport massive stone sleds on the sand while building the pyramids, without any formal knowledge of capillarity. Mentions about the calming effect of oil films on the rough sea waves could be found [11] in ancient texts by Aristotle, Plinius Secundus (the Elder), and Plutarch.

The work of Extrand [12] provides a historical account of the evolution of the formal field of capillarity and wetting. Much of the early works focused on deciphering the spontaneous rise of liquids in small-diameter capillary tubes. Some of the early observations in this regard were made by Hauskbee [5] in 1706, and Jurin [6] in 1717. Subsequently, in 1751, Segner established surface tension as an intrinsic property of a liquid, because of which its surface behaves like an elastic membrane. In the early 19^{th} century, Young reported

[8] his pioneering observation that the angle of contact between a solid and a liquid is independent of the geometry and concluded: "all the phenomena of capillary action may be accurately explained and mathematically demonstrated from the general law of equable tension of the surface of the fluid, together with the consideration of the angle of contact appropriate to every combination of a fluid with a solid." Laplace, who was active almost at the same time, was the first one to perform rigorous mathematical treatment [9] of a variety of wetting phenomena, including the capillary rise. The early analyses of Young and Laplace were based on force balance and pressure arguments. The foundational concepts of classical thermodynamics were not established back then. Gibbs [13], and Dupré [14] are credited with incorporating the energy approach in wetting studies. Subsequently, an upsurge in efforts [15–21] to recast the problems previously solved using the force approach to the energy formulation could be observed in the early 20^{th} century.

Despite its long-standing history, the field of capillarity and wetting remains evergreen to date mainly due to its fundamentally rich physics [22] coupled with the outstanding ramifications [23] of capillary-inspired processes in day-to-day life as well as commercial applications. Wetting and capillarity lie central to multiple industrial processes, including lubrication & fluid handling, surface coating, and printing.

Capillarity, wetting, and interfaces have been a long-standing research direction of our lab, Micro & Nano-scale Transport (MNT) Lab. Saha *et al.* [24] studied the capillary flow inside microchannels containing integrated pillars with variable wettabilities. Gunda *et al.* [25] introduced the concept of 'Reservoir-on-a-Chip,' a microfluidic chip with the features of a realistic pore network capable of performing the necessary waterflooding experiments routinely done in reservoir engineering. Das *et al.* [26, 27] revisits the different regimes of vertical capillary filling and report several previously unknown theoretical scaling relationships. Waghmare *et al.* [28] developed a needle-free drop deposition technique particularly suitable for the wetting characterization of superhydrophobic surfaces using the favorable interfacial interaction between a droplet and a needle tip at a three-fluid interface. Kumari *et al.* [29] performed underliquid wetting experiments on multiple substrates of different wettabilities and reported an anomalous wetting behavior that cannot be predicted with conventional wetting theories. With theoretical arguments, they attribute it to the formation of a sandwiched thin film of the surrounding medium between the droplet and

the test substrate. The present thesis is built upon the foundation of these works. It aims to further enhance the understanding of this rich area at the intersection of mechanical engineering, chemical engineering, chemistry, and condensed matter physics.

1.2 Scope of the thesis

This thesis looks into different aspects of capillarity and wetting with a general attempt to resolve some of the unresolved challenges of pertinent practical and commercial relevance, as we highlight in the subsequent chapters. The scope of the thesis can be split into two broad themes: thin film-mediated wetting and accurate quantification of droplet-surface interaction.

The dynamics of wetting can be significantly altered by the formation or presence of micro to nanoscale thin film [29] in the domain of interaction. Such a thin film either spontaneously form as a result of interaction between the surface, droplet, and the surrounding (e.g., formation of a precursor film during spontaneous drop spreading on a fully wettable surface [30], formation of an ultrathin air cushion during droplet impact on solid surface kept in the air [31, 32] or possible entrapment of a thin film of the surrounding medium in between a droplet and the surface during drop deposition on a surface submerged in a viscous bath [29]) or is intentionally infused in a system (e.g., liquid-infused surfaces [33, 34]) because of its favorable attributes.

The ability to understand and control the mentioned thin film dynamics gives us enormous capabilities to solve major practical challenges, for example, drug targeting via encapsulation [35, 36], condensation heat transfer enhancement [37], design of pressure stable, omniphobic repellent surfaces [33, 34]. It inspires us to pursue thin-film dynamics as a major direction of the present thesis. Under thin film-mediated wetting, three different research objectives are pursued, namely, liquid-liquid encapsulation, interferometric observation of nanometric thin films, and the development of lubricant-infused porous surfaces with exceptional outdoor durability.

Further, a critical step in realizing the practical potential of thin film-mediated wetting is to understand how the thin film changes the interaction of a liquid droplet with a solid

and the first step towards this is the ability to quantify the said liquid-solid interfacial interaction. The second thematic objective of this thesis stems from the need to accurately predict how the droplets interact with solids. The droplet-surface wetting interaction [1, 8] has conventionally been characterized by performing wetting studies via optical goniometry. However, goniometry suffers from significant imaging challenges due to optical noise by scattering and diffraction near the three-phase contact line [38–42]. which significantly compromises its accuracy [43], especially on superhydrophobic surfaces. In this thesis, we look into an alternative force-based approach to quantify this interaction using a flexible capillary probe. We demonstrate that this approach can unravel previously unknown physical insights of practical implications, including the interaction of bacteria/microbes with surfaces.

The general scope and thematic organization of the thesis are outlined in Figure 1.1.

1.3 Organization of the Thesis

This thesis is based on published or under-review journal articles.

Chapter 1 (the present chapter) discusses the general motivation of the study and outlines the scope and organization of the presented thesis.

In Chapter 2, the development of a novel, impact-driven, ultrafast liquid-liquid encapsulation framework is discussed. Exploiting liquid-liquid interfacial energy differences, we demonstrate a simple, ultrafast, and low-cost method for stably encapsulating a liquid core with a thin film of another shell-forming liquid.

Chapter 3 expands the applicability of the impact-driven method described in Chapter 2 kinetic energy independent. In doing so, we elaborate on an interfacially trapped configuration where the impacting core droplet cannot separate from the interfacial layer and rather gets trapped inside. We demonstrate that subject to adherence to a thermodynamic threshold, the trapped state is also an encapsulated state. Further, using polydimethylsiloxane as the shell-forming liquid, we demonstrate the wrapping and subsequent extraction of various core analytes with direct relevance in the food and beverages

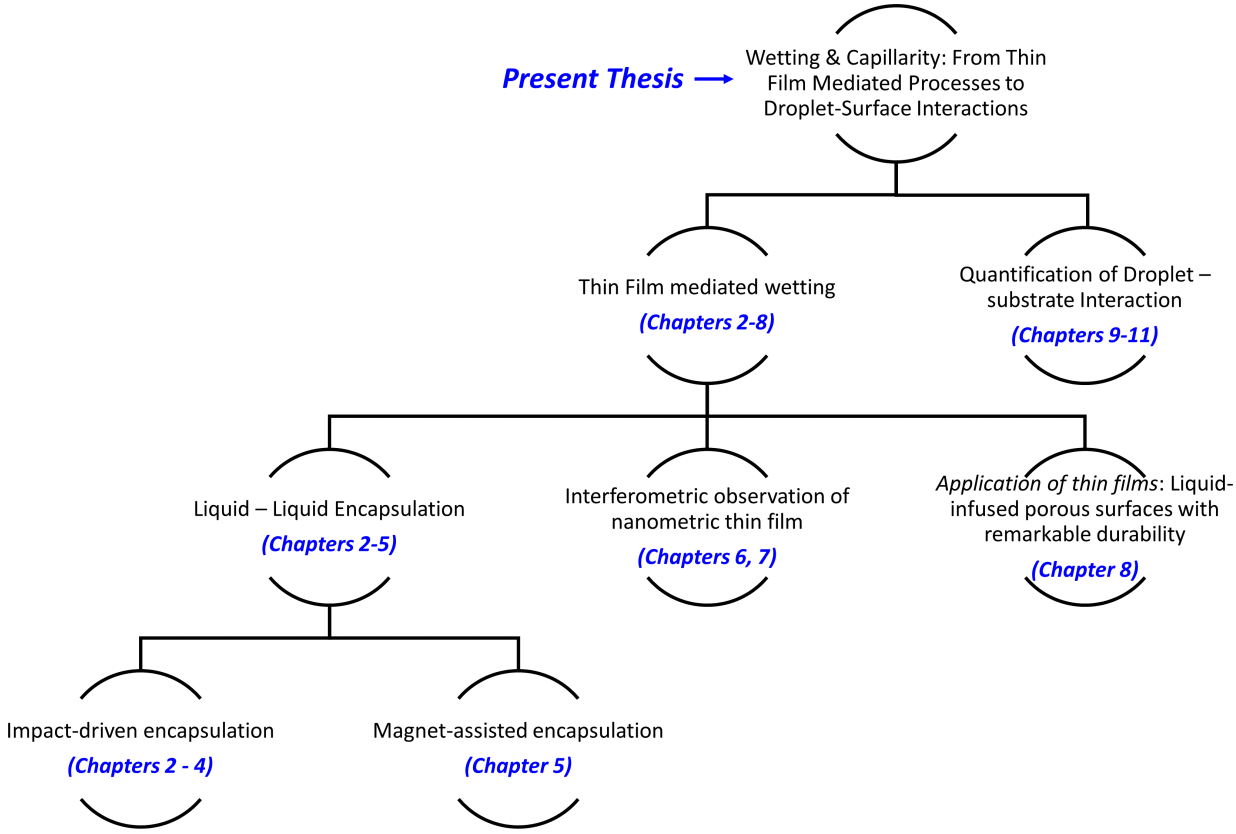

Figure 1.1: Outline of the thesis: Thematic alignment of different chapters is indicated in the outline.

industry. We also report the development of encapsulated Janus droplets with multiple cores bearing different functionalities using the interfacial trapping mechanism.

In Chapter 4, we use the liquid-liquid encapsulation framework discussed in Chapters 2 & 3, to achieve the underwater formation of encapsulated cargo with magnetoresponsive (ferrofluid) shell. We exploit the magnetic manipulability of the shell to demonstrate controlled actuation, coalescence of water-soluble cargo, and the release of the cargo inside a water bath.

In Chapter 5, we demonstrate an alternate pathway to form underwater encapsulated drops with magnetoresponsive (ferrofluid) core via liquid-liquid encapsulation. We utilize

the same experimental paradigm of Chapters 2 - 4 involving a floating interfacial layer on top of a host bath. However, instead of impact, we utilize magnetic actuation of ferrofluid core droplets to achieve encapsulation. We discuss the involved mechanism of encapsulation and delineate the different possible outcomes.

Chapters 6 and 7 provide a tool for direct non-contact visualization of nanoscale thin liquid films which is otherwise extremely challenging using optical means. interferometric observation.

Chapter 6 discusses the development of a non-invasive framework to probe nanometric thin liquid films using reflected laser interferometry.

In chapter 7, utilizing the framework described in Chapter 6, we report a novel spontaneous motion during the condensation of low-surface-tension test liquids on high energy surfaces, where nucleated smaller microdroplets spontaneously migrated towards nearby bigger microdroplets.

Chapter 8 discusses a direct application of thin film-mediated wetting in designing functional materials with desired wetting characteristics. We utilize the fundamentals of capillarity-driven lubricant transport via a bi-continuous porous base layer of a composite to develop slippery lubricant-infused porous surfaces with excellent self-recoverability and outdoor durability. This work was carried out at the National Institute for Materials Science (NIMS), Tsukuba, Japan as part of a collaborative research internship.

Chapters 9-11 deal with the direct quantification of the droplet-substrate interfacial interaction in terms of adhesion signature.

In Chapter 9, we introduce a force-based characterization method to probe both friction and adhesion forces of microparticle-laden aqueous droplets over various repellent/ (super)hydrophobic surfaces.

The cantilever deflection-based adhesion quantification method discussed in Chapter 9 is restricted to (super)hydrophobic surfaces where the interacting probe droplet can completely detach from the test substrate. The method, in its conventional form, loses applicability on high-energy surfaces where instead of complete retraction, the probe droplet splits into two daughter droplets. In Chapter 10, through critical arguments and mechanistic analysis of the motion of the cantilever, we augment the cantilever-based method to

be applicable for higher energy surfaces and also link the characteristic adhesion with the motion of the cantilever.

In chapter 11 we use the method outlined in Chapter 9 to study how bacteria-laden droplets interact with (super)repellent surfaces and in the process, uncover an anomalous adhesion behavior when live bacteria is used as a dopant inside the probe droplet.

Finally, Chapter 12 summarizes the research, discusses the major outcomes of the thesis, and introduces possible directions for future work.

Chapters 2-11 are self-contained. They independently define the problem, discuss the current state of literature & identify the research gaps, explain the methodology, report new findings, and provide a summarized conclusion focusing on the impact of new observations. An exhaustive review of the literature is therefore omitted here for the sake of brevity.

References

[1] P.-G. Gennes, F. Brochard-Wyart, D. Quéré, *et al.*, *Capillarity and Wetting Phenomena: Drops, Bubbles, Pearls, Waves*. Springer, 2004.

[2] R. Boyle, *New Experiments Physico-mechanical Touching the Spring of the Air and its Effects*. H. Hall: Oxford, England, 1662.

[3] R. Hooke, *An Attempt for the Explication of the Phœnomena Observable in an Experiment Published by the Honourable Robert Boyle, Esq., in the XXXV Experiment of his Epistolical Discourse Touching the Aire in Confirmation of a Former Conjecture Made by RH.* Thomson: London, 1661.

[4] R. Boyle, "New experiments made and communicated by the honourable robert boyle esquire, about the superficial figures of fluids, especially of liquors contiguous to other liquors: likely to conduce much to the physical theory of the grand system of the world," *Philosophical Transactions of the Royal Society of London*, vol. 11, no. 131, pp. 775–787, 1676.

[5] F. Hauksbee, "VIII. An experiment made at Gresham-College, shewing that the seemingly spontaneous ascention of water in small tubes open at both ends is the same in vacuo as in the open air," *Philosophical Transactions of the Royal Society of London*, vol. 25, no. 305, pp. 2223–2224, 1706.

[6] J. Jurin, "II. An account of some experiments shown before the Royal Society; with an enquiry into the cause of the ascent and suspension of water in capillary tubes.," *Philosophical Transactions of the Royal Society of London*, vol. 30, no. 355, pp. 739–747, 1717.

[7] I. Newton, *Opticks*. Prometheus Books, 1730.

[8] T. Young, "III. An essay on the cohesion of fluids," *Philosophical Transactions of the Royal Society of London*, no. 95, pp. 65–87, 1805.

[9] P. S. Laplace, *Traité de mécanique céleste, 1.* Typ. Crapelet, 1823.

[10] A. Fall, B. Weber, M. Pakpour, N. Lenoir, N. Shahidzadeh, J. Fiscina, C. Wagner, and D. Bonn, "Sliding friction on wet and dry sand," *Physical Review Letters*, vol. 112, no. 17, p. 175502, 2014.

[11] W. Alpers and H. Hühnerfuss, "The damping of ocean waves by surface films: A new look at an old problem," *Journal of Geophysical Research: Oceans*, vol. 94, no. C5, pp. 6251–6265, 1989.

[12] C. W. Extrand, "Origins of wetting," *Langmuir*, vol. 32, no. 31, pp. 7697–7706, 2016.

[13] J. W. Gibbs, "On the equilibrium of heterogeneous substances," *American Journal of Science*, vol. s3-16, no. 96, pp. 441–458, 1878.

[14] A. Dupré, *Théorie Mécanique de la Chaleur*. Gauthier-Villars: Paris, 1869.

[15] R. Brown, "Note on the energy associated with capillary rise," *Proceedings of the Physical Society*, vol. 53, no. 3, pp. 233–234, 1941.

[16] N. Adam, *The Physics and Chemistry of Surfaces*. Oxford University Press: London, 1941.

[17] F. Bashforth and J. C. Adams, *An attempt to test the theories of capillary action by comparing the theoretical and measured forms of drops of fluid.* University Press: Cambridge, England, 1883.

[18] W. Thorpe and D. Crisp, "Studies on plastron respiration; the biology of aphelocheirus," *The Journal of Experimental Biology*, vol. 24, no. 3-4, pp. 227–269, 1947.

[19] A. B. D. Cassie and S. Baxter, "Wettability of Porous Surfaces," *Transactions of the Faraday Society*, vol. 40, pp. 546–551, 1944.

[20] A. B. D. Cassie, "Contact Angles," *Discussions of the Faraday Society*, vol. 3, pp. 11–16, 1948.

[21] R. J. Good, "A Thermodynamic Derivation of Wenzel's Modification of Young's Equation for Contact Angles; Together with a Theory of Hysteresis," *Journal of the American Chemical Society*, vol. 74, no. 20, pp. 5041–5042, 1952.

[22] D. Quéré, "Wetting and roughness," *Annu. Rev. Mater. Res.*, vol. 38, pp. 71–99, 2008.

[23] K. Liu, X. Yao, and L. Jiang, "Recent developments in bio-inspired special wettability," *Chemical Society Reviews*, vol. 39, no. 8, pp. 3240–3255, 2010.

[24] A. A. Saha and S. K. Mitra, "Effect of dynamic contact angle in a volume of fluid (VOF) model for a microfluidic capillary flow," *Journal of colloid and interface science*, vol. 339, no. 2, pp. 461–480, 2009.

[25] N. S. K. Gunda, B. Bera, N. K. Karadimitriou, S. K. Mitra, and S. M. Hassanizadeh, "Reservoir-on-a-Chip (ROC): A new paradigm in reservoir engineering," *Lab on a Chip*, vol. 11, no. 22, pp. 3785–3792, 2011.

[26] S. Das, P. R. Waghmare, and S. K. Mitra, "Early regimes of capillary filling," *Physical Review E*, vol. 86, no. 6, p. 067301, 2012.

[27] S. Das and S. K. Mitra, "Different regimes in vertical capillary filling," *Physical Review E*, vol. 87, no. 6, p. 063005, 2013.

[28] P. R. Waghmare, S. Das, and S. K. Mitra, "Drop deposition on under-liquid low energy surfaces," *Soft Matter*, vol. 9, no. 31, pp. 7437–7447, 2013.

[29] K. Trinavee, N. S. K. Gunda, and S. K. Mitra, "Anomalous wetting of underliquid systems: Oil drops in water and water drops in oil," vol. 34, no. 39, pp. 11695–11705, 2018.

[30] L. Tanner, "The spreading of silicone oil drops on horizontal surfaces," *Journal of Physics D*, vol. 12, no. 9, p. 1473, 1979.

[31] J. de Ruiter, F. Mugele, and D. van den Ende, "Air cushioning in droplet impact. i. dynamics of thin films studied by dual wavelength reflection interference microscopy," *Physics of fluids*, vol. 27, no. 1, p. 012104, 2015.

[32] J. de Ruiter, D. van den Ende, and F. Mugele, "Air cushioning in droplet impact. ii. experimental characterization of the air film evolution," *Physics of fluids*, vol. 27, no. 1, p. 012105, 2015.

[33] A. Lafuma and D. Quéré, "Slippery pre-suffused surfaces," *Europhysics Letters*, vol. 96, no. 5, p. 56001, 2011.

[34] T.-S. Wong, S. H. Kang, S. K. Tang, E. J. Smythe, B. D. Hatton, A. Grinthal, and J. Aizenberg, "Bioinspired self-repairing slippery surfaces with pressure-stable omniphobicity," *Nature*, vol. 477, no. 7365, p. 443, 2011.

[35] J. Pessi, H. A. Santos, I. Miroshnyk, D. A. Weitz, S. Mirza, *et al.*, "Microfluidics-assisted engineering of polymeric microcapsules with high encapsulation efficiency for protein drug delivery," *International journal of pharmaceutics*, vol. 472, no. 1-2, pp. 82–87, 2014.

[36] R. K. Shah, H. C. Shum, A. C. Rowat, D. Lee, J. J. Agresti, A. S. Utada, L.-Y. Chu, J.-W. Kim, A. Fernandez-Nieves, C. J. Martinez, *et al.*, "Designer emulsions using microfluidics," *Materials Today*, vol. 11, no. 4, pp. 18–27, 2008.

[37] S. Anand, A. T. Paxson, R. Dhiman, J. D. Smith, and K. K. Varanasi, "Enhanced condensation on lubricant-impregnated nanotextured surfaces," *ACS nano*, vol. 6, no. 11, pp. 10122–10129, 2012.

[38] C. Extrand and S. Moon, "Contact angles of liquid drops on super hydrophobic surfaces: Understanding the role of flattening of drops by gravity," *Langmuir*, vol. 26, no. 22, pp. 17090–17099, 2010.

[39] J. A. Kleingartner, S. Srinivasan, J. M. Mabry, R. E. Cohen, and G. H. McKinley, "Utilizing dynamic tensiometry to quantify contact angle hysteresis and wetting state transitions on nonwetting surfaces," *Langmuir*, vol. 29, no. 44, pp. 13396–13406, 2013.

[40] J. T. Korhonen, T. Huhtamäki, O. Ikkala, and R. H. Ras, "Reliable measurement of the receding contact angle," *Langmuir*, vol. 29, no. 12, pp. 3858–3863, 2013.

[41] M. G. Cabezas, A. Bateni, J. M. Montanero, and A. W. Neumann, "Determination of surface tension and contact angle from the shapes of axisymmetric fluid interfaces without use of apex coordinates," *Langmuir*, vol. 22, no. 24, pp. 10053–10060, 2006.

[42] A. Kalantarian, R. David, and A. W. Neumann, "Methodology for high accuracy contact angle measurement," *Langmuir*, vol. 25, no. 24, pp. 14146–14154, 2009.

[43] K. Liu, M. Vuckovac, M. Latikka, T. Huhtamäki, and R. H. Ras, "Improving surface-wetting characterization," *Science*, vol. 363, no. 6432, pp. 1147–1148, 2019.

Chapter 2

Encapsulation with interfacial liquid layer [1]

2.1 Overview

Hypothesis:

We developed an impact-driven liquid-based encapsulation method by utilizing the fundamental thermodynamic tendency of a suitable three-liquid combination towards formation of a core-shell structure.

Experiments:

Stable wrapping is achieved by impinging a core drop from a vertical separation on an interfacial liquid film floating on a host liquid bath. The resulting interfacial dynamics is captured using a high-speed camera. Several combinations of impact height and interfacial film thickness are investigated for a quantitative description of the phenomena.

[1] Adapted with permission from **Misra, S**; Trinavee, K.; Gunda, N. S. K.; Mitra, S.K. *J. Colloid Interface Sci*, 558C (2020) pp. 334-344. Copyright ©2019, Elsevier Inc.

Findings:

The stability and integrity of the liquid encapsulating layer are confirmed both experimentally (by analyzing the under-liquid wetting signature) and theoretically (by equilibrium thermodynamic analysis). The effect of viscous dissipation on the dynamics is explained and a consequent theoretical threshold for minimum allowable drop size is provided. A non-dimensional experimental regime is also constructed for successful encapsulation in terms of impact kinetic energy and interfacial layer thickness. Additionally, the encapsulating layer is shown to protect the core drop even when the core and host liquids are miscible. The demonstrated method is simple to implement yet robust, offers flexibility regarding varying both the size and the material properties of the core and shell liquids and consistently produces stable monodispersed encapsulated drops in an ultrafast manner.

2.2 Introduction

Encapsulation bears significant practical relevance [1–6] in a broad range of applications including pharmaceutics, agriculture, food processing, personal care, inkjet printing and even in oil and gas industries. Encapsulation generates a protective outer layer around a core substance, which is crucial to safeguard an unstable component from an aggressive environment or to protect essential bio-active components for targeted drug delivery [7, 8]. This work focuses on developing a new method to stably encapsulate a liquid core by another liquid film.

Liquid-liquid encapsulation is of particular importance because of the relatively higher bio-availability and dosage efficiency of resulting capsules owing to the existence of both the core and the shell in liquid phase. Double emulsification has been an interesting choice for producing such liquid in liquid drops. However, despite their high throughput, most conventional batch emulsification techniques generate highly polydisperse encapsulated drops with low stability and offer poor control over the size distribution. To obtain double emulsions with controllable monodispersity, droplet microfluidic techniques [9–15] need to be adopted. However, these methods operate on intricate microfabricated devices - either glass microcapillaries or planar devices made of poly(dimethylsiloxane) (PDMS) elastomer

by soft lithography. Additionally, precise control of the wettability of the channels, the flow rates and the orifice dimensions are crucial to ensure monodispersity and desired size of the core drop. Also, these microfluidic devices are restrictive in terms of allowable variability in size of the core drop. Fabrication of a new device becomes necessary if a core size beyond the allowable limit is required. Also, their applicability is limited to pico-litre to micro-litre scale.

Encapsulation of a liquid drop can also be achieved by wrapping it in a solid/semi-solid membrane or in an assembly of dense macroscopic particles. Soft gel capsules (bio-active solution or suspension or semi-solid analyte hermetically sealed in a soft gelatin shell) have been the accepted industry standard for a long time in pharmaceutical practices especially for drugs which have poor aqueous solubility but have a better solubility in a pharmaceutically acceptable non-aqueous solvent. Soft gel capsules offer multiple advantages over other forms of oral dosages including improved bioavailability (due to containment of the core analyte in liquid/semi-solid form), ease in oral administration, better masking of unpleasant taste or odor, ability to deliver low/ultra-low dosages, higher shelf life etc. A review on the working principles and developments on soft gel encapsulation can be found in the work of Gullapalli [16]. However, soft gel encapsulation is infrastructurally demanding as it requires both specialized expensive equipment as well as operational expertise. Additionally, flexibility regarding the choice of shell material is rather limited. Recently another set of methods have been developed [17–22] that use thin polymer sheets to wrap a liquid droplet. These methods have some similarity with the aforementioned soft gel encapsulation. Fundamentally they work on the interaction between the elasticity and capillarity to spontaneously form a thin shell membrane around the core drops. Recently Kumar *et al.* [22] reported a method where they use the fast dynamics of impact with a floating thin polymeric sheet (thickness range: 46 - 372 nm) to create a wrapping layer around oil drops. However, the handling of such ultrathin polymer sheets can be technologically intricate and it requires multiple steps before it could be transferred to the experimental set up, as also noted by the authors. Another alternative approach to encapsulate a liquid core has been reported in recent works [23, 24] by using an assembly of granular particles. Encapsulation of liquid drops in these methods is achieved by destabilization (either spontaneous gravity driven or externally actuated) and consequent collapse of an interfacial

raft of dense granular particles. Although it offers interesting avenues for applications such as oil-water separation/ spillage control, acceptability in pharmaceutical/food-processing operations remains under question because of the involvement of dense granular particles.

In the present work, we propose a simple, ultrafast method for liquid-liquid encapsulation utilizing a fundamental characteristic of liquid, i.e., minimization of its interfacial energy. The proposed method is built upon the fundamentals of the impact driven water entry problem. A wide volume of scientific endeavour [25–33] is dedicated to understand the dynamics of impact of solid objects as well as liquid drops on a liquid pool. In this work we additionally introduce an intermediate liquid layer in the traversal path of the drop. This intermediate liquid layer can be dispensed on top of the host liquid pool by a needle and syringe pump assembly, without any complicated handling steps. Interfacial interaction of the core drop with this intermediate liquid layer leads to formation of a stable and consistent liquid based wrapping. Additionally, unlike droplet microfluidic emulsification techniques, the size of the core droplet can be varied controllably in a broad range without any major changes in the experimental setup. Moreover, this method allows easy switching between different shell and core materials, as long as the necessary requirements for interfacial energies and density are satisfied, which can be a highly desirable attribute for experimental trials on new drug development. Also, unlike some of the double emulsification methods, maintaining monodispersity is not a concern in this method because of the inherent aspect of encapsulating one core drop at a time.

2.3 Experimental Section

Materials

The proposed method involves three liquids, namely the core drop (liquid L1), the interfacial layer forming the shell (liquid L2) and the host liquid (liquid L3) that houses the encapsulated drop after it settles down. In this work, the host liquid is chosen to be deionized (DI) water (purified by Milli-Q, MilliPoreSigma, Ontario, Canada) with density $\rho_3 = 1000$ kg/m^3, dynamic viscosity $\mu_3 = 1$ mPa-s and liquid-air surface tension $\gamma_3 =$

72 mN/m. The interfacial layer that ultimately wraps the core drop is composed of canola oil (manufactured and marketed under the brand name of Clic International Inc., Ottawa, Canada), with density $\rho_2 = 913$ kg/m^3, dynamic viscosity $\mu_2 = 63.5$ mPa-s, liquid-air surface tension $\gamma_2 = 31.3$ mN/m and liquid-water interfacial tension, $\gamma_{23} = 18.01$ mN/m. If not otherwise mentioned, a particular class of laser liquid - a mixture of silicanes and polyphenol ethers, with a water solubility of $< 0.1\%$ (Product Code: 57B63, Cargille Laboratories Inc., Cedar Grove, NJ, USA) is used to form the core drop. The relevant material properties are as follows: density $\rho_1 = 1900$ kg/m^3, dynamic viscosity $\mu_1 = 1024$ mPa-s, liquid-air surface tension $\gamma_1 = 50$ mN/m, liquid-canola oil interfacial tension $\gamma_{12} = 2.22$ mN/m and liquid-water interfacial tension $\gamma_{13} = 39.4$ mN/m.

The experiments were conducted in a distortion-free glass cuvette (Product Code: SC-02, Krüss GmbH, Hamburg, Germany) of inner dimension 36 mm $\times$ 36 mm $\times$ 30 mm with 2.5 mm wall thickness. The solid substrate used for studying the wetting signature is poly(methyl methacrylate) (PMMA). PMMA sheets of dimensions 150 mm $\times$ 150 mm with 1 mm thickness (Plaskolite Inc., Columbus, Ohio, United States) were diced into 25 mm $\times$ 25 mm square pieces before using as substrates. Polished and passivated stainless-steel disposable needle tips with gauge 14 and inner diameter of 0.060" (Part No. 7018035, Nordson EFD, East Province, RI, USA) mounted on 1 ml NORM-JECT® sterile luer-slip syringes (Henke-Sass, Wolf GmbH, Tuttlingen, Germany) were used for dispensing the liquids.

Method

In the proposed method, first, the cuvette is partially filled with 24 ml of host liquid (here DI water). The aforementioned needle-syringe assembly mounted on a syringe pump is used thereafter to dispense the interfacial liquid at a flow rate of 36 μl/min concentrically on the water - air interface from close proximity. It is important to have a slow and controlled liquid dispensation to prevent disruption of the interfacial layer due to sudden influx of the discharged liquid. The core drop is generated thereafter by pumping the liquid L1 at the same flow rate. While dispensing the core drop, a vertical separation H is maintained between the drop and interfacial layer.

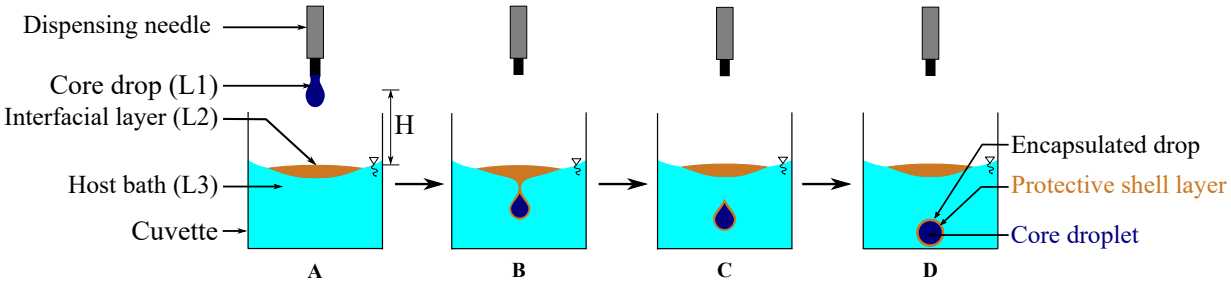

Figure 2.1: Step-by-step schematic representation (not to scale) of the liquid-liquid encapsulation process. (A) The core drop (L1) is dispensed from a height H above the interfacial layer (L2). **(B)** Neck formation takes place as the core drop attempts to penetrate through the interfacial layer. **(C)** The core drop successfully penetrates through the interfacial layer and an encapsulating layer of L2 is formed around it. **(D)** The encapsulated drop settles at the bottom of the cuvette where it is surrounded by the host liquid (L3).

We have not induced any external actuation to force drop detachment from the needle. During the generation process, the core drop grows till a volume when the surface tension forces at the needle tip can no longer sustain its weight and it detaches from the needle tip thereafter due to gravity. This volume is determined by the outer diameter of the needle, the liquid-air surface tension and the effect of gravity [34]. Therefore, it remains invariant as long as the same class of needle tip and liquid combination is used. In our experiments the average volume of the core drop is found to be 15.5 μl with a standard deviation of 0.8 μl. If we assume spherical geometry, this average volume corresponds to a radius of 1.54 mm, which is below the capillary length-scale of the problem. Upon detachment from the needle, the drop accelerates downward due to gravity and comes in contact with the interfacial layer of liquid L2. If the drop has sufficient kinetic energy to penetrate through this interfacial layer, it gets encapsulated with a liquid layer of L2, provided formation of such a layer around the core drop is thermodynamically favorable (elaborated later). A step-wise schematic representation of the entire process is provided in Figure 5.1.

Other than the laser oil-canola oil combination, the surface and interfacial tension values are measured by pendant drop tensiometry using the open source software OpenDrop v1.1

developed by Berry *et al* [35]. Due to very low interfacial energy, a pendant drop shape is not applicable for the laser oil - canola oil combination. For this case, the interfacial tension is determined by implementing a balance between hydrostatic and Laplace pressure, as reported by Waghmare *et al*[36].

The experiments reported here are performed on a vibration isolating optical table to eliminate unwanted movement of interfacial layer and consequent loss of concentricity in liquid dispensing during the experiments.

2.4 Results and discussion

2.4.1 Experimental visualization of a typical encapsulation process

A typical encapsulation process is illustrated in Figure 2.2 for interfacial film volume V_{film} = 350 μL and impact height H = 6.5 cm. Figure 2.2A illustrates the dynamics of water (L3) entry of a laser oil (L2) drop in the absence of any interfacial layer (L2), while Figure 2.2B demonstrates the penetration process after an interfacial oil layer (L2) is introduced at the water-air interface in the same experimental set up, which leads to formation of an encapsulated drop. Intentionally the unencapsulated drop from the earlier experiment of Figure 2.2A is not removed while conducting the encapsulation experiment of Figure 2.2B, so that the two drops (encapsulated and unencapsulated) can be visually compared side-by-side.

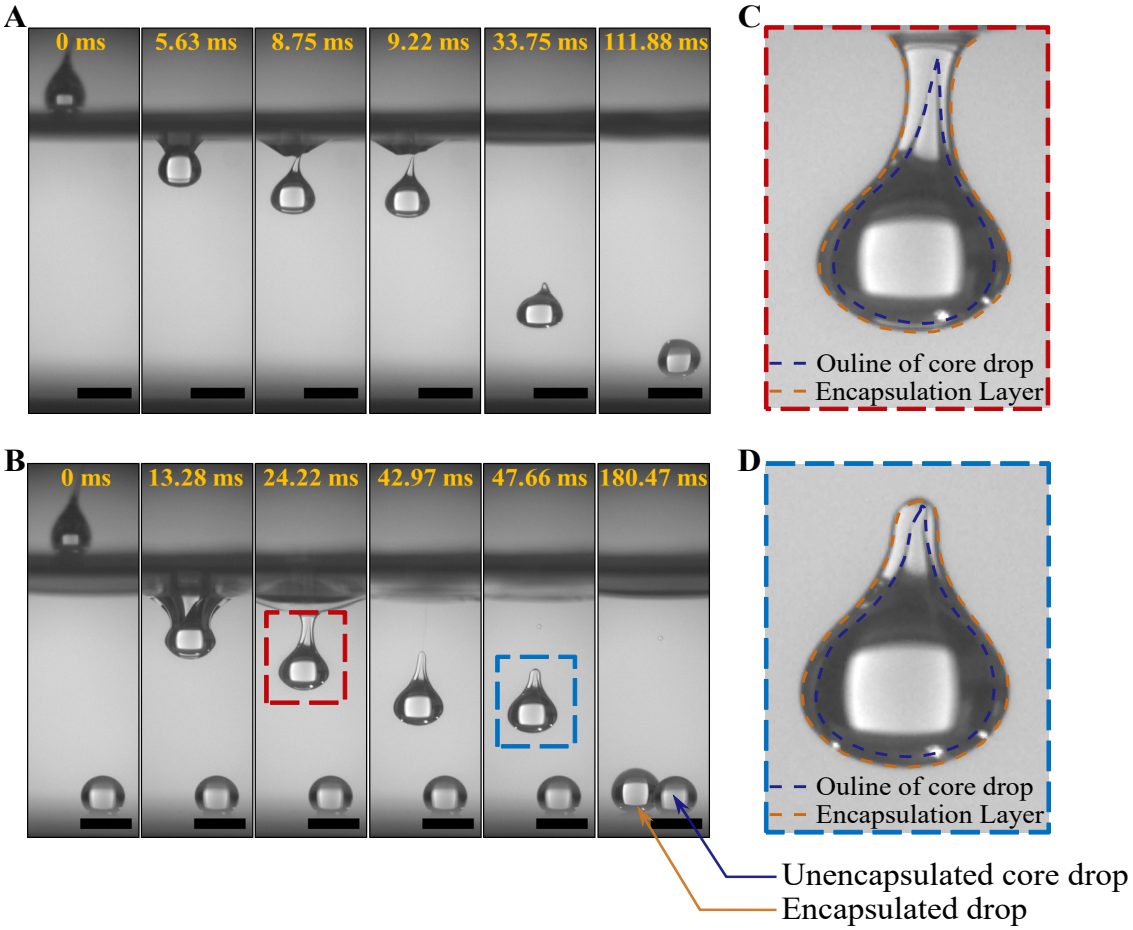

Figure 2.2: Illustration of the process leading to liquid-liquid encapsulation and visual characterization of encapsulation layer. (A) Time series demonstrating the interfacial phenomena of the entry of the core drop (consisting of liquid L1, here laser oil) inside liquid bath L3 (here water) when there is no interfacial film (i.e., absence of liquid L2) and therefore no encapsulation. Here impact height, $H = 6.5$ cm **(B)** Time series illustrating the encapsulation process in the same experimental set up as (A) after a thin interfacial film (here L2 is canola oil) of volume $V_{\text{film}} = 350\mu$L has been dispensed on top of the host water bath. The fourth time stamp denotes successful shell formation and therefore the completion of encapsulation process, with the required time being 42.97 ms. **(C)** Zoomed in view of the formation process of the shell layer (made of the interfacial liquid L2), the corresponding region of interest is highlighted in red dotted rectangle on time snap T = 24.22 ms in (C). (. . . continuing to the next page)

Figure 2.2: (. . . continued from the previous page) **(D)** Zoomed in view of an encapsulated drop corresponding to the region of interest highlighted in cyan dotted rectangle on time snap T = 47.66 ms in (C), with distinctively identifiable outlines of the core and shell. The scale bar represents 4 mm wherever applicable throughout the figure.

Upon detachment from the dispensing needle, the core drop traverses through air before it comes in contact with the interfacial layer of L2. At the point of its first contact with this interfacial layer, the drop possesses a kinetic energy equal to the weight of the drop multiplied by the impact height H (assuming negligible viscous dissipation in air). Upon contact with the interfacial layer, the core drop attempts to penetrate through this intermediate layer. There are three competing effects that govern the penetration process. The core drop drags the L2 layer downward due to its momentum, which deforms the interface and increases its surface area. However, interfacial forces acting on the deformed L3-L2 and L2-L1 interfaces attempt to restore the interface back to its original position to minimize the interfacial energy. The viscous resistance of the interfacial layer also opposes the downward motion of the drop by dissipating its momentum. This competition leads to neck formation (time stamp T = 24.22 ms in Figure 2.2B). If the drop has sufficient momentum to overcome the barrier imposed by both the interfacial forces and the viscous resistance, then it can penetrate through the interfacial L2 layer, as is the case illustrated in Figure 2.2B (see the time stamp T = 42.97 ms). In this process the core drop detaches a part of the film from the interfacial layer. This detached layer forms a thin enclosure (the encapsulating shell) around the core drop. To elaborate this dynamic interface evolution further, two different stages of encapsulation process have been zoomed in Figure 2.2C and 2.2D. Figure 2.2C demonstrates the necking process that leads to separation of drop from interfacial layer while Figure 2.2D illustrates the enclosure formation around the core drop. In both the cases the outlines of the core drop and shell layer are distinctively visible and are highlighted for clarity. This process is ultrafast with a typical successful encapsulation requiring only tens of milliseconds to complete.

The translucent nature of both the core and shell liquid makes the visualization of the encapsulating layer difficult. To facilitate objective visualization of the encapsulation process, a separate experiment is performed where a partially oil soluble particle based

dye (yellow in color) is thoroughly mixed with canola oil to prepare an opaque interfacial liquid layer. The opaque yellow encapsulating layer can unambiguously be identified in the post-encapsulation drop after it settles down at the bottom of the host cuvette. Further information on this experiment can be found in section A.4 of Appendix A.

2.4.2 Shape of the interfacial oil layer

Another interesting consideration here is the equilibrium shape of the interfacial layer L2 that depends on the values of surface and interfacial tensions and the dispensed volume. In our case upon being dispensed on the water-air interface, canola oil forms a floating bi-convex oil lens with one side in contact with water while the other side is exposed to air. The floating liquid lens has two different contact angles as well, with the water side contact angle ($25.6 \pm 3.4°$) registering a higher value than the air side one ($9.7 \pm 2.6°$) in our experiments. Contextually, as shown in Figure A.1 in Appendix A, it might appear from the experimental images that the bi-convex canola lens is covered by a thin water film that prevents direct contact of the canola lens with air. This resembles the pseudo-total wetting state reported by Sebilleau [37]. It is important to investigate this further as the formation of such a state would mean that the core drop would come into contact with a thin film of the host liquid (here water) first before it could interact with the interfacial layer. In the present context, any direct contact between the core drop and the host liquid is undesirable, especially when the two are not physicochemically compatible. However, the possibility of formation of such a pseudo-total wetting state has been nullified both theoretically and experimentally (see section A.1 in Appendix A). It has been confirmed that this is an imaging artifact arising out of the concave shape of water meniscus on the quartz cuvette.

The interfacial layer has the maximum film thickness, δ_{max} at the centre of the lens. Although, in the experiments V_{film} is the parameter that can be precisely controlled, it is desirable to map the output quantities (resulting shell thickness, encapsulated volume etc.) with respect to δ_{max} instead of V_{film}. This is because δ_{max} is a more fundamental representation of the effect (e.g., the imposed viscous resistance) of the interfacial layer on the process dynamics. However, due to the concave shape of the water meniscus, the

complete profile of the bi-convex floating lens could not be captured. The downward curved meniscus obscures the side view of the top portion (air-side) of the lens. However, the shape of the water side could be captured. To reconstruct the entire profile, we have assumed the lens to be an intersection of two spheres of different radii along a common circular plane, the diameter of which is equal to the diameter of the contact line. Thereafter, with some geometric calculations, the profile of the air side is reconstructed using the known value of V_{film} and measured shape of the bottom part of lens. This allows us to estimate δ_{max} for different values of V_{film}. Details on this estimation method can be found in Appendix A.

2.4.3 Theoretical threshold for the applicability and success of the process

For the proposed liquid-liquid encapsulation method to be applicable, two main criteria need to be fulfilled. As the interfacial layer (L2) maintains direct contact with the host liquid (L3), L2 and L3 needs to be physicochemically compatible (i.e., mutually unreactive, immiscible). Additionally, as the interfacial layer is required to float stably on top of the host liquid and the motion of the core drop inside the liquid pool is assisted by gravity, a favorable density regime for this method would require the core drop (L1) to have the highest density among three participating liquids, followed by the host liquid (L3) and the interfacial layer (L2) respectively ($\rho_1 > \rho_3 > \rho_2$).

In addition to the above two criteria regarding the applicability of the proposed method, the interfacial energies of the three participating liquids need to satisfy certain necessary conditions for the formation of a stable encapsulated drop to be thermodynamically feasible. The relevant necessary theoretical thresholds for both formation and stability of encapsulated drops are derived here under the following assumptions:

- The drops (both encapsulated and unencapsulated) are spherical in shape.
- The shell layer has an uniform thickness δ which is much less compared to the radius of the core drop, R_c i.e. $\delta << R_c$.

- The change in surface area of the interfacial oil layer before and after encapsulation is negligible. Therefore, the change in interfacial energy of this layer due to encapsulation does not need to be accounted for.

Assuming both the unencapsulated and encapsulated drops to be spherical in shape is a reasonable approximation. For a given enclosed volume, a spherical shape has the lowest surface area and consequently, the lowest surface energy, making it the thermodynamically most stable shape among all possible configurations. Therefore, it can be inferred that the criterion governing successful encapsulation for the most stable initial configuration is a conservative one and automatically holds true for the actual pendant drop shape that has a higher surface area. For the encapsulated drops, we consider the drops after the post encapsulation interfacial disturbances have subsided. The drops then are seen to attain near-spherical shape, as can also be confirmed from the experimental videos.

The third approximation can also be justified with the experimental observation that the volume of the detached (shell forming) layer accounts to no more than 10% of V_{film}. So, for a ballpark estimate if we assume a spherical shape, then the change in surface area comes out to be $< 6.67\%$, which can justifiably be neglected.

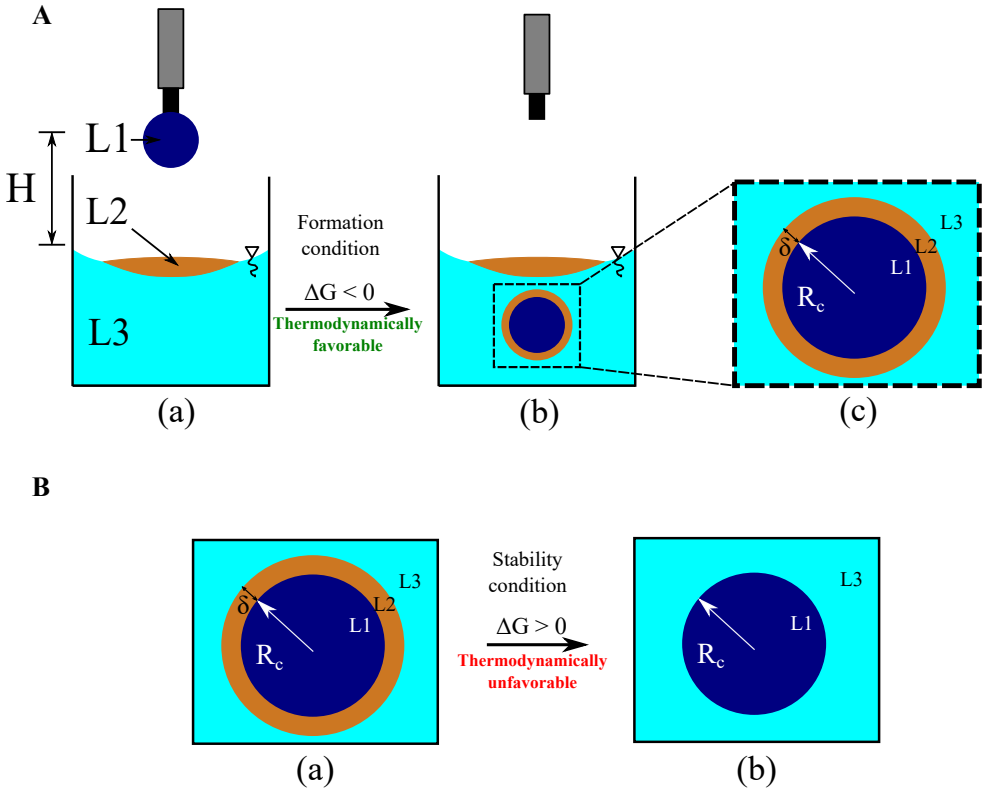

Figure 2.3: Schematic illustration (not to scale) of the criteria for the formation and stability of the encapsulated state. **(A)** Formation of an encapsulated drop is thermodynamically feasible when the Gibbs free energy change during the transition from state (a) to (b) is negative. A zoomed in view of the encapsulated drop is provided in (c) with relevant geometric parameters used in the calculation of free energy change. **(B)** The encapsulated drop remains stable upon formation only if the transition from state (a) to state (b) is thermodynamically unfavorable i.e. has an associated positive free energy change.

Criterion for the formation of an encapsulating layer around the core drop

From equilibrium thermodynamic perspective, the transition of the core drop in air at a height H above the interface to an encapsulated drop is spontaneous only when the change in Gibbs potential is negative in the process (see Figure 2.3A).

With the aforementioned approximations, the change in Gibbs potential between the states A(a) and A(b) as represented in Figure 2.3A can be calculated as

$$\begin{aligned}\Delta G_{\text{formation}} = G_{\text{A(b)}} - G_{\text{A(a)}} &= A_{12}\gamma_{12} + A_{23}\gamma_{23} - A_1\gamma_1 - m_d g H; \\ &= 4\pi R_{\text{c}}^2\gamma_{12} + 4\pi(R_{\text{c}}+\delta)^2\gamma_{23} - 4\pi R_{\text{c}}^2\gamma_1 - \frac{4}{3}\pi R_{\text{c}}^3\rho_1 g H.\end{aligned}$$

$$\text{As } \delta << R_{\text{c}}; \qquad 4\pi(R_{\text{c}}+\delta)^2 \approx 4\pi R_{\text{c}}^2$$

$$\therefore \Delta G_{\text{formation}} = 4\pi R_{\text{c}}^2(\gamma_{12}+\gamma_{23}-\gamma_1) - \frac{4}{3}\pi R_{\text{c}}^3\rho_1 g H.$$

Here m_d is the mass of the core drop, γ_{ij} is the interfacial tension between phases i and j, γ_i is the surface tension (with air) of phase i and A_{ij} is the area of contact between phases i and j, where $(i, j) \in 1, 2, 3$.

For the process to be thermodynamically feasible,

$$\begin{aligned}\Delta G_{\text{formation}} &< 0 \\ \therefore H &> \frac{3(\gamma_{12}+\gamma_{23}-\gamma_1)}{\rho_1 g R_{\text{c}}}\end{aligned} \tag{2.1}$$

Eq. (2.1) is the necessary condition for the formation of an encapsulated drop from a purely equilibrium thermodynamic perspective. However, H being a positive variable, $(\gamma_{12}+\gamma_{23}-\gamma_1) < 0$ is sufficient for Eq. (2.1) to be satisfied.

Criterion for the stability of encapsulated drops

Merely attaining an encapsulated structure does not assure its stability as the wrapping layer (L2) might get detached from the core leaving the core drop (L2) exposed to the host

liquid (L3), if such a transition is energetically favorable. Therefore, for the encapsulated drop to be stable, the free energy change between encapsulated state (denoted as B(a), Figure 2.3B) and the unwrapped state (where the core drop exposed to the host liquid bath after detachment of the shell layer, denoted as B(b), Figure 2.3B) should be positive. The free energy change between the two states can be expressed as,

$$\begin{aligned}\Delta G_{\text{detachment}} &= G_{\text{B(b)}} - G_{\text{B(a)}} = A_1\gamma_{13} - A_{12}\gamma_{12} - A_{23}\gamma_{23};\\ &= 4\pi R_{\text{c}}^2\gamma_{13} - 4\pi R_{\text{c}}^2\gamma_{12} - 4\pi(R_{\text{c}}+\delta)^2\gamma_{23};\\ &= 4\pi R_{\text{c}}^2(\gamma_{13} - \gamma_{12} - \gamma_{23}).\end{aligned}$$

It has been assumed here that once wrapping layer of thickness δ gets detached from the encapsulated drop, its surface area is negligible and therefore can be neglected in the calculation of free energy change. If the wrapping layer gets detached from the encapsulated drop, it attains a spherical shape before it floats up to the air-water interface due to buoyancy. For a thin wrapping layer ($\delta << R_{\text{c}}$), the volume of the shell layer is much low compared to that of the core drop. Therefore, when that wrapping layer of negligible volume attains a spherical shape, its surface area can reasonably be neglected. For the encapsulated drop to be stable,

$$\begin{aligned}\Delta G_{\text{detachment}} &> 0;\\ \therefore \gamma_{13} &> (\gamma_{12} + \gamma_{23}).\end{aligned} \tag{2.2}$$

In our experiments with water (L3), canola oil (L2) and laser oil (L1),

$$\begin{aligned}(\gamma_{12} + \gamma_{23} - \gamma_1) &= (2.22 + 18.01 - 50)\ \text{mN/m} = -29.77\ \text{mN/m} < 0,\\ (\gamma_{13} - \gamma_{12} - \gamma_{23}) &= (39.4 - 2.22 - 18.01)\ \text{mN/m} = 19.17\ \text{mN/m} > 0.\end{aligned}$$

Therefore, not only is the formation of encapsulated drops thermodynamically feasible but the resulting encapsulated drops are stable as well.

2.4.4 Experimental confirmation of stability and integrity of encapsulation

In the encapsulated drops, the shell layer being lighter than the surrounding host medium and intrinsically mobile (liquid phase), it exhibits a tendency to move up (without

getting detached from the core) and form a crown like structure at the apex. Consequently confirmation of the integrity and all-around existence of the shell layer stands out to be of particular concern, as otherwise existence of the encapsulating layer at the bottom part of the drop can be questioned. We have analyzed the wetting signature of the concerned entities to validate this important aspect of integrity of encapsulation. Numerous studies in literature [38–48], both experimental as well as theoretical, have studied the evolution of wetting signature as an unique identifier of solid-liquid surface interaction, both for ambient as well as under-liquid applications.

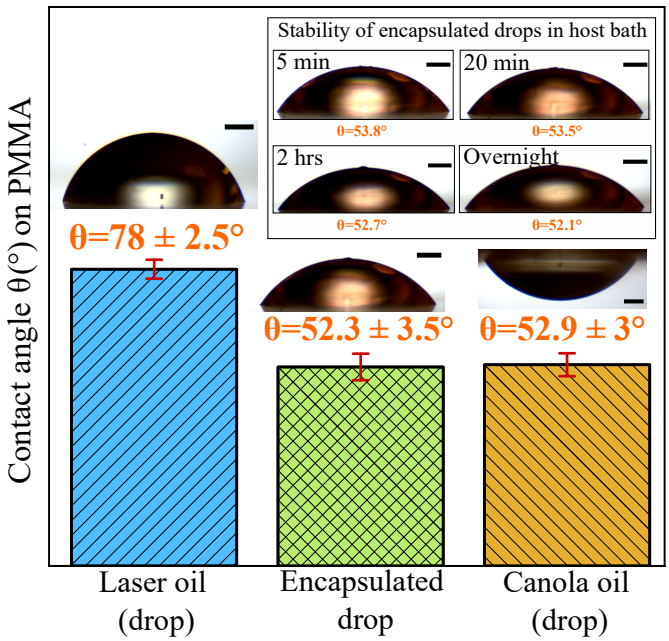

Figure 2.4: Stability and integrity of encapsulating layer: Wetting signature of core liquid (laser oil), shell liquid (canola oil) and the encapsulated drop on PMMA substrate. The inset provides the equilibrium shapes and the corresponding contact angle values of the encapsulated drop after it is allowed to settle for 5 minutes, 20 minutes, 2 hours and overnight. The scale bar represents 0.75 mm wherever applicable throughout the figure.

For this purpose, separate under water contact angle measurements of laser oil (core liquid) drop, canola oil (interfacial liquid) drop and encapsulated drop have been carried

out after the drops are allowed to settle down on a Poly(methyl methacrylate) (PMMA) substrate kept on the bottom of the cuvette that holds the host liquid (water) and if applicable, the interfacial layer of canola oil (for generating the encapsulated drop only). As can be seen from the experimental results plotted in Figure 2.4, the wetting signature of the laser oil drop in water (with a measured contact angle, $\theta = 78 \pm 2.5^{\circ}$) differs significantly from that of a canola oil drop in water ($\theta = 52.9 \pm 3^{\circ}$). However, the wetting characteristic of the encapsulated drop (i.e., laser oil core drop enclosed in a thin layer of canola oil) exhibits a contact angle of $\theta = 52.3 \pm 3.5^{\circ}$, resembling the wetting signature of pure canola oil drop in water medium ($\theta = 52.9 \pm 3^{\circ}$). This similarity in wetting signature serves as a conclusive evidence of the integrity and all-around existence of canola oil encapsulation layer around the laser oil core drop.

Also, the settled encapsulated drop is left overnight in the surrounding host liquid (water) and its shape is captured after different exposure times. In the inset of Figure 2.4, the equilibrium drop shapes and the corresponding contact angle values on PMMA substrate are presented at four different times of exposure to the host liquid. It can be concluded from the inset that the encapsulated drop undergoes negligible change in equilibrium shape with time. This reaffirms the stability of the encapsulated drop experimentally, which was proven earlier theoretically by equilibrium thermodynamic stability analysis.

2.4.5 Role of impact Weber number and interfacial layer thickness: deviation from idealized thermodynamic estimate

In experiments merely satisfying the condition: $\gamma_{12} + \gamma_{23} < \gamma_1$ does not guarantee successful encapsulation. This is because, this thermodynamic estimate only considers the Gibbs free energy (G) differences between the two equilibrium states. And G being a state variable, the change in Gibbs potential does not reflect anything about process that lead to the transformation. The key underlying assumption in obtaining the thermodynamic threshold is that the path leading to encapsulation is reversible and there is no loss of energy in the process. However, in practice the process is irreversible with the viscous dissipation during the motion of the drop through the interfacial layer being the primary source of irreversibility that remains unaccounted for. $\gamma_{12} + \gamma_{23} < \gamma_1$, therefore, is a necessary

condition, not a sufficient one and there remains a possibility that the drop would not get encapsulated even after the above condition is satisfied. This is because the drop needs to possess sufficient kinetic energy not only to overcome any energy barrier posed by the interfacial energy difference between the two states but also to compensate for the viscous dissipation while breaking through the interfacial layer. Otherwise, even after having an energetically favorable interfacial tension combination, the drop can not penetrate through the interfacial layer and instead gets trapped in there.

During its traversal through air before its impact with the interfacial layer, the core drop gains a kinetic energy (manifested in the form of impact Weber number $\mathrm{We_i}$, calculated as $\mathrm{We_i} = \frac{\rho_1 v^2 R_c}{\gamma_1} \approx \frac{2\rho_1 g H R_c}{\gamma_1}$ where v is the velocity of the core drop immediately before its impact with the interfacial layer, R_c is the radius of the core drop assuming spherical shape and g is the acceleration due to gravity) proportional to the impact height H. Now as the droplet moves downward through the interfacial layer (L2), it experiences a viscous drag which slows it down. If the kinetic energy of the impinging droplet is not sufficient to overcome this viscous barrier, the drop gets trapped at the interfacial layer and cannot get encapsulated despite having a thermodynamically favorable tendency of encapsulation by L2 (i.e., $\Delta G_{\mathrm{formation}} < 0$). However complete theoretical estimation of this viscous drag is particularly challenging because of the involvement of three continually deforming fluid interfaces. A detailed numerical investigation is needed for proper estimation of this energy loss, which is beyond the scope of the present work.

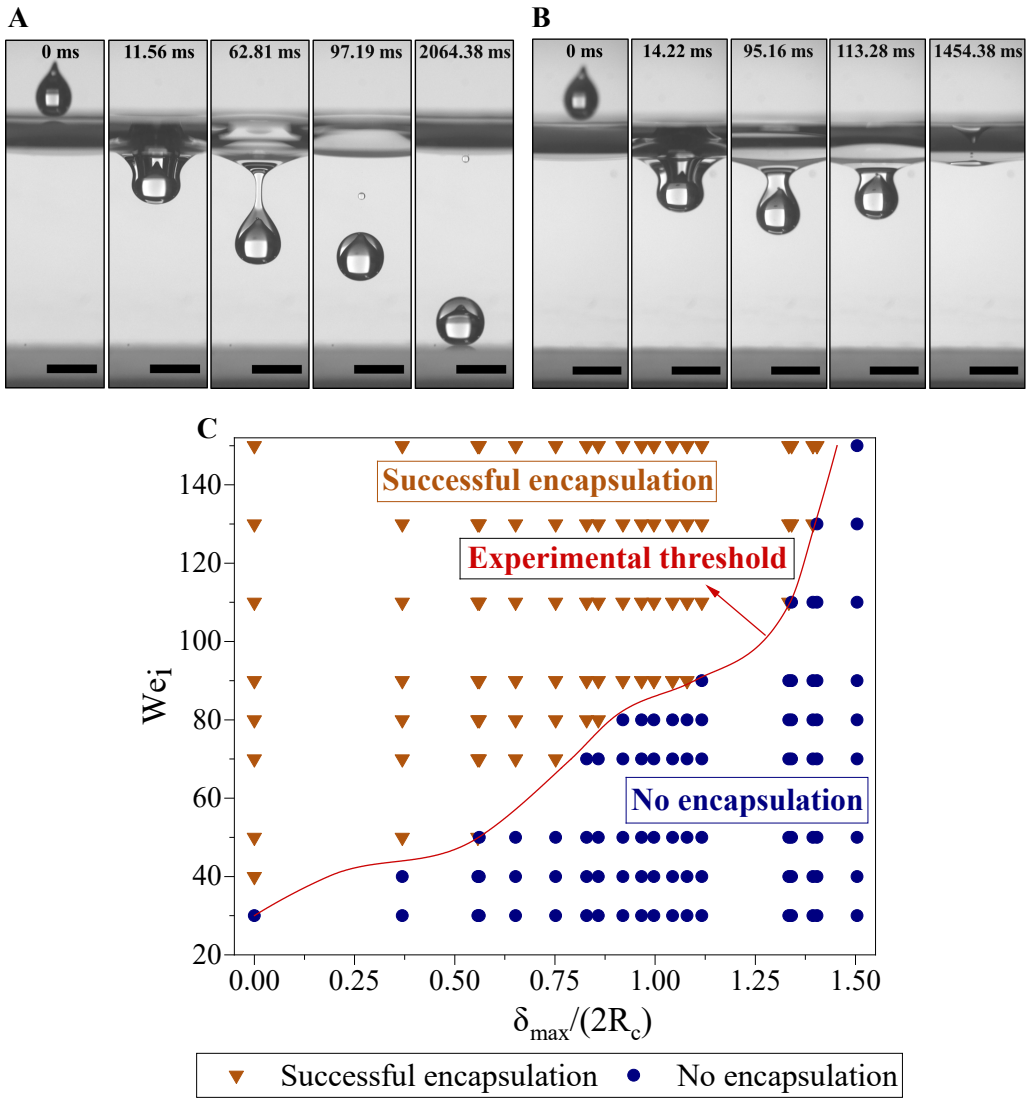

Figure 2.5: Success of encapsulation: Dependence on impact Weber number, We_i and non-dimensionalized interfacial layer thickness, $\delta_{max}/(2R_c)$. **(A)** Successful encapsulation: Time series depicting successful encapsulation process for $We_i = 130$ and $\delta_{max}/(2R_c) = 1.394$ (corresponding $V_{film} = 1150\ \mu L$). **(B)** No encapsulation: Time series demonstrating the unsuccessful attempt of the drop towards encapsulation and consequent entrapment at the interfacial layer for the same impact Weber number, $We_i = 130$ but an increased interfacial film volume with $\delta_{max}/(2R_c) = 1.404$ (corresponding $V_{film} = 1200\ \mu L$). (...continuing to the next page)

Figure 2.5: (...continued from the previous page) **(C)** A regime map demonstrating the dependence of the success of encapsulation process on We_i and $\delta_{max}/(2R_c)$. The experimental threshold for the same is illustrated by the red zone boundary separating the two regimes - successful encapsulation and no encapsulation. The scale bar represents 4 mm wherever applicable throughout the figure.

As the thickness of the interfacial layer increases, the resistance in the penetration process also increases. Therefore, for successful encapsulation even at an increased layer thickness, the core drop needs to possess higher impact kinetic energy which, in the proposed method, is fulfilled by appropriately increasing the impact height H. As can be inferred from Figure 2.5A and 2.5B, even though the core drops have the same kinetic energy at the time of impact (same We_i), in the first case the drop encounters lower viscous resistance in the process of penetration due to a relatively lower value of $\delta_{max}/(2R_c)$. Consequently, the core drop gets successfully encapsulated in the first case, while it fails to separate from the interfacial layer in the later.

In Figure 2.5C, we identified a non-dimensional experimental regime for successful encapsulation in terms of the impact Weber number (We_i) and interfacial film thickness non-dimensionalized with respect to the diameter of the core drop ($\delta_{max}/(2R_c)$). For lower δ_{max}, successful encapsulation is achieved even at low Weber number while a higher δ_{max} requires a higher impact Weber number for success in encapsulation, owing to the augmented kinetic energy requirement to overcome the viscous energy barrier.

2.4.6 Dependence of extent of encapsulation on the thickness of interfacial layer

The fluidic properties of the interfacial layer and its thickness are the two main parameters that dictate the extent of encapsulation. In Figure 2.6 the dependence on interfacial film thickness is explored by varying the value of V_{film} in the range of 0 - 500 μl, while keeping the liquid combination fixed. The encapsulation experiments are carried out for five different values of V_{film}, namely, 0, 120, 220, 320 and 420 μl. For every value of V_{film}, the

maximum thickness of the interfacial layer, δ_{max} is estimated using the method described in subsection 2.4.2 and is found to be 0, 2024, 2276, 2565 and 2845 μm respectively. The kinetic energy at impact is also kept constant by maintaining the same impact height H (7.5 cm in this case). Any increment in δ_{max} results in an enhancement in the viscous resistance which slows the drop down by dissipating its momentum. As a result the residence time of the core drop inside the interfacial layer increases. The increasing trend of residence time with increasing interfacial film thickness is captured in Figure 2.6A in the form of penetration time, which is defined (even when there is no interfacial film) as the difference in time between two instances, namely, the first instance when the entire drop is inside the host liquid and the last instance when the drop is completely in air. Also, as the residence time increases, the core drop detaches a higher volume of liquid L2 from the interfacial layer upon successful penetration, resulting in a higher post-encapsulation drop volume and estimated shell thickness, as can be noted from the reported trend in Figure 2.6. The reported shell thickness is a theoretical estimate assuming spherical drop shape and uniform thickness of encapsulating layer. For estimating shell thickness we consider the drops just before it reaches the bottom of cuvette so that the drop shape is affected neither by the post-encapsulation interfacial disturbances nor by the surface interaction at the bottom of the cuvette. Under these circumstances spherical geometry with uniform film thickness is a reasonable assumption when we operate with a moderately low value of V_{film} (< 500 μL). The details on the numerical method for calculation of drop volume using image processing and estimation of thickness of the encapsulating layer from calculated volume can be found in section A.3 of Appendix A. As mentioned earlier, the volume of the laser oil core drop (the volume of the drop before it comes in contact with the interfacial layer) remains invariant (within the limit of experimental errors) in our experiments as we use the same class of dispensing needle throughout. Nevertheless, as shown in the inset of Figure 2.6, an increase in δ_{max} corresponds to a consequent increment in the shell volume.

We would also like to comment here that there is a possibility of air entrapment [49–54] when a drop impacts on and enters a liquid pool. However, as highlighted in earlier works [53, 54], there exists a minimum impact height below which there is practically no air entrapment. From the high-speed photographs of our experiments, it has been confirmed that within the operating height (H) range of the study, air entrapment does not take place.

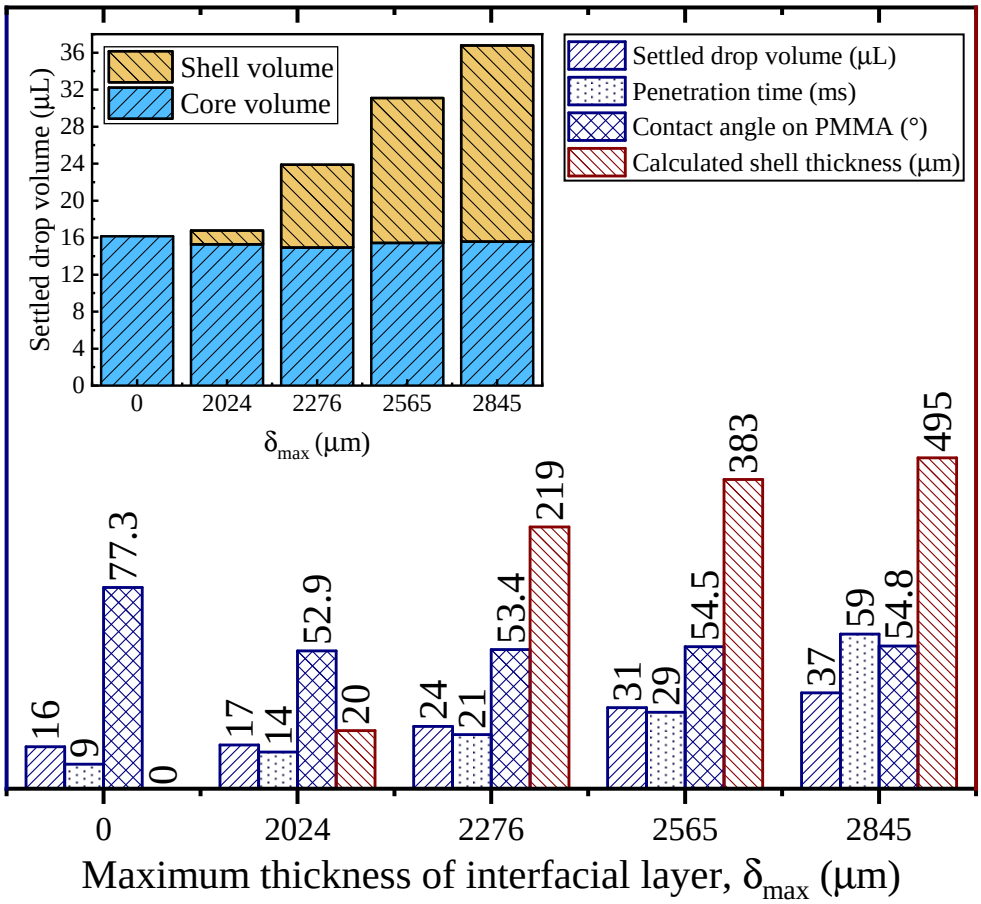

Figure 2.6: Quantification of the extent of encapsulation with change in the maximum thickness of interfacial layer: Dependence of encapsulated drop volume, theoretically estimated encapsulated film thickness, penetration time and contact angle (on PMMA) on the maximum layer thickness, $\delta_{\max}$. The calculated shell thickness is plotted in a semi-log scale in the right Y axis, while the rest are represented in linear scale on the left Y axis. The inset demonstrates the variation in core drop volume and the corresponding encapsulated shell volume with $\delta_{\max}$.

Therefore, this volume enhancement can unambiguously be attributed to the volume gain of the core drop during the process of its interfacial interaction with the intermediate liquid layer (consisting of liquid L2) and the subsequent formation of a liquid shell layer.

The macroscopic contact angle being a thermodynamically intensive property (independent of the volume of the drop) of the substrate-liquid combination, the dependence of observed contact angle on layer thickness is insignificant. Even an interfacial canola film volume as low as 120 μl is found (Figure 2.6) to be sufficient to form to an outer encapsulation layer that suppresses the intrinsic wetting signature of the core laser oil drop and exhibits conclusive resemblance with the wetting pattern of canola oil (the shell liquid), with a measured value of contact angle of $\theta = 52.9^{\circ}$ on PMMA substrate.

2.4.7 Assessment of practical applicability: protection of core drop from incompatible (miscible) surrounding

Practical applicability of an encapsulation protocol depends extensively on its ability in safeguarding the core drop from aggressive environment. To assess this aspect, an experiment is designed where the core drop (L1) and host liquid medium (L3) are not internally compatible. For this purpose, ethylene glycol (density $\rho_1 = 1115$ kg/m^3, dynamic viscosity $\mu_1 = 16.9$ mPa-s and liquid-air surface tension $\gamma_1 = 48$ mN/m) is chosen as the core liquid (L1) keeping other two liquids unaltered.

Due to its miscibility in water, ethylene glycol drop can not retain its shape if it enters the host water bath directly (see Figure 2.7A). However, when the same drop is made to pass through an intermediate layer of canola oil (with $V_{\text{film}} = 220$ μL) prior to entering the water bath, the drop attains an encapsulation layer of canola oil all around itself, which protects it from getting dissolved in the surrounding medium and consequently it retains itself even after settling down at the bottom of the water bath (see Figure 2.7B).

Also, as the encapsulation process is preceded by necking at the interface, a part of the core drop gets pinched off and trapped at the interfacial layer upon successful encapsulation, as also noted by Kumar *et al* [22]. In the post-encapsulation top view of the interfacial layer presented in Figure 2.7C, we notice the existence of the left over portion of the impinging ethylene glycol drop inside the interfacial canola layer. Additionally, the existence of an encapsulating layer in the settled drop can also be confirmed from the bottom view of the encapsulated drop captured by bright-field optical microscopy (see Figure 2.7D).

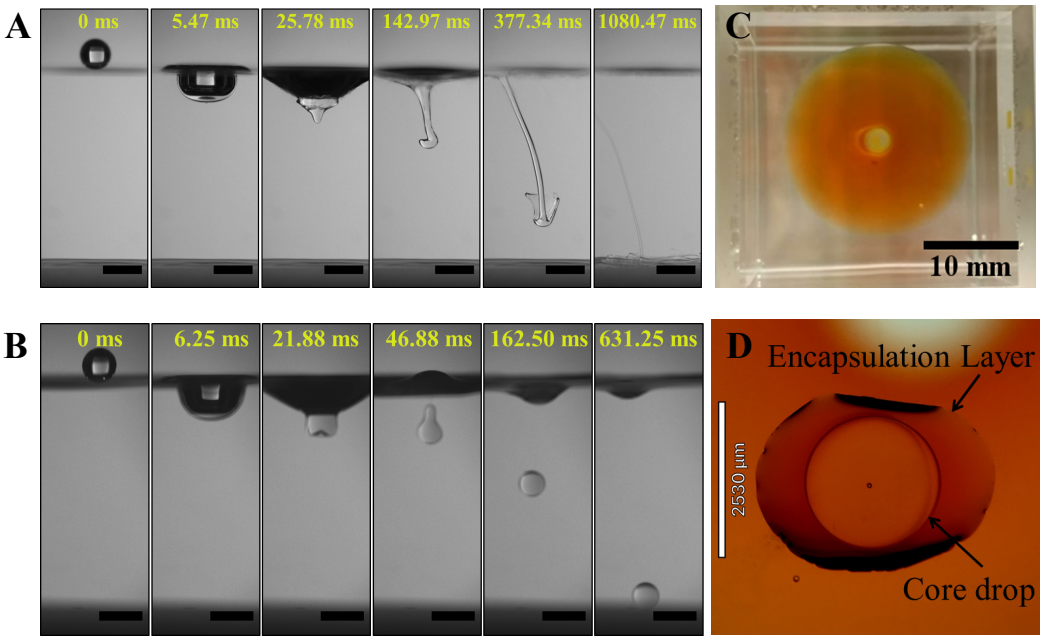

Figure 2.7: Evaluation of potential of the proposed method in safeguarding the core drop from an aggressive (miscible) environment. **(A)** Time series illustrating the water entry of an ethylene glycol drop. Due to its miscibility in water, the drop gets dissolved in the surrounding medium upon its entrance. **(B)** Time series demonstrating the water entry of another ethylene glycol drop of same volume - this time the drop passes through an interfacial layer of canola oil ($V_{\text{film}} = 220\mu\text{L}$) before it enters the water bath. **(C)** Post-encapsulation top-view of the interfacial canola layer. **(D)** Bottom view of the encapsulated drop captured via bright-field optical microscopy. If not explicitly mentioned otherwise, the scale bar represents 4 mm wherever applicable.

2.5 Conclusion

In this work we propose and demonstrate a first of its kind impact driven liquid based encapsulation method. We choose an eligible liquid triplet and utilize gravity driven impact to exploit its energetically favourable tendency towards wrapping ($\Delta G_{\text{formation}} < 0$) for achieving ultra-fast yet controllable and reproducible encapsulation of a core drop inside another thin liquid layer. The stability and integrity of the resulting encapsulated drops

are confirmed experimentally. The fundamental theoretical criteria for formation of such stable encapsulated drops are also derived from an equilibrium thermodynamic perspective. Moreover, the influence of viscous dissipation on the process dynamics during the drop's downward motion through the interfacial layer is explored theoretically assuming spherical non-deformable drop shape. This enabled us to obtain a minimum critical drop size for successful encapsulation for a certain impact height and interfacial layer thickness. From the perspective of execution, the proposed method is extremely straightforward, which can be conducted as a tabletop experiment with minimal infrastructural requirements. However, it offers several competitive advantages over its counterparts. Unlike the soft gel encapsulation techniques [16] or the methods involving wrapping with polymeric sheet [17, 20, 22], our method does not require any complex intermediate material processing steps. Appropriate volume of the interfacial layer can be dispensed in its bulk form on top of the host liquid using a syringe pump. When compared to the droplet microfluidics based emulsification techniques [9–15], our method caters to a much broader range of core drop volume and allows possibility of switching between drop sizes without major changes in the experimental embodiment. It offers more flexibility in the choice of core and shell materials as well. Perhaps mechanical shear based bulk emulsification techniques are comparable to the proposed method in terms to their simplicity. However, the control over the size of the core drop and the monodispersity of the resulting core-shell structure is much superior in our method. Additionally, this method allows us to obtain stably encapsulated drops even when the core and the host liquids are miscible. These operational advantages make the proposed method a simple yet robust and efficient alternative towards stable encapsulation of a liquid droplet with another liquid layer. This method can also be used as a precursor to the existing encapsulation techniques where a wrapped liquid drop is enclosed by a polymer sheet or interfacial assembly of particles (viz. granular materials/ colloidal surfactants etc.). Solidification of the liquid shell by established curing techniques (e.g., ultraviolet treatment [55, 56] or coacervate formation [57, 58]) and exploring the possibility of extending the proposed method to form multiple shell layers around a single core fall under the future scope of this work [59].

References

[1] A. King, "Encapsulation of food ingredients: A review of available technology, focusing on hydrocolloids," *Encapsulation and Controlled Release of Food Ingredients*, vol. 590, pp. 26–39, 1995.

[2] B. Gibbs, S. Kermasha, I. Alli, and C. Mulligan, "Encapsulation in the food industry: A review," *International Journal of Food Sciences and Nutrition*, vol. 50, no. 3, pp. 213–224, 1999.

[3] J. Lakkis, *Encapsulation and Controlled Release in Bakery Applications*. 2007.

[4] V. Nedovic, A. Kalusevic, V. Manojlovic, S. Levic, and B. Bugarski, "An overview of encapsulation technologies for food applications," *Procedia Food Science*, vol. 1, pp. 1806–1815, 2011.

[5] J. Van Soest, *Encapsulation of fragrances and flavours: A way to control odour and aroma in consumer products*. 2007.

[6] F. Casanova and L. Santos, "Encapsulation of cosmetic active ingredients for topical application-a review," *Journal of Microencapsulation*, vol. 33, no. 1, pp. 1–17, 2016.

[7] E. Cole, D. Cadé, and H. Benameur, "Challenges and opportunities in the encapsulation of liquid and semi-solid formulations into capsules for oral administration," *Advanced Drug Delivery Reviews*, vol. 60, no. 6, pp. 747–756, 2008.

[8] M. Singh, K. Hemant, M. Ram, and H. Shivakumar, "Microencapsulation: A promising technique for controlled drug delivery," *Research in Pharmaceutical Sciences*, vol. 5, no. 2, pp. 65–77, 2010.

[9] I. Loscertales, A. Barrero, I. Guerrero, R. Cortijo, M. Marquez, and A. Gañán-Calvo, "Micro/nano encapsulation via electrified coaxial liquid jets," *Science*, vol. 295, no. 5560, pp. 1695–1698, 2002.

[10] S. Anna, N. Bontoux, and H. Stone, "Formation of dispersions using "flow focusing" in microchannels," *Applied Physics Letters*, vol. 82, no. 3, pp. 364–366, 2003.

[11] A. Utada, E. Lorenceau, D. Link, P. Kaplan, H. Stone, and D. Weitz, "Monodisperse double emulsions generated from a microcapillary device," *Science*, vol. 308, no. 5721, pp. 537–541, 2005.

[12] L.-Y. Chu, J.-W. Kim, R. Shah, and D. Weitz, "Monodisperse thermoresponsive microgels with tunable volume-phase transition kinetics," *Advanced Functional Materials*, vol. 17, no. 17, pp. 3499–3504, 2007.

[13] A. Utada, L.-Y. Chu, A. Fernandez-Nieves, D. Link, C. Holtze, and D. Weitz, "Dripping, jetting, drops, and wetting: The magic of microfluidics," *MRS Bulletin*, vol. 32, no. 9, pp. 702–708, 2007.

[14] A. Utada, A. Fernandez-Nieves, H. Stone, and D. Weitz, "Dripping to jetting transitions in coflowing liquid streams," *Physical Review Letters*, vol. 99, no. 9, 2007.

[15] J.-W. Kim, A. Utada, A. Fernández-Nieves, Z. Hu, and D. Weitz, "Fabrication of monodisperse gel shells and functional microgels in microfluidic devices," *Angewandte Chemie - International Edition*, vol. 46, no. 11, pp. 1819–1822, 2007.

[16] R. Gullapalli, "Soft gelatin capsules (softgels)," *Journal of Pharmaceutical Sciences*, vol. 99, no. 10, pp. 4107–4148, 2010.

[17] C. Py, P. Reverdy, L. Doppler, J. Bico, B. Roman, and C. Baroud, "Capillary origami: Spontaneous wrapping of a droplet with an elastic sheet," *Physical Review Letters*, vol. 98, no. 15, 2007.

[18] A. Antkowiak, B. Audoly, C. Josserand, S. Neukirch, and M. Rivetti, "Instant fabrication and selection of folded structures using drop impact," *Proceedings of the National Academy of Sciences of the United States of America*, vol. 108, no. 26, pp. 10400–10404, 2011.

[19] H. King, R. Schroll, B. Davidovitch, and N. Menon, "Elastic sheet on a liquid drop reveals wrinkling and crumpling as distinct symmetry-breaking instabilities," *Proceedings of the National Academy of Sciences of the United States of America*, vol. 109, no. 25, pp. 9716–9720, 2012.

[20] J. Paulsen, V. Démery, C. Santangelo, T. Russell, B. Davidovitch, and N. Menon, "Optimal wrapping of liquid droplets with ultrathin sheets," *Nature Materials*, vol. 14, no. 12, pp. 1206–1209, 2015.

[21] B. Davidovitch, R. Schroll, D. Vella, M. Adda-Bedia, and E. Cerda, "Prototypical model for tensional wrinkling in thin sheets," *Proceedings of the National Academy of Sciences of the United States of America*, vol. 108, no. 45, pp. 18227–18232, 2011.

[22] D. Kumar, J. Paulsen, T. Russell, and N. Menon, "Wrapping with a splash: High-speed encapsulation with ultrathin sheets," *Science*, vol. 359, no. 6377, pp. 775–778, 2018.

[23] M. Abkarian, S. Protière, J. Aristoff, and H. Stone, "Gravity-induced encapsulation of liquids by destabilization of granular rafts," *Nature Communications*, vol. 4, 2013.

[24] E. Jambon-Puillet, C. Josserand, and S. Protière, "Drops floating on granular rafts: A tool for liquid transport and delivery," *Langmuir*, vol. 34, no. 15, pp. 4437–4444, 2018.

[25] A. Worthington, "On impact with a liquid surface," *Proc. R. Soc. Lond.*, vol. 34, no. 220-223, pp. 217–230, 1882.

[26] A. Worthington and R. Cole, "Impact with a liquid surface, studied by the aid of instantaneous photography," *Phil. Trans. R. Soc. Lond. A*, vol. 189, pp. 137–148, 1897.

[27] S.-M. Yang and L. Leal, "Motions of a fluid drop near a deformable interface," *International Journal of Multiphase Flow*, vol. 16, no. 4, pp. 597–616, 1990.

[28] J. Aristoff and J. Bush, "Water entry of small hydrophobic spheres," *Journal of Fluid Mechanics*, vol. 619, pp. 45–78, 2009.

[29] A. Prosperetti and H. Oguz, "The impact of drops on liquid surfaces and the underwater noise of rain," *Annual Review of Fluid Mechanics*, vol. 25, no. 1, pp. 577–602, 1993.

[30] C. Josserand and S. Zaleski, "Droplet splashing on a thin liquid film," *Physics of Fluids*, vol. 15, no. 6, pp. 1650–1657, 2003.

[31] R. Bergmann, D. van der Meer, S. Gekle, A. van der Bos, and D. Lohse, "Controlled impact of a disk on a water surface: Cavity dynamics," *Journal of Fluid Mechanics*, vol. 633, pp. 381–409, 2009.

[32] T. Truscott, B. Epps, and A. Techet, "Unsteady forces on spheres during free-surface water entry," *Journal of Fluid Mechanics*, vol. 704, pp. 173–210, 2012.

[33] H. Lhuissier, C. Sun, A. Prosperetti, and D. Lohse, "Drop fragmentation at impact onto a bath of an immiscible liquid," *Physical Review Letters*, vol. 110, no. 26, 2013.

[34] B.-B. Lee, P. Ravindra, and E.-S. Chan, "New drop weight analysis for surface tension determination of liquids," *Colloids and Surfaces A: Physicochemical and Engineering Aspects*, vol. 332, no. 2-3, pp. 112–120, 2009.

[35] J. Berry, M. Neeson, R. Dagastine, D. Chan, and R. Tabor, "Measurement of surface and interfacial tension using pendant drop tensiometry," *Journal of Colloid and Interface Science*, vol. 454, pp. 226–237, 2015.

[36] P. Waghmare, S. Das, and S. Mitra, "Drop deposition on under-liquid low energy surfaces," *Soft Matter*, vol. 9, no. 31, pp. 7437–7447, 2013.

[37] J. Sebilleau, "Equilibrium thickness of large liquid lenses spreading over another liquid surface," *Langmuir*, vol. 29, no. 39, pp. 12118–12128, 2013.

[38] P.-G. De Gennes, F. Brochard-Wyart, and D. Quéré *Capillarity and Wetting Phenomena: Drops, Bubbles, Pearls, Waves*, 2004.

[39] O. Voinov, "Hydrodynamics of wetting," *Fluid Dynamics*, vol. 11, no. 5, pp. 714–721, 1976.

[40] R. Cox, "The dynamics of the spreading of liquids on a solid surface. part 1. viscous flow," *Journal of Fluid Mechanics*, vol. 168, pp. 169–194, 1986.

[41] B. Binks and J. Clint, "Solid wettability from surface energy components: Relevance to pickering emulsions," *Langmuir*, vol. 18, no. 4, pp. 1270–1273, 2002.

[42] D. Bonn, J. Eggers, J. Indekeu, and J. Meunier, "Wetting and spreading," *Reviews of Modern Physics*, vol. 81, no. 2, pp. 739–805, 2009.

[43] P. Waghmare, S. Das, and S. Mitra, "Under-water superoleophobic glass: Unexplored role of the surfactant-rich solvent," *Scientific Reports*, vol. 3, 2013.

[44] P. Waghmare, N. Gunda, and S. Mitra, "Under-water superoleophobicity of fish scales," *Scientific Reports*, vol. 4, 2014.

[45] S. Mitra and S. Mitra, "Understanding the early regime of drop spreading," *Langmuir*, vol. 32, no. 35, pp. 8843–8848, 2016.

[46] S. Mitra, N. Gunda, and S. Mitra, "Wetting characteristics of underwater micro-patterned surfaces," *RSC Advances*, vol. 7, no. 15, pp. 9064–9072, 2017.

[47] B. Sahoo, N. Gunda, S. Nanda, J. Kozinski, and S. Mitra, "Development of dual-phobic surfaces: Superamphiphobicity in air and oleophobicity underwater," *ACS Sustainable Chemistry and Engineering*, vol. 5, no. 8, pp. 6716–6726, 2017.

[48] K. Trinavee, N. Gunda, and S. Mitra, "Anomalous wetting of underliquid systems: Oil drops in water and water drops in oil," *Langmuir*, vol. 34, no. 39, pp. 11695–11705, 2018.

[49] H. Oguz and A. Prosperetti, "Bubble entrainment by the impact of drops on liquid surfaces," *Journal of Fluid Mechanics*, vol. 219, pp. 143–179, 1990.

[50] T. Tran, H. De Maleprade, C. Sun, and D. Lohse, "Air entrainment during impact of droplets on liquid surfaces," *Journal of Fluid Mechanics*, vol. 726, p. R3, 2013.

[51] A. Wang, C. Kuan, and P. Tsai, "Do we understand the bubble formation by a single drop impacting upon liquid surface?," *Physics of Fluids*, vol. 25, no. 10, 2013.

[52] M. Hendrix, W. Bouwhuis, D. Van Der Meer, D. Lohse, and J. Snoeijer, "Universal mechanism for air entrainment during liquid impact," *Journal of Fluid Mechanics*, vol. 789, pp. 708–725, 2016.

[53] A. Jones, "The sounds of splashes," *Science*, vol. 52, no. 1343, pp. 295–296, 1920.

[54] C. Raman and A. Dey, "On the sounds of splashes," *Phil. Mag.*, vol. 39, no. 229, pp. 145–147, 1920.

[55] S. Li, H. Boyter, and L. Qian, "Uv curing for encapsulated aroma finish on cotton," *Journal of the Textile Institute*, vol. 96, no. 6, pp. 407–411, 2005.

[56] D. Xiao, M. Rong, and M. Zhang, "A novel method for preparing epoxy-containing microcapsules via uv irradiation-induced interfacial copolymerization in emulsions," *Polymer*, vol. 48, no. 16, pp. 4765–4776, 2007.

[57] E. Onder, N. Sarier, and E. Cimen, "Encapsulation of phase change materials by complex coacervation to improve thermal performances of woven fabrics," *Thermochimica Acta*, vol. 467, no. 1-2, pp. 63–72, 2007.

[58] Z. Fang and B. Bhandari, "Encapsulation of polyphenols - a review," *Trends in Food Science and Technology*, vol. 21, no. 10, pp. 510–523, 2010.

[59] S. Mitra, N. S. K. Gunda, S. Misra, and K. Trinavee, "Liquid encapsulation method and compositions and uses related thereto," Feb. 2022.

Chapter 3

Liquid-liquid encapsulation: Penetration vs. trapping at a liquid interfacial layer [1]

3.1 Overview

Encapsulation protects vulnerable cores in an aggressive environment and imparts desirable functionalities to the overall encapsulated cargo, including control of mechanical properties, release kinetics, and targeted delivery. Liquid-liquid encapsulation to create such capsules, where a liquid layer (shell) is used to wrap another liquid (core), is an attractive value proposition for ultrafast encapsulation ($\sim$ 100 ms). Here, we demonstrate a robust framework for stable liquid-liquid encapsulation. Wrapping is achieved by simple impingement of a target core (in liquid form) on top of an interfacial layer of another shell-forming liquid floating on a host liquid bath. Polydimethylsiloxane (PDMS) is chosen as the shell-forming liquid due to its biocompatibility, physicochemical stability, heat curability, and acceptability as both a drug excipient and food additive. Depending

[1] Adapted from an article of the same title by **Misra, S***, Banerjee, U*; Mitra, S.K., just accepted for publication in *ACS Applied Materials & Interfaces* (manuscript id: am-2023-021773). *: Equally contributing first-authors

on the kinetic energy of the impinging core droplet, encapsulation is accomplished by either of the two pathways - necking-driven complete interfacial penetration and subsequent generation of encapsulated droplets inside the host bath or trapping inside the interfacial layer. Combining thermodynamic argument with experimental demonstration, we show that the interfacially trapped state, which results in a low kinetic energy of impact, is also an encapsulated state where the core droplet is wholly enclosed inside the floating interfacial layer. Therefore, despite being impact-driven, our method remains kinetic energy independent and minimally restrictive. We describe the underlying interfacial evolution behind encapsulation and experimentally identify a non-dimensional regime of occurrence for the two pathways mentioned above. Successful encapsulation by either path offers efficient long-term protection of the encased cores in aggressive surroundings (e.g., protection of honey/maple syrup inside a water bath despite their miscibility). We enable the generation of multifunctional compound droplets via interfacial trapping, where multiple core droplets with different compositions are encapsulated within the same wrapping shell. Further, we demonstrate the practical utility of the interfacially trapped state by showing successful heat-curing of the shell and subsequent extraction of the capsule. The cured capsules are sufficiently robust and remain stable under normal handling.

3.2 Introduction

Encapsulation is immensely relevant in multiple industrial applications, including pharma & nutraceuticals [1], agriculture [2], food processing [3, 4], cosmetics [5], and efficient energy management systems [6, 7]. Encapsulation shields a vulnerable core from an aggressive environment, such as in protecting enzymes from denaturing solvents [8], shielding the core from oxidation, moisture [9], and improving the delivery of bioactive molecules [10], (e.g., antioxidants, vitamins, minerals, fatty acids, and antioxidants) and living cells (e.g., probiotics) into foods as well as in the pharmaceutical industry, where expensive active pharmaceutical ingredients are protected by encapsulating inside a suitable shell [11, 12].

A critical aspect of any encapsulated system is the properties of the shell material, which have a significant impact on the overall functionality of the encapsulated core. The

shell is responsible for providing structural integrity and stability to the core. Moreover, the shell should manifest desirable attributes to facilitate various release mechanisms as desired for the intended application. In this regard, polydimethylsiloxane (PDMS) is an excellent choice for shell material [13–17]. PDMS offers several advantages [18], including functionalizing the shell surfaces and controlling the shell's permeability and physical strength. Apart from these, the non-toxicity, biocompatibility, chemical stability, transparency, flexibility, low-cost preparation, and acceptability as both food additives [19, 20], and pharmaceutical excipients [21–23], bolster its utility as the shell material [13] even in consumable products. In a recent evaluation [20], the European Food Safety Authority (EFSA) concluded that oral exposure to PDMS did not lead to any systemic adverse effects in any species or at any dose tested. They observed that the absorption of PDMS from the gastrointestinal tract was minimal, and most consumed dimethylpolysiloxane was excreted via feces. The conclusion of the study [20] allowed them to increase the Acceptable daily intake limit from 1.5 mg/kg to 17 mg/kg of bodyweight. This is a significantly high upper limit if the consumption of PDMS in the form of the thin shell layer of cured capsules is considered. Further, the water-permeable elastomeric network of PDMS allows for stimuli-responsive [16, 24, 25], release of the encapsulated core and has been extensively explored as a platform for controlled drug release [21, 22, 26–30] in pharmaceutical applications in its cross-linked form.

Encapsulation techniques can be classified into chemical, physical, and physicochemical methods. Chemical methods include *in situ* polymerization [31]; physical methods include spray-drying [32], and fluidized bed coating [33], and physicochemical methods include complex coacervation [34], and sol-gel encapsulation [35]. However, these processes suffer from several restrictions, including difficulty in controlling the thickness of the shell, low yield, presence of coacervating materials on the surface of capsules, low stability, low yield, use of toxic chemicals in the process, etc., which limits the utility of these conventional techniques. On the other hand, microfluidics-based systems [36–39], would require the fabrication of microfluidic devices, involvement of multiple syringe pumps for fluid infusion, and controlled wetting conditions [40, 41], of the microfluidic device for the generation of microcapsules [42]. Therefore, efficient alternative encapsulation systems are much sought after.

In this regard, we previously demonstrated a simple yet robust platform for liquid-liquid encapsulation [43, 44], where stable and ultrafast wrapping was achieved by impact-driven water entry of a liquid analyte (core) through the floating interfacial layer of another liquid (shell). Using our patent-pending technique, Yin *et al.,* [45] further demonstrated stable triple-layer encapsulation and subsequent extraction of the encapsulated cargo via UV-curing of the outer shell. However, our previous approach [43], had three primary restrictions. First, the generation of practically utilizable encapsulated droplets is possible only after successful interfacial penetration of the core droplet. It puts a stringent restriction on both the minimum allowable size of the core drop and the height of impact. In other words, the success of the previous method was kinetic energy dependent. The insufficient kinetic energy of the impacting core droplet leads to the drop being unable to penetrate through the interfacial layer and instead getting trapped at the interface. Second, the participating liquid triplet (the core, the shell, and the host liquid) needs to adhere to a density criterion. The core liquid needs to be the heaviest as the encapsulated cargo needs to separate from the interfacial layer and settle down at the bottom of the host bath. Third, being an all-liquid system, the encapsulated droplet is only stable as long as it is inside the host bath. The cargo cannot be extracted from the host bath for further processing/handling, often desired in multiple practical applications. In the present work, we show a holistic platform for liquid-liquid encapsulation using PDMS as the shell-forming liquid, which resolves all three above issues while retaining the simplicity and robustness of our previous approach [43]. We demonstrate that complete interfacial penetration is not a strict prerequisite for successfully encapsulating the impacting core. Instead, stable wrapping is achieved even if the core cannot penetrate the floating interfacial layer and attains an interfacially trapped state owing to insufficient kinetic energy. It eliminates the minimum size restriction, the impact height limitation, and the density criteria and renders the method universal in terms of kinetic energy requirement. We also identify the relevant theoretical threshold for the thermodynamic favorability of an encapsulated state in the interfacially trapped configuration. Further, we provide a detailed kinetic description of the interfacial interaction that leads to successful encapsulation. The developed technique can effectively wrap and protect a target analyte in an aggressive surrounding, as demonstrated by the successful formation of encapsulated cargo with water-soluble cores inside

a host water bath. We specifically chose food ingredients (honey/maple syrup) to show the potential of this approach in creating novel experience-driven beverages with localized flavoring. For example, the demonstrated method can generate honey-flavored beverages with multiple dispersed honey capsules where the honey content is not homogeneously mixed in the bulk of the drink and instead is released only upon chewing the capsules, an upcoming trend in the consumer beverage industry. We also demonstrate the successful generation of encapsulated magnetoresponsive droplets underwater and in the interfacially trapped state where a water-soluble ferrofluid core is stably wrapped using a PDMS interfacial layer. We also show that our framework allows simultaneous encapsulation of multiple core droplets of different compositions in the same cargo leading to the formation of novel encapsulated compound droplets with multiple functionalities. Further, owing to the usage of PDMS as the interfacial layer, we could also cure the shell of the interfacially trapped cargo by simple heating, enabling extraction of the encapsulated cargo for practical utilization. The cured capsules are sufficiently robust for regular handling, as we show via both experimental demonstrations as well as compressive stress testing. This work opens up a paradigm for minimally restrictive fabrication of practically relevant multifunctional encapsulated cargos.

3.3 Experimental Section

Materials

The framework involves three liquids, namely the core drop (liquid L_1), the interfacial layer forming the shell (liquid L_2), and the host liquid (liquid L_3), on top of which the interfacial layer is dispensed. If not otherwise mentioned, a class of laser liquid - a mixture of silicanes and polyphenol ethers with a water solubility of < 0.1 % (Product Code: 57B63, Cargille Laboratories Inc., Cedar Grove, NJ, USA) is used to form the core drop. The relevant material properties are as follows: density $\rho_1 = 1900$ kg/m^3, dynamic viscosity $\mu_1 = 1024$ mPa $-$ s, liquid-air surface tension $\gamma_1 = 50$ mN/m, and liquid-water interfacial tension $\gamma_{13} = 39.4$ mN/m. Freshly prepared polydimethylsiloxane (PDMS) (Sylgard 184, Dow Chemicals) by mixing the base elastomer and the cross-linker in a $10:1$

weight ratio is used to form the interfacial layer. The relevant thermophysical properties are as follows: density $\rho_2 = 965$ kg/m^3, dynamic viscosity $\mu_2 = 3500$ mPa $-$ s, and liquid-air surface tension $\gamma_2 = 22$ mN/m, liquid-water surface tension [17] $\gamma_{23} = 42.1$ mN/m. The interfacial tension between L_1 (laser oil) and L_2 (PDMS), $\gamma_{12} = 5.67$ mN/m is calculated using the interfacial tension formula [46] for non-polar liquids as $\gamma_{12} = \gamma_1 + \gamma_2 - 2\sqrt{\gamma_1\gamma_2}$. The host liquid is deionized (DI) water (purified by Milli-Q, MilliPoreSigma, Ontario, Canada) with density $\rho_3 = 1000$ kg/m^3, dynamic viscosity $\mu_3 = 1$ mPa $-$ s and liquid-air surface tension $\gamma_3 = 72$ mN/m. The experiments were conducted in a distortion-free glass cuvette (Product Code: SC-02, Krüss GmbH, Hamburg, Germany) of inner dimension 36 mm $\times$ 36 mm $\times$ 30 mm with a 2.5 mm wall thickness. Polished and stainless-steel disposable needle tips with gauge 14 and inner diameter of 0.060″ (Part No. 7018035, Nordson EFD, East Province, RI, USA) mounted on 1 ml NORM-JECT® sterile luer-slip syringes (Henke-Sass, Wolf GmbH, Tuttlingen, Germany) were used for dispensing the liquids. The dispenser is mounted on a linear translating stage (A-BLQ0595, Zaber) which controls the impact height. Honey, maple syrup, and polyethylene glycol-based water-soluble ferrofluid are used as the core liquids to demonstrate the practical use cases. The ferrofluid (PBG 900, density 1860 kg/m^3) was purchased from Ferrotec, USA, and diluted 10-fold with DI water before experiments. Honey and maple syrup were purchased from Walmart, Canada, and used as purchased.

Methods

Before each experiment, the glass cuvette is thoroughly cleaned by dipping it in a glass beaker containing hexane and ultrasonication (Branson 5800, Emerson Electric Co., USA) in hexane for 30 minutes. The cuvette is then thoroughly rinsed with DI water before drying with compressed nitrogen. Next, a freshly plasma-cleaned glass slide (thickness 1 mm) is placed at the bottom of the experimental cuvette to allow easy retrieval of the encapsulated cargo from the experimental cuvette. The cuvette is then partially filled with 20 ml of DI water. First, the base elastomer and the curing agent are thoroughly mixed in a 10:1 weight ratio to prepare the interfacial layer. Then the mixture is degassed in a desiccator to remove trapped air bubbles. Subsequently, a predetermined volume of PDMS, V_{PDMS}

in the range of 30 $-$ 1000 μl is dispensed on top of the water bath from close proximity using a 1 ml syringe and allowed to spread uniformly [47], for $\sim$ 2 minutes resulting in the formation of a thin PDMS layer of uniform thickness, $\delta = \frac{V_{PDMS}}{A_C}$, where A_C is the inner cross-sectional area of the cuvette Using the linear translating stage, the dispenser is then taken to the predetermined height, H. The core drop is generated by pumping the liquid L_1 slowly through the syringe mounted on the pump. The core droplet's average volume, V_{core} for laser oil is 15.5 μl with a standard deviation of 0.8 μl, which corresponds to a drop radius of 1.54 mm (assuming spherical geometry) below the system's capillary length scale. Upon detachment from the needle, the drop accelerates downward due to gravity and comes in contact with the interfacial layer of liquid L_2. Suppose the droplet has sufficient kinetic energy to overcome the interfacial and viscous barrier, which assists the droplet in penetrating through this interfacial layer. In that case, it gets encapsulated with a liquid layer of L_2 as it separates from the interfacial layer (Method 1). On the other hand, if the droplet's kinetic energy is insufficient to overcome the interfacial and viscous barrier, the droplet cannot penetrate through the interfacial layer. In this case, the droplet gets trapped at the interface and remains encapsulated (Method 2). A step-wise schematic representation of the impact-driven encapsulation process is provided in Figure 3.1. The complete dynamics of the encapsulation were captured using a high-speed camera (Photron, FASTCAM Mini AX200) at 6400 fps. A Zoom Lens (Navitar 7000 Zoom with an effective focal length of 18 – 108 mm) was coupled with a high-speed camera to capture the dynamics. The used high-speed camera has an internal memory of 32 GB. At 6400 fps, it allows a maximum recording window of 3.412656 s at full resolution (1024 px $\times$ 1024 px), which is enough to capture the entire time-resolved dynamics of encapsulation, typically completed within 500 ms. We used the 'end' trigger mode for image acquisition to apply the trigger by visually confirming the completion of encapsulation, and the preceding events corresponding to the interface dynamics could be conveniently recorded. For further analysis, the captured data was transferred to a connected personal computer using the high-speed Gigabit ethernet connection between the camera and the computer.

For the curing of the encapsulated cargo, the experiments are conducted on top of a hot plate (preheated at 70°C). Following encapsulation, the experimental cuvette containing the host bath, floating interfacial layer, and the encapsulated drop is left undisturbed

overnight on the hot plate at 70°C, which allows solidification of the PDMS shell and subsequent extraction of the encapsulated cargo. Note that it is critical to clean the reusable cuvette thoroughly between two subsequent curing experiments. Once cured, it is extremely challenging to completely eliminate the PDMS residues from the walls of the cuvette by solvent cleaning. It can lead to local roughness features and consequent spatially varying wettability along the cuvette walls. We noticed that it could significantly alter the spreading behavior of the PDMS interfacial film on the host water bath. Therefore, for curing experiments, once the cuvette is cleaned using hexane, we additionally expose the cuvette to air plasma (PE-25, PLASMA ETCH, USA). The compression testing of the cured capsules was performed using a tribometer (CETR UMT-2, Bruker).

3.4 Results and Discussion

In this method, the core drop is dispensed from a vertical separation H onto the PDMS interfacial layer floating on top of the host liquid bath (see Figure 3.1 for a schematic representation of the process). The impact of the core drop onto the interfacial PDMS layer can lead to two possibilities. With sufficient kinetic energy to overcome the viscous and interfacial resistance offered by the floating PDMS layer, the core drop can penetrate through the PDMS layer. However, the drop can also get trapped at the interface if the kinetic energy is dissipated by viscous resistance before the drop can detach from the interface. The kinetic energy requirement is reflected in terms of the impact Weber number We_i and the thickness of the interfacial layer δ. The impact Weber number (We_i) is defined as $We_i = \frac{\rho_1 v^2 R_c}{\gamma_1} \approx \frac{2gH\rho_1 R_c}{\gamma_1}$. Here v is the velocity of the core droplet just before its contact with the interfacial layer, R_c is the radius of the core droplet assuming spherical geometry, and g is the acceleration due to gravity. For a particular δ, if We_i is higher than a critical Weber number $We_{cr}(\delta)$, impact results in complete separation of the impinging droplet from the interfacial layer while $We_i < We_{cr}(\delta)$ leads to interfacial trapping. Subject to adherence to a favorable thermodynamic threshold, the droplet gets encapsulated by the interfacial layer in both cases, which is discussed later. Encapsulation via the first path involving complete detachment of the impinging core drop from the interfacial layer and subsequent under-liquid formation of the standalone encapsulated droplet is termed

method 1. In contrast, encapsulation via the second route involving interfacial trapping is named method 2.

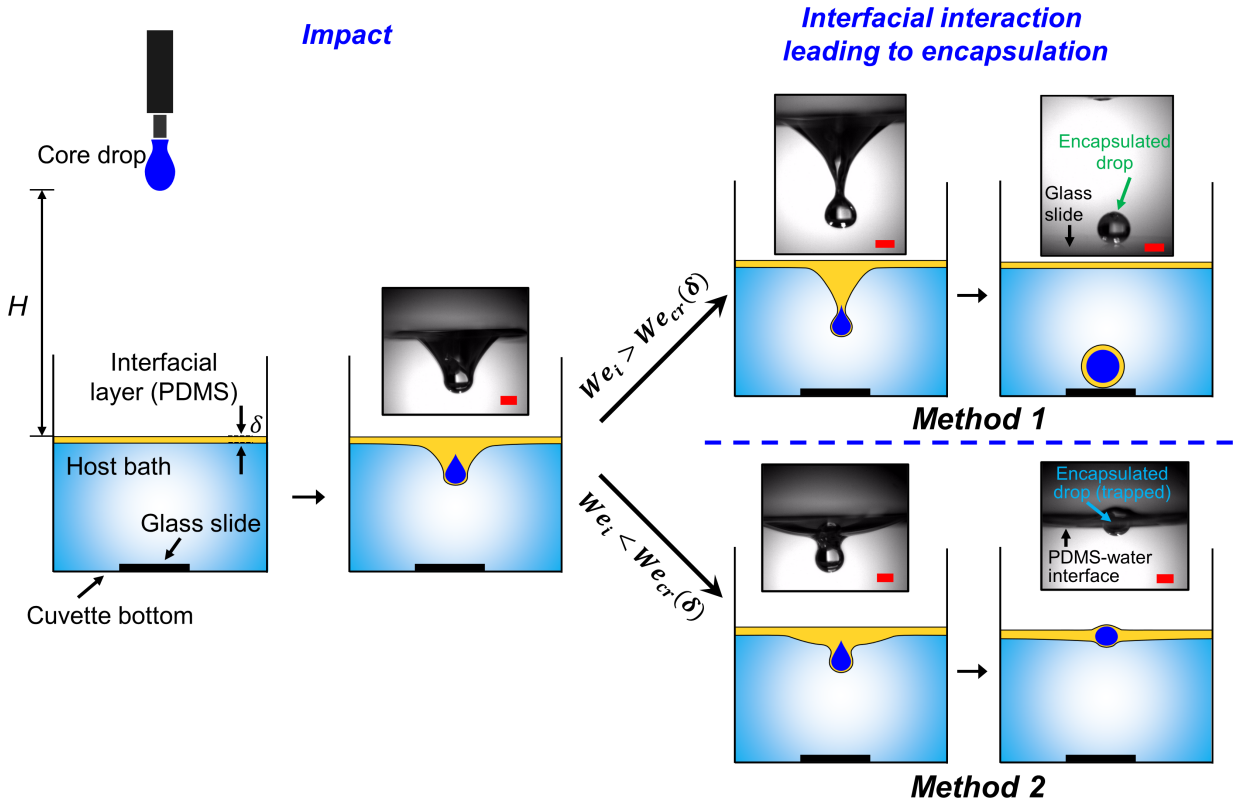

Figure 3.1: Schematic representation of the liquid-liquid encapsulation framework. Method 1 demonstrates the necking-assisted encapsulation mechanism leading to the formation of wrapped droplets at the bottom of the cuvette. In contrast, Method 2 corresponds to the interfacial trapping process where the oncoming core drop gets encapsulated while still being attached to the floating interfacial layer. The scale bar represents 2 mm in all the experimental images of the inset.

3.4.1 The underlying mechanism of encapsulation

The encapsulation methods described herein are impact-driven, which involve a complex interplay between interfacial (surface) tension forces, viscous forces, and momentum at the

four fluids (namely, air, interfacial layer, host liquid, and the core drop) interface. The involved competing forces are schematically shown in **Figure 3.2**A. Owing to the vertical separation H between the interfacial layer (L_2) and the dispensing needle, the core drop gains kinetic energy, termed hereafter as the kinetic energy of impact ($\boldsymbol{KE}_{impact}$) before it comes in contact with the interfacial layer. At the moment of impact, the core droplet has an associated initial momentum, $\boldsymbol{p}_{\text{in}}$ defined as $\boldsymbol{p}_{\text{in}} = \rho_1 V_{core} v \approx \rho_1 V_{core}\sqrt{2gH}$. Upon contact, the core drop attempts to penetrate through this intermediate layer. At this point, the core drop drags the PDMS (L_2) layer down through the water (L_3) bath due to its momentum, which deforms the PDMS-water interface and increases its surface area. The downward-acting gravitational force, $\boldsymbol{F}_g$ assists in the downward motion of the core drop. However, interfacial forces, $\boldsymbol{F}_\gamma$ acting on the deformed L_2-L_3 interface, attempt to restore the interface to its original position to minimize the interfacial energy. Further, the viscous force, $\boldsymbol{F}_{visc}$ offered by the interfacial layer also opposes the downward motion of the drop by dissipating its initial momentum, $\boldsymbol{p}_{\text{in}}$. This competition leads to neck formation. We describe the geometry of the neck in terms of two characteristic non-dimensional parameters, namely, non-dimensional cusp length L^* and non-dimensional neck-diameter D^*, as shown in Figure 3.2A. L^* is defined as $L^* = L_{\text{cusp}}/R_{\text{c}}$where L_{cusp} is the vertical separation of the lowest point of L_3-L_2 interface and the location of the L_3-L_2 interface in its unperturbed state (before impact). D^*, on the other hand, is defined as $D^* = D_{\text{neck}}/R_{\text{c}}$where D_{neck} is the width of the neck formed by the deformed L_3-L_2 interface, as shown in Figure 3.2A. Note that the neck represents the point of inflection of the L_3-L_2 interface where the curvature of the interface switches sign. Above the neck, the curvature of the interface is directed concave downward, while it is concave upwards below the neck. In other words, the neck is the location of zero Laplace pressure due to zero local curvature.

Competition between these three forces dictates the droplet's fate, which involves encapsulation either by necking-driven interfacial penetration or by trapping at the PDMS-water interface. We present the underlying interfacial evolution corresponding to either of these two outcomes in Figures 3.2B and 3.2C in terms of time-resolved (high-speed) experimental snapshots. If the drop has sufficient momentum to overcome the barrier imposed by both the interfacial forces and the viscous resistance, it can penetrate through the interfacial layer (L_2). In this process, the core drop detaches a part of the film from the interfacial

layer. This detached layer forms a thin enclosure (the encapsulating shell) around the core drop. Once the wrapped droplet separates from the interfacial layer, the residual interfacial layer reinstates to its unperturbed state. This pathway is termed **method 1** (Figure 3.2B). On the other hand, the impacting core droplet encounters a different fate in the absence of sufficient kinetic energy to penetrate through the interfacial layer, as shown in Figure 3.2C. Although it initially tries to separate from the interfacial layer by elongating the L_2-L_3 interface, it fails to attain a complete separation from L_2 because of the dissipation of $\boldsymbol{KE}_{impact}$ before separation. As a result, the drop returns to the host bath-air interface while being trapped in the interfacial layer. This pathway towards encapsulation via interfacial trapping is identified as **method 2** (Figure 3.2C).

In Figures 3.2D and 3.2E, we provide a kinetic description of the wrapping dynamics in the form of the temporal evolution of L^* and D^*. Figure 3.2D describes the encapsulation process via method 1 for two different We_i, where the PDMS interfacial layer (L_2) thickness is kept fixed at $\delta = 38.6$ μm. The process leading to encapsulation in method 1 can be split into two sequential steps: rapid elongation of the PDMS cusp and viscoelastic neck thinning, leading to complete separation of the encapsulated cargo from the interfacial layer, as shown in Figure 3.2D. Immediately upon impact with the interfacial layer, the core drop moves fast through the interfacial layer as the magnitude of $\boldsymbol{KE}_{impact}$ dominates over the viscous and interfacial forces. As a result, the PDMS-water cusp undergoes a rapid elongation, as confirmed by the fast-increasing trend of L^* with time. It also leads to fast neck thinning, manifested in an associated sharp decrease in D^*. This stage continues until the L_2-L_3 interface touches the glass slide at the bottom of the cuvette. This event is marked in the relevant timestamp $t \sim 63$ ms in Figure 3.2B as 'touchdown' and is also indicated by black colored arrows in Figure 3.2D. For $We_i = 214$, the touchdown happens at $t \sim 63$ ms, while for $We_i = 261$, it takes a lesser time, $t \sim 30$ ms, due to a higher value of $\boldsymbol{KE}_{impact}$. Evidently, L_{cusp} cannot elongate any further once the touchdown happens. Therefore, following the touchdown, L^* remains constant. However, at this stage, the neck undergoes a slow thinning process. This is due to the time-dependent straining behavior of the viscoelastic [48] PDMS, which results in the viscoelastic thinning of the PDMS neck. Finally, the neck thins beyond a critical thickness, separating the wrapped core drop from the interfacial layer (timestamps, $t \sim 171$ ms for $We_i = 261$ and

$t \sim 146$ ms for $We_i = 214$). As seen in Figure 3.2D, for a fixed δ, the viscoelastic thinning happens faster if We_i is lower. For $We_i = 261$, the viscoelastic thinning stage (defined as the gap between the touchdown and the completion of necking) lasts for ~ 141 ms, while the duration is ~ 83 ms for $We_i = 214$. It could be attributed to two possible reasons. First, a higher $\boldsymbol{KE}_{impact}$ associated with higher We_i leads to a faster touchdown which corresponds to a higher value of D^* at the point of touchdown. For example, at $We_i = 261$, $D^* \sim 0.17$ at touchdown ($t \sim 30$ ms) while $D^* \sim 0.11$ when the L_2-L_3 interface touches down the bottom of the cuvette for $We_i = 214$ (corresponding $t \sim 63$ ms). As a result, at a higher impact Weber number, the slow viscoelastic thinning stage constitutes a higher fraction of the total neck thinning process (e.g., for $We_i = 261$, $\sim 6.7\%$ of neck thinning takes place in the viscoelastic thinning regime, compared to $\sim 4.4\%$ for $We_i = 214$). A second possible factor is a higher associated value of remaining downward momentum at higher We_i just before the touchdown, which, once the droplet makes contact with the bottom surface and comes to rest, gets converted into an upward-directed reaction force and slows down the necking process.

Next, Figure 3.2E provides a kinetic description of the encapsulation process in method 2 for two different We_i with $V_{PDMS} = 50$ μl and a corresponding $\delta = 38.6$ μm. As seen from a side-by-side comparison between Figure 3.2D and 3.2E, the first stages in method 1 and method 2 are similar. Upon impact, the droplet drags the L_2-L_3 interface downward due to its momentum. For $We_i = 191$, a downward motion of the interface is observed for about ~ 19 ms, while the L_2-L_3 interface elongates downward for ~ 16.4 ms for $We_i = 145$. Once the viscous and interfacial resistance dissipates the initial momentum, $\boldsymbol{p}_{\text{in}}$, the interface starts to return to its undeformed state (before impact) owing to the restorative interfacial tension forces. The onset of interface retraction is indicated by black colored arrows on the L^* vs. t plot for both the We_i values in Figure 3.2E. The direction reversal of the motion of the L_2-L_3 interface is also marked on the relevant timestamp, $t \sim 19$ ms in Figure 3.2C. Note that the neck thinning significantly slows down once the interface starts retracting. The slight reduction in D^*, even beyond the onset of interface retraction, could be attributed to viscoelastic effects. Finally, the interface reinstates to its unperturbed position, with the core droplet trapped inside the interfacial layer, as shown in Figure 3.2B (see time stamp, $t = 59$ ms). Note that, despite a lower $\boldsymbol{KE}_{impact}$, the total encapsulation

time is lower in method 2 compared to method 1. As can be seen from Figure 3.2C and 3.2D, encapsulation via method 1 takes $\sim$ 146 ms for $We_i = 214$, while successful encapsulation is achieved in the trapped configuration (method 2) within $\sim$ 59 ms for a lower $We_i = 191$. This is because successful encapsulation is achieved in method 1 only after a slow viscoelastic neck thinning stage and subsequent separation of the encapsulated cargo from the interfacial layer, which is absent in method 2. A simple workaround to achieve faster encapsulation, even in method 1, is to use a taller cuvette so that the height of the host water column can be increased. It will allow the completion of necking and the consequent separation of the encapsulated cargo to be achieved during the rapid first stage of interface evolution while the L_{cusp} is still elongating (i.e. before the touchdown happens). Note that in our previous work [43], where we first introduced the impact-driven platform for liquid-liquid encapsulation, we achieved successful encapsulation within $\sim$ 50 ms via interfacial penetration (similar to method 1 described here) of an impacting core droplet through the floating interfacial layer of a non-viscoelastic edible oil.

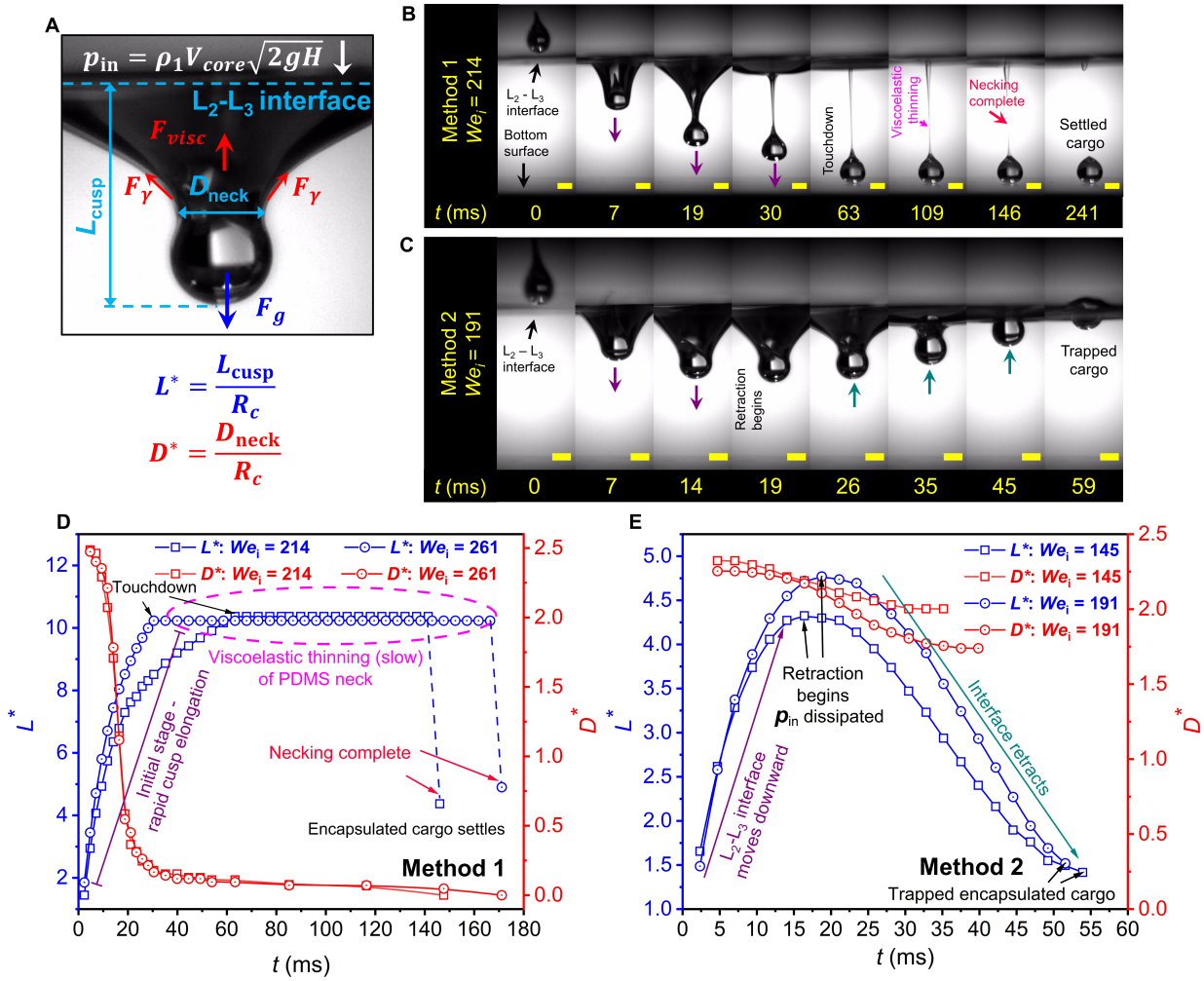

Figure 3.2: Kinetic description of the encapsulation process: (A) schematically represents the involved competing forces and consequent geometry of the neck in terms of the cusp length (L_{cusp}) and neck diameter (D_{neck}) on a typical experimental snap. (B-C) shows the interface evolution leading to the encapsulated droplet formation in the form of a time series for method 1 and method 2, respectively. Scale bar 2 mm. The L_2-L_3 interface indicated by black colored arrows in the first snaps of both (B) and (C) denotes the unperturbed state of the interface before impact. Upon impact, the direction of motion of the L_2-L_3 interface is marked with different colored arrows. The downward purple arrows denote the downward motion of the interface, while the upward, teal-colored arrows indicate the retraction of the interface. (...continuing to the next page)

Figure 3.2: (...continued from the previous page) (D-E) provides a kinetic description of the encapsulation process in terms of the temporal variation of the non-dimensionalized cusp length (L^*) and the neck- diameter (D^*) for both method 1 and method 2, respectively, for two different We_i in each case. $V_{PDMS} = 50$ μl for all the reported experiments in this figure, which corresponds to $\delta = 38.6$ μm.

3.4.2 Thermophysical criteria for successful encapsulation via interfacial trapping

In the interfacially trapped state, the floating interfacial layer wholly encloses the oncoming core drop and no core drop–host bath or core drop–air interface exists. In our method, the controlled proximal dispensation of the core droplet(s) onto the interfacial layer leads to monodispersed encapsulated droplets with a highly predictive and regular morphology. We identify that for successful interfacial trapping, the following criteria should be satisfied –

1. As the interfacial layer (L_2) needs to float stably on top of the host bath (L_3), the density of L_2 needs to be lower than L_3, i.e., $\rho_2 < \rho_3$. Further, as L_2 and L_3 are in direct contact, they need to be physicochemically compatible. The same criteria for mutual compatibility apply to L_1 and L_2 as well.

2. L_2 should spread on top of the host bath, which is feasible if the spreading parameter of L_2 on L_3, $S_{23} < 0$. S_{23} is defined as $S_{23} = \gamma_3 - \gamma_2 - \gamma_{23}$. For water as the host bath (L_3) and PDMS as the interfacial layer (L_2), S_{23} can be estimated as $S_{23} = 72 - 22 - 42.1 \ \frac{\text{mN}}{\text{m}} > 0$. It justifies the spreading of PDMS on water [47].

3. The criteria for attaining the interfacially trapped state can also be expressed in terms of the spreading parameters between the core drop (L_1) and the interfacial layer (L_2). For the interfacially trapped state to be thermodynamically feasible, L_2 should spread on top of L_1, not vice-versa. It translates to the thermodynamic requirement that the spreading parameter of L_2 on L_1, S_{21} should be positive, while

the spreading parameter of L_1 on L_2, S_{12} should be negative. For laser oil as the core liquid (L_1) and PDMS as the interfacial layer (L_2), we can estimate that -

$$S_{21} = \gamma_1 - \gamma_2 - \gamma_{12} = 50 - 22 - 5.67 \ \frac{\text{mN}}{\text{m}} > 0$$
$$S_{12} = \gamma_2 - \gamma_1 - \gamma_{12} = 22 - 50 - 5.67 \ \frac{\text{mN}}{\text{m}} < 0$$

It confirms the thermodynamic feasibility of the interfacially trapped configuration for the demonstrated liquid triplet. In addition to the thermodynamic favorability, we confirm the wrapping by practically demonstrating the non-coalescence of multiple identical/miscible droplets. The interfacially trapped configuration that we demonstrate here is analogous to the pseudo-total wetting state discussed in the work [49] of Sebilleau. It can also be thought equivalent to the cloaked state [50, 51] occurring on lubricant-infused surfaces where the infused lubricant layer spreads all over the oncoming droplet and cloaks it within. Typically, the interfacially trapped state will be thermodynamically unfavorable for low-surface-tension core liquids (e.g., ethanol) due to a negative spreading parameter of liquid PDMS on the core droplet. Note that, in our previous work [43, 44], where we first introduced the impact-driven liquid-liquid encapsulation framework, we used laser oil as the core drop (L_1), canola oil as the interfacial layer (L_2), and DI water as host bath (L_3). If we apply the above criteria to the liquid triplet, we can find that the triad satisfies all the thermophysical requirements for successful encapsulation via interfacial trapping. Canola oil (L_2) has a positive spreading coefficient on water (L_3) ($S_{23} = \gamma_3 - \gamma_2 - \gamma_{23} = 72 - 31.3 - 18.01 \frac{\text{mN}}{\text{m}} > 0$), thus forming an interfacial film on water. Further, canola oil (L_2) has a positive spreading coefficient on laser oil (L_1) core ($S_{21} = \gamma_1 - \gamma_2 - \gamma_{12} = 50 - 31.3 - 2.22 \ \frac{\text{mN}}{\text{m}} > 0$) as well, while the spreading coefficient of laser oil on canola oil is negative ($S_{12} = \gamma_2 - \gamma_1 - \gamma_{12} = 31.3 - 50 - 2.22 \ \frac{\text{mN}}{\text{m}} < 0$). Therefore, in our previous study, the drops that failed to detach from the interfacial layer due to insufficient kinetic energy, attain an equilibrium configuration where they are wholly engulfed by the floating interfacial layer. However, being in an all-liquid state, the interfacially trapped cargo was of no practical utility in the case of canola oil shell, as it can neither be detached from the interfacial layer nor can be packaged or utilized along with the interfacial layer.

3.4.3 Regime map of applicability of method 1 vs. method 2

Understandably, thermodynamic favorability alone cannot dictate the fate of the impinging core droplet as it only considers the energetic suitability of the equilibrium configuration at the encapsulated state and does not account for the irreversible non-equilibrium process during the interaction of the core droplet with the interfacial layer. The viscous dissipation during the core droplet's journey through the interfacial layer plays a pivotal role here, and competition between the momentum of the impacting droplet, the viscous resistance, and the restorative interfacial forces at the deformed L_2-L_3 interface decide whether encapsulation is achieved by method 1 or method 2, as discussed in subsection 3.4.1. Once the involved liquid triad satisfies the thermodynamic threshold for stable encapsulation identified in subsection 3.4.2, encapsulation by method 1 is achieved if the kinetic energy of the impacting droplet is adequate to overcome the viscous resistance and the interfacial forces offered by the interfacial layer and a transition to method 2 is observed otherwise. In Figure 3.3, a non-dimensional experimental regime for successful encapsulation is identified in terms of the impact Weber number (We_i), and interfacial film thickness non-dimensionalized with respect to the diameter of the core drop (δ/R_c). In our experiments, We_i is varied in discrete intervals between $75 - 550$ by changing the vertical separation H between the interfacial layer and the dispensing needle. For lower δ, the oncoming droplet can penetrate through the interfacial layer even with low We_i due to the low viscous resistance offered by the thin interfacial layer. Therefore, upon impact, successful encapsulation is achieved by method 1, where the encapsulated droplet is generated inside the host bath. For a higher value of δ/R_c, a higher We_i is required for encapsulation by method 1, owing to the augmented kinetic energy needed to overcome the viscous energy barrier. Consequently, a gradual transition from method 1 to method 2 could be observed in the regime map presented in Figure 3.3 with an increase in δ/R_c. The dashed blue line, demarcating the two regimes, experimentally maps the critical Weber number, We_{cr} as a function of δ.

Beyond an interfacial PDMS film thickness $\delta \sim 123\ \mu$m (and a corresponding $\delta/R_c \sim 0.08$), encapsulation was achieved only by interfacial trapping (method 2) for the range of

We_i explored in this study. In our previous work [43], we reported the successful underwater generation of encapsulated droplets using canola oil as the interfacial layer. The study demonstrated successful encapsulation by complete interfacial penetration (analogous to method 1) for a much higher δ/R_c ($\sim$ 2.8) with a lower We_i ($\sim$ 160). This is an expected outcome as PDMS is $\sim$ 55 times more viscous than canola oil. This high viscosity leads to a significant increase in the viscous resistance offered by the PDMS interfacial layer causing interfacial trapping at a much lower interfacial film thickness. However, with PDMS as the interfacial layer, the transition to interfacial trapping at low δ/R_c is not a functional bottleneck and could be advantageous for two primary reasons. First, with suitable structural stability, a capsule with a thin wrapping shell is often more desirable in several applications due to improved dosage efficiency and release profile. Using PDMS as the shell-forming material allows us to generate excellently stable encapsulated droplets even in aggressive surroundings despite having a very thin shell layer, as we demonstrate in subsection 3.4.4. Second, even if the impinging droplet is trapped at the interface, the heat curability of PDMS allows extraction and subsequent handling of the encapsulated drops, as also shown later in this study. Further, there is no upper limit for interfacial film thickness for the applicability of method 2. We could achieve successful encapsulation of target analytes for δ as high as 0.77 mm (corresponding V_{PDMS} = 1 ml). Thus, the demonstrated liquid-liquid encapsulation framework involving PDMS allows the generation of encapsulated drops with on-demand shell thickness control without any restrictions on kinetic energy requirement.

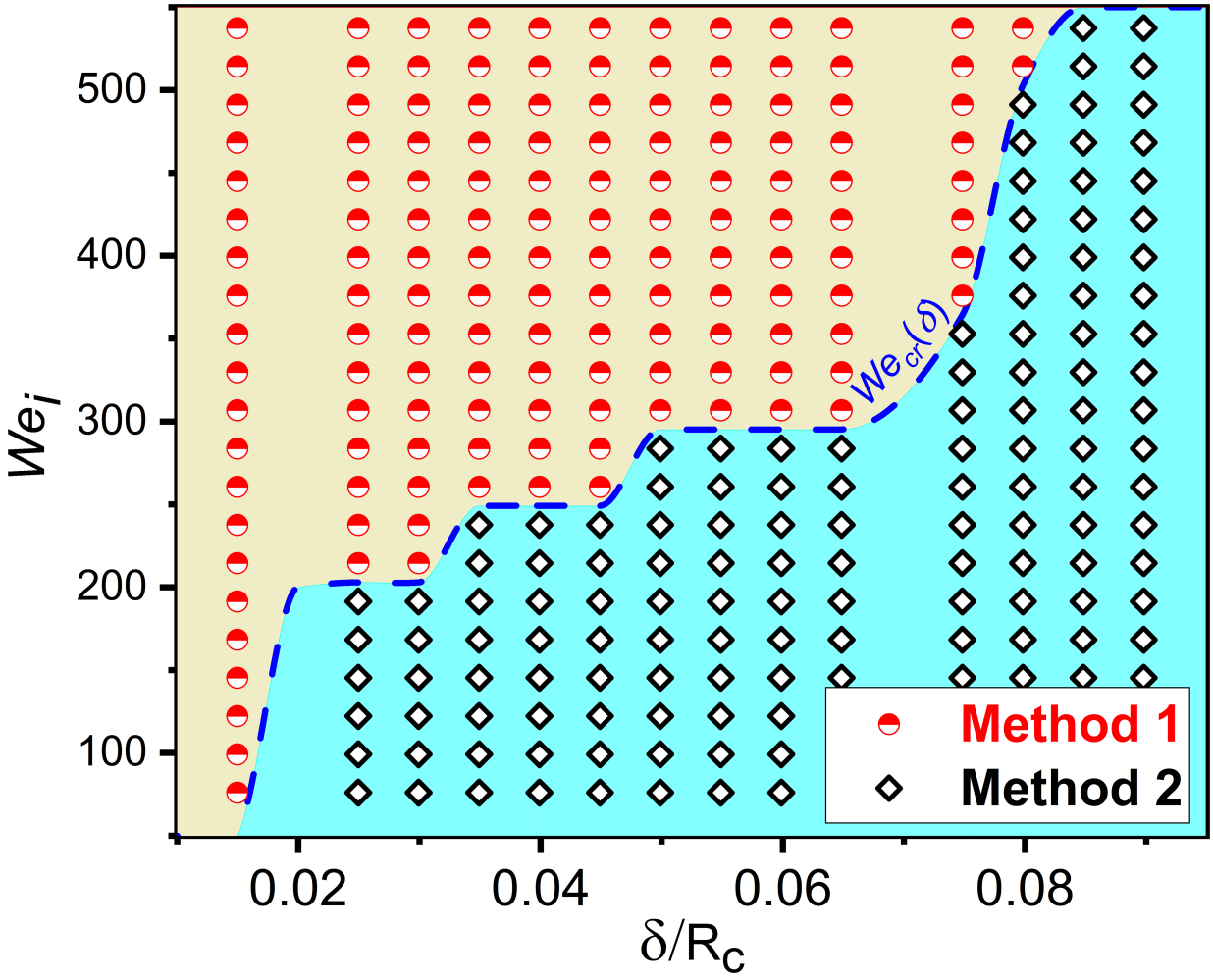

Figure 3.3: Regime map showing the region of applicability of method 1 and method 2. The blue dashed line demarcates the two regimes. Successful encapsulation is achieved by method 1 (interfacial penetration) above the blue line, while operating below the blue line leads to encapsulation by method 2 (interfacial trapping)

3.4.4 Practical use cases - Development of robust, multifunctional encapsulated drops

The practical utility of efficient encapsulation lies in providing efficient protection to target analytes by safeguarding them in aggressive surroundings and preventing the unwanted release. Figure 3.4 demonstrates the applicability of the developed impact-driven framework in this regard. We have used three test liquids of practical relevance as core liquids - two food ingredients (honey and maple syrup) and the other one a ferrofluid suspension that offers several functional advantages, including magnetic manipulation [17, 52], analyte targeting, etc. The core liquids were chosen such that all of them are miscible in the used host bath (DI water), allowing us to evaluate the robustness and protection achieved upon successful encapsulation.

In panel A of Figure 3.4, we show the impact-driven underwater formation of PDMS-wrapped stable capsules of the three tested core liquids using method 1. A relatively high impact height of $H = 46.6$ cm (corresponding $We_i \sim 537$) is used to ensure that the impinging droplets have sufficient kinetic energy $\boldsymbol{KE}_{impact}$ to penetrate through the interfacial layer. After successful penetration, all three droplets are wrapped by a thin PDMS layer. In addition to the formation, here we also confirm that despite the thinness of the PDMS wrapping layer, the encapsulated cargo remained stable in water, and no sign of perishing/dissolution of the miscible core in water could be observed.

Further, for a low impact height $H = 16.6$ cm (and consequently a low $We_i \sim 191$), encapsulation by interfacial trapping was achieved for the same core liquid compositions. The all-around existence of the PDMS wrapping layer could be observed in the digital photographs presented in panel B of Figure 3.4. Note that we have intentionally demonstrated the use cases for a thin interfacial layer to affirm the robustness of the PDMS wrapper. However, encapsulation by interfacial trapping (method 2) could also be realized for higher PDMS film volume (as shown in the regime map in Figure 3.3), allowing us to obtain thicker cured capsules on demand, as we show in Figure 3.5.

Additionally, as shown in panel C of Figure 3.4, interfacial trapping was further extended to encapsulate multiple core droplets of different compositions simultaneously. It allows the formation of encapsulated multicomponent droplets with multiple functional-

ities in the same cargo. The multicomponent encapsulated configuration with the same wrapping shell was achieved by dispensing various core droplets (honey, maple syrup, and ferrofluid), as shown in Figure 3.4C, on top of the floating interfacial layer one-after-another from proximity. The corresponding volumes of the dispensed core droplets and the volume of the interfacial layer are noted in the caption of Figure 3.4C. Once dispensed, the core droplets get individually encapsulated by the PDMS interfacial layer in a trapped state. Additionally, the low $\boldsymbol{KE}_{impact}$ associated with proximal dispensation coupled with the high viscosity of PDMS prevents complete drainage of the intermediate PDMS film between the neighboring droplets, thereby preventing unwanted direct interaction/contact and subsequent coalescence between the different core droplets. As a result, multiple droplets with different physicochemical properties could be individually wrapped inside the same outer wrapping shell. This leads to the formation of multicomponent compound droplets, where multiple droplets individually carry different functionalities without interacting among themselves while residing in the same outer wrapper. Note that the ferrofluid suspension has dynamic viscosity $\sim O(10^1$ mPa-s) and maple syrup has a viscosity $\sim O(10^2$ mPa-s), while honey is significantly more viscous with viscosity $\sim O(10^3$ mPa-s). Core droplets of all three liquids could not only be individually encapsulated via successful interfacial trapping but two or more droplets of dissimilar compositions could also be wrapped inside the same outer PDMS shell despite their significant difference in viscosities. It implies that the feasibility of interfacial trapping is not dependent on the viscosity of the core liquid. Rather interfacial energies of the participating entities play a much more crucial role, as we discussed in subsection 3.4.2.

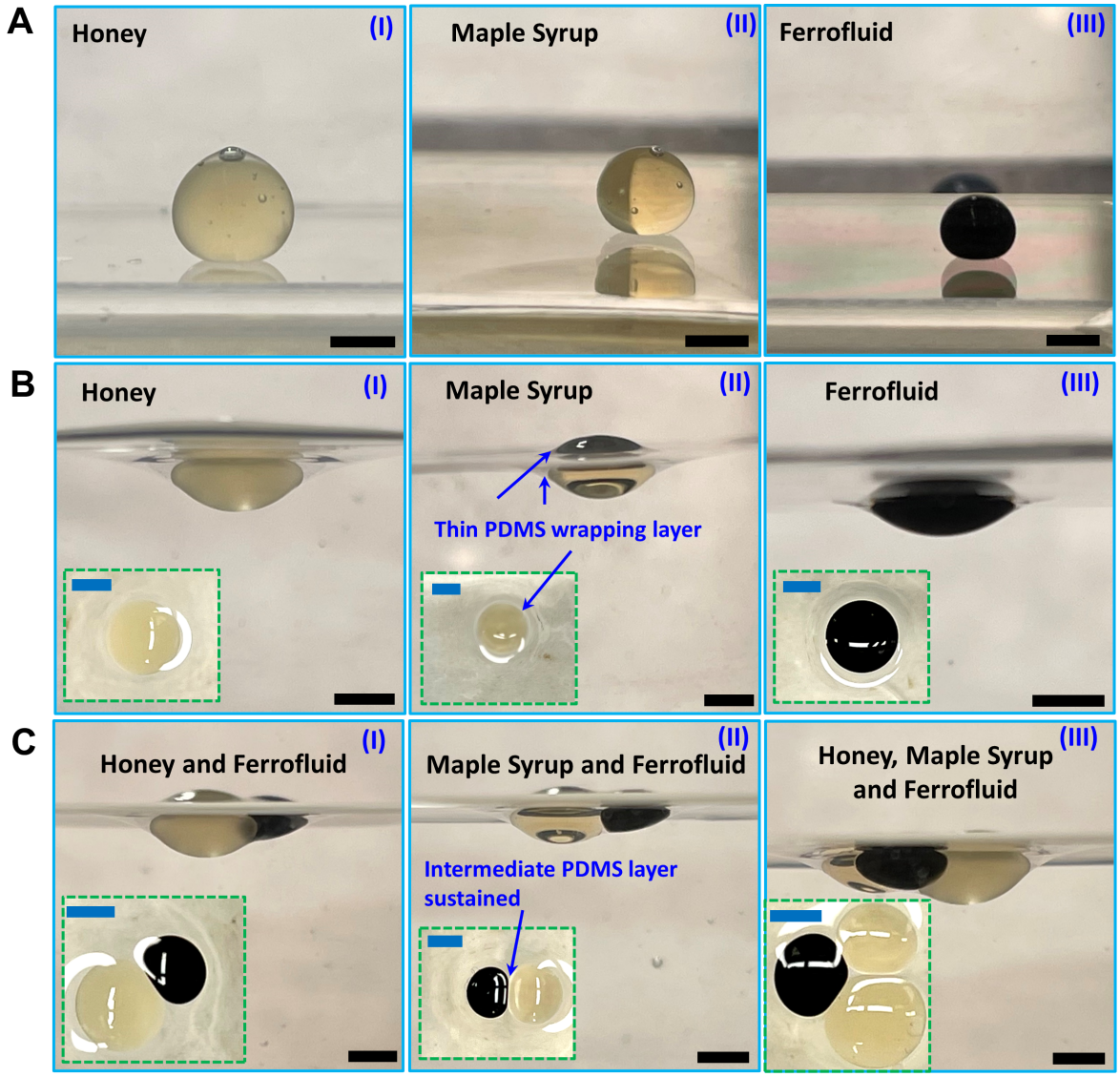

Figure 3.4: Demonstration of applicability in practical use cases involving miscible core liquid-host bath combinations - (A) Underwater formation of encapsulated droplets using method 1 with a thin PDMS wrapping layer containing (I) honey, (II) maple syrup, (III) PEG-based ferrofluid as core drops. Impact height $H = 46.6$ cm ($We_i \sim 537$). (B) Generation of interfacially trapped encapsulated droplets using method 2 containing (I) honey, (II) maple syrup, and (III) ferrofluid solution. Impact height $H = 16.6$ cm ($We_i \sim 191$). (...continuing to the next page)

Figure 3.4: (...continued from the previous page) (C). Encapsulation using method 2 with multiple interfacially trapped droplets leading to Janus configuration containing (I) Honey and ferrofluid, (II) Maple syrup and ferrofluid, and (III) Honey, maple syrup, and ferrofluid. The droplets were dispensed sequentially on the floating interfacial layer from proximity ($H \sim 5$ mm), maintaining $We_i < 10$. Insets present the top view of the corresponding cases. For all the cases reported in Figure 3.4, the average dispensed volume of the core droplet, $V_{core} \sim 22.4$ μl, 12.9 μl and 9.4 μl for honey, maple syrup, and ferrofluid, respectively. In all cases, 50 μl freshly prepared PDMS was used to create the floating interfacial layer, resulting in a thin interfacial layer with thickness $\delta = 38.6$ μm. The scale bar is 2 mm throughout the figure.

3.4.5 Practical utility of the interfacially trapped state: Curing and mechanical characterization of encapsulated drops

Figure 3.5 shows the curing and subsequent characterization of the encapsulated droplets generated by the interfacial trapping mechanism (method 2). The encapsulated drops are generated by dispensing the laser oil core droplets proximally ($We_i < 10$) on top of a floating PDMS layer and subsequently heating the experimental cuvette on a hot plate overnight at 70°C. The volume of the core drop (V_{core}) and the interfacial PDMS layer (V_{PDMS}) can both be varied on-demand over a broad range to suit different sizes and hardness requirements of the final capsules. We explored a range of 15.5 μl $\leq V_{core} \leq$ 250 μl and 50 μl $\leq V_{PDMS} \leq$ 1000 μl for our curing experiments.

Figures 3.5A-B present the experimental images of the cured capsules for two different V_{core}, 15.5 μl and 250 μl, respectively, for a fixed volume of PDMS interfacial layer, $V_{PDMS} = 1000$ μl. Heating the cuvette containing the host water bath (with a bath height of ~ 15.5 mm) after proximally dispensing the core drop onto the interfacial layer leads to the solidification of the entire interfacial PDMS layer with the liquid core trapped inside. We could remove the cured interfacial layer and the trapped core from the host cuvette by cutting the PDMS layer adjacent to the cuvette walls using a knife/scalpel. The snaps presented herein are captured after removing the cured interfacial layer from the cuvette.

The solidified excess interfacial layer around the cured encapsulated drop is visible in the snaps. Once extracted from the cuvette, this excess PDMS layer can be trimmed off by cutting around the periphery of the trapped core using scissors before packaging. The capsules can also be cut on-demand into various complex designer shapes using profiled cutters like cookie cutters for improved consumer perception. These capsules resemble commercially available soft gelatin capsules with liquid cores (e.g., omega 3/fish oil, vitamin D3, or ibuprofen). It is apparent from Figures 3.5A & 3.5B that the method is capable of generating capsules of vastly varying dimensions/core-shell volume ratios. Note that, in the interfacially trapped configuration, the floating PDMS interfacial layer that wraps the core drop has two dissimilar interfaces, namely, the top air-PDMS interface and the bottom PDMS-water interface. Once the core drop is dispensed, the PDMS-water interface sags downward due to the combined weight of the core drop and the interfacial layer. The sagging becomes prominent when V_{core} is high (see Figure 3.5B). As a result, the bottom interface of the encapsulated droplet attains a higher curvature than the relatively flatter top interface, which is sustained even after the cured (shell-hardened) cargo is extracted from the experimental cuvette, as shown in Figure 3.5B. We have confirmed that once cured, the wrapping layer is sufficiently robust to withstand normal handling, including exposure to drying under hot air, repeated hand-to-hand transfer, and shaking/tumbling inside a bottle. The cargo remained stable, and no sign of perishing or leakage of the core could be observed during normal handling.

Subsequently, we performed compressive stress testing to quantify the mechanical strength of the cured capsules. For compressive stress testing, the cured capsule is first placed on a clean glass slide with its flatter top interface facing the glass slide. Subsequently, the load cell with a maximum load capacity of 1000 N is brought close to the capsule. Then the load cell is made to traverse downward at a velocity of 0.05 mm/s using the tribometer's computer-controlled program, which leads to squeezing the capsule. The reaction force, $\boldsymbol{F_z}$, is recorded by the load cell as a function of the traversal distance, z. The reaction force, $\boldsymbol{F_z}$ is directed upward, opposite to the direction of z (downward). That is why $\boldsymbol{F_z}$ carries a negative sign.

We first study the influence of the variation of V_{core} on the resulting mechanical properties of the capsules (Figures 3.5C, 3.5D) while maintaining $V_{PDMS} = 1000$ μl. The core

volume was varied in a range 50 μl $\leq V_{core} \leq$ 250 μl. As we can see in Figure 3.5C, $|\boldsymbol{F}_z|$ increases initially with increasing z. However, at one point, a sharp reduction in $|\boldsymbol{F_z}|$ could be observed. We confirmed that this point corresponds with the rupture of the shell, which leads to leakage of the trapped liquid core. The trapped liquid gets pressurized as the load cell squeezes the capsule. Eventually, rupture leads to a sudden release of this pressure which manifests in a sharp reduction in the reaction force. Point R, marked in Figure 3.5C, indicates the point of rupture. The absolute magnitude of the reaction force recorded at the point of rupture is termed the crushing force ($\boldsymbol{F_{cr}}$). After the sudden reduction in $|\boldsymbol{F_z}|$ immediately following the rupture, $|\boldsymbol{F}_z|$ again start increasing with increasing z as the load cell continues compressing the broken capsule until the maximum load capacity of 1000 N is reached. In Figure 3.5C, two distinct trends can be observed in the $\boldsymbol{F}_z$ vs. z plots with varying V_{core}. First, at a higher V_{core}, the slope of the $\boldsymbol{F}_z$ vs. z curve before rupture is low. This is because a higher volume fraction of the liquid core in the cured capsule leads to a more deformable capsule. As a result, during the downward traversal of the load cell, the capsule gets deformed relatively easily, leading to dissipation of the downward applied compressive load. Consequently, in the case of a higher V_{core}, the load cell experiences a lower upward reaction force, $\boldsymbol{F}_z$, for the same traversal distance, z, compared to capsules with a lower V_{core}, which is reflected in the slope of the $\boldsymbol{F}_z$ vs. z curves. Second, $\boldsymbol{F}_{cr}$ decreases with increasing V_{core}. For the same V_{PDMS}, increasing V_{core} corresponds to a lower volume fraction of the solidified shell material in the cured capsule (i.e., a thinner shell). It leads to a lower resistance to crushing under compressive load, which is manifested in the reducing trend of $\boldsymbol{F}_{cr}$ with increasing V_{core}. We further estimate the crushing strength (pressure), P_{cr}, by dividing $\boldsymbol{F}_{cr}$ with the projected cross-sectional area of the droplet as follows, $P_{cr} = \frac{4*F_{cr}}{\pi D_{proj}^2}$. The projected diameter, D_{proj} of the capsule is obtained from the experimental image of the cured capsule, as shown in the inset of Figure 3.5C. Both P_{cr} and $\boldsymbol{F}_{cr}$ are plotted side-by-side in the form of a bar graph in Figure 3.5D for the three different V_{core} values reported here, and we notice a consistent, sharp reducing trend of both parameters with increasing V_{core}. Note that there is a practical limitation on the maximum allowable core volume, V_{core} that can be encapsulated via interfacial trapping, which depends on the density of the core liquid, ρ_1 and the volume of the interfacial PDMS layer, V_{PDMS}. For example, in our experiments involving laser oil as

the core droplet (ρ_1= 1900 kg/m^3), we observed that for V_{PDMS}= 1000 μl, if we increase V_{core} beyond 250 μl, the floating interfacial layer cannot sustain the weight of the dispensed core drop and ultimately sags down to the bottom of the cuvette. In the process, the core droplet detaches from the interfacial layer and forms a standalone underwater encapsulated droplet similar to those produced by method 1 (i.e., complete interfacial penetration).

To understand the relative influence of the variation of core and interfacial layer volume on the resulting mechanical properties of the cured capsules, we have additionally performed experiments where we have kept V_{core} fixed at 150 μl and varied V_{PDMS} in the range of 500 μl$\leq V_{PDMS} \leq$1000 μl. The recorded force ($\boldsymbol{F}_z$) vs. displacement of the load cell (z) plots with varying V_{PDMS} is shown in Figure 3.5E, while Figure 3.5F summarizes the variation of crushing force, $\boldsymbol{F}_{cr}$, and crushing strength, P_{cr} with different tested V_{PDMS}. It is evident that the change in V_{PDMS} has a much less pronounced effect on the mechanical properties of the cured capsules in comparison to changes in V_{core}. As we increased V_{PDMS} from 500 μl to 1000 μl, $\boldsymbol{F}_{cr}$ undergoes a slight increment of $\sim$ 18.1 %. The higher sensitivity of $\boldsymbol{F}_{cr}$ and P_{cr} towards V_{core} is not a surprising outcome. Any change in V_{core} is directly manifested in its entirety in the morphology of the interfacially trapped capsule. On the contrary, V_{PDMS} being the volume of the floating interfacial layer and not the shell volume of the trapped cargo, changes in V_{PDMS} is reflected over the entire surface area of the interfacial layer (which can be assumed equal to the free-surface area of the host bath). As we are utilizing only a small fraction (< 10 %) of the free surface area of the interfacial layer to generate the interfacially trapped capsules, the effect of changing V_{PDMS} on the morphology of the resulting capsules remains significantly less pronounced. To elaborate, V_{core}= 150 μl, the projected cross-sectional area of the trapped capsules is $\sim$ 70 mm^2 which is $\sim$ 5.4 % of the total surface area of the interfacial layer, given the inner dimension of the cuvette housing the host bath, and the interfacial layer is 36 mm x 36 mm. Therefore if we assume uniform spreading47 of PDMS on water, for an increase of 500 μl to 1000 μl, the effective increase of shell volume of the encapsulated cargo can be roughly estimated to be only $\sim$ 27 μl. This explains the lower sensitivity of mechanical properties toward changing V_{PDMS}. These results and the associated discussions serve as design guidelines for developing interfacially trapped capsules with varied hardness via varying V_{core} and/or V_{PDMS}.

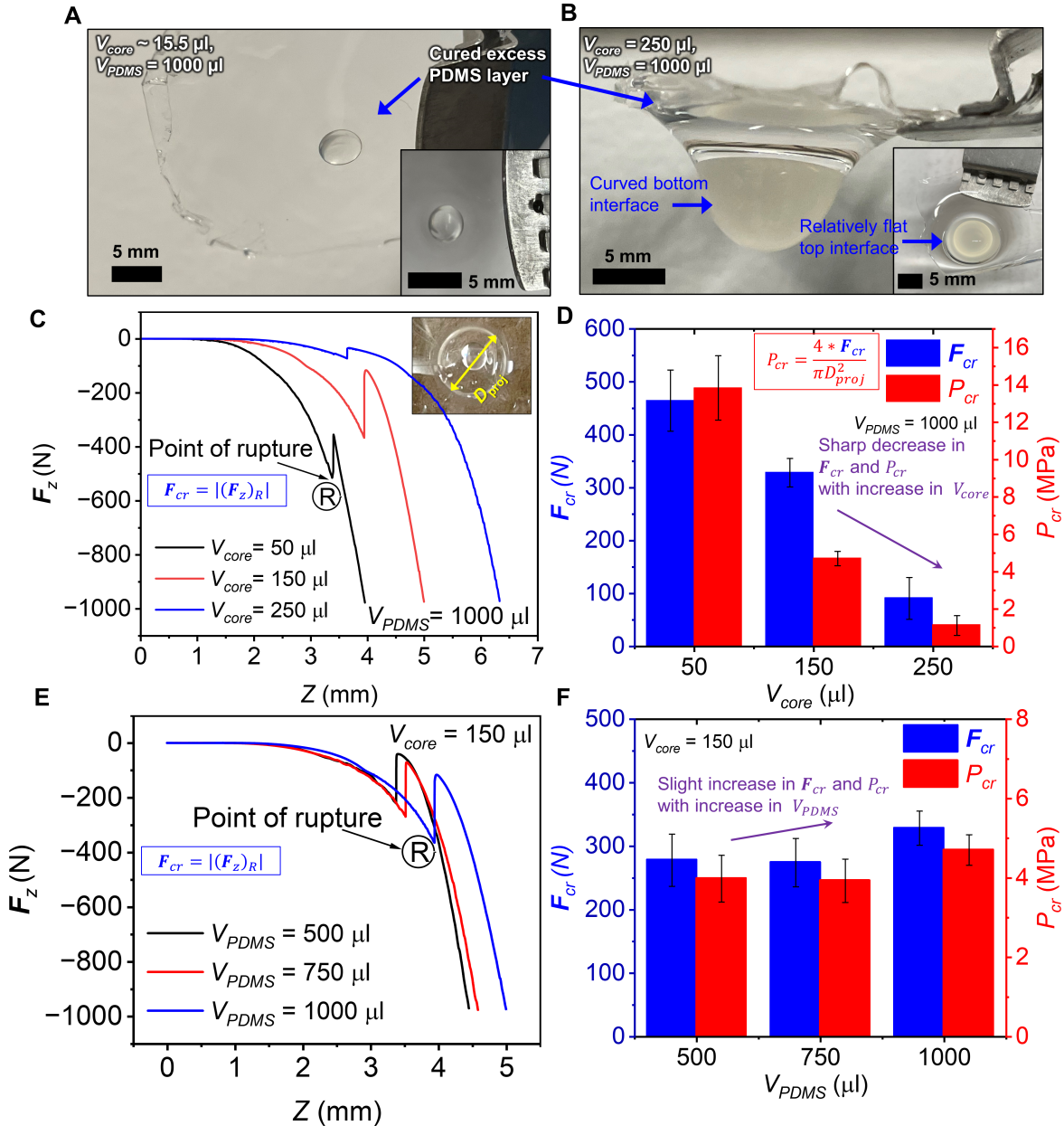

Figure 3.5: Curing and mechanical characterization of the interfacially trapped (method 2) capsules - (A-B) shows the images of the cured capsules containing laser oil core wrapped in a PDMS layer with $V_{core} \sim 15.5$ μl and 250 μl, respectively. The volume of the PDMS interfacial layer is kept fixed at $V_{PDMS} = 1000$ μl. (...continuing to the next page)

Figure 3.5: (...continued from the previous page) (B) shows the side-view of the cured capsule, while the capsule had to be tilted upward while capturing the image presented in (A), as the side-view projection could not reveal the contour of the encapsulated drop owing to the smaller size of the core drop. The insets show the corresponding top views of the cured capsules. (C-D) report the mechanical characterization of the cured capsules of varying V_{core} with V_{PDMS} fixed at 1000 μl. (C) shows the plots of reaction force, $\boldsymbol{F}_z$ vs. traversal distance, z recorded by a load cell on a tribometer during compression testing of cured capsules for three different V_{core} with a fixed V_{PDMS}. (D) tabulates the crushing force, $\boldsymbol{F}_{cr}$, and crushing strength, P_{cr} of the capsules corresponding to the data presented in (C). (E-F) discusses the compression testing of the cured capsules with varying V_{PDMS} while V_{core} is kept fixed at 150 μl. (E) shows the variation of reaction force, $\boldsymbol{F}_z$ vs. traversal distance, z recorded by a load cell on a tribometer during compression testing of cured capsules for three different V_{PDMS} values with a fixed V_{core}. (F) summarizes the crushing force, $\boldsymbol{F}_{cr}$, and crushing strength, P_{cr} of the capsules corresponding to the data presented in (E). The error bars reported in (D) & (F) indicate the standard deviation of $\boldsymbol{F}_{cr}$ and, P_{cr} of at least three independent measurements carried out on three different capsules for each data point.

However, it is understandable that in some cases, one might want to tune the hardness of capsules while not varying the core/shell volumes. The tunable mechanical properties of PDMS can be leveraged in this regard. It is well established in literature [53, 54] that by changing the mixing ratio of the base elastomer and the curing agent, the stiffness of PDMS can be varied over a broad range. Seghir *et al.* [53] showed that the stiffness of PDMS (tangent modulus) could be varied from 800 kPa to 10 MPa by changing the base elastomer to curing agent mixing ratio between 19:1 to 2:1 and the curing conditions. It directly influences the rupture limit. In our case, we can leverage this dependence to tune the mechanical strength of our capsules by suitably varying the mixing ratio. It will allow us to achieve the desired hardness/softness over a broad range without having to change the core/shell volumes.

The interfacial trapping approach demonstrated herein is minimally restrictive in terms

of allowable core-shell portfolio. As long as the participating liquid triplet (core, interfacial layer and host bath) adhere to the thermodynamic thresholds identified in subsection 3.4.2, we can generate interfacially trapped droplets. However, the practical applicability of the interfacially trapped state depends upon the curability of the interfacial layer, which allows subsequent extraction of the enclosed cargo. Therefore, choosing an interfacial liquid that can subsequently be cured is essential. In the present work, the heat curability of PDMS was leveraged in this regard. However, subject to adherence to the identified thermodynamic thresholds, other shell-forming materials can also be used as the interfacial layer. Starch-based biopolymers [55] or thiol-ene biopolymers [56] could be interesting alternative shell materials to explore, especially due to their tunable mechanical properties. Also, if intended for food/drug applications, the acceptability of chosen shell-forming liquid in such applications, including biocompatibility, biodegradability, and non-toxicity, must be thoroughly assessed. In this work, we have demonstrated heating-driven shell hardening of the interfacially trapped droplets with PDMS shell and subsequent release of the entrapped core via mechanical deformation. Suitable functionalization of the PDMS shell to achieve additional stimuli-responsiveness [57] remains an exciting future scope of this work.

We should also mention here that although we have demonstrated the approach to form one encapsulated droplet per cuvette, the method can be readily scaled up by increasing the surface area of the cuvette. Note that we adopted a sequential core droplet dispensation approach while generating the multicomponent compound droplets presented in Figure 3.4C. Once the first droplet is dispensed on the interfacial layer, it gives rise to a downward curvature in the interfacial layer due to its weight. Owing to this curvature, when the subsequent droplets are dispensed in the proximity of the first dispensed drop, they all migrate towards the first droplet leading to the formation of a multicomponent encapsulated droplet with the same outer wrapping shell, as shown in Figure 3.4C. However, depending on the requirement, the approach can be tweaked by dispensing multiple core droplets using multiple injection syringes with a predefined in-plane separation. Due to simultaneous dispensation, the dispensed drops will not experience the curvature effect and, therefore, will be interfacially trapped at the original place of dispensation without migrating towards each other. It will enhance the utilization of the available surface area and will subsequently reduce PDMS consumption and the associated cost. Here we provide

a simple engineering estimate. In our lab-scale experiments performed in a cuvette with an inner cross-section of 36 mm x 36 mm, we have shown that we can generate sufficiently robust capsules with V_{core}= 50 μl for V_{PDMS}= 500 μl. If we scale the cross-section of the host cuvette up to 30 cm x 30 cm, we can estimate that we can achieve the same effective interfacial layer thickness with a PDMS volume of $\sim$ 35 ml owing to the near-uniform spreading of PDMS on water [47]. We have measured that for laser oil as the core liquid, a core droplet with a volume of 50 μl will have a projected diameter onto the interfacial layer of $\sim$ 6.5 mm. Suppose we allow for an inter-droplet spacing of 5 mm and leave a gap of 7.5 mm all along the wall of the cuvette to avoid near wall curvature effects. In that case, we can estimate that we will be able to simultaneously generate 625 interfacially trapped capsules by utilizing the entire available surface area of the host bath. A recent purchase price of PDMS $\sim$ 200 CAD per 0.5 kg will correspond to a per capsule production cost for the shell material of just above 2 cents, which affirms the economy of scale of our method.

3.5 Conclusions

In summary, this work demonstrates a platform for the fabrication of robust multifunctional capsules with core-shell morphology using a simple, rapid, impact-driven liquid-liquid encapsulation framework. Depending on the kinetic energy of impact, $\boldsymbol{KE}_{impact}$ (manifested in the impact Weber number, We_i), encapsulation can be achieved either by interfacial penetration or via interfacial trapping. A complex interplay between the force associated with the momentum, $\boldsymbol{F}_{\boldsymbol{KE}}$, the viscous dissipation, $\boldsymbol{F}_{\boldsymbol{visc}}$, and the restorative interfacial tension force, $\boldsymbol{F}_{\boldsymbol{\gamma}}$ acting on the deformed interfacial layer-host bath interface, dictate the pathway towards encapsulation. Encapsulation via interfacial penetration consists of two sequential steps - rapid cusp elongation and consequent fast thinning of the PDMS neck followed by a slow viscoelastic thinning stage which ultimately leads to complete necking and separation of the encapsulated cargo from the interfacial layer. On the contrary, for interfacial trapping, although the interfacial layer-host bath interface undergoes an initial downward elongation phase, the interface retracts upward toward its initial unperturbed state due to $\boldsymbol{F}_{\boldsymbol{\gamma}}$ once $\boldsymbol{KE}_{impact}$ is dissipated by the viscous resistance. We present a non-dimensional experimental regime for the occurrence of both cases in terms of

We_i and the non-dimensional interfacial layer thickness (δ/R_c). We also identify a critical Weber number, We_{cr}, as a function of δ that demarcates the two outcomes. However, we show that in either of the cases, the resulting configuration is an encapsulated state where the interfacial layer wholly encloses the core droplet. It demonstrates the universality of our framework in terms of kinetic energy requirement. Further, the presented framework is minimally restrictive regarding thermophysical property requirements. Stable encapsulation can be achieved as long as the participating liquid triplet (core, shell, and host liquid) adheres to an interfacial energy criterion. We show that successful wrapping can safeguard liquid cores despite their miscibility with the host bath. We also leverage the interfacial trapping mechanism to create multifunctional compound capsules. Subsequently, the extraction of the interfacially trapped capsules is demonstrated via heat curing of the PDMS outer shell, where we confirm the robustness of the wrapping layer in the cured state. We show that the interfacially trapped capsule with $V_{core} = 150$ μl and $V_{PDMS} = 1000$ μl possesses a crushing strength value of $P_{cr} \sim 4.7$ MPa. We also demonstrate that increasing V_{core} with a fixed V_{PDMS} leads to a reduction in both crushing force, $\boldsymbol{F}_{cr}$, and crushing strength, P_{cr} owing to a decrease in shell thickness in the cured capsules. To the best of our knowledge, this is the first time the practical utility of the interfacially trapped encapsulated state is being demonstrated. We believe the present work builds the foundation of a robust and minimally restrictive liquid-liquid encapsulation technology well suited for both commercial production and exploratory endeavors toward novel encapsulated material synthesis.

References

[1] M. Singh, K. Hemant, M. Ram, and H. Shivakumar, "Microencapsulation: A promising technique for controlled drug delivery," *Research in Pharmaceutical Sciences*, vol. 5, no. 2, pp. 65–77, 2010.

[2] J. L. de Oliveira, E. V. R. Campos, M. Bakshi, P. C. Abhilash, and L. F. Fraceto, "Application of nanotechnology for the encapsulation of botanical insecticides for sus-

tainable agriculture: Prospects and promises," *Biotechnology Advances*, vol. 32, no. 8, pp. 1550–1561, 2014.

[3] A. H. King, "Encapsulation of Food Ingredients," in *Encapsulation and Controlled Release of Food Ingredients*, vol. 590 of *ACS Symposium Series*, pp. 26–39, American Chemical Society, 1995.

[4] V. Nedovic, A. Kalusevic, V. Manojlovic, S. Levic, and B. Bugarski, "An overview of encapsulation technologies for food applications," *Procedia Food Science*, vol. 1, pp. 1806–1815, 2011.

[5] F. Casanova and L. Santos, "Encapsulation of cosmetic active ingredients for topical application – a review," *Journal of Microencapsulation*, vol. 33, no. 1, pp. 1–17, 2016.

[6] F. Wang, R. Deng, J. Wang, Q. Wang, Y. Han, H. Zhu, X. Chen, and X. Liu, "Tuning upconversion through energy migration in core–shell nanoparticles," *Nature Materials*, vol. 10, no. 12, pp. 968–973, 2011.

[7] Y. E. Milián, A. Gutiérrez, M. Grágeda, and S. Ushak, "A review on encapsulation techniques for inorganic phase change materials and the influence on their thermophysical properties," *Renewable and Sustainable Energy Reviews*, vol. 73, pp. 983–999, 2017.

[8] F. Caruso, D. Trau, H. Möhwald, and R. Renneberg, "Enzyme Encapsulation in Layer-by-Layer Engineered Polymer Multilayer Capsules," *Langmuir*, vol. 16, no. 4, pp. 1485–1488, 2000.

[9] R. Vidhyalakshmi, R. Bhakyaraj, and R. S. Subhasree, "Encapsulation "The Future of Probiotics"-A Review," p. 9, 2009.

[10] P. de Vos, M. M. Faas, M. Spasojevic, and J. Sikkema, "Encapsulation for preservation of functionality and targeted delivery of bioactive food components," *International Dairy Journal*, vol. 20, no. 4, pp. 292–302, 2010.

[11] M. Peanparkdee, S. Iwamoto, and R. Yamauchi, "MICROENCAPSULATION: A REVIEW OF APPLICATIONS IN THE FOOD AND PHARMACEUTICAL INDUSTRIES," *Reviews in Agricultural Science*, vol. 4, no. 0, pp. 56–65, 2016.

[12] P. Venkatesan, R. Manavalan, and K. Valliappan, "MICROENCAPSULATION: A VITAL TECHNIQUE IN NOVEL DRUG DELIVERY SYSTEM," *J. Pharm. Sci.*, p. 10, 2009.

[13] R. F. A. Teixeira, O. van den Berg, L.-T. T. Nguyen, K. Fehér, and F. E. Du Prez, "Microencapsulation of Active Ingredients Using PDMS as Shell Material," *Macromolecules*, vol. 47, no. 23, pp. 8231–8237, 2014.

[14] A. Simmons, A. D. Padsalgikar, L. M. Ferris, and L. A. Poole-Warren, "Biostability and biological performance of a PDMS-based polyurethane for controlled drug release," *Biomaterials*, vol. 29, no. 20, pp. 2987–2995, 2008.

[15] P. Mazurek, A. E. Daugaard, M. Skolimowski, S. Hvilsted, and A. L. Skov, "Preparing mono-dispersed liquid core PDMS microcapsules from thiol–ene–epoxy-tailored flow-focusing microfluidic devices," *RSC Advances*, vol. 5, no. 20, pp. 15379–15386, 2015.

[16] J. Huang, C. Luo, W. Li, Y. Li, Y. Shrike Zhang, J. Zhou, and Q. Jiang, "Eccentric magnetic microcapsules for orientation-specific and dual stimuli-responsive drug release," *Journal of Materials Chemistry B*, vol. 3, no. 22, pp. 4530–4538, 2015.

[17] U. Banerjee, S. Misra, and S. K. Mitra, "Liquid–Liquid Encapsulation of Ferrofluid Using Magnetic Field," *Advanced Materials Interfaces*, vol. 9, no. 21, p. 2200288, 2022.

[18] M. P. Wolf, G. B. Salieb-Beugelaar, and P. Hunziker, "PDMS with designer functionalities—Properties, modifications strategies, and applications," *Progress in Polymer Science*, vol. 83, pp. 97–134, 2018.

[19] World Health Organization, Food and Agriculture Organization of the United Nations, and I. Joint FAO/WHO Expert Committee on Food Additives. Meeting (74th : 2011 : Rome, "Evaluation of certain food additives and contaminants: seventy-fourth [74th] report of the Joint FAO/WHO Expert Committee on Food Additives," 2011.

[20] EFSA Panel on Food Additives and Flavourings (FAF), M. Younes, G. Aquilina, L. Castle, K.-H. Engel, P. Fowler, M. J. Frutos Fernandez, P. Fürst, R. Gürtler, U. Gundert-Remy, T. Husøy, M. Manco, W. Mennes, S. Passamonti, R. Shah, D. H. Waalkens-Berendsen, D. Wölfle, M. Wright, P. Boon, P. Tobback, A. Giarola, A. M. Rincon, A. Tard, and P. Moldeus, "Re-evaluation of dimethyl polysiloxane (E 900) as a food additive," *EFSA Journal*, vol. 18, no. 5, p. e06107, 2020.

[21] T. C. Dahl and I. T. Sue, "The Effects of Heat and Desiccation Treatment on the Controlled Release Properties of Aqueous Silicone Latex Coated Tablets," *Drug Development and Industrial Pharmacy*, vol. 16, no. 14, pp. 2097–2107, 1990.

[22] L. C. Li and G. E. Peck, "Water Based Silicone Elastomer Controlled Release Tablet Film Coating 1: Free Film Evaluation," *Drug Development and Industrial Pharmacy*, vol. 15, no. 1, pp. 65–95, 1989.

[23] J. Schulze Nahrup, Z. M. Gao, J. E. Mark, and A. Sakr, "Poly(dimethylsiloxane) coatings for controlled drug release—polymer modifications," *International Journal of Pharmaceutics*, vol. 270, no. 1, pp. 199–208, 2004.

[24] J. Huang, W. Li, Y. Li, C. Luo, Y. Zeng, Y. Xu, and J. Zhou, "Generation of uniform polymer eccentric and core-centered hollow microcapsules for ultrasound-regulated drug release," *Journal of Materials Chemistry B*, vol. 2, no. 39, pp. 6848–6854, 2014.

[25] J. Huang, W. Huang, Y. Chen, Y. S. Zhang, J. Zhong, Y. Li, and J. Zhou, "Eccentric magnetic microcapsules for MRI-guided local administration and pH-regulated drug release," *RSC Advances*, vol. 8, no. 73, pp. 41956–41965, 2018.

[26] L. C. Li and G. E. Peck, "Water Based Silicone Elastomer Controlled Release Tablet Film Coating III - Drug Release Mechanisms," *Drug Development and Industrial Pharmacy*, vol. 15, no. 12, pp. 1943–1968, 1989.

[27] T. C. Dahl and I.-I. T. Sue, "Mechanisms to Control Drug Release from Pellets Coated with a Silicone Elastomer Aqueous Dispersion," *Pharmaceutical Research*, vol. 9, no. 3, pp. 398–405, 1992.

[28] V. Carelli, G. Di Colo, E. Nannipieri, and M. F. Serafini, "Evaluation of a silicone based matrix containing a crosslinked polyethylene glycol as a controlled drug delivery system for potential oral application," *Journal of Controlled Release*, vol. 33, no. 1, pp. 153–162, 1995.

[29] Z. Gao, J. S. Nahrup, J. E. Mark, and A. Sakr, "Poly(dimethylsiloxane) coatings for controlled drug release. i. preparation and characterization of pharmaceutically acceptable materials," *Journal of Applied Polymer Science*, vol. 90, no. 3, pp. 658–666, 2003.

[30] B. Ratner, C. Kwok, K. Walline, E. Johnston, and R. Miller, "Silicone blends and composites for drug delivery," 2006.

[31] O. Nguon, F. Lagugné-Labarthet, F. A. Brandys, J. Li, and E. R. Gillies, "Microencapsulation by *in situ* Polymerization of Amino Resins," *Polymer Reviews*, vol. 58, no. 2, pp. 326–375, 2018.

[32] A. Gharsallaoui, G. Roudaut, O. Chambin, A. Voilley, and R. Saurel, "Applications of spray-drying in microencapsulation of food ingredients: An overview," *Food Research International*, vol. 40, no. 9, pp. 1107–1121, 2007.

[33] K. Dewettinck and A. Huyghebaert, "Fluidized bed coating in food technology," *Trends in Food Science & Technology*, vol. 10, no. 4-5, pp. 163–168, 1999.

[34] Y. P. Timilsena, T. O. Akanbi, N. Khalid, B. Adhikari, and C. J. Barrow, "Complex coacervation: Principles, mechanisms and applications in microencapsulation," *International Journal of Biological Macromolecules*, vol. 121, pp. 1276–1286, 2019.

[35] R. Ciriminna and M. Pagliaro, "Sol–gel microencapsulation of odorants and flavors: opening the route to sustainable fragrances and aromas," *Chemical Society Reviews*, vol. 42, no. 24, p. 9243, 2013.

[36] I. G. Loscertales, A. Barrero, I. Guerrero, R. Cortijo, M. Marquez, and A. M. Gañán-Calvo, "Micro/Nano Encapsulation via Electrified Coaxial Liquid Jets," *Science*, vol. 295, no. 5560, pp. 1695–1698, 2002.

[37] S. L. Anna, N. Bontoux, and H. A. Stone, "Formation of dispersions using "flow focusing" in microchannels," *Applied Physics Letters*, vol. 82, no. 3, pp. 364–366, 2003.

[38] A. S. Utada, E. Lorenceau, D. R. Link, P. D. Kaplan, H. A. Stone, and D. A. Weitz, "Monodisperse Double Emulsions Generated from a Microcapillary Device," *Science*, vol. 308, no. 5721, pp. 537–541, 2005.

[39] L.-Y. Chu, J.-W. Kim, R. K. Shah, and D. A. Weitz, "Monodisperse Thermoresponsive Microgels with Tunable Volume-Phase Transition Kinetics," *Advanced Functional Materials*, vol. 17, no. 17, pp. 3499–3504, 2007.

[40] V. Barbier, M. Tatoulian, H. Li, F. Arefi-Khonsari, A. Ajdari, and P. Tabeling, "Stable Modification of PDMS Surface Properties by Plasma Polymerization: Application to the Formation of Double Emulsions in Microfluidic Systems," *Langmuir*, vol. 22, no. 12, pp. 5230–5232, 2006.

[41] T. Nisisako, S. Okushima, and T. Torii, "Controlled formulation of monodisperse double emulsions in a multiple-phase microfluidic system," *Soft Matter*, vol. 1, no. 1, p. 23, 2005.

[42] U. Banerjee, S. K. Jain, and A. K. Sen, "Particle encapsulation in aqueous ferrofluid drops and sorting of particle-encapsulating drops from empty drops using a magnetic field," *Soft Matter*, vol. 17, no. 24, pp. 6020–6028, 2021.

[43] S. Misra, K. Trinavee, N. S. K. Gunda, and S. K. Mitra, "Encapsulation with an interfacial liquid layer: Robust and efficient liquid-liquid wrapping," *Journal of Colloid and Interface Science*, vol. 558, pp. 334–344, 2020.

[44] S. MITRA, N. S. K. GUNDA, S. Misra, and K. Trinavee, "Liquid encapsulation method and compositions and uses related thereto," 2022.

[45] S. Yin, Y. Huang, X. Shen, C. Zhang, X. Chen, Marcos, H. Li, and T. Neng Wong, "Triple-layered encapsulation through direct droplet impact," *Journal of Colloid and Interface Science*, vol. 615, pp. 887–896, 2022.

[46] V. P. Carey, *Liquid-Vapor Phase-Change Phenomena: An Introduction to the Thermophysics of Vaporization and Condensation Processes in Heat Transfer Equipment, Third Edition*. Boca Raton: CRC Press, 3 ed., 2020.

[47] D. Kim, S.-H. Kim, and J. Y. Park, "Floating-on-water Fabrication Method for Thin Polydimethylsiloxane Membranes," *Polymers*, vol. 11, no. 8, p. 1264, 2019.

[48] Y. Hu, X. Chen, G. M. Whitesides, J. J. Vlassak, and Z. Suo, "Indentation of polydimethylsiloxane submerged in organic solvents," *Journal of Materials Research*, vol. 26, no. 6, pp. 785–795, 2011.

[49] J. Sebilleau, "Equilibrium Thickness of Large Liquid Lenses Spreading over Another Liquid Surface," *Langmuir*, vol. 29, no. 39, pp. 12118–12128, 2013.

[50] J. D. Smith, R. Dhiman, S. Anand, E. Reza-Garduno, R. E. Cohen, G. H. McKinley, and K. K. Varanasi, "Droplet mobility on lubricant-impregnated surfaces," *Soft Matter*, vol. 9, no. 6, pp. 1772–1780, 2013.

[51] F. Schellenberger, J. Xie, N. Encinas, A. Hardy, M. Klapper, P. Papadopoulos, H.-J. Butt, and D. Vollmer, "Direct observation of drops on slippery lubricant-infused surfaces," *Soft Matter*, vol. 11, no. 38, pp. 7617–7626, 2015.

[52] M. R. Gunjan, U. Banerjee, S. Misra, and S. K. Mitra, "Manipulation of ferrofluid wrapped drops: Translation, coalescence and release (Under Review)," 2023.

[53] R. Seghir and S. Arscott, "Extended PDMS stiffness range for flexible systems," *Sensors and Actuators A: Physical*, vol. 230, pp. 33–39, 2015.

[54] F. C. P. Sales, R. M. Ariati, V. T. Noronha, and J. E. Ribeiro, "Mechanical Characterization of PDMS with Different Mixing Ratios," *Procedia Structural Integrity*, vol. 37, pp. 383–388, 2022.

[55] L. Ceseracciu, J. A. Heredia-Guerrero, S. Dante, A. Athanassiou, and I. S. Bayer, "Robust and Biodegradable Elastomers Based on Corn Starch and Polydimethylsiloxane (PDMS)," *ACS Applied Materials & Interfaces*, vol. 7, no. 6, pp. 3742–3753, 2015.

[56] T. O. Machado, C. Sayer, and P. H. H. Araujo, "Thiol-ene polymerisation: A promising technique to obtain novel biomaterials," *European Polymer Journal*, vol. 86, pp. 200–215, 2017.

[57] M. Delcea, H. Möhwald, and A. G. Skirtach, "Stimuli-responsive LbL capsules and nanoshells for drug delivery," *Advanced Drug Delivery Reviews*, vol. 63, no. 9, pp. 730–747, 2011.

Chapter 4

Liquid-liquid encapsulation with magnetoresponsive shell: Translation, coalescence and cargo release [1]

4.1 Overview

Magnetic manipulation of droplets has emerged as a promising strategy to achieve several complex tasks ranging from targeted drug delivery and micro-robotics to controlled chemical synthesis. In this regard, proper control in creating magnetically responsive droplets is indispensable for successful implementation. Here, an impact-based encapsulation technique is employed to create stable ferrofluid-wrapped single liquid droplets and compound droplets inside a water bath. Thereafter, a permanent magnet is used to manipulate the resulting encapsulated cargo and demonstrate its feasibility for various applications. The manipulations reported herein are underwater magnet-assisted drop translation and coalescence of compound droplets. The release of the innermost cargo in the compound droplet is also experimentally demonstrated via magnetic actuation. Importantly, for the first time, magnetically controlled coalescence of ferrofluid encapsulated

[1] Adapted from Gunjan, M.R.*, Banerjee, U*, **Misra, S***, Mitra, S.K., under review (manuscript id: admi.202300144) in *Advanced Materials Interfaces*. *: Equally contributing first-authors

compound droplets containing water-soluble species in a water pool is demonstrated. The non-contact manipulation technique presented in this work promises significant implications for magnet-assisted actuation technologies.

4.2 Introduction

Manipulation of droplets has recently gained immense attention from the research community owing to its application in microfluidics systems [1–8], drug delivery [9–12], controlled reactions [1, 13–16], DNA analysis [17, 18], and microfabrication [19, 20], among others. In this regard, significant effort has been directed toward the development of droplet manipulation/actuation techniques using active stimulus. The various active techniques comprise electric field [21], acoustic waves [22, 23], thermal gradient [24], optical actuation [25], and magnetic field [6, 13, 26–28]. However, despite the advancements, most of the strategies mentioned above suffer from inherent design complexities. For example, manipulation *via* an electric field necessitates the incorporation of a complex electrode array along with a digital device [12, 21, 29]. Similarly, as noted by Huang *et al.* [12], acoustic actuation requires compatible materials with reflecting properties and demands a complex fabrication of the device. While optical methods facilitate non-contact manipulation, they suffer from low throughput and can cause chemical changes due to photosensitivity. Thermally actuated droplet migration requires continuous heat flux as well as wettability gradient surfaces and thus has limited maneuverability [24].

Alternatively, magnetic manipulation is a relatively simple and easy-to-implement strategy, which has become quite popular due to the non-contact control of droplets [26, 30–35]. The presence of magnetically responsive agents inside or on the droplet's surface makes it easily maneuverable [36]. Unlike other techniques, magnetic systems lead to minimum heat generation in the case of electromagnets and no heat generation in the case of permanent magnets. Owing to the high saturation magnetization, better stability, and low toxicity of magnetic nanoparticles (MNPs) [10, 11, 37, 38], the droplets are loaded with magnetic nanoparticles, which is commonly referred to as an MNP-laden droplet [12], or by coating its surface with a magnetic powder, which is popularly known as magnetic liq-

uid marble (MLM) [12, 15, 39–42]. Conversely, ferrofluids, which are colloidal suspensions of magnetic nanoparticles in a base fluid, have emerged as a popular choice in magnetic manipulation systems [12, 43]. Ferrofluid manipulation finds application in liquid cargo transportation [44–46], micro-lens fabrication [19, 20], droplet sorting [13, 34, 47], controlled chemical synthesis [13], oil recovery [48], among others. Importantly, it has been shown that manipulation of encapsulated magnetic cargo can be used for targeted drug delivery for therapeutic applications [10, 11, 49–51]. For example, Kato *et al.* [50] showed that magnetic microcapsules containing anticancer drugs could be successfully manipulated to deliver the medicine at the tumor site. Chen *et al.* [10] fabricated magnetic nanocapsules consisting of nano iron core encapsulated by a mesoporous silica shell. The space between the shell and the iron core was loaded with an anti-cancer drug. The drug was then controllably released by varying the pH of the outermost silica shell. The applications mentioned above demand the encapsulation of the target cargo (core) by a magnetic layer or encapsulation of magnetic fluids inside a non-magnetic shell, such that it can be manipulated by magnetic forces. In this regard, a robust and efficient encapsulation technique should facilitate strong protection of the core from the aggressive environment and provide stability to the encapsulated cargo. It should also facilitate a wider range of core and shell volume as required. In this regard, the research community has investigated various encapsulation techniques for magnetic fluids which include phase-separation [48, 52], microfluidics [8, 34, 47, 53], and emulsification [54].

Recently, Banerjee *et al.* [55] from our group demonstrated a facile magnet-assisted framework that facilitates the encapsulation of multiple ferrofluid droplets inside a thin polydimethylsiloxane (PDMS) shell. Their technique uses a magnet to pull the ferrofluid (FF) droplets through a thin PDMS layer floating on a water pool. It is observed that the PDMS acts as a durable shell that prevents coalescence of the ferrofluid droplets and also protects the ferrofluid core (miscible with water) which remains stable in the water bath. The study has also demonstrated the magnet-assisted underwater manipulation of the encapsulated cargo, affirming the stability and integrity of the wrapping. While most of the literature is dedicated to the encapsulation of ferrofluids inside another liquid, studies related to the encapsulation of non-magnetic liquids by ferrofluids are scarce. Note that, non-magnetic droplets wrapped by a thin ferrofluid shell can be of immense practical

relevance as they can impart manipulability to non-magnetic cargo with a small volumetric doping of magneto-responsive liquid. A non-magnetic droplet encapsulated inside a ferrofluid shell is analogous to a magnetic liquid marble (MLM), which is a droplet coated with ferromagnetic particles. MLMs have been shown to facilitate controlled chemical reactions [15], micro-mixing [1], on-demand wrapping and unwrapping of the magnetic coating [39]. However, despite the interfacial analogies between magnetic liquid marbles and ferrofluid encapsulated droplets, the latter remains much less explored. Importantly, MLMs suffer from the lack of mechanical robustness [56] due to interfacial breakage and particle jamming and thus have limited magnetic maneuverability. A survey of relevant papers on magnetic manipulation reveals that most of the effort is directed toward the manipulation of ferrofluid droplets and the fabrication of MLMs and MNP-Laden droplets. Few of the studies [42, 57], report the magnetic actuation of liquid metal droplets.

Herein, we demonstrate the underwater magnet-assisted manipulation of ferrofluid-wrapped droplets. The encapsulation of the core liquid (laser oil) inside the oil-based ferrofluid is achieved by using the robust impact-driven liquid-liquid encapsulation technique developed by our group [58]. In that work, Misra *et al.* [58] exploited the thermodynamically favorable tendency of a liquid-triplet to demonstrate impact-driven stable and ultrafast encapsulation by impinging a target core analyte on the interfacial layer of a shell-forming liquid floating on the pool of another host liquid. This technique is further utilized by Yin *et al.*[59] for the fabrication of triple-layered encapsulated droplets, indicating the robustness of the technique. Here, based on the above-mentioned technique, the droplets of laser oil are allowed to impact the interfacial layer (oil-based ferrofluid) floating on a quiescent water pool resulting in the formation of the ferrofluid-wrapped droplets inside the water bath. Thereafter, we employ a cubic Neodymium permanent magnet fixed on a computer-controlled linear translator to demonstrate the post-encapsulation manipulation of the encapsulated cargo. Under the manipulations, we demonstrate the underwater magnet-assisted transportation of the encapsulated cargo and its characteristics. We show that the ferrofluid layer protecting the laser oil (core) plays a significant role in the manipulation of the encapsulated cargo. We further demonstrate the stability of the ferrofluid layer (shell) by wrapping and unwrapping the ferrofluid shell using the magnetic field.

Further, we exploit the magnetic manipulability of the encapsulated cargo to design

and demonstrate a novel platform for controlled actuation, coalescence of water-soluble analyte and the release of the cargo inside a water bath. This system bears a high degree of practical relevance in controlled reactions, drug targeting, and release. We use ethylene glycol (EG) as the model water-soluble analyte. We first enclose the EG droplet inside a carrier droplet of laser oil using a Y-junction flow arrangement and then encapsulate the laser oil - EG compound droplet with a ferrofluid shell layer using the same impact-driven liquid-liquid encapsulation technique [58]. Subsequently, we use controlled actuation of an external permanent magnet to manipulate the compound cargo and demonstrate on-demand coalescence which allows controlled mixing of the inner EG core without perishing in the surrounding aqueous medium. Finally, we show the release of the EG core inside the water bath using the magnetic field. The necessity of employing carrier droplets in this platform and the rationale behind its selection are elaborated in subsection 4.4.1. To the best of our knowledge, this is a first-time demonstration of the controlled coalescence of the encapsulated compound droplets *via* magnetic manipulation.

4.3 Experimental Section

Materials

The materials used in this work and their relevant properties are mentioned as follows. The core droplet of laser oil (Cargille Laboratories Inc., Cedar Grove, NJ, USA) has a density $\rho_{lo} = 1900$ kg m^{-3}, dynamic viscosity $\mu_{lo} = 1024$ mPa s, and liquid-air surface tension $\gamma_{lo} = 50$ mN m^{-1}. The host liquid is deionized water (Milli-Q, Millipore Sigma, Ontario, Canada) with density $\rho_w = 1000$ kg m^{-3}, dynamic viscosity $\mu_w = 1$ mPa s, and liquid-air surface tension $\gamma_w = 72$ mN m^{-1}. A commercially available oil-based ferrofluid (EMG900, Ferrotec, USA) with density $\rho = 1740$ kg m^{-3} is mixed with a solvent (density 790 kg m^{-3}) in the volumetric ratio of 1:10 (ferrofluid: solvent). The density of the prepared 10-fold diluted ferrofluid suspension used as the interfacial layer is $\rho_{ff} = 885$ kg m^{-3}. The surface tension of the interfacial layer in the air $\gamma_{ff} = 25.7$ mN m^{-1} and in water $\gamma_{ff-w} = 23.6$ mN m^{-1}. The laser oil-water interfacial tension $\gamma_{lo-w} = 39.4$ mN m^{-1}. The laser oil-ferrofluid interfacial tension $\gamma_{lo-ff} = 4$ mN m^{-1} is calculated using the interfacial

tension formula for non-polar liquids as $\gamma_{lo-ff} = \gamma_{lo} + \gamma_{ff} - 2\sqrt{\gamma_{lo}\gamma_{ff}}$ [60]. Ethylene glycol is purchased from Sigma-Aldrich, USA which has a density $\rho_{gly} = 1110$ kg m^{-3}, dynamic viscosity $\mu_{gly} = 16.1$ mPa s, and liquid-air surface tension $\gamma_{gly} = 48.6$ mN m^{-1}. Distortion free glass cuvettes are purchased from cuvet.co (Hong Kong) with inner dimensions 50 mm x 50 mm x 50 mm.

Method

Figure 4.1 shows the schematic of the experimental setup for the underwater generation of ferrofluid-wrapped droplets. Before each experiment, we thoroughly clean the glass cuvette by dipping it in a glass beaker containing hexane, followed by ultrasonication (Branson 5800, Emerson Electric Co., USA) for 30 minutes. Thereafter, the cuvette is thoroughly rinsed with DI water and acetone, followed by drying with compressed nitrogen. Next, we treat the cleaned cuvette in air plasma (PE-25, PLASMA ETCH, USA) for 10 minutes. Then cuvette is placed over a vertically movable stage (Kruss GmbH, Hamburg, Germany). At first, the cuvette is partially filled with host liquid (DI water, 90 ml), resulting in a water column height of ~ 36 mm. Then, 200 μl of the 10-fold diluted oil-based ferrofluid suspension was dispensed on the host bath using a pipette (DiaPETTE, Canada) which is allowed to spread uniformly on the water surface, leading to the formation of the floating interfacial layer (i.e., which acts as the shell layer).

Single droplet generation

Figure 4.1a shows the impact of a laser oil droplet on the interfacial layer. In this case, the laser oil droplets are dispensed using a disposable flat-tipped stainless needle (gauge 14, part no. 7018035, Nordson EFD, USA) having an inner diameter of 1.53 mm attached to a 1 ml NORM-JECT sterile luer-slip plastic syringe (Henke-Sass, Wolf GmbH, Germany). The syringe containing laser oil is securely affixed vertically using a retort stand and centrally positioned over the cuvette (see Figure 4.1a). Laser oil droplets of volume 15 ± 0.8 μl are dispensed using a programmable syringe pump (Chemyx Fusion 4000) at a controlled rate of 36 μL min^{-1} from a height of 5 cm.

Compound droplet generation

Figure 4.1b shows the impact of a compound droplet on the interfacial layer. Throughout the study, compound droplet indicates an ethylene glycol (EG) droplet wrapped by laser oil. To generate a compound droplet, we employ a Y-junction flow arrangement as shown in Figure 4.1b. Here, laser oil is pushed through the vertically oriented microtip (inner diameter of 2 mm) attached to a syringe, while ethylene glycol is introduced from the side using a flat-tipped stainless needle (gauge 25, part no. 7018339, Nordson EFD, USA) of internal diameter 0.25 mm mounted on a 1 ml NORM-JECT syringe. Using a programmable syringe pump (Chemyx Fusion 4000), we first introduce 0.5 μL of ethylene glycol in the laser oil microtip at a controlled rate of 3 μL min^{-1}. Then the compound droplet is dispensed by pumping laser oil using the programmable syringe pump (Chemyx Fusion 4000) at a controlled rate of 36 μL min^{-1}.

For both single and compound droplet generation, the impact height, which is the difference between the needle tip and the ferrofluid interfacial layer, is kept constant at 5 cm which corresponds to an impact Weber number $We_i = 57$ for single droplet impact and $We_i = 68$ for compound droplet impact. The impact Weber number $We_i = \frac{\rho_{lo} v^2 R_d}{\gamma_{lo}} \approx \frac{2\rho_{lo} g H R_d}{\gamma_{lo}}$ is estimated by considering the properties of laser oil droplets. Here, $v = \sqrt{2gH}$ is the velocity of impact, g is the acceleration due to gravity and H is the impact height and R_d is the radius of the droplet (assuming a spherical shape) before impact. For magnetic manipulation, we used a cubic neodymium (NdFeB) permanent magnet of size 1.27 cm (N52, remnant flux density $B_r = 1.48$ T, K&J Magnetics Inc. USA), which is placed over a movable linear translator (Zaber Technologies, Canada) and is positioned beneath the cuvette. The magnetic field is estimated using a three-dimensional numerical simulation carried out in the computational framework of COMSOL Multiphysics®. The variation of the magnetic field and the details of the COMSOL simulation are provided in Appendix B (section B.1).

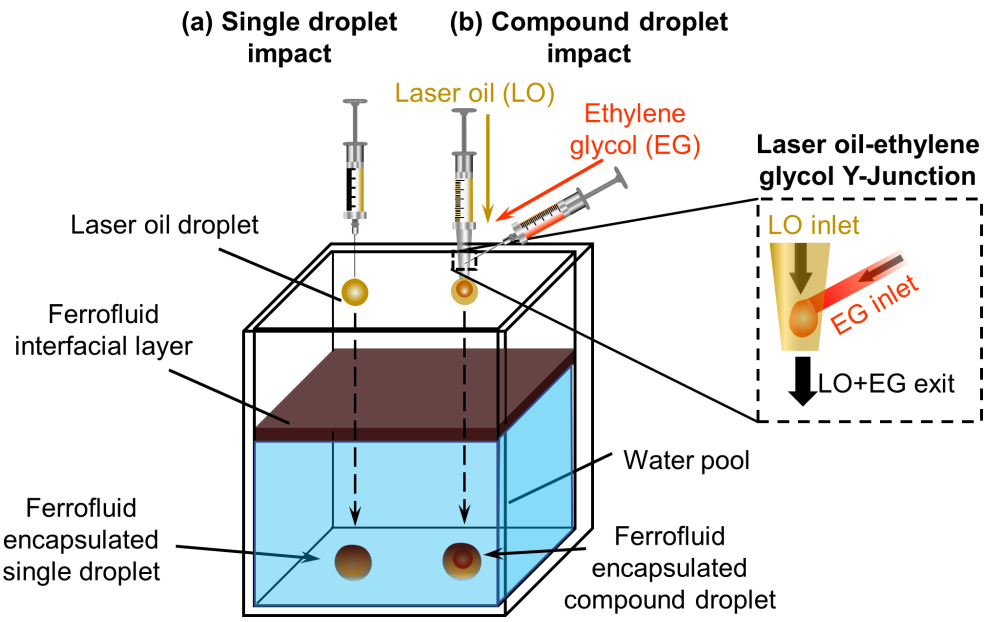

Figure 4.1: Schematic showing the (a) encapsulation of the laser oil droplet inside the ferrofluid as an interfacial layer, (b) encapsulation of the compound droplet of laser oil as the outer fluid and ethylene glycol as the inner fluid by the ferrofluid interfacial layer. Inset shows a zoomed in illustration of the Y-junction flow arrangement for generating compound droplets. Here laser oil flows through the vertically oriented microtip while ethylene glycol is introduced from the side leading to the formation of a laser oil-ethylene glycol compound droplet at the microtip exit.

The complete dynamics of the encapsulation process were captured using a high-speed camera (Photron, FASTCAM Mini AX200) coupled with a lens interfaced with a personal computer. The manipulation of the encapsulated cargo and the color images in the study are captured using a macro lens (Tokina, 100 mm F2.8 MACRO) coupled with a DSLR camera (Nikon D5200). The post-processing of the raw video files is done using an in-house MATLAB script to acquire relevant quantitative data reported here.

4.4 Results and Discussion

In this section, we discuss the impact-driven encapsulation of a single laser oil droplet and the compound droplet (EG drop engulfed within the laser oil drop) using the ferrofluid shell layer as the wrapping layer. Following that, we demonstrate the underwater magnetic manipulation of the ferrofluid-wrapped laser oil droplet by studying its transportation characteristics and the role played by the ferrofluid shell layer in the magnetic manipulation. Finally, we discuss the magnetic manipulation of the compound droplets where we studied the role of magnetic field in the underwater coalescence of two compound droplets. In addition, we also experimentally demonstrate, a sample case of release of the innermost EG core in the compound droplet. In doing so, we demonstrate a novel platform that addresses the physiologically relevant problem of controlled underwater mixing of water-soluble analytes.

4.4.1 Encapsulation of a single core droplet and compound droplet using ferrofluid wrapping layer

Figure 4.2 shows the interfacial evolution during the encapsulation process when a laser oil drop and a compound drop pierces through the interfacial layer (ferrofluid) giving rise to encapsulated droplets. The impact is captured at 5000 frames per second. In both cases, the laser oil droplet and the compound droplet are released from a height of 5 cm onto the interfacial layer. The generation process of the compound droplet remains the same as discussed in section 4.3. Owing to the sufficient kinetic energy, the droplet pierces through the interfacial layer where it overcomes the interfacial barrier offered by the ferrofluid-water interface and results in the formation of the encapsulated droplet as reported by Misra *et al* [58]. In both situations, the interface undergoes a similar evolution process as evident from the high-speed time-stamped images of Figure 4.2a and 4.2b, respectively. The color images of the final encapsulated droplets are shown in Figure 4.2a (rightmost) and Figure 4.2b (rightmost). It can be observed from the colour images that, there is a significant difference in the concentration of the magnetic nanoparticles (MNPs) between the apex and the bottom of the droplet as evident from the appearance of the dark spherical cap

at the apex of the droplet. This excess layer forms due to the extra ferrofluid volume that the droplet pulls inward during impact. Ferrofluid ($\rho_{ff} = 885$ kg m^{-3}) being lighter than water ($\rho_w = 1000$ kg m^{-3}), the excess ferrofluid accumulates at the top due to buoyancy. This excess layer plays a significant role in the magnetic manipulation of the encapsulated cargo as discussed in the subsequent sections.

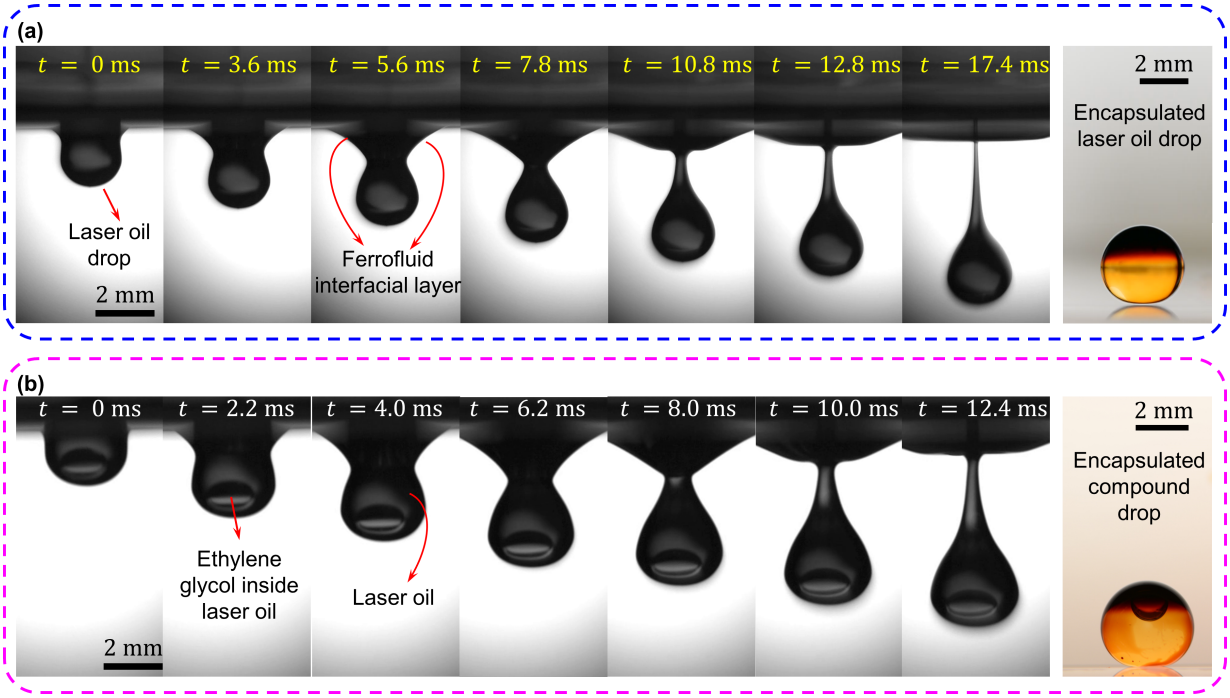

Figure 4.2: Timestamped high-speed images of the interfacial evolution during the encapsulation of (a) laser oil by the ferrofluid layer. (b) compound droplet by the ferrofluid layer. The rightmost images (colour) in both cases depict the final encapsulated cargo inside the water bath.

Misra *et al.* [58] elucidated the thermodynamic criterion for the formation of a stable encapsulated droplet. They showed that for liquid-liquid encapsulation, the interfacial tension of the participating fluids should satisfy the following criteria:

$$\gamma_{lo-ff} + \gamma_{ff-w} - \gamma_{lo} < 0 \tag{4.1}$$

$$\gamma_{lo-w} - \gamma_{lo-ff} - \gamma_{ff-w} > 0 \tag{4.2}$$

The above equations are based on surface energy minimization before and after impact and as such, depend only on the surface and interfacial tensions. If we substitute the various interfacial tensions as mentioned in the previous section in Equation (4.1) and (4.2), we get that for our combination involving laser oil (core), ferrofluid (shell) and water (host liquid):

$$(4 + 23.6 - 50)\ \text{mN m}^{-1} = -22.4\ \text{mN m}^{-1} < 0$$
$$(39.4 - 4 - 23.6)\ \text{mN m}^{-1} = 11.8\ \text{mN m}^{-1} > 0$$

which satisfies both the above criteria. It is to be noted for the compound droplet, the core liquid that is playing the role in surface energy minimization during the impact-driven encapsulation process is laser oil, as in the case of the single core droplet. Thus, based on the experimental images and the fulfilment of the above-mentioned criteria, we can confirm that, the laser oil droplet is stably encapsulated inside the ferrofluid layer. In the case of a compound droplet, the droplet of ethylene glycol (marked with the red arrow in Figure 4.2b) remains stable during the interfacial evolution as evident from the high-speed images of Figure 4.2b. In addition to that, the EG droplet remains stable after encapsulation. Note that EG being lighter than laser oil ($\rho_{gly} = 1110$ kg m^{-3}, $\rho_{lo} = 1900$ kg m^{-3}) migrates to the apex of the compound droplet because of buoyancy (see the colour image, Figure 4.2b). By employing the ferrofluid interfacial layer, we fulfill two important aspects - (i) controlling the mixing of the ethylene glycol droplet (miscible in water) which affirms the robustness of the encapsulation technique and (ii) providing the magnetic responsiveness to the compound droplet which is exploited for the magnet-assisted manipulation of the compound droplet as shown in subsection 4.4.4.

4.4.2 Mechanism of droplet manipulation

Figure 4.3 represents the schematic for the manipulation of the ferrofluid-wrapped droplets. In the preceding discussions, we emphasized the role of the non-contact manipulation of droplets and how it can be useful in related applications. In this regard, the ability to controllably manipulate encapsulated droplets using a moving magnet is indispensable. Here we demonstrate the controlled actuation of the ferrofluid-wrapped droplet via two

different motions of an external permanent magnet, as shown in Figure 4.3. First, *magnet motion along the x-axis* where we fix the gap D_m between the cuvette bottom and the magnet top and translate the magnet horizontally along the x-axis. Second, *magnet motion along the z-axis* where the magnet is positioned at a fixed x-location and moved up and down along the z-axis. In both cases, the interaction between the magnetic field and the MNPs gives rise to the actuation of the ferrofluid layer, which in turn results in controlled droplet manipulation, as discussed subsequently. The variation in the magnetic field is accounted for by using the magnetic Bond number, defined as $Bo_m = \frac{\mu_0 H^2 R_d}{\gamma_{ff-w}}$ [7, 55], which is the ratio of magnetic force and interfacial tension force. Here $\mu_0 = 4\pi \times 10^{-7}$ H m^{-1} is the magnetic permeability of free space, H is the magnitude of the applied H-field (A m^{-1}), R_d is droplet radius and γ_{ff-w} is the ferrofluid-water interfacial tension. Thus, if the value of H-field (magnetic field) is known at a particular magnet height D_m, then Bo_m can be calculated. The variation of H-field of the magnet and the associated simulation details used in this work are discussed in Appendix B section B.1.

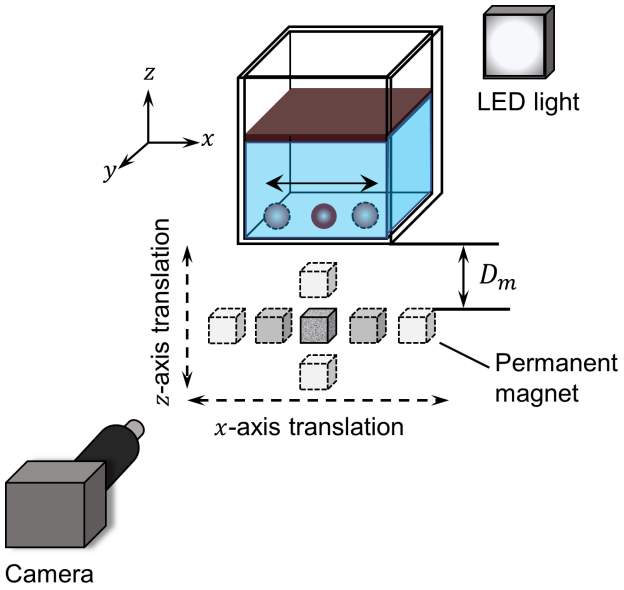

Figure 4.3: Schematic showing the experimental setup for the manipulation of the encapsulated droplet by the magnet motion along x and z axes.

Figure 4.4 illustrates the complete mechanism of actuation of the ferrofluid-wrapped

droplets *via* the movement of the permanent magnet in the respective x and z directions. Note that during the motion of the magnet, there always exists a finite time delay between the movement of the magnet and the effect of that movement being realized by the magneto-responsive droplet, irrespective of the direction of the motion. During translation in the x-direction, this delay in response results in a horizontal offset (x-offset) between the axis of magnetization and the axis of the droplet. Consequently, the direction of overall magnetic force, $\boldsymbol{F}_m$ experienced by the ferrofluid-wrapped droplet is not vertical, as shown schematically in Figure 4.4(a1). Thus, the ferrofluid wrapping layer experiences an attractive pull both in the x-direction as well as downward in the z-direction. The vertically downward z component of the net the force, $\boldsymbol{F}_{m,z}$ brings the excess ferrofluid layer down near the bottom of the droplet while the horizontal component pulls the compound droplet along the x-direction as the magnet traverses along the x-axis. An interplay between the horizontal component of the magnetic pull, $\boldsymbol{F}_{m,x}$ and the viscous resistance offered by the surrounding water bath, $\boldsymbol{F}_{visc}$ governs the resulting x-motion of the ferrofluid-wrapped laser oil droplet during the x-axis translation of the magnet. Figure 4.4(a2) experimentally delineates the translation motion of the ferrofluid-wrapped laser oil droplet owing to the motion of the magnet along the x-axis. In this case, the magnet-cuvette gap is kept fixed, i.e., $D_m = 1.5$ cm which corresponds to $Bo_m = 88.8$ and the magnet is moved with a speed $v_m = 3.8$ cm s^{-1}. As explained previously, in the absence of an external magnetic field (i.e., when the permanent magnet is far away from the cuvette) the excess ferrofluid layer predominantly remains at the top ($t = 0$ s) as it has a lower density than the surrounding medium (water). When the magnet moves closer to the droplet from the left, owing to the interaction between the MNPs and the magnetic field, the ferrofluid layer experiences an attractive magnetic force toward the oncoming magnet. The MNPs always try to attain the position of maximum magnetic field and try to migrate towards the magnet. Owing to the attractive force experienced by the MNPs due to the incoming magnet from the left-hand side, the excess ferrofluid layer starts to rotate in an anti-clockwise direction ($t = 0.2 - 0.8$ s). During this motion, when the magnet is directly beneath the droplet at $t = 0.9$ s, the ferrofluid layer attains a position closest to the magnet. At this position, the axis of magnetization coincides with the axis of the droplet, and the MNPs experience the maximum magnetic force. Beyond this point ($t \geq 1.0$ s), the droplet begins to translate

along the direction of the magnet (along the x-axis). It can be noted that the excess layer remains firmly attached to the droplet and causes it to translate which affirms the stability of the magnetic manipulation. Once the droplet starts to move along the magnet motion, it experiences a viscous drag (due to the surrounding water bath) opposing its motion. Depending on the competition between the magnetic pull and viscous retardation, the droplet moves a certain distance before coming to rest (termed as 'disengagement', see the timestamp $t = 3.5$ s in Figure 4.4(a2)). The disengagement is defined as the condition when the encapsulated droplet can no longer follow the motion of the magnet and comes to rest instead. It is interesting to note that, just after the disengagement, the excess ferrofluid layer moves back to the top of the droplet due to buoyancy. The translational behaviour of the ferrofluid-wrapped droplets is discussed in detail in subsection 4.4.3, where the mechanism of disengagement is explained. Thus, the movement of the encapsulating ferrofluid layer is what propels the droplet. Unlike bulk ferrofluid droplets or magnetic liquid marbles, here we achieve translation with a thin encapsulating layer of low concentration ferrofluid. We estimate that our protocol allows robust, controlled actuation of the wrapped cargo with less than 0.5 % volumetric concentration of the magnetic fluid (EMG-900) in the final encapsulated droplet, which is indicative of the sustainability of our framework.

Figure 4.4(b1) shows the manipulation of the ferrofluid layer across the droplet when the magnet is moved along the z-axis. We schematically show the involved forces and the resulting morphology of the compound droplet during the magnet's motion along the z-axis. In this case, the magnet's axis of magnetization coincides with the encapsulated droplet's axis which ensures that there is no x-component of the magnetic force experienced by the droplet and, therefore, no translational motion along the x-axis. The net magnetic force, $\boldsymbol{F}_m$ acting vertically downward on the magneto-responsive encapsulated droplet, increases as the cuvette-magnet separation, D_m reduces due to the magnet approaching the base of the cuvette from the bottom. As a result, the excess ferrofluid layer experiences an increased attractive pull toward the bottom of the droplet. This is manifested in a visible decrease in the width of the excess ferrofluid layer, w_{ff}. Herein, we experimentally capture the response of the encapsulated droplet towards the motion of the magnet along the z-axis for a single encapsulated droplet (laser oil) of radius 1.86 mm, the results of which are shown in Figure 4.4(b2)-4(b5). The total experimental time is 30 minutes during which the

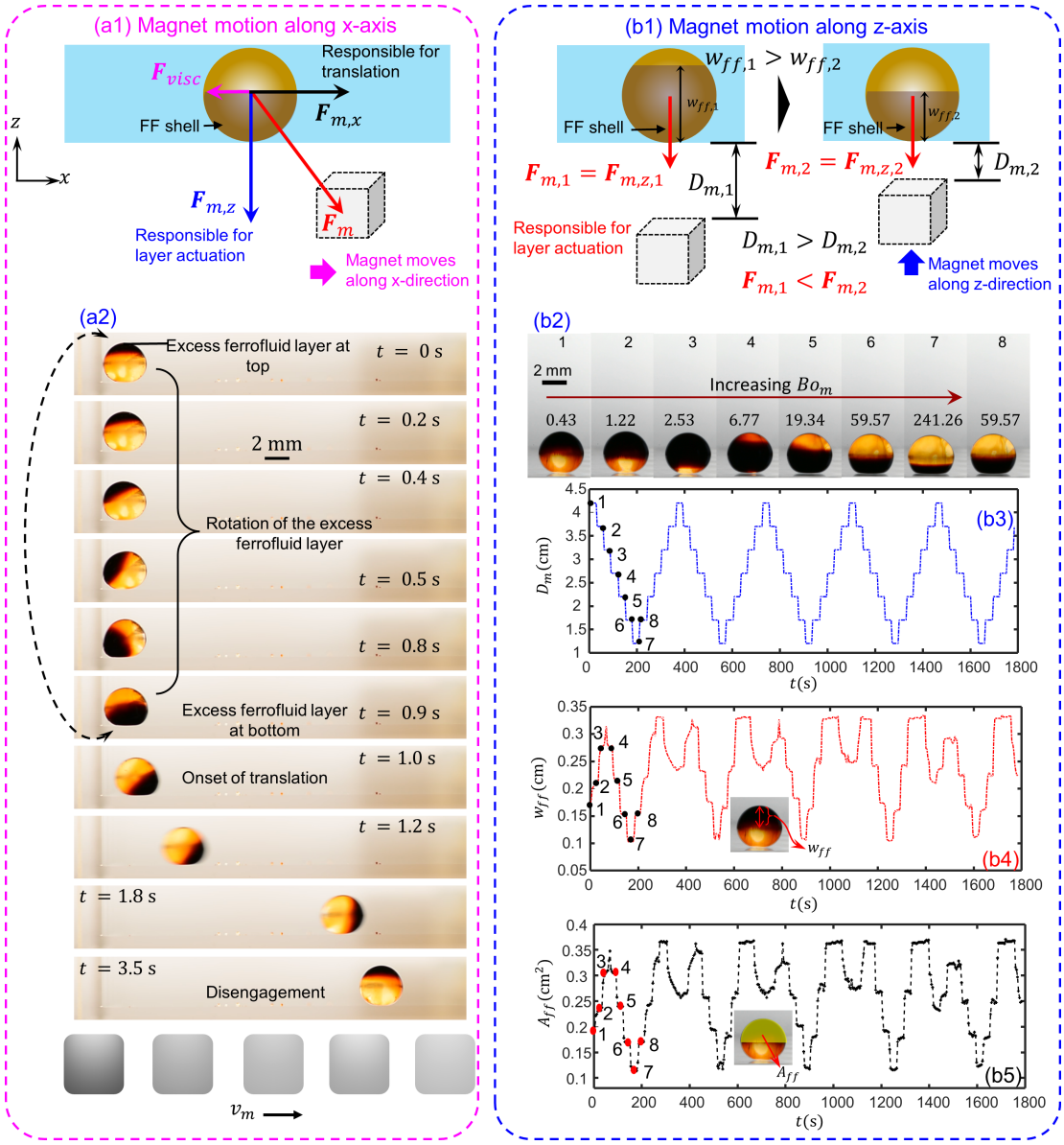

Figure 4.4: (a1) Schematic showing the magnetic and viscous forces acting on the encapsulated droplet for magnet motion along the x-axis. F_m is the net magnetic force acting on the droplet with x and z components represented by $F_{m,x}$ and $F_{m,z}$, respectively. F_{visc} is the viscous drag due to the surrounding water medium. FF shell represents the excess ferrofluid layer over the droplet. (...continuing to the next page)

Figure 4.4: (...continued from the previous page) (a2) Timestamped color images showing the translation of an encapsulated droplet when the magnet is kept fixed at $D_m = 1.5$ cm (Bo_m= 88.8) and moved with a speed v_m= 3.8 cm s^{-1} along the x-axis. The images show the rotation of the excess layer, translation, and disengagement (b1) Schematic showing the magnetic force F_m acting on the encapsulated droplet for magnet motion along the z-direction for two different magnet-cuvette gaps D_m. Here $D_{m,1} > D_{m,2}$ such that $F_{m,1} < F_{m,2}$. Note that there is no x-component of the magnetic force in this case, hence the z-component $F_{m,z}$ is equal to the net magnetic force F_m. w_{ff} represents the span of the excess ferrofluid layer over the droplet along the vertical direction. w_{ff} decreases with an increase in F_m, such that $w_{ff,1} > w_{ff,2}$. (b2) Timestamped color experimental images showing the magnetic manipulation of the ferrofluid shell (dark encapsulating layer) across the droplet surface when the magnet is moved in multiple cycles along the z-axis. (b3) Variation of D_m with a staircase feature. The points denoted by numeric $1-8$ represent the various instants for which the corresponding droplet images are shown in (b2). The variation of the excess layer is quantified in terms of ferrofluid layer width w_{ff} and coverage area A_{ff} as shown in (b4) and (b5), respectively. The color inset images in (b4) and (b5) illustrate the definition of w_{ff} and A_{ff}, respectively. The black and red dots in (b4) and (b5) correspond to the images in (b2).

magnet is moved up and down in discrete steps with a waiting time of 30 seconds at each value of D_m. In Figure 4.4(b2), images are denoted by numeric $1-8$ which corresponds to the different values of D_m marked by black dots in Figure 4.4(b3), which represents the temporal variation of the magnet position D_m for the complete experimental time (30 minutes). Initially, the encapsulated droplet is brought under the influence of the magnet which is positioned at $D_m = 4.2$ cm for 30 s (see image 1 Figure 4.4(b2)). Following this, the gap is reduced in a step of 0.5 cm until the gap becomes $D_m = 1.2$ cm (see image 7 in Figure 4.4(b2)). At each position (D_m), the magnet is kept fixed for 30 s which allows the MNPs to interact with the magnetic field. As a result of the magnetic interaction, the MNPs tend to migrate toward the zone of maximum magnetic field (closest to the magnet) leading to the gradual relocation of the excess ferrofluid layer from the apex (image 1 in Figure 4.4(b2)) to the bottom of the droplet (image 7 in Figure 4.4(b2)). In this regard,

images 3 and 4 stands as the interim stage of the excess layer relocation process where the excess ferrofluid layer is seen to be distributed across the entire x-z cross-section of the encapsulated droplet. This corresponds to $D_m = 3.2$ cm ($Bo_m = 2.53$) and $D_m = 2.7$ cm ($Bo_m = 6.77$), respectively. On the further decrease of D_m, the excess layer begins to move downwards and at $D_m = 1.2$ cm (corresponding $Bo_m = 241.26$), the excess ferrofluid layer lies completely at the bottom of the droplet as shown by image number 7. This concludes the forward half-cycle of the magnet motion. The reverse half-cycle of the magnet motion is executed subsequently where D_m is gradually increased in steps of 0.5 cm until $D_m = 4.2$ cm is reached, while maintaining the same hold time of 30 s at each step. Note that the ferrofluid layer attains the same morphology for a fixed D_m during the forward and the reverse half-cycle, which can be found *via* a qualitative comparison between image 6 (forward half-cycle) and image 8 (reverse half-cycle) of Figure 4.4(b2) for both of which, $D_m = 1.7$ cm. The experiment is repeated for a total of five complete cycles in a similar manner during which the ferrofluid layer undergoes the aforementioned morphological evolution cyclically. The cyclic variation of the layer morphology during the experiment can be confirmed by the quantitative estimation of the ferrofluid layer width w_{ff} and the ferrofluid layer coverage area A_{ff} with time as shown in Figure 4.4(b4) and 4(b5). Here, w_{ff} is the width of the excess ferrofluid layer across the droplet along the vertical direction as shown in Figure 4.4(b4) which is calculated after processing the images in MATLAB. Similarly, A_{ff} is the area of the excess layer on the droplet as shown in Figure 4.4(b5) which is calculated assuming spherical cap geometry. The details of image processing and calculation scheme of w_{ff} and A_{ff} can be found in Appendix B section B.2. It can be observed from Figure 4.4(b4) and (b5) that, the variation w_{ff} and A_{ff} follows a similar cyclic pattern. Both w_{ff} and A_{ff} first increase owing to a decrease in D_m, reach a maximum value, and then begin to decrease again, which affirms the stability of the ferrofluid layer. One of the implications of the layer manipulation discussed above is that it allows one to expose the core droplet to the water environment by varying the magnetic field (Bo_m). This can be useful in the controlled coalescence of the core droplet by unwrapping the ferrofluid shell layer in a controlled fashion. Please note that we are not unwrapping the laser oil drop (core) completely as demonstrated by Wang *et al.* [13]. In this case, the magnetic force can only actuate the excess ferrofluid layer and cannot

unwrap the thin ferrofluid layer that has an intrinsic thermodynamic tendency to adhere to the laser oil core, as shown theoretically in subsection 4.4.1. The next sections will discuss the translational characteristic of the ferrofluid-wrapped laser oil droplets and the manipulation of compound droplets based on the above mechanisms.

4.4.3 Translational characteristics of the ferrofluid-wrapped droplets

Based on the above discussion, it can be understood that using a moving magnet, a ferrofluid-wrapped droplet can be transported from one location to another inside the water bath. **Figure 4.5** shows the translational characteristics of the ferrofluid-wrapped laser oil droplets based on the magnet speed v_m and the magnetic Bond number Bo_m. The experimental procedure adopted to obtain the results shown in Figure 4.5 are described in Appendix B section B.3. The side view image sequence (denoted by numeric $1-5$) shown in Figure 4.5a is obtained from high-speed imaging at a frame rate of 50 frames per second and represents the disengagement length δ of the droplets for five different magnet speeds v_m at a particular $Bo_m = 42$. Here we define the disengagement length δ as the distance traversed by the droplet before it can no longer follow the motion of the magnet and comes to rest instead. Thus, δ is estimated as the absolute value of the difference between the initial and final location of the droplet (along the x-axis) for a given magnet speed v_m at which the droplet ceases to follow the motion of the magnet. It can be observed from Figure 4.5a that as the magnet speed is decreased from $v_m = 4$ cm s^{-1}, to $v_m = 2$ cm s^{-1}, the difference $v_m - v_d$ reduces which indicates that the tendency of the droplet to follow the magnet increases. Also, the corresponding disengagement length of the droplet increases (δ_1 to δ_5) which can be observed in Figure 4.5a. This fact can be understood in the following manner as discussed here. It is mentioned that the interaction between the magnetic field and the MNPs gives rise to the actuation of the ferrofluid layer which in turn results in the manipulation of the encapsulated cargo. The droplet motion is governed by the interplay between the magnetic force on the MNPs and the viscous drag between the encapsulated droplet and the host water bath. Once the droplet starts to move along the magnet motion, it experiences a viscous drag opposing its motion. At a lower magnet speed $v_m = 2$ cm s^{-1}, the viscous drag experienced by the encapsulated

cargo is less as compared to the same at higher magnet speed $v_m = 4$ cm s^{-1} as also noted by Mandal *et al.* [45]. Thus, at a higher magnet speed, the magnetic force on the MNPs is unable to overcome the viscous drag experienced by the encapsulated cargo resulting in a shorter disengagement length. Figure 4.5b and 5c show the temporal variation of the droplet displacement l and the droplet velocity v_d for various magnet speed v_m and at a fixed Bo_m.

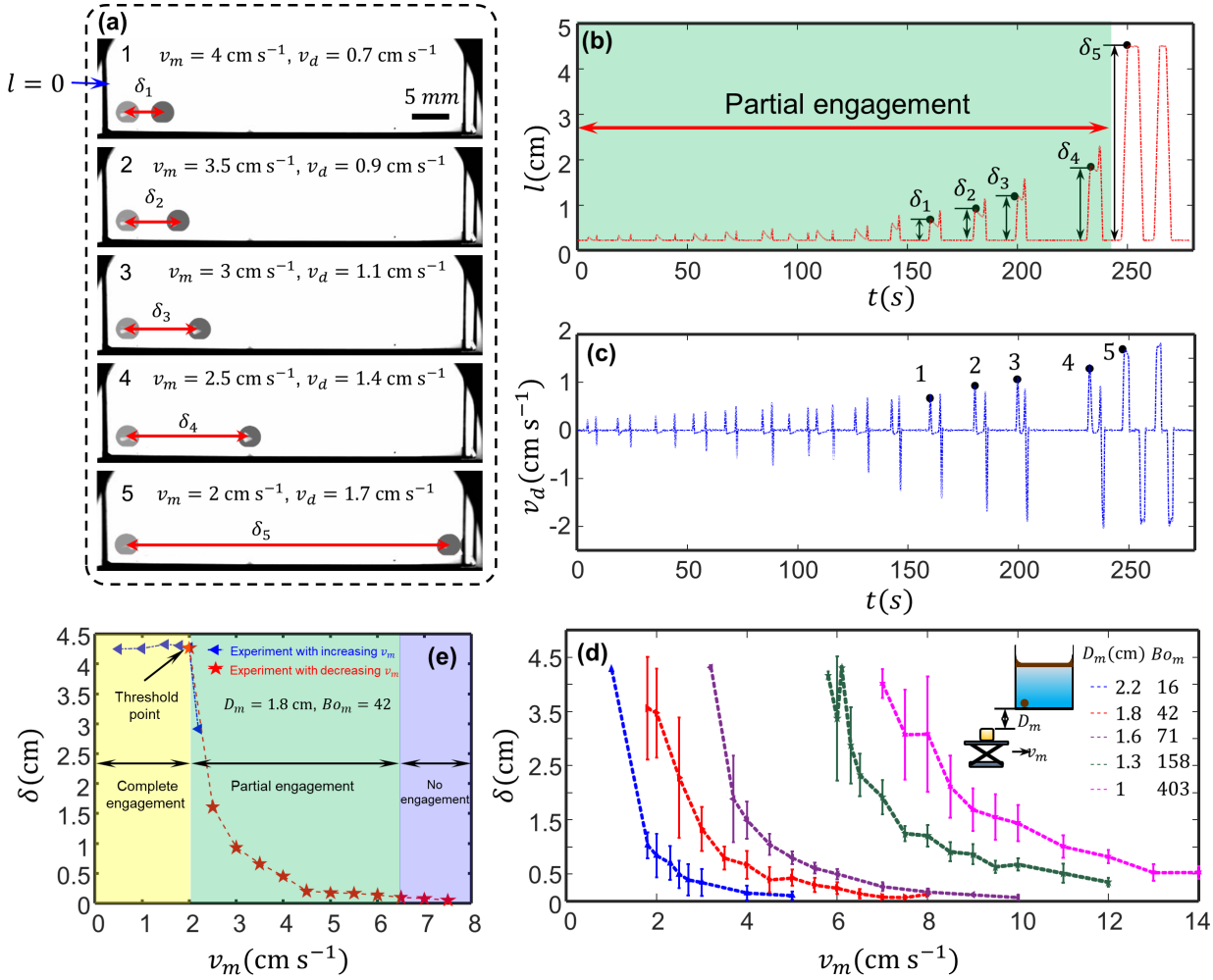

Figure 4.5: Results of magnet-assisted drop translation. (a) Sideview snapshots from the high-speed video for droplet disengagement length δ at different magnet speeds v_m. (b) The plot showing the temporal variation of the droplet displacement l. The peaks and valleys in the plot denote the translation and disengagement of the droplet with the moving magnet. The disengagement lengths δ corresponding to the snapshots in (a) are denoted by numeric $1-5$. (c) The plot showing the temporal variation of the droplet velocity v_d corresponding to the droplet displacement shown in (b). The black dots in (c) denote the points corresponding to the snapshots shown in (a). (d) Results of droplet translation for different values of Bo_m. The gap D_m and the corresponding magnetic Bond number Bo_m are shown in the legend. (...continuing to the next page)

Figure 4.5: (...continued from the previous page) (e) Plot showing the variation of disengagement length with the increasing and decreasing v_m at a fixed magnetic Bond number $Bo_m = 42$. For the experiment with increasing v_m, the starting magnet speed is 0.5 cm s^{-1}, whereas for experiments with decreasing v_m, the starting magnet speed is 7.5 cm s^{-1}. The threshold point denotes the location at which the droplet transitions to partial engagement for increasing v_m or to complete engagement for decreasing v_m.

Here the droplet displacement l is defined as the total horizontal length traveled by the droplet as v_m is varied. Here the left wall of the cuvette (marked with the blue arrow in Figure 4.5a) denotes $l = 0$. A detailed discussion on image processing methodology to obtain droplet displacement and velocity is presented in Appendix B, section B.4. The corresponding disengagement lengths and the droplet velocities for the cases shown in Figure 4.5a are marked in Figure 4.5b and 5c, respectively.

The above discussion corresponds to a fixed Bo_m and it is important to obtain the translational characteristics of the encapsulated cargo for a wide range of Bo_m and v_m. Thus, to obtain the experimental data, we performed the translation experiments for different values of Bo_m and measured the disengagement length δ at different values of v_m. We present the variation of δ with v_m for 5 different values of Bo_m in Figure 4.5d. Let us consider the variation of $D_m = 1.8$ cm ($Bo_m = 42$) shown by the red dotted line in Figure 4.5d. As v_m increases, δ decreases, such that at a sufficiently high v_m, the droplet practically remains stationary. This is reflected in the near flat nature of the curve between $7 - 8$ cm s^{-1}. Conversely, at a sufficiently low v_m, δ approaches the value of maximum traversal length, which is found to be $\sim$ 4.5 cm (see Appendix B, section B.3). As we increase the magnetic field, by lowering the gap D_m (i.e., increase Bo_m), the curve shifts rightwards, which means that the magnet speed at which droplet disengagement occurs increases. Moreover, it can be assumed that for the cuvette size used in the current work, if $\delta \approx 4.5$ cm, one would not observe disengagement below that corresponding v_m. This fact can be understood from Figure 4.5d. For every value of Bo_m, we see that there is a minimum threshold value of v_m, corresponding to $\delta \approx 4.5$ cm, which is the maximum available length for the droplet to travel. Now, if v_m were to decrease even further, the

droplet would remain engaged completely with the magnet. We tested this hypothesis by doing a separate experiment, wherein the starting magnet speed is kept sufficiently low at 0.5 cm s^{-1}, and is then increased in discrete steps for $D_m = 1.8$ cm. The results are presented in Figure 4.5e**,** wherein the blue dotted line represents the experiment with increasing magnet speed. For increasing v_m, the droplet remains completely engaged with the magnet until $v_m = 1.8$ cm s^{-1}. Beyond this value of v_m, droplet starts to disengage and with further increase in v_m it travels shorter distances. Conversely, for the experiments on decreasing v_m, the droplet approaches the same threshold point found in the case when v_m is increased, which is found to be $\sim$ 2 cm s^{-1}. Hence, in our experiments, we observe the same threshold value of v_m for disengagement, irrespective of the starting magnet speed indicating a robust magnetic manipulation. In addition, we also demarcate the result of Figure 4.5(e) into complete, partial, and no engagement zones. Note that, the partial engagement zone is a particularly important attribute of efficient targeted delivery systems where it is often necessary to be able to retrieve the magnet without disturbing the target analyte once the analyte has been delivered to the target. Therefore, this demarcation of the various zones is critical for the efficient design of magnetic manipulation systems, where one can appropriately estimate the dimensions for the actuation length or the required magnet speeds for the target application.

In the next section, we discuss the underwater magnetic manipulation of the encapsulated compound droplet, controlled coalescence, and the release of the inner core.

4.4.4 Underwater manipulation of encapsulated compound droplets

As discussed in the introduction section, one of the major motivations for the development of magnet-assisted manipulation techniques is its suitability for non-contact transport and release of targeted materials packaged inside tiny droplets. Secondly, as noted by many authors [1, 15, 27], the technique can also be applied for applications such as micro-mixing and micro-reactions, wherein two droplets can be controllably coalesced for miniaturized applications. Naturally, these applications involve droplet manipulation such as translation, rupture, or wrapping/unwrapping. With this motivation, herein we demonstrate a robust platform for controlled actuation and mixing of water-soluble cargo inside a water

medium. As discussed in the introduction section, a water-soluble EG core is used as the model analyte. EG is first enclosed inside a carrier medium of laser oil before executing the impact-driven wrapping process of the compound droplet by the magneto-responsive ferrofluid layer. The laser oil carrier phase serves two distinct purposes here. First, as identified in our previous work [58], a critical condition for the success of the impact-driven liquid-liquid encapsulation is the mutual compatibility between the shell layer and the core droplet as they remain in direct contact in the final encapsulated cargo. However, in our experiment, we found that if EG droplets are used for core, they are not compatible with the oil-based ferrofluid suspension, during the encapsulation process. Upon contact with the ferrofluid interfacial layer, EG core droplet immediately disrupts the colloidal stability of dispersed superparamagnetic particles of the interfacial layer leading to a depletion zone. See Figure B.5 for Appendix B, which shows the alternation in the morphology of the floating ferrofluid interfacial layer on top of the water host after its contact with an EG droplet, wherein we dispensed EG droplet directly on to the floating ferrofluid interfacial layer. It is likely due to the attractive interaction between the EG and the oleic acid surfactant present in the ferrofluid suspension. Therefore, unlike laser oil, EG can not be wrapped directly using the ferrofluid interfacial layer. However, to impart underwater magnetic manipulability to EG, it needs to be packaged alongside the ferrofluid. Introducing an intermediate carrier phase of non-polar laser oil which is compatible with both EG and the ferrofluid suspension, solves this challenge. Second, the ferrofluid-wrapped compound droplet essentially has a triple-layered morphology where the inner EG core is surrounded by two shell layers, namely, a laser oil shell that is in direct contact with EG and the outer ferrofluid layer. The intermediate viscous laser oil provides an additional diffusion barrier that prevents unwanted mixing of the EG droplet with the surrounding water bath. It improves the controllability of the manipulation and subsequent coalescence of the encapsulated cargo and aids in the robustness of the developed platform.

Figure 4.6 shows the experimental scheme adopted in studying the magnet-assisted coalescence of two compound droplets inside the water bath.

The compound droplet consists of an ethylene glycol (EG) droplet encapsulated inside a laser oil. The compound droplet is then encapsulated inside a ferrofluid shell wrapping layer using the impact-driven technique discussed in subsection 4.4.1. The controlled coalescence

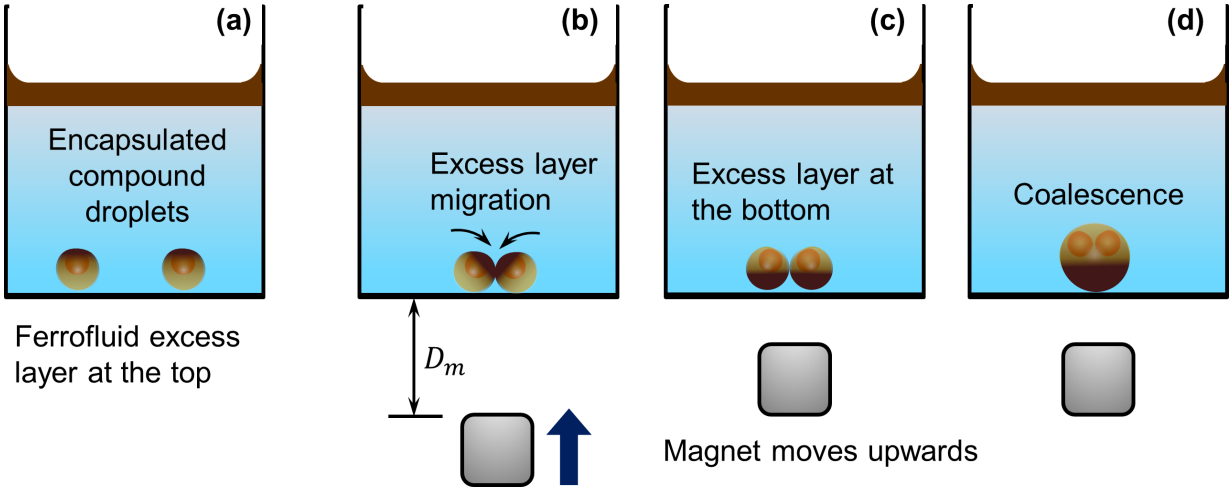

Figure 4.6: (a) Two compound droplets generated at a distance apart are shown with a brownish appearance at the top to illustrate the presence of an excess ferrofluid layer. (b) The droplets come toward each other due to the magnetic force experienced by the MNPs as soon as the magnet is brought under the cuvette and fixed at a gap D_m. This also causes the droplets to come in contact and leads to the onset of excess layer migration towards the bottom (shown by the arrowheads). (c) With a further decrease in D_m, the excess layer is pulled further below and settles at the bottom. (d) Droplets finally coalesce owing to the migration of the excess ferrofluid layer from the apex of the droplet to the bottom of the droplet.

of the two compound droplets is achieved in four steps - (*i*) two compound droplets are generated inside the water bath with an excess ferrofluid layer at the apex of the droplet (Figure 4.6a), (*ii*) then the magnet is brought beneath the cuvette and fixed at a gap D_m which causes the two compound droplets to come in contact and also causes the excess layer to migrate towards the bottom (Figure 4.6b), (*iii*) the gap D_m is then reduced (increasing the magnetic field) which causes the excess ferrofluid layer to settle at the bottom of the droplet (Figure 4.6c), (*iv*) keeping the magnet at the same location D_m for a while results in the migration of the MNPs toward the zone of the highest magnetic field which results in the continuous drainage of the excess ferrofluid layer, which in turn results in the coalescence of the compound droplets (Figure 4.6d).

We discuss the results of compound droplet coalescence through the timestamped color images shown in **Figure 4.7**, which are obtained from a single experiment by varying the gap D_m. The coalescence of compound droplets indicates the merging of the two outer laser oil droplets (containing the EG drops) with each other when the ferrofluid layer is brought to the droplet's bottom. The coalescence of the EG droplets encapsulated inside the laser oil is discussed separately. Initially, the magnet is positioned at a distance of $D_m = 2.3$ cm ($Bo_m = 15.6$) beneath the cuvette when the first compound droplet of radius 1.8 mm impacts the ferrofluid interfacial layer (Figure 4.7a) resulting in the formation of the "first encapsulated compound droplet." Owing to the magnetic pull experienced by the MNPs due to the magnet, the encapsulated droplet attains the position of the highest magnetic field and stays there as shown in Figure 4.7a ($t = 0$ s). Then, the second compound droplet impacts the ferrofluid interfacial layer at a distance apart from the first impact point resulting in the formation of the "second encapsulated compound droplet" at $t = 1.2$ s. The droplet upon experiencing the magnetic pull migrates ($t = 1.2$ s to 2.1 s) toward the highest magnetic field and eventually comes in contact with the first droplet at $t = 2.5$ s. It can be observed from Figure 4.7a, that the magnetic interaction between the MNPs and the magnetic field at $Bo_m = 15.6$ is not sufficient to bring the ferrofluid layer from the apex of the encapsulated droplet to the bottom of the droplet. Owing to this fact, the drainage of the ferrofluid does not occur, thus, the coalescence of the droplets is not observed even after 63 seconds. The EG droplets remain intact inside the laser oil droplet which affirms the fact that the laser oil and the ferrofluid layer are successful in preventing the mixing of the EG droplets and the water.

On the contrary, when the magnetic field is enhanced by bringing the magnet closer to a location $D_m = 1.8$ cm ($Bo_m = 50.3$), the excess ferrofluid layer migrates from the apex of the droplet toward the bottom of the droplet. This fact can be visually confirmed from the experimental images shown in Figure 4.7b ($t = 162.6$ s to 219.3 s). It is interesting to observe that, even though during the whole process the two droplets remain in contact with each other, the ferrofluid layer is unable to migrate below the contact point even at $t = 219.3$ s which prevents the coalescence of the two laser oil droplets (containing EG drops). Thereafter, we further increase the magnetic field by reducing the gap to $D_m = 1.5$ cm ($Bo_m = 105.1$) at around 220 s (see Figure 4.7c). The increase in magnetic

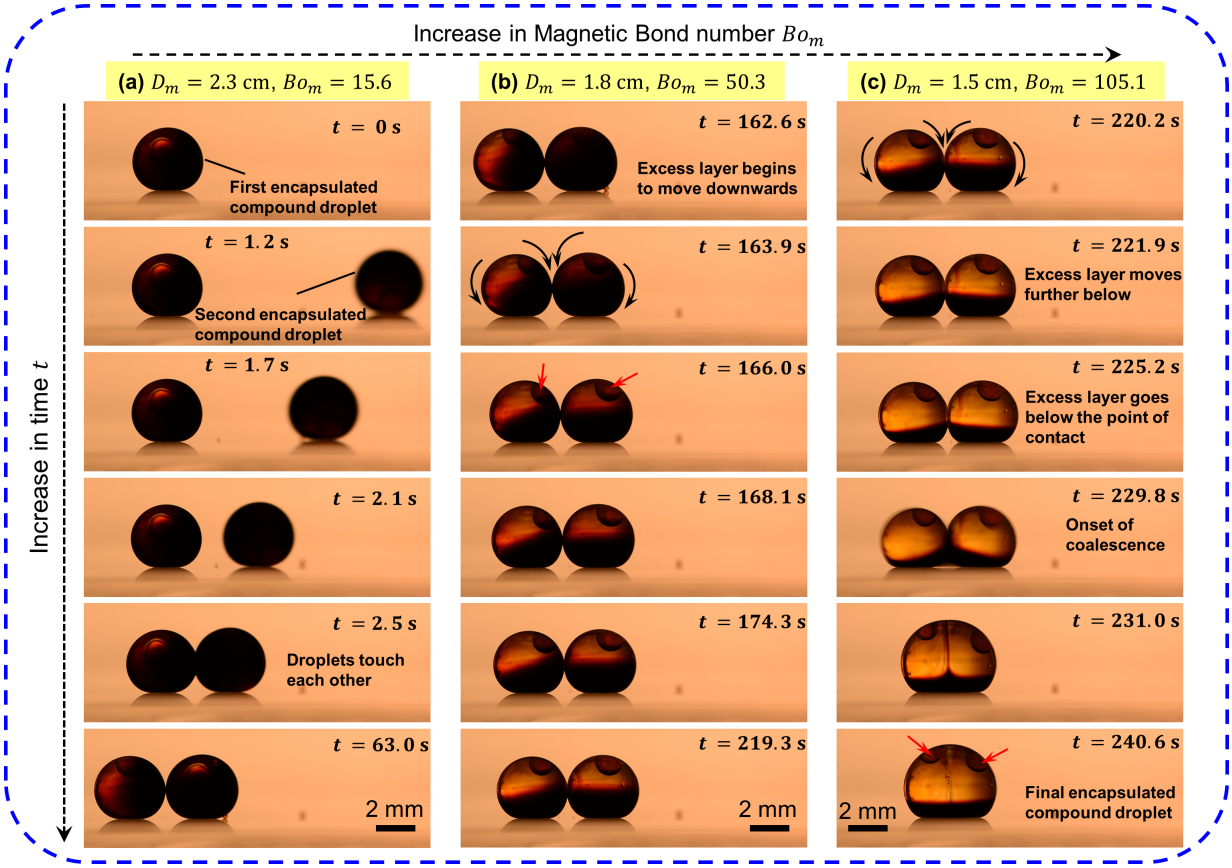

Figure 4.7: Timestamped images of compound droplet coalescence for a single experiment with increasing Bo_m - (a) droplets do not coalesce at $Bo_m = 15.6$. (b) The excess ferrofluid layer migrates from the apex of the droplet to the bottom of the droplet and the droplets do not coalesce at $Bo_m = 50.3$. (c) Laser oil droplets coalesce with each other at $Bo_m = 105.1$. In all the cases, the ethylene glycol droplets remain intact inside the laser oil droplet as marked by the red arrows.

force pulls the excess ferrofluid layer below the point of contact between the two laser oil drops (t = 225.2 s). Owing to the drainage of the ferrofluid layer at the point of contact, the interface of the laser oil drops begins to fuse ("onset of coalescence" at t = 229.8 s) as shown in Figure 4.7c. Finally, the two laser oil drops merge at t = 240 s with two EG droplets intact inside the laser oil. This experiment provides an insightful

understanding that the coalescence time of the two drops can be controlled by the magnetic field. Also, the experimental demonstration further affirms the stability of our impact-driven encapsulation technique and the role of the laser oil and the ferrofluid layer in preventing the mixing between the EG drops and the water. Thus, the ferrofluid layer not only facilitates translation but also provides an ingenious way to control coalescence.

The above results indicate that the position of the excess ferrofluid layer has a significant role in controlling the coalescence time of the two laser oil drops containing the EG drops. Based on the experimental observations, we theorize that in the absence of the magnetic field, the drainage of the ferrofluid film at the point of contact would have occurred due to the combined effect of Laplace pressure and disjoining pressure [61], and hence would have taken much longer time for coalescence. However, in the presence of the magnetic field, the magnetic force pulls a significant portion of the ferrofluid layer from the droplet's apex to the bottom of the droplet such that only a thin nanometric ferrofluid film is present at the point of contact. Thereafter, the attractive disjoining pressure causes this thin ferrofluid film to rupture resulting in the coalescence of the laser oil droplets (containing EG drops). Based on this premise, it should be possible to facilitate immediate coalescence of the laser oil drops if the magnet is positioned closer to the cuvette bottom, i.e., the magnetic force is sufficiently strong to bring the ferrofluid excess layer below the point of contact. To test this hypothesis, we performed another experiment wherein, instead of varying D_m from 2.3 cm to 1.5 cm (as in the case of Figure 4.7), we positioned the magnet at $D_m = 1.5$ cm before impacting the first droplet. The experimental results are shown in **Figure 4.8a**. Please note that this is the same value of D_m at which the ferrofluid layer moves below the point of contact between the two droplets as shown in Figure 4.7c. Thereafter, we continue to record the observation till the inner EG drops present inside the laser oil coalesce with each other.

Let us first discuss the coalescence of the outer laser oil droplets as shown in Figure 4.8a. At $t = 0$ s, the first encapsulated compound droplet is shown. Since the magnet is already placed at a position ($D_m = 1.5$ cm) where the droplet experiences a stronger magnetic force. Thus, we see that the excess ferrofluid layer occupies a position at the bottom of the encapsulated cargo ($t = 0$ s). Thereafter, at $t = 0.4$ s, the second encapsulated compound droplet forms and eventually comes in contact ($t = 7.0$ s) with the first droplet due to the

strong magnetic pull.

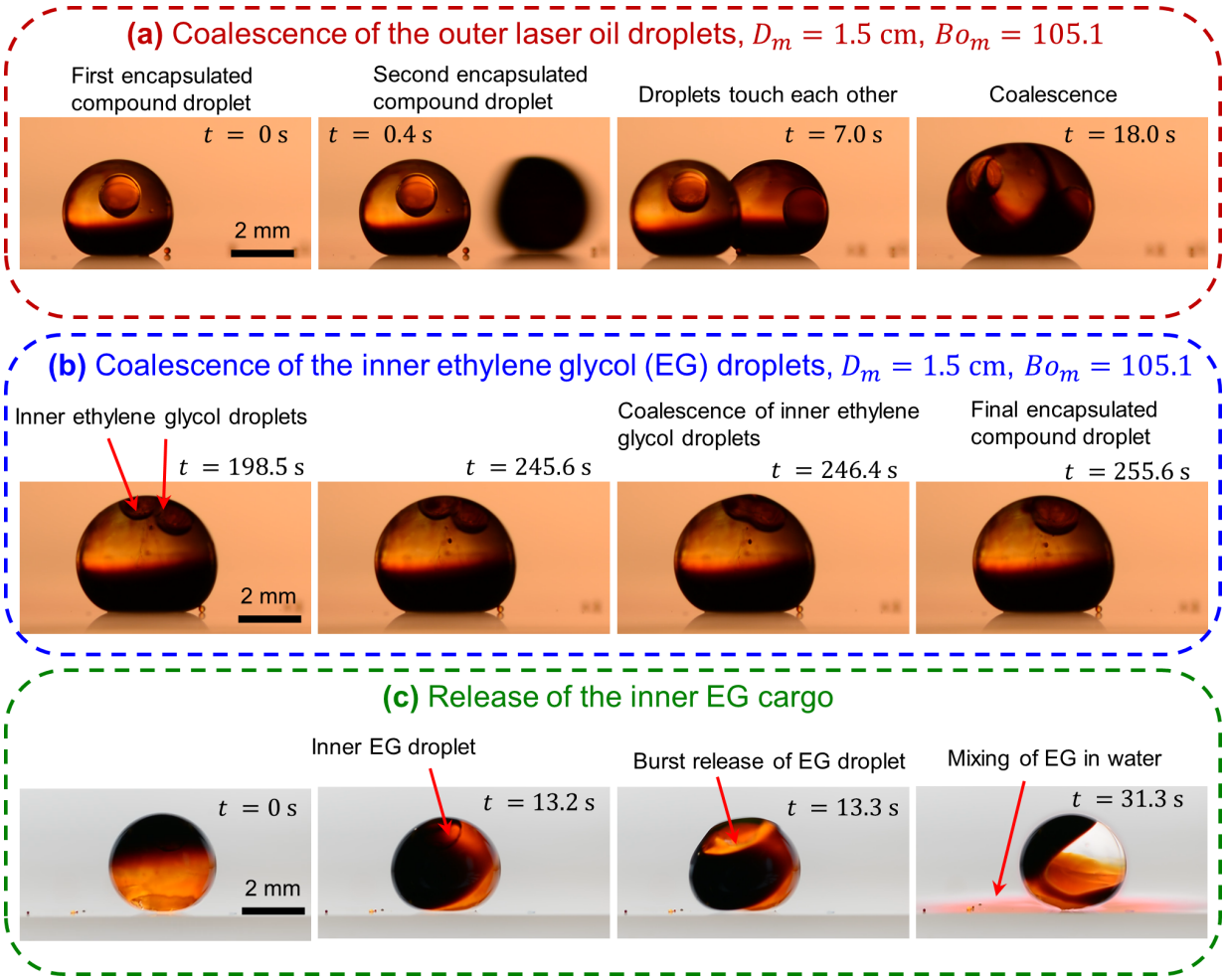

Figure 4.8: (a) Timestamped images for the magnet-assisted immediate coalescence of the outer laser oil droplets leading to an encapsulated compound droplet containing two ethylene glycol drops. (b) Timestamped images showing the coalescence of the inner ethylene glycol droplets for the final compound droplet (shown in (a)). (c) Experimental demonstration of the release of the inner EG cargo in the surrounding water medium. The inner EG droplet is visible at $t = 13.2$ s, due to the migration of the excess ferrofluid layer. The outer laser oil droplet ruptures and releases the inner EG droplet at $t = 13.3$ s. The dyed EG droplet settles at the bottom and mixes with the surrounding water.

Shortly after this, the outer laser oil droplets coalesce at $t = 18.0$ s which follows the same mechanism as discussed before. Thus, unlike the results shown in Figure 4.7, here we achieve the coalescence of outer laser oil drops in a much shorter time after the impact of the initial droplet. Please note that the coalescence of the outer laser oil droplets leads to a single encapsulated compound droplet with two ethylene glycol droplets inside the laser oil droplet (at $t = 18.0$ s in Figure 4.8a). For the applications such as micro-mixing and micro-reactions, the fusion of the cargo packaged inside encapsulated droplets is an important aspect that should be addressed. In this regard, we next show the merging of the two ethylene glycol droplets (inside the laser oil) for the same experiment as shown in Figure 4.8b. It is found that owing to the buoyancy, the two inner EG droplets slowly approach each other at the apex of the droplet ($t = 198.5$ s) and finally coalesce at $t = 246.4$ s. It is to be noted that due to the high viscosity of the laser oil ($\mu_{lo} = 1024$ mPa s), it takes much longer for the inner ethylene glycol droplets to coalesce.

We mentioned in the introduction section that, a major driving motivation for the development of magnetically active materials is their ability for targeted cargo delivery and release. In this context, we now present a sample experimental result of the release of the inner EG core in a compound droplet *via* magnetic actuation. For visualization, we dyed EG with a commercially available orange dye (Bright Dyes® FLT Orange Liquid, Product number: 106006, Kingscote CHEMICALS, USA) and used a white LED light for better color contrast to show post-release mixing. The results are presented in Figure 4.8c. In this experiment, we generate an encapsulated compound droplet as described in subsection 4.4.1. The initial value of $D_m = 4$ cm, which corresponds to $Bo_m = 0.56$. Then the magnet is quickly moved upwards to $D_m = 2.0$ cm ($Bo_m = 27.3$), which causes the migration of the excess layer from the droplet's apex toward the bottom in a short time. As a result, the EG core becomes visible at $t = 13.2$ s (marked with a red arrow). We postulate the following event taking place at this time instant. A high shear rate is applied on the laser drop by the excess ferrofluid layer due to the quick migration of the excess ferrofluid layer from the apex to the bottom of the droplet. This results in the immediate rupture of the laser oil drop (which otherwise is under stable encapsulation in water during the normal impact-driven liquid-liquid encapsulation process [58]) and releases the inner EG core (which has moved near the apex of the compound droplet due to the density

stratification) into the surrounding water medium as shown at $t = 13.3$ s. Thereafter, EG being heavier than water flows toward the bottom and slowly dissolves as evidenced by the misty orange appearance in the vicinity of the droplet bottom at $t = 31.3$ s. It can be clearly noted that the ruptured EG core displaces the ferrofluid layer after the release ($t = 31.3$ s), thus indicating their mutual incompatibility, as we discussed previously.

While we have not performed dedicated experiments for the controlled release of the inner cargo, we attribute the thinning of the laser oil film contained between the inner EG drop and the outer ferrofluid film to the abrupt release of the EG drop. The thinning can be accelerated *via* magnetic actuation which pulls the excess layer and in turn distorts the droplet shape at the apex (see Figure 4.8c, $t = 13.2$ s). Any deviation from the spherical cap shape leads to non-uniform curvature along the interface which may accelerate thinning of the laser oil film. However, other factors such as droplet pinning, offset with the axis of magnetization, and post-impact internal movement of the inner droplet may also contribute significantly to the release phenomenon. A detailed analysis of each of these factors is beyond the scope of the current work. Nonetheless, we show that magnetic manipulation of encapsulated droplets is well-suited for targeted cargo delivery and can be enhanced further in future works.

Thus, in this section, we demonstrate that using magnetic actuation we can control the total time of coalescence of the outer layer (laser oil) of the encapsulated compound droplets. In addition, we also show that the inner EG droplets contained inside the laser oil drop spontaneously coalesce to form a larger encapsulated compound droplet. Note that the buoyancy-driven coalescence of the internal EG core droplets inside the laser oil carrier medium is a hydrodynamic phenomenon that can be tailored further by tuning the viscosity of the carrier phase and the density ratio between the carrier phase and the target analyte. Optimization of the fluidic properties of the carrier phase, therefore, remains an exciting avenue for future research towards both a fundamental understanding of the dynamics of compound droplet coalescence as well as controlled on-demand micro-mixing and micro-reaction. Importantly, we also demonstrate the release of the inner EG cargo, which can be taken up as a stepping stone to develop magnet-assisted controlled release technologies.

4.5 Conclusions

In summary, we report the underwater magnet-assisted manipulation of ferrofluid-wrapped droplets. We use an impact-driven liquid-based encapsulation technique to encapsulate laser oil drops and compound drops inside an oil-based ferrofluid shell inside a water bath. The compound droplets consist of an ethylene glycol droplet encapsulated inside a laser oil drop. We found that the magnetic interaction between the magnetic nanoparticles with the magnetic field results in the migration of the ferrofluid shell layer from the apex to the bottom of the droplet. The migration of the shell layer is found to occur in two situations such as the magnet is translated along the horizontal direction (x-axis) at a fixed gap from the cuvette bottom or by moving the magnet along the vertical direction (z-axis) at a fixed location. In this case, we find that even after multiple cycles of magnet motion along the vertical direction (z-axis), the ferrofluid shell layer remains intact. We quantify the shell layer characteristics in terms of the variation of ferrofluid layer width w_{ff} and ferrofluid layer coverage area on the droplet A_{ff}. We exploit the first mechanism of shell layer migration to study the transportation characteristics of the encapsulated droplet where we quantify the translational characteristics in terms of disengagement length (δ), magnet speed (v_m) and the magnetic Bond number (Bo_m). We found that at a fixed Bo_m, increase in v_m results in a decrease in δ and at a fixed v_m, an increase in Bo_m results in the increment in δ. We also show that for every Bo_m, there is a threshold value of v_m below which the droplet travels all along the cuvette length, and disengagement is not observed. Then, we use the second mechanism of shell layer migration to demonstrate the underwater coalescence of the encapsulated compound droplets. We, for the first time, show the magnet-assisted coalescence of compound droplets, wherein we conclusively demonstrate that magnetic Bond number has a significant influence on the coalescence time of the compound droplets. We found that the increase in Bo_m, results in the faster coalescence of the laser oil droplets by partially unwrapping the ferrofluid shell layer resulting in the formation of a larger encapsulated compound droplet containing two drops of ethylene glycol. We then observe that owing to the buoyancy, the two inner ethylene glycol droplets slowly approach each other toward the apex of the droplet and finally coalesce. Finally, we show that magnetic actuation can also be used to release the

inner cargo in compound droplets, thus paving the way for targeted cargo delivery. We believe that the present study provides an insightful understanding of the magnet-assisted manipulation of the encapsulated droplets and coalescence of the encapsulated compound droplets and is expected to be useful in experiments or applications that require targeted drug delivery, micro-mixing or micro-reaction, controlled release of the encapsulated core.

References

[1] X. Zhang, L. Sun, Y. Yu, and Y. Zhao, "Flexible ferrofluids: Design and applications," *Advanced Materials*, vol. 31, 2019.

[2] L. Agiotis, I. Theodorakos, S. Samothrakitis, S. Papazoglou, I. Zergioti, and Y. S. Raptis, "Magnetic manipulation of superparamagnetic nanoparticles in a microfluidic system for drug delivery applications," *Journal of Magnetism and Magnetic Materials*, vol. 401, pp. 956–964, 2016.

[3] D. Liu, H. Zhang, F. Fontana, J. T. Hirvonen, and H. A. Santos, "Microfluidic-assisted fabrication of carriers for controlled drug delivery," *Lab on a Chip*, vol. 17, pp. 1856–1883, 2017.

[4] Y. Zhang, A. Zhou, S. Chen, G. Z. Lum, and X. Zhang, "A perspective on magnetic microfluidics: Towards an intelligent future," *Biomicrofluidics*, vol. 16, 2022.

[5] D. P. Regan and C. Howell, "Droplet manipulation with bioinspired liquid-infused surfaces: A review of recent progress and potential for integrated detection," *Current Opinion in Colloid and Interface Science*, vol. 39, pp. 137–147, 2019.

[6] Y. Zhan, S. Yu, A. Amirfazli, A. R. Siddiqui, and W. Li, "Magnetically responsive superhydrophobic surfaces for microdroplet manipulation," *Advanced Materials Interfaces*, vol. 9, 2022.

[7] S. G. Jones, N. Abbasi, B. U. Moon, and S. S. Tsai, "Microfluidic magnetic self-assembly at liquid-liquid interfaces," *Soft Matter*, vol. 12, pp. 2668–2675, 2016.

[8] U. Banerjee, M. Sabareesh, and A. K. Sen, "Manipulation of magnetocapillary flow of ferrofluid in a microchannel," *Sensors and Actuators, B: Chemical*, vol. 246, pp. 487–496, 2017.

[9] A. Q. Alorabi, M. D. Tarn, J. Gómez-Pastora, E. Bringas, I. Ortiz, V. N. Paunov, and N. Pamme, "On-chip polyelectrolyte coating onto magnetic droplets-towards continuous flow assembly of drug delivery capsules," *Lab on a Chip*, vol. 17, pp. 3785–3795, 2017.

[10] H. Chen, D. Sulejmanovic, T. Moore, D. C. Colvin, B. Qi, O. T. Mefford, J. C. Gore, F. Alexis, S. J. Hwu, and J. N. Anker, "Iron-loaded magnetic nanocapsules for ph-triggered drug release and mri imaging," *Chemistry of Materials*, vol. 26, pp. 2105–2112, 2014.

[11] M. K. Manshadi, M. Saadat, M. Mohammadi, M. Shamsi, M. Dejam, R. Kamali, and A. Sanati-Nezhad, "Delivery of magnetic micro/nanoparticles and magnetic-based drug/cargo into arterial flow for targeted therapy," *Drug Delivery*, vol. 25, pp. 1963–1973, 2018.

[12] G. Huang, M. Li, Q. Yang, Y. Li, H. Liu, H. Yang, and F. Xu, "Magnetically actuated droplet manipulation and its potential biomedical applications," *ACS Applied Materials and Interfaces*, vol. 9, pp. 1155–1166, 2017.

[13] W. Wang, J. V. Timonen, A. Carlson, D. M. Drotlef, C. T. Zhang, S. Kolle, A. Grinthal, T. S. Wong, B. Hatton, S. H. Kang, S. Kennedy, J. Chi, R. T. Blough, M. Sitti, L. Mahadevan, and J. Aizenberg, "Multifunctional ferrofluid-infused surfaces with reconfigurable multiscale topography," *Nature*, vol. 559, pp. 77–82, 2018.

[14] S. K. Saroj, M. Asfer, A. Sunderka, and P. K. Panigrahi, "Two-fluid mixing inside a sessile micro droplet using magnetic beads actuation," *Sensors and Actuators, A: Physical*, vol. 244, pp. 112–120, 2016.

[15] Y. Xue, H. Wang, Y. Zhao, L. Dai, L. Feng, X. Wang, and T. Lin, "Magnetic liquid marbles: A "precise" miniature reactor," *Advanced Materials*, vol. 22, pp. 4814–4818, 2010.

[16] Z. Xin and T. Skrydstrup, "Flüssigmurmeln: Eine vielversprechende und vielseitige plattform für miniaturisierte chemische reaktionen," *Angewandte Chemie*, vol. 131, pp. 12078–12080, 2019.

[17] Z. J. Chu, S. J. Xiao, Y. H. Liu, G. L. Xiong, D. J. Huang, S. ping Wang, X. J. Zhao, and Z. B. Zhang, "Rapid and sensitive detection of the is6110 gene sequences of mycobacterium tuberculosis based on hybridization chain reaction and reusable magnetic particles," *Sensors and Actuators, B: Chemical*, vol. 282, pp. 904–909, 2019.

[18] L. D. Lapitan, Y. Xu, Y. Guo, and D. Zhou, "Combining magnetic nanoparticle capture and poly-enzyme nanobead amplification for ultrasensitive detection and discrimination of dna single nucleotide polymorphisms," *Nanoscale*, vol. 11, pp. 1195–1204, 2019.

[19] M. Falahati, W. Zhou, A. Yi, and L. Li, "Fabrication of polymeric lenses using magnetic liquid molds," *Applied Physics Letters*, vol. 114, 2019.

[20] C. P. Lee, Y. H. Chen, and M. F. Lai, "Ferrofluid-molding method for polymeric microlens arrays fabrication," *Microfluidics and Nanofluidics*, vol. 16, pp. 179–186, 2014.

[21] W. C. Nelson and C. J. C. Kim, "Droplet actuation by electrowetting-on-dielectric (EWOD): A review," *Journal of Adhesion Science and Technology*, vol. 26, pp. 1747–1771, 2012.

[22] Z. Wang and J. Zhe, "Recent advances in particle and droplet manipulation for lab-on-a-chip devices based on surface acoustic waves," *Lab on a Chip*, vol. 11, pp. 1280–1285, 2011.

[23] T. Franke, A. R. Abate, D. A. Weitz, and A. Wixforth, "Surface acoustic wave (SAW) directed droplet flow in microfluidics for pdms devices," *Lab on a Chip*, vol. 9, pp. 2625–2627, 2009.

[24] S. Huang, S. Yin, F. Chen, H. Luo, Q. Tang, and J. Song, "Directional transport of droplets on wettability patterns at high temperature," *Applied Surface Science*, vol. 428, pp. 432–438, 2018.

[25] K. Dholakia and T. Čižmár, "Shaping the future of manipulation," *Nature Photonics*, vol. 5, pp. 335–342, 2011.

[26] Y. Fang, J. Liang, X. Bai, J. Yong, J. Huo, Q. Yang, X. Hou, and F. Chen, "Magnetically controllable isotropic/anisotropic slippery surface for flexible droplet manipulation," *Langmuir*, vol. 36, pp. 15403–15409, 2020.

[27] G. P. Zhu, Q. Y. Wang, Z. K. Ma, S. H. Wu, and Y. P. Guo, "Droplet manipulation under a magnetic field: A review," *Biosensors*, vol. 12, 2022.

[28] M. A. Bijarchi, A. Favakeh, E. Sedighi, and M. B. Shafii, "Ferrofluid droplet manipulation using an adjustable alternating magnetic field," *Sensors and Actuators, A: Physical*, vol. 301, 2020.

[29] J. Gong and C. J. Kim, "All-electronic droplet generation on-chip with real-time feedback control for ewod digital microfluidics," *Lab on a Chip*, vol. 8, pp. 898–906, 2008.

[30] K. Han, Z. Wang, X. Han, X. Wang, P. Guo, P. Che, L. Heng, and L. Jiang, "Active manipulation of functional droplets on slippery surface," *Advanced Functional Materials*, vol. 32, 2022.

[31] D. Hu, H. Lai, Z. Cheng, Y. Song, X. Luo, D. Zhang, Z. Fan, Z. Xie, and Y. Liu, "A magnetic-driven switchable adhesive superhydrophobic surface for in situ sliding control of superparamagnetic microdroplets," *Advanced Materials Interfaces*, vol. 9, 2022.

[32] U. Banerjee and A. K. Sen, "Shape evolution and splitting of ferrofluid droplets on a hydrophobic surface in the presence of a magnetic field," *Soft Matter*, vol. 14, pp. 2915–2922, 2018.

[33] C. Yang and G. Li, "A novel magnet-actuated droplet manipulation platform using a floating ferrofluid film," *Scientific Reports*, vol. 7, 2017.

[34] U. Banerjee, S. K. Jain, and A. K. Sen, "Particle encapsulation in aqueous ferrofluid drops and sorting of particle-encapsulating drops from empty drops using a magnetic field," *Soft Matter*, vol. 17, pp. 6020–6028, 2021.

[35] S. K. Jain, U. Banerjee, and A. K. Sen, "Trapping and coalescence of diamagnetic aqueous droplets using negative magnetophoresis," *Langmuir*, vol. 36, pp. 5960–5966, 2020.

[36] M. K. Khaw, C. H. Ooi, F. Mohd-Yasin, R. Vadivelu, J. S. John, and N. T. Nguyen, "Digital microfluidics with a magnetically actuated floating liquid marble," *Lab on a Chip*, vol. 16, pp. 2211–2218, 2016.

[37] E. Katz, "Magnetic nanoparticles," *Magnetochemistry*, vol. 6, pp. 1–6, 2020.

[38] L. Liu, Y. Pan, B. Bhushan, F. Li, and X. Zhao, "Core-shell magnetic nanoparticles for substrate-independent super-amphiphobic surfaces and mechanochemically robust liquid marbles," *Chemical Engineering Journal*, vol. 391, 2020.

[39] Y. Zhao, J. Fang, H. Wang, X. Wang, and T. Lin, "Magnetic liquid marbles: Manipulation of liquid droplets using highly hydrophobic Fe_3O_4 nanoparticles," *Advanced Materials*, vol. 22, pp. 707–710, 2010.

[40] S. Fujii, "Liquid marble as an amphibious carrier for the controlled delivery and release of substances," *Langmuir*, vol. 38, pp. 12757–12763, 2022.

[41] C. H. Ooi and N. T. Nguyen, "Manipulation of liquid marbles," *Microfluidics and Nanofluidics*, vol. 19, pp. 483–495, 2015.

[42] R. Chen, Q. Xiong, R. Z. Song, K. L. Li, Y. X. Zhang, C. Fang, and J. L. Guo, "Magnetically controllable liquid metal marbles," *Advanced Materials Interfaces*, vol. 6, 2019.

[43] R. Deb, B. Sarma, and A. Dalal, "Magnetowetting dynamics of sessile ferrofluid droplets: a review," *Soft Matter*, vol. 18, pp. 2287–2324, 2022.

[44] H. Feng, X. Xu, W. Hao, Y. Du, D. Tian, and L. Jiang, "Magnetic field actuated manipulation and transfer of oil droplets on a stable underwater superoleophobic surface," *Physical Chemistry Chemical Physics*, vol. 18, pp. 16202–16207, 2016.

[45] C. Mandal, U. Banerjee, and A. K. Sen, "Transport of a sessile aqueous droplet over spikes of oil based ferrofluid in the presence of a magnetic field," *Langmuir*, 2019.

[46] X. Fan, X. Dong, A. C. Karacakol, H. Xie, and M. Sitti, "Reconfigurable multifunctional ferrofluid droplet robots," *Proceedings of the National Academy of Sciences*, vol. 117, no. 45, pp. 27916–27926, 2020.

[47] U. Banerjee, A. Raj, and A. K. Sen, "Dynamics of aqueous ferrofluid droplets at coflowing liquid-liquid interface under a non-uniform magnetic field," *Applied Physics Letters*, vol. 113, 2018.

[48] M. Kostrzewska, L. Yu, Y. Li, J. Li, B. Wenzell, T. Kasama, and A. L. Skov, "Magnetically activated microcapsules as controlled release carriers for a liquid pdms crosslinker," *Materials Research Express*, vol. 6, 2019.

[49] C. Prabu, S. Latha, P. Selvamani, F. Ahrentorp, C. Johansson, R. Takeda, Y. Takemura, and S. Ota, "Layer-by-layer assembled magnetic prednisolone microcapsules (MPC) for controlled and targeted drug release at rheumatoid arthritic joints," *Journal of Magnetism and Magnetic Materials*, vol. 427, pp. 258–267, 2017.

[50] T. Kato, R. Nemoto, H. Mori, R. Abe, K. Unno, A. Goto, H. Murota, M. Harada, and M. Homma, "Magnetic microcapsules for targeted delivery of anticancer drugs," 1984.

[51] P. M. Price, W. E. Mahmoud, A. A. Al-Ghamdi, and L. M. Bronstein, "Magnetic drug delivery: Where the field is going," *Frontiers in Chemistry*, vol. 6, 2018.

[52] B. Ma, J. H. Hansen, S. Hvilsted, and A. L. Skov, "Control of pdms crosslinking by encapsulating a hydride crosslinker in a pmma microcapsule," *RSC Advances*, vol. 4, pp. 47505–47512, 2014.

[53] X. H. Ge, J. P. Huang, J. H. Xu, and G. S. Luo, "Controlled stimulation-burst targeted release by smart decentered core-shell microcapsules in gravity and magnetic field," *Lab on a Chip*, vol. 14, pp. 4451–4454, 2014.

[54] E. Zwar, A. Kemna, L. Richter, P. Degen, and H. Rehage, "Production, deformation and mechanical investigation of magnetic alginate capsules," *Journal of Physics Condensed Matter*, vol. 30, 2018.

[55] U. Banerjee, S. Misra, and S. K. Mitra, "Liquid–liquid encapsulation of ferrofluid using magnetic field," *Advanced Materials Interfaces*, vol. 9, 2022.

[56] P. Aussillous and D. Quéré, "Properties of liquid marbles," *Proceedings of the Royal Society A: Mathematical, Physical and Engineering Sciences*, vol. 462, pp. 973–999, 2006.

[57] X. Li, S. Li, Y. Lu, M. Liu, F. Li, H. Yang, S. Y. Tang, S. Zhang, W. Li, and L. Sun, "Programmable digital liquid metal droplets in reconfigurable magnetic fields," *ACS Applied Materials and Interfaces*, vol. 12, pp. 37670–37679, 2020.

[58] S. Misra, K. Trinavee, N. S. K. Gunda, and S. K. Mitra, "Encapsulation with an interfacial liquid layer: Robust and efficient liquid-liquid wrapping," *Journal of Colloid and Interface Science*, vol. 558, pp. 334–344, 2019.

[59] S. Yin, Y. Huang, X. Shen, C. Zhang, X. Chen, Marcos, H. Li, and T. N. Wong, "Triple-layered encapsulation through direct droplet impact," *Journal of Colloid and Interface Science*, vol. 615, pp. 887–896, 2022.

[60] V. P. Carey, *Liquid-Vapor Phase-Change Phenomena: An Introduction to the Thermophysics of Vaporization and Condensation Processes in Heat Transfer Equipment, Third Edition*. Boca Raton: CRC Press, 3 ed., 2020.

[61] J. B. Boreyko, G. Polizos, P. G. Datskos, S. A. Sarles, and C. P. Collier, "Air-stable droplet interface bilayers on oil-infused surfaces," *Proceedings of the National Academy of Sciences of the United States of America*, vol. 111, pp. 7588–7593, 2014.

Chapter 5

Liquid-liquid encapsulation of ferrofluid using magnetic field [1]

5.1 Overview

Encapsulated magnetic microdroplets are of paramount importance in drug targeting and therapeutic applications. However, conventional techniques for generating encapsulated magnetic microdroplets suffer from several challenges, including lack of monodispersity, inflexibility in core-shell combinations, and complex device architecture to achieve encapsulation. Herein, a facile magnet-assisted framework to controllably wrap ferrofluid (FF) droplets inside polydimethylsiloxane (PDMS) floating on a water bath is developed. A permanent magnet placed at the bottom of a static glass cuvette pulls the ferrofluid droplet across the PDMS-water interface, which results in the wrapping of the FF droplet by a thin PDMS layer. The deformation of the FF-PDMS interface and the encapsulation of FF inside PDMS thereof is attributed to the interplay of magnetic force and force due to PDMS-water interfacial tension. Based on the experimental observations, three regimes are identified, namely, stable encapsulation, unstable encapsulation, and no encapsulation,

[1] Adapted with permission from Banerjee, U*; **Misra, S***; Mitra, S.K. *Advanced Materials Interfaces*, 9(21), 2022, 2200288. *: Equally contributing first-authors.

which depends on the magnetic Bond number (Bo_m) and the thickness of the PDMS layer (δ). The versatility of the technique is demonstrated further by showing stable wrapping of multiple ferrofluid droplets inside the same encapsulated cargo and successful underwater manipulation of the encapsulated droplets, which finds relevance in the encapsulation and magnet-assisted actuation of novel encapsulated materials.

5.2 Introduction

Drug delivery is one of the primary focuses of therapeutics in which drugs need to be delivered inside the body. Conventionally, drugs are either consumed orally or administered via injections. In this way, the drugs are delivered throughout the whole body, which causes adverse effects such as reduced efficacy, damage to healthy cells, etc. On the other hand, target drug delivery delivers the drug at the desired lesion inside the body, thereby improving the efficacy, reduction in dosage frequency, and concomitant side effects [1]. Several techniques utilize external stimuli such as acoustics, optics, electric and magnetic field for target drug delivery [2, 3]. Among these techniques, drug targeting using a magnetic field offers several advantages, including simplified device architecture for controlled droplet actuation and contactless manipulation with minimal heat generation. Magnetic drug targeting (MDT) [4] is a technique in which an external magnetic field assists the delivery and the controlled release of magnetic cargos containing the drugs at the desired lesion inside the body [5–7]. The magnetic cargos consist of magnetic nanoparticles [8–10], magnetic microspheres, or encapsulated magnetic microdroplets [11]. In general, encapsulated magnetic microdroplets consist of a magnetic fluid (core) wrapped by a polymeric membrane (shell) which can be employed as cargo for drug targeting [12–14]. Owing to the high saturation magnetization, better stability, and low toxicity of iron oxide, magnetic nanoparticles (MNPs) [15, 16], are the preferred choice. The ferrofluids, which are colloidal suspensions of iron oxide MNPs (size $\sim$ 10 nm) in oil or water dispersion medium, are exceedingly used for magnetic drug targeting [17–19], and antibody extraction [20].

Encapsulated magnetic microdroplets can be fabricated using techniques involving polymerization-based chemical methods [13, 21, 22], emulsification [22], phase separation

[23–25], layer-by-layer templating [26–28], and droplet microfluidics [29–37]. In the case of the polymerization-based method, an emulsion consisting of the magnetic liquid and an immiscible dispersed phase (such as water) is synthesized. Then, a copolymer is precipitated at the interface between a magnetic fluid and the dispersed phase, resulting in the formation of encapsulated magnetic microdroplets. However, these processes suffer from several restrictions, including a lack of suitable core-shell combination due to strict chemical property requirements for successful polymerization reaction, challenges in ensuring monodispersity of the encapsulated drops, and limited control over the volume of the encapsulated core, and the thickness of the shell layer. In addition to these challenges, the possibility of losing the stability of the magnetic fluid and the lack of sensitivity of the magnetic microdroplet towards the externally applied magnetic field remains another set of challenges. Similarly, microfluidic-based systems would require the fabrication of microfluidic devices, involvement of multiple syringe pumps for fluid infusion, and controlled wetting conditions [38, 39] of the microfluidic device for the generation of encapsulated magnetic microdroplets [40].

Herein, we demonstrate a facile liquid-liquid encapsulation technique in which polyethylene glycol (PEG) based ferrofluid (miscible with water) droplet is encapsulated inside a PDMS shell using a magnetic field. Briefly, the to-be-encapsulated ferrofluid droplet ('core' droplet) is gently dispensed on top of a PDMS layer floating on a water bath (**Figure 5.1**). As the dispensed ferrofluid droplet gets deformed in response to the externally applied magnetic field, it also deforms the PDMS layer underneath. Eventually, a competition between the disruptive magnetic force and the restorative interfacial tension force at the PDMS-water interface leads to the formation of a thin wrapping layer of PDMS all-around the ferrofluid droplet. Once encapsulated, the PEG-based ferrofluid droplet remains stable in the water bath despite its complete miscibility in water, affirming the stability and integrity of the wrapping. The non-toxicity, biocompatibility, and bio-stability of PDMS are the primary reason behind its selection as the shell material [41]. A prolific development has happened in the direction of under-liquid systems investigating the wetting signature [42–48], encapsulation of liquid inside thin elastic sheets [49], and manipulation of droplets [50]. The present study is motivated by a simple and robust technique developed by our research group in which droplets of laser oil (core), generated by a nozzle, are impinged on

a layer of canola oil (shell layer floating on a water bath), resulting in the encapsulation of laser oil inside canola oil [51, 52]. The techniques in which encapsulation is achieved by droplet impact demand a threshold kinetic energy of the droplet for successful encapsulation, which makes the droplet size and height of impact limiting parameters compared to its unprecedented throughput ($\sim$ 300,000 encapsulations/hr using four injection nozzles). In addition to that, issues of air entrapment during droplet impact [53], and splashing [54] remain significant challenges in these techniques. Thus, to overcome these challenges, we have proposed a technique that exploits the interplay of magnetic force and the force due to interfacial tension for successful encapsulation of ferrofluid inside PDMS, resulting in the formation of encapsulated magnetic microdroplets with better control over the encapsulation process. Based on the magnetic Bond number (Bo_m), the thickness of the PDMS layer (δ), three regimes are identified as stable encapsulation, unstable encapsulation and no encapsulation. The influence of δ on the final volume of the encapsulated droplet and shell volume is also investigated. Finally, the technique is exploited to encapsulate multiple ferrofluid droplets inside a single shell layer and their sensitivity toward the magnetic field. This technique demonstrates a facile way to efficiently wrap and protect a ferrofluid droplet and enables responsive manipulation of the encapsulated cargo inside water, a physiologically relevant medium. At first, the schematic representation of the encapsulation process is presented. Then, the effect of magnetic Bond number (Bo_m) on the shape evolution of the FF-PDMS interface and various regimes are delineated. Finally, the effect of the thickness of the PDMS interfacial layer on the encapsulated droplet and the encapsulation of multiple ferrofluid droplets inside a PDMS shell is presented.

5.3 Results and Discussions

Figure 5.1 depicts the magnet-assisted encapsulation of a ferrofluid (FF) droplet inside a shell of polydimethylsiloxane (PDMS) floating on a water bath. The degassed PDMS mixture (10:1) is dispensed on the water bath and allowed to spread uniformly for a sufficient time [55], resulting in the formation of a thin PDMS layer of thickness δ (Figure 5.1a). A neodymium iron boron (NdFeB) permanent magnet (B_r = 1.48 T), fixed on a vertical moving stage, is placed at a gap (g >> δ) below the bottom surface of the cuvette, which

provides a non-uniform magnetic field (Figure 5.1a). Then, a ferrofluid droplet is gently dispensed on the PDMS layer from close proximity so that the effect of droplet impact on the encapsulation process can be neglected. The droplet, upon dispensation, experiences magnetic force $\boldsymbol{F_m}$ due to the presence of the magnet resulting in the elongation of the FF-PDMS interface toward the magnet, as shown in Figure 5.1b. The PDMS-water interfacial tension opposes the elongation of the FF-PDMS interface with a force, $\boldsymbol{F_i}$ acting along the interface, as shown in Figure 5.1b. The interplay of $\boldsymbol{F_m}$ and $\boldsymbol{F_i}$ results in the deformation of the PDMS-water interface as depicted in the schematic (Figure 5.1b) and observed in the experiments (Figure 5.1d). Eventually, during the course of deformation, the PDMS-water interface comes in contact with the bottom surface of the cuvette, which restricts its movement further. Subsequently, as the ferrofluid droplet is pushed further downward, the deformed PDMS-water interface above the FF droplet starts to narrow down, leading to the formation of a PDMS neck. Eventually, the neck thins down and splits into two parts where the bottom part engulfs the FF core droplet leading to successful encapsulation as shown in the schematic (Figure 5.1c) and observed in the experiments (Figure 5.1e). At this stage, the flat shape of the PDMS-water interface gets restored, and the encapsulated FF droplet detaches from the interfacial layer and settles down at the bottom of the cuvette. Due to the presence of the magnet at the bottom of the cuvette, the encapsulated droplet is deformed in shape. The detailed mechanism of the encapsulation process is discussed further in this section.

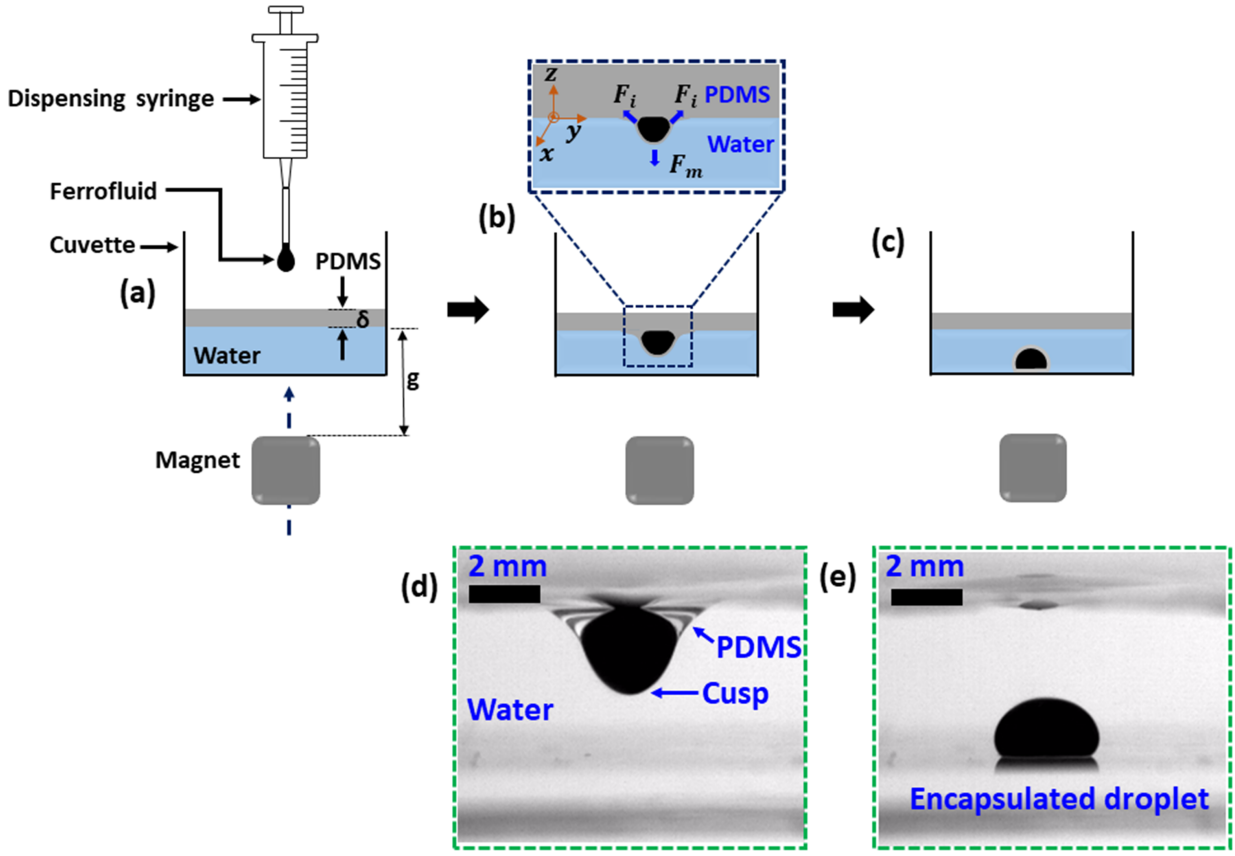

Figure 5.1: Schematic representation of the encapsulation process. a) A ferrofluid droplet is dispensed on the PDMS interfacial layer. The axis of magnetization is shown as a blue dotted arrow. b) The interplay of magnetic force and interfacial tension force results in the deformation of the PDMS-water interface, the schematic illustrating the forces acting at the interface is shown inside the blue box (dotted). c) The encapsulated droplet settles down at the bottom of the cuvette surrounded by the water bath. d) Experimental image depicting the deformation of the PDMS-water interface corresponding to the schematic shown in (b). e) Experimental image showing the ferrofluid droplet encapsulated inside PDMS shell corresponding to the schematic shown in (c).

Figure 5.2a depicts the temporal evolution of the FF-PDMS interface, and Figures 2b, Figure 5.2c, and Figure 5.2d delineate the time-lapse image of the deformed FF-PDMS interface for the corresponding three cases (Bo_m = 90, 99, and 112, respectively). The ferrofluid droplet volume and the gap (g) corresponding to the magnetic Bond number are as follows: for Bo_m = 90, the gap g = 1.33 cm, and ferrofluid volume V_{FF} = 15 μl, for Bo_m = 99, the gap g = 1.23 cm, and ferrofluid volume V_{FF} = 12 μl and, for Bo_m = 112, the gap g = 1.13 cm, and ferrofluid volume V_{FF} = 9 μl. The volume of PDMS is 100 μl and is kept constant for all three cases. The magnetic Bond number (Bo_m) which compares the magnetic force ($\boldsymbol{F_m}$) to the interfacial tension force ($\boldsymbol{F_i}$) is estimated as $Bo_m = \frac{\mu_0 H^2 R}{\gamma_i}$ [56], where $\mu_0 = 4\pi \times 10^{-7}$ H-m^{-1} is the magnetic permeability of free space, H is the magnitude of the applied H-field (A-m^{-1}), R is the radius of the ferrofluid droplet (m) estimated assuming a spherical shape of the FF droplet, γ_i is the interfacial tension between the PDMS-water interface. The deformed shape of the FF-PDMS interface is characterized by the width (D) and height (L) along the y-direction and the z-direction, respectively, as shown in the inset (green box, Figure 5.2a). The width (D) and height (L) are non-dimensionalized by the respective initial width and height (at t = 0) for estimating D* and L*. The time scale (t) is also non-dimensionalized by the total time, T, to obtain t* where T is given by T= t_2 - t_1, t_1 corresponds to the instance of the dispensation of the FF droplet on top of the PDMS interfacial layer, while t_2 is the temporal instance just before the deformed PDMS-water interface touches the bottom of the cuvette. Therefore at t* = 1, the PDMS-water interface is barely above the bottom surface of the cuvette, and at the immediate next time instance, it touches the cuvette's bottom. The ferrofluid droplet, upon dispensation on the PDMS interfacial layer, experiences a magnetic force $\boldsymbol{F_m}$ along the negative z-direction as shown in Figure 5.1b. In addition to that, the presence of the PDMS-water interface gives rise to the interfacial tension force $\boldsymbol{F_i}$ acting at the interface as shown in Figure 5.1b. The component of $\boldsymbol{F_i}$ along the z-direction attempts to restrict the deformation of the FF-PDMS interface due to the magnetic force (along the negative z-direction). Due to the magnetic force, the MNPs present inside the FF droplet tends to migrate and accumulate at the cusp [57], giving rise to an increased concentration of MNPs at the cusp and the elongation of the FF-PDMS interface. Due

to the elongation of the FF-PDMS interface, the interface moves closer to the magnet. The cumulative effect of the accumulation of MNPs at the cusp and the movement of the FF-PDMS interface closer to the magnet gives rise to enhanced magnetic interaction. Ferrofluid droplets of volume ranging from 6 μl to 15 μl are used in the experiments. The H-field ($\boldsymbol{H}$, in A m^{-1}) produced by the rectangular permanent magnet is estimated using the analytical expression, as shown in Appendix C (**Figure C.2**). As discussed previously, the interplay of magnetic force and force due to interfacial tension plays a vital role in the deformation of the FF-PDMS interface. Thus magnetic Bond number (Bo$_m$), which compares the magnetic force ($\boldsymbol{F_m}$) to the interfacial tension force ($\boldsymbol{F_i}$) is used to represent the experimental results. It can be seen from Figure 5.2a, for Bo$_m$ = 90, the width (D*) along y-direction reduces slightly and remain constant (from t* = 0.2 to 0.76). On the other hand, the height (L*) along the z-direction keeps on increasing. After t* = 0.76, the rapid decrease in D* and rapid increase in L* leads to the formation of a downward bell shape (at t* = 1), as shown in Figure 5.2b. On the contrary, as Bo$_m$ is increased (Figure 5.2a) from Bo$_m$ = 90 to 112, the time over which D* remains constant reduces significantly, and the rapid decay in D* and rapid increase in L* begins at an early stage (at t* = 0.50) which can be attributed to the increase in the magnetic interaction between the MNPs and the H-field. In each case, the interplay of magnetic force and the force due to interfacial tension leads to a downward bell shape of the FF-PDMS interface, as shown in Figure 5.2b, Figure 5.2c, and Figure 5.2d.

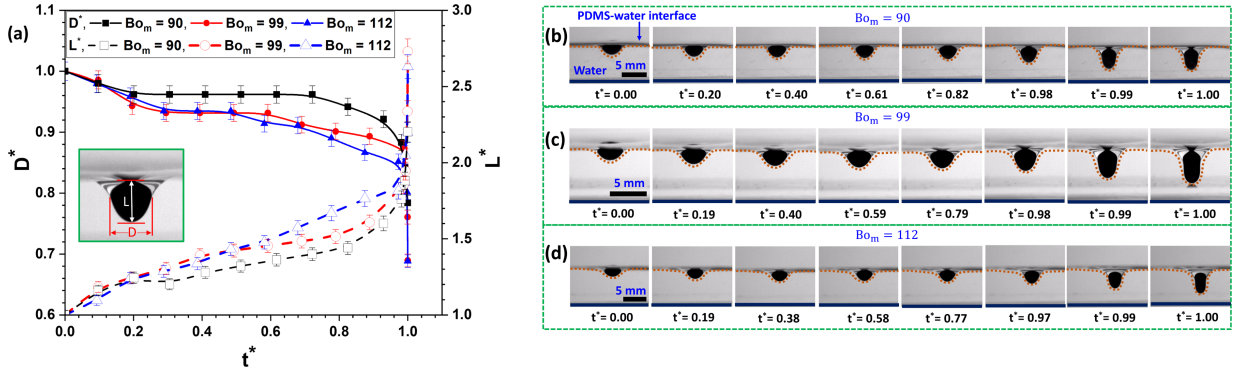

Figure 5.2: Characterization of the deformed shape of the FF-PDMS interface. a) Variation in the width (D^*) and height (L^*) of the FF-PDMS interface along the y-direction and the z-direction, respectively, for three magnetic Bond numbers (Bo_m). Time-lapse images showing the evolution of the FF-PDMS interface for (a) $Bo_m = 90$, (b) $Bo_m = 99$, and (c) $Bo_m = 112$.

Figure 5.3a depicts the regime map consisting of three regimes, namely stable encapsulation, unstable encapsulation, and no encapsulation, as observed in the experiments. An extensive set of experiments are performed by varying the gap (g = 0.83 – 1.33 cm), FF droplet volume (V_{FF} = 6 – 15 μl), and the volume of the PDMS interfacial layer (V_{PDMS} = 100 – 500 μl). The ferrofluid droplet volume, the gap (g) and the volume of PDMS corresponding to the magnetic Bond number are as follows: for $Bo_m = 99$, the gap g = 1.23 cm, ferrofluid volume V_{FF} = 12 μl, and, PDMS volume V_{PDMS} = 100 μl, for $Bo_m = 298$, the gap g = 0.93 cm, ferrofluid volume V_{FF} = 6 μl, and, the PDMS volume V_{PDMS} = 500 μl and, for $Bo_m = 392$, the gap g = 0.83 cm, ferrofluid volume V_{FF} = 12 μl, and, PDMS volume V_{PDMS} = 100 μl. The variation of the gap, FF droplet volume, and the volume of PDMS gives rise to the variation in the magnetic H-field (H), FF droplet size (R), and the thickness of the PDMS interfacial layer (δ), respectively. Based on the experimental observations, the regimes of encapsulation are presented using the magnetic Bond number (Bo_m) and the non-dimensional encapsulation time (T^*), as shown in Figure 5.3a. The encapsulation time (t_{en}) is defined as the time gap between the dispensation of the ferrofluid droplet on the interfacial PDMS layer and the necking of the PDMS-water interface that leads to the formation of the encapsulated droplet. The encapsulation time

is non-dimensionalized as $T^* = \frac{\gamma_i t_{en}}{\mu\delta}$ [58], where μ is the dynamic viscosity of PDMS (Pa-s), and δ represents the thickness of the PDMS interfacial layer. Since the PDMS spreads uniformly over the water [55], the thickness of the PDMS layer can be estimated as $\delta = \frac{V_{PDMS}}{A_c}$, where V_{PDMS} represents the volume of PDMS dispensed and A_c is the inner cross-sectional area of the cuvette. It can be seen from Figure 5.3a that the blue color regime is identified as the stable regime ($80 \leq \text{Bo}_m < 296$) in which the ferrofluid droplet encapsulated inside the PDMS shell remains stable. For $\text{Bo}_m < 80$, the deformation of the FF-PDMS interface is not significant, which can be attributed to the fact that the magnetic force ($\boldsymbol{F_m}$) is not sufficient to overcome the force due to interfacial tension ($\boldsymbol{F_i}$) offered by the PDMS-water interface. As discussed previously, the migration of MNPs toward the cusp and the interplay of $\boldsymbol{F_m}$ and $\boldsymbol{F_i}$ results in the deformed shape of the FF-PDMS interface as depicted in Figure 5.3c (t = 0.00 to 172.00 s). During the deformation, the PDMS-water interface comes in contact with the bottom of the cuvette, as shown in Figure 5.3c (t = 172.02 s), and due to the magnetic force, the interface is pushed further down against the cuvette bottom. This leads to the formation of a PDMS bridge which slowly thins down as time progresses. Eventually, necking takes place, causing the splitting of the PDMS bridge and consequent formation of the encapsulated droplet, as shown in Figure 5.3c (t = 172.94 s). For a particular Bo_m, an increase in δ results in a higher encapsulation time, which is attributed to the higher viscous resistance offered by the PDMS interfacial layer. The high viscous resistance slows down the necking of the PDMS bridge, which delays the encapsulation process resulting in a longer encapsulation time. In the case of unstable encapsulation, the PDMS shell ruptures for the given $\text{Bo}_m = 298$, and the ferrofluid droplet dissolves in the water bath. This corresponds to a Bo_m in the range of $296 \leq \text{Bo}_m < 358$, as shown in Figure 5.3a. To understand the underlying mechanism behind the rupture in the unstable encapsulation regime, we performed a separate experiment where an encapsulated droplet was exposed to a gradually increasing H-field (H) till the point of rupture of the shell layer and consequent leakage of the encapsulated FF core. The H-field is varied by varying the distance between the magnet and the encapsulated droplet. The deformation of the encapsulated droplet with the H-field is captured in Figure 5.3b. The deformation is presented by the settled encapsulated droplet aspect ratio when it rests on the bottom of the cuvette, which is defined as the ratio of the height (d_1) and the width

(d_2) of the droplet. The parameters d_1 and d_2 for a deformed droplet are schematically shown in the bottom inset of Figure 5.3b. The H-field is also non-dimensionalized by the maximum H-field (H_{max}) to obtain H^*. The maximum H-field (H_{max}) is defined as the magnitude of the H-field at the point of rupture of the PDMS shell. It can be seen that, in the absence of the H-field, the encapsulated droplet adopts a spherical shape (d_1/d_2 = 0.96), as shown in the inset of Figure 5.3b (green dotted box). As the magnet is brought closer to the droplet (at H^* = 0.34), the droplet gets deformed, where d_1 gradually increases while d_2 decreases resulting in a reduction in d_1/d_2 (d_1/d_2 = 0.82), as shown in the inset of Figure 5.3b (yellow dotted box). The deformation of the droplet is due to the magnetic force which pushes the droplet against the bottom of the cuvette giving rise to magnetic stress and concomitant deformation. As the H-field is further enhanced (at H^* = 1), the droplet deforms to the maximum extent (d_1/d_2 = 0.62) before the shell ruptures, as shown in Figure 5.3b (red dotted box). At a lower value of H-field, the interfacial tension between FF-PDMS competes against the magnetic force to restrict the deformation of the encapsulated droplet. The encapsulated FF core elongates in width as the magnet is brought closer. The magnet exerts a magnetic force on the encapsulating PDMS shell layer, which leads to the accumulation of elastic stress in the shell. Beyond a threshold H-field (H_{max}), the shell layer cannot withstand the generated elastic stress, which initiates rupture of the shell at the maximum stress point of occurrence. In our experiments, we observed that the rupture occurs from a point underneath the droplet near the three-phase contact line between the bottom surface, PDMS shell, and the surrounding water medium (see Figure 5.3d, t = 2.60 s). This stands in agreement with a previous theoretical study [21], where maximum elastic stress in a deformed encapsulated droplet with a magnetic core and an elastic shell was estimated to occur near the curved region at the bottom of the droplet. If the magnetic Bond number is very high ($Bo_m \geq 358$), the PDMS shell can no longer encapsulate the ferrofluid droplet, and rupture occurs before the necking of the PDMS-water interface, as shown in Figure 5.3e (t = 0.14 s). This regime is marked as the no encapsulation regime in Figure 5.3a.

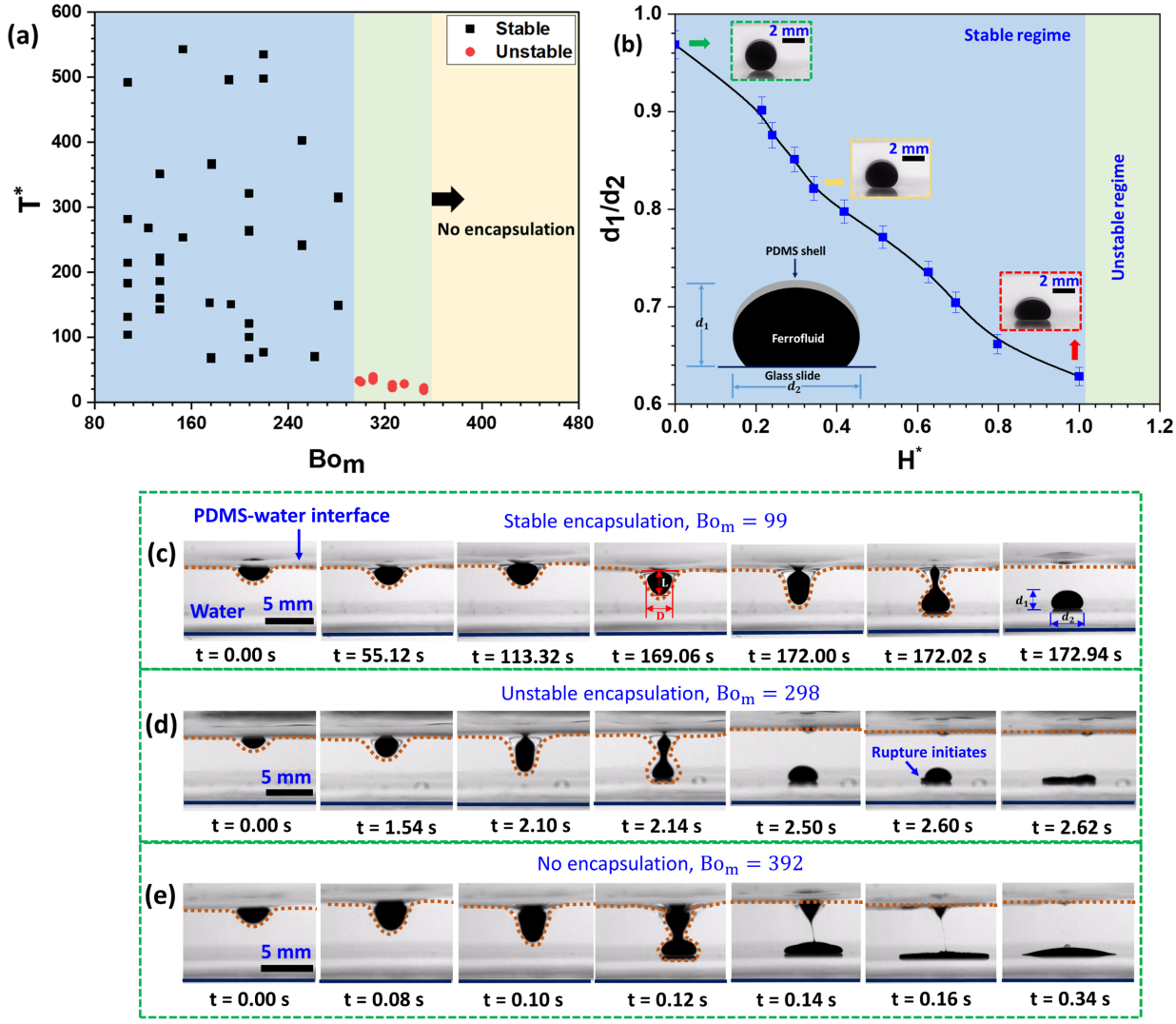

Figure 5.3: a) Regime map manifesting various regimes of encapsulation and the dependence of magnetic Bond number (Bo_m), the thickness of PDMS shell layer (δ) on the non-dimensional encapsulation time (T^*). b) Deformation of a ferrofluid droplet with the gradual increase in the H-field. Regimes of encapsulation - (c) Stable encapsulation for $Bo_m = 99$. (d) Unstable encapsulation for $Bo_m = 298$. (e) No encapsulation for $Bo_m = 392$.

Figure 5.4 explores the effect of the thickness of the PDMS interfacial layer, δ, on the volume of the encapsulated drop, V_{encap}. By varying the volume of the dispensed PDMS, we were able to control δ. The experiments are performed for five different PDMS volumes, which are 100, 200, 300, 400, and 500 μl. The corresponding thickness of the PDMS interfacial layer (δ) is estimated to be 77, 154, 231, 308, and 385 μm, respectively. The magnetic Bond number ($Bo_m = 175$) in each case is kept constant by keeping the ferrofluid volume (9 μl) and the gap (g) fixed. In the experiments, a plasma-treated glass slide of a thickness of 1 mm is placed on the cuvette bottom so that the encapsulated droplet adopts a spherical shape when the H-field is removed. The encapsulated droplet volume is estimated using the spherical geometry in each case. It can be seen from Figure 5.4 that an increase in the volume of PDMS (increase in thickness δ) results in an increment in the volume of the encapsulated droplet. This can be attributed to the fact that, as the PDMS thickness increases, the time of encapsulation increases (explained in Figure 5.3) due to a stronger viscous resistance offered by the PDMS interfacial layer. Due to this increase in encapsulation time, the residence time inside the interfacial layer for FF increases before the formation of an encapsulated droplet. Thus, the FF droplet detaches a higher volume of PDMS from the interfacial layer upon successful encapsulation, which leads to a larger encapsulated droplet volume and the corresponding shell volume. The experimental images corresponding to the encapsulated droplets in each case are also shown as insets of Figure 5.4. If the volume of the PDMS layer is increased significantly, it may happen that the PDMS would not form a uniformly stratified layer on top of the water bath. The small density gap might lead to the sagging of the PDMS-water interface towards the water bath. Second, if the thickness is too high, the applied magnetic field strength might turn insufficient for the core drop to overcome the viscous resistance posed by the PDMS interfacial layer. Therefore, the core drop might not even detach from the interfacial layer preventing the formation of the encapsulated cargo. Finally, if the encapsulation is indeed successful, it is possible that with the increase in δ, the shell thickness of the encapsulated droplet will not increase monotonically. It is likely that after a certain δ, the shell thickness will saturate, and further increment in δ will not lead to any further increase in V_{encap}. This expectation stems from the observation in Figure 5.4, where a 400% increment in δ corresponds to only a 60% increase in shell thickness.

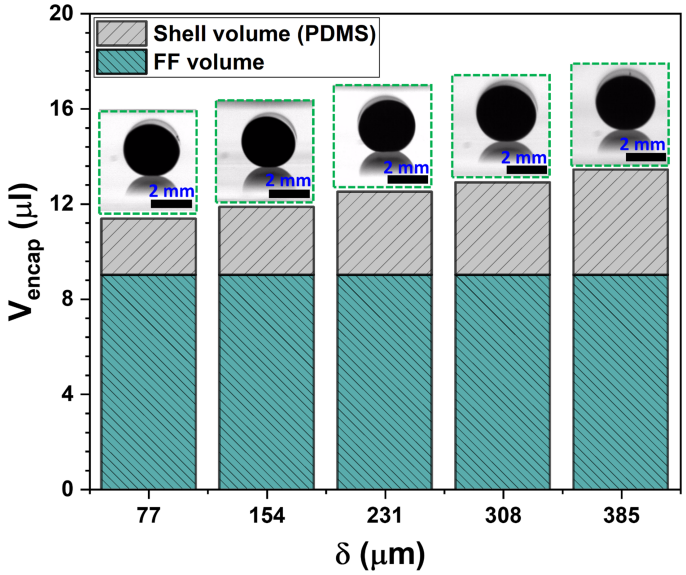

Figure 5.4: (a) The variation of encapsulated droplet volume with the interfacial layer thickness, δ

Figure 5.5 depicts the encapsulation of multiple ferrofluid droplets inside the PDMS shell and the encapsulation of a single ferrofluid droplet inside the shell of canola oil. In the case of multiple droplet encapsulation, multiple FF droplets are dispensed on a PDMS interfacial layer of volume = 300 μl. The magnetic Bond number (Bo_m = 107) is kept fixed for each case. The FF droplets are dispensed on the PDMS interfacial layer slowly and in a controlled manner. This process rules out the possibility of coalescence during multiple encapsulations due to the momentum associated with dispensation if a core drop is dispensed right on top of another previously dispensed core drop. Although once dispensed, a core droplet gets engulfed in the PDMS shell layer and thus always has a consistent PDMS wrapping layer all around it. But, the sudden dispensation of another droplet right on top can cause rupture of the PDMS shell, which is undesired in case of multiple encapsulations of FF droplets. Upon dispensation, the droplets start experiencing the magnetic pull, which brings them toward the axis of magnetization (as shown in Figure 5.1). However, at this point, due to the presence of a thin layer of PDMS

between each droplet, coalescence is hindered. The complete encapsulation process of multiple FF droplets is similar to that of a single FF droplet, as explained previously in Figure 5.3. It can be seen from Figure 5.5a-c that even after encapsulation, the droplets do not coalesce with each other. Apart from the outer PDMS shell layer encasing multiple FF droplets, each ferrofluid droplet is wrapped inside an individual PDMS shell. Therefore, a PDMS layer exists between the encapsulated droplets, which restricts the inter-droplet interaction and thus the coalescence, ultimately providing stability to the encapsulated cargo. This intermediate layer can be visualized in Figure 5.5a-c. The manipulation of an encapsulated droplet containing two ferrofluid droplets inside a PDMS shell using a permanent magnet is also achieved. Thus, the technique may find its potential application in the under-liquid formation of magnetic Janus droplets [59], packaging of drugs with multiple functionalities in the same encapsulated cargo, and it's delivery in therapeutic applications. The encapsulation layer is stable if the PDMS is in liquid form and the encapsulated droplet is inside the water bath. However, if the PDMS layer is cured at the desired temperature of 60° C for 4-5 hours inside an oven, the encapsulated droplet can be taken out of the water bath. As the present study focuses on understanding the mechanism of ferrofluid droplet encapsulation inside a PDMS shell inside a water bath, the curing of PDMS has not been studied.

Further, we also realized successful encapsulation (Figure 5.5d) of a FF droplet using less viscous canola oil (μ = 63.5 mPa-s) as the shell-forming liquid instead of PDMS. The dyed canola oil (300 μl) is dispensed on the water bath, which forms an interfacial layer, as seen in the encapsulation technique developed by our research group [51]. A ferrofluid droplet (9 μl) is then dispensed on the canola oil in the presence of a magnet (Bo_m = 93), resulting in the formation of an encapsulated droplet, as shown in Figure 5.5d. This indicates that the viscoelastic property of the PDMS is not essential for the success of the demonstrated technique and shows the possible direction of the future expansion of the repertoire of appropriate shell materials toward the development of novel encapsulated functional materials.

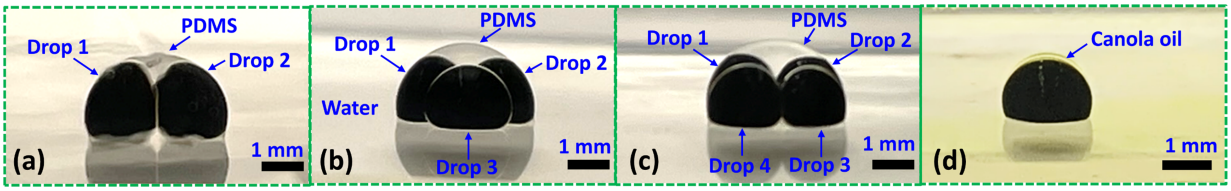

Figure 5.5: (a) Encapsulation of two ferrofluid droplets inside PDMS shell. (b) Encapsulation of three ferrofluid droplets inside the PDMS shell. (c) Encapsulation of four ferrofluid droplets inside the PDMS shell. (d) Encapsulation of a single ferrofluid droplet inside canola oil as an interfacial layer.

5.4 Conclusions

In summary, our work demonstrates a magnet-assisted facile encapsulation technique in which ferrofluid (FF) droplets are encapsulated inside polydimethylsiloxane (PDMS) floating on a water bath. A complex interplay between the magnetic force $\boldsymbol{F_m}$ and the interfacial tension force $\boldsymbol{F_i}$ results in the formation of a thin PDMS layer around the FF droplet which efficiently protects the PEG-based FF droplet underwater despite its complete miscibility in water. Based on the experimental observations, three regimes are identified: stable encapsulation, unstable encapsulation, and no encapsulation, which depends on the magnetic Bond number (Bo_m) and the thickness of the PDMS layer (δ). The technique is exploited to demonstrate stable wrapping of multiple ferrofluid droplets inside a single PDMS shell and successful underwater manipulation of the encapsulated droplets, which finds relevance in the formation and magnet-assisted actuation of novel encapsulated materials.

5.5 Experimental section

Materials

The proposed technique involves three liquids, a commercially available polyethylene glycol-based ferrofluid (PBG 900, Ferrotec, USA) with density $\rho = 1860$ kg-m^{-3}. The ferrofluid is diluted using DI water, and the resulting solution (10 % FF) is used as core liquid wrapped inside a shell layer consisting of polydimethylsiloxane (PDMS, Sylgard 184) with density $\rho = 965$ kg-m^{-3}, viscosity $\mu = 5.5$ Pa-s. The complete encapsulation process occurs inside a host liquid bath of deionized (DI) water (purified by Milli-Q, MilliporeSigma, Ontario, Canada) with density $\rho = 1000$ kg-m^{-3}, viscosity $\mu = 1$ mPa-s. The interfacial tension between PDMS and water is $\gamma_i = 42.1$ mN-m^{-1}.

Method

The PDMS monomer and curing agent at a ratio of 10:1 (by weight) were mixed and degassed inside a desiccator in order to remove the bubbles entering the PDMS solution. The experiments were conducted in a distortion-free glass cuvette (Product Code: SC-02, Krüss GmbH, Hamburg, Germany) of inner dimension 36 mm $\times$ 36 mm $\times$ 30 mm with 2.5 mm wall thickness fixed on a vertical moving stage (non-magnetic) using a double-sided tape. At first, the cuvette was partially filled with the host liquid (water, 6500 μl), resulting in a water column height of 0.5 cm using a pipette (Eppendorf, Canada). The PDMS mixture was then dispensed on the water layer using a syringe (1 ml NORM-JECT® sterile luer-slip syringes (Henke-Sass, Wolf GmbH, Tuttlingen, Germany) with appropriate volume control. The PDMS layer was then allowed to spread uniformly on the water surface for 30 s. A neodymium iron boron (NdFeB) permanent magnet of cubicle shape (2a = 2b = 2c = 12.7 cm, N52, magnetic strength $B_r = 1.48$ T, K&J Magnetics Inc., USA) was placed below the cuvette bottom surface fixed on a vertical moving stage using double-sided tape to control the H-field. The axis of magnetization of the magnet (Figure S1) is normal to the bottom surface of the cuvette. The variation of the H-field is shown in Appendix C (Figure C.2). In order to avoid any interference with the H-field,

non-magnetic materials (except the ferrofluid and magnet) were used in the experimental setup. Finally, ferrofluid droplets of volume ranging from 6 to 15 μl were gently dispensed on the PDMS interfacial layer using a pipette (Eppendorf, Canada) so that the effect of droplet impact could be neglected. The complete dynamics of the encapsulation process were captured using a high-speed camera (Photron, FASTCAM Mini AX200) coupled with a lens interfaced with a personal computer at 50 fps.

References

[1] Y. L. Liu, D. Chen, P. Shang, and D. C. Yin, "A review of magnet systems for targeted drug delivery," *Journal of Controlled Release*, vol. 302, no. April, pp. 90–104, 2019.

[2] C. Y. Lin, M. Javadi, D. M. Belnap, J. R. Barrow, and W. G. Pitt, "Ultrasound sensitive eLiposomes containing doxorubicin for drug targeting therapy," *Nanomedicine: Nanotechnology, Biology, and Medicine*, vol. 10, no. 1, pp. 67–76, 2014.

[3] S. Sengupta and V. K. Balla, "A review on the use of magnetic fields and ultrasound for non-invasive cancer treatment," *Journal of Advanced Research*, vol. 14, pp. 97–111, 2018.

[4] P. M. Price, W. E. Mahmoud, A. A. Al-Ghamdi, and L. M. Bronstein, "Magnetic drug delivery: Where the field is going," *Frontiers in Chemistry*, vol. 6, no. DEC, pp. 1–7, 2018.

[5] T. Kato, R. Nemoto, H. Mori, R. Abe, K. Unno, A. Goto, H. Murota, M. Harada, and M. Homma, "Magnetic microcapsules for targeted delivery of anticancer drugs," *Applied Biochemistry and Biotechnology*, vol. 10, no. 1-3, pp. 199–211, 1984.

[6] D. V. Voronin, O. A. Sindeeva, M. A. Kurochkin, O. Mayorova, I. V. Fedosov, O. Semyachkina-Glushkovskaya, D. A. Gorin, V. V. Tuchin, and G. B. Sukhorukov, "In Vitro and in Vivo Visualization and Trapping of Fluorescent Magnetic Microcapsules in a Bloodstream," *ACS Applied Materials and Interfaces*, vol. 9, no. 8, pp. 6885–6893, 2017.

[7] X. H. Ge, J. P. Huang, J. H. Xu, and G. S. Luo, "Controlled stimulation-burst targeted release by smart decentered core-shell microcapsules in gravity and magnetic field," *Lab on a Chip*, vol. 14, no. 23, pp. 4451–4454, 2014.

[8] E. Katz, "Magnetic Nano-Particles," *Magnetochemistry*, vol. 6, no. 1, pp. 2–7, 2020.

[9] A. S. Kumar, N. Bharath, M. D. S. Rao, P. Venkatesh, D. Hepcykalarani, and R. Prema, "A Review on Mucoadhesive Drug Delivery Systems," *Research Journal of Pharmaceutical Dosage Forms and Technology*, vol. 11, no. 4, p. 280, 2019.

[10] M. K. Manshadi, M. Saadat, M. Mohammadi, M. Shamsi, M. Dejam, R. Kamali, and A. Sanati-Nezhad, "Delivery of magnetic micro/nanoparticles and magnetic-based drug/cargo into arterial flow for targeted therapy," *Drug Delivery*, vol. 25, no. 1, pp. 1963–1973, 2018.

[11] M. Lengyel, N. Kállai-Szabó, V. Antal, A. J. Laki, and I. Antal, "Microparticles, microspheres, and microcapsules for advanced drug delivery," *Scientia Pharmaceutica*, vol. 87, no. 3, 2019.

[12] H. Chen, D. Sulejmanovic, T. Moore, D. C. Colvin, B. Qi, O. T. Mefford, J. C. Gore, F. Alexis, S. J. Hwu, and J. N. Anker, "Iron-loaded magnetic nanocapsules for pH-triggered drug release and MRI imaging," *Chemistry of Materials*, vol. 26, no. 6, pp. 2105–2112, 2014.

[13] S. Neveu-Prin, V. Cabuil, R. Massart, P. Escaffre, and J. Dussaud, "Encapsulation of magnetic fluids," *Journal of Magnetism and Magnetic Materials*, vol. 122, pp. 42–45, 1993.

[14] C. Wischnewski and J. Kierfeld, "Spheroidal and conical shapes of ferrofluid-filled capsules in magnetic fields," *Physical Review Fluids*, vol. 3, no. 4, pp. 1–40, 2018.

[15] D. Hu, H. Lai, Z. Cheng, Y. Song, X. Luo, D. Zhang, Z. Fan, Z. Xie, and Y. Liu, "A Magnetic-Driven Switchable Adhesive Superhydrophobic Surface for In Situ Sliding Control of Superparamagnetic Microdroplets," *Advanced Materials Interfaces*, vol. 2101660, pp. 1–9, 2021.

[16] Y. Zhan, S. Yu, A. Amirfazli, A. R. Siddiqui, and W. Li, "Magnetically Responsive Superhydrophobic Surfaces for Microdroplet Manipulation," *Advanced Materials Interfaces*, vol. 2102010, p. 1, 2022.

[17] R. Ganguly, A. P. Gaind, S. Sen, and I. K. Puri, "Analyzing ferrofluid transport for magnetic drug targeting," *Journal of Magnetism and Magnetic Materials*, vol. 289, pp. 331–334, 2005.

[18] L. Agiotis, I. Theodorakos, S. Samothrakitis, S. Papazoglou, I. Zergioti, and Y. S. Raptis, "Magnetic manipulation of superparamagnetic nanoparticles in a microfluidic system for drug delivery applications," *Journal of Magnetism and Magnetic Materials*, vol. 401, pp. 956–964, 2016.

[19] C. Scherer and A. M. F. Neto, "Ferrofluids — Properties and applications," *Brazillian Journal of Physics*, vol. 35, no. 3, pp. 718–727, 2005.

[20] H. H. Al-terke, M. Latikka, J. V. I. Timonen, L. Vékás, A. Paananen, J. Joensuu, and R. H. A. Ras, "Functional Magnetic Microdroplets for Antibody Extraction," *Advanced Materials Interfaces*, vol. 2101317, pp. 1–8, 2021.

[21] C. Wischnewski, E. Zwar, H. Rehage, and J. Kierfeld, "Strong Deformation of Ferrofluid-Filled Elastic Alginate Capsules in Inhomogenous Magnetic Fields," *Langmuir*, vol. 34, no. 45, pp. 13534–13543, 2018.

[22] E. Zwar, A. Kemna, L. Richter, P. Degen, and H. Rehage, "Production, deformation and mechanical investigation of magnetic alginate capsules," *Journal of Physics Condensed Matter*, vol. 30, no. 8, 2018.

[23] M. Kostrzewska, L. Yu, Y. Li, J. Li, B. Wenzell, T. Kasama, and A. L. Skov, "Magnetically activated microcapsules as controlled release carriers for a liquid PDMS crosslinker," *Materials Research Express*, vol. 6, no. 1, 2019.

[24] L. González, M. Kostrzewska, M. Baoguang, L. Li, J. H. Hansen, S. Hvilsted, and A. L. Skov, "Preparation and characterization of silicone liquid core/polymer shell microcapsules via internal phase separation," *Macromolecular Materials and Engineering*, vol. 299, no. 10, pp. 1259–1267, 2014.

[25] B. Ma, J. H. Hansen, S. Hvilsted, and A. L. Skov, "Control of PDMS crosslinking by encapsulating a hydride crosslinker in a PMMA microcapsule," *RSC Advances*, vol. 4, no. 88, pp. 47505–47512, 2014.

[26] P. Chakkarapani, L. Subbiah, S. Palanisamy, A. Bibiana, F. Ahrentorp, C. Jonasson, and C. Johansson, "Encapsulation of methotrexate loaded magnetic microcapsules for magnetic drug targeting and controlled drug release," *Journal of Magnetism and Magnetic Materials*, vol. 380, pp. 285–294, 2015.

[27] Y. Wang, A. S. Angelatos, and F. Caruso, "Template synthesis of nanostructured materials via layer-by-layer assembly," *Chemistry of Materials*, vol. 20, no. 3, pp. 848–858, 2008.

[28] E. Donath, G. B. Sukhorukov, F. Caruso, S. A. Davis, and H. Möhwald, "tion are fabricated by stepwise adsorption of oppositely charged polyelectrolytes onto melamin resin templates which are subsequently solubilized . P olyelectrolyte shells with controlled thickness and composi- T he confocal micrograph of a shell that is," *Angewandte Chemie (International ed. in English)*, vol. 37, no. 16, pp. 2201–2205, 1998.

[29] D. Liu, H. Zhang, F. Fontana, J. T. Hirvonen, and H. A. Santos, "Microfluidic-assisted fabrication of carriers for controlled drug delivery," *Lab on a Chip*, vol. 17, no. 11, pp. 1856–1883, 2017.

[30] S. Okushima, T. Nisisako, T. Torii, and T. Higuchi, "Controlled production of monodisperse double emulsions by two-step droplet breakup in microfluidic devices," *Langmuir*, vol. 20, no. 23, pp. 9905–9908, 2004.

[31] Q. Xu, M. Hashimoto, T. T. Dang, T. Hoare, D. S. Kohane, G. M. Whitesides, R. Langer, D. G. Anderson, and H. David, "Preparation of monodisperse biodegradable polymer microparticles using a microfluidic flow-focusing device for controlled drug delivery," *Small*, vol. 5, no. 13, pp. 1575–1581, 2009.

[32] M. Navi, J. Kieda, and S. S. Tsai, "Magnetic polyelectrolyte microcapsules: Via water-in-water droplet microfluidics," *Lab on a Chip*, vol. 20, no. 16, pp. 2851–2860, 2020.

[33] C. H. Yang, K. S. Huang, Y. S. Lin, K. Lu, C. C. Tzeng, E. C. Wang, C. H. Lin, W. Y. Hsu, and J. Y. Chang, "Microfluidic assisted synthesis of multi-functional polycaprolactone microcapsules: Incorporation of CdTe quantum dots, Fe3O4 superparamagnetic nanoparticles and tamoxifen anticancer drugs," *Lab on a Chip*, vol. 9, no. 7, pp. 961–965, 2009.

[34] A. Q. Alorabi, M. D. Tarn, J. Gómez-Pastora, E. Bringas, I. Ortiz, V. N. Paunov, and N. Pamme, "On-chip polyelectrolyte coating onto magnetic droplets-towards continuous flow assembly of drug delivery capsules," *Lab on a Chip*, vol. 17, no. 22, pp. 3785–3795, 2017.

[35] S. S. H. Tsai, J. S. Wexler, J. Wan, and H. A. Stone, "Conformal coating of particles in microchannels by magnetic forcing," *Applied Physics Letters*, vol. 99, no. 15, pp. 1–4, 2011.

[36] B.-u. Moon, N. Hakimi, D. K. Hwang, S. S. H. Tsai, B.-u. Moon, N. Hakimi, D. K. Hwang, and S. S. H. Tsai, "Microfluidic conformal coating of non-spherical magnetic particles Microfluidic conformal coating of non-spherical magnetic particles," vol. 052103, 2014.

[37] U. Banerjee, S. K. Jain, and A. K. Sen, "Particle encapsulation in aqueous ferrofluid drops and sorting of particle-encapsulating drops from empty drops using a magnetic field," *Soft Matter*, vol. 17, no. 24, pp. 6020–6028, 2021.

[38] V. Barbier, M. Tatoulian, H. Li, F. Arefi-Khonsari, A. Ajdari, and P. Tabeling, "Stable modification of PDMS surface properties by plasma polymerization: Application to the formation of double emulsions in microfluidic systems," *Langmuir*, vol. 22, no. 12, pp. 5230–5232, 2006.

[39] T. Nisisako, S. Okushima, and T. Torii, "Controlled formulation of monodisperse double emulsions in a multiple-phase microfluidic system," *Soft Matter*, vol. 1, no. 1, pp. 23–27, 2005.

[40] C. X. Zhao, "Multiphase flow microfluidics for the production of single or multiple

emulsions for drug delivery," *Advanced Drug Delivery Reviews*, vol. 65, no. 11-12, pp. 1420–1446, 2013.

[41] B. C. Leopércio, S. Ribeiro, F. Gomes, M. Michelon, and M. S. Carvalho, "Microcapsules with controlled magnetic response," *Microfluidics and Nanofluidics*, vol. 25, no. 12, pp. 1–12, 2021.

[42] K. Trinavee, N. S. K. Gunda, and S. K. Mitra, "Anomalous Wetting of Underliquid Systems: Oil Drops in Water and Water Drops in Oil," *Langmuir*, vol. 34, no. 39, pp. 11695–11705, 2018.

[43] B. N. Sahoo, N. S. K. Gunda, S. Nanda, J. A. Kozinski, and S. K. Mitra, "Development of Dual-Phobic Surfaces: Superamphiphobicity in Air and Oleophobicity Underwater," *ACS Sustainable Chemistry and Engineering*, vol. 5, no. 8, pp. 6716–6726, 2017.

[44] S. Mitra, N. S. K. Gunda, and S. K. Mitra, "Wetting characteristics of underwater micro-patterned surfaces," *RSC Advances*, vol. 7, no. 15, pp. 9064–9072, 2017.

[45] P. R. Waghmare, S. Das, and S. K. Mitra, "Drop deposition on under-liquid low energy surfaces," *Soft Matter*, vol. 9, no. 31, pp. 7437–7447, 2013.

[46] P. R. Waghmare, N. S. K. Gunda, and S. K. Mitra, "Under-water superoleophobicity of fish scales," *Scientific Reports*, vol. 4, pp. 1–5, 2014.

[47] P. R. Waghmare, S. Das, and S. K. Mitra, "Under-water superoleophobic glass: Unexplored role of the surfactant-rich solvent," *Scientific Reports*, vol. 3, pp. 1–7, 2013.

[48] S. Mitra and S. K. Mitra, "Understanding the Early Regime of Drop Spreading," *Langmuir*, vol. 32, no. 35, pp. 8843–8848, 2016.

[49] D. Kumar, J. D. Paulsen, T. P. Russell, and N. Menon, "Wrapping with a splash: High-speed encapsulation with ultrathin sheets," *Science*, vol. 359, no. 6377, pp. 775–778, 2018.

[50] C. Yang and G. Li, "A novel magnet-actuated droplet manipulation platform using a floating ferrofluid film," *Scientific Reports*, vol. 7, no. 1, p. 15705, 2017.

[51] S. Misra, K. Trinavee, N. S. K. Gunda, and S. K. Mitra, "Encapsulation with an interfacial liquid layer: Robust and efficient liquid-liquid wrapping," *Journal of Colloid and Interface Science*, vol. 558, pp. 334–344, 2019.

[52] S. MITRA, N. S. K. GUNDA, S. MISRA, and K. TRINAVEE, "LIQUID ENCAPSULATION METHOD AND COMPOSITIONS AND USES RELATED THERETO," 2020.

[53] T. Tran, H. De Maleprade, C. Sun, and D. Lohse, "Air entrainment during impact of droplets on liquid surfaces," *Journal of Fluid Mechanics*, vol. 726, pp. 1–11, 2013.

[54] C. Josserand and S. Zaleski, "Droplet splashing on a thin liquid film," *Physics of Fluids*, vol. 15, no. 6, pp. 1650–1657, 2003.

[55] D. Kim, S. H. Kim, and J. Y. Park, "Floating-on-water fabrication method for thin polydimethylsiloxane membranes," *Polymers*, vol. 11, no. 8, 2019.

[56] S. G. Jones, N. Abbasi, B. U. Moon, and S. S. Tsai, "Microfluidic magnetic self-assembly at liquid-liquid interfaces," *Soft Matter*, vol. 12, no. 10, pp. 2668–2675, 2016.

[57] U. Banerjee and A. K. Sen, "Shape evolution and splitting of ferrofluid droplets on a hydrophobic surface in the presence of a magnetic field," *Soft Matter*, vol. 14, no. 15, pp. 2915–2922, 2018.

[58] A. S. Geller, S. H. Lee, and L. G. Leal, "The creeping motion of a spherical particle normal to a deformable interface," *Journal of Fluid Mechanics*, vol. 169, no. -1, p. 27, 1986.

[59] I. U. Khan, C. A. Serra, N. Anton, X. Li, R. Akasov, N. Messaddeq, I. Kraus, and T. F. Vandamme, "Microfluidic conceived drug loaded Janus particles in side-by-side capillaries device," *International Journal of Pharmaceutics*, vol. 473, no. 1-2, pp. 239–249, 2014.

Chapter 6

Reflected laser interferometry: A versatile tool to probe condensation of low surface tension droplets [1]

6.1 Overview

Experimental investigation of dropwise condensation of low surface tension liquids remains prone to error owing to the imaging difficulties caused by the typically low droplet height. Using reflection interference contrast microscopy in confocal mode, we demonstrate a non-invasive framework to accurately capture this condensation dynamics of volatile liquids with low surface tension. The capability of the developed framework is demonstrated in studying condensation dynamics of acetone where it accurately describes the growth mechanism of condensed microdroplets with excellent spatiotemporal resolution even for sub-micron range drop height and a three-phase contact angle of $<5°$. From experimentally obtained interferograms, the framework can reconstruct the three-dimensional topography of the microdroplets even when the contact line of the droplet is distorted due to strong

[1] Adapted with permission from **Misra, S**; Teshima, H., Takahashi, K.; Mitra, S.K. *Langmuir*, 37(27), 2021, 8073-8082. Copyright

local pinning. The obtained results exhibit excellent quantitative agreement with several theoretically predicted trends. The proposed protocol overcomes the limitation of conventional techniques (e.g., optical imaging/ environmental scanning electron microscopy) and provides an efficient alternative for studying condensation of low surface tension liquids under atmospheric conditions.

6.2 Introduction

Microdroplet condensation has attracted sustained attention because of its various engineering applications, such as water harvesting [1], design of efficient microscale thermal management systems including micro heat pipe [2] and condensation heat transfer [3]. Environmental scanning electron microscopy (ESEM) has extensively been used to study microscale droplet condensation because of good spatiotemporal resolution [3–5]. However, ESEM has two major restrictions. First, the operating conditions inside the ESEM chamber, namely, electron beam irradiation and the presence of low pressure, can impact the properties of condensing droplets [4, 6, 7], giving an inaccurate representation of the ensuing dynamic behavior. Additionally, ESEM primarily deals with condensation of water vapor which results in a high contact angle due to relatively high air-liquid surface tension. We have to rely on optical microscopy [8] for studying condensation of low surface tension liquids, such as organic solvents or refrigerants. However, in optical microscopy, low spatial resolution and depth of focus severely restrict the precision in measurement. On macroscale, side-view imaging is a possibility. However, when moving to microscale, the accuracy gets compromised because of the low droplet height, which makes the influence of uncertainty in determining the baseline of the droplet [9] more pronounced. Consequently, there exist major gaps in our understanding of the condensation behavior of microdroplets with low contact angles. Reflection interference contrast microscopy (RICM) offers an excellent alternative way to capture the condensation dynamics in three dimensions because of good resolution along the height direction of the droplets (i.e., along the optical axis of the microscope which is perpendicular to the base plane of the condensing droplets) and large depth of focus. When operating in confocal mode, RICM can capture suffi-

ciently sharp interferograms corresponding to the three-dimensional (3D) droplet shapes, enabling us to analyze the dynamic behavior of microdroplet condensation, even for test liquids with low surface tension. However, scientific endeavor to develop a comprehensive framework to study such condensation phenomena using RICM is rather scarce with only a few sporadic attempts [10, 11].

In this work, we use dual-wavelength reflection interference contrast microscopy in confocal mode to develop a framework to capture and quantify the dynamics of droplet condensation and demonstrate the capability of our framework by studying the dynamics of condensation of acetone, a test liquid with low surface tension and high vapor pressure, on quartz, a surface with high surface energy. Sharp interferograms are obtained by controlling the confocal pinhole of the RICM imaging setup. A novel image processing framework is also developed to interpret the experimental interferograms. Utilizing the reflected intensity pattern corresponding to two monochromatic laser sources, the drop shape is reconstructed unambiguously. Unlike the work by Sundberg *et al.* [11], our technique is not limited to only determining the contact angles. We perform a complete 3D reconstruction of the drop shape as well which allows us to extract several other valuable quantitative data, namely, evolution of drop volume, liquid–vapor surface area and footprint of the droplets. The developed framework is utilized for analyzing a test case of acetone condensation, where it is found that the condensed microdroplets grow in constant contact angle mode with the drop shape bearing reasonable resemblance with spherical cap. It is to be noted here that the developed interferometric protocol enables studies on droplet condensation at precisely controlled pressure, humidity, and temperature, which is not achievable in ESEM. Although demonstrated for droplet condensation, this framework can be applied directly to study other relevant physical phenomena involving droplet dynamics (e.g., wetting, spreading, droplet coalescence, motion of droplets etc.). Hence, it finds applicability not only in studying dropwise condensation but also in several other practical applications including droplet microfluidics [12, 13], water harvesting [14], fog collection [1, 15], design of functional surfaces with self-cleaning [16, 17] and ice phobic properties [18, 19]18,19 and even in the assessment of stability of alternative liquid wrapped dosage forms [20] for pharmaceutical applications.

6.3 Experimental Section

Condensation of acetone microdroplets was studied in a demountable quartz flow cell with a light path of 2 mm (Type 49, FireflySci Inc., Staten Island, New York). American Chemical Society reagent grade acetone (Sigma Aldrich Canada Ltd.) was used as test liquid. First the liquid cell, placed on the sample stage, was partially filled with 5 ml of acetone through one of the openings in the demountable lid. The inner surface of this lid was our target surface for observing the condensation of sessile acetone microdroplets, as shown in Figure 6.1A. The surface roughness of this surface was measured using a stylus type surface profiler (P-6, KLA-Tencor) and the arithmetic mean surface roughness was found to be 2.9 nm. The inner surfaces of the flow cell (including the lid) were thoroughly rinsed in ethanol (Sigma Aldrich Canada Ltd.) and Milli-Q water (MilliPore Sigma, Canada) and then dried under N_2 gas prior to conducting experiments. Then a small volume of air (ca. 2–3 ml) was injected into the flow cell through the same opening via a glass syringe. This infused air formed a bubble inside the flow cell (please see Figure 6.1A). The cell was then tilted slightly to position this air bubble near the observation area of the microscope (around the center of the flow cell). Both inlets of the flow cell were covered thereafter with glass coverslips to minimize evaporation and consequent unwanted escape of the volatile test liquid into external atmosphere. After that, a drop of cold water (temperature $\sim 4^\circ$ C) was deposited on the outer surface of the lid on top of the observation area to locally reduce the temperature. It helped to promote condensation of the vapor of the high vapor pressure test liquid on the inner surface of the lid. The outside temperature was maintained at 22° C. We maintained a time delay of ~ 10 s between the deposition of the cold water drop on the outer surface of the lid and the start of the acquisition of data for the condensation experiment.

The condensation dynamics was captured with LSM 800 (Carl Zeiss, Canada), a confocal dual-wavelength reflection interference contrast microscope (DW- RICM), using an objective lens with magnification 10X and numerical aperture 0.3 (EC Plan-Neofluar, Carl Zeiss, Canada). The flow cell had a light path of 2 mm and the bottom wall of the cell had a thickness of 1.25 mm, which made the distance between the inner surface of the top lid (the target surface for studying condensation) and the bottom outer surface of the cell (the

surface having direct contact with the sample stage of the microscope – see Figure 6.1A) 3.25 mm. As a result, the working distance of 5.2 mm of the chosen objective allowed us to successfully focus on the inner surface of the lid from below the sample stage. A simplified light path of the used DW-RICM system is shown schematically in Figure 6.1B. In the data acquisition phase, the observation area was raster scanned pixelwise using two focused monochromatic laser beams with wavelengths 488 nm and 561 nm. Then the reflected light was routed through the pinhole of the confocal microscope before being split into two different signals by a dichroic mirror and collected by two photomultiplier tubes, each corresponding to one of the two laser wavelengths. An algorithm inbuilt into the LSM system was then used to convert the detected analog optical signal to a digital image. The pinhole size was kept at 1 Airy unit corresponding to the 488 nm laser light, the one with the lower wavelength among the two used monochromatic laser sources. For the used objective lens, this setting yields an in-focus axial slice thickness of ~ 11 μm when operating in dual-wavelength mode. It is sufficient for capturing the entire 3D topography of low surface tension microdroplets with maximum height $\sim$ 4–5 μm. At this pinhole size, we were able to get sufficiently strong signal from region of interest, while avoiding stray light (noise) from out of focus planes. The pixel size and scan area were optimized such that the scan time for each pixel was < 1 μs, which was essential for obtaining necessary temporal resolution to capture the transient dynamics. To give a perspective, in the experiments reported here, we could acquire a set of two simultaneous frames corresponding to the two imaging wavelengths with dimensions 512 pixels * 512 pixels within 410 ms, where each pixel corresponds to a physical dimension of 0.489 μm.

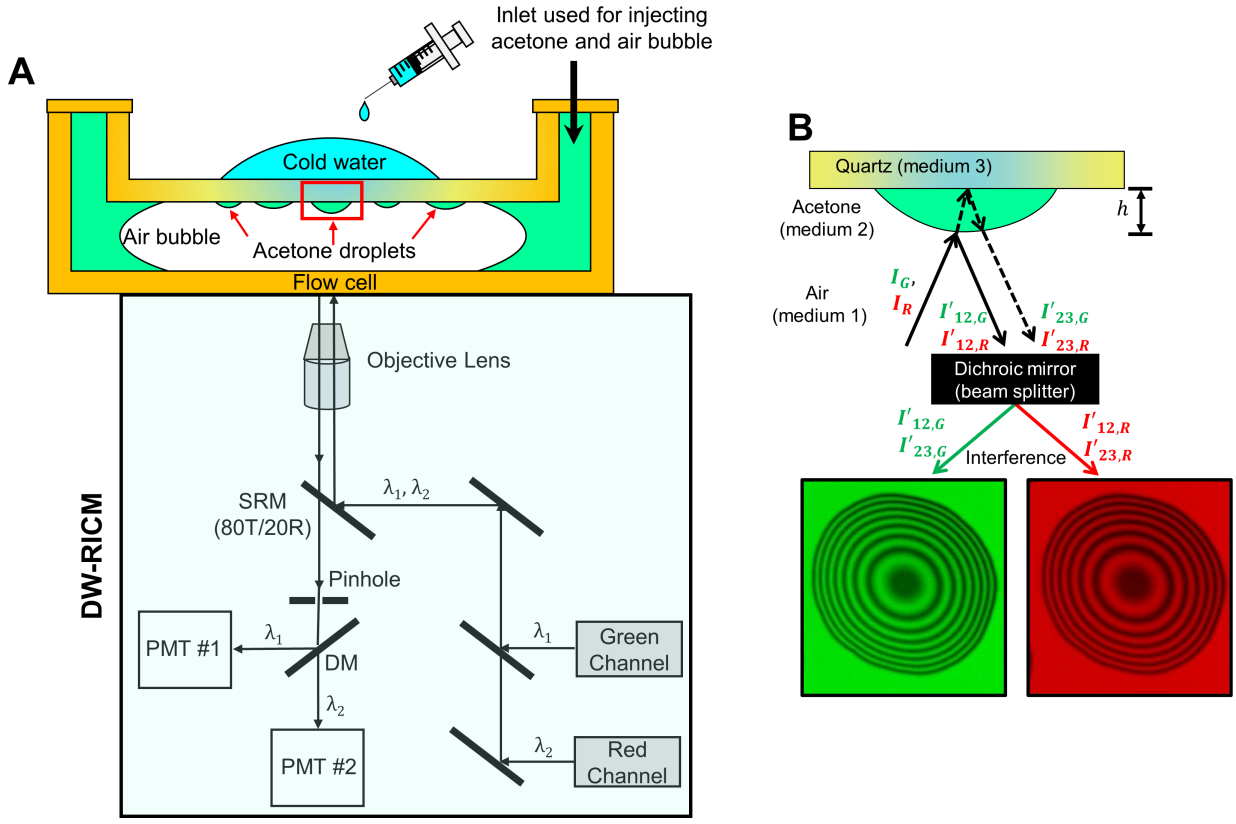

Figure 6.1: (A) **Schematic representation (not to scale) of the experimental setup for droplet condensation and the simplified light path of the DW-RICM used for capturing the condensation dynamics from bottom view**. λ_1 and λ_2 represent the two monochromatic laser wavelengths of 488 nm and 561 nm, corresponding to the green and red channels, respectively. It is to be noted that 'green' and 'red' are just the labels for the imaging channels and not the actual colors of corresponding laser beams. SRM (80T/20R): semi reflective mirror that transmits 80% of the incident signal while reflecting the remaining 20%. In the illustrated configuration, it allows 20% of the incident laser intensity to be directed to the specimen and 80% of the reflected signal coming from the specimen to be routed to the pinhole, DM: long pass dichroic mirror that splits the reflected signal into two signals with wavelengths λ_1 and λ_2 and reflects the signal with wavelength λ_1 (corresponding to the Green channel) to detector (PMT) #1 while transmitting the signal with wavelength λ_2 to detector (PMT) #2, PMT: photomultiplier tubes used as detectors for the reflected signal. (...continuing to the next page)

Figure 6.1: (. . . continued from the previous page) (B) **Schematic representation (not to scale) of the process of formation of interferometric image in the present experimental setup.** The local height of the droplet, h gives rise to a path difference of $2h$ between the reflected signals from the air (medium 1)–acetone (medium 2) interface ($I'_{12,G}$ for green channel and $I'_{12,R}$ for the red channel) and from the acetone (medium 2)–quartz (medium 3) interface ($I'_{23,G}$ for green channel and $I'_{23,R}$ for the red channel). The dichroic mirror, which acts as a beam splitter, splits the reflected signals into two wavelengths before routing them to the two detectors corresponding to the two imaging channels**.** The two pairs of reflected signals **(***$I'_{12,G}$, $I'_{23,G}$**)** *and* **(***$I'_{12,R}$, $I'_{23,R}$**)** then interfere to form the dual-wavelength interferometric image.

6.4 Results and Discussion

6.4.1 Interpretation of experimental results by image processing

DW-RICM works on the principle of interference of the light reflected from different interfaces. In our case, the incident laser beam gets reflected from two consecutive interfaces, namely, the air bubble–droplet interface and the droplet–quartz interface, as shown schematically in Figure 6.1B. These two reflected beams have a geometric path difference equal to twice the local height of the droplet at the point of incidence of laser beam, h. It corresponds to a phase difference $\Delta\varphi$ where

$$\Delta\varphi = \frac{2\pi n}{\lambda} \cdot 2h = \frac{4\pi n h}{\lambda} \tag{6.1}$$

where n is the refractive index of the droplet and λ is the wavelength of the laser source. Contextually, it is to be mentioned that the overall phase difference between the two interfering reflected beams also depends on the relationship between the refractive indices of the media on either side of the two participating reflective interfaces (here, air–acetone and acetone–quartz interfaces). Specifically, when light travels from a lower refractive

index medium to a higher refractive index medium, reflection at the interface introduces an additional phase shift [21] of π. However, in the studied case, the relationship between the refractive indices is monotonic ($n_{air} < n_{acetone} < n_{quartz}$). Therefore, the additional phase shifts of π incurred upon each reflection (from the air–acetone interface and the acetone–quartz interface, respectively) cancel each other. The effective phase difference between the two interfering beams is, therefore, only due to the local separation, h (see Figure 6.1B) between the two participating interfaces.

In our analysis, the base plane of the droplet is chosen to be the XY plane, and the image frame is considered to be the absolute frame of reference where the origin of the coordinate system is fixed at the top left corner of the acquired image, maintaining consistency with the traditional imaging convention.

Depending on the value of $\Delta\varphi$, two extreme cases of interference between the two reflected beams are possible, namely constructive, and destructive interference, resulting in the occurrence of either bright fringes (intensity maxima) or dark fringes (intensity minima). The criteria are the following

$$\Delta\varphi = \begin{cases} 2m\pi & \Rightarrow \text{Constructive Interference} \\ (2m+1)\pi & \Rightarrow \text{Destructive Interference,} \end{cases} \tag{6.2}$$

where m is an integer.

Evidently, bright, and dark fringes appear alternatively in the interference pattern as the phase difference changes by π. From Eqs. (6.1) and (6.2), it follows that the local height of the droplet changes by $\lambda/4n$ between any two consecutive extrema. Thus, by detecting the occurrence of maxima and minima in the interference pattern, the relative evolution of droplet profile can be obtained even with one single laser source illuminating the region of interest as long as a reference plane with a known height can be identified in the experimental system. In the present system, the base plane (i.e., the solid–liquid contact surface) of the droplet serves as the known reference plane. It is to be mentioned here that a diffusively grown precursor film [22, 23] with thickness of a few angstrom to several ten nm may form around the macroscopic contact line when a droplet of a low

surface tension liquid (e.g., acetone) sits on a hydrophilic surface (e.g., quartz). However, the precursor film is so thin that it does not affect the observations. Therefore, the droplet–solid contact surface can effectively be assigned a zero height which allows us to assume the local height of the droplet at the three phase contact line to be zero.

Based on the abovementioned fundamentals, an image processing algorithm has been developed in MATLAB to reconstruct the droplet shape from the experimentally obtained dual-wavelength interference patterns. A typical reconstruction process is illustrated in Figure 6.2. An experimental image of a condensed acetone microdroplet strongly pinned at one end is represented in Figure 6.2A. First, the intensity profiles corresponding to both the wavelengths are sampled along a randomly chosen vertical slice through the droplet apex (e.g., slice AB in Figure 6.2A). Let us assume that the vertical slicing yields n points on the base plane (XY) at which the intensity profile has been sampled. Let us also assume that in the absolute frame of reference, these points have cartesian coordinates (x_i, y_i) where $i \in \{1, 2, 3, \ldots, n\}$. In our reconstruction routine, we first define a one-dimensional (1D) base coordinate σ along the chosen slicing direction where $\sigma_i = \sqrt{(x_i - x_1)^2 + (y_i - y_1)^2}$. The sampled intensity profiles along the slice AB are plotted against this 1D base coordinate, σ in Figure 6.2B. The red channel corresponds to the intensity of the reflected signal for imaging with the 'red' laser with $\lambda = 561$ nm, while the green channel represents the intensity profile corresponding to the reflected 'green' laser ($\lambda = 488$ nm). The extrema are detected thereafter by computing the local derivatives of the intensity profile. In our reconstruction algorithm, we approach the apex of the droplet separately from either end of the slice.

Note that the reflected signals corresponding to both the red and the green laser lights attain maxima at the edges of the contact line as the virtually zero local height at the contact line leads to constructive interference for both the wavelengths. There is a steep decrease in intensity thereafter as we move inside towards the apex of the droplet. Therefore, the edge of the droplet can be identified as the location where the reflected intensities corresponding to both the wavelengths start decreasing sharply. In the studied case, this location is always the same for both the wavelengths since the local height at the edges can effectively be assumed to be zero. However, when no a-priori information is available regarding a reference height (e.g., fluctuating membranes or colloidal beads in a buffer

medium [24, 25], droplet impact on surfaces [26–28] or even dropwise condensation on lubricant infused surfaces [29]), usage of simultaneous dual-wavelength intensity signal becomes indispensable. One way to identify a reference plane in such cases is to theoretically determine the optical path lengths and fringe orders of the coincident extrema corresponding to the two imaging wavelengths. It can be obtained by computing the least common multiple (LCM) of the vertical separations (i.e., the differences in local profile heights in Z direction) between two sets of consecutive interference extrema corresponding to the two imaging wavelengths. In other words, integer multiples of the LCM of $(\lambda_1/4n)$ and $(\lambda_2/4n)$ correspond to local droplet heights for which one observes coincident extrema in the fringe patterns recorded with the two wavelengths. The calculated locations of coincident extrema then need to be compared against the location and fringe order of coincident peaks in the experimentally obtained intensity spectrum. With sufficiently spatially resolved interferograms, a known reference plane can be set by comparing these two data, which can then be used for reconstructing the entire profile. Alternatively, the normalized intensity corresponding to the two imaging wavelengths can be plotted against each other. Comparing this with the theoretically expected Lissajous curve, the height profile can be resolved [25, 30] unambiguously. This approach can be especially useful in test cases where the maximum measured profile height is too low to detect a coincident extremum.

Additionally, we should always encounter same number of extrema as we traverse from the contact line to the apex. This is because the maximum height of the droplet (i.e., the apex height) remains the same, irrespective of the direction of approach towards the apex from the contact line. Therefore, for any arbitrarily chosen slicing direction, there should be an equal number of intensity extrema on either side of the droplet's apex. In other words, the base location of the central extremum in the sampled interferogram between any two diametrically opposite points on the three-phase contact line (e.g., AB in Figure 6.2A) corresponds to the base location of the apex. We utilize this physical constraint to determine the base coordinate of the apex of the droplet at the beginning of our computational routine. For the demonstrated test case, the detected edges across the slice AB are highlighted in red in Figure 6.2A while the center (apex) is indicated in cyan.

Evidently, the base coordinates of the extrema do not always coincide in the two sampled interferograms owing to the difference in wavelengths of the two lasers. The extrema

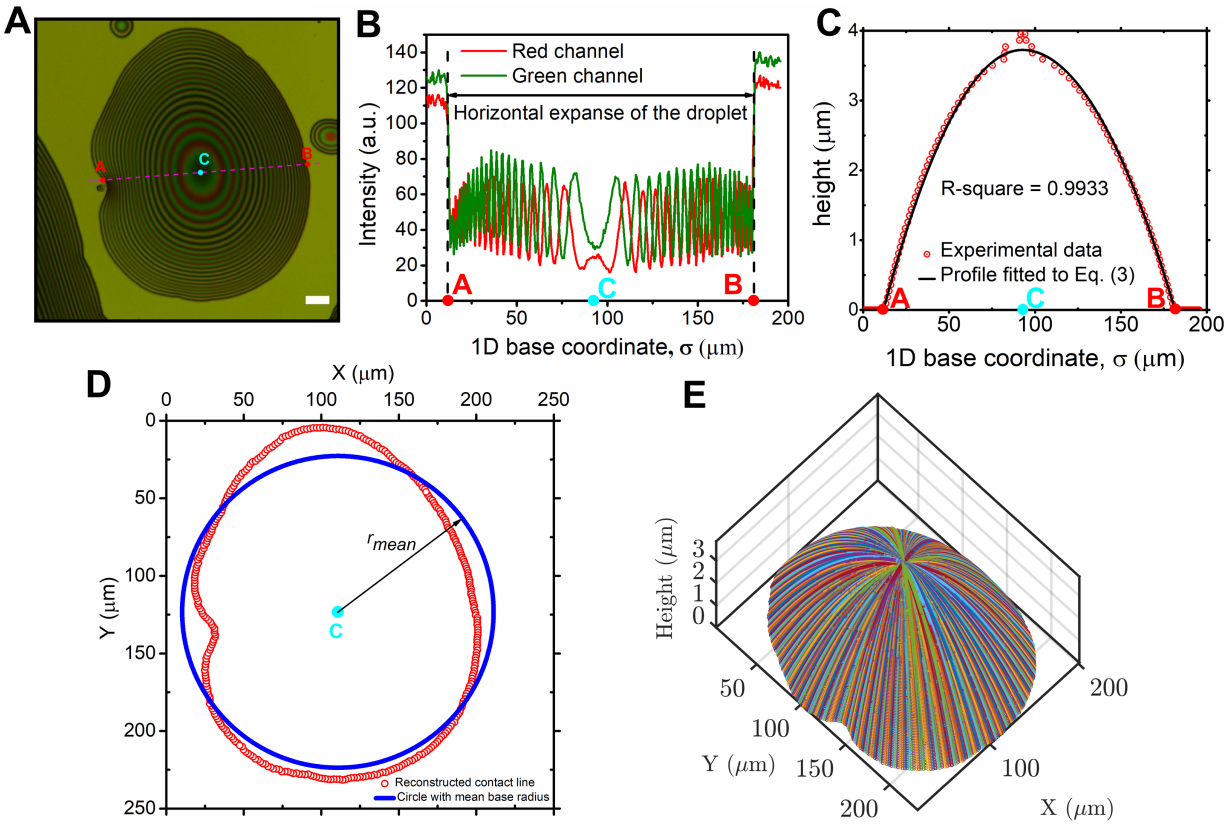

Figure 6.2: Reconstruction of three-dimensional droplet shape from the experimental interferogram. **(A)** A typical experimental snap showing a pinned acetone microdroplet. AB is a randomly chosen vertical slice across the microdroplet of interest. Red dots labeled A, B indicate the locations of the droplet contact line while the cyan dot labeled C indicates the projected location of the droplet apex on the base (XY) plane. The scale bar represents 20 μm. **(B)** The intensity profiles of the reflected signal along the line AB (as shown in part **A)** corresponding to both the red and green imaging channels. **(C)** The height profile of the droplet along the line AB (as shown in part **A)**. The red circled dots represent the experimentally acquired data and the black line shows the fitted trend using the asymmetric piecewise quadratic function described by Eq. (6.3). **(D)** The reconstructed shape of the contact line (red circular markers). A circle with the center at C and radius equal to r_{mean} is also shown to illustrate the concept of mean base radius (blue line). **(E)** The reconstructed 3D topography of the entire droplet.

coincide at the edge of the three-phase contact line and then red extrema appear more sparsely in comparison to the green signal, as can be seen from Figure 6.2B. Once the edges are determined, we can work with either one of the reflected signals. We work with the green signal as it provides a better spatial resolution owing to its smaller wavelength ($\lambda = 488$ nm). First, we assign a reference height of zero at the detected edges and then approach inward towards the apex. As mentioned earlier, the difference in local height of the droplet between two consecutive extrema (a minimum and an adjacent maximum, or vice versa) is $\lambda/4n$. Using this, the local height profile of the droplet can be obtained as a function of base coordinate σ with a resolution of $\lambda/4n$ from the experimentally acquired interferograms, where $n = 1.36$ (for acetone). The extracted experimental profile for the demonstrated test case is plotted in Figure 6.2C in red dots. It is to be noted here that false extrema might occur at the central region of the droplet (near the apex). It is because the slope of the interface is very low near the apex and variation in local height is minimal making the intensity profile almost uniform near the apex. Therefore, unavoidable background noise might manifest itself as false extrema. To avoid overestimation of maximum droplet height, we track any drastic increase in the slope of the experimentally obtained height profile near the apex, thereby detecting, and eliminating false extrema.

Generally speaking, a vertical cross-section of spherical cap shaped droplet can be well represented by a symmetric quadratic fit. However, a regular quadratic fit does not provide a reasonable representation when the drop shape is not symmetric. Such a situation can arise due to contact angle hysteresis induced by strong pinning. Here we define a modified piecewise quadratic fitting function to account for the asymmetry. The definition of the function is as follows,

$$h(\bar{r}) = \begin{cases} \alpha\bar{r}\left(1 - \dfrac{\bar{r}}{2\bar{r}_p}\right), & \text{for } (0 \leq \bar{r} \leq \bar{r}_p) \\ -\dfrac{\alpha\bar{r}_p}{2(1-\bar{r}_p)^2}\bar{r}^2 + \dfrac{\alpha\bar{r}_p^2}{(1-\bar{r}_p)^2}\bar{r} + \dfrac{\alpha\bar{r}_p}{2(1-\bar{r}_p)^2}(1 - 2\bar{r}_p) & \text{for } (\bar{r}_p < \bar{r} \leq 1). \end{cases} \tag{6.3}$$

Here $\bar{r}$ is the normalized base coordinate along the direction of the slice and $h(\bar{r})$ is the local height of the droplet at $\bar{r}$. $\bar{r}$ is defined as $\bar{r} = \frac{\sigma - \sigma_L}{\sigma_R - \sigma_L}$, with $0 \leq \bar{r} \leq 1$. σ_L, σ_R

denote the one-dimensional base coordinates of the detected left and right edges of the droplet, respectively. $\bar{r_p}$ is the normalized base coordinate corresponding to the apex of the droplet. α is a positive free parameter, bearing the dimension of height, fitted based on the experimental data. For the test case demonstrated in Figure 6.2C, $\bar{r_p}$= 0.48 and the value of α is found to be 15.61 μm after fitting, which corresponds to a maximum droplet height of 3.75 μm. A total of 82 interference extrema (experimental data points), with 41 extrema on either side of the apex, have been used in this case to evaluate the fit. As can be seen in Figure 6.2C, the fit provides a satisfactory representation of the experimental data with an R-square value of 0.9933.

In our algorithm, once the fitted profile for the chosen first slice (here AB) is obtained, the same process is repeated in an automated manner by rotating the slicing direction by 1° at a time for total of 180 times. The two edges of each of the 180 slices, computed as per the procedure outlined above, represent two diametrically opposite points on the contact line, allowing us to detect a total of 360 points on the contact line with 1° angular separation between two neighboring points. It enables us to capture the irregularities (pinning, contact angle hysteresis) along the contact line and the resulting distortion of the drop shape. Ultimately the shape of the contact line is reconstructed (shown in Figure 6.2D). The reconstructed contact line in Figure 6.2D represents the experimental data accurately even though the drop is distorted due to the pinning. The 3D topography is also obtained as can be seen in Figure 6.2E. It is to be mentioned here that once the location of the droplet apex is determined from the first slice, the (X, Y) coordinates of the apex in the absolute frame of reference are then used as known input parameters to compute $\bar{r_p}$ while performing subsequent h vs $\bar{r}$ fits corresponding to other slicing directions. It ensures that the locations of the droplet apex coincide in the height profiles reconstructed along different slicing directions. This analysis framework enables us to obtain quantitative data regarding the growth and motion of the droplets (e.g., contact angle, height, surface area, volume, velocity of motion etc.).

Once the profiles are fitted to Eq. (6.3), the contact angle values are obtained by calculating the slope of the profile tangents at the detected profile edges lying on the contact line. The analytical expression for local contact angle, θ can be derived from Eq. (6.3) as follows,

$$\theta = \tan^{-1}\left(\left|\frac{dh}{d\sigma}\right|\right) = \tan^{-1}\left(\left|\frac{dh}{d\bar{r}}\cdot\frac{d\bar{r}}{d\sigma}\right|\right) = \tan^{-1}\left(\left|\frac{1}{(\sigma_R-\sigma_L)}\frac{dh}{d\bar{r}}\right|\right)$$
$$= \begin{cases} \tan^{-1}\left(\left|\frac{\alpha}{(\sigma_R-\sigma_L)}\right|\right) & \text{for } \bar{r}=0 \text{ (left edge)} \\ \tan^{-1}\left(\left|\frac{\alpha\bar{r_{\mathrm{p}}}}{(\sigma_L-\sigma_R)(1-\bar{r_{\mathrm{p}}})}\right|\right) & \text{for } \bar{r}=1 \text{ (right edge)} \end{cases} \tag{6.4}$$

We calculate the volume and liquid–vapor surface area of the droplet thereafter. The height profiles, reconstructed along different slicing directions, provide us with an ensemble of points in three-dimensional space enveloping the droplet. We calculate the volume of the droplet, V by computing a 3D convex hull [31] of this 3D point cloud.

For computing the liquid–vapor surface area, we first evaluate the total surface area (S_{tot}) of the previously computed 3D convex hull which is basically the sum of the liquid–vapor surface area, S_{lv} and the liquid–solid surface area, S_{ls}. For this purpose, let us assume that $\overrightarrow{P1}$, $\overrightarrow{P2}$ and $\overrightarrow{P3}$ are the position vectors of the three vertices of a facet of the triangulation that comprises the convex hull. The surface area of this triangular facet is computed by,

$$S_F = \frac{1}{2}\left|\left|\overrightarrow{P1}\times\overrightarrow{P2}+\overrightarrow{P2}\times\overrightarrow{P3}+\overrightarrow{P3}\times\overrightarrow{P1}\right|\right| \tag{6.5}$$

S_{tot} is evaluated thereafter by summing S_F over all the facets of the triangulated hull profile.

Then the points on the base plane (XY) of the droplet (points with Z coordinates equal to 0) are extracted from the abovementioned 3D point ensemble. These points on the XY plane represent the boundary of the solid–liquid contact surface (i.e., the three-phase contact line) of the droplet. A two-dimensional hull is computed thereafter enclosing these points on the base plane of the droplet which allowed us to evaluate the liquid–solid surface area (S_{ls}). Once we have both S_{tot} and S_{ls}, S_{lv} is readily obtained as $S_{lv} = S_{tot} - S_{ls}$. Our framework allows fine sampling in both XY plane (owing to slicing at 1° angular interval) as well as in the Z direction (due to the RICM height resolution of ~ 90 nm). Consequently, the reconstructed hull geometry could accurately represent the actual drop shape.

It is to be noted here that there is a limit on the maximum resolvable contact angle using the interference pattern and it is determined by the lateral resolution of the objective. If the horizontal separation between an interference maximum and its adjacent minimum, or vice versa is smaller than the lateral resolution of the used objective, the two interference fringes can not be resolved and instead they appear merged/overlapped. We have observed this in our previous work[16] for condensation of ethanol microdroplets on PDMS. The average contact angle of ethanol on PDMS, as measured from contact angle goniometry, was $\sim 39^\circ$ and RICM could not resolve the vertical profile near the contact line, instead the area near the contact line appeared dark because of overlapping/very closely spaced fringes. In-depth calculation of an upper limit of the resolvable contact angle in the present set up is beyond the scope of current work as it requires detailed consideration of the effect of cone of illumination, manifested in the form illumination numerical aperture. However, the classical work of Rädler and Sackmann [21] provides a ballpark estimate for the resolution: they calculated an upper resolvable profile inclination of 34° for their optics with numerical aperture 1.25 and illumination numerical aperture 0.48. In the present study focusing on the condensation of low surface tension liquids, this upper limit of slope does not pose a serious restriction as by suitably varying the objective lenses (choosing an objective with higher numerical aperture) we can cover almost all the typical combinations of low surface tension liquids and high surface energy solid surfaces.

6.4.2 Studying growth and coalescence of condensed acetone microdroplets

Using the DW-RICM framework, we experimentally captured the growth of acetone microdroplets on the quartz surface. A total of two such observation sets are reported in this work, namely, observation set #1 (Figure 6.3) and observation set #2 (Figure D.1 in Appendix D). During its lifecycle, a condensing droplet undergoes two different types of events, namely, growth events – when the droplet grows uninterruptedly due to condensation without encountering nearby droplets and coalescence events – when, as the droplet grows, its contact line touches other neighboring droplets, and they merge to form a bigger droplet. In observation set #1, the droplet of interest (denoted by 1) underwent four

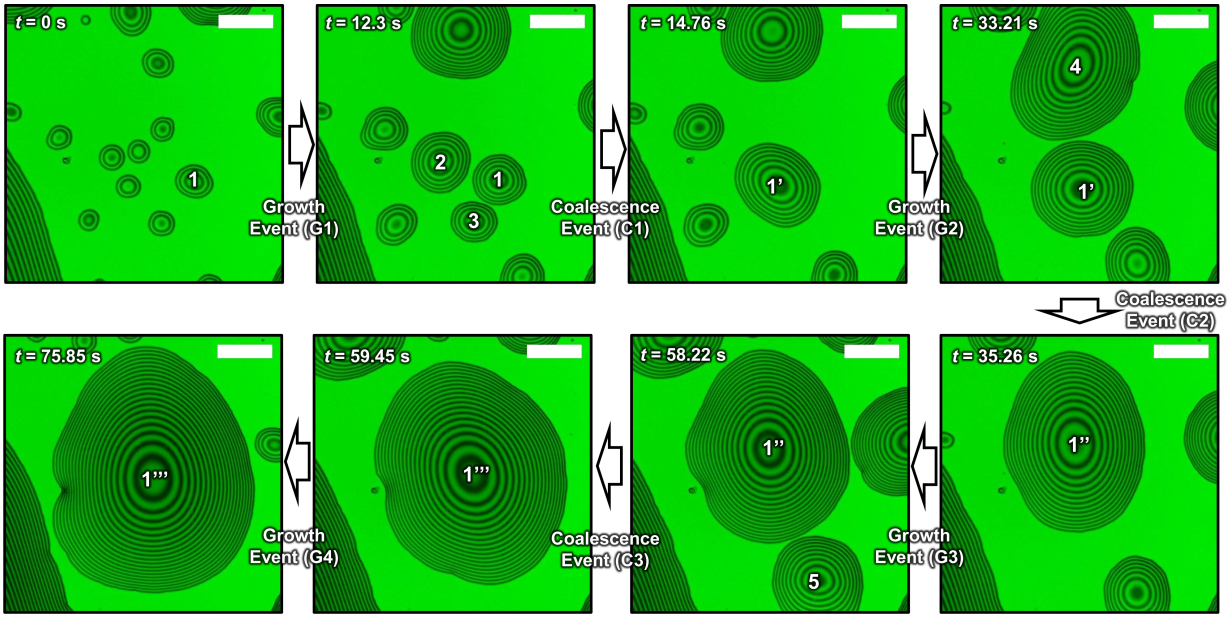

Figure 6.3: Time evolution of a typical acetone microdroplet condensation event (observation set #1). During the observation period of 75.85 s, the droplet of interest (denoted by 1) underwent four events of gradual growth (namely, G1, G2, G3 and G4) and three coalescence events (namely, C1, C2 and C3). The droplet number is kept the same during the pure growth phases while it has been updated after each coalescence. During C1, droplet numbered 1, merges with droplets numbered 2 and 3 to form droplet numbered 1'. Similarly, droplets 1' and 4 merge to from droplet 1" during C2 and droplets 1" and 5 merge to form droplet 1"' during C3. The scale bar is 50 μm.

such growth events (namely, G1, G2, G3 and G4) and three coalescence events (namely, C1, C2 and C3) during a total observation period of 75.85 s, as indicated in Figure 6.3. A total of 185 frames for each of the two wavelengths were captured over this observation window, which provided us with sufficient temporal resolution to capture the dynamics of the process.

Using the algorithm described earlier, we analyzed the growth of the microdroplet denoted by 1 in Figure 6.3. The results are presented in Figure 6.4. The measured values of volume, V and the liquid–vapor surface area, S_{lv} are plotted for different mean base radii in Figure 6.4A. Mean base radius, r_{mean} is defined as the average distance of a point on the contact line from the center of the droplet, the projection of the apex of the droplet on the base (XY) plane. We computed this average while reconstructing the drop shape from experimental image by taking multiple vertical slices at 1° angular separation. By fitting a power law profile to the experimentally determined dependences $S_{lv}\left(r_{mean}\right)$, $V(r_{mean})$, we obtained $S_{lv} \sim {r_{mean}}^{1.99}$ and $V \sim {r_{mean}}^{3.04}$, which stand in excellent agreement with the analytical formulas for an ideal spherical cap [32] with a constant contact angle where $S_{lv} \sim {r_{mean}}^{2}$ and $V \sim {r_{mean}}^{3}$, implying that the shape of the condensed microdroplets during condensation and growth phase can reasonably be approximated by the spherical cap shape.

Further, the values of mean contact angle, θ, which is the spatial average of all the 360 local contact angle values along the three-phase contact line of the droplet at a particular time instant, have also been plotted against r_{mean} in Figure 6.4B. It can be seen that the contact angle remained almost constant (within 3.25°–5.25°) and the values were effectively invariant with respect to changes of the base radii, which is an expected outcome resulting from the combination of a low surface tension condensate and a surface with arithmetic mean surface roughness as low as 2.9 nm. For the particular condensation experiment reported in Figure 6.3 and 4, the time average of the mean (spatially averaged over the contact line) contact angle, θ over the entire observation window of 75.85 s was found to be 4.13°, with a standard deviation of 0.26°. Contextually, the observed trends remained consistent across different sets of observation involving different droplets with the volume and liquid–vapor surface area following similar scaling with mean base radius and mean contact angle remaining invariant over the observation window. Another set of data from

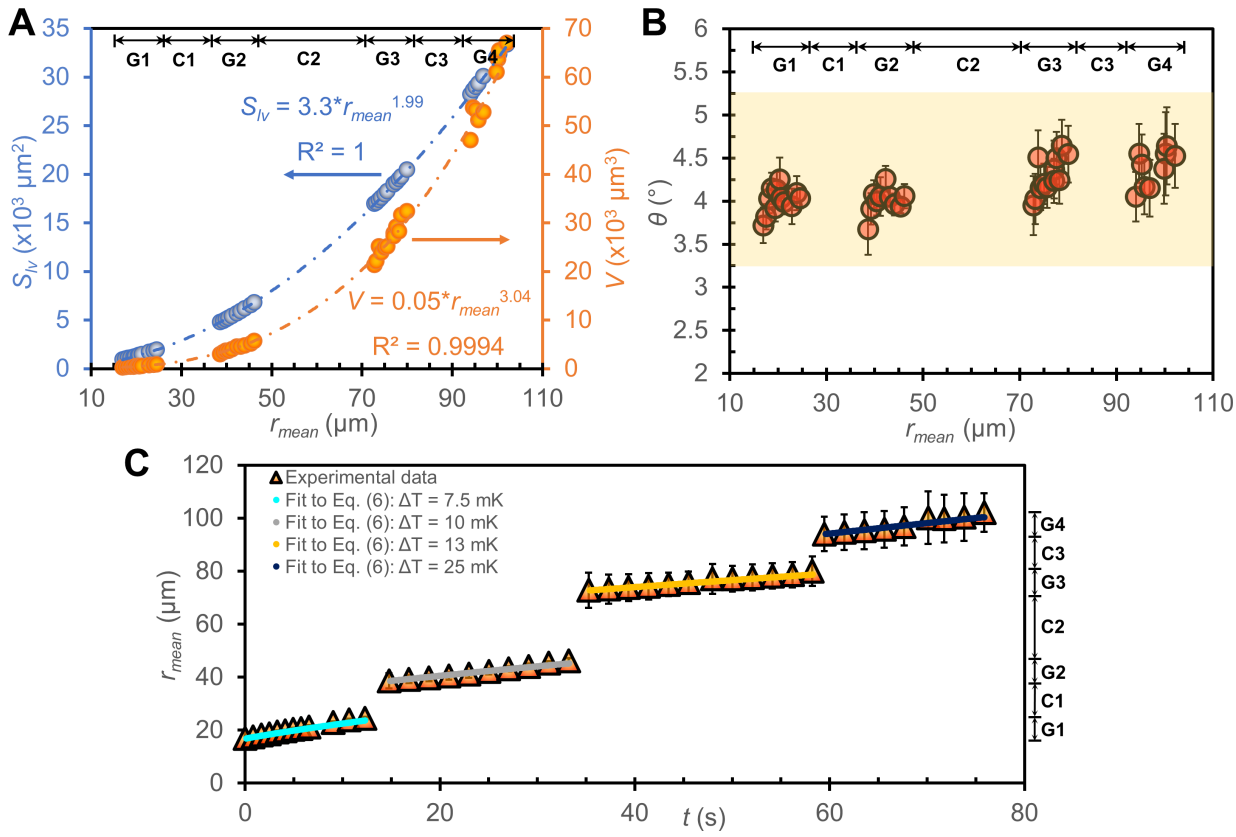

Figure 6.4: Quantitative analysis of the dynamics of growth of a condensing acetone microdroplet corresponding to observation set #1. (A) Variation of droplet volume V and liquid–vapor surface area S_{lv} with mean base radius. **(B)** Dependence of the mean contact angle θ on mean base radius. A total of 360 local contact angles were averaged across the contact line of the droplet at each instance. The error bars represent the standard deviation of these 360 local values, which gives an indication of the contact angle heterogeneity across the contact line. **(C)** The evolution of mean base radius r_{mean} with time during condensation. Similar to Figure 6.4**B**, a total of 360 local values of base radii were considered along the 180 different slicing direction with 1° angular interval to evaluate the mean base radius. The error bars represent the standard deviation of these 360 local base radius values. The presented plots characterize the evolution of the droplet denoted by 1 in Figure 6.3, with G1, G2, G3 and G4 indicating the individual growth events and C1, C2 and C3 denoting the coalescence events.

the same experiment (observation set #2) has been analyzed to establish the consistency. Please see Figures D.1 and D.2 of Appendix D for further details. The observed scaling behavior of S_{lv} and V with r_{mean} and the experimentally observed invariance of θ over r_{mean} clearly indicate that the condensed droplets grow in constant contact angle mode (even when the drop undergoes multiple coalescence events) and it is reasonable to approximate the drop shape by spherical cap geometry.

Additionally, we have also captured the experimentally observed trend of growth of the mean base radius r_{mean} with time in Figure 6.4C and compared it to the theoretical prediction of Rykaczewski4 for droplet growth in constant contact angle mode. Assuming the solid surface underneath the condensed droplet to be at uniform temperature, Rykaczewski proposed the following formula to define the growth rate of a condensed droplet given the growth is essentially in constant contact angle mode,

$$\frac{dr_c}{dt} = \frac{\Delta T \ \left(1 - \frac{r_{\min}}{r_c}\right)}{2H_{lv}\rho_l \left(\frac{1}{2h_i} + \frac{r_c\phi(1-\cos\phi)}{4k_l \sin\phi}\right)} \tag{6.6}$$

where r_c is the radius of curvature of the droplet at time instant t. ΔT is the effective subcooling given by the temperature difference between the vapor phase inside the flow cell, T_{vapor} and the underlying solid surface T_{surf}. In our case ΔT is a free parameter (not an experimental input) and is therefore estimated from the evaluated fit to the experimental data. Also, the acetone vapor inside the flow cell is considered to be in thermal equilibrium with the ambient atmosphere and therefore T_{vapor} is assumed to be 295 K. H_{lv}, ρ_l and k_l are the latent heat of vaporization, density and thermal conductivity of the test liquid, respectively. ϕ is the contact angle, which effectively remains constant throughout the observation period. We chose ϕ to be equal to the time averaged value of mean contact angle over the entire observation window. For observation set #1, $\phi = 4.13°$. $r_{\min}$ denotes the critical radius of curvature for condensation, given by4 $r_{\min} = \frac{2T_{vapor}\ \sigma_{lg}}{H_{lv}\rho_l \Delta T}$, with σ_l being the surface tension of the test liquid. Additionally, the assumption of uniform temperature across the base surface leads to a constant interfacial heat transfer coefficient h_i, which is defined as [33]

Parameters	Values
Latent heat of vaporization, H_{lv}	536.7 kJ/kg
Density, ρ_l	788 kg/m^3
Thermal conductivity, k_l	0.162 W/m-K
Surface tension, σ_l	23.09 mN/m
Molecular weight, $\bar{M}$	0.058079 kg/mol
Molar gas constant, $\bar{R}$	8.314472 J/mol-K

Table 6.1: Thermophysical parameters [34] of the test liquid (here acetone) used to compare experimental results to the theoretical predictions given by Eq. (6.6).

$$h_i = \left(\frac{2\widehat{\sigma}}{2-\widehat{\sigma}}\right)\frac{\rho_l H_{lv}^2}{T_{vapor}}\left(\frac{\bar{M}}{2\pi T_{vapor}\bar{R}}\right)^{\frac{1}{2}} \tag{6.7}$$

where $\bar{M}$ is the molecular weight of the test liquid, $\bar{R}$ is the universal molar gas constant and $\widehat{\sigma}$ is an accommodation coefficient that accounts for the experimental condition. The relevant parameters are tabulated in Table 6.1.

In our study $\widehat{\sigma}$ is assumed to be 0.04 [35, 36] considering the fact that the experiment is carried out essentially in atmospheric condition and non-condensable gases coexist alongside condensable vapor in the experimental domain.

To obtain the value of r_c, Eq. (6.6) was solved numerically with a sufficiently small timestep size of 100 μs. The base radius r was calculated thereafter from the numerical solution of r_c by $r = r_c \sin\phi$. This procedure was repeated for a discrete range of ΔT and in each case, the values of r were compared with the experimentally obtained values of r_{mean} to find the value of ΔT that gives the optimal fit. As can be seen in Figure 6.4C, the experimental data could be excellently fitted to the model of Rykaczewski4 represented by Eq. (6.6) with ΔT being the fitting parameter. It is to be noted that ΔT was assumed to be constant during each of the pure growth phases as a simplification and updated after each coalescence event. After each coalescence event, the fit yielded a higher ΔT value for the next growth phase, as the drop height underwent a noticeable increase following

each coalescence, and consequently, the heat transfer resistance between saturated vapor and the base surface increased. Contextually, a similar comparison was carried out for the observation set #2 as well (please see Figure D.2 of Appendix D for further details) and the range of fitted values of ΔT (9.5–14 mK) was comparable with that of the observation set #1 (7.5–25 mK).

6.5 Conclusion

Using reflected laser interferometry, we have developed a simple yet accurate non-invasive protocol to study the dynamic behavior of condensed microdroplets even for droplets with the maximum height as small as $\sim$1 μm. For low surface tension liquids, sufficiently sharp experimental interferograms have been obtained by appropriately controlling the confocal pinhole. An automated numerical framework has also been developed to dynamically reconstruct the three-dimensional topography of the droplets from the obtained interferograms. The proposed framework allows us to determine the droplet shape with a vertical resolution of $\sim$90 nm (i.e., one-quarter of the effective wavelength of the 488 nm laser light propagating through acetone with refractive index 1.36). Although we have illustrated the framework for studying dropwise condensation, the protocol, in its present form, finds direct applicability in the study of a wide range of fundamental phenomena involving droplet dynamics including wetting, spreading, droplet pinning and motion, contact angle hysteresis, droplet coalescence etc., In fact, in a recent work [23] we used a modified single-wavelength version of the same framework to detect and analyze a unique precursor-film-mediated spontaneous thermocapillary motion of ethanol microdroplets nucleated on quartz surface. We believe that suitable adaptation of the developed protocol will assist in unveiling previously unknown fundamental physical insights of practical relevance in the fields of physical chemistry of surfaces, micro/nanoscale fluid dynamics or heat transfer.

References

[1] J. Ju, H. Bai, Y. Zheng, T. Zhao, R. Fang, and L. Jiang, "A multi-structural and multi-functional integrated fog collection system in cactus," *Nature Communications*, vol. 3, pp. 1–6, 2012.

[2] J. Qu, H. Wu, P. Cheng, Q. Wang, and Q. Sun, "Recent advances in MEMS-based micro heat pipes," *International Journal of Heat and Mass Transfer*, vol. 110, pp. 294–313, 2017.

[3] N. Miljkovic and E. N. Wang, "Condensation heat transfer on superhydrophobic surfaces," *MRS Bulletin*, vol. 38, no. 5, pp. 397–406, 2013.

[4] K. Rykaczewski, "Microdroplet growth mechanism during water condensation on superhydrophobic surfaces," *Langmuir*, vol. 28, no. 20, pp. 7720–7729, 2012.

[5] Y. Yamada, T. Ikuta, T. Nishiyama, K. Takahashi, and Y. Takata, "Droplet nucleation on a well-defined hydrophilic-hydrophobic surface of 10 nm order resolution," *Langmuir*, vol. 30, no. 48, pp. 14532–14537, 2014.

[6] N. A. Stelmashenko, J. P. Craven, A. M. Donald, E. M. Terentjev, and B. L. Thiel, "Topographic contrast of partially wetting water droplets in environmental scanning electron microscopy," *Journal of Microscopy*, vol. 204, no. 2, pp. 172–183, 2001.

[7] A. Méndez-Vilas, A. B. Jódar-Reyes, and M. L. González-Martín, "Ultrasmall liquid droplets on solid surfaces: Production, imaging, and relevance for current wetting research," *Small*, vol. 5, no. 12, pp. 1366–1390, 2009.

[8] S. Sett, P. Sokalski, K. Boyina, L. Li, K. F. Rabbi, H. Auby, T. Foulkes, A. Mahvi, G. Barac, L. W. Bolton, and N. Miljkovic, "Stable Dropwise Condensation of Ethanol and Hexane on Rationally Designed Ultrascalable Nanostructured Lubricant-Infused Surfaces," *Nano Letters*, vol. 19, no. 8, pp. 5287–5296, 2019.

[9] K. Liu, M. Vuckovac, M. Latikka, T. Huhtamäki, and R. H. Ras, "Improving surface-wetting characterization," *Science*, vol. 363, no. 6432, pp. 1147–1148, 2019.

[10] S. J. Gokhale, S. DasGupta, J. L. Plawsky, and P. C. Wayner, "Reflectivity-based evaluation of the coalescence of two condensing drops and shape evolution of the coalesced drop," 2004.

[11] M. Sundberg, A. Månsson, and S. Tågerud, "Contact angle measurements by confocal microscopy for non-destructive microscale surface characterization," *Journal of Colloid and Interface Science*, vol. 313, no. 2, pp. 454–460, 2007.

[12] Z. Yan, M. Jin, Z. Li, G. Zhou, and L. Shui, "Droplet-based microfluidic thermal management methods for high performance electronic devices," *Micromachines*, vol. 10, no. 2, pp. 1–16, 2019.

[13] S. Y. Teh, R. Lin, L. H. Hung, and A. P. Lee, "Droplet microfluidics," *Lab on a Chip*, vol. 8, no. 2, pp. 198–220, 2008.

[14] D. Seo, C. Lee, and Y. Nam, "Influence of geometric patterns of microstructured superhydrophobic surfaces on water-harvesting performance via dewing," *Langmuir*, vol. 30, no. 51, pp. 15468–15476, 2014.

[15] B. S. Lalia, S. Anand, K. K. Varanasi, and R. Hashaikeh, "Fog-harvesting potential of lubricant-impregnated electrospun nanomats," *Langmuir*, vol. 29, no. 42, pp. 13081–13088, 2013.

[16] T. S. Wong, S. H. Kang, S. K. Tang, E. J. Smythe, B. D. Hatton, A. Grinthal, and J. Aizenberg, "Bioinspired self-repairing slippery surfaces with pressure-stable omniphobicity Supplementary Information," *Nature*, vol. 477, no. 7365, pp. 443–447, 2011.

[17] R. Blossey and C. Scientifique, "Self-cleaning surfaces — virtual realities," pp. 301–306, 2003.

[18] M. J. Kreder, J. Alvarenga, P. Kim, and J. Aizenberg, "Design of anti-icing surfaces: Smooth, textured or slippery?," *Nature Reviews Materials*, vol. 1, no. 1, 2016.

[19] T. Yamazaki, M. Tenjimbayashi, K. Manabe, T. Moriya, H. Nakamura, T. Nakamura, T. Matsubayashi, Y. Tsuge, and S. Shiratori, "Antifreeze Liquid-Infused Surface with

High Transparency, Low Ice Adhesion Strength, and Antifrosting Properties Fabricated through a Spray Layer-by-Layer Method," *Industrial and Engineering Chemistry Research*, vol. 58, no. 6, pp. 2225–2234, 2019.

[20] S. Misra, K. Trinavee, N. S. K. Gunda, and S. K. Mitra, "Encapsulation with an interfacial liquid layer: Robust and efficient liquid-liquid wrapping," *Journal of colloid and interface science*, vol. 558, pp. 334–344, 2020.

[21] J. Rädler and E. Sackmann, "Imaging optical thicknesses and separation distances of phospholipid vesicles at solid surfaces," *Journal de Physique II*, vol. 3, no. 5, pp. 727–748, 1993.

[22] M. N. Popescu, G. Oshanin, S. Dietrich, and A. M. Cazabat, "Precursor films in wetting phenomena," *Journal of Physics Condensed Matter*, vol. 24, no. 24, pp. 243102–243130, 2012.

[23] H. Teshima, S. Misra, K. Takahashi, and S. K. Mitra, "Precursor-Film-Mediated Thermocapillary Motion of Low-Surface-Tension Microdroplets," *Langmuir*, vol. 36, no. 19, pp. 5096–5105, 2020.

[24] J. Schilling, K. Sengupta, S. Goennenwein, A. R. Bausch, and E. Sackmann, "Absolute interfacial distance measurements by dual-wavelength reflection interference contrast microscopy," *Physical Review E - Statistical, Nonlinear, and Soft Matter Physics*, vol. 69, no. 2 1, pp. 1–9, 2004.

[25] L. Limozin and K. Sengupta, "Quantitative reflection interference contrast microscopy (RICM) in soft matter and cell adhesion," *ChemPhysChem*, vol. 10, no. 16, pp. 2752–2768, 2009.

[26] J. De Ruiter, R. Lagraauw, D. Van Den Ende, and F. Mugele, "Wettability-independent bouncing on flat surfaces mediated by thin air films," *Nature Physics*, vol. 11, no. 1, pp. 48–53, 2015.

[27] J. de Ruiter, F. Mugele, and D. van den Ende, "Air cushioning in droplet impact. I. Dynamics of thin films studied by dual wavelength reflection interference microscopy," *Physics of Fluids*, vol. 27, no. 1, 2015.

[28] T. Tran, H. J. Staat, A. Prosperetti, C. Sun, and D. Lohse, "Drop impact on superheated surfaces," *Physical Review Letters*, vol. 108, no. 3, pp. 1–5, 2012.

[29] J. Y. Ho, K. F. Rabbi, S. Sett, T. N. Wong, and N. Miljkovic, "Dropwise condensation of low surface tension fluids on lubricant-infused surfaces: Droplet size distribution and heat transfer," *International Journal of Heat and Mass Transfer*, vol. 172, pp. 16–20, 2021.

[30] D. Daniel, J. V. Timonen, R. Li, S. J. Velling, and J. Aizenberg, "Oleoplaning droplets on lubricated surfaces," *Nature Physics*, vol. 13, no. 10, pp. 1020–1025, 2017.

[31] H. T. Barber, C. B., Dobkin, D. P., and Huhdanpaa, "The Quickhull algorithm for convex hulls," *ACM Trans. on Mathematical Software*, vol. 22, no. 4, pp. 469–483, 1996.

[32] J. Israelachvili, *Intermolecular and Surface Forces*. Academic Press, 3 ed., 2011.

[33] V. P. Carey, *Liquid-vapor phase-change phenomena*. New York: Taylor and Francis, 2nd ed. ed., 2008.

[34] J. R. Rumble, ed., *CRC Handbook of Chemistry and Physics*. CRC Press/Taylor & Francis, Boca Raton, FL., 101st edit ed.

[35] A. Phadnis and K. Rykaczewski, "The effect of Marangoni convection on heat transfer during dropwise condensation on hydrophobic and omniphobic surfaces," *International Journal of Heat and Mass Transfer*, vol. 115, pp. 148–158, 2017.

[36] S. Chavan, H. Cha, D. Orejon, K. Nawaz, N. Singla, Y. F. Yeung, D. Park, D. H. Kang, Y. Chang, Y. Takata, and N. Miljkovic, "Heat Transfer through a Condensate Droplet on Hydrophobic and Nanostructured Superhydrophobic Surfaces," *Langmuir*, vol. 32, no. 31, pp. 7774–7787, 2016.

Chapter 7

Precursor Film Mediated Thermocapillary Motion of Low Surface Tension Microdroplets [1]

7.1 Overview

In contrast to microdroplet condensation with high contact angles, the one with low contact angles remains unclear. In this study, we investigated dynamics of microdroplet condensation of low surface tension liquids on two flat substrate surfaces by using reflection interference confocal microscopy. Spontaneous migration towards relatively larger droplets was first observed for the microdroplets nucleated on hydrophilic quartz surface. The moving microdroplets showed a contact angle hysteresis of $\sim 0.5^{\circ}$, which is much lower than the values observed on typical flat substrates and is within the range observed on slippery lubricant-infused porous surfaces. Because the microdroplets on hydrophobic polydimethylsiloxane surface did not move, we concluded that the ultrathin precursor film is formed only on the hydrophilic surface, which reduces a resistive force to migration.

[1] Adapted with permission from Teshima, H.,**Misra, S**; Takahashi, K.; Mitra, S.K. *Langmuir*, 36(19), 2020, 5096-5105. Copyright ©2020, American Chemical Society.

Also, reduced size of droplets promotes the thermocapillary motion, which is induced by a gradient in local temperature inside a small microdroplet arising due to the difference in size of adjacent droplets.

7.2 Introduction

Study of droplet condensation in microscale does not only contain scope for exploring a broad variety of fundamentally rich thermophysical processes (which often differs significantly from its macroscale counterpart) but also holds promising potential in a multitude of practical purposes including microscale heat exchangers and heat pipes, bearing extensive implication in electronic circuitry. On the fundamental side, several experimental results have shown that microdroplets exhibit significantly lower contact angles compared to those observed on the macroscale [1, 2]. This may arise from line tension and/or pinning effect [3, 4]; however, a definitive explanation of extremely low contact angle is still lacking. On the application side, microdroplet condensation plays a key role, especially in phase change heat transfer [5–9]. For example, condensed microdroplets with a diameter of less than 100 μm account for approximately 80 % of the total heat transfer of dropwise condensation [9–12] and thus quick and continuous nucleation and departure of microdroplets are required for effective heat transfer. Several attempts are made to facilitate continuous removal of these condensed microdroplets and subsequent recovery of nucleation sites. Superhydrophobic surfaces with nanofabricated roughness features [13–16] and slippery lubricant-infused porous surfaces (SLIPS) [8, 17, 18] are two of them, which have garnered significant interest in recent past. However, ensuring long term durability of these surfaces remains challenging [11, 17, 19] for either of them. Therefore, to unveil the fundamental problems and optimize the microdroplet condensation in such applications, further understanding of the dynamics of condensed microdroplets based on detailed observations is indispensable.

To observe the dynamics of microdroplet condensation, environmental scanning electron microscopy (ESEM) has been widely used because of good spatiotemporal resolution [6, 20, 21]. Due to the provision of precisely controlling the internal vapor pressure and the

temperature of the sample stage, ESEM can easily induce the water droplet condensation with a size range of sub-micrometer to micrometer [20–25]. However, ESEM has two drawbacks. One is that the specific conditions in the ESEM chamber, such as low vapor pressure and electron beam irradiation, can affect the properties of droplets [23, 24, 26]. The other is that the vapor available for droplet condensation is restricted to water. Reflection interference contrast microscopy (RICM) is an alternative and promising way to observe the dynamics of droplet condensation. RICM can provide interference patterns corresponding to droplet thickness, which are essential for understanding the dynamic behavior of microdroplet condensation. In addition, microdroplet condensation of low surface tension liquids can be observed because there is no restriction of liquids and pressure. However, such studies using RICM are rare [1, 27–30], and thus the scientific endeavor on the characterization of microdroplet condensation of low surface tension fluids consisting of alcohol and refrigerant is relatively scarce.

In this study, we observed the microdroplet condensation of low surface tension liquids on two different surfaces with different surface energy, namely, quartz and polydimethylsiloxane (PDMS) using RICM. By constructing the profile of microdroplets from the experimentally captured interference patterns, growth and dynamics of the droplets with extremely low contact angles (approximately 4°) were investigated. We found that droplets which nucleated on hydrophilic quartz surface spontaneously moved to relatively larger droplets and merged, while droplets on hydrophobic PDMS surface did not move and coalesced only when the three-phase contact line touched to neighboring droplets. In addition, the moving droplets showed extremely low contact angle hysteresis, like droplets observed on SLIPS surfaces. From these results, we attribute the mobility of droplets to thermocapillary motion mediated by a very thin precursor film, which reduces the contact angle hysteresis yielding a resistive force for the movement. This motion of small microdroplets towards large ones could be explained by taking a condensation induced local gradient in temperature into consideration. We also estimated the temperature gradient of the substrate surface underneath small microdroplets from the force balance analysis of the pinned microdroplets. Consequently, the temperature gradient was 2.3 ± 1.1 K/mm, which is comparable to those used in the previous reports on thermocapillary motion [31, 32]. The reported motion can be realized on flat featureless surfaces and it does not require the

above-mentioned complex surface features for droplet movement, such as nanofabricated superhydrophobic surfaces and SLIPS. These results will extend our fundamental knowledge about microdroplet condensation and will be valuable not only for condensation heat transfer but also in the various engineering applications, such as droplet-based microfluidics [33–36], anti-icing [19, 37–39], water harvesting [40–43], and self-cleaning surface [44–47].

7.3 Experimental Section

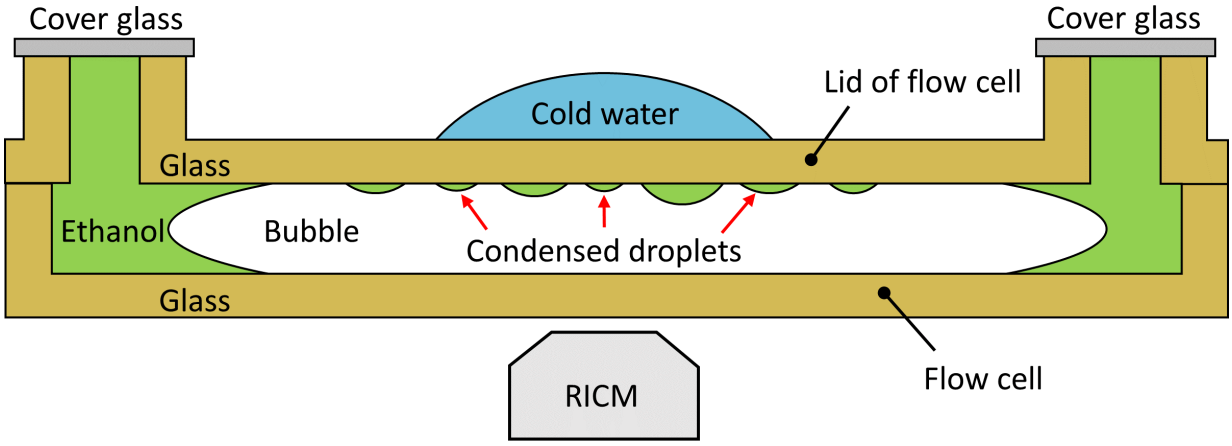

Figure 7.1: Schematic diagram of the experimental setup for RICM observation of microdroplet condensation. This image is not represented to scale for clarity.

The condensation experiments were carried out in a flow cell made of UV quartz (Type 49 Micro Demountable Flow Through Cell, Fireflysci Inc., NY). A schematic representation of the experimental set up is shown in Figure 7.1. First, 5 ml of test liquid was partially filled into the flow cell with the lid in place using a glass syringe. Then, 2-3 ml of air was infused into the liquid cell, which forms an air bubble. The liquid cell was slightly tilted to move the bubble up to the center of the liquid cell. The two inlets of the flow cell were then covered with glass coverslips to prevent evaporation of the test liquid. After putting the experimental setup on the observation stage of RICM, a drop of cold water (approximately 0.2 ml) was placed by a syringe on the top of the lid of the liquid cell to reduce the local temperature, resulting in the condensation of the test liquid vapor inside the liquid cell.

Before the experiment, the syringe filled with 5 ml of deionized water was preserved in a refrigerator at a temperature of 4°C for at least 1 hour. The cold droplet was then placed immediately after taking it out from the refrigerator. During the observation, we frequently added cold droplets on the top of the lid to sustain the condensation process. Even without the addition of such liquid, condensation normally lasted for about 5 minutes. The room temperature was 22°C.

We have studied the condensation of two low surface tension liquids (i.e., ethanol and acetone) and a high surface tension liquid (i.e., deionized water). The ethanol and acetone are American Chemical Society reagent grade chemicals and purchased from Sigma Aldrich Canada Ltd. Deionized water was prepared using a water purifier (Milli-Q, 18.2 MΩ cm, MilliPore Sigma, Ontario, Canada). Droplet condensation on quartz was observed at the inner surface of the lid of the flow cell. For experiments on a PDMS surface, a thin slice of freshly prepared PDMS was utilized. Specifically, the PDMS substrates was prepared by thoroughly mixing the base reagent of the Sylgard 184 elastomer kit with the curing agent (Dow Inc.) in 10:1 weight ratio followed by degassing and subsequent curing at 60°C for 12 hours. Young's modulus of the PDMS prepared by this procedure is 1.7 MPa [48]. The PDMS slice was placed on the inner surface of the lid of the flow cell by gently pressing it with a stainless steel tweezer, making use of the adhesive nature of PDMS. Water contact angles on quartz and PDMS surfaces are 31.7 ± 4 ° and 104.3 ± 2.5 °, respectively. Arithmetic mean surface roughness of the quartz and PDMS surface were measured by profilometer (P-6 stylus profiler, KLA Corp., vertical spatial resolution is 0.001 nm) and were 2.9 nm and 0.45 nm, respectively. Although both quartz and PDMS are non-conductive, static charges should not be present since the sample stage is grounded and humidity inside the liquid cell is very high. For every experiment, the microdroplets with various base radii were nucleated immediately after placing the cold water.

The condensation dynamics were captured by a custom-built LSM 800 (Carl Zeiss, Canada) RICM with a 10x objective lens with numerical aperture of 0.3 (EC Plan-Neofluar, Carl Zeiss, Canada). The observation area was scanned pixel-by-pixel using focused beam of monochromatic laser with wavelength 488 nm. The incident light was collected through the pinhole with the size of 1 airy unit, which corresponds to an in-focus axial slice length of ∼11 μm in our experiment. This pinhole improves signal to noise ratio by blocking out

of focus light. The detected analog optical signal is then converted to a digital image using an inbuilt deconvolution algorithm. The dwell time at each pixel was less than 1 μs, which is necessary to have a satisfactory temporal resolution for capturing the dynamic behavior of droplet condensation.

In RICM setup, the incident light rays reflected from two interfaces, namely solid/liquid and liquid/air interfaces, interfere with one another. This interference results in the occurrence of bright and dark fringes depending on the difference in the light path. Difference in local height of the droplet between adjacent bright and dark fringes corresponds to $\lambda/(4n)$, where λ is the wavelength of the used laser source and n is the refractive index of the droplet. Using this interference pattern, we can construct the height profile of microdroplets. Detailed principle of generation of interference patterns is provided in Chapter 6. The shapes of deformed droplets caused by pinning of three-phase contact line were fitted by asymmetric quadratic function, enabling us to measure the contact angle hysteresis (see Chapter 6).

7.4 Results and Discussion

Figure 7.2 shows condensation of ethanol microdroplets on a PDMS surface. The entire observation area is shown in Figure 7.2(a). Microdroplets of several different sizes nucleated instantaneously and appeared as black regions on the surface. Figure 7.2(b) shows the dynamics of droplet growth in the form of a time series in the region indicated by a red square in Figure 7.2(a). We observed the temporal evolution of 8 microdroplets (numbered 1-8 in the time series). As the droplets grew in size, the contact line expanded in all directions. Eventually, small droplets coalesced and formed bigger droplets when their three-phase contact lines touched. The projection of the apex of the droplets on the contact surface (termed as the center of the droplets henceforth) remained almost stationary during the growth phase and it shifted only after merging with another neighboring droplet.

Note that we could not obtain the height of these microdroplets on PDMS surface because the region near the three-phase contact line did not show the interference patterns and appeared dark. This is because the rate of change in local height with respect to the

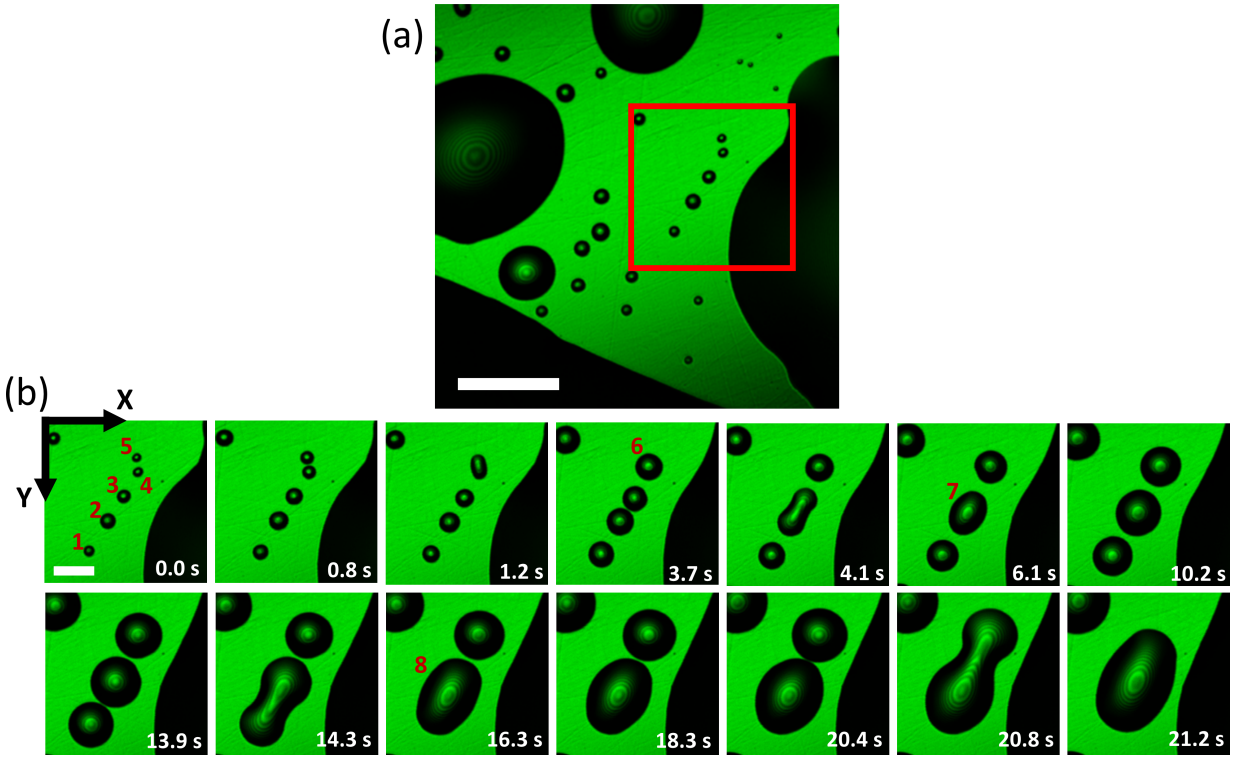

Figure 7.2: Ethanol microdroplet condensation on a PDMS surface. (a) The initial snap showing the entire observation area. The regions with dark edges are the nucleated microdroplets. (b) Time series demonstrating the dynamics of microdroplet condensation in the region indicated by a red square in (a). Scale bars are (a) 50 μm and (b) 20 μm, respectively.

base coordinate is so fast due to large contact angles that interference patterns appear very closely spaced, making the region dark.

It is known that a droplet on a soft substrate pulls the surface and makes a rim at the three-phase contact line, causing the self-pinning effect [49]. However, we did not observe such a deformation of the PDMS surface in our experiments. This is because Young's modulus of our PDMS is 1.7 MPa [48], which is higher than the values which cause non-negligible surface deformation [50]. Therefore, we assume that the self-pinning effect can be neglected on this PDMS surface.

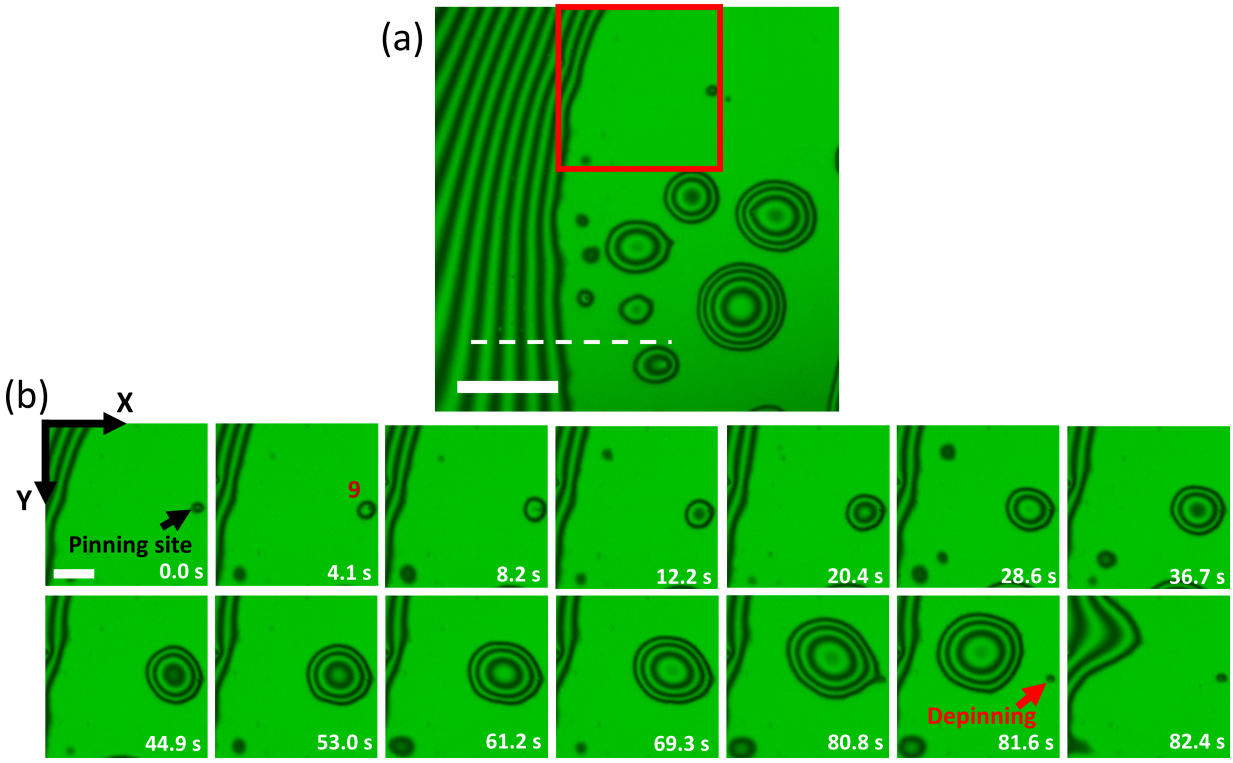

Figure 7.3: Ethanol microdroplet condensation on a quartz surface. (a) The initial snap showing the entire observation area containing the nucleated microdroplets. Normalized intensity profile along the white broken line is shown in Figure S2. (b) Time series demonstrating the dynamics of microdroplet condensation in the region indicated by a red square in (a). Scale bars are (a) 50 μm and (b) 20 μm, respectively.

Figure 7.3 shows an ethanol condensation experiment on a quartz surface. The entire observation area is shown in Figure 7.3(a). Interference patterns were observed throughout the nucleated microdroplets. This indicates that the contact angles of the microdroplets on the quartz are lower in comparison to those on the PDMS surface. Indeed, their contact angles and heights estimated from the constructed shapes were approximately 4 ° and less than 1 μm, which are very difficult to be measured by normal optical microscopy due to the diffraction limit of light [51]. In Figure 7.3(b), temporal evolution of a microdroplet numbered 9 was tracked from its nucleation. The droplet was nucleated and pinned at an impurity indicated by a black arrow. During its growth, the center of the droplet clearly shifted to the left side. At 81.6 seconds, the three-phase contact line was eventually depinned from the impurity, as indicated by the red arrow. After the depinning, the microdroplet immediately moved to the left side and then merged with a bigger droplet. This indicates that a driving force is acting on the droplet and makes it move towards the left side.

Wayner's group has also observed droplet condensation of ethanol on a glass surface [28–30]. However, they reported that no significant flow from the small droplet towards the large droplet was observed and the spontaneous flow between them occurred only when three-phase contact lines comes into contact with each other [30], while in our experiments we observed spontaneous movement of small microdroplets towards big ones even without coalescence and merging of contact lines, as shown in the snap corresponding to 81.6 seconds in Figure 7.3(b). This may be because they could not find the phenomenon due to the short time scale of their observation (a few seconds) compared to that of the spontaneous movement of the microdroplets (several ten seconds).

In Figure 7.4, we tracked the center positions of the aforementioned 9 microdroplets. The base plane of the droplet is defined to be the XY plane and the top left corner of the time series images shown in Figure 7.2(b) and 3(b) was chosen as the origin of the coordinate system. The center positions of the microdroplets on the PDMS surface (number 1-8) almost overlapped. In contrast, the center position of the microdroplet on the quartz surface clearly shifted by around 40 μm towards left. This result indicates that low surface tension microdroplets nucleated on a surface with low surface energy remained almost stationary until they coalesced, while the microdroplets of the same liquid

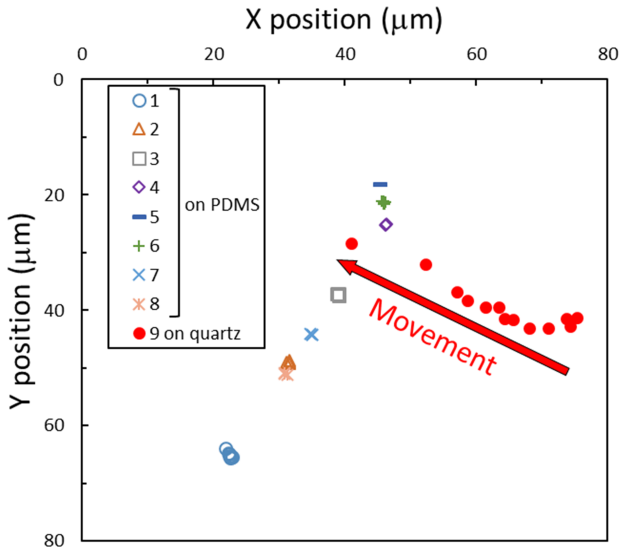

Figure 7.4: Scatter plot of center positions of ethanol droplets nucleated on PDMS and quartz surfaces. The numbers in legends correspond to droplet numbers shown in Figures 7.2(b) and 7.3(b).

showed a mobile nature when they nucleated on a high energy surface. The mobility of nucleated microdroplets was also observed when we used the acetone as a low surface tension liquid. However, when we conducted water condensation on the quartz surface, the nucleated microdroplets did not move and showed the similar tendency as those observed on the PDMS surface. These results are an unambiguous indication that the spontaneous movement is realizable exclusively for a combination of low surface tension liquid and high surface energy solid surface.

To investigate the mechanism behind the motion of low surface tension microdroplets on high energy surface, we analyzed another instance of ethanol condensation on the quartz surface as shown in Figure 7.5. Several small ethanol microdroplets with different base radii were nucleated in the center of the observation area. In addition, there are two large droplets in the left and right sides of the observation area. The trajectory of the center positions of the droplets in the left and right sides are shown by red and yellow arrows, respectively. It was found that the microdroplets in the left side of the observation area moved to the big droplet in the left, while the droplets on the right side approached and

merged with the big droplet present on the right edge. From this observation, it is obvious that small droplets moved towards a bigger droplet close to them and not just towards a direction. It is to be emphasized that only the small microdroplets moved towards relatively large droplets and not vice versa. The migration of small droplets towards the nearest large droplet has been reported on SLIPS surfaces8. Sun and Weisensee explained that the mechanism of the migration is that the broad lubricant meniscus around a large droplet causes a difference in the inclination of the lubricant meniscus between the proximal and distal sides of nearby small droplets, resulting in a driving force towards the large droplet. In our case, however, we cannot explain the spontaneous movement of small droplets in the same manner because there are no such menisci around the droplets.

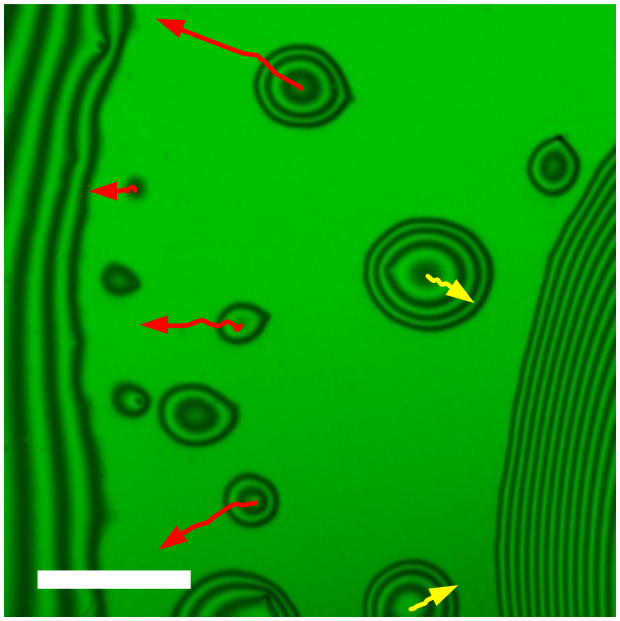

Figure 7.5: Trajectory of mobile ethanol droplets on the quartz surface. Red and yellow arrows track the center positions of mobile droplets. Scale bar is 50 μm.

As a mechanism behind the movement, a vapor mediated movement on high energy surfaces can be considered [52–56]. For example, Cira et al. reported that two component droplets such as propylene glycol and water deposited on clean glass cause the motion of neighboring droplets over a distance, which is attributed to differential evaporation

induced local imbalance in surface tension and consequent Marangoni flow [52]. Their system is clearly different from ours with only single test liquid. However, the motion of pure droplets, which is more similar to our system, has been theoretically and experimentally reported [53–55]. They proposed that, even in the absence of Marangoni effect, motion of pure droplets can be realized by a gradient in evaporation rate, which makes the droplets move from the high evaporation side to the low evaporation side. This is because a replenishing flow inside the droplet towards the high evaporation side pushes it towards the opposite, high evaporation side by viscous friction from the substrate (Vapor-gradient mechanism) [55]. However, they experimentally observed the movement of bigger droplets towards small droplets as well [54], while we only observed that the small droplets moved towards big ones. Another definite difference is that the previously reported movements were only observed during evaporation. We also investigated evaporation of acetone droplets on the quartz surface and confirmed that the microdroplets did not move during evaporation. This may be because that the sizes of microdroplets in our study are much smaller than those of previous reports ($\sim$ several mm), reducing the difference in vapor between proximal and distal side of the droplets.

We also consider the effect of vapor for the droplet motion during condensation based on Sadafi et al.'s theory [55]. They proposed that there are two vapor-induced mechanisms that affect the interaction between two evaporating pure droplets; (i)Vapor-gradient mechanism as mentioned above and (ii)Vapor-induced temperature gradient mechanism that decreases local temperature at higher evaporation side (i.e. distal side) by latent heat, leading to thermocapillary motion away from the other droplet. Vapor also should affect the motion of microdroplets during condensation in a similar manner. For simplification, although there are several droplets in our observation, we consider the motion of two droplets. In regard to (i)Vapor-gradient mechanism, since the vapor near the proximal side is used for condensation of two droplets, the vapor influx to each droplet may become smaller at the proximal side than that at the distal side. Therefore, a replenishing flow will go into the proximal side, pushing the droplet towards the opposite (distal) direction. Therefore, the viscous force from the mechanism (i) will act as a resistance to the observed movement of smaller droplets towards large ones. On the other hand, the thermocapillary force induced by the mechanism (ii) enhances the droplet motion towards the other droplet

since the local temperature rise by condensation at the distal side is higher than that at the proximal side. In our experiments, the effect of (i) is not dominant because we observed the motion of the droplets towards the other ones, not the opposite direction. In contrast, the thermocapillary motion from the mechanism (ii) helps the droplets to move towards the other ones.

From the above discussions, we conclude that the underlying mechanism behind the droplet motion that we observed here is different from the vapor-gradient mechanism.

In addition, we also rule out the possible mechanism from the capillary pressure. If we assume that a fluid can flow inside the precursor film (or a suddenly formed liquid tunnel), mass transfer derived from the difference in Laplace pressure between large and small droplets occurs. In such a case, however, the movement of small droplets towards large droplets will not occur since viscous drag acts in the opposite direction to the flow. In addition, the moving droplets clearly increased their volume although the smaller droplets should become smaller and eventually disappear in case of a capillary pressure driven mass transfer process. Therefore, the capillary pressure cannot explain our observation results.

In our experiments, the moving microdroplets showed very low contact angle hysteresis (defined as the difference between the maximum and minimum contact angles measured for a single droplet). In Figure 7.3(c), the moving droplet at 81.6 seconds showed a contact angle hysteresis of approximately 0.5°, which is much lower than the ones observed for macroscopic droplets (20-50°) [57] and is within the typical hysteresis range observed on slippery lubricant-infused porous (SLIPS) surfaces ($< 3°$) [18]. Based on these observations, we conclude that vapor of low surface tension liquid adheres to high energy surface and forms an ultrathin liquid film during condensation, which has been called film-like condensate [58] or precursor film [59]. Our results indicate that the precursor film works as a lubricant layer and thus decreases the resistance for droplet movement. It is known that a lubricant on SLIPS surfaces also works in a similar manner to the precursor film, although there are two significant difference; the precursor film component is that of fluid, while it is the lubricant oil in the case of SLIPS; The droplets in our experiments just sit on the precursor film, while the droplets on lubricant film can be encapsulated within the lubricant or create a rim at the three-phase contact line. Such encapsulation or the rim sometimes act opposing to coalescence [60].

To explain the movement of smaller microdroplets towards larger droplets, we propose the following mechanism. Temperature of microdroplets can increase in the process of condensation due to release of latent heat. However, the rate of temperature increment is low in large droplets due to the large heat capacity. In addition, thermal diffusion through the underlying substrate is also large due to large contact area with the quartz surface. Therefore, the temperature rise due to condensation is considered to be negligible for the large droplets. Rather, since the droplet acts as a thermal resistance, the substrate surface underneath the droplet attains a lower local temperature than that of the surrounding substrate surface [55]. In contrast, the temperature rise of small microdroplet becomes larger compared to that of large droplets because they have small heat capacity and contact area with the quartz surface. Therefore, a local temperature gradient is formed between the neighboring small and large droplets, causing a heat flow from the small droplet towards the bigger droplet. Essentially, the bigger droplet acts as a heat sink. This results in a local temperature gradient inside the small droplet where the edge of droplet closer to the bigger droplet has a lower local temperature than that of the edge away from it. It gives rise to a surface tension imbalance inside the small droplet, resulting in a thermocapillary motion towards the large droplet. Although such temperature profiles also appear on ethanol droplets on the PDMS surface and on water droplets on the quartz surface, they cannot move along the surface because of absence of the precursor film, without which the thermocapillary force cannot overcome the resistance in motion arising because of direct droplet-substrate contact. It has been indeed reported that the contact angle hysteresis prevents the droplet from thermocapillary motion [31, 32, 61].

To validate this mechanism, we first provide a theoretical prediction of the presence or absence of the precursor film on quartz and PDMS surfaces. The existence of precursor film is determined by the sign of the difference in two Hamaker constants $A = A_{SL} - A_{LL}$ and the spreading coefficient $S{=}\gamma_{SV} - \gamma_{SL} - \gamma_{LV}$ [62], where γ is surface tension and the subscripts S, L, and V indicate the solid, liquid, and vapor, respectively. Here, A_{SL} can be expressed as $A_{SL} \approx \sqrt{A_{SS}A_{LL}}$ [63]. A_{SS} for quartz and PDMS surfaces are $6.5{\times}10^{-20}$ J and $4.4{\times}10^{-20}$ J and A_{LL} for water, ethanol and acetone are $3.7{\times}10^{-20}$, $4.2{\times}10^{-20}$ J and $4.1{\times}10^{-20}$ J, respectively [63, 64]. Therefore, for all the cases we used in our experiments (i.e., quartz-water/ethanol/acetone and PDMS-ethanol combinations), the sign of A was

positive. In addition, the positive and negative value of S corresponds to the wetting states, namely complete wetting and partial wetting. In addition to the water droplet on a quartz surface as shown in the experimental section, the ethanol droplet on a PDMS surface also showed the finite contact angles of 39 $\pm$ 1 °, indicating the negative sign of S. In contrast, the ethanol and acetone droplets spread completely on a quartz surface, and thus the sign of S is positive.

It has been reported that the precursor film appears when both the sign of A and S are positive, while it does not appear on the combination of positive A and negative S [62, 65]. Therefore, this theoretical prediction indicates that the ethanol and acetone form the precursor films on the hydrophilic quartz surface while the PDMS surface has no liquid film, which is consistent with our assumption. The sign of A and S and the existence of precursor film are summarized in Table 7.1. We also theoretically predicted that the precursor films around large and small microdroplets spread sufficiently and connect to each other (see Appendix E, Section E.1).

Solid	Liquid	A	S	Precursor film
PDMS	Ethanol	Positive	Negative	No
Quartz	Water	Positive	Negative	No
Quartz	Ethanol	Positive	Positive	Yes
Quartz	Acetone	Positive	Positive	Yes

Table 7.1: Sign of the difference in two Hamaker constants A and spreading coefficient S, and the existence of precursor film.

Unfortunately, we could not experimentally observe the precursor film using our RICM because the reflected signal received from such an ultrathin film is essentially indistinguishable from the background intensity (see Appendix E, Section E.2). The precursor film has been observed by the methods, such as Brewster angle microscopy [66] and ellipsometry [67]. Indeed, the existence of ultrathin film during ethanol condensation on a quartz surface has been reported in a previous report [29].

Next, we provide a simplified theoretical framework to qualitatively explain the differ-

ence in temperature rise between large and small microdroplets. Let us take a microdroplet of volume V at time t. Let us say that the drop volume increases by ΔV due to condensation in a differential time interval Δt. The heat energy ΔQ released from condensation during this process is

$$\Delta Q = \rho \Delta V H \tag{7.1}$$

where ρ is the density of condensed liquid and H is the specific latent heat of condensation. Here, if we consider that the timescale Δt is sufficiently small, we can assume that the heat generated due to droplet condensation is used solely to increase the temperature of the droplet by ΔT. We use $\Delta t = 0.1$ ms for the estimation, which is much shorter than the time scale of the conduction [20] through the quartz, $t_{\text{conduction}} \approx L^2/\alpha \approx 3$ ms, where $L = 2$ mm and $\alpha = 1.4 \times 10^{-3} m^2/s$ are the thickness and thermal diffusivity of quartz, respectively. By considering the energy balance, we obtain

$$\Delta T = \frac{H}{C_p} \frac{\Delta V}{V + \Delta V} \tag{7.2}$$

where C_p is the specific heat capacity. The volume V can be geometrically expressed as

$$V = \frac{1}{3} \pi r^3 \frac{(2 + \cos\theta)(1 - \cos\theta)^2)}{\sin^3\theta} \tag{7.3}$$

where r and θ are the mean base radius and contact angle of a microdroplet, respectively. Figure 7.6(a) shows a plot of contact angles of an ethanol droplet on the quartz surface as a function of mean base radius. It was found that the contact angles were almost constant at ~ 4 ° and independent on the mean base radius. Therefore, by differentiating Eq. (7.3) by the time t under the assumption that contact angle is constant, we obtain

$$\frac{dV}{dt} = \pi r^2 \frac{(2 + \cos\theta)(1 - \cos\theta)^2)}{\sin^3\theta} \frac{dr}{dt} \tag{7.4}$$

For a sufficiently small Δt, ΔV can be expressed as $\Delta V = \frac{dV}{dt} \Delta t$. Therefore, Eq. (7.2) can be written as

$$\Delta T = \frac{H}{C_p} \frac{3\Delta t \frac{dr}{dt}}{r + 3\Delta t \frac{dr}{dt}} \tag{7.5}$$

Experimentally obtained values of base radii r of the ethanol microdroplet at different time t are plotted in Figure 7.6(b). A linear fit between r and t clearly represented the experimentally obtained plot reasonably well (R-square value of 0.9929). Therefore, we can assume $\frac{dr}{dt}$ to be constant for our analysis. In addition, the value of $\frac{dr}{dt}$ shown in Figure 7.6(b) was 0.15. Using the experimentally obtained values in Eq. (7.5), we finally obtained a theoretical trend for variation of ΔT with mean base radius r, as shown in Figure 7.6(c). Note that this equation (7.5) is derived to qualitatively discuss the trend of the temperature difference between small and large droplets.

From the trend in Figure 7.6(c), we can conclude that the smaller microdroplets experience a higher temperature increment during condensation than that of the bigger ones. This result is in agreement with our assumption that the temperature rise of small microdroplets becomes larger compared to that of large droplets. Large droplets have a higher heat dissipation to the substrate (acting as a local heat sink) and therefore temperature rise becomes much smaller, while the temperature of small microdroplets becomes high due to small heat dissipation. Therefore, within the small microdroplet, a local temperature gradient is established between the edge closer to the bigger droplet and the edge away from it, resulting in thermocapillary motion.

From the force balance of the pinned ethanol microdroplets, we quantitatively estimate the driving force responsible for the spontaneous movement and the temperature gradient inside small microdroplets. On the pinned microdroplets as shown in Figure 7.3(b), hydrodynamic force induced by the thermocapillary flow, $F_{\mathrm{h}} = \frac{\partial \gamma_{\mathrm{LV}}}{\partial T} \frac{\partial T}{\partial x} \frac{\pi r^2}{2}$ and the force at three-phase contact line arising from the surface tension, $F_{\mathrm{cl}} = \frac{\partial \gamma_{\mathrm{LV}}}{\partial T} \frac{\partial T}{\partial x} \pi r^2 \cos\theta$ act in the direction of the larger droplet [31, 68]. In addition, the pinning force, $F_{\mathrm{P}} = \frac{\Delta S \gamma}{h}$ works at the pinning site (i.e., the impurity) in the opposite direction [69]. Here, h is the length of the neck pulled up by F_{h} and F_{cl}, and $\Delta S \gamma$ is the change in surface energy of the droplet, where $\Delta S = S_{\mathrm{pulled}} - S_{\mathrm{unpulled}}$ is the difference in the surface area between the pulled and unpulled microdroplets, which can be estimated from the experimental data. Because the pinned droplet is static, these forces should be in balance. By assuming that the base area

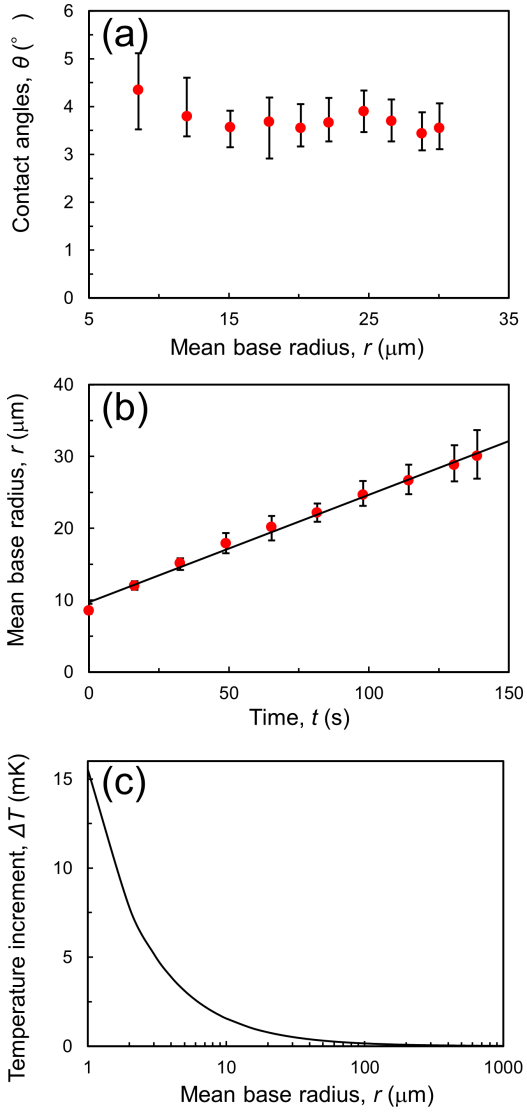

Figure 7.6: Analysis of the dynamics of growth of an ethanol microdroplet on a quartz surface. (a) Contact angle θ vs mean base radius r of an ethanol droplet nucleated on a quartz surface. (b) Mean base radius r vs time t. The slope of the fitting line in (b) is $\frac{dr}{dt} = 0.15$ and the R-square value is 0.9929. Upper and lower limits of error bars shown in (a) and (b) indicate the maximum and minimum values obtained by our analysis. (c) Theoretical trend of temperature increment ΔT during Δt= 0.1 ms as a function of base radius. The material parameters of ethanol are H= 838 J/g, $C_{\rm p}$= 2.42 J/g-K, and an averaged value of the contact angles θ= 3.7°.

is a circle, the force balance can be written as follows

$$\frac{\partial \gamma_{\mathrm{LV}}}{\partial T}\frac{\partial T}{\partial x}\frac{\pi r^2}{2}(1+2\cos\theta) = \frac{\Delta S_\gamma}{h} \tag{7.6}$$

The rate of change of the ethanol-vapor interfacial tension with temperature $\frac{\partial \gamma_{\mathrm{LV}}}{\partial T}$ was estimated as 6.37×10^{-5} N/(m-K) from literature [70]. Since the small microdroplets start to move immediately after depinning, the values of the pinning force F_{P} at the maximal extension of the neck, as shown in the 80.8 seconds of Figure 7.3(b), should be almost the same as the driving force on the moving microdroplet. Hence, from several microdroplets just before the depinning, the driving force was estimated as 208 ± 50 pN. The spontaneous movement despite extreme smallness of the forces is attributed to the reduction of resistive force from the solid surface by formation of the precursor film.

From the equation (7.6), the temperature gradient inside small microdroplets along the direction of the spontaneous movement $\frac{\partial T}{\partial x}$ was also estimated as 2.3 ± 1.1 K/mm, which is comparable to the value typically used to induce the thermocapillary motion [31, 32]. However, although the microdroplets on a PDMS surfaces also experience the similar temperature gradient, the droplets did not move. This is because there is the critical radius below which the droplets cannot move even on the thermal-gradient surface due to the contact angle hysteresis [31, 32, 61]. For example, Pratap et al. reported the critical radius of decane droplets on a PDMS surface with the temperature gradient of 1.05 - 2.77 K/mm is approximately 0.27 mm [31]. Therefore, it can be considered that the ethanol microdroplets on a PDMS surface did not move because their sizes were smaller than the critical radius induced by the contact angle hysteresis. In contrast, the ethanol microdroplets on the quartz surface were spontaneously moved even when the base radii of them are less than 20 μm, which are much smaller than the typical critical radius [31, 32, 61]. This indicates that the critical radius of the ethanol droplets on the hydrophilic quartz surface was significantly decreased because the precursor film reduced the resistive force exerted from the quartz surface, resulting in the extremely small contact angle hysteresis ($\sim 0.5^\circ$).

In our experiments, the minimum base radius at which the spontaneous movement occurred was approximately 3.5 μm. We noted that the spontaneous movement takes place

when the neck of the droplets that is pulled by the pinning sites becomes unstable and pinches off, as shown in Figure 7.3(b). The neck becomes unstable as the size of the droplet increases and/or the size of the pinning site decreases [69]. Therefore, it can be considered that larger droplets are more likely to detach on the surface and the minimum base radius for the spontaneous movement becomes smaller on smoother and cleaner surfaces.

Lastly, we analyzed the migration velocity of the depinned microdroplet shown in the frame at 81.6 seconds in Figure 7.3(b) and quantitatively compared with the theoretical value. Pratap et al. reported that the temperature-induced induced motion of the droplet can be modeled as a quasi-steady process and the migration velocity V can be written as follows [31]

$$V = \frac{r\frac{\partial \gamma_{LV}}{\partial T}\frac{\partial T}{\partial x}(1+2\cos\theta)}{12\mu\left[g(\theta,1-\epsilon)-g(\theta,0)\right]} \tag{7.7}$$

where

$$g(\theta,\zeta) = \cot\theta\left[1-\ln(\sqrt{\mathrm{cosec}^2\theta-\zeta^2}-\cot\theta\right]-\sqrt{\mathrm{cosec}^2\theta-\zeta^2} \tag{7.8}$$

$\mu = 1.2\times10^{-3}$ Pa-s is the viscosity of ethanol and ϵ is a constant value that is defined as $\epsilon = L_s/r$, where $L_s = 0.5$ nm is a cutoff length value of the order of molecular dimensions, introduced solely to avoid mathematical singularity. By applying the equation (7.7) to the depinned droplet, the migration velocity can be estimated. Accordingly, the value was approximately 4.2 μm/s. On the other hand, the experimental value of the migration velocity of the same microdroplet (defined as the rate of the change of the center position with respect to time) was approximately 12.7 μm/s, which is higher than the theoretical value. This may be because the droplet still does not reach the quasi-steady condition since the sudden depinning breaks the balance of the forces working on the droplet, resulting in sudden acceleration of the droplet. Further quantitative characterization of the spontaneous motion remains an interesting topic for future studies, but beyond the scope of the present work that focuses on the mechanism of the spontaneous motion.

7.5 Conclusions

In this work, we report experimental observation of condensation of microdroplets with extremely low contact angles. We found that contact angles of ethanol microdroplets condensed on a hydrophilic quartz surface were constant (approximately 4°) and did not depend on the base radius. The small microdroplets spontaneously moved to relatively large droplets during condensation. Although we conducted the microdroplet condensation by using high surface tension liquid (i.e. deionized water) and a hydrophobic PDMS surface, this movement occurred only when we used the combination of a low surface tension liquid and a hydrophilic surface. In addition, the moving droplets showed extreme low contact angles hysteresis. From these results, we attributed this motion to two factors, namely, formation of an ultrathin precursor film and a gradient in local temperature inside the small microdroplet caused by the difference in adjacent droplet sizes. The local temperature gradient causes thermocapillary effect and thus makes the small microdroplets move towards the large droplet close to them. The presence of the ultrathin precursor film underneath the nucleated droplets facilitates the motion by reducing the resistive force to migration. The driving force for the migration and the temperature gradient inside a small microdroplet were quantitatively calculated from the force balance of the pinned microdroplets. The extremely small driving force and the onset of the movement of the microdroplets with the very small base radius are the incontrovertible evidence of the existence of precursor film. These results will extend our fundamental knowledge about microdroplet condensation and will be valuable for condensation heat transfer.

References

[1] K. W. Stöckelhuber, B. Radoev, and H. J. Schulze, "Some new observations on line tension of microscopic droplets," *Colloids and Surfaces A: Physicochemical and Engineering Aspects*, vol. 156, no. 1-3, pp. 323–333, 1999.

[2] L. O. Heim and E. Bonaccurso, "Measurement of line tension on droplets in the submicrometer range," *Langmuir*, vol. 29, no. 46, pp. 14147–14153, 2013.

[3] H. Zhang, S. Chen, Z. Guo, Y. Liu, F. Bresme, and X. Zhang, "Contact Line Pinning Effects Influence Determination of the Line Tension of Droplets Adsorbed on Substrates," *Journal of Physical Chemistry C*, vol. 122, no. 30, pp. 17184–17189, 2018.

[4] D. Lohse and X. Zhang, "Surface nanobubbles and nanodroplets," *Reviews of Modern Physics*, vol. 87, no. 3, pp. 981–1035, 2015.

[5] S. Daniel, M. K. Chaudhury, and J. C. Chen, "Fast drop movements resulting from the phase change on a gradient surface," *Science*, vol. 291, no. 5504, pp. 633–636, 2001.

[6] N. Miljkovic and E. N. Wang, "Condensation heat transfer on superhydrophobic surfaces," *MRS bulletin*, vol. 38, no. 5, pp. 397–406, 2013.

[7] F. Chu, X. Wu, B. Zhu, and X. Zhang, "Self-propelled droplet behavior during condensation on superhydrophobic surfaces," *Applied Physics Letters*, vol. 108, no. 19, p. 194103, 2016.

[8] J. Sun and P. B. Weisensee, "Microdroplet self-propulsion during dropwise condensation on lubricant-infused surfaces," *Soft Matter*, vol. 15, no. 24, pp. 4808–4817, 2019.

[9] D. Orejon, O. Shardt, P. R. Waghmare, N. S. Kumar Gunda, Y. Takata, and S. K. Mitra, "Droplet migration during condensation on chemically patterned micropillars," *RSC Advances*, vol. 6, no. 43, pp. 36698–36704, 2016.

[10] P. B. Weisensee, Y. Wang, H. Qiang, D. Schultz, W. P. King, and N. Miljkovic, "Condensate droplet size distribution on lubricant-infused surfaces," *International Journal of Heat and Mass Transfer*, vol. 109, pp. 187–199, 2017.

[11] J. W. Rose, "Dropwise condensation theory and experiment: A review," *Proceedings of the Institution of Mechanical Engineers, Part A: Journal of Power and Energy*, vol. 216, no. 2, pp. 115–128, 2002.

[12] D. Orejon, O. Shardt, N. S. K. Gunda, T. Ikuta, K. Takahashi, Y. Takata, and S. K. Mitra, "Simultaneous dropwise and filmwise condensation on hydrophilic mi-

crostructured surfaces," *International Journal of Heat and Mass Transfer*, vol. 114, pp. 187–197, 2017.

[13] A. Lafuma and D. Quéré, "Superhydrophobic states," *Nature Materials*, vol. 2, no. 7, pp. 457–460, 2003.

[14] X. Yan, L. Zhang, S. Sett, L. Feng, C. Zhao, Z. Huang, H. Vahabi, A. K. Kota, F. Chen, and N. Miljkovic, "Droplet Jumping: Effects of Droplet Size, Surface Structure, Pinning, and Liquid Properties," *ACS Nano*, vol. 13, no. 2, pp. 1309–1323, 2019.

[15] N. Miljkovic, R. Enright, Y. Nam, K. Lopez, N. Dou, J. Sack, and E. N. Wang, "Jumping-droplet-enhanced condensation on scalable superhydrophobic nanostructured surfaces," *Nano letters*, vol. 13, no. 1, pp. 179–187, 2013.

[16] J. B. Boreyko and C. H. Chen, "Self-propelled dropwise condensate on superhydrophobic surfaces," *Physical Review Letters*, vol. 103, no. 18, p. 184501, 2009.

[17] S. Anand, A. T. Paxson, R. Dhiman, J. D. Smith, and K. K. Varanasi, "Enhanced condensation on lubricant-impregnated nanotextured surfaces," *ACS Nano*, vol. 6, no. 11, pp. 10122–10129, 2012.

[18] A. Lafuma and D. Quéré, "Slippery pre-suffused surfaces," *Europhysics Letters*, vol. 96, no. 5, p. 56001, 2011.

[19] M. J. Kreder, J. Alvarenga, P. Kim, and J. Aizenberg, "Design of anti-icing surfaces: Smooth, textured or slippery?," *Nature Reviews Materials*, vol. 1, no. 1, 2016.

[20] K. Rykaczewski, "Microdroplet growth mechanism during water condensation on superhydrophobic surfaces," *Langmuir*, vol. 28, no. 20, pp. 7720–7729, 2012.

[21] Y. Yamada, T. Ikuta, T. Nishiyama, K. Takahashi, and Y. Takata, "Droplet nucleation on a well-defined hydrophilic-hydrophobic surface of 10 nm order resolution," *Langmuir*, vol. 30, no. 48, pp. 14532–14537, 2014.

[22] S. Anand and S. Y. Son, "Sub-micrometer dropwise condensation under superheated and rarefied vapor condition," *Langmuir*, vol. 26, no. 22, pp. 17100–17110, 2010.

[23] N. A. Stelmashenko, J. P. Craven, A. M. Donald, E. M. Terentjev, and B. L. Thiel, "Topographic contrast of partially wetting water droplets in environmental scanning electron microscopy," *Journal of Microscopy*, vol. 204, no. 2, pp. 172–183, 2001.

[24] K. Rykaczewski, J. H. Scott, and A. G. Fedorov, "Electron beam heating effects during environmental scanning electron microscopy imaging of water condensation on superhydrophobic surfaces," *Applied Physics Letters*, vol. 98, no. 9, p. 093106, 2011.

[25] N. Miljkovic, R. Enright, and E. N. Wang, "Effect of droplet morphology on growth dynamics and heat transfer during condensation on superhydrophobic nanostructured surfaces," *ACS Nano*, vol. 6, no. 2, pp. 1776–1785, 2012.

[26] A. Méndez-Vilas, A. B. Jódar-Reyes, and M. L. González-Martín, "Ultrasmall liquid droplets on solid surfaces: Production, imaging, and relevance for current wetting research," *Small*, vol. 5, no. 12, pp. 1366–1390, 2009.

[27] M. Sundberg, A. Månsson, and S. Tågerud, "Contact angle measurements by confocal microscopy for non-destructive microscale surface characterization," *Journal of Colloid and Interface Science*, vol. 313, no. 2, pp. 454–460, 2007.

[28] Y. X. Wang, J. L. Plawsky, and P. C. Wayner, "Optical measurement of microscale transport processes in dropwise condensation," *Microscale Thermophysical Engineering*, vol. 5, no. 1, pp. 55–69, 2001.

[29] S. J. Gokhale, J. L. Plawsky, P. C. Wayner, and S. DasGupta, "Inferred pressure gradient and fluid flow in a condensing sessile droplet based on the measured thickness profile," *Physics of Fluids*, vol. 16, no. 6, pp. 1942–1955, 2004.

[30] P. C. Wayner, "Nucleation, growth and surface movement of a condensing sessile droplet Peter," *Colloids and Surfaces A: Physicochemical and Engineering Aspects*, vol. 206, pp. 157–165, 2002.

[31] V. Pratap, N. Moumen, and R. S. Subramanian, "Thermocapillary motion of a liquid drop on a horizontal solid surface," *Langmuir*, vol. 24, no. 9, pp. 5185–5193, 2008.

[32] J. Z. Chen, S. M. Troian, A. A. Darhuber, and S. Wagner, "Effect of contact angle hysteresis on thermocapillary droplet actuation," *Journal of Applied Physics*, vol. 97, no. 1, p. 014906, 2005.

[33] S. Y. Teh, R. Lin, L. H. Hung, and A. P. Lee, "Droplet microfluidics," *Lab on a Chip*, vol. 8, no. 2, pp. 198–220, 2008.

[34] Z. Yan, M. Jin, Z. Li, G. Zhou, and L. Shui, "Droplet-based microfluidic thermal management methods for high performance electronic devices," *Micromachines*, vol. 10, no. 2, pp. 1–16, 2019.

[35] C. G. Yang, Z. R. Xu, and J. H. Wang, "Manipulation of droplets in microfluidic systems," *Trends in Analytical Chemistry*, vol. 29, no. 2, pp. 141–157, 2010.

[36] J. L. Garcia-Cordero and Z. H. Fan, "Sessile droplets for chemical and biological assays," *Lab on a Chip*, vol. 17, no. 13, pp. 2150–2166, 2017.

[37] T. Yamazaki, M. Tenjimbayashi, K. Manabe, T. Moriya, H. Nakamura, T. Nakamura, T. Matsubayashi, Y. Tsuge, and S. Shiratori, "Antifreeze Liquid-Infused Surface with High Transparency, Low Ice Adhesion Strength, and Antifrosting Properties Fabricated through a Spray Layer-by-Layer Method," *Industrial and Engineering Chemistry Research*, vol. 58, no. 6, pp. 2225–2234, 2019.

[38] P. W. Wilson, W. Lu, H. Xu, P. Kim, M. J. Kreder, J. Alvarenga, and J. Aizenberg, "Inhibition of ice nucleation by slippery liquid-infused porous surfaces (SLIPS)," *Physical Chemistry Chemical Physics*, vol. 15, no. 2, pp. 581–585, 2013.

[39] P. Kim, T. S. Wong, J. Alvarenga, M. J. Kreder, W. E. Adorno-Martinez, and J. Aizenberg, "Liquid-infused nanostructured surfaces with extreme anti-ice and anti-frost performance," *ACS Nano*, vol. 6, no. 8, pp. 6569–6577, 2012.

[40] B. S. Lalia, S. Anand, K. K. Varanasi, and R. Hashaikeh, "Fog-harvesting potential of lubricant-impregnated electrospun nanomats," *Langmuir*, vol. 29, no. 42, pp. 13081–13088, 2013.

[41] K. C. Park, S. S. Chhatre, S. Srinivasan, R. E. Cohen, and G. H. McKinley, "Optimal design of permeable fiber network structures for fog harvesting," *Langmuir*, vol. 29, no. 43, pp. 13269–13277, 2013.

[42] D. Seo, C. Lee, and Y. Nam, "Influence of geometric patterns of microstructured superhydrophobic surfaces on water-harvesting performance via dewing," *Langmuir*, vol. 30, no. 51, pp. 15468–15476, 2014.

[43] J. Ju, H. Bai, Y. Zheng, T. Zhao, R. Fang, and L. Jiang, "A multi-structural and multi-functional integrated fog collection system in cactus," *Nature Communications*, vol. 3, pp. 1–6, 2012.

[44] V. A. Ganesh, H. K. Raut, A. S. Nair, and S. Ramakrishna, "A review on self-cleaning coatings," *Journal of Materials Chemistry*, vol. 21, no. 41, pp. 16304–16322, 2011.

[45] T. S. Wong, S. H. Kang, S. K. Tang, E. J. Smythe, B. D. Hatton, A. Grinthal, and J. Aizenberg, "Bioinspired self-repairing slippery surfaces with pressure-stable omniphobicity," *Nature*, vol. 477, no. 7365, pp. 443–447, 2011.

[46] Y. Lu, S. Sathasivam, J. Song, C. R. Crick, C. J. Carmalt, and I. P. Parkin, "Robust self-cleaning surfaces that function when exposed to either air or oil," *Science*, vol. 347, no. 6226, pp. 1132–1135, 2015.

[47] R. Blossey, "Self-cleaning surfaces - Virtual realities," *Nature Materials*, vol. 2, no. 5, pp. 301–306, 2003.

[48] I. D. Johnston, D. K. McCluskey, C. K. Tan, and M. C. Tracey, "Mechanical characterization of bulk Sylgard 184 for microfluidics and microengineering," *Journal of Micromechanics and Microengineering*, vol. 24, no. 3, p. 035017, 2014.

[49] J. H. Snoeijer, E. Rolley, and B. Andreotti, "Paradox of Contact Angle Selection on Stretched Soft Solids," *Physical Review Letters*, vol. 121, no. 6, p. 68003, 2018.

[50] R. Pericet-Cámara, A. Best, H. J. Butt, and E. Bonaccurso, "Effect of capillary pressure and surface tension on the deformation of elastic surfaces by sessile liquid micro-

drops: An experimental investigation," *Langmuir*, vol. 24, no. 19, pp. 10565–10568, 2008.

[51] M. Born and E. Wolf, *Principles of optics: electromagnetic theory of propagation, interference and diffraction of light*. 6th ed., 2013.

[52] N. J. Cira, A. Benusiglio, and M. Prakash, "Vapour-mediated sensing and motility in two-component droplets," *Nature*, vol. 519, no. 7544, pp. 446–450, 2015.

[53] X. Man and M. Doi, "Vapor-Induced Motion of Liquid Droplets on an Inert Substrate," *Physical Review Letters*, vol. 119, no. 4, p. 044502, 2017.

[54] Y. Wen, P. Y. Kim, S. Shi, D. Wang, X. Man, M. Doi, and T. P. Russell, "Vapor-induced motion of two pure liquid droplets," *Soft Matter*, vol. 15, no. 10, pp. 2135–2139, 2019.

[55] H. Sadafi, S. Dehaeck, A. Rednikov, and P. Colinet, "Vapor-Mediated versus Substrate-Mediated Interactions between Volatile Droplets," *Langmuir*, pp. 1–9, 2019.

[56] B. Majhy and A. K. Sen, "Evaporation-induced transport of a pure aqueous droplet by an aqueous mixture droplet," *Physics of Fluids*, vol. 32, no. 3, 2020.

[57] D. Quéré, "Non-sticking drops," *Reports on Progress in Physics*, vol. 68, no. 11, pp. 2495–2532, 2005.

[58] Q. Sheng, J. Sun, Q. Wang, W. Wang, and H. S. Wang, "On the onset of surface condensation: Formation and transition mechanisms of condensation mode," *Scientific Reports*, vol. 6, no. 30764, pp. 1–9, 2016.

[59] M. N. Popescu, G. Oshanin, S. Dietrich, and A. M. Cazabat, "Precursor films in wetting phenomena," *Journal of Physics Condensed Matter*, vol. 24, no. 243102, pp. 1–30, 2012.

[60] J. B. Boreyko, G. Polizos, P. G. Datskos, S. A. Sarles, and C. P. Collier, "Air-stable droplet interface bilayers on oil-infused surfaces," *Proceedings of the National Academy of Sciences of the United States of America*, vol. 111, no. 21, pp. 7588–7593, 2014.

[61] J. B. Brzoska, F. Brochard-Wyart, and F. Rondelez, "Motions of Droplets on Hydrophobic Model Surfaces Induced by Thermal Gradients," *Langmuir*, vol. 9, no. 8, pp. 2220–2224, 1993.

[62] F. Brochard-Wyart, J. M. di Meglio, D. Quéré, and P. G. de Gennes, "Spreading of Nonvolatile Liquids in a Continuum Picture," *Langmuir*, vol. 7, no. 2, pp. 335–338, 1991.

[63] J. Israelachvili, *Intermolecular and Surface forces, 1985.* Academic Press, 3rd ed., 2011.

[64] C. J. Drummond and D. Y. Chan, "van der Waals interaction, surface free energies, and contact angles: Dispersive polymers and liquids," *Langmuir*, vol. 13, no. 14, pp. 3890–3895, 1997.

[65] D. Bonn, J. Eggers, J. Indekeu, and J. Meunier, "Wetting and spreading," *Reviews of Modern Physics*, vol. 81, no. 2, pp. 739–805, 2009.

[66] I. Ueno, K. Hirose, Y. Kizaki, Y. Kisara, and Y. Fukuhara, "Precursor film formation process ahead macroscopic contact line of spreading droplet on smooth substrate," *Journal of Heat Transfer*, vol. 134, no. 5, pp. 1–4, 2012.

[67] E. Shoji, A. Komiya, J. Okajima, M. Kubo, and T. Tsukada, "Three-step phase-shifting imaging ellipsometry to measure nanofilm thickness profiles," *Optics and Lasers in Engineering*, vol. 112, no. August 2018, pp. 145–150, 2019.

[68] F. Brochard, "Motions of Droplets on Solid Surfaces Induced by Chemical or Thermal Gradients," *Langmuir*, vol. 5, no. 2, pp. 432–438, 1989.

[69] B. H. Tan, H. An, and C.-D. Ohl, "Resolving the Pinning Force of Nanobubbles with Optical Microscopy," *Physical Review Letters*, vol. 118, no. 5, p. 054501, 2017.

[70] F. A. Gonalves, A. R. Trindade, C. S. Costa, J. C. Bernardo, I. Johnson, I. M. Fonseca, and A. G. Ferreira, "PVT, viscosity, and surface tension of ethanol: New measurements and literature data evaluation," *Journal of Chemical Thermodynamics*, vol. 42, no. 8, pp. 1039–1049, 2010.

Chapter 8

Bioinspired Scalable Lubricated Bi-continuous-porous Composites with self-recoverability and exceptional outdoor durability [1]

8.1 Overview

Lubricant impregnated surfaces (LIS) are promising as robust liquid-repellent surfaces, which comprise a surface lubricant layer stabilized by base solid structures. However, the lubricant layer is susceptible to depletion upon exposure to degrading stimuli, leading to the loss of functionality. Lubricant depletion becomes even more pronounced in exposed outdoor conditions, restricting LIS to short-term lab-scale applications. Thus, the development of scalable and long-term stable LIS suitable for practical outdoor applications remains challenging. In this work, we designed "Lubricated Bi-Continuous porous Composites" (LuBiCs) by infusing a silicone oil lubricant into a bi-continuous porous composite

[1] Adapted from a manuscript of same title by **Misra, S**; Tenjimbayashi, M.; Weng, W.; Mitra, S.K. & Naito, M., under review (manuscript id: am-2023-031282) in *ACS Applied Materials & Interfaces*.

matrix of tetrapod-shaped Zinc Oxide micro fillers and poly(dimethylsiloxane). LuBiCs are prepared in meter-scale by a facile drop-casting inspired wet process. The bi-continuous porous feature of the LuBiCs enables capillarity-driven spontaneous lubricant transport throughout the surface without any external driving force. Consequently, the LuBiCs can regain liquid-repellent function upon lubricant depletion via capillary replenishment from a small, connected lubricant reservoir, making them tolerant to lubricant degrading stimuli (e.g., rain shower, surface wiping, and shearing). As a proof-of-concept, we show that the large-scale "LuBiCs roof" retains slippery behavior even after more than 9 months of outdoor exposure.

8.2 Introduction

Surfaces that can fully repel oncoming liquids are significant in many industrial applications such as corrosion-resistant [1]/self-cleaning [2] coatings, anti-fogging [3]/anti-icing [4], and oil/water separation [5]. Lotus-leaf inspired [6] rough structured superhydrophobic (SHPO) surfaces [7] with low surface energy have been extensively used to achieve water-repellent functionality in synthetic surfaces where the sustenance of a trapped air cushion into the surface roughness underneath an oncoming water droplet (the Cassie-Baxter wetting state [8]) enables removal of water. However, associated functional challenges [9] such as the inability to repel low surface tension liquids, weak pressure/impact [10] stability, and susceptibility to failure upon mechanical damage [11] to delicate surface structures restrict the long-term applicability of conventional SHPO surfaces in the outdoor environment. In the past two decades, increasingly complex geometrical structures have been proposed to combat some of these challenges. Examples include the development of re-entrant [12, 13]/ doubly re-entrant geometry [14] to achieve omniphobicity and multiscale microcones and nanograss geometry [15] or armored structures [16] to improve mechanical robustness. Although fundamentally interesting, the challenges associated with intricate surface texturing and the lack of scalability thereof limits their practical applicability.

Another type of liquid-repellent surface, Lubricant impregnated surface (LIS), [17, 18] are promising as repellent surfaces for their omniphobicity. LIS is prepared by infusing

a compatible lubricant into a textured/porous [17–19] solid or into the molecular matrix of an absorbent/swellable polymer [20–23]. When the surface lubricant is thermodynamically stable and immiscible with oncoming droplets [17], the surface slides them off with negligible sliding angle and contact angle hysteresis. Thus, proper lubricant and base layer selection enables the LIS to repel liquids over a wide surface tension range. Moreover, thanks to the surface fluidity by the lubricant layer, LIS is pressure-stable and exhibits self-repairing property against mechanical damage. Owing to their promising prospects, the applicability of LIS has been explored in multiple practical purposes since their discovery including enhancement of condensation [24, 25], drag reduction [26, 27], anti-icing coatings [28, 29], prevention of biofouling in marine [30, 31] as well as, medical applications [20, 32] and in the rational design of stimuli-responsive interfaces for smart liquid manipulation [33–37].

However, this surface lubricant is depleted by droplet sliding [38–40], which limits the lifetime of the LIS. Several efforts to design the sustainable, lubricant-depletion resistant LIS have been made. Cui et al. demonstrated a supramolecular polymer-gel system [22] that self-reports lubricant loss by the change in optical transparency and accordingly self-regulates lubricant secretion from the bulk to achieve self-repairability. Howell et al. mimicked the vascular network [41] of a leaf to maintain lubricant supply to the surface. Tenjimbayashi et al. reported liquid-infused smooth coating [42], which exhibits liquid repellence regardless of the lubricant thickness. Urata et al. designed swollen elastomer gels [43] which can supplement the surface lubricant layer from the bulk via syneresis. Several other studies [20, 21, 44, 45] also report the formation of self-replenishing LIS by post-crosslinking infusion of silicone oil into a silicone-based elastomer network. These works showed the promising possibility of the lubricant transport from the bulk of the coating to the LIS surface. However, as noted in a study [45] on the lubrication dynamics of syneresis-driven systems, the syneresis rates gradually decrease over time as the system approaches the crosslinking equilibrium, and therefore, the self-lubricating capability of such surfaces can only be realized for a finite duration. As the lubricant content stored in bulk cannot be scaled up without prohibitive compromises on the thickness and integrity of the coating, a rational design of a truly maintenance-free, long-term durable, self-recovering system would require a source of lubricant attached to the desired surface

from where the lubricant can be transported throughout the material as and when needed without any external support (e.g., pumping). Overall, capillary transport could be useful here for sustainable lubricant replenishment.

Inspired by this rationale, herein we report the scalable formation of "Lubricated Bi-Continuous porous Composites" (LuBiCs), which exhibit slippery function with remarkable long-term stability. LuBiCs comprise a silicone oil lubricant layer stabilized into a bi-continuous micro-porous base layer of self-assembled tetrapod-shaped ZnO [46] covered with polydimethylsiloxane (PDMS) elastomer. Because of the wurtzite structure, ZnO can be grown into tetrapod shape [47], which then loosely assembles into the PDMS matrix to impart a high porosity to the base layer. Owing to the bi-continuous porous feature and high affinity between silicone oil and PDMS, lubricant can be transported to the whole of the solid structure via capillary force. This enables continuous unassisted lubricant transport from separately attached lubricant reservoir to LuBiCs surface (**Figure 8.1**). As a result, the LuBiCs are tolerant to lubricant-degrading stimuli (e.g., rain shower, surface wiping, and shearing). Additionally, the selection of non-volatile silicone oil as the infused lubricant enhances the service life of LuBiCs by reducing evaporation-driven lubricant loss during exposed outdoor operation. We confirmed that meter-scale LuBiCs coating maintained slippery behavior during outdoor exposure for over 9 months.

Furthermore, due to the usage of non-toxic, biocompatible silicone [48, 49] materials both as the backbone of the base layer and the infused lubricant, the LuBiCs stand out as an environmentally friendlier and sustainable alternative to LIS employing fluorinated surfaces and lubricants [17, 19, 50].

It is also reported that silicone fluids (liquid PDMS) degrade in typical agricultural soil within days via clay-catalyzed-rearrangement [52–54] resulting in the formation of low-molecular-weight water soluble silanols along with some volatile cyclic or trimethylsiloxy end-blocked linear oligomers. Thus, although the infused lubricant can leach into the soil during outdoor operation, silicone oils are significantly less environmentally persistent and easier to remediate than perfluorinated carbon-based lubricants, which are particularly resistant to environmental degradation [55, 56] owing to the stable C−F bonds. Further, from the viewpoint of sustainability, we propose the idea to collect the lubricant spilled by water sliding/ rain shower on LuBiCs into the same lubricant reservoir by integrating

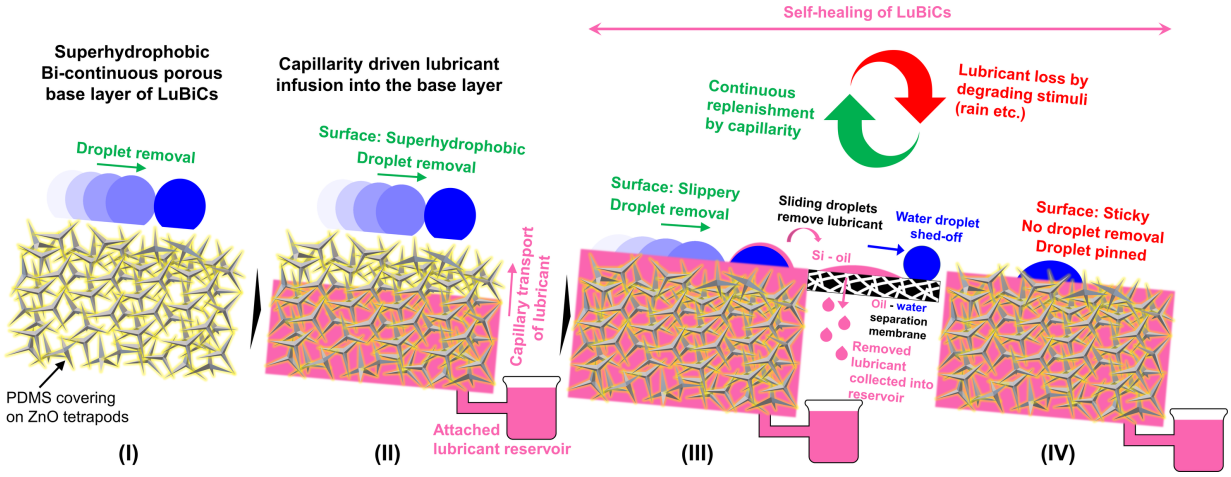

Figure 8.1: Research concept: Self-lubricating LuBiCs with exceptional durability. The ZnO-PDMS composite base layer is superhydrophobic and possesses bicontinuous porosity (state I). Silicone oil lubricant can spontaneously wick through (state II) the interconnected pores of the base layer by capillary action, which turns the initially superhydrophobic base layer slippery (state III). Exposure to degrading stimulus, e.g., rain shower, wiping, or high shear, might lead to a partial loss of lubricant covering from the surface and can consequently turn the surface sticky (state IV), causing droplet pinning and temporary loss of repellent behavior. However, owing to bicontinuous porosity and the chemical compatibility between the PDMS backbone and the infused silicone oil, the surface can self-recover its slippery behavior by capillary action. This is realizable even at large scale and over many lubricant loss-recovery cycles, as evident from the successful large-scale, multi-month outdoor durability test. Further, a self-standing, attachable oil-water separation membrane, demonstrated in a previous work [51], can be integrated with LuBiCs, as shown here schematically. It will allow us to collect the lubricant removed from LuBiCs surface by droplet sliding/rain shower back into the same attached lubricant reservoir.

an oil/water separation filter [51, 57] at the bottom of the LuBiCs. In a previous study, Tenjimbayashi *et al.* [51] reported a self-standing, attachable nanofibrous membrane with $> 99\%$ oil-water separation efficiency. Once integrated in-between the LuBiCs surface and the lubricant reservoir (see the schematic representation in Figure 8.1), the membrane

with selective wettability (hydrophobic/ superoleophilic) can shed off water while allowing silicone oil to pass through enabling us to recollect > 99 % of the spilled lubricant back to the lubricant reservoir. This will not only circumvent the possibility of fouling of the soil by the released silicone lubricant but will also significantly reduce silicone oil consumption during the service life of LuBiCs through material circularity. We envision that with their excellent performance, remarkable maintenance-free outdoor durability, and scalability, LuBiCs will emerge as a key enabler toward developing market-ready LIS well-suited for outdoor applications which meet the United Nations' Sustainable Development Goals [58].

8.3 Results and Discussion

8.3.1 Surface morphology of the base layer

The base layer of the LuBiCs is a bi-continuous porous composite with an acicular structure. The design is inspired by the protective outer structure of porcupine fish where hard spines protrude through the elastic skin. We mimicked the unique structure of porcupinefish in the micrometer scale by embedding tetrapod-shaped ZnO microfillers in the elastic matrix of PDMS. Each of the two components of the resulting composite serves different purposes. The ZnO tetrapods provide roughness to the matrix. It is responsible for the bicontinuous porosity in the bulk, while on the surface, it provides capillary force to retain the lubricant in place. The PDMS backbone provides elasticity to the matrix and also facilitates the retention and transport of silicone oil lubricant throughout the base layer owing to its chemical compatibility with the infused lubricant. The surface roughness (RMS roughness, $R_q \approx 5.70 \pm 0.43\ \mu$m) introduced by the ZnO tetrapods make the base layer superhydrophobic with advancing contact angle (ACA), receding contact angle (RCA), contact angle hysteresis (CAH), and sliding angle (SA) for water being 157.0±2.5°, 152.5±2.1°, 4.4±2.8°, and 2.8±0.8°, respectively. The superhydrophobic properties of the base layer were explored in detail in a previous publication [46] of the group. The base composite is excellently mechanical damage, deformation, and defect tolerant. We have shown that the superhydrophobic composite maintains stable water repellency after 1000 abrasion and 1000 bending cycles, and even after their surfaces were sliced off many times.

Thus, the rough, bicontinuous porous structure all-around the composite matrix not only facilitates unassisted capillary transport of lubricant throughout the surface but also prevents loss in functionality upon mechanical damage. The coating was fabricated using a drop-casting process. Owing to the geometric hindrance offered by the tetrapod shape, the ZnO microfillers assemble loosely in the PDMS matrix, forming a highly porous elastic coating with interconnected pores (**Figure 8.2**A, B). Note that the porosity of the base matrix is controlled [46] by the weight ratio (r) of ZnO microfillers and PDMS. With increasing r, the porosity increases while the elasticity decreases. As our proposed application is in capillarity-driven self-replenishing roof coatings, higher porosity of the matrix is more critical than achieving flexibility. That is why we have chosen a high ZnO to PDMS weight ratio while fabricating our coatings. The fabrication process of the base layer is versatile and can be achieved using other wet processes, including spraying, dipping, or bar coating, as shown in a previous work [46]. The interconnected pores enable efficient capillary transport through the porous network. Assuming circular pore geometry, we have estimated the pore size distribution (in terms of pore diameter, d_{pore}) on the top surface of the base layer (Figure 8.2C) as well as along its cross-section (Figure 8.2D). More than 94% of the total number of pores have pore diameters in the range 0.5 - 2.5 μm. We estimated that LuBiCs coating with a thickness of 181.8 $\pm$ 1.1 μm could retain 11.84 mg cm^{-2} of silicone oil even after being subjected to shear at 5000 RPM. Owing to the bi-continuous structure and high porosity, the lubrication capacity of this base layer is higher than other reported LIS [42, 50, 59–65]. We also observed that the surface of the ZnO tetrapods was mostly covered by a layer of RTV silicone, as can be confirmed from the Energy-dispersive X-Ray spectroscopy (EDX) elemental mapping (Figure 8.2E) and Raman spectral imaging (Figure 8.2F) of the surface of the base layer. The covering of RTV silicone on ZnO microfillers reduces the interfacial energy between the base layer and silicone oil lubricant while retaining the roughness features. It leads to improved lubricant immobilization on the surface. We also performed Raman mapping of the surface after lubricant infusion into the porous base layer (Figure 8.2G). As expected, the surface scan did not identify any ZnO phase on the lubricated surface due to a lubricant overlayer.

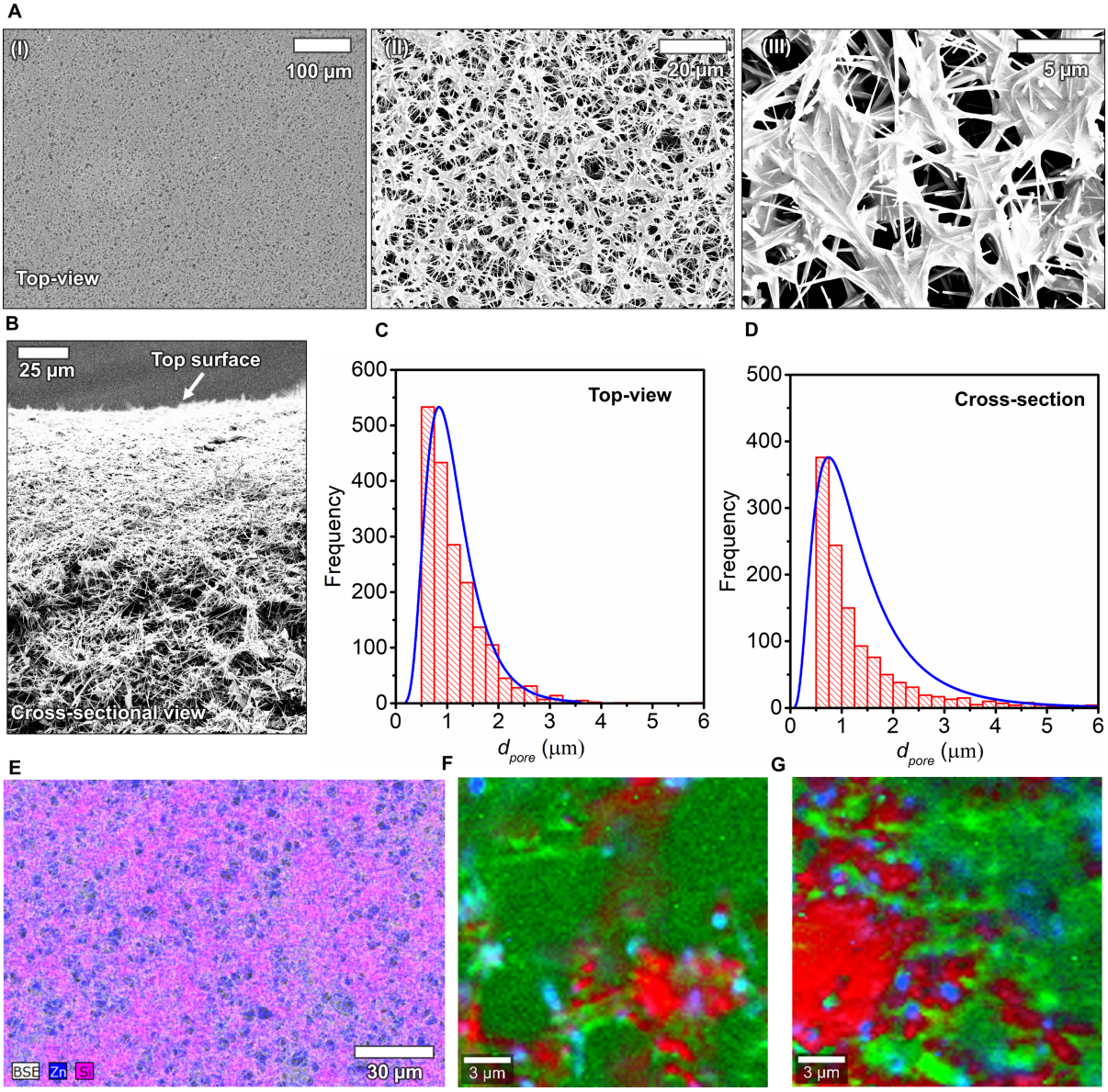

Figure 8.2: Surface morphology of the base layer. (A) Scanning electron microscopy (SEM) images of the top surface of the base layer at different magnifications. (B) Cross-sectional SEM image of the base layer, (C-D) show pore diameter distribution over a scan area of 120 μm x 80 μm both on the top surface as well as along the cross-section of the 3D porous base layer, respectively. The distributions were calculated from the SEM data. The histograms were fitted with lognormal distribution. (. . . continuing to the next page)

Figure 8.2: (...continued from the previous page) (E) Elemental mapping of the top surface of the base layer showing the distribution of Zn and Si, obtained from Energy dispersive X-ray (EDX) spectroscopy. The EDX spectra and component-wise elemental map for Zn and Si are shown in Figure F.1 of Appendix F. (F) Raman composite image of the top surface of the base layer - the green and red phases correspond to PDMS while the blue phase is ZnO. (G) Raman composite image of the top surface of the lubricated composite - all three phases (red, green, and blue) correspond to PDMS while no ZnO signal was found on the surface. Note that in (F), the database matching procedure inbuilt into the Raman software identified the red and green phases to be two different phases due to slight differences in spectra and consequent differences in the Hit Quality Index (HQI). However, it was verified that they represent the same chemical composition and that is of PDMS/dimethicone. Similarly, for the lubricated surface, all three identified phases in (G) correspond to PDMS with slightly different HQI scores. The Raman spectra of the individually identified components as well as the component-wise Raman images for both the base layer (Figure F.2) and the lubricated composite (Figure F.3) are given in Appendix F.

8.3.2 Omniphobicity of the LuBiCs surface

The LuBiCs repelled various test liquids of a broad surface tension range (21.91 mN/m - 72.06 mN/m), with contact angle hysteresis, CAH $< 5°$, and sliding angle, SA $< 5°$ for 2μl droplet volume, as shown in **Figure 8.3**A. LuBiCs repelled liquids with roughly constant CAH irrespective of their surface tension, which is different from classical superomniphobic surfaces [13], where contact angle hysteresis increases with a decrease in the surface tension of the liquid to be repelled. We present the side view optical images of 2 μl droplets of several test liquids of varying surface tension sliding on LuBiCs in Figure 8.3B. The droplets were placed on an initially horizontal LuBiCs-coated glass slide mounted on a tilting platform and subsequently tilted to allow sliding. The snaps represent the drop shapes just at the onset of the sliding. Further, Figure 8.3C shows the self-cleaning ability of LuBiCs after being fouled by particulate contaminants, including sand. The surface was

intentionally covered with a generous amount of sand, and then water jet was impinged on it. As shown in Figure 8.3C, the oncoming water carried the sand away from the surface, and the surface was clean again.

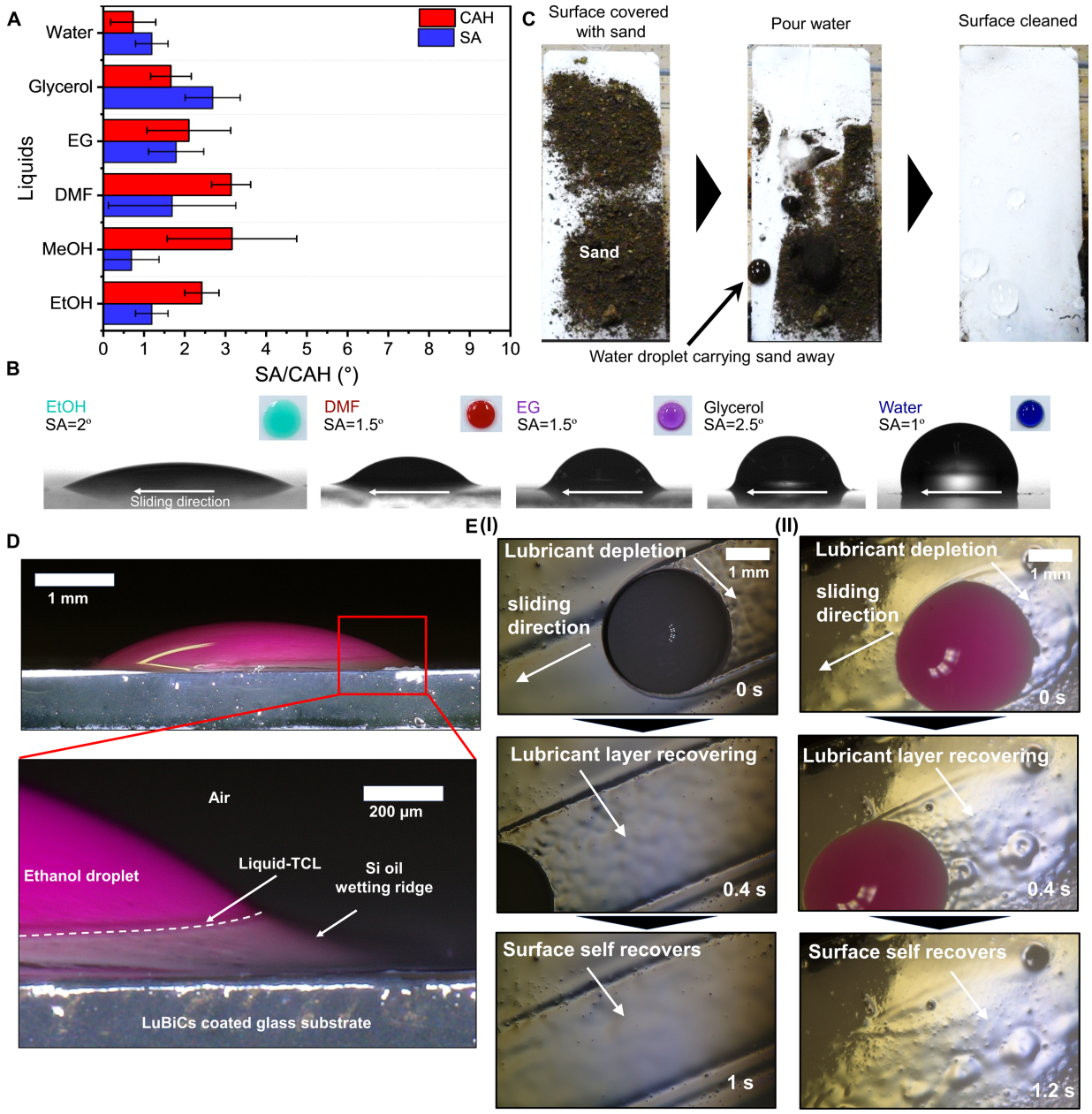

Figure 8.3: Omniphobicity of the LuBiCs surface.(A) Contact angle hysteresis (CAH) and sliding angle values (SA) of different liquids with varying surface tension, measured on a glass slide with LuBiCs coating. 2μl droplets were used for SA measurement. (. . . continuing to the next page)

Figure 8.3: (...continued from the previous page) (B) Side view optical images of 2 μl droplets of 5 different liquids placed on LuBiCs coated surfaces mounted on a tilting platform. The tilting stage is continually tilted at a rate of 0.5 deg s^{-1}, and the snaps capture the droplet shapes just at the onset of sliding. Inset shows top-view optical images of the respective droplets on the LuBiCs surface. Droplets were dyed for visualization. The abbreviations for liquid names in (A-B) are as follows: EtOH: Ethanol, MeOH: Methanol, DMF: *N, N*-Dimethylformamide, EG: Ethylene Glycol. (C) Self-cleaning of LuBiCs surface by oncoming water after being fouled by sand. (D) Side view optical image of an ethanol droplet on a LuBiCs surface showing the lubricant ridge and the liquid TCL, (E) Top view sliding sequence of (I) a water droplet with 2% sodium alginate and (II) an ethanol droplet (dyed with Nile red) on a LuBiCs surface kept at a fixed angle of inclination of 11.3°.

Oncoming droplets of different surface tension can attain different equilibrium thermodynamic states (cloaked vs non-cloaked) upon contact with the surface lubricant layer of LuBiCs. The lubricant cloaks a droplet of high surface tension test liquid [66–68] as the combined interfacial tension of the lubricant-air interface and lubricant-water interface is still lower than the water-air interface, making the cloaked state a thermodynamically favorable one. In contrast, complete cloaking by lubricant remains energetically unfavorable for low surface tension oncoming liquids (e.g., ethanol). Therefore, although a low surface tension droplet can pull the lubricant up from the surface due to capillary pressure, causing the formation of a curved lubricant meniscus around the base (Figure 8.3D), it does not extend all the way to the apex and instead forms an annular ridge around the rim of the droplet. In this configuration, the droplet, the pulled-up lubricant, and the surrounding air meet along a line termed the liquid three-phase contact line (liquid-TCL), which can be seen in the microscopy image of ethanol droplet on LuBiCs, presented in Figure 8.3D.

Figure 8.3E shows the time-resolved sliding sequence of water and ethanol droplets on LuBiCs which demonstrates the self-repairing ability of the surface. In the presence of sufficient lubricant on the surface, the surface can spontaneously recover from local damages/ lubricant depletion by means of surface energy driven capillary wicking [17, 69], as can be seen during the sliding of both water as well as ethanol droplets (Figure 8.3E).

Although some local depletion of the lubricant layer is observed underneath the sliding droplets, lubricant from the surrounding areas flows to the depleted region and the surface self-heals within a second. Further, we also confirmed that the LuBiCs coating is pressure (section F.2, Figure F.4, Appendix F) and UV stable (section F.3, Figure F.5, Appendix F).

8.3.3 Capillarity-driven self-lubrication through the base layer

Owing to the interconnected pores and the low interfacial tension between the dry base layer of LuBiCs and the infused silicone oil, the silicone oil lubricant can be carried within the base layer by capillary transport without any external assistance. **Figure 8.4** provides experimental evidence of capillarity-driven lubricant transport and discusses the consequent changes in wetting states and surface properties in LuBiCs. One end of a glass slide coated with the dry superhydrophobic base layer was immersed in a silicone oil bath to a depth of δ = 6 mm. Then the wetting properties and surface microstructure were monitored for 24 hours in the target region (marked by hashed lines in Figure 8.4A) which is d = 50 mm away from the oil level in the reservoir. Once the lubricant reaches a dry superhydrophobic region by capillary transport, the reflectivity of the surface reduces, which can be easily detected both in digital photographs (Figure 8.4B) as well as confocal microscopy images (Figure 8.4C) of the surface. The capillary wicking front was tracked from the digital photographs by analyzing the change in intensity of the reflected signal at the wicking front (Figure 8.4B). The tracked location of the wicking front, z_c is plotted against time, t in Figure 8.4D. Considering a force balance between capillarity, gravity, and viscous forces, we have derived a closed-form analytical equation (Eq. (8.1)) to model the capillary wicking process through the base layer of LuBiCs. Note that the inertia forces are negligible for our context due to narrow (sub)micron scale porosity and the high viscosity of the rising lubricant. Even at the very early stage of the rise (t = 1 ms), where we expect a fast-rising capillary wicking front (i.e., high velocity of capillary rise), we can estimate a Reynolds number, $Re = \frac{\rho v d_{pore}}{\eta} \approx 8.65 \times 10^{-5} << 1$. It indicates that the inertia forces can be neglected throughout the rise. See section F.4 of Appendix F for the derivation of the analytical formulation of Eq. (8.1) and a detailed discussion on the applicable capillary

transport model.

$$z_c = \frac{2\gamma\left(W\left(-\mathrm{e}^{-\frac{1}{16}\left(\frac{Bo}{Oh}\right)\frac{t}{\sqrt{\frac{\gamma}{Rg^2\rho}}}-1}\right)+1\right)}{Rg\rho} \tag{8.1}$$

where R, $Bo = \frac{\rho R^2 g}{\gamma}$, and $Oh = \frac{\eta}{(\rho R\gamma)^{1/2}}$ are the equivalent pore radius of the matrix, Bond number, and Ohnesorge number, respectively. $\gamma \approx 20$ mN m^{-1}, $\rho \approx 1069$ kgm^{-3}, and $\eta \approx 106.9$ mPa-s are the surface tension, density, and dynamic viscosity of the infused lubricant, respectively. g is the acceleration due to gravity. W is the Lambert W (Product Logarithm) function. As shown in Figure 8.4D, the experimental data can be fitted to Eq. (8.1) with a coefficient of determination $R^2 = 0.9961$. From the evaluated fit, we estimate the equivalent pore diameter of the porous network, $d_{pore} = 2R \approx 1.86$ μm which is consistent with the pore size distribution obtained from the SEM data (Figure 8.2C-D).

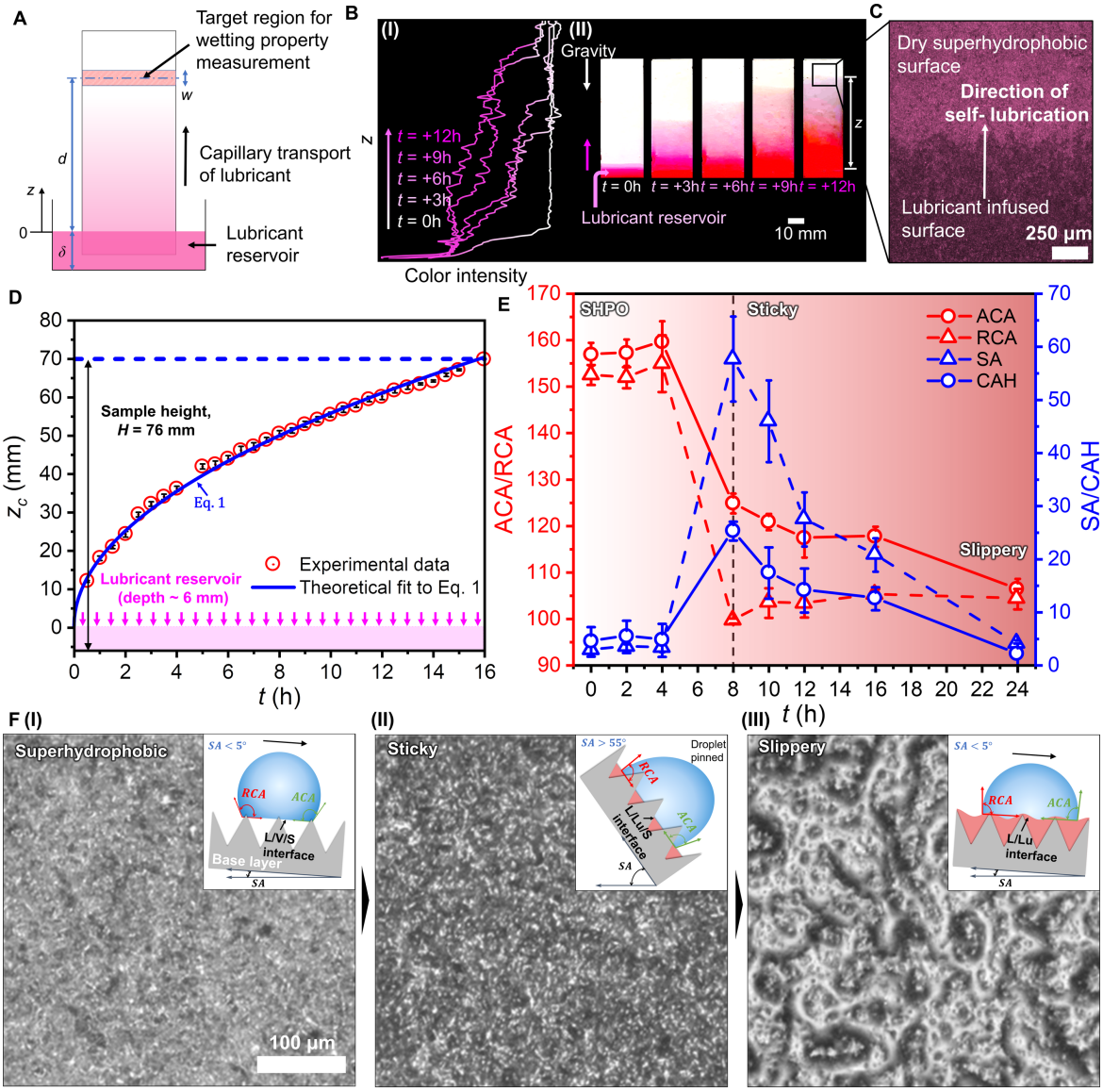

Figure 8.4: Capillarity-driven self-lubrication through the base layer. (A) Controlled experiment to observe capillarity-driven self-lubrication in a glass slide of dimension 76 mm x 26 mm coated with the 3D porous superhydrophobic base material. One end of the glass slide is immersed in a silicone oil reservoir till a depth of 6 mm and the capillary wicking front is tracked with time. The wetting properties are measured in the hatched 10 mm x 26 mm region located 50 mm above the lubricant level in the reservoir. (. . . continuing to the next page)

Figure 8.4: (...continued from the previous page) (B) shows the upward propagation of the capillary wicking front by highlighting the change in reflectivity of the surface from time-resolved digital photographs. (C) shows a zoomed-in optical micrograph around the capillary wicking front. (D) plots the lubricant infusion height (z_c) vs. time (t). The open red circles represent the experimentally observed location of the wicking front, while the blue line is the theoretical fit to the experimental data to Eq. (8.1), a gravity-inclusive analytical description of vertical capillary wicking. (E) denotes the evolution of wetting properties (ACA, RCA, CAH, and SA) in the hatched target region as the lubricant moves through the surface. (F) shows the change in surface microstructure as the surface evolves from superhydrophobic to sticky to slippery state during the self-lubrication process. The inset to (F) illustrates the corresponding wetting states by schematically showing the configuration of a water droplet on the surface.

Figure 8.4E elaborates on the dynamics of self-lubrication of LuBiCs in terms of the evolution of the wetting properties of our target region with time, while Figure 8.4F captures the corresponding microstructural changes of the surface in the form of confocal microscopy images of the surface texture. The insets to Figure 8.4F schematically illustrate the corresponding wetting states by showing the configuration of an oncoming water droplet on the surface. The target region is initially superhydrophobic; an air cushion underneath the droplet and a consequent solid (base layer)/vapor (air)/liquid (water) interface (S/V/L interface) is responsible (inset to Figure 8.4F (I)) for the water repellent property. In this state, the surface exhibits CAH $= 4.4 \pm 2.9°$ and SA $= 2.8 \pm 0.8°$. Subsequently, once the capillary wicking front reaches the target region, the vapor layer responsible for superhydrophobicity gets replaced by the infused silicone oil. However, in this state, the amount of surface lubricant is not sufficient to cover the roughness features on the surface, and hence it cannot prevent direct contact between the oncoming droplet and the solid base layer. It leads to the formation of a heterogeneous liquid (water)-lubricant (silicone oil)- solid (base layer) interface (L/Lu/S interface) underneath an oncoming droplet (inset to Figure 8.4F (II)). This state neither supports an air cushion nor a homogeneous lubricant film and instead, this interface leads to strong pinning of oncoming droplets into surface microstructure and consequent temporary degradation in the ability of the surface to remove

water droplets as evident from the increased CAH and SA values (CAH = $25.3 \pm 1.8°$ and SA = $57.7 \pm 8°$). This intermediate state is termed the 'sticky' state (t $\sim$ 8h). As more lubricant is carried to the surface with time by capillary action, a lubricant overlayer is formed on the surface microstructures, which prevents the oncoming droplet from coming in direct contact with the base layer and allows them to slide off the surface on this lubricious overlayer. The homogeneous liquid (water)-lubricant (silicone oil) interface (L/Lu interface) formed underneath the droplet (inset to Figure 8.4F (III)) is responsible for the slippery behavior of the surface. In the 'slippery' state (t$\sim$24 h), the surface shows a CAH = $2.1 \pm 2.1°$ and can remove water droplets with a SA = $4.0 \pm 0.7°$. It is apparent from this discussion that there exists a time lag between the capillary wicking front reaching a target location and that location turning slippery. At t $\sim$ 8h, the capillary wicking front reached our identified target zone (Figure 8.4D). However, as can be noted from Figure 8.4E, at t $\sim$ 8h, the target region is in sticky state, and only at t $\sim$ 24 h the region turns completely slippery. Also, during the self-lubrication process (Figure 8.4E), the ACA reduces consistently as the surface wetting state changes from superhydrophobic (ACA = $157 \pm 2.5°$) to sticky (ACA = $124.9 \pm 2.1°$) and finally to slippery state (ACA = $106.4 \pm 2.3°$). The RCA undergoes a steeper decline during the transition from superhydrophobic (RCA = $152.5 \pm 2.1°$)to sticky state (RCA = $99.6 \pm 0.5°$) and then increases slightly as the surface subsequently turns completely slippery (RCA = $104.3 \pm 2.2°$). The RCA records the lowest value when the surface is in sticky state, indicating the enhanced pinning effect offered by the surface in the partially lubricated state. We also recorded the evolution of RMS roughness (R_q) of the surface in the self-lubrication process from the confocal microscopy images. In the superhydrophobic state, the surface records $R_q = 5.70 \pm 0.43$ μm while it increases to $R_q = 8.49 \pm 0.74$ μm in the sticky state and then decreases again to $R_q = 6.98 \pm 0.41$ μm as the surface turns slippery by self-lubrication.

8.3.4 Shear tolerance of LuBiCs

The infused lubricant in slippery surfaces is naturally susceptible to shear damage which can restrict the functionality of slippery material for practical application. Even in outdoor conditions, the surfaces are continually exposed to environmental shear (e.g., from rain).

Therefore, an assessment of shear stability is necessary to evaluate the performance of a slippery material. To examine the shear stability of LuBiCs, we exposed the LuBiCs coated surfaces to varying shear rates, ω in the range of 0-6000 rpm. **Figures 8.5**A and **8.5**B summarize the wettability variation of LuBiCs with different applied shear for water and ethanol, respectively. The samples were mounted firmly on the rotary spindle of a spin-coater and were subsequently exposed to shear by spinning at the mentioned spin rate, ω. Note that the flow of another liquid over the lubricated surface also exposes the LIS to shear-driven lubricant decay. However, we have chosen spinning as the method to generate shear for the evaluation of the shear tolerance of LuBiCs as spinning exposes the LIS to an overall higher shear force [70, 71] per unit area. The inset to Figure 8.5A schematically shows the experimental procedure to impart shear to LuBiCs samples. In general, with an increased rate of shear, ACA underwent an increment while RCA decreased for both water and ethanol, resulting in an increase in CAH and SA with increasing shear. However, despite that, the LuBiCs coated surfaces consistently maintained a CAH $< 5^\circ$ and SA $<10^\circ$ for 2 μl water droplets even at a shear rate of 5000 rpm. Figure 8.5C captures the shear-driven lubricant decay and consequent evolution of surface roughness of LuBiCs. As expected, with an increase in shear rate, the volume of lubricant impregnated into the base layer of LuBiCs gradually decreases. The trapped lubricant volume is computed by comparing the weight of the sample before and after exposure to shear. In the low rpm range, the volume of lubricant per unit surface area undergoes a steep decline with an increase in shear rate followed by a slow decay at the later stage. This is expected as there remains some excess lubricant on the surface that gets shed off fast. Once the excess lubricant is lost, the lubricant is primarily stored in bulk, and the surface lubricant remains adherent to the surface textures by capillary force resulting in a reduced rate of lubricant decay with rpm. Figure 8.5C also shows the evolution of RMS roughness, R_q of LuBiCs with applied shear. R_q increases with an increase in RPM till 5000 rpm. However, R_q shows a decrease with increasing shear beyond 5000 rpm. This trend is similar to the observed trend of surface roughness evolution during the self-lubrication process of a LuBiCs-coated glass slide where the partially lubricated/sticky state recorded higher surface roughness than both superhydrophobic and slippery states, as reported in subsection 2.3. Therefore 5000 rpm can be marked as the onset of the transition of the surface from slippery state

to the sticky state, as can also be confirmed from the wettability variation presented in Figures 8.5A, 8.5B. Although the surface is still slippery and can remove the oncoming liquids even after being sheared at 6000 rpm, a noticeable increase in both CAH and SA could be observed between 5000 rpm and 6000 rpm. At 5000 rpm, the LuBiCs surface recorded an average CAH value of 3.7° and an average SA value of 6° for water, while at 6000 rpm, the average CAH and SA values were 14.5° and 32°, respectively. Thus, based on the wettability data and the trend of evolution of surface roughness, we can assume 5000 RPM to be the limit at which the pores of the superhydrophobic base layer are just saturated with the lubricant. With this assumption, we used the total amount of lubricant stored by the coated sample at 5000 rpm (as obtained from Figure 8.5C) to estimate the volumetric porosity, ϕ of the coating. In our case, $\phi \sim 61\%$. Figure 8.5D presents the evolution of surface microstructure with increasing shear in the form of confocal microscopy images. The illustrative line scan roughness profiles corresponding to the applied shear, as presented in the insets of Figure 8.5D, also clearly illustrate the increase in surface heterogeneity with increasing shear.

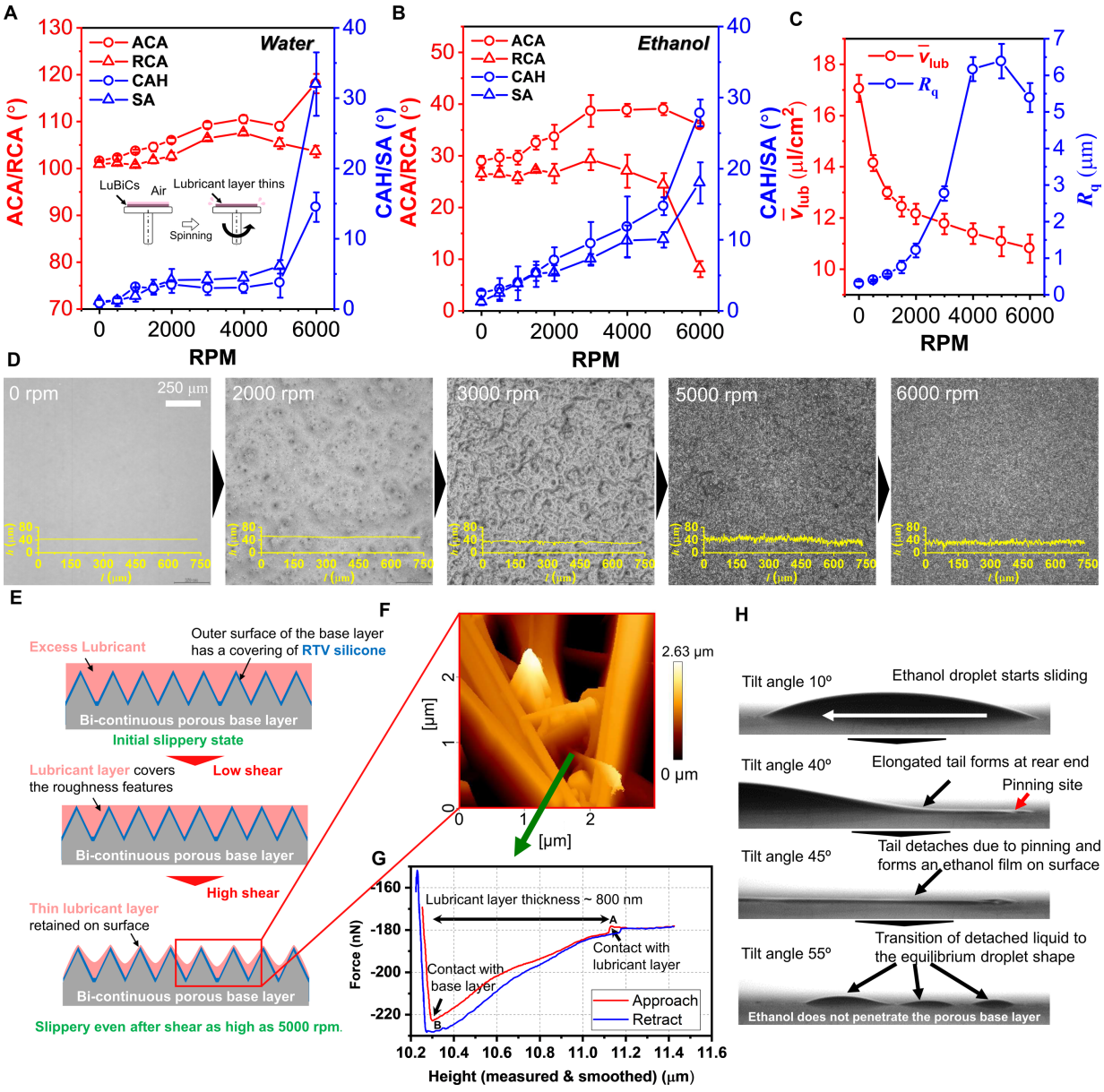

Figure 8.5: Shear tolerance of LuBiCs. (A) Variation of wetting properties (ACA, RCA, CAH, and SA) for water with applied shear rate. Inset schematically shows the experimental framework where the shear was applied to the LuBiCs samples by mounting them on the stage of a spin coater and spinning at the mentioned spin rate. (...continuing to the next page)

Figure 8.5: (...continued from the previous page) (B) variation of wetting parameters (ACA, RCA, CAH, and SA) for ethanol with applied shear rate, (C) variation of surface area averaged lubricant volume and RMS roughness with applied shear rate. (D) Surface microstructure observed under a confocal optical microscope after the surfaces are exposed to the mentioned shear. Insets show corresponding illustrative line-scan roughness profiles obtained from the optical micrographs. (E) Schematic representation of the shear-driven lubricant depletion process of the LuBiCs and the corresponding surface morphology. Although some surface roughness features are exposed due to shearing, the exposed surface features retain a thin lubricant covering, leading to the surface still being able to maintain both water as well as ethanol repellence. (F) AFM height image of a LuBiCs coated surface exposed to 5000 RPM shear for 1 min. (G) AFM force curve showing the presence of a thin (∼800 nm) lubricant layer for the point indicated by the green arrow. (H) Dynamics of sliding of a 2 μl ethanol droplet on a LuBiCs coated surface exposed to 5000 RPM shear for 1 min. The surfaces were sheared for 1 min in all the experiments reported in Figure 8.5.

Note that the roughness features present on the surface give rise to a capillary force that attempts to lock the lubricant film in place upon exposure to centrifugation. The ratio between the centrifugal forces and the capillary forces is a key parameter [72–76] that controls the lubricant depletion due to centrifugation. The theoretical limit of shear stability of the surface lubricant layer can be evaluated from a force balance between the applied shear force and the capillary forces. The balance yields a critical length scale, l_c for the surface roughness. The capillary forces cannot retain a lubricant overlayer upon exposure to shear-driven centrifugal forces if l_c is lower than the length scale of the roughness textures present on the surface [65]. l_c can be thought to be equivalent to the capillary length scale, obtained from a balance between surface tension and gravitational forces. In our case, $l_c = \frac{60}{2\pi\omega}\sqrt{\frac{\gamma}{\rho s_r}}$ where s_r is the radial separation of the area of measurement from the axis of rotation. For $\omega = 5000$ rpm, at the distal edge of the sample (corresponding $s_r = 38$ mmfor sample dimensions of 76 mm $\times$ 26 mm), the value of l_c turns out to be ~ 42 μm which is higher than the nominal length (~ 10 μm) of the ZnO microfillers responsible for the roughness of the base layer. It explains the sustained shear stable liquid-repellent

performance of our microstructured LuBiCs coating even after centrifugation at 5000 rpm.

From the experimentally obtained wettability variation (Figure 8.5A, 5B) and the surface microstructure images (Figure 8.5D), the evolution of the surface morphology of LuBiCs with applied shear is schematically presented in Figure 8.5E. Although the lubricant layer thins down and the microscale surface textures start getting exposed with increasing shear, the surface can retain a thin, integral lubricant covering on the exposed microstructures even at a shear rate as high as 5000 rpm owing to the combined effect of favorable surface microstructure and the chemical compatibility between the base layer and infused lubricant. The presence of this oil overlayer was confirmed using Atomic Force Microscopy (AFM) force imaging. Figure 8.5F presents the AFM height map of a 3 μm $\times$ 3 μm surface area of a LuBiCs coated surface exposed to 5000 rpm shear, while Figure 8.5G shows the recorded force curve for the point indicated by the green arrow in Figure 8.5F. 'A' denotes the point of contact of the AFM tip with the lubricant layer where a snap-in could be observed due to the formation of a lubricant meniscus that pulls the tip down. 'B' is the point where the AFM tip makes hard contact with the underlying base layer, beyond which the force curve changes direction. The separation between A and B, therefore, provides the lubricant thickness, which is $\sim$ 800 nm. Sustenance of this lubricant layer enables LuBiCs to repel water droplets with a CAH $< 5^\circ$ and SA $< 10^\circ$ even after exposure to 5000 rpm shear. Note that, from the observed lubricant thickness and the shear rate, we can estimate the shear stress imposed on the LuBiCs samples $\tau \sim O(10^6$ Pa), which is indicative of its impressive performance under high applied shear. Further, the time-resolved sliding dynamics of ethanol (Figure 8.5H) on the LuBiCs coated surface after exposure to 5000 rpm shear also validate the wetting state with a thin lubricant cover shown in Figure 8.5E. The sliding experiment of Figure 8.5H was conducted using the continuous tilt method, where the surface containing the drop was continually tilted even after the drop started sliding on it. A tilt angle of 10° marks the onset of sliding. However, as the tilt angle increases, the sliding ethanol droplet experiences an increased pinning effect from the exposed microscale protrusions (proposed to be still covered with a lubricant layer) of the surface owing to increased sliding speed. Consequently, the droplet elongates and forms a film on the surface at the rear end (see the snaps corresponding to tilt angles 40° and 45° in Figure 8.5H). However, once the trailing film detaches from the original droplet due to

depinning, it regroups and attains the shape of a smaller droplet with a similar contact angle as that of the original droplet instead of fouling into the microstructure. This is a clear indication that there exists a barrier (a thin lubricant film) on the surface that prevents direct contact between ethanol and the underlying porous base layer and ultimately promotes the transition of the detached film to an equilibrium slippery droplet shape.

8.3.5 Self-replenishing ability of the LuBiCs coating

Figure 8.6 demonstrates the self-replenishing ability of the LuBiCs. As noted previously, a truly maintenance-free, long-term durable, practical LIS will require the integration of a lubricant reservoir into the material architecture. We developed a system (Figure 8.6A) where one end of the lubricant-infused surfaces was immersed into a lubricant reservoir to a small depth (here $\sim$ 6 mm for a coated glass slide of dimensions 76 mm $\times$ 26 mm). If the surface loses the lubricant layer due to exposure to degrading stimuli (e.g., extreme shear, surface wiping, or direct water shower), the lubricant is transported from the reservoir to the LuBiCs surface without any external assistance. Eventually, the lubricant covering is re-established on the surface, allowing the surface to recover its slippery behavior. Figure 8.6B shows the evolution of surface morphology upon exposure to the degrading stimuli and the subsequent self-recovery. Three different degrading stimuli were explored in this work, namely, shear at 6000 rpm for 1 min, manually wiping the sample with Kim wipes, and exposure to water shower with a flow rate of 8 L min^{-1} for 2 hours. Different stimuli have different aggravating effects on the wetting properties of the surface, as can be seen in the CAH/SA data in the degraded state presented in Figure 8.6C. For example, surface wiping does not only remove the lubricant from the surface but also leads to the generation of abrasion-driven surface defects (see Figure 8.6B), which can act as local pining sites to restrict droplet mobility. Consequently, the surface exposed to wiping exhibits the highest CAH/SA values in the degraded state. Further, water shower demonstrates the most aggravating effect in removing lubricant as the impacting water jet can penetrate through the pores of the base layer and remove the lubricant from the bulk. In contrast, shear and wiping-driven lubricant loss is typically confined to the surface.

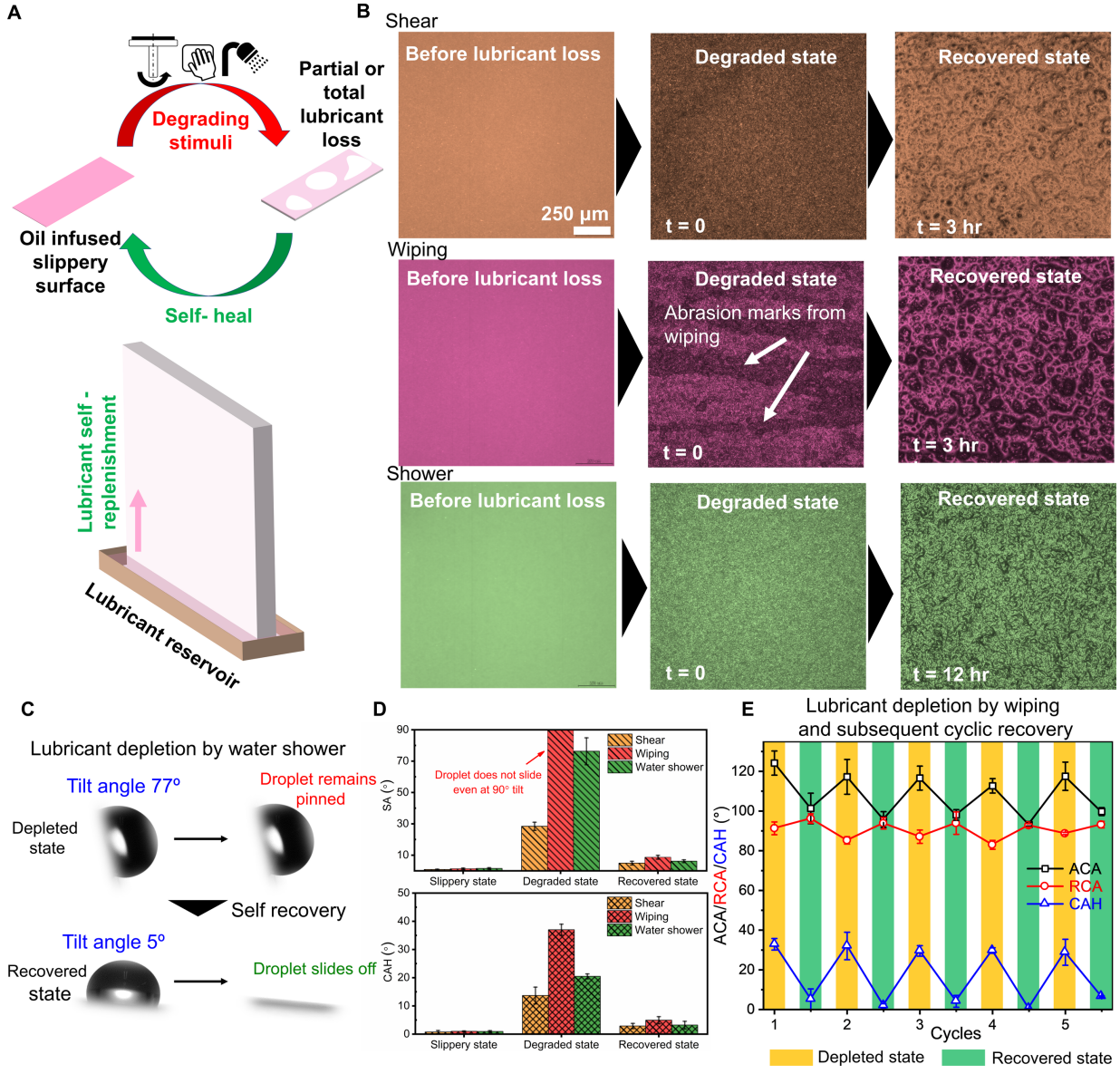

Figure 8.6: Self-replenishing ability of the LuBiCs coating. (A) Schematic representation of the system with an integrated reservoir that allows self-recovery upon exposure to degrading stimuli (shear, wiping, or water shower). (B) Evolution of surface microstructure of LuBiCs upon lubricant depletion and subsequent recovery. (...continuing to the next page)

Figure 8.6: (...continued from the previous page) (C) Direct visualization of the evolution of the wetting state during the lubricant depletion - recovery process. Upon lubricant depletion due to exposure to water shower, a 2μl droplet remains strongly pinned on the surface even at a tilt angle of 77°, while after self-recovery, a water droplet of the same volume slides on the same surface at a tilt angle of 5°. (D) Evolution of wetting properties (presented in terms of sliding angle and contact angle hysteresis) of the surface before application of the stimulus ('slippery state'), immediately after the application of the degrading stimulus ('degraded state') and after self-recovery ('recovered state'), (E) Cyclic self-healing ability of LuBiCs surface from wiping driven lubricant depletion.

Consequently, in our experiments, the surface exposed to water shower took the longest (∼12 h) time to recover, while the surfaces exposed to wiping or shear recovered within ∼3h. Also, contrary to the conventional LIS, the surface structure in the recovered state is not exactly smooth, as can be seen in the third panel of Figure 8.6B. There are some roughness features on the free surface, even in the recovered state. However, those are totally covered by a layer of lubricant, which, as evident from the measured $< 5°$ CAH and $<10°$ SA for 2 μl water droplets (Figure 8.6C) in the recovered state, is enough for the restoration of the slippery functionality. As an example, after exposure to water shower, a 2 μl water droplet remained strongly pinned on the surface and did not slide till a tilting angle of 77°. However, in the recovered state, a tilt angle of 5° was enough to slide the droplet off the surface (Figure 8.6D). Further, Figure 8.6E shows the cyclic self-healing ability of LuBiCs from repeated lubricant depletion. We have used wiping as the stimulus here. The sample was stamped and gently wiped using a Kim wipe until the lubricant was visibly removed from the surface. It leads to noticeable degradation of slippery performance, as evident from the average CAH $> 30°$ immediately after lubricant loss ('depleted state'). The sample was then left overnight with one end immersed in a small lubricant reservoir. Dynamic contact angle measurements were taken the next morning, where it was confirmed that the surface regained its water-repellent functionality with an average CAH $< 5°$ ('recovered state'). This process was repeated for five cycles on the same sample, and every time the surface self-healed from lubricant loss via capillarity-assisted lubricant replenishment.

8.3.6 Scalability of the LuBiCs

The overall scalability of the LuBiCs concept depends upon two facets - first, scalability in the fabrication of the coating, and second, the applicability of capillary transport in the large-scale fabricated sample. Owing to an all-wet fabrication process, the formation of LuBiCs coating is excellently scalable. Using the same drop-casting method, we successfully applied the bi-continuous porous ZnO-PDMS superhydrophobic base layer on 0.3 m x 0.3 m glass slabs (hereafter termed the large-scale sample). The coating was able to survive outdoor exposure involving torrential rain, snow as well as strong wind flow for over a year, indicating good adhesion between the base layer and the underlying glass slab. Moreover, we could apply LuBiCs coating on a variety of substrates including metals, polymers, wood, paper, and even cotton, and turn them slippery (see Figure F.9, Appendix F). Further, **Figure 8.7** shows capillarity-driven self-lubrication in large-scale LuBiCs applied to two different test cases. Figure 8.7 A-B shows self-lubrication in LuBiCs coating applied on a meter-scale glass slab, while Figure 8.7 C-E demonstrates self-lubrication in self-standing monolithic LuBiCs blocks.

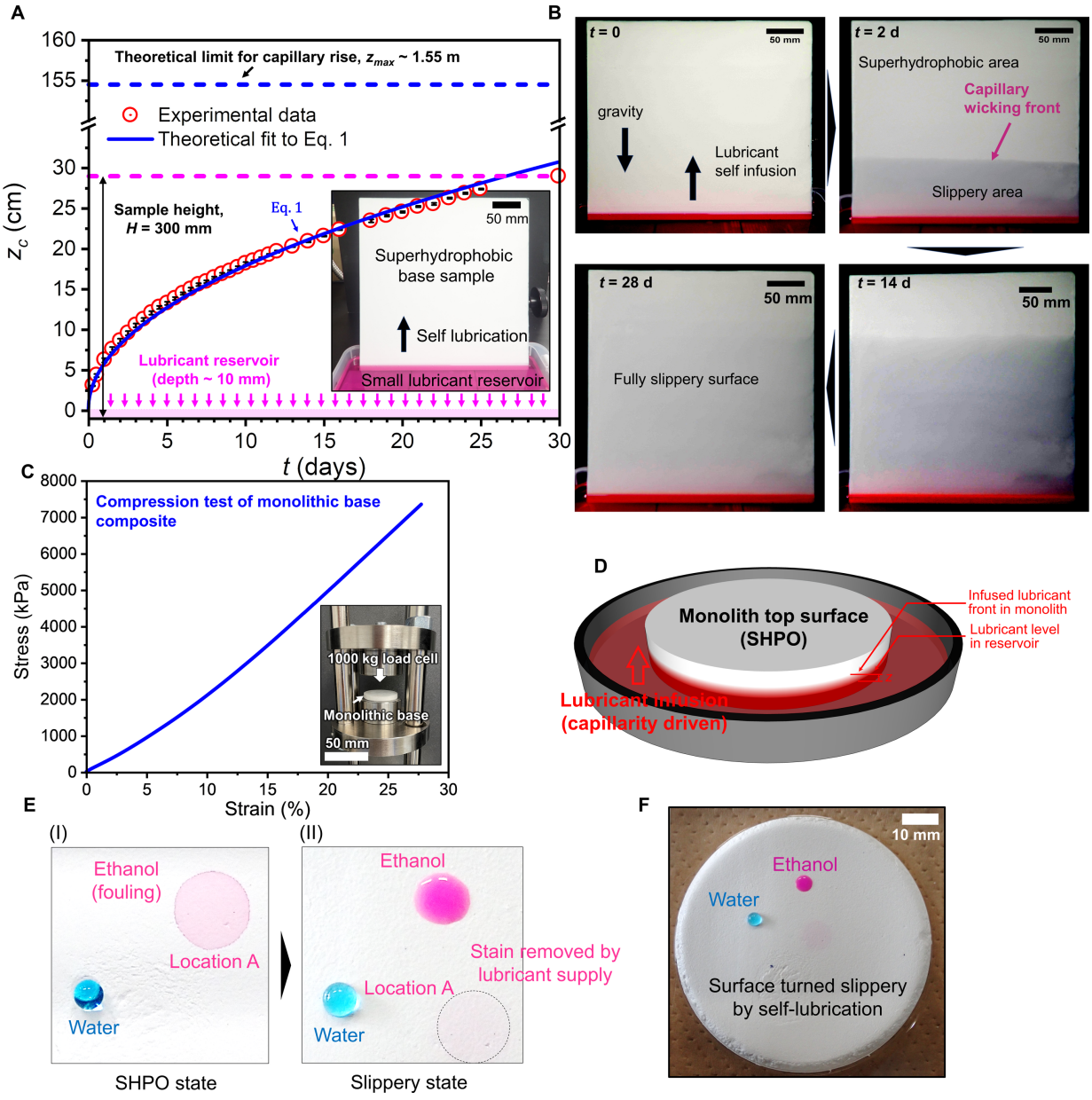

Figure 8.7: Scalability of the LuBiCs: Fabrication of large-scale porous base layer and capillarity-driven self-lubrication through the same. (A-B) show self-lubrication through LuBiCs coating applied on a large-scale (0.3 m x 0.3 m) glass slab. (...continuing to the next page)

Figure 8.7: (...continued from the previous page) (A) tracks the propagation of the capillary wicking front of silicone oil with time through the base layer for the experimental configuration shown in the inset. One end of the dry sample with the base coating was immersed in a small silicone oil reservoir till a depth of $\sim$ 10 mm. The sample was then kept in a near-vertical configuration, and digital images of the sample were captured at regular intervals to track the location of the wicking front. The experimental data can be fitted excellently to the analytical formulation of Eq. (8.1). (B) shows timelapse images of the sample, which clearly demonstrates the upward transport of silicone oil through the base layer. The capillary wicking front reached the top of the surface within a month. The photographs were post-processed uniformly for contrast and clarity. (C-F) show the formation, mechanical characterization and self-lubrication through self-standing monolithic blocks of LuBiCs. (C) shows compression test results of the dry monolithic base composite. (D) Schematically shows the experimental configuration for capillarity driven self-lubrication through the dry, initially superhydrophobic monolith. (E) shows the wetting transition of the monolith from superhydrophobic to slippery state. Water (dyed with methylene blue) and ethanol (dyed with Nile red) droplets are used as probe droplets to differentiate between the two wetting states, (F) presents the digital photograph of the lubricated monolithic block.

For the first demonstrated case (Figure 8.7 A-B), one end of the dry large-scale sample with the porous base coating was immersed into a silicone oil reservoir to a depth of $\sim$ 10 mm. Figure 8.7A tracks the upward propagation of the capillary wicking front with time, while the time-resolved digital photographs of the sample presented in Figure 8.7B show the location of the capillary front at different time instances. As shown in Figure 8.7A, the experimentally obtained z_c vs. t profile can be fitted excellently to the gravity-inclusive theoretical formulation of capillary transport described by Eq.(8.1) with an $R^2 = 0.99209$. We confirmed that the entire sample surface (surface area 900 cm^2) turned slippery within 30 d. It confirms the continuity of pores in the sample and the occurrence of capillary transport at a large scale. For an estimated volumetric porosity of 61% ($\phi = 0.61$)and an average pore diameter for the large-scale sample, d_{pore} (calculated from the fit to Eq.(8.1) in Figure 8.7A) of 0.79 μm, we can also theoretically estimate [77] the maximum height

z_{max} for capillary imbibition through the porous base layer as $z_{\max} = \frac{(1-\phi)(\gamma_S - \gamma_{SL})}{\phi \rho d_{pore} g} = \frac{(1-\phi)\gamma_L \cos(\theta)}{\phi \rho d_{pore} g} \approx \frac{(1-\phi)\gamma_L}{\phi \rho d_{pore} g} \approx 1.55$ m (see also section F.4 of Appendix F). Here, γ_S and $\gamma_L$are the surface energies of the dry base layer and the infused lubricant.γ_{SL} is the interfacial energy between the dry base layer and the lubricant. Due to the PDMS covering on ZnO microfillers, γ_S can be approximated by the surface energy of PDMS and γ_{SL} can be assumed zero due to chemically identical nature of the silicone oil and PDMS. Note that there exists a competition between ϕ and the speed of capillary wicking through LuBiCs. With increasing mixing ratio, r between ZnO and PDMS, ϕ increases with an associated decrease in d_{pore}, as was shown in a previous study [46] on the superhydrophobic properties of the base composite. Therefore, although the increased porosity at higher r corresponds to higher volumetric storage of lubricant in the bulk of LuBiCs, the speed of capillary transport through the base matrix slows down due to narrower pore size. Careful optimization of the mixing ratio, therefore, is an interesting direction of future study toward further enhancement of the durability and self-recovery process of LuBiCs.

For the second test case (Figure 8.7C-E), we created self-standing cylindrical monolith blocks of the 3D porous base material simply by curing the coating solution at room temperature in a beaker for a week. The PDMS backbone in the elastomeric base matrix provides compressibility to LuBiCs as we confirmed in Figure 8.7C by conducting compression test on the dry self-standing monolithic base composite. The base composite reports $\sim 30\%$ compressive strain under the peak load of 10000 N (equivalent compressive stress ~ 7.5 MPa) without fracture/compressive failure. Further, the superhydrophobic monolith sample turns slippery just by immersing one end in a lubricant reservoir, as shown schematically in Figure 8.7D. This transition in the wetting state is captured in Figure 8.7D. Initially, water (dyed blue) beads up on the superhydrophobic surface while ethanol (dyed red) penetrates through the pores and stains the surface (Figure 8.7D(I)). One end of the monolithic block was then left immersed in a shallow silicone oil pool of depth ~ 2 mm, and 4 h later we confirmed that the block turned slippery. This is apparent from the wetting state of ethanol and water (Figure 8.7D(II)) as well as from the visual appearance of the block (Figure 8.7E). Subsequently, we also confirmed successful lubricant infusion into the bulk of the monolith by slicing it and touching the internal surface. Notably, in this experiment, we also observed the stain-removal capability of LuBiCs. The red dye

stain formed due to the impregnation of dyed ethanol into the pores of the initially superhydrophobic base layer was visibly removed by capillarity-assisted lubricant supply from the bottom as the surface turned slippery (Figure 8.7D).

8.3.7 Long-term outdoor durability of large-scale LuBiCs coating

Figure 8.8 evaluates the long-term outdoor durability of the LuBiCs coating where a large-scale LuBiCs coated sample of dimension 0.3 m x 0.3 m was kept outdoors on the top of our building in the humid subtropical climate of Tsukuba, Japan. One end of the surface was inserted in a sealed lubricant reservoir to a depth of $\sim$ 10 mm (Figure 8.8A (I)). The coated sample was kept at an angle of $\sim 45^{\circ}$ with the horizontal, which is lower than the sliding angle of water recorded on LuBiCs exposed to water shower (Figure 8.7C, 7D) so that the pinning of water droplets can be observed in the degraded state. Two different tests were conducted thereafter on the same sample. First, the sample was exposed to an artificial water shower at 6 L min^{-1} for 6 h. Immediately after the shower was turned off, multiple droplets were seen to be stuck/pinned to the surface of the sample, confirming the expected loss of slippery functionality upon exposure to water shower. Further, a dry, relatively bright patch (see Figure 8.8A(II)) was observed around the center of the surface where the water jet from the shower directly hit. Around the area of direct impact, the water jet was able to completely remove the lubricant even from the bulk of the base layer, effectively turning the region locally superhydrophobic. This region is super-repellent to water - impinging water jets were also seen to bounce off from this region, while water droplets impacting the surrounding region either slid off or got stuck on the surface. Figure 8.8A (III) represents the reflected greyscale intensity sampled along the red line AB shown in the second snippet (corresponding to $t = 2$ d) of Figure 8.8A (II). The difference in the greyscale intensity clearly demarcates the side-by-side existence of two zones with different wettability, namely, the dry (brighter) region which is superhydrophobic in nature, and the lubricant wetted region (relatively darker) which is in 'sticky' state. Once the shower was turned off, the surface was left on the roof to allow capillarity-driven self-recovery. Water contact tests were conducted at regular intervals where water (dyed blue with methylene blue) was generously dispensed on the surface in the form of impinging water jets, and the

sliding behavior of the oncoming droplets was captured. Initially, multiple water droplets were seen to remain pinned on the surface on regions that turned 'sticky' due to exposure to water shower. However, as time passed, fewer droplets remained adhered on the surface after the completion of the water contact test. The superhydrophobic region also shrank over time and turned slippery by self-replenishment, as shown in the time series of Figure 8.8A (II). As can be confirmed from Figure 8.8A (II), the surface regains its functionality within 12 days.

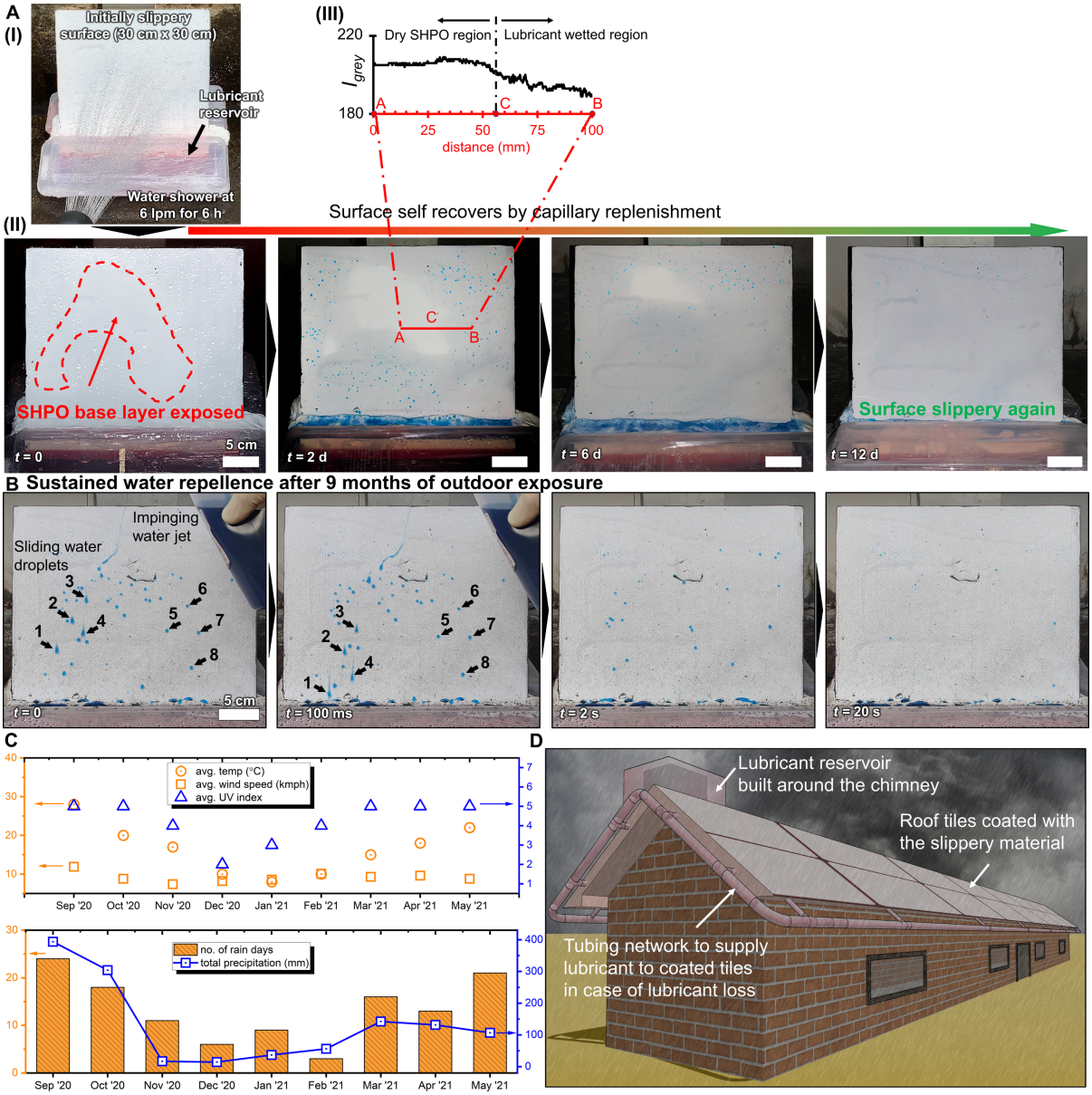

Figure 8.8: Long-term outdoor durability of large-scale LuBiCs coating. (A) Exposure to artificial rain shower - a 0.3 m x 0.3 m glass slab was coated with the LuBiCs coating, and then one end of it was immersed in a lubricant reservoir till a depth of 10 mm. The surface was then placed on a rooftop and exposed to an artificial shower at a flow rate of 6 L min^{-1} for 6 h. (B) Water spray test on the surface after over 9 months of outdoor exposure. (. . . continuing to the next page)

Figure 8.8: (...continued from the previous page) (C) Summarized monthly averaged climate data of Tsukuba, Japan (the location of the outdoor field test) over the duration of the test, (D) Schematic of a proposed engineering framework to integrate LuBiCs in large-scale application on roof tiles. The coating can be applied on the tiles while a lubricant reservoir can be integrated around the chimney with a tubing network running along the eavestrough connecting the tiles to the reservoir.

Once the sample completely recovered from the artificial water shower, it was left unattended on the roof for over 9 months when it got exposed to harsh outdoor conditions, including elevated temperature, UV irradiation, and, most importantly, heavy rainfall. The monthly averaged weather data of Tsukuba over the test duration is summarized in Figure 8.8C. In brief, the surface encountered more than 47 inches of total rainfall and a total of 121 rain days. Also, the temperature varied between a maximum of 31°C in September and a minimum of 2°C in January. Despite exposure to repeated rain showers and varying temperature conditions, the LuBiCs-coated surface could maintain its slippery functionality as we confirmed by performing water contact test on the surface after more than 9 months of outdoor exposure. Note that LuBiCs can retain their slippery functionality over a broad operating temperature range. LuBiCs-coated samples maintained their water repellence (see Figure F.10 of Appendix F) at elevated ($\sim$ Leidenfrost point) as well as near freezing temperatures. As demonstrated in the form of a time series in Figure 8.8B, the oncoming water droplets slid on the surface, and almost all the droplets were removed within 20 s. It was apparent from the sliding dynamics that the sample repels water, not because of the superhydrophobic base layer but owing to the sustained slippery nature of its surface. Further, during its outdoor exposure, the surface has undergone multiple lubricant depletion events due to rain showers. Despite that, it recovered and maintained its functionality even after 9 months, indicating its sustained self-healing performance after repeated lubricant loss. We also present a minimalistic, practical design in the concept sketch of Figure 8.8D that will allow the integration of the LuBiCs in roof coating. The lubricant reservoir can be built around the chimney, and a piping network can be installed which will connect the reservoir to the LuBiCs-coated tiles placed on the roof. Once the pipes are primed with the lubricant during installation, no further maintenance should be

necessary, and the coated tiles will be able to maintain their water-repellent functionality in the long-term owing to capillarity-driven spontaneous self-recovery. Previously we have estimated that ~ 11.08 μl lubricant is required per cm^2 surface area to saturate the pores of the base layer. We can reasonably approximate the year-round lubricant depletion effect of rainfall by an average of 90 days of extreme rainfall per year when the entire lubricant content from the roof tiles will get washed away. With the integrated oil-water separation filter bearing the previously reported separation efficiency [51] of > 99 %, we can estimate that a 30 US gallon-sized lubricant tank can serve a house with a roof area of 1000 ft^2 for 12 years without any refill/maintenance.

8.4 Conclusion

To summarize, we have succeeded in designing lubricant depletion tolerant, long-term stable, large-scale slippery surfaces by infusing a silicone oil into a bicontinuous porous composite of ZnO and PDMS. Capillary transport through the interconnected pores of the base layer allowed the surface to recover the surface lubricant layer even after exposure to severe depleting stimuli. As a proof of concept, we prepared large-scale "LuBiCs roof" which retained water-repellent behavior even after continuous outdoor exposure for over 9 months. Owing to the white color of the ZnO microfillers, the porous elastomeric base layer of LuBiCs is white in appearance and therefore is highly reflective, making them well-suited as coating materials for energy-efficient cool-roofing [78]. In addition to roof coating, LuBiCs are suitable for implementation in other applications that require durable omniphobic performance without strictly demanding optical transparency. Examples include coatings on bathroom/shower walls, anti-biofouling coatings on ships and submarines, etc. With the aforementioned functional advantages, we envision this work will pave the way toward the market entry of sustainable LIS for outdoor applications. We also believe that future studies specifically targeted at investigating the temporal dynamics of the self-recovery process of LuBiCs will push the boundaries for the development of more efficient LIS.

8.5 Experimental Section

Materials

The materials used to prepare the acicular superhydrophobic coating are the following - one part polydimethylsiloxane (PDMS) - room temperature vulcanizing (RTV) silicone (HC2100, DOWSIL, Toray Industries), tetrapod-shaped ZnO microparticles with ca. 10 μm length of the leg (Pana-Tetra WZ-0501, Panasonic) and Ethyl acetate solvent (EtOAc, 99.5%, Wako Pure Chemical Industries). Additionally, silicone oil (ASO-100, viscosity 100 cSt, AS ONE) is used as the lubricating liquid for preparing the slippery surfaces.

LuBiCs formation

First, 5 g of RTV silicone was dissolved in 300 ml EtOAc solvent by stirring at 1000 rpm for 5 min at room temperature. Then 45 g of ZnO powder was weighed and added to the solution. The resulting suspension was then thoroughly stirred again at 1000 rpm for 10 min. Finally, 1-2 ml of this suspension was carefully poured drop-by-drop onto a freshly cleaned and oxygen plasma-treated glass slide (dimensions: 76 mm * 26 mm). Once the solvent evaporates, the coated substrates are kept in a humidity-controlled desiccator for 72 h to allow complete curing of RTV silicone.

Then, the coated glass slides were immersed entirely in a Si oil bath overnight to let the Si oil soak into the 3D porous structure of the coating. Afterward, it is taken out from the oil bath and held vertically for 10 min to allow gravity-driven removal of excess oil before conducting experiments.

Large-scale samples (dimensions: 0.3 m * 0.3 m) were prepared using the same protocol after proportionately scaling up the volume of the used suspension to 45 ml to account for the increased surface area of the coated sample while maintaining the same 9:1 weight ratio between the ZnO and PDMS. It ensures morphological consistency across samples of different scales.

For the capillarity-driven self-replenishment test, only one end of the dry superhydrophobic coating was dipped in the lubricant reservoir till a specified depth ($\sim$ 6 mm for

the glass slides and $\sim$ 10 mm for the large-scale samples).

Characterization

All lab experiments were conducted at room temperature. Outdoor durability tests are performed in outdoor conditions outlined in Figure 8.8C. Contact angle measurements were performed using a contact angle meter (Drop master-DMs-401, Kyowa Interface Science Co., Ltd., Japan). A droplet volume of 2 μl is used for measuring sliding angles. SEM micrographs were obtained using either a Benchtop SEM (Miniscope TM 3000, Hitachi) or a field emission SEM (S-4800, Hitachi). EDS data was captured using the EDS module built into the Miniscope TM 3000 Benchtop SEM. Raman images were captured using a confocal Raman imaging microscope (alpha300AR, WiTec). The Raman images were acquired using a 40 mW, 532 nm excitation laser, and the True Surface^{TM} module was used to account for the roughness features of the surface. An inbuilt correlation coefficient-based Hit-Quality Index (HQI) algorithm was used for component identification from the ST Japan 5.1 spectra database. AFM measurements were performed using Bruker's NanoWizard 4 BioAFM with OLTESPA probe (force constant 2 Nm^{-1}) using the Quantitative imaging mode. Digital photographs of experiments were taken using Olympus Tough TG-5 digital camera. Wherever applicable, digital images are processed uniformly for clarity and contrast. Sliding videos of ethanol and water on the slippery surface were recorded using a tilting microscope (DSX1000 TILT MODEL, Olympus, Japan). Droplet impact dynamics were captured with a high-speed camera (FASTCAM Mini AX100, Photron Ltd.) at 4000 fps. Confocal images of the surface microstructure were captured using a hybrid laser microscope (OPTELICS HYBRID, Lasertec Co., Japan). ImageJ software [79] was used for processing experimental images.

References

[1] E. Vazirinasab, R. Jafari, and G. Momen, "Application of superhydrophobic coatings as a corrosion barrier: A review," *Surface and Coatings Technology*, vol. 341, pp. 40–56, 2018.

[2] R. Fürstner, W. Barthlott, C. Neinhuis, and P. Walzel, "Wetting and Self-Cleaning Properties of Artificial Superhydrophobic Surfaces," *Langmuir*, vol. 21, no. 3, pp. 956–961, 2005.

[3] Z. Sun, T. Liao, K. Liu, L. Jiang, J. H. Kim, and S. X. Dou, "Fly-Eye Inspired Superhydrophobic Anti-Fogging Inorganic Nanostructures," *Small*, vol. 10, no. 15, pp. 3001–3006, 2014.

[4] L. Cao, A. K. Jones, V. K. Sikka, J. Wu, and D. Gao, "Anti-Icing Superhydrophobic Coatings," *Langmuir*, vol. 25, no. 21, pp. 12444–12448, 2009.

[5] X. Zhou, Z. Zhang, X. Xu, F. Guo, X. Zhu, X. Men, and B. Ge, "Robust and Durable Superhydrophobic Cotton Fabrics for Oil/Water Separation," *ACS Applied Materials & Interfaces*, vol. 5, no. 15, pp. 7208–7214, 2013.

[6] W. Barthlott and C. Neinhuis, "Purity of the sacred lotus, or escape from contamination in biological surfaces," *Planta*, vol. 202, no. 1, pp. 1–8, 1997.

[7] M. Ma and R. M. Hill, "Superhydrophobic surfaces," *Current Opinion in Colloid &amp Interface Science*, vol. 11, no. 4, pp. 193–202, 2006.

[8] A. B. D. Cassie and S. Baxter, "Wettability of porous surfaces," *Transactions of the Faraday Society*, vol. 40, p. 546, 1944.

[9] X.-M. Li, D. Reinhoudt, and M. Crego-Calama, "What do we need for a superhydrophobic surface? A review on the recent progress in the preparation of superhydrophobic surfaces," *Chemical Society Reviews*, vol. 36, no. 8, p. 1350, 2007.

[10] D. Bartolo, F. Bouamrirene, Verneuil, A. Buguin, P. Silberzan, and S. Moulinet, "Bouncing or sticky droplets: Impalement transitions on superhydrophobic micropatterned surfaces," *Europhysics Letters (EPL)*, vol. 74, no. 2, pp. 299–305, 2006.

[11] A. Milionis, E. Loth, and I. S. Bayer, "Recent advances in the mechanical durability of superhydrophobic materials," *Advances in Colloid and Interface Science*, vol. 229, pp. 57–79, 2016.

[12] A. Tuteja, W. Choi, M. Ma, J. M. Mabry, S. A. Mazzella, G. C. Rutledge, G. H. McKinley, and R. E. Cohen, "Designing Superoleophobic Surfaces," *Science*, vol. 318, no. 5856, pp. 1618–1622, 2007.

[13] A. Tuteja, W. Choi, J. M. Mabry, G. H. McKinley, and R. E. Cohen, "Robust omniphobic surfaces," *Proceedings of the National Academy of Sciences*, vol. 105, no. 47, pp. 18200–18205, 2008.

[14] T. iu and C.-J. im, "Turning a surface superrepellent even to completely wetting liquids," *Science*, vol. 346, no. 6213, pp. 1096–1100, 2014.

[15] V. Kondrashov and J. Rühe, "Microcones and Nanograss: Toward Mechanically Robust Superhydrophobic Surfaces," *Langmuir*, vol. 30, no. 15, pp. 4342–4350, 2014.

[16] D. Wang, Q. Sun, M. J. Hokkanen, C. Zhang, F.-Y. Lin, Q. Liu, S.-P. Zhu, T. Zhou, Q. Chang, B. He, Q. Zhou, L. Chen, Z. Wang, R. H. A. Ras, and X. Deng, "Design of robust superhydrophobic surfaces," *Nature*, vol. 582, no. 7810, pp. 55–59, 2020.

[17] T.-S. Wong, S. H. Kang, S. K. Y. Tang, E. J. Smythe, B. D. Hatton, A. Grinthal, and J. Aizenberg, "Bioinspired self-repairing slippery surfaces with pressure-stable omniphobicity," *Nature*, vol. 477, no. 7365, pp. 443–447, 2011.

[18] A. Lafuma and D. Quéré, "Slippery pre-suffused surfaces," *EPL (Europhysics Letters)*, vol. 96, no. 5, p. 56001, 2011.

[19] A. K. Epstein, T.-S. Wong, R. A. Belisle, E. M. Boggs, and J. Aizenberg, "Liquid-infused structured surfaces with exceptional anti-biofouling performance," *Proceedings of the National Academy of Sciences*, vol. 109, no. 33, pp. 13182–13187, 2012.

[20] N. MacCallum, C. Howell, P. Kim, D. Sun, R. Friedlander, J. Ranisau, O. Ahanotu, J. J. Lin, A. Vena, B. Hatton, T.-S. Wong, and J. Aizenberg, "Liquid-Infused Silicone As a Biofouling-Free Medical Material," *ACS Biomaterials Science & Engineering*, vol. 1, no. 1, pp. 43–51, 2015.

[21] I. Sotiri, A. Tajik, Y. Lai, C. T. Zhang, Y. Kovalenko, C. R. Nemr, H. Ledoux, J. Alvarenga, E. Johnson, H. S. Patanwala, J. V. I. Timonen, Y. Hu, J. Aizenberg, and

C. Howell, "Tunability of liquid-infused silicone materials for biointerfaces," *Biointerphases*, vol. 13, no. 6, p. 06D401, 2018.

[22] J. Cui, D. Daniel, A. Grinthal, K. Lin, and J. Aizenberg, "Dynamic polymer systems with self-regulated secretion for the control of surface properties and material healing," *Nature Materials*, vol. 14, no. 8, pp. 790–795, 2015.

[23] H. Liu, P. Zhang, M. Liu, S. Wang, and L. Jiang, "Organogel-based Thin Films for Self-Cleaning on Various Surfaces," *Advanced Materials*, vol. 25, no. 32, pp. 4477–4481, 2013.

[24] S. Anand, A. T. Paxson, R. Dhiman, J. D. Smith, and K. K. Varanasi, "Enhanced Condensation on Lubricant-Impregnated Nanotextured Surfaces," *ACS Nano*, vol. 6, no. 11, pp. 10122–10129, 2012.

[25] S. Sett, P. Sokalski, K. Boyina, L. Li, K. F. Rabbi, H. Auby, T. Foulkes, A. Mahvi, G. Barac, L. W. Bolton, and N. Miljkovic, "Stable Dropwise Condensation of Ethanol and Hexane on Rationally Designed Ultrascalable Nanostructured Lubricant-Infused Surfaces," *Nano Letters*, vol. 19, no. 8, pp. 5287–5296, 2019.

[26] B. R. Solomon, K. S. Khalil, and K. K. Varanasi, "Drag Reduction using Lubricant-Impregnated Surfaces in Viscous Laminar Flow," *Langmuir*, vol. 30, no. 36, pp. 10970–10976, 2014.

[27] M. K. Fu, I. Arenas, S. Leonardi, and M. Hultmark, "Liquid-infused surfaces as a passive method of turbulent drag reduction," *Journal of Fluid Mechanics*, vol. 824, pp. 688–700, 2017.

[28] P. Kim, T.-S. Wong, J. Alvarenga, M. J. Kreder, W. E. Adorno-Martinez, and J. Aizenberg, "Liquid-Infused Nanostructured Surfaces with Extreme Anti-Ice and Anti-Frost Performance," *ACS Nano*, vol. 6, no. 8, pp. 6569–6577, 2012.

[29] P. W. Wilson, W. Lu, H. Xu, P. Kim, M. J. Kreder, J. Alvarenga, and J. Aizenberg, "Inhibition of ice nucleation by slippery liquid-infused porous surfaces (SLIPS)," *Phys. Chem. Chem. Phys.*, vol. 15, no. 2, pp. 581–585, 2013.

[30] S. Amini, S. Kolle, L. Petrone, O. Ahanotu, S. Sunny, C. N. Sutanto, S. Hoon, L. Cohen, J. C. Weaver, J. Aizenberg, N. Vogel, and A. Miserez, "Preventing mussel adhesion using lubricant-infused materials," *Science*, vol. 357, no. 6352, pp. 668–673, 2017.

[31] C. S. Ware, T. Smith-Palmer, S. Peppou-Chapman, L. R. J. Scarratt, E. M. Humphries, D. Balzer, and C. Neto, "Marine Antifouling Behavior of Lubricant-Infused Nanowrinkled Polymeric Surfaces," *ACS Applied Materials & Interfaces*, vol. 10, no. 4, pp. 4173–4182, 2018.

[32] C. Howell, A. Grinthal, S. Sunny, M. Aizenberg, and J. Aizenberg, "Designing liquid-infused surfaces for medical applications: A review," *Advanced Materials*, vol. 30, no. 50, p. 1802724, 2018.

[33] Z. Wang, Y. Liu, P. Guo, L. Heng, and L. Jiang, "Photoelectric Synergetic Responsive Slippery Surfaces Based on Tailored Anisotropic Films Generated by Interfacial Directional Freezing," *Advanced Functional Materials*, vol. 28, no. 49, p. 1801310, 2018.

[34] K. Han, L. Heng, Y. Zhang, Y. Liu, and L. Jiang, "Slippery Surface Based on Photoelectric Responsive Nanoporous Composites with Optimal Wettability Region for Droplets' Multifunctional Manipulation," *Advanced Science*, vol. 6, no. 1, p. 1801231, 2019.

[35] K. Han, Z. Wang, L. Heng, and L. Jiang, "Photothermal slippery surfaces towards spatial droplet manipulation," *Journal of Materials Chemistry A*, vol. 9, no. 31, pp. 16974–16981, 2021.

[36] S. Cheng, P. Guo, X. Wang, P. Che, X. Han, R. Jin, L. Heng, and L. Jiang, "Photothermal slippery surface showing rapid self-repairing and exceptional anti-icing/deicing property," *Chemical Engineering Journal*, vol. 431, p. 133411, 2022.

[37] P. Guo, Z. Wang, X. Han, and L. Heng, "Nepenthes pitcher inspired isotropic/anisotropic polymer solid–liquid composite interface: preparation, function, and application," *Materials Chemistry Frontiers*, vol. 5, no. 4, pp. 1716–1742, 2021.

[38] M. J. Hoque, S. Sett, X. Yan, D. Liu, K. F. Rabbi, H. Qiu, M. Qureshi, G. Barac, L. Bolton, and N. Miljkovic, "Life Span of Slippery Lubricant Infused Surfaces," *ACS Applied Materials & Interfaces*, vol. 14, no. 3, pp. 4598–4611, 2022.

[39] M. J. Kreder, D. Daniel, A. Tetreault, Z. Cao, B. Lemaire, J. V. Timonen, and J. Aizenberg, "Film Dynamics and Lubricant Depletion by Droplets Moving on Lubricated Surfaces," *Physical Review X*, vol. 8, no. 3, p. 031053, 2018.

[40] S. Nishioka, M. Tenjimbayashi, K. Manabe, T. Matsubayashi, K. Suwabe, K. Tsukada, and S. Shiratori, "Facile design of plant-oil-infused fine surface asperity for transparent blood-repelling endoscope lens," *RSC Advances*, vol. 6, no. 53, pp. 47579–47587, 2016.

[41] C. Howell, T. L. Vu, J. J. Lin, S. Kolle, N. Juthani, E. Watson, J. C. Weaver, J. Alvarenga, and J. Aizenberg, "Self-Replenishing Vascularized Fouling-Release Surfaces," *ACS Applied Materials & Interfaces*, vol. 6, no. 15, pp. 13299–13307, 2014.

[42] M. Tenjimbayashi, R. Togasawa, K. Manabe, T. Matsubayashi, T. Moriya, M. Komine, and S. Shiratori, "Liquid-Infused Smooth Coating with Transparency, Super-Durability, and Extraordinary Hydrophobicity," *Advanced Functional Materials*, vol. 26, no. 37, pp. 6693–6702, 2016.

[43] C. Urata, G. J. Dunderdale, M. W. England, and A. Hozumi, "Self-lubricating organogels (SLUGs) with exceptional syneresis-induced anti-sticking properties against viscous emulsions and ices," *Journal of Materials Chemistry A*, vol. 3, no. 24, pp. 12626–12630, 2015.

[44] X. Zhu, J. Lu, X. Li, B. Wang, Y. Song, X. Miao, Z. Wang, and G. Ren, "Simple Way to a Slippery Lubricant Impregnated Coating with Ultrastability and Self-Replenishment Property," *Industrial & Engineering Chemistry Research*, vol. 58, no. 19, pp. 8148–8153, 2019.

[45] N. Lavielle, D. Asker, and B. D. Hatton, "Lubrication dynamics of swollen silicones to limit long term fouling and microbial biofilms," *Soft Matter*, vol. 17, no. 4, pp. 936–946, 2021.

[46] Y. Yamauchi, M. Tenjimbayashi, S. Samitsu, and M. Naito, "Durable and Flexible Superhydrophobic Materials: Abrasion/Scratching/Slicing/Droplet Impacting/Bending/Twisting-Tolerant Composite with Porcupinefish-Like Structure," *ACS Applied Materials & Interfaces*, vol. 11, no. 35, pp. 32381–32389, 2019.

[47] Y. K. Mishra, G. Modi, V. Cretu, V. Postica, O. Lupan, T. Reimer, I. Paulowicz, V. Hrkac, W. Benecke, L. Kienle, *et al.*, "Direct growth of freestanding zno tetrapod networks for multifunctional applications in photocatalysis, uv photodetection, and gas sensing," *ACS applied materials & interfaces*, vol. 7, no. 26, pp. 14303–14316, 2015.

[48] M. Andriot, J. V. DeGroot, R. Meeks, A. T. Wolf, S. Leadley, J. L. Garaud, F. Gubbels, J. P. Lecomte, B. Lenoble, S. Stassen, C. Stevens, and X. Thomas, "Silicones in Industrial Applications," *Inorganic polymers*, pp. 61–161, 2007.

[49] M. Nendza, "Hazard assessment of silicone oils (polydimethylsiloxanes, PDMS) used in antifouling-/foul-release-products in the marine environment," *Marine Pollution Bulletin*, vol. 54, no. 8, pp. 1190–1196, 2007.

[50] N. Vogel, R. A. Belisle, B. Hatton, T.-S. Wong, and J. Aizenberg, "Transparency and damage tolerance of patternable omniphobic lubricated surfaces based on inverse colloidal monolayers," *Nature Communications*, vol. 4, no. 1, p. 2176, 2013.

[51] M. Tenjimbayashi, K. Sasaki, T. Matsubayashi, J. Abe, K. Manabe, S. Nishioka, and S. Shiratori, "A biologically inspired attachable, self-standing nanofibrous membrane for versatile use in oil–water separation," *Nanoscale*, vol. 8, no. 21, pp. 10922–10927, 2016.

[52] R. R. Buch and D. N. Ingebrigtson, "Rearrangement of poly (dimethylsiloxane) fluids on soil," *Environmental Science & Technology*, vol. 13, no. 6, pp. 676–679, 1979.

[53] R. Lehmann, S. Varaprath, and C. Frye, "Degradation of silicone polymers in soil," *Environmental Toxicology and Chemistry*, vol. 13, no. 7, pp. 1061–1064, 1994.

[54] R. Lehmann, S. Varaprath, and C. Frye, "Fate of silicone degradation products (silanols) in soil," *Environmental Toxicology and Chemistry*, vol. 13, no. 11, pp. 1753–1759, 1994.

[55] R. Mahinroosta and L. Senevirathna, "A review of the emerging treatment technologies for PFAS contaminated soils," *Journal of Environmental Management*, vol. 255, p. 109896, 2020.

[56] C. D. Vecitis, H. Park, J. Cheng, B. T. Mader, and M. R. Hoffmann, "Treatment technologies for aqueous perfluorooctanesulfonate (PFOS) and perfluorooctanoate (PFOA)," *Frontiers of Environmental Science & Engineering in China*, vol. 3, no. 2, pp. 129–151, 2009.

[57] T. Matsubayashi, M. Tenjimbayashi, M. Komine, K. Manabe, and S. Shiratori, "Bioinspired Hydrogel-Coated Mesh with Superhydrophilicity and Underwater Superoleophobicity for Efficient and Ultrafast Oil/Water Separation in Harsh Environments," *Industrial & Engineering Chemistry Research*, vol. 56, no. 24, pp. 7080–7085, 2017.

[58] L. Pokrajac, A. Abbas, W. Chrzanowski, G. M. Dias, B. J. Eggleton, S. Maguire, E. Maine, T. Malloy, J. Nathwani, L. Nazar, A. Sips, J. Sone, A. van den Berg, P. S. Weiss, and S. Mitra, "Nanotechnology for a sustainable future: Addressing global challenges with the international network4sustainable nanotechnology," *ACS Nano*, vol. 15, no. 12, pp. 18608–18623, 2021.

[59] M. Yan, C. Zhang, R. Chen, Q. Liu, J. Liu, J. Yu, L. Gao, G. Sun, and J. Wang, "Fast self-replenishing slippery surfaces with a 3D fibrous porous network for the healing of surface properties," *Journal of Materials Chemistry A*, vol. 7, no. 43, pp. 24900–24907, 2019.

[60] T. Yamazaki, M. Tenjimbayashi, K. Manabe, T. Moriya, H. Nakamura, T. Nakamura, T. Matsubayashi, Y. Tsuge, and S. Shiratori, "Antifreeze Liquid-Infused Surface with High Transparency, Low Ice Adhesion Strength, and Antifrosting Properties Fabricated through a Spray Layer-by-Layer Method," *Industrial & Engineering Chemistry Research*, vol. 58, no. 6, pp. 2225–2234, 2019.

[61] M. Muschi, B. Brudieu, J. Teisseire, and A. Sauret, "Drop impact dynamics on slippery liquid-infused porous surfaces: influence of oil thickness," *Soft Matter*, vol. 14, no. 7, pp. 1100–1107, 2018.

[62] R. Togasawa, M. Tenjimbayashi, T. Matsubayashi, T. Moriya, K. Manabe, and S. Shiratori, "A Fluorine-free Slippery Surface with Hot Water Repellency and Improved Stability against Boiling," *ACS Applied Materials & Interfaces*, vol. 10, no. 4, pp. 4198–4205, 2018.

[63] C. Wei, G. Zhang, Q. Zhang, X. Zhan, and F. Chen, "Silicone Oil-Infused Slippery Surfaces Based on Sol–Gel Process-Induced Nanocomposite Coatings: A Facile Approach to Highly Stable Bioinspired Surface for Biofouling Resistance," *ACS Applied Materials & Interfaces*, vol. 8, no. 50, pp. 34810–34819, 2016.

[64] S. Sunny, N. Vogel, C. Howell, T. L. Vu, and J. Aizenberg, "Lubricant-Infused Nanoparticulate Coatings Assembled by Layer-by-Layer Deposition," *Advanced Functional Materials*, vol. 24, no. 42, pp. 6658–6667, 2014.

[65] P. Kim, M. J. Kreder, J. Alvarenga, and J. Aizenberg, "Hierarchical or Not? Effect of the Length Scale and Hierarchy of the Surface Roughness on Omniphobicity of Lubricant-Infused Substrates," *Nano Letters*, vol. 13, no. 4, pp. 1793–1799, 2013.

[66] J. D. Smith, R. Dhiman, S. Anand, E. Reza-Garduno, R. E. Cohen, G. H. McKinley, and K. K. Varanasi, "Droplet mobility on lubricant-impregnated surfaces," *Soft Matter*, vol. 9, no. 6, pp. 1772–1780, 2013.

[67] F. Schellenberger, J. Xie, N. Encinas, A. Hardy, M. Klapper, P. Papadopoulos, H.-J. Butt, and D. Vollmer, "Direct observation of drops on slippery lubricant-infused surfaces," *Soft Matter*, vol. 11, no. 38, pp. 7617–7626, 2015.

[68] D. Daniel, J. V. I. Timonen, R. Li, S. J. Velling, and J. Aizenberg, "Oleoplaning droplets on lubricated surfaces," *Nature Physics*, vol. 13, no. 10, pp. 1020–1025, 2017.

[69] C. Ishino, M. Reyssat, E. Reyssat, K. Okumura, and D. Quéré, "Wicking within forests of micropillars," *Europhysics Letters (EPL)*, vol. 79, no. 5, p. 56005, 2007.

[70] C. Howell, T. L. Vu, C. P. Johnson, X. Hou, O. Ahanotu, J. Alvarenga, D. C. Leslie, O. Uzun, A. Waterhouse, P. Kim, M. Super, M. Aizenberg, D. E. Ingber, and J. Aizenberg, "Stability of Surface-Immobilized Lubricant Interfaces under Flow," *Chemistry of Materials*, vol. 27, no. 5, pp. 1792–1800, 2015.

[71] X. Chen, G. Wen, and Z. Guo, "What are the design principles, from the choice of lubricants and structures to the preparation method, for a stable slippery lubricant-infused porous surface?," *Materials Horizons*, vol. 7, no. 7, pp. 1697–1726, 2020.

[72] J. H. Hwang and F. Ma, "On the flow of a thin liquid film over a rough rotating disk," *Journal of Applied Physics*, vol. 66, no. 1, pp. 388–394, 1989.

[73] F. Ma and J. H. Hwang, "Stochastic simulation of the flow of a thin liquid film over a rough rotating disk," *Journal of Applied Physics*, vol. 66, no. 10, pp. 5026–5033, 1989.

[74] L. E. Stillwagon, R. G. Larson, and G. N. Taylor, "Planarization of Substrate Topography by Spin Coating," *Journal of The Electrochemical Society*, vol. 134, no. 8, pp. 2030–2037, 1987.

[75] L. E. Stillwagon and R. G. Larson, "Leveling of thin films over uneven substrates during spin coating," *Physics of Fluids A: Fluid Dynamics*, vol. 2, no. 11, pp. 1937–1944, 1990.

[76] L. M. Peurrung and D. B. Graves, "Film Thickness Profiles over Topography in Spin Coating," *Journal of The Electrochemical Society*, vol. 138, no. 7, pp. 2115–2124, 1991.

[77] P.-G. De Gennes, F. Brochard-Wyart, and D. Quéré, *Capillarity and wetting phenomena: drops, bubbles, pearls, waves*, vol. 336. Springer, 2004.

[78] H. Akbari and R. Levinson, "Evolution of Cool-Roof Standards in the US," *Advances in Building Energy Research*, vol. 2, no. 1, pp. 1–32, 2008.

[79] C. A. Schneider, W. S. Rasband, and K. W. Eliceiri, "NIH Image to ImageJ: 25 years of image analysis," *Nature Methods*, vol. 9, no. 7, pp. 671–675, 2012.

Chapter 9

Friction and Adhesion of Microparticle Suspension on Repellent Surfaces [1]

9.1 Overview

With the recent advancements in the development and application of repellent surfaces, both in air and under liquid medium, accurate characterization of repellence behavior is critical in understanding the mechanism behind many observed phenomena and exploiting them for novel applications. Conventionally, the repellence behavior of a surface is characterized by optical measurement of the dynamic contact angle of the target (to be repelled) liquid on the test surface. However, as already established in the literature, optical measurements are prone to appreciable error, especially for repellent surfaces with high contact angles. Here, we present an alternative, more accurate force-based characterization method of both friction and adhesion forces of microparticle-laden aqueous droplets over various repellent surfaces, where the force signature is captured by probing the surface with a droplet of the test liquid mounted at the tip of a flexible cantilever and then tracking the deflection of the tip of the cantilever as the probe droplet interacts with the surface.

[1] Adapted with permission from M., Kiran Raj, **Misra, S**, Mitra, S.K., *Langmuir*, 2020, 36, 45, 13689–13697. Copyright ©2020, American Chemical Society.

A systematic investigation of the response of repellent surfaces towards droplets with different microparticle concentrations revealed the dependency and sensitivity of measured adhesion and friction signature towards particle concentration. A comparison of theoretical estimates with optical goniometry highlights the deviation of the theoretical data from experimentally measured values and further substantiates the need for such a force-based approach for the accurate characterization of repellence behavior.

9.2 Introduction

Understanding the phenomena of adhesion is of vital importance in a spectrum of applications, especially in bioengineering and surface science [1]. The interaction of bacteria and pathogens with a given substrate is critical toward our understanding of how mitigation strategies can be designed to kill, repel and dislodge the harmful bio-agents from surfaces [2]. To understand this interaction, it is important to first characterize the adhesion force between the substrate and a model system. Typically, the microbes have a characteristics length scale of a few microns, therefore, here we aim to elucidate the interaction between a target substrate and bio-agents by measuring the adhesion force between microparticle-laden drops and the substrate.

Repellant surfaces have garnered considerable attention in the past decade. With the origin in biomimetics and termed it accordingly as the lotus leaf effect, it led to the development of a plethora of engineered surfaces known as 'superhydrophobic' (SHP) or that with extreme water repellency [3]. However, an accurate estimation of the relevant properties like the surface energy has always been a challenge [4]. Among the methods of surface characterization like Wilhemy plate method, du Noüy ring method and capillary rise method, the contact angle measurement is the most commonly used one, but not without complications [5]. Simple to carry out, the results depend crucially on the accuracy of image acquisition and its processing [6, 7]. A more reliable estimate is the dynamic contact angle, which takes into account the contact line movement [8]. This method gives the contact angle hysteresis (CAH), conventionally given as the difference in the advancing (θ_a) and receding contact angle (θ_r). All of the imaging-based techniques

falter at extremely high contact angles primarily owing to the difficulty and uncertainty in detecting the baseline [6]. This is where the precision of force-based techniques finds relevance [9]. They can be deflection-based like Atomic Force Microscope (AFM) [10] or piezoelectric sensors [11] or microelectronic balance systems [12]. Nonetheless, they all require expensive instrumentation and complicated procedures to yield the final result.

Recent attempts have been focused on quantifying both adhesion and friction with cantilever-based sensors and by skilfully tuning the existing framework of tools like AFM. Daniel *et al.*, have used capillary tubes as cantilevers to measure the dissipative forces when a droplet attached to the capillary is bought in contact with repellent surfaces, which translates at a fixed velocity [9]. By attaching a microlitre-sized droplet of the test liquid on the cantilever and then using the droplet to probe the surface response, detailed mapping can be carried out [13]. They have studied the three main classes of liquid-repellent surfaces with varying physical mechanisms at the contact line: micro/nanostructures showing the lotus-leaf effect, polymeric brush-grafted surfaces, and lubricated surfaces. They found that the dissipative force is independent of the velocity of droplet movement on superhydrophobic surfaces, but it depends non-linearly with the velocity for polymer brush grafted and lubricated surfaces. The results were also corroborated with the observations from optical interferometry. The same study was extended to underliquid systems [14, 15] where a thin liquid film exists between the droplet and the solid surface, and the forces involved are a function of the nondimensional capillary number (ratio of viscous force to surface tension force) [16]. However, they have not investigated how particle-laden drops can affect adhesion and friction behavior.

When the constitution of the droplet is not homogenous and consists of another phase as micro/nanoparticles, it can affect the dynamics of wetting significantly [17, 18]. The introduction of microparticles can affect the fundamental interaction of the fluid with the solid surface due to a number of aspects like adsorption, agglomeration and the internal convection and particle-particle interactions [17, 19, 20]. The interfacial interaction of a particle-laden droplet with a solid surface gives rise to a wide range of interesting physical phenomena, among which evaporation is a major one. In evaporating particle laden droplets with pinned contact line, radially varying rate of evaporation induces a capillary flow directed towards the contact line which drags the suspended particles outward, ulti-

mately leaving behind a ring-like stain along the contact line after the drop is evaporated (the so-called coffee stain effect) [21]. By appropriately tuning the size, volume fraction of suspended particles and the structure and wettability of the underlying surface, this aggregation process can be controlled to produce self-assembled micro/nanoscale structures in varied geometrical arrangements [22–29]. Such evaporation driven colloidal self-assembly from particle-laden suspension has garnered extensive interest in the scientific community because of its practical relevance including its potential in creating photonic bandgap crystals [30, 31], applicability in metamaterials research [32–35], its mixed implication in inkjet printing and others [36, 37]. Additionally, with suitable modification, this system involving microparticle-laden droplets can be extended to assess the response of non-living surfaces towards active pathogenic loads, which finds direct relevance in the present novel coronavirus pandemic scenario. One way to understand the role of microparticles in the ensuing interfacial dynamics is to study the CAH of particle-laden droplets on the target surface. The effect of microparticle concentrations on the CAH has been investigated over hydrophobic glass surfaces [38]. However, the impact of particle concentrations has not been studied systematically for repellent surfaces [39].

As evident from existing literature, understanding the interaction between particle-laden drops and a given repellant surface is still an ongoing research direction. Fundamental to this understanding is the ability to experimentally measure the force signature (namely, the adhesion and friction forces) as the microparticle-laden droplet comes in contact with the target substrate. To investigate such interactions which consist of forces in the range of micro/nanonewtons, complex equipment like AFM [40] or highly sensitive force sensors [11] are often needed. Here, we have attempted to address this challenge with the aid of simple instrumentation, circumventing the use of such sophisticated tools. Droplet interaction experiments are conducted with an in-house developed experimental setup that combines the simplicity of a capillary tube-based cantilever sensor with the accuracy of high-resolution image acquisition and processing. Imaging-based techniques are exploited in the analysis for the time tracking of the displacement and force signature with a high spatiotemporal resolution, yielding a cost-effective and rapid tool to decipher such force and wetting signatures.

9.3 Experimental Section

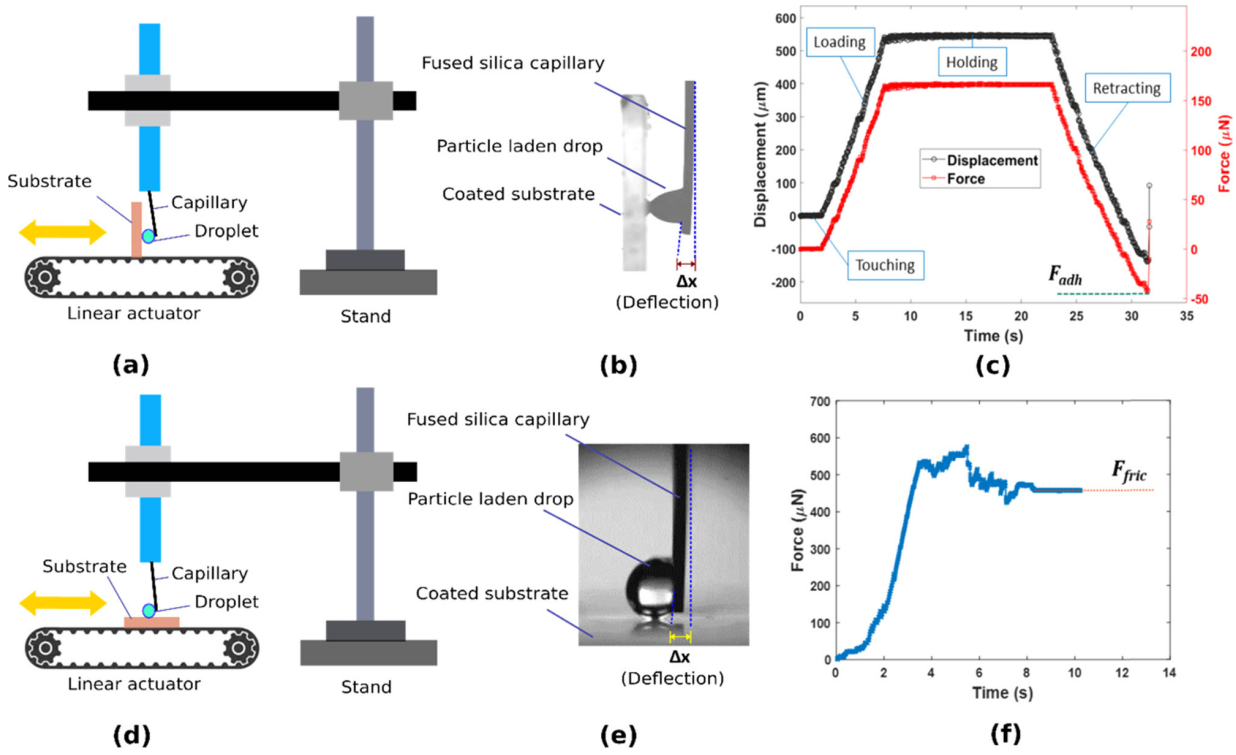

Figure 9.1: (a) Experimental setup showing the linear stage on which the test surface is held vertically. The droplet is dispensed at the tip of the cantilever which is aligned vertically with a stand. (b) Photograph of the droplet detaching from the surface and the deflection of the cantilver Δx. (c) Typical displacement curve and the force curve showing the steps involved in the adhesion measurement and the point corresponding to F_{adh}. (d) Experimental setup in which the sample is held horizontally to measure the friction. (e) Photograph of the deflection due friction between the droplet and the substrate (f) Typical force curve for friction measurent and the final plateau region gives F_{fric}.

The adhesion measurement setup consists of in-house made instrumentation as shown in Figure 9.1 (a). A fused silica capillary tube (Polymicro Capillary Tubing, Molex, AZ, USA) with length $L = 70$mm and external diameter $d = 410\mu$m (see Figure 9.1 (b)) is used as a cantilever sensor with a stiffness constant $k = 305$ mN/m (see Appendix G, Section

G.1 for calibration details). A similar experimental system has been used to investigate the adhesion of underliquid droplets on polyzwitterionic brushes [16]. A 5μl droplet is dispensed at the tip of the cantilever manually with a micropipette. The glass slides with the coating were fixed vertically over a linear motor stage (Zaber Technologies Inc., BC, Canada) and were translated at a velocity U = 0.5mm/s. The entire process is captured using a video camera (Photron FASTCAM Mini) at 60fps with a strong LED backlight. Video analysis is carried out using an open-source video analysis platform [41] from which the deflection profile of the cantilever tip (Δx) with respect to time is extracted. Based on this, adhesion measurement consists of four steps – (i) touching, where the droplet made the first contact with the substrate (ii) loading where the substrate is pushed against the droplet for a distance of 500μm (iii) holding where the droplet stays on the substrate for 15s and (iv) retracting where the substrate is translated in the opposite direction at a velocity U = 0.5mm/s. These events are shown in the typical displacement curve in Figure 9.1 (c) from which, the force acting on the cantilever can be easily estimated as $F = k\Delta x$ and is also depicted in the same figure. At the end of the retraction step, the droplet is detached from the substrate when the maximum deflection is achieved (Δx_{max}). Then, adhesion force is calculated as $F_{adh} = k\Delta x_{max}$ as shown in Figure 9.1 (c). The detachment is fairly quick and the inertia on the cantilever results in an overshoot of Δx from the mean position. For measuring friction, the same setup is used with the exception that the substrate is held horizontally against the droplet dispensed on the cantilever as shown in Figure 9.1(d & e) and was translated at a velocity of U = 0.5 mm/s. Here again, the temporal variation of the cantilever deflection (Δx) is recorded as shown in Figure 9.1(f) and is converted into the force using $F = k\Delta x$ as shown in Figure 9.1(f). After an initial peak similar to the static friction between two solid surfaces, the curve attains a steady state force which is taken as the friction force F_{fric}. It should be noted that though the deflection of the cantilever is recorded against time during the experiment, the value of F_{adh} and F_{fric} corresponds to a point and a steady state value, respectively, in the curve.

An important consideration while conducting this experiment would be to ensure that the adhesion between the probing droplet and the target surface is lower than that between the probing droplet and the cantilever, as otherwise the probing droplet might get detached from the cantilever tip and get deposited on the target surface in the retraction

phase of the adhesion measurement cycle. On the other hand, we will also need to ensure that the probing droplet does not spread on the cantilever surface and therefore a hydrophilic cantilever would not work either. One way to ensure this is to use a moderately hydrophobic cantilever tip (with a static water contact angle 70°-100°) to probe superhydrophobic surfaces with a typical water contact angle higher than 140°. Applying a thin polydimethylsiloxane (PDMS) coating on the surface of the capillary helps in this regard. Another important aspect is to choose the outer diameter of the capillary tube and droplet volume accordingly so that the surface tension force at the tip of the capillary can sustain the weight of the probing droplet. For our chosen capillary tube with an outer diameter 410μm, we could stably attach probing droplets with volume 10 μL or lower. However, droplets bigger than 10 μL in volume tend to detach from the tip due to gravity.

We used three coatings to fabricate repellent surfaces on glass slides: Soot (S1), commercially available single-part spray (Glaco - 'Soft99', S2), and a double-part spray (Rust-Oleum- 'NeverWet', S3). All glass slides were sonicated in ethanol and then rinsed in deionized (DI) water and dried with nitrogen gas before coating. For S1 (soot), we kept the glass slide over a flame for 5 min to allow soot to deposit onto the glass slide and then baked at 100° C for 30min. In the last decade, candle soot-inspired repellent coatings have been extensively explored [42–46] in literature because of the possibility of creating excellently stable, omniphobic surfaces. The fractal-like assembly of nanoscopic soot particles helps sustain a Cassie-Baxter state with a typical water contact angle higher than 150°. For S2, the spray was applied on the glass slide twice with a 30 min intervals and cured at ambient temperature for 4 hours. For S3, the base and top coatings were applied on a glass slide with 30 min intervals and cured at ambient temperature for 4 hours. Scanning Electron Microscopic (SEM) images, shown in Figure 9.2 elucidates the presence of hierarchical micro/ nanostructures, which is responsible for the superhydrophobicity. All three coatings are well established in the literature as structured superhydrophobic surfaces with a very high static contact angle and fairly durable for normal operating conditions if not extreme [42, 47, 48]. Prepared samples were safely kept in a vacuum desiccator before the experiments to avoid contamination. The contact angle was measured using a goniometer (Holmarc Opto-Mechatronics, Kerala, India) by systematic characterization using a 3μl droplet on these substrates, dispensed quasi-statically using a needle dispenser.

For dynamic contact angle measurements, the probe liquid is first slowly infused and then withdrawn from the test surface using a dispensing needle tip at a flowrate of 0.5 μl/min connected to a syringe pump (Chemyx, Stafford, TX) and the contact line movement is captured for both the growing as well as shrinking phase of the probe droplet. Subsequently, the contact angles at these phases are extracted using ImageJ which gives θ_a and θ_r respectively. We used polystyrene latex particles with a nominal diameter of 1μm (Magsphere Inc., Pasadena, CA, USA), diluted in deionized (DI) water as the working fluid. The concentrations of these microparticles were varied from 0 (no particles) to 5% (w/v) and their interfacial tension (IFT) values were measured with pendant drop method [49] (see Appendix G, Section G.2).

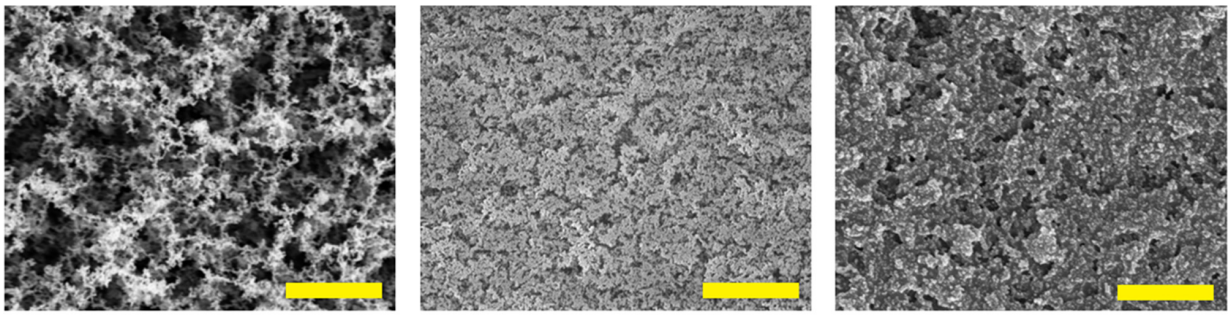

Figure 9.2: SEM images of (a) S1 (b) S2 (c) S3 coatings on glass surface. Scale bar represents 1μm

9.4 Results & Discussion

The static contact angle gives an outline of the wetting characteristics based on the equilibrium state of the three-phase contact line. Within the range of experiments, the static contact angle remained almost independent of the concentration for all the substrates as shown in Figure 9.3(a). This occurred despite the reduction in the interfacial tension with an increase in the concentration of the microparticles. S2 showed a smaller contact angle compared to S1 and S3, pointing to a reduced repellency for the same concentration of the microparticles. For the dynamic contact angle measurements expressed in the form

of contact angle hysteresis (CAH = θ_a $-\theta_r$)) as shown in Figure 9.3(b) for S2, it is observed that CAH is monotonously increasing with the concentration. A similar increase in CAH was observed for microbead suspensions over a hydrophilic glass surface ($\theta < 90^0$) with the increase in volume fraction of the microparticles [38]. For S1 and S3, the CAH is minimal and shows no variation with respect to a change in the concentration. This shows the importance of dynamic characterization in addition to the static contact angle measurement while dealing with repellant surfaces as the behavior of the surface while approaching a previously unwet surface (advancing stage) and receding from an already wet surface (receding stage) are different. Further, the dynamics involved in the very process of dispensing a sessile droplet may cause errors if not operated correctly [8].

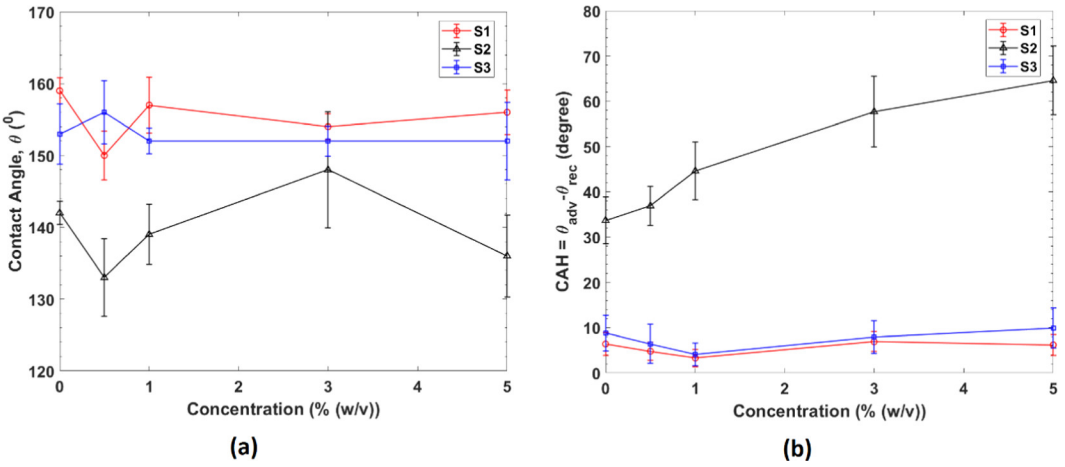

Figure 9.3: (a) Static contact angle (θ) and (b) Contact angle hysteresis for different concentrations of the microparticles in aqueous solution for the three repellent surfaces studied.

We estimated the friction force acting on the droplet during the contact line motion using Furmidge's relation as [50]

$$F_{th} = 2a\gamma_{LV}(\cos\theta_r \ - \cos\theta_a \ ), \tag{9.1}$$

where a is base radius and γ_{LV} is the surface tension and is plotted in Figure 9.4(a). F_{th} is almost invariable for S1 and S3 with the change in the concentration of the microparticles and the values obtained are comparable to that reported for structured superhydrophobic

surfaces using a cantilever-based force sensor ($\sim$ 5 μN) [9]. However, for S2, it shows a linearly increasing behavior. The friction force obtained from the cantilever-based measurement (F_{fric}), is plotted in Figure 9.4(b), which shows an increasing trend with an increase in the concentration of microparticles for S2 an S3 and a plateau for S1 after the initial rise. To validate our force estimation, we have also measured the tilting angle required for a droplet of chosen volume to start sliding down the surface of interest. The recorded tilt angle was then used in conjunction with the drop size to indirectly estimate the friction force, which is equal to the component of gravity acting along the inclined surface just at the moment when the droplet starts sliding down. For the surface-droplet combination with the lowest friction force (pure water droplet on S1), the calculated average friction from sliding angle data was 27.55 μN while our force apparatus registered an average value of 36.78 μN for a 10 μL droplet. This deviation of ca. 25% is within acceptable accuracy considering the base value in itself is very small. For further details on the sliding angle measurement, please refer to section G.3 in Appendix G.

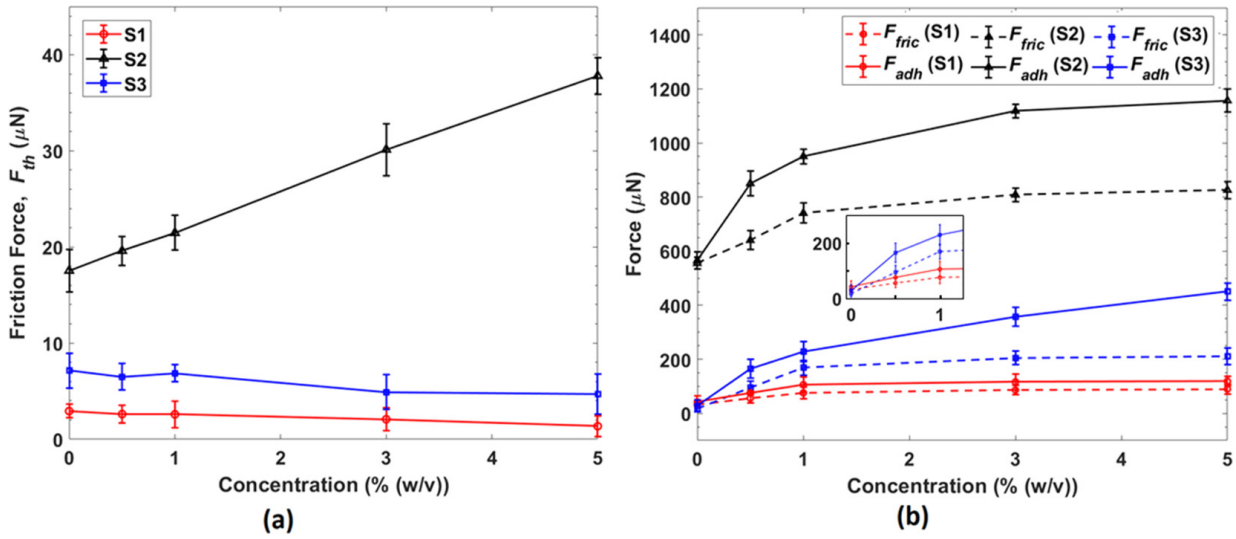

Figure 9.4: (a) Friction force from Furmidge equation (F_{th}) and (b) Friction (F_{fric}) and Adhesion force (F_{adh}) from for different concentration of the microparticles in aqueous solution for the three repellent surfaces studied. The inset shows values for S1 and S3 for low concentrations.

It is to be noted here that F_{th} estimated using the optically measured dynamic contact angle values differ significantly from the experimentally obtained F_{fric} values using the cantilever-based droplet force apparatus. This arises due to the well-known difficulty [6, 51] in determining the baseline of the droplet from the shadow images of the contact angle goniometer, which significantly affects the accuracy of measurement of contact angle data in superhydrophobic surfaces (contact angle $> 150°$). For a nominal static contact angle of 162°, an error as small as 1 pixel in fixing the baseline of the droplet can result in an uncertainty of 5° in contact angle measurement.6 To illustrate its impact on the calculated value of F_{th}, let us assume an instance where the advancing contact angle is 162° and the receding contact angle is 157°. Now, if the receding angle is measured as 152° (an underprediction of 5°) due to the aforementioned error in accurate determination of the baseline, the value of $\Delta cos\theta$ ($= \cos\theta_r - \cos\theta_a$) experiences a 123% increment, which, assuming there is no other sources of error, directly corresponds to an error of 123% in the calculated value of friction force. Another responsible factor behind this difference is the possibility of local pinning of probing droplets on the target surface during friction measurement, which gives to a higher measured friction. This is more pronounced in the case of S2 (Glaco coating – the one that consistently shows the highest friction and adhesion force among all the three coatings) where the surface contains random agglomeration of nanoscopic structures, as can be seen in the SEM image in Figure 9.2 (b). Similar observation with Glaco surface coating has earlier been reported by previous researchers [52, 53] as well. Such agglomerations act as local pinning sites, which contribute to a higher absolute friction and adhesion force as well as a higher difference between experimentally obtained data and the theoretical estimates using Furmidge's equation. Further, Furmidge's equation relies on the contact line motion and thus the energy dissipation at the vicinity of the three-phase contact line is considered. This is analogous to the Landau-Levich-Derjaugin (LLD) law for estimating the thickness of lubricant film between a drop and a solid surface, where the dissipation is considered only over the rim for a small width [1]. The above-mentioned arguments substantiate the requirement of force-based measurement techniques, as the one reported here, for direct evaluation of adhesion and friction characteristics of super-repellent surfaces where the optically captured contact angle signature can be a source of significant uncertainty.

Now, let us look at the second force estimate from our experiments: F_{adh} plotted

along with F_{fric} in Figure 9.4(b). For F_{adh}, the entire droplet surface that encountered the solid surface (circular area with radius a) contributes to the force measurement and thus in the deflection of the cantilever. It is perceived as the resistance to disengagement in the normal direction while the experimentally measured frictional force in the present context (F_{fric}) is considered as the resistance to detachment in the lateral direction of the substrate. Even though both adhesion and friction correspond to the energy dissipation at the contact line, they differed in their magnitudes. It is clear from Figure 9.4(b) that F_{fric} is lower than F_{adh} for all coatings and concentrations. This could be attributed to the fundamental difference in the way adhesion and friction contribute to the dissipation at the solid-liquid interface. Adhesion is measured by forceful complete removal of a test droplet from the surface while friction corresponds to the lateral migration of the droplet, where the droplet always maintains contact with the surface. While probing on the surface, adhesion measurement is confined to the area of contact (with radius a) whereas friction is extended over a strip with a width a.

Another observation is that F_{fric} flattened with respect to the concentration at a lower value than F_{adh}. A 20% reduction in the interfacial tension (see Appendix G, Figure G.2 (b)) due to the increased concentration of the particles has resulted in about more than 100% increase in F_{adh}. For structured superhydrophobic surfaces, F_{fric} is a function of the solid surface fraction (φ) and is independent of the contact line velocity [9]. A number of theories has been proposed towards the functional relationship with φ based on the energy considerations of the capillary bridges formed over the micro/nanostructures and their rupture [54–57]. It should be noted that F_{th} based on the Furmidge relation considers an ideal flat surface without any roughness or impurities on the surface ($\varphi = 1$). In the present case, φ cannot be quantified accurately as the coating process is mostly uncontrolled on this aspect and it is only ensured that the fractal structures are formed on the substrate, leading to a Cassie-Baxter state of wetting [1]. This is verified through roughness measurement and reflection interference contrast microscopy (RICM) with the particle-laden droplet over it for S2, the surface that offers the highest adhesion force to the oncoming droplets among all the tested substrates (see Appendix G, Section G.4 for details). The topological mapping of S2 was carried out using Atomic Force Microscopy (AFM), as shown in Figure 9.5(a). It shows the random micro/nanostructures that are

responsible for the Cassie-Baxter state of wetting and the consequent superhydrophobicity [58]. This is further elucidated by means RICM observation as shown schematically in Figure 9.5(b). Figure 9.5(c) illustrates the change in reflected intensity signal from the same observation area before (Figure 9.5(c-i)) and after (Figure 9.5(c-ii)) a microparticle-laden (5% w/v) water droplet is placed on the surface. The observed interference rings in Figure 9.5(c-ii) confirm the formation of air pockets underneath the dispensed droplet, resulting in a Cassie - Baxter wetting state.

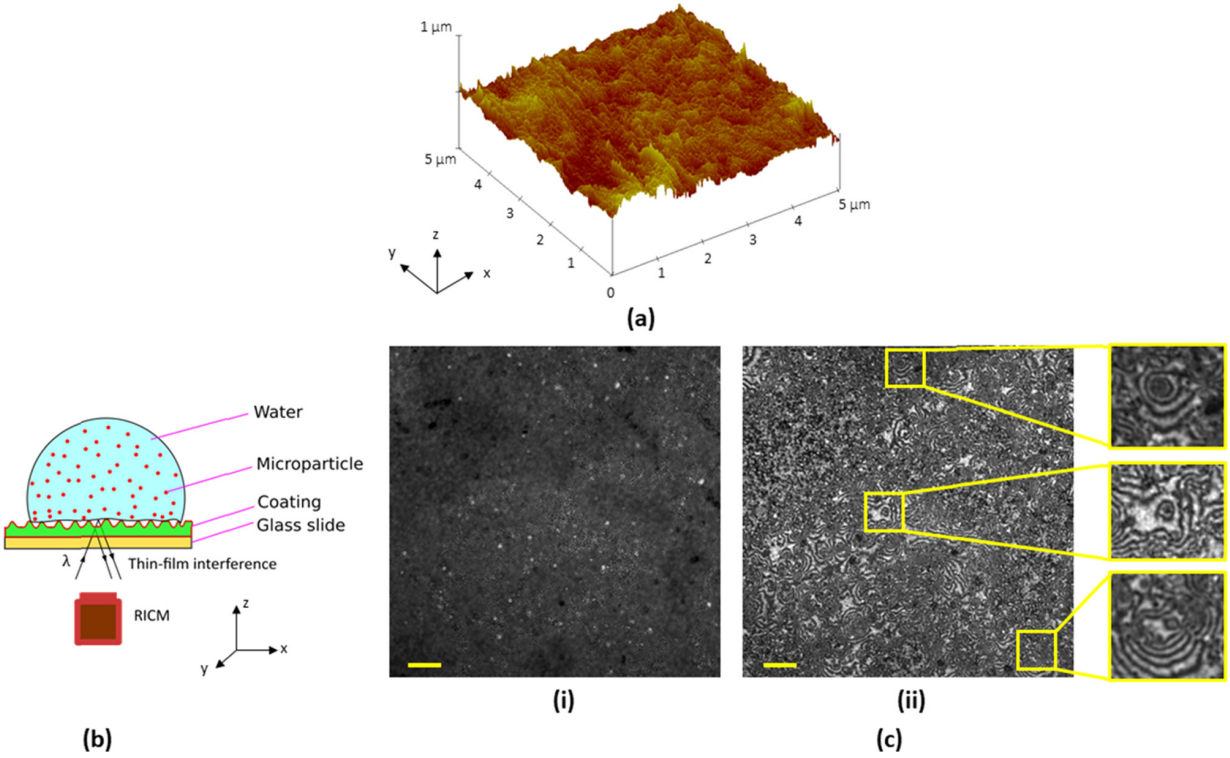

Figure 9.5: (a) AFM image showing the random roughness on the surface with the heights of the micro/nano features (b) Schematic of the RICM setup to probe at the location of the liquid-coating interface (c) RICM micrograph of (i) The sample without any water droplet on the surface (ii) The same position as in (i) with a droplet sitting over as shown in (b), clearly revealing the interference fringes corresponding to the capillary bridges formed between the micro/nanostructures. Scale bar represents 50μm.

In our experiments, we also observed that F_{fric} was independent of the contact line velocity U (see Appendix G, Section G.5). From a measurement perspective, F_{adh} and F_{fric} are directly-measured from the cantilever deflection while F_{th} is obtained from image analysis of both contact radius and the contact angles, making it more prone to appreciable errors in the case of highly repellant surfaces like the ones used in the present study. Contextually, it is to be noted here that the directly measured friction values using our force sensor provide a true representation of the actual response of the surface towards the oncoming droplet and therefore are more reliable than the theoretical estimate using Furmidge's equation.

To understand the role of any force component due to the sedimentation of the particles with time along the contact line (coffee-ring effect), experiments are conducted by systematically varying the holding time (the time of direct contact of the droplet with the test surface) of the probing droplet on the test surface. It did not affect the adhesion force as shown in Figure 9.6 for a time interval up to 5 min even when we used a probe droplet with 5% (w/v) microdroplet concentration (the highest concentration used in the present study). It is to be noted that the substrates being highly repellant, the droplet is completely detached from the surface once the maximum deflection point of the cantilever is reached during the measurement of F_{adh}, without leaving any residues on the surface. In the case of hydrophilic substrates like normal quartz glass, the droplet is partially detached and splits into daughter droplets on the substrate, and thus the force measured will correspond to the separation force, which is also associated with formation of a new interface [12, 59]. Further, we also confirmed that the chemical inhomogeneities were not significant by conducting FTIR (Fourier-transform infrared spectroscopy) measurements over random locations across the sample (see Appendix G, Section G.6), which confirms acceptable spatial uniformity of the measured interaction signature.

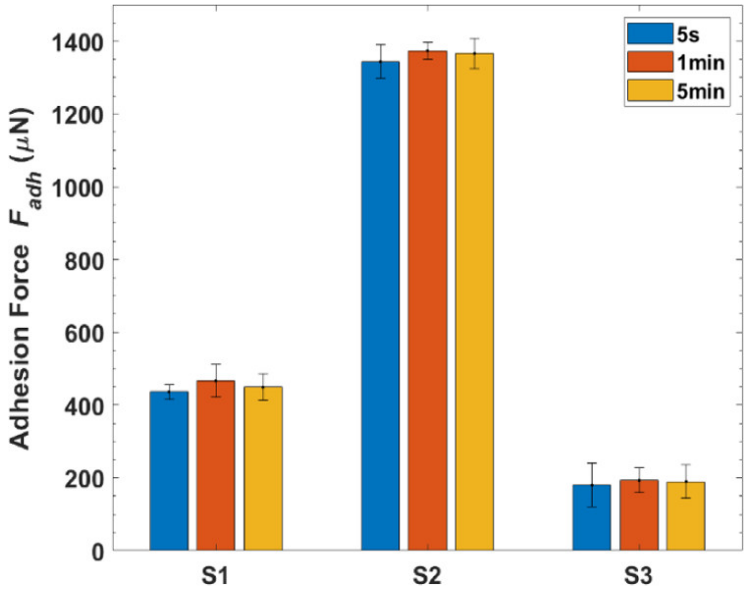

Figure 9.6: Adhesion force (F_{adh}) measured for different holding times over the substrates for a concentration of 5% (w/v).

The results presented here show that F_{adh} and F_{fric} can be a reliable estimate to classify different repellant surfaces. For better accuracy and spatial averaging, AFM will definitely yield finer measurements [13], however, customization of such an expensive instrument is not practical for most research groups. The present setup offers simplicity in construction, data collection, and analysis with minimal infrastructure and investment. With controlled vertical rastering, an adhesion map may be constructed for repellent surfaces. Several factors can potentially introduce errors in the present system like localized variation in the concentration within the droplet, agglomeration of the microparticles, and improper placing of the droplet on the cantilever. Further, the sole dependence on the bending of the cantilever as the measurement mechanism may lead to errors due to fatigue and variation in the k value over time. Nevertheless, it is useful in capturing the fundamental repellence signature, can help differentiate between seemingly similar repellent surfaces with similar static contact angle values, and can also be used as a generic interfacial force measuring apparatus.

9.5 Conclusion

We have investigated the frictional and adhesion characteristics of microparticle-laden drops over repellent surfaces utilizing a simple yet efficient experimental setup. We have shown that the direct force measurements using a droplet attached to a cantilever mechanism are more reliable than regular optical goniometry for surfaces having high contact angle values where the inherent difficulties in optically imaging the solid-liquid interface and the challenges associated with the dispensation of the probe liquid significantly compromise the accuracy of measurements. Three coatings with different physicochemical properties but similar static water contact angles were investigated using the cantilever-based setup. Further, using the same setup, we were able to quantify the differences in the magnitudes of these forces for spherical polymeric microparticle-laden water droplets. Based on the framework laid in this study, future structured investigations targeted at probing the molecular origin and nature of the interaction forces (contribution of van der Waals forces, capillary adhesion, steric effects, etc.) between particle-laden suspensions and solid surfaces could be developed. This study also provides a foundation for the development of rapid and cost-effective techniques to investigate the mechanism of interaction between surfaces and droplets with active bacterial or viral loads to evaluate the efficiency of antimicrobial/antiviral coatings and to understand the physics of their attachment to specific materials and fabrics, provided appropriate consideration given to account for the viability and motility of the live agents.

References

[1] P.-G. De Gennes, F. Brochard-Wyart, and D. Quéré *Capillarity and Wetting Phenomena: Drops, Bubbles, Pearls, Waves*, 2004.

[2] H. Song, Y. Ahmad Nor, M. Yu, Y. Yang, J. Zhang, H. Zhang, C. Xu, N. Mitter, and C. Yu, "Silica nanopollens enhance adhesion for long-term bacterial inhibition," *Journal of the American Chemical Society*, vol. 138, no. 20, pp. 6455–6462, 2016.

[3] M. Nosonovsky and B. Bhushan, "Superhydrophobic surfaces and emerging appli-

cations: Non-adhesion, energy, green engineering," *Current Opinion in Colloid and Interface Science*, vol. 14, no. 4, pp. 270–280, 2009.

[4] A. Neumann and R. Good, "Techniques of measuring contact angles," *Surface and Colloid Science*, vol. 11, pp. 31–91, 1979.

[5] D. Kwok and A. Neumann, "Contact angle measurement and contact angle interpretation," *Advances in Colloid and Interface Science*, vol. 81, no. 3, pp. 167–249, 1999.

[6] K. Liu, M. Vuckovac, M. Latikka, T. Huhtamäki, and R. Ras, "Improving surface-wetting characterization," *Science*, vol. 363, no. 6432, pp. 1147–1148, 2019.

[7] S. Srinivasan, G. McKinley, and R. Cohen, "Assessing the accuracy of contact angle measurements for sessile drops on liquid-repellent surfaces," *Langmuir*, vol. 27, no. 22, pp. 13582–13589, 2011.

[8] T. Huhtamäki, X. Tian, J. Korhonen, and R. Ras, "Surface-wetting characterization using contact-angle measurements," *Nature Protocols*, vol. 13, no. 7, pp. 1521–1538, 2018.

[9] D. Daniel, J. Timonen, R. Li, S. Velling, M. Kreder, A. Tetreault, and J. Aizenberg, "Origins of extreme liquid repellency on structured, flat, and lubricated hydrophobic surfaces," *Physical Review Letters*, vol. 120, no. 24, 2018.

[10] R. Sullan, A. Churnside, D. Nguyen, M. Bull, and T. Perkins, "Atomic force microscopy with sub-piconewton force stability for biological applications," *Methods*, vol. 60, no. 2, pp. 131–141, 2013.

[11] V. Liimatainen, M. Vuckovac, V. Jokinen, V. Sariola, M. Hokkanen, Q. Zhou, and R. Ras, "Mapping microscale wetting variations on biological and synthetic water-repellent surfaces," *Nature Communications*, vol. 8, no. 1, 2017.

[12] Y. Sun, Y. Li, X. Dong, X. Bu, and J. Drelich, "Spreading and adhesion forces for water droplets on methylated glass surfaces," *Colloids and Surfaces A: Physicochemical and Engineering Aspects*, vol. 591, 2020.

[13] D. Daniel, C. Lay, A. Sng, C. Lee, D. Neo, X. Ling, and N. Tomczak, "Mapping micrometer-scale wetting properties of superhydrophobic surfaces," *Proceedings of the National Academy of Sciences of the United States of America*, vol. 116, no. 50, pp. 25008–25012, 2019.

[14] P. Waghmare, S. Das, and S. Mitra, "Drop deposition on under-liquid low energy surfaces," *Soft Matter*, vol. 9, no. 31, pp. 7437–7447, 2013.

[15] S. Mitra and S. Mitra, "Symmetric drop coalescence on an under-liquid substrate," *Physical Review E - Statistical, Nonlinear, and Soft Matter Physics*, vol. 92, no. 3, 2015.

[16] D. Daniel, A. Chia, L. Moh, R. Liu, X. Koh, X. Zhang, and N. Tomczak, "Hydration lubrication of polyzwitterionic brushes leads to nearly friction- and adhesion-free droplet motion," *Communications Physics*, vol. 2, no. 1, 2019.

[17] S. Vafaei, T. Borca-Tasciuc, M. Podowski, A. Purkayastha, G. Ramanath, and P. Ajayan, "Effect of nanoparticles on sessile droplet contact angle," *Nanotechnology*, vol. 17, no. 10, pp. 2523–2527, 2006.

[18] K. Sefiane, J. Skilling, and J. MacGillivray, "Contact line motion and dynamic wetting of nanofluid solutions," *Advances in Colloid and Interface Science*, vol. 138, no. 2, pp. 101–120, 2008.

[19] K. Kendall, M. Kendall, and F. Rehfeldt, "Adhesion of nanoparticles," *Adhesion of Cells, Viruses and Nanoparticles*, pp. 169–193, 2011.

[20] S. Du, K. Kendall, P. Toloueinia, Y. Mehrabadi, G. Gupta, and J. Newton, "Aggregation and adhesion of gold nanoparticles in phosphate buffered saline," *Journal of Nanoparticle Research*, vol. 14, no. 3, 2012.

[21] R. Deegan, O. Bakajin, T. Dupont, G. Huber, S. Nagel, and T. Witten, "Capillary flow as the cause of ring stains from dried liquid drops," *Nature*, vol. 389, no. 6653, pp. 827–829, 1997.

[22] F. Fan and K. Stebe, "Assembly of colloidal particles by evaporation on surfaces with patterned hydrophobicity," *Langmuir*, vol. 20, no. 8, pp. 3062–3067, 2004.

[23] I. Hosein and C. Liddell, "Convectively assembled asymmetric dimer-based colloidal crystals," *Langmuir*, vol. 23, no. 21, pp. 10479–10485, 2007.

[24] D. Harris, H. Hu, J. Conrad, and J. Lewis, "Patterning colloidal films via evaporative lithography," *Physical Review Letters*, vol. 98, no. 14, 2007.

[25] Marín, H. Gelderblom, D. Lohse, and J. Snoeijer, "Order-to-disorder transition in ring-shaped colloidal stains," *Physical Review Letters*, vol. 107, no. 8, 2011.

[26] O. Velev, A. Lenhoff, and E. Kaler, "A class of microstructured particles through colloidal crystallization," *Science*, vol. 287, no. 5461, pp. 2240–2243, 2000.

[27] A. Dinsmore, M. Hsu, M. Nikolaides, M. Marquez, A. Bausch, and D. Weitz, "Colloidosomes: Selectively permeable capsules composed of colloidal particles," *Science*, vol. 298, no. 5595, pp. 1006–1009, 2002.

[28] V. Manoharan, M. Elsesser, and D. Pine, "Dense packing and symmetry in small clusters of microspheres," *Science*, vol. 301, no. 5632, pp. 483–487, 2003.

[29] Marín, H. Gelderblom, A. Susarrey-Arce, A. Van Houselt, L. Lefferts, J. Gardeniers, D. Lohse, and J. Snoeijer, "Building microscopic soccer balls with evaporating colloidal fakir drops," *Proceedings of the National Academy of Sciences of the United States of America*, vol. 109, no. 41, pp. 16455–16458, 2012.

[30] Y. Vlasov, X.-Z. Bo, J. Sturm, and D. Norris, "On-chip natural assembly of silicon photonic bandgap crystals," *Nature*, vol. 414, no. 6861, pp. 289–293, 2001.

[31] K. Busch and S. John, "Photonic band gap formation in certain self-organizing systems," *Physical Review E - Statistical Physics, Plasmas, Fluids, and Related Interdisciplinary Topics*, vol. 58, no. 3, pp. 3896–3908, 1998.

[32] A. Van Blaaderen, R. Ruel, and P. Wiltzius, "Template-directed colloidal crystallization," *Nature*, vol. 385, no. 6614, pp. 321–323, 1997.

[33] P. Jiang, J. Bertone, K. Hwang, and V. Colvin, "Single-crystal colloidal multilayers of controlled thickness," *Chemistry of Materials*, vol. 11, no. 8, pp. 2132–2140, 1999.

[34] I. Hosein, S. Lee, and C. Liddell, "Dimer-based three-dimensional photonic crystals," *Advanced Functional Materials*, vol. 20, no. 18, pp. 3085–3091, 2010.

[35] K. Stebe, E. Lewandowski, and M. Ghosh, "Oriented assembly of metamaterials," *Science*, vol. 325, no. 5937, pp. 159–160, 2009.

[36] J. Park and J. Moon, "Control of colloidal particle deposit patterns within picoliter droplets ejected by ink-jet printing," *Langmuir*, vol. 22, no. 8, pp. 3506–3513, 2006.

[37] M. Kuang, L. Wang, and Y. Song, "Controllable printing droplets for high-resolution patterns," *Advanced Materials*, vol. 26, no. 40, pp. 6950–6958, 2014.

[38] P. Waghmare and S. Mitra, "Contact angle hysteresis of microbead suspensions," *Langmuir*, vol. 26, no. 22, pp. 17082–17089, 2010.

[39] L. Brannon-Peppas, "Recent advances on the use of biodegradable microparticles and nanoparticles in controlled drug delivery," *International Journal of Pharmaceutics*, vol. 116, no. 1, pp. 1–9, 1995.

[40] A. Alessandrini and P. Facci, "Afm: A versatile tool in biophysics," *Measurement Science and Technology*, vol. 16, no. 6, pp. R65–R92, 2005.

[41] D. Brown, "Tracker video analysis and modeling tool," *Tracker Video Analysis and Modeling Tool*, 2009.

[42] X. Deng, L. Mammen, H.-J. Butt, and D. Vollmer, "Candle soot as a template for a transparent robust superamphiphobic coating," *Science*, vol. 335, no. 6064, pp. 67–70, 2012.

[43] B. Sahoo, S. Nanda, J. Kozinski, and S. Mitra, "Pdms/camphor soot composite coating: towards a self-healing and a self-cleaning superhydrophobic surface," *RSC Advances*, vol. 7, no. 25, pp. 15027–15040, 2017.

[44] R. Iqbal, B. Majhy, and A. Sen, "Facile fabrication and characterization of a pdms-derived candle soot coated stable biocompatible superhydrophobic and superhemophobic surface," *ACS Applied Materials and Interfaces*, vol. 9, no. 36, pp. 31170–31180, 2017.

[45] B. Sahoo, N. Gunda, S. Nanda, J. Kozinski, and S. Mitra, "Development of dual-phobic surfaces: Superamphiphobicity in air and oleophobicity underwater," *ACS Sustainable Chemistry and Engineering*, vol. 5, no. 8, pp. 6716–6726, 2017.

[46] B. Majhy, R. Iqbal, and A. Sen, "Facile fabrication and mechanistic understanding of a transparent reversible superhydrophobic – superhydrophilic surface," *Scientific Reports*, vol. 8, no. 1, 2018.

[47] I. Vakarelski, N. Patankar, J. Marston, D. Chan, and S. Thoroddsen, "Stabilization of leidenfrost vapour layer by textured superhydrophobic surfaces," *Nature*, vol. 489, no. 7415, pp. 274–277, 2012.

[48] X. Zhao, M. Khandoker, and K. Golovin, "Non-fluorinated omniphobic paper with ultralow contact angle hysteresis," *ACS Applied Materials and Interfaces*, vol. 12, no. 13, pp. 15748–15756, 2020.

[49] J. Berry, M. Neeson, R. Dagastine, D. Chan, and R. Tabor, "Measurement of surface and interfacial tension using pendant drop tensiometry," *Journal of Colloid and Interface Science*, vol. 454, pp. 226–237, 2015.

[50] C. Furmidge, "Studies at phase interfaces. i. the sliding of liquid drops on solid surfaces and a theory for spray retention," *Journal of Colloid Science*, vol. 17, no. 4, pp. 309–324, 1962.

[51] M. Vuckovac, M. Latikka, K. Liu, T. Huhtamäki, and R. Ras, "Uncertainties in contact angle goniometry," *Soft Matter*, vol. 15, no. 35, pp. 7089–7096, 2019.

[52] C. Lv, P. Hao, Z. Yao, and F. Niu, "Departure of condensation droplets on superhydrophobic surfaces," *Langmuir*, vol. 31, no. 8, pp. 2414–2420, 2015.

[53] P. Bourrianne, C. Lv, and D. Quéré, "The cold leidenfrost regime," *Science Advances*, vol. 5, no. 6, 2019.

[54] M. Reyssat and D. Quéré, "Contact angle hysteresis generated by strong dilute defects," *Journal of Physical Chemistry B*, vol. 113, no. 12, pp. 3906–3909, 2009.

[55] L. Gao and T. McCarthy, "Contact angle hysteresis explained," *Langmuir*, vol. 22, no. 14, pp. 6234–6237, 2006.

[56] C. Extrand, "Model for contact angles and hysteresis on rough and ultraphobic surfaces," *Langmuir*, vol. 18, no. 21, pp. 7991–7999, 2002.

[57] H.-J. Butt, N. Gao, P. Papadopoulos, W. Steffen, M. Kappl, and R. Berger, "Energy dissipation of moving drops on superhydrophobic and superoleophobic surfaces," *Langmuir*, vol. 33, no. 1, pp. 107–116, 2016.

[58] B. Bhushan and Y. Jung, "Natural and biomimetic artificial surfaces for superhydrophobicity, self-cleaning, low adhesion, and drag reduction," *Progress in Materials Science*, vol. 56, no. 1, pp. 1–108, 2011.

[59] B. Samuel, H. Zhao, and K.-Y. Law, "Study of wetting and adhesion interactions between water and various polymer and superhydrophobic surfaces," *Journal of Physical Chemistry C*, vol. 115, no. 30, pp. 14852–14861, 2011.

Chapter 10

A Universal Capillary-deflection Based Adhesion Measurement Technique [1]

10.1 Overview

Hypothesis

Contact angle goniometry suffers from inherent optical challenges such as scattering and diffraction near the triple contact line (TCL) rendering erroneous results. Alternatively, the cantilever-based direct adhesion measurement was constrained to low-energy surfaces to date due to the inability of the probe droplet to retract (pull-off) from high-energy surfaces completely. The present study revisits the cantilever approach from a fundamental physical perspective and generalizes the approach to render it wettability invariant.

Experiments

The adhesive wetting interaction between a probe droplet (attached to a cantilever) with the test substrate is recorded with a high-speed camera. Image processing and subsequent

[1] Adapted with permission from Shyam, S*; **Misra, S***; Mitra, S.K. *J. Colloid Interface Sci*, 630 (2023) pp. 322-333. *: Equally contributing first-authors.

motion analysis enable us to accurately calculate the adhesion force (in the sub-micron range) exhibited by the test substrate.

Findings

We experimentally demonstrate the contact line depinning (and not the droplet pull-off) to be the only prerequisite for accurately quantifying the characteristic adhesion force. We also reveal that depinning precedes the onset of cantilever retraction due to the inertia effect. Further, we establish that the characteristic adhesion corresponds to zero acceleration of the cantilever and not to its maximum deflection. The inferences of the study will be beneficial in the rational design of direct wetting characterization methods for any substrate.

10.2 Introduction

An accurate understanding of the wetting signature of liquid-solid interactions has been an area of great interest owing to its tremendous implications in many contemporary engineering applications such as ink-jet printing, self-assembly, water transport, and many more [1–9]. For instance, a fundamental understanding of the adhesive interactions between toner and the print surface is of prime importance pertaining to the development of the printing process in general [10]. Similarly, biological and synthetic surfaces usually present inhomogeneity in texture, thereby leading to spatial heterogeneity in wetting properties. Therefore, accurate spatial estimation of the wetting interaction between such substrates and liquid is important for the fundamental understanding of various physical processes such as droplet mobility, condensation, and many more [11–14].

To date, contact angle goniometry has been accepted as the golden standard for the characterization of liquid-solid wetting interactions [15, 16]. With a history of more than a century, the characterization of a substrate via advancing, receding, and static contact angle is still widely accepted as benchmark wetting behaviour [10, 17, 18]. However, goniometry suffers from significant imaging challenges arising from optical noise caused by

scattering and diffraction near the three-phase contact line [19–23]. It leads to inaccurate identification of the baseline of the droplet, thereby causing the propagation of substantial systematic errors [24] in measurement. It is worth mentioning that in superhydrophobic surfaces, an error of one pixel in baseline identification can lead to almost a 300% error in estimating the adhesion force [24–26]. Further, contact angle goniometry provides only an indirect estimation of the adhesion & friction forces, which is often empirical [17].

Due to these shortcomings, recent research attention shifted towards direct quantification of wetting forces, essentially for an accurate understanding of the liquid-solid wetting interactions [27–32]. Researchers have shown that a microbalance coupled with a CCD (charge coupled device) camera can effectively characterize a substrate [33]. Similarly, other precision-based techniques, like atomic force microscope (AFM) [34–37], piezoelectric sensor [38], acoustic sensor [39], and many more [40–43], have also garnered attention amongst researchers worldwide. Despite their accuracy, all the approaches mentioned above suffer from complex protocols and expensive instrumentations. A few researchers have shown a possible way to tactfully translate the AFM-based approach to a cantilever-based sensor technique for a simple yet accurate estimation of the wetting characteristics [27, 31, 44–52].

In the cantilever-based approach, a micro-droplet attached to the tip of a polymeric cantilever is used for probing the adhesion and frictional characteristics of substrates [53, 54]. The force acting on the droplet is calculated from the deflection of the cantilever. After sensing the maximum adhesion force, the probe droplet is pulled-off from the substrate by the retracting cantilever in this method. It is important to mention that the pull-off is realizable only with low-energy surfaces for which droplet-substrate adhesion forces are small. However, for substrates with moderately high surface energies, the pull-off of the probe droplet (by the cantilever) is not possible. As will be shown later in this work, on such surfaces, the droplet splits into two parts: one remains attached to the characterizing substrate while the other part is extracted by the cantilever. It is to be emphasized here that the event of the pull-off of the probe droplet from the substrate has been an essential requirement of the cantilever-based adhesion measurement methodology. Researchers attribute the force exhibited by the cantilever at the pull-off stage as the characteristic adhesion force [31]. Thus, the absence of the pull-off stage on surfaces with

relatively higher energies has constrained the applicability of this method to low-energy, (super)hydrophobic surfaces. To date, the suitability of this method applied to high-energy surfaces remains completely unexplored.

In this work, we elucidate for the first time a generalized methodology for direct force measurement of the liquid-solid wetting interactions using the cantilever-based approach, which is applicable over a broad surface energy spectrum (ranging from hydrophilic to superhydrophobic). We show that by accurately tracking the contact line of the probe droplet, the depinning point can be observed. By motion analysis, we correlate the depinning dynamics of the contact line with the motion of the cantilever. We show that the temporal instance at which the acceleration of the cantilever equates to zero marks the depinning of the probe droplet from the target substrate. We argue that the corresponding force at the instant of zero acceleration is the characteristic adhesion force exhibited by the substrate. As such, the whole study is divided into four parts. In the first part, we explore the cantilever-based adhesion measurement methodology for high-energy substrates, clearly delineating all the available zones. In the second part, we explore the depinning dynamics of the probe droplet on a high-energy substrate in greater detail, which enables the generalization of the approach. In the third part, we reaffirm the validity of the proposed hypothesis by benchmarking the adopted methodology to a different set of experimental situations. Further, in the last part of the study, we comment on some critical insights regarding the applicability of the methodology for low-energy substrates. We believe this work reports some significant conceptual advances towards force-based direct wetting characterization, and suitable adaptation of the demonstrated framework will enable surface energy invariant characterization of liquid-solid wetting interactions. Further, owing to its simplicity and generalizability, it also bears the potential to emerge as a simple yet more accurate alternative to optical goniometry.

10.3 Experimental Section

Method

We show in Figure 10.1 the schematic representation of the capillary-based adhesion characterization methodology. The experimental setup consists of a polymeric capillary (which is used as a cantilever), a probe droplet, a test substrate, and a linear actuator. First, a probe droplet of de-ionized (DI) water is dispensed onto the tip of the cantilever. The volume of the probe droplet is 5 μl, if not mentioned otherwise. A polymeric capillary tube length of 70 mm, and a diameter of 410 μm are used as a cantilever. Prior to the measurement, the cantilever is calibrated, rendering a spring constant of k $\sim$ 305$\pm$6.1 nN/μm [55]. Readers are referred to section H.5 of Appendix H for the calibration details of the cantilever. The test substrate (placed on a linear actuator) approaches the probe droplet at a prescribed velocity, U(0.1 mm/s $-$ 0.5 mm/s) and undergoes a series of stages, i.e., snap-in, holding, retraction of the substrate, and a complete/partial detachment of the probe droplet, as can be observed from Figure 10.1(a). The linear actuator enables us to control the translational velocity of the substrate during its approach and retraction to/from the cantilever probe. The substrate is directly mounted on the actuator and translates at the same velocity as the linear actuator. The individual stages of the measurement cycle are discussed in detail in Section 3. Due to the adhesive interaction between the probe droplet and the test substrate, the cantilever undergoes deflection.

The deflection of the cantilever can be further converted to the adhesion force experienced by the probe droplet using the following equation,

$$\Delta X = X_0 - X(t) \tag{10.1}$$

$$\boldsymbol{F} = k\Delta X \tag{10.2}$$

where k, X_0, $X(t)$ denotes the spring coefficient of the cantilever, the equilibrium position, and instantaneous positions of the cantilever at time t, respectively. In Figure 10.1(b), we show a typical force curve calculated from Eq. (10.1)-(10.2), exhibiting all the

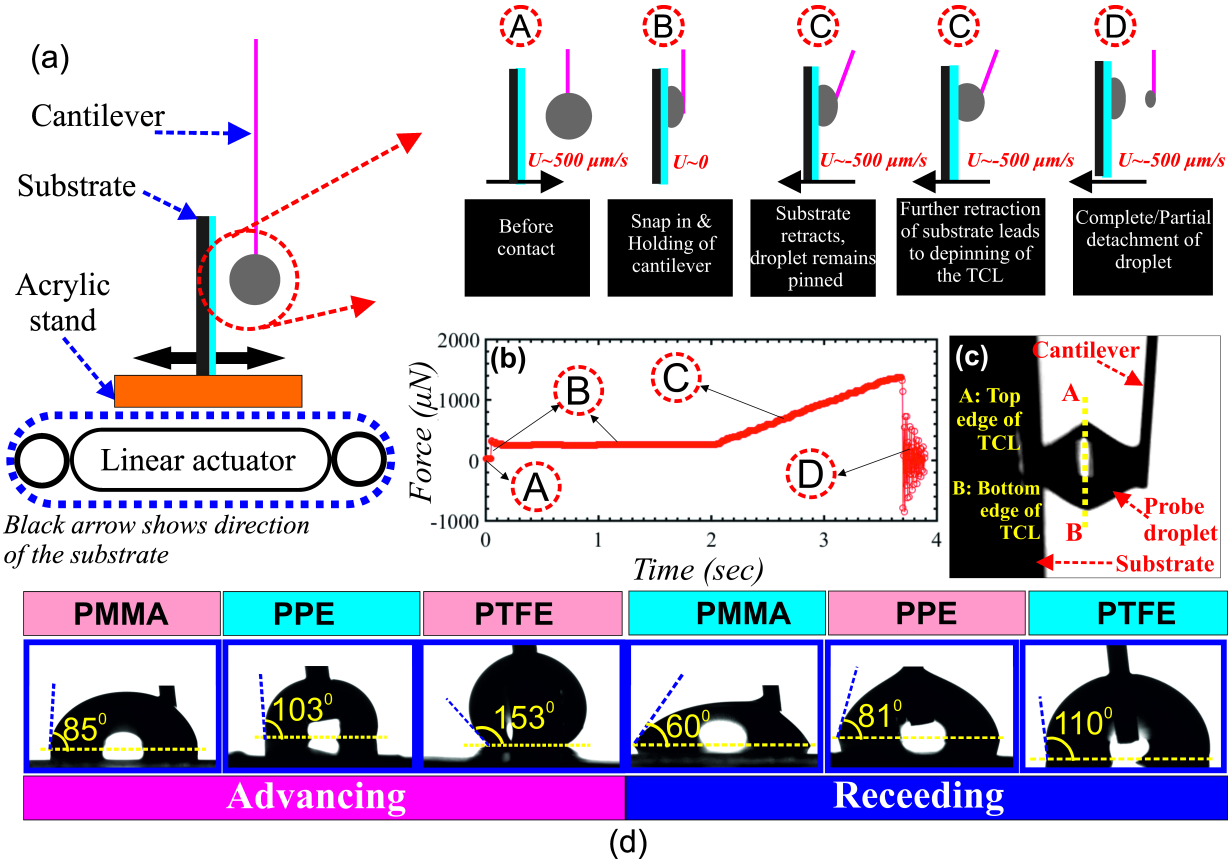

Figure 10.1: (a) Schematic representation of the adhesion measurement experimental setup. A substrate placed on a linear actuator approaches a cantilever containing the probe microdroplet. The subsequent stages of interactions are schematically represented as Stages A, B, C, and D, respectively. (b) Plot depicts a typical force-time curve that measures the adhesion characteristics of the substrates. The four previously highlighted stages, i.e., stage A, stage B, stage C, and stage D, are marked in the force-time curve. (c) Image shows a cantilever-adhered probe droplet snapped onto the test substrate. A and B positions refer to the top and bottom edge of the triple contact line (TCL), respectively. (d) Advancing and receding contact angle of DI water droplet on a PMMA, PP, and PTFE substrate.

reported stages (Stages A-D). Figure 10.1(c) shows a typical probe droplet snapped-in onto the substrate.

Materials

Three polymer substrates of dimensions 30 mm × 20 mm × 1.1mm each are used in the present work, namely, Polymethyl methacrylate (PMMA), Polypropylene (PP), and polytetrafluoroethylene (PTFE). These substrates are chosen because of the range of their surface energies. For instance, PTFE exhibits low surface energy, while PP and PMMA exhibit moderately high surface energies. Water droplets on PTFE, PP, and PMMA record static contact angles around 135°, 95°, and 70°, respectively. Before conducting each experiment, the substrates were cleaned with isopropanol and water. The substrates were then dried in an oven at 60°c for 30 minutes.

Contact angle measurement

We use an optical goniometer (DSA 30, KRÜSS USA) for the measurement of the static, advancing, and receding contact angles of a DI water droplet on the various substrates under consideration. For the measurement of static contact angle, a water droplet of volume 5 μl is dispensed onto the substrate, and the contact angles were obtained using the Young-Laplace fitting algorithm. For the measurement of the advancing contact angle, deionized water (15 mL) was injected onto the substrate at a rate of $\sim$ 0.1 mL/s and as the contact line advances, the value of the contact angle is recorded. Similarly, for the measurement of the receding contact angle, the liquid was aspirated from the droplet at a rate of $\sim$ 0.1 mL/s. The receding contact angle is measured as the contact line of the droplet recedes. Figure 10.1(d) shows the typical advancing and receding contact angles of a DI water droplet on PMMA, PP, and PTFE substrate, respectively. Each experiment is repeated three times to ensure repeatability.

Imaging system

We capture the wetting interaction between the probe droplet and the solid substrate with a high-speed camera (Photron Fastcam Mini). The high-speed camera is coupled with an 18-108 mm macro lens (Navitar ZOOM 7000). We use a brightness-controlled Fiber optic illuminator along with a diffuser as a backlight. Images are recorded at frame rates between 125 - 500 frames per second with a resolution of 1024×1024 pixels^2. The instantaneous motion of the cantilever tip is measured using an in-house developed code [56]. All the experiments are carried out at a controlled ambient temperature of around 21^0C and relative humidity of 60 %, respectively.

10.4 Results and Discussion

10.4.1 Droplet-Substrate Wetting Interactions on High Energy Substrate

In Figure 10.2(a)-(b), we show the displacement (X) vs. time (t) profiles of the cantilever tip during typical adhesion measurement cycles on different substrates. Here we explore the adhesion interaction of water droplets on two typical substrates, i.e., PMMA (Polymethyl methacrylate) (Fig 2(a)), and PP (Polypropylene) (Figure 10.2(b)). These two substrates are chosen specifically due to the range of wettability that they offer. For instance, PMMA exhibits a static water contact angle $\theta_s \sim 65^\circ - 70^\circ$, whereas $\theta_s \sim 95^\circ$ for PP (see Figure 10.1(d) for detailed wetting characterization of the test substrates). As can be observed from Figure 10.2(a)-(b), for both the test substrates, the $X - t$ curves exhibit characteristic similarity with four distinctively identifiable stages (termed stage A, stage B, stage C, and stage D) in each case. In stage A, the probe droplet is attached to the cantilever while the substrate approaches the droplet at a constant velocity, $U = 0.5$ mm/s. The position of the undeflected cantilever in this state is referred to as its equilibrium position, where the test substrate is yet to come in contact with the probe droplet. Subsequently, as the separation between the probe droplet and the test surface reduces below a nanometric critical threshold, the probe droplet experiences an attractive pull by the

substrate. Consequently, it gets snapped towards the approaching surface along with the cantilever tip. This is marked in the $X-t$ curve by a sudden deflection of the tip from its equilibrium position during the transition from stage A to stage B, as can be observed in Figure 10.2(a)-(b). The snap-in is followed by stage B (i.e., holding), in which the snapped-in droplet-substrate assembly is held stationary for around ten seconds. The holding stage ensures that the probe droplet spreads over the substrate in accordance with the involved surface energies. In stage C, the substrate is retracted in the opposite direction (away from the cantilever) with $U = -0.5$ mm/s. Note that throughout this work, we consider the direction of approach of the cantilever towards the surface to be positive X direction while retraction away from the surface is considered to be the negative X direction. In stage C, owing to the droplet-surface adhesive interaction, the tip of the cantilever starts moving (deflecting) away from its equilibrium position along with the probe droplet, which remains adhered to the retracting test substrate. However, beyond a critical point, any further retraction of the substrate leads to depinning of the three-phase contact line of the probe droplet. Beyond this point, the deflected cantilever tip starts returning to its equilibrium position, which is opposite to the direction of the substrate retraction.

It is important to note here that depending on the surface energy (γ) of the test substrate, the probe droplet can encounter two possible fates during the retraction of the substrate. In the first scenario, when the cantilever retracts from the substrate, it brings the entire probe droplet along, leading to its complete detachment from the test substrate. This is commonly encountered on low-surface-energy/ (super)hydrophobic substrates (e.g., on PTFE in our experiments), where the droplet-substrate adhesion is typically low. We discuss the adhesion measurement methodology on a PTFE substrate in greater detail in the last section of this work. However, on higher energy surfaces, a competition between the test substrate and the cantilever leads to a different fate of the droplet where it splits into two parts (e.g., on PMMA/PP as shown in Figure 10.2(c)-(d))- one remains attached to retracting surface while the other gets reclaimed by the detaching cantilever. This leads to the final stage (stage D) in the measurement cycle. In stage D, the cantilever is detached from the moving substrate, and it oscillates around its equilibrium position before coming to rest, as can be observed in Figure 10.2(a)-(b). It is worth mentioning here that the maximum deflection of the cantilever during the transition from stage C to

stage D (the magnitude of the minima, X_{min} of the $X-t$ profile, encountered during the transition from stage C to stage D, as seen from Figure 10.2(a)-(b)) is indicative of the droplet-surface characteristic adhesion. In our experiments, PMMA records a higher value of $|X_{\text{min}}|$ compared to PP, which stands in accordance with the order of surface energies(γ) where γ_{PMMA} (41.1 mN/m) $> \gamma_{\text{PP}}$ (29.6 mN/m) [57].

Notably, the research on cantilever-based adhesion measurement, which has essentially been limited to characterizing low-energy surfaces to date, marks the force corresponding to the pull-off event (i.e., the instant at which the probe droplet snaps off from the surface in its entirety) as the characteristic droplet–surface adhesion force. Also, the pull-off has conventionally been correlated to the maximal deflected state of the cantilever. However, the pull-off stage, where the probe droplet completely detaches from the test substrate, is absent on high-energy substrates (e.g., PMMA and PP), as can be clearly observed in Figure 10.2(a)-(d). The absence of the pull-off triggers an intriguing question: "*How do you characterize a higher energy substrate following the cantilever-based adhesion measurement technique, where the pull-off stage is absent?*".

In Figure 10.2(e), we show the force-time curves corresponding to the $X-t$ curves (Figure 10.2(a)-(b)) of the cantilever for all the test substrates. The force recorded by the cantilever, $\boldsymbol{F}$, could be calculated from the deflection profile $x(t) : |\boldsymbol{F}| = k\,|X|$ where k is the spring constant of the cantilever. Qualitatively, the adhesion forces on different test substrates are in accordance with their surface energies. But the main complication lies here with the inference of the characteristic adhesion force. As such, the question still remains: *Which point in the force-time curve should we refer to as the* characteristic *adhesion force* ($\boldsymbol{F}_{adh}$)*?* We have already shown in the preceding discussion that only partial retraction of the probe droplet is realizable on higher energy substrates, and there is no pull-off stage. Thus from a general perspective, the question remains: *Does the peak of the* $|\boldsymbol{F}| - t$ *curve, which corresponds to the maximum deflected stage of the cantilever, implies the characteristic adhesion,* $\boldsymbol{F}_{adh,}$*? And if it is so, then how does it translate to higher energy surfaces (e.g., PMMA/PP) where the maximum deflected state of the cantilever does not correspond to the event of pull-off and therefore has no physical significance either?* These questions remain unanswered in the literature and form the fundamental basis of our present investigation.

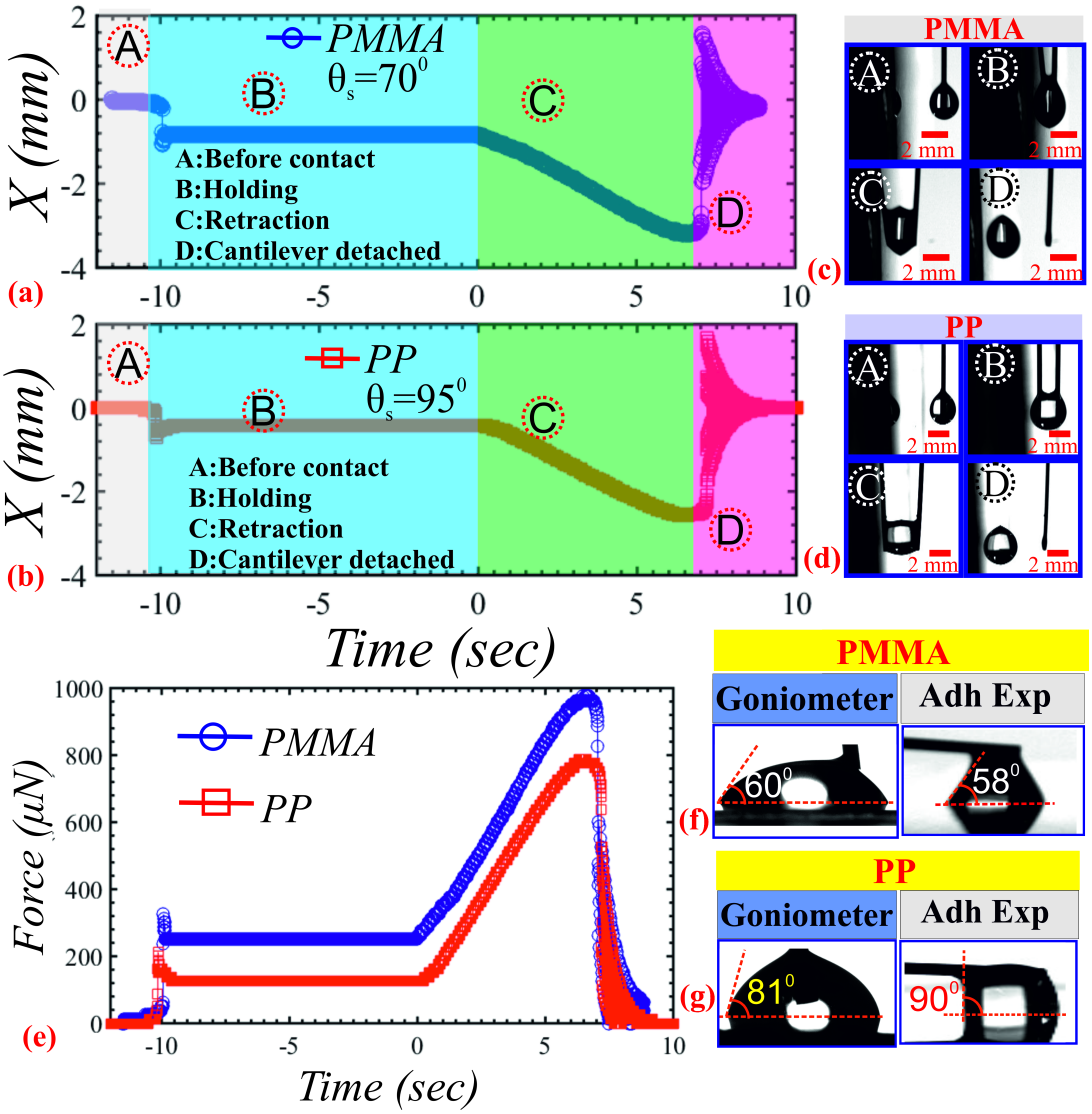

Figure 10.2: Displacement(X)-time(t) curves of the cantilever tip for (a) PMMA, (b) PP, extracted from high-speed images captured during a typical adhesion measurement experiment. Snapshots of the individual stages are referred to as A, B, C, and D for (c) PMMA, (d) PP. (e) Absolute Force(F)-time(t) curves for PMMA and PP substrates estimated from the deflection profile presented in (a-b), Receding contact angle measured with contact angle goniometer and during adhesion experiments for (f) PMMA, and (g) PP.

It should be mentioned here that on both PMMA and PP, although the probe droplet could not be completely detached from the surface, we were able to confirm the depinning of the three-phase contact line (TCL) of the probe droplet before the droplet splits. Further, we also noticed a close match (see Figure 10.2(f)-(g)) between the contact angle of the probe droplet at the moment of depinning of TCL and the receding contact angle of water measured on the target substrates using contact angle goniometry. It is well-established in the wetting literature that the adhesion force between a droplet and a target substrate is a function of the receding contact angle [10, 58–60]. Therefore, we argue that cantilever-based adhesion characterization of high-energy surfaces should not be restricted by an incomplete detachment of the probe droplet. Rather, as long as we can confirm depinning of the TCL of the probe droplet and capture the deflection of the cantilever at that temporal instance, we should be able to estimate the characteristic droplet-surface adhesion from that information alone. This fact, in particular, enables us to generalize the methodology for substrates over a broad spectrum of surface energies. Important to note that the occurrence of TCL depinning prior to droplet splitting/cantilever detachment makes the fate of the probe droplet after cantilever detachment irrelevant from the perspective of adhesion characterization. As long as the TCL of the probe droplet depins before the cantilever probe detaches from the substrate, the methodology remains independent of the morphological evolution of the probe droplet (i.e., splitting vs. complete retrieval from the test substrate), which is consequent of the adhesive-cohesive interactions between cantilever-probe droplet-test substrate triad.

However, despite the conceptual advancement, the method remains reliant upon accurate detection of the onset of TCL motion, which is susceptible to similar sets of imaging uncertainties and subsequent inaccuracies (as incurred in contact angle goniometry) due to the optical distortions near the contact line vicinity [60]. Nevertheless, tracking the tip of the cantilever from optical images is a much more reliable alternative than tracking the TCL. This leads us to another critical question: *Is there a way to correlate the depinning initiation with the cantilever motion? If so, how?*

10.4.2 Determination of the characteristic Adhesion force: correlation with the cantilever motion

To find an answer to these fundamental questions, we separately track and correlate the cantilever deflection during stage C and the TCL motion of the probe droplet on PMMA. We specifically choose PMMA due to its high surface energy, which has remained a research gap to date on cantilever-based adhesion measurement. We show in Figure 10.3(a) the time-resolved snapshots of the cantilever adhered probe droplet snapped onto the substrate. We mark the position of the cantilever's tip as $X = 0\ px$, the moment the probe droplet gets snapped in onto the substrate. We could clearly observe from Figure 10.3(a) that initially (during the retraction phase of the substrate), the cantilever gets deflected in the negative-X direction; however, beyond a particular deflection, the cantilever initiates its motion in the opposite direction (see the snapshots corresponding to $t = 7.01$ s) of the substrate's motion, i.e., the positive-X direction.

To further understand the involved dynamics, we plot the grayscale intensity value across the yellow line AB (see Figure 10.3(a)) in Figure 10.3(b), which covers the projected footprint of the probe droplet on our plane of observation. Note that the line AB should intersect with the triple contact line of the adhered probe droplet twice, and at both these intersection points, a grayscale intensity $I_{gray} \sim 0$ is expected. As one progresses from $A - B$, we can see the intensity value drops to $I_{gray} \sim 0$, indicating the top edge of the triple contact line (see Figure 10.3(a)-(b) for details). Following this, we could see a rise in the intensity value. This rise in the intensity value is due to the reflection of light and does not hold a real physical significance. As we progress towards B, we could see the intensity value again drops to $I_{gray} \sim 0$. This marks the location of the bottom edge of the triple contact line (see Figure 10.3(a)). Thus the plot gives us an idea of pinned diameter of the probe droplet in pixels. For a particular time, if we could measure the number of pixels between the top and bottom edge of the triple contact lines, we should be able to estimate the contact line diameter and the initiation of the contact line depinning. As can be observed from Figure 10.3(b), for $t \sim 0\ s$ and $t \sim 2\ s$, the contact line diameter remains the same. However, the diameter starts changing at $\sim 4.3\ s$, indicating that the TCL has already depinned. Note that the cantilever reverses its motion only beyond $t \sim$

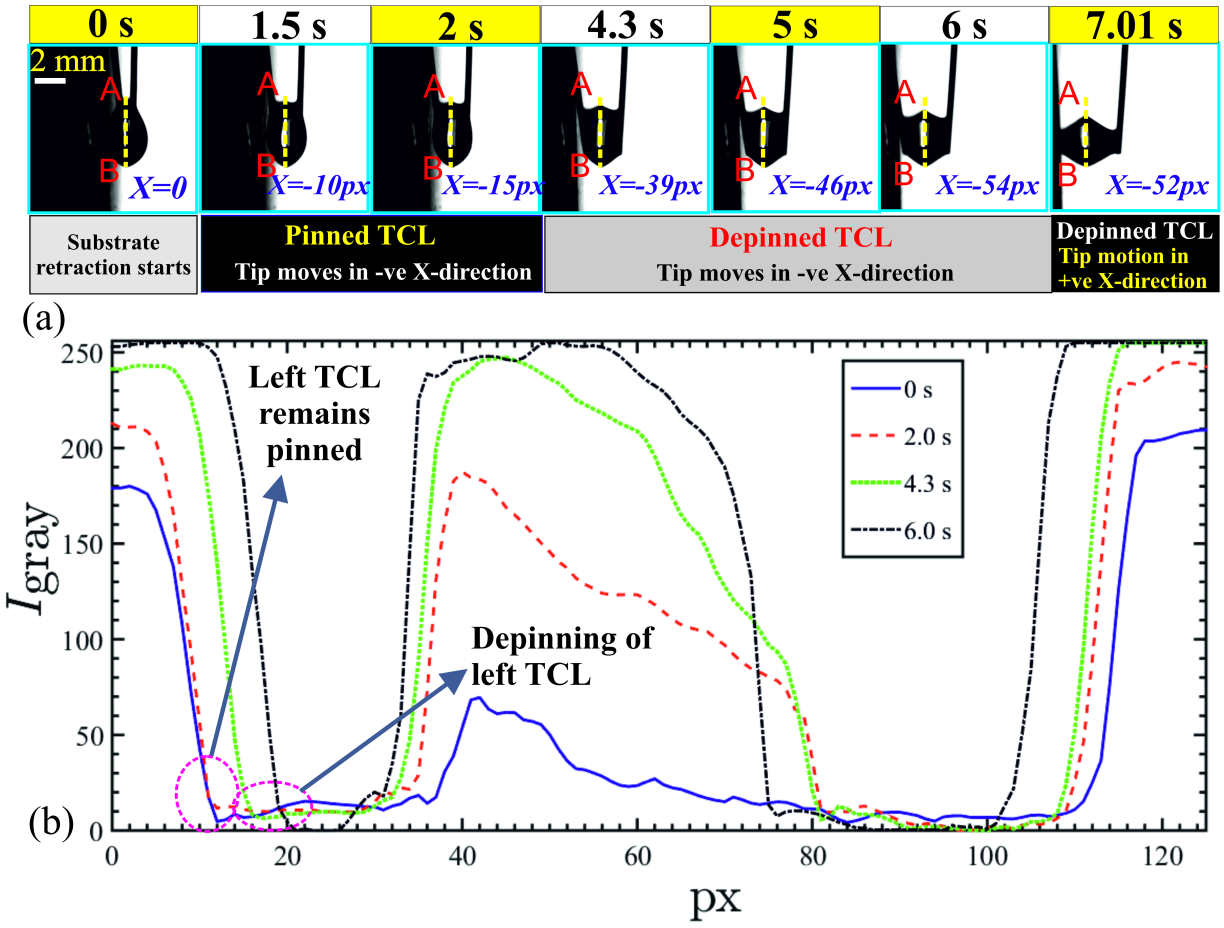

Figure 10.3: (a) Time-resolved snapshots of substrate adhered probe droplet-cantilever assembly showing the motion of the TCL and the tip of the cantilever, $X = 0$ reflects the position of the cantilever tip at $t = 0$ s. Increasing values of X indicate the cantilever tip moves along with the retracting substrate. Reducing values of X, indicates the cantilever tip's motion in the opposite direction of the substrate's motion. (b) Variation of the grayscale intensity (I_{gray}) along the yellow dotted line as highlighted in (a) at various temporal instances. $I_{gray} \sim 0$, indicates the triple contact line. The line AB is chosen along the line of symmetry of the probe droplet and its reflection on the substrate, which allows us to accurately and unambiguously identify the projected TCL at each presented time instance.

7.01 s. Thus, to sum it up, Figure 10.3(a)-(b) points towards a temporal gap between the initiation of the depinning of the contact line ($t \sim 4.3$ s) and the reversal motion of the cantilever (beyond $t \sim 7$ s).

Further, we could confirm from the bright field visualization videos that the TCL depins at $t \approx 4$ s. while the cantilever reverses its direction of motion at $t \approx 6.6$ s. As mentioned previously, it indicates a prominent time gap Δt between contact line depinning and maximum deflection of the cantilever ($\Delta t = 2.6\ s$ for water-PMMA pair). It means that even after depinning of the contact line of the probe droplet, the cantilever continued to move in the same direction as the retracting substrate for a brief period of time, as can be seen in the snaps corresponding to $t \sim 4.3$ s, $t \sim 5$ s, $t \sim 6$ s in Figure 10.3(a). The cantilever reverses its motion only after a substantial time gap. In other words, the effect of the depinning of TCL is reflected on the cantilever's motion only after a physical span of time.

To further understand the time gap between the TCL depinning and the cantilever receding, we performed a detailed motion analysis of the tip of the cantilever. In this analysis, a 5^{th} order polynomial function was fitted to the time-resolved trajectory of the tip (during stage C) with an adjusted R-square value of 0.9998. A fitting function was used here because the experimental data is intermittent in nature. If used as is, it would result in spurious unphysical oscillations once we differentiate it to obtain velocity/acceleration profiles. To decide the order of the polynomial, we perform fitting with polynomials with different orders (m) in the range of $m = 3$ to $m = 9$ and note that only beyond order $m = 5$, the fitted polynomial reasonably approximates the experimental data. Further, to avoid overfitting driven unphysical oscillations, we analyzed the change in the squared residual of the fit with the order of polynomial and have concluded that an order higher than fifth does not significantly improve the quality of the fit (see Appendix H section H.1).

We use the fitted polynomial to estimate the velocity ($\dot{X} = \frac{dX}{dt}$) and acceleration ($\ddot{X} = \frac{d^2X}{dt^2}$) of the tip of the cantilever. The temporal variations of X, $\dot{X}$, $\ddot{X}$ and the diameter (d) of the probe droplet (for stage C, i.e., the retraction phase of the substrate), are plotted in Figure 10.4. The contact diameter (d) corresponds to the base diameter of the adhered probe droplet on the substrate. Two critical points of physical relevance,

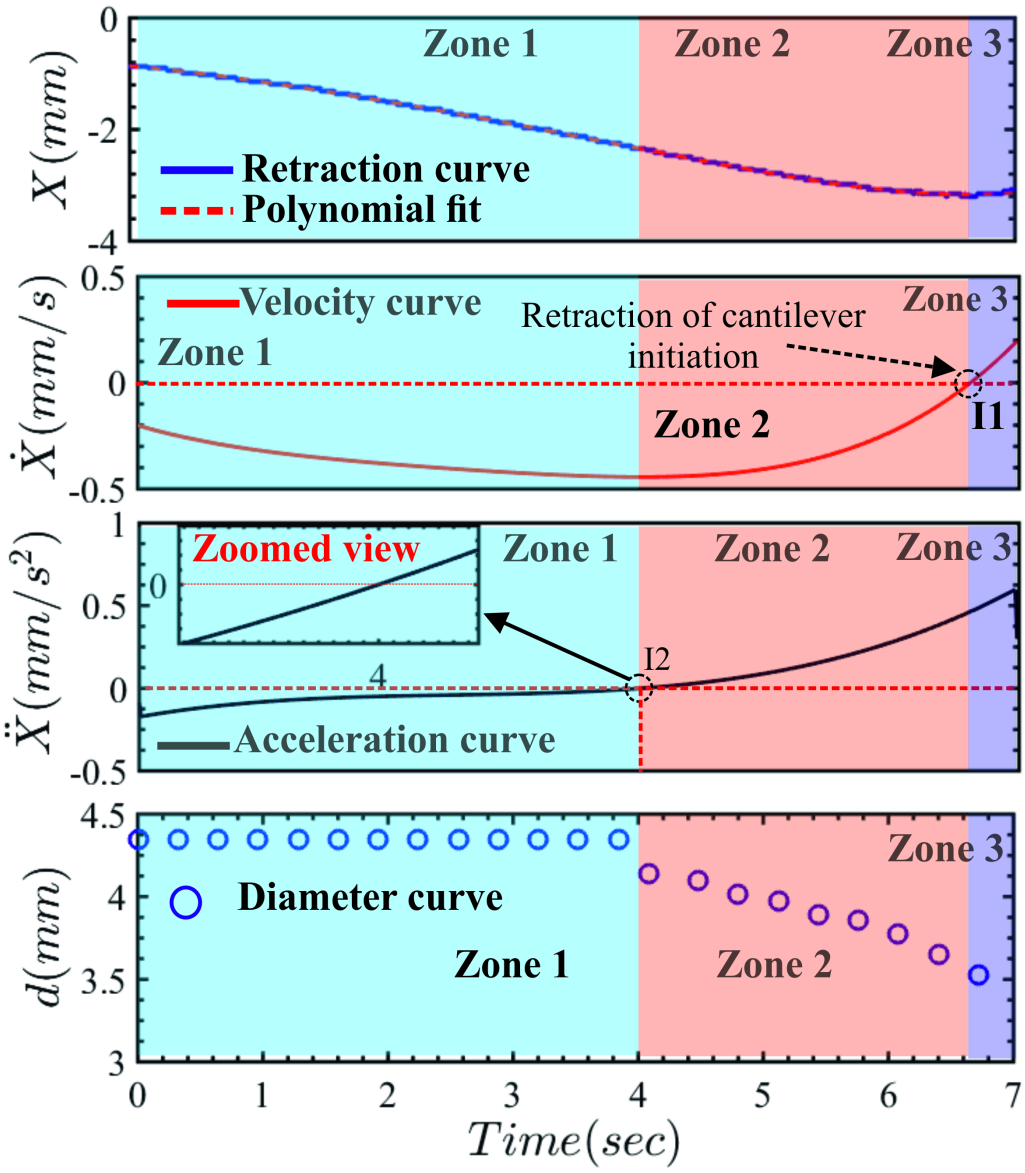

Figure 10.4: Temporal variation of the displacement (X), velocity ($\dot{X}$) and acceleration ($\ddot{X}$) of the cantilever tip and the contact diameter of the probe droplet during the retraction of the test substrate (i.e., stage C). The curves are divided into Zones I, II, and III with respect to points $I1$ and $I2$. $I1$ indicates the velocity of the cantilever tip, $\dot{x} = 0$. $I2$ indicates the acceleration of the cantilever's tip, $\ddot{X} = 0$.

marked by $I1$ and $I2$, could be noted in Figure 10.4. I1 corresponds to the point of zero velocity of the cantilever tip. It physically represents the instance of maximum deflection of the cantilever at which the direction of motion of the cantilever reverses, i.e., the cantilever starts returning to its equilibrium position. I2 represents the point of zero acceleration of the cantilever. Comparing $\ddot{X} - t$, curve vis-à-vis $d - t$, we could comprehend that the point of depinning of TCL (marked by the first noticeable decrease in d) coincides with point I2, the point of zero acceleration of the cantilever.

The observed trend of acceleration reveals that at the beginning of the retraction phase (of the substrate), the cantilever accelerates in the negative-X direction as the retracting substrate pulls the cantilever (Zone I) along with the probe droplet. The value of $\left|\ddot{X}\right|$ gradually decreases as the substrate moves further apart from the initial position of contact. At the moment of depinning (point I2 in $\ddot{X} - t$, curve), the cantilever's acceleration becomes zero, and beyond that, it starts accelerating in the opposite (positive-X) direction. This observation indicates that the point of depinning corresponds to a switchover in the cantilever's inertia from negative-X direction to positive-X direction. Further, it also explains the observed time lag between the depinning of the droplet and the reversal of the cantilever's direction of motion. The motion of the cantilever in the negative-X direction is sustained for a brief period even after depinning. However, after contact line depinning, the cantilever starts slowing down, as indicated by its recorded acceleration in the positive-X direction and gradual reduction in $\left|\dot{X}\right|$ in zone 2 (Figure 10.4). We can therefore substantiate that the point of zero acceleration of the cantilever tip (marked by I2) corresponds to contact line depinning and the onset of TCL motion. Thus, we can correlate it to the occurrence of $\boldsymbol{F}_{adh}$. This is a particularly enabling conclusion as it eliminates the requirement of optically tracking the TCL. However, we should mention that an accurate quantitative correlation between the adhesion force/the work of adhesion and the macroscopic wetting parameters (i.e., static/dynamic contact angle) is indeed a tricky one, as noted in past literature [60]. The seminal work of Butt et al. [60] outlines a theoretical approach to correlate tensile adhesion with droplet geometry by assuming axisymmetric profile shape and solving the Laplace equation. The present work does not attempt to address that. Although we analyzed the temporal evolution of the left and the right contact angle of the probe droplet (see Figure H.6 of Appendix H) during the adhesion measure-

ment cycle, however, we could not observe any strong correlation between the contact angle and the adhesion force. Direct measurement of adhesion force, as demonstrated in the present work, thus remains a more sensitive and accurate alternative for quantifying the wetting properties of substrates with varied wettability.

10.4.3 Depinning corresponds to $\ddot{X} = 0$: Verification of Universality

In the previous subsection, we have established a correlation between the initiation of the depinning and the cantilever's motion. We have shown that the moment at which the TCL of the probe droplet gets depinned, the cantilever demonstrates zero acceleration. We also show that the inertia of the cantilever is critical in accurately characterizing the adhesion interaction as it directly influences the gap between the occurrences of zero acceleration and maximum deflection of the cantilever. To critically evaluate our hypothesis further, we conducted two different sets of experiments. In the first set, we have varied the volume of the probe droplet, while in the second one, we have altered the speed of approach/retraction of the test substrate by changing the translation velocity of the linear actuator. Both these events have direct implications on the inertia of the system and allow us to verify our hypothesis and, in turn, establish its universality, as described below.

Variation of the volume of probe droplet:

We carried out further experimentation with a different volume of the probe droplet to reconfirm that the depinning of the contact line of the probe droplet corresponds to $\ddot{X} = 0$ of the cantilever. We used PMMA as the test substrate, while the probe droplet volume was changed to 3μl. The basic intention of changing the volume of the probe droplet is to alter the overall adhesion force and, in turn, the inertia exhibited by the cantilever.

Figure 10.5 shows the deflection of the cantilever, its corresponding velocity $\left(\dot{X}\right)$ and acceleration$\left(\ddot{X}\right)$. As can be observed from Figure 10.5(a) (top right-inset), the cantilever acceleration becomes zero at $t = 3.24$ *sec*. The adhesion force corresponding to $\ddot{X} = 0$,

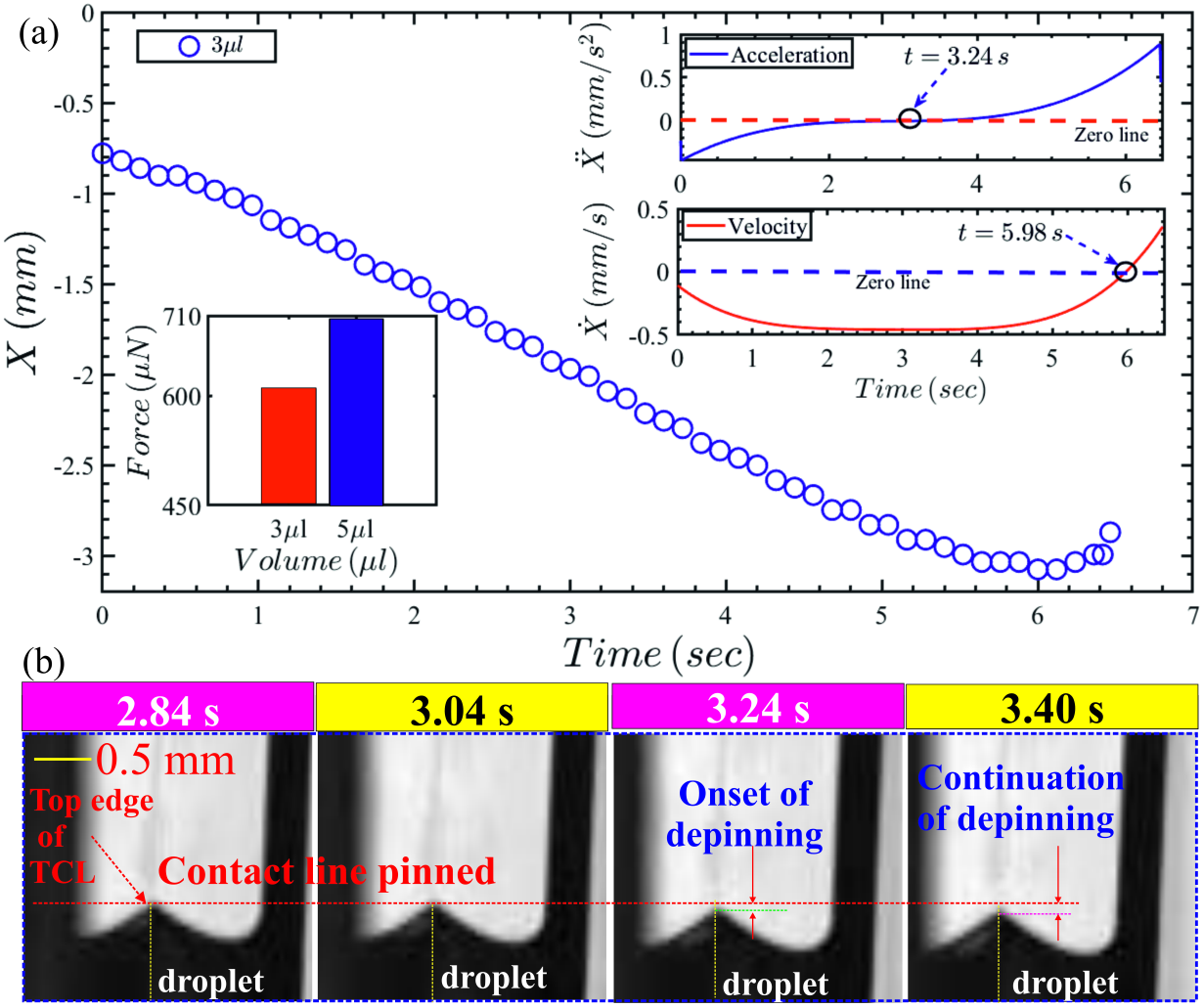

Figure 10.5: (a) Temporal variation of the displacement (X) of the cantilever tip. The top-right inset shows the velocity ($\dot{X}$) and acceleration ($\ddot{X}$) profiles of the cantilever tip with time t. Bottom-left inset shows the adhesion force exhibited by the PMMA-water pair for different volumes of the probe droplet. The adhesion force is measured corresponding to $\ddot{X} = 0$. (b) Snapshots show the temporal evolution of the contact line of the probe droplet around the temporal vicinity of the point of zero acceleration (t = 3.24 s). The red-dotted line marks the position of the top edge of the triple contact line corresponding to 2.84 seconds. The volume of the droplet is 3 μl.

equals $\sim$ 610 μN, while the characteristic adhesion force for a 5 μl probe droplet is $\sim$ 705 μN (see Figure 10.5(a), bottom-left inset). Thus, as argued before, the alteration in the volume of the probe droplet directly influences the adhesion force, thereby affecting the inertia of the cantilever probe.

From the preceding discussion, it is evident that the acceleration of the cantilever becomes zero at $\sim$ 3.24 seconds. Therefore, for our hypothesis to be true, the depinning of the contact line of the probe droplet should also be at 3.24 seconds. In Figure 10.5(b), we arrange the snapshots of the probe droplet's contact line in the temporal vicinity of 3.24 seconds. It can be clearly observed from Figure 10.5(b) that the depinning of the TCL of the probe droplet is also initiated at around 3.24 seconds. Although the characteristic adhesion force itself is different for various volumes of the probe droplet, our hypothesis regarding the coincident occurrence of zero acceleration and TCL depinning holds true either way.

Variation of the translation velocity of the substrate:

For these experiments, we choose three substrate velocities, $U = 0.1$ mm/s, 0.3 mm/s, and 0.5 mm/s respectively. If the characteristic adhesion force thus obtained from the cantilever deflection at the point of its zero acceleration is truly an intrinsic property of the droplet-substrate combination, it should remain invariant upon changing substrate speeds even though it has a direct impact on the inertia of the system. We show in Figure 10.6(a)-(f) the $X-t$, $\ddot{X}-t$ curve, and the characteristics adhesion force (see the bar graph in Figure 10.7) for the different substrate velocities, during the retraction phase of the cantilever. As can be observed from Figure 10.6(a)-(c), the $X-t$ curve is different for all the substrate velocities. Consequently, the time instance at which the acceleration of the cantilever becomes zero ($\ddot{X} \sim 0$) is different for all the cases as well. For instance, $\ddot{X} \sim 0$ at $t = 18.2$ s when the substrate velocity is maintained at 0.1 mm/s (Figure 10.6(d)), while it is 5.8 s (Figure 10.6(e)) and 4 s (Figure 10.6(f)) for $U =$ 0.3 mm/s and 0.5 mm/s, respectively.

Despite that, in calculating the force corresponding to this deflection (i.e., the point at which $\ddot{X} \sim 0$), we found almost identical values for all the cases. As can be observed from

Figure 10.7 although $\ddot{X}$ became zero at different temporal instances, the corresponding deflection, X, and therefore the estimated adhesion force, F_{adh} remains almost invariant upon changing substrate velocities. The characteristic adhesion force was estimated to be around 671 μN ($X \sim 2.21$ mm) 658 μN ($X \sim 2.17$ mm), and 705 μN ($X \sim 2.32$ mm) for the substrate velocities 0.1 mm/s, 0.3 mm/s, and 0.5 mm/s respectively. This observation further justifies that the depinning of the contact line is indeed a property of the droplet substrate interaction and substantiates our hypothesis of characterizing the adhesion force from the deflection at the point of zero acceleration of the cantilever tip.

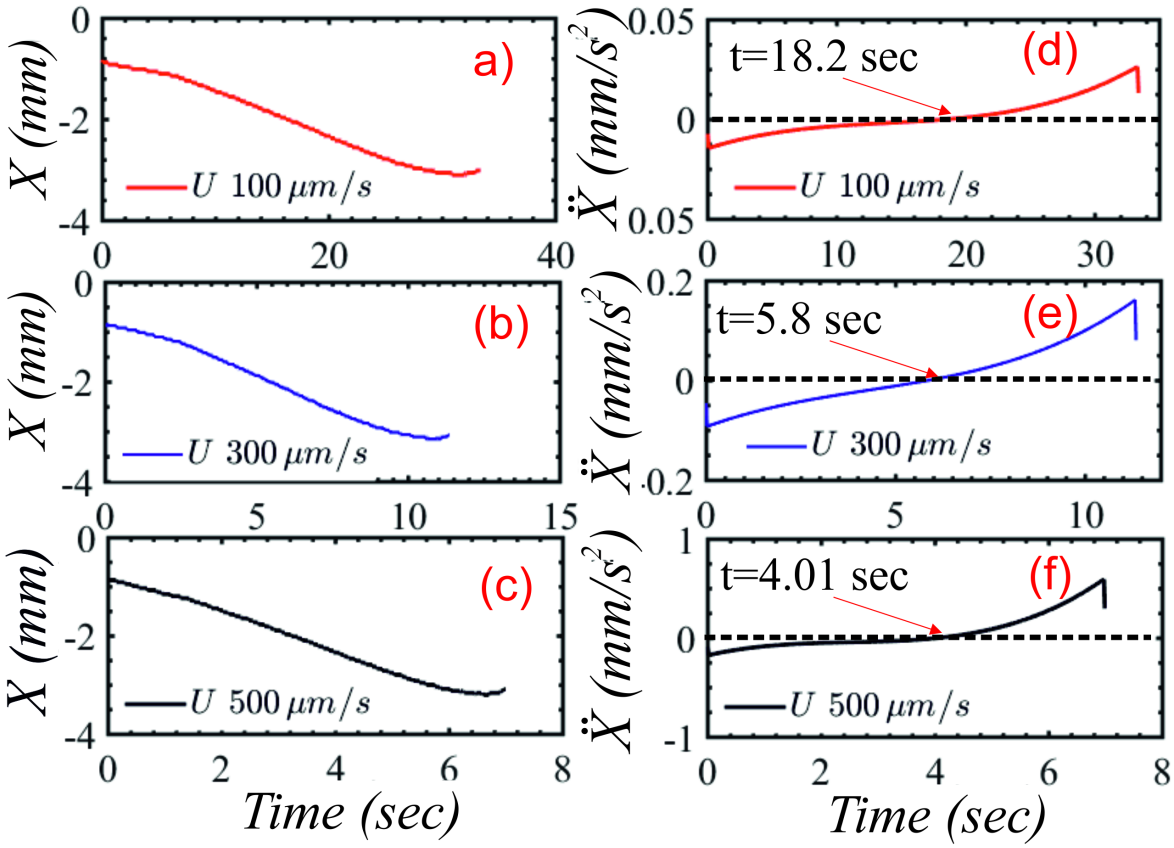

Figure 10.6: The retraction curves for substrate velocities (a) 0.1 mm/s, (b) 0.3 mm/s, (c) 0.5 mm/s . The acceleration profile of the cantilever tip during the retraction stage for substrate velocities (d) 0.1 mm/s, (e) 0.3 mm/s, (f) 0.5 mm/s. The size of the probe droplet is maintained at 5 μl for all the experiments.

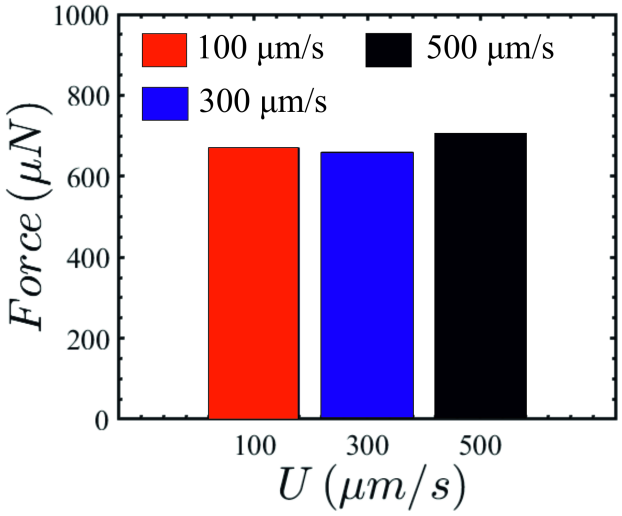

Figure 10.7: The characteristic adhesion force estimated from the deflection at the point of zero acceleration of the cantilever tip for substrate velocities of 0.1 mm/s, 0.3 mm/s, and 0.5 mm/s. The corresponding motion analysis of the cantilever tip is presented in Figure 10.6.

10.4.4 Adhesion Characterization of Low Energy Surfaces

The adhesion characterization of the low-energy substrate following cantilever-based methodology is well explored in numerous literature [31, 38, 45, 48]. In the present section, we revisit the adhesion measurement technique on a typical low-energy substrate, i.e., a PTFE substrate, and in doing so, we comment on the physical significance of the peak of the $F - t$ graph, the depinning point, and the pull-off stage in particular. The wettability characterization of PTFE substrate using contact angle goniometry is shown in Figure 10.1(d). We show in Figure 10.8(a) the measured force corresponding to the cantilever deflection. The $X - t$ curve of the deflecting cantilever tip is shown in the top inset of Figure 10.8(a). As mentioned previously, for low-energy substrates the probe droplet fully detaches from the substrate, thereby exhibiting all the reported stages, i.e., stages A, B, C, and D. Thus it was well accepted in the literature that, for low-energy substrates, the peak of the force-time graph (which presumably is coincident with the point of pull-off of

the probe droplet) corresponds to the characteristic adhesion.

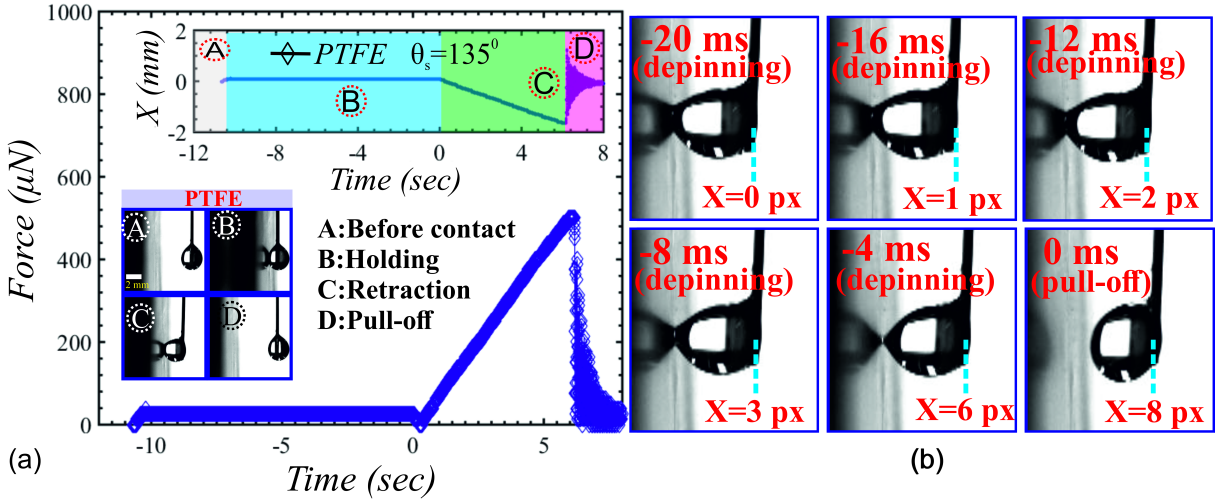

Figure 10.8: (a) Plot shows the force-time curve for a PTFE substrate. The top inset shows the displacement-time curve of the PTFE substrate. The shaded regions identify the various stages of the adhesion-measurement methodology, i.e., stages A, B, C, and D, respectively. The bottom inset shows the snapshots of the respective stages A, B, C, and D. (b) Time-resolved snapshots showing the cantilever motion in the temporal vicinity of the pull-off stage on PTFE. $t \sim 0\ ms$ marks the pull-off event. $X = 0$ indicates the position of the cantilever's tip at $t \sim -20\ ms$.

Here, we used high-speed imaging to study the interaction of the probe droplet with the PTFE substrate to check whether distinctly identifiable intermediate zones (e.g., depinning, maximum deflection or cantilever detachment) similar to higher energy surfaces are present on lower energy surfaces as well. Upon observing the phenomena at 250 frames per second, we found intermediate temporal instances at which the probe droplet remains in contact with the substrate while the cantilever has started receding, as can be observed in Figure 10.8(b). In Figure 10.8(b), we show the contact line motion of the probe droplet in the temporal vicinity of the pull-off stage. $t = 0$ refers to the instant the probe droplet is pulled-off from the substrate. The negative temporal instances indicate the preceding events. We mark the position of the cantilever tip at $t = -$ 20 ms as $X = 0$ pixel and subsequently

track the position of the tip in the interval of 4 ms till the point of detachment of the droplet from the surface ($t = 0$). As per our sign convention, increasing pixel values of X, indicates the motion of the cantilever tip in a direction opposite to the retracting substrate. It can be clearly observed that although the retraction of the cantilever has started, the probe droplet is still attached to the substrate. It implies that maximum deflection of the cantilever occurs slightly ahead of the pull-off event. Interestingly, as the cantilever retracts towards its equilibrium position, the contact line of the probe droplet continues to recede from the substrate, as evident from its shrinking contact diameter in Figure 10.8(b). Due to the high contact angle of the PTFE substrate, observing the initiation of the depinning phenomena becomes a very challenging task, therefore, we do not comment on this perspective. However, it is worth mentioning that the time gap between the onset of depinning and the pull-off phenomena is almost negligible on low-energy superhydrophobic surfaces due to the limited adhesion interaction between the PTFE substrate and the probe droplet. Thus the time delay between the initiation of depinning and the droplet pull-off becomes not so critical for low-energy substrates. In other words, for low surface energy substrates, the initiation of TCL depinning, the peak of the force-time curve, and the pull-off event almost coincide. As established in the preceding discussions, the time delay between these characteristic points becomes prominent only for higher energy substrates.

10.5 Conclusion

To summarize, the present work critically revisits, augments, and redefines the cantilever deflection-based direct force measurement framework towards a more accurate and wettability invariant characterization of droplet-surface adhesion interaction. The cantilever-based adhesion measurement technique to date has been limited to characterizing low-energy substrates, mainly due to the inability of the probe droplet to fully retract on high-energy surfaces [31, 45]. The present study generalizes this methodology, in particular, toward characterizing maximum substrate adhesion force over a broad surface energy spectrum. In doing so, we raise and subsequently answer some fundamental questions pertaining to the cantilever-based adhesion measurement approach.

We use three substrates with different characteristic wettability, namely, PMMA (hydrophilic), PP (hydrophobic) and PTFE (superhydrophobic), to demonstrate the wettability invariance of our adopted approach. Based on high-speed imaging and subsequent image processing, we quantify the adhesive interaction between the probe droplet and the test substrates. We provide direct experimental evidence of a time gap between the occurrence of maximum deflection of the cantilever ($x_{\min}$ in $x-t$ curve) and the event of pull-off of probe droplet. Important to mention that literature to date attributes the pull-off stage (of the probe droplet from the test substrate) as the occurrence of maximum deflection of the cantilever. The observed time-gap pinpoints the involved inaccuracies incurred in the conventional approach of characterizing adhesion ($\boldsymbol{F}_{adh}$) by pull-off of the probe droplet. The gap becomes more prominent as the surface energy of the test substrate is increased. Following this, we further demonstrate that even $x_{\min}$ does not correspond to $\boldsymbol{F}_{adh}$, as the depinning of TCL, the sole physical criterion with direct correspondence to $\boldsymbol{F}_{adh,}$ precedes the onset of the retraction of the cantilever by a prominent time gap. This insight, in particular, expands the applicability of the cantilever-based approach to higher energy surfaces, where we show that $\boldsymbol{F}_{adh}$ could be estimated just by detecting the depinning initiation of the TCL. Further, with detailed motion analysis, we also establish that the point of zero acceleration of the cantilever corresponds to the point of depinning of the TCL and, thus, to the point of occurrence of $\boldsymbol{F}_{adh.}$ It eliminates the need to optically track the TCL, which is often plagued by imaging challenges near the contact line.

We reaffirm our hypothesis regarding the coincident occurrence of depinning of probe droplet and zero acceleration of the cantilever by altering the size of the probe droplet. The prime intention of altering the size of the probe droplet is that it should change the overall inertia force experienced by the cantilever probe. We could verify from accurate high-speed visualization that although $\boldsymbol{F}_{adh}$ values are different for different volumes of probe droplet, the depinning initiation always coincides with zero acceleration of the cantilever. Further, we also establish that the characteristic adhesion force, $\boldsymbol{F}_{adh}$ estimated from the cantilever deflection at $\ddot{X} = 0$ is indeed an intrinsic property of the droplet-substrate combination by showing that $\boldsymbol{F}_{adh}$ remains invariant of changing substrate speed. . We have also demonstrated that the fate of the droplet after cantilever detachment, which is dictated primarily by an interplay between the surface energies of the test substrate-probe droplet-

cantilever triad, does not influence the definition of $\boldsymbol{F}_{adh}$. The characteristic adhesion is defined at the point of depinning of the droplet's triple contact line irrespective of whether the droplet splits into two or gets pulled-off from the substrate by the cantilever as a whole.

Further, from the execution perspective, the present methodology is general and straightforward. Simple tracking of the motion of the cantilever and subsequent computation of its acceleration, which can be automated, enable the user to characterize the ensuing maximum adhesion between the probe droplet and the test substrate, irrespective of the surface energies, which has remained a significant bottleneck in literature [31, 45, 49, 50]. Thus the generalized adhesion characterization framework demonstrated here provides a simple, fast, and accurate way of quantifying liquid-solid wetting interactions without any high-end instrumentation. The methodology also offers an alternative to contact angle goniometry in which the droplet-surface adhesion force is often calculated empirically [32].

References

[1] B. Qian and K. S. Breuer, "The motion, stability and breakup of a stretching liquid bridge with a receding contact line," *Journal of Fluid Mechanics*, vol. 666, pp. 554–572, 2011.

[2] A. A. Darhuber, S. M. Troian, and S. Wagner, "Physical mechanisms governing pattern fidelity in microscale offset printing," *Journal of Applied Physics*, vol. 90, no. 7, pp. 3602–3609, 2001.

[3] D. Bonn, J. Eggers, J. Indekeu, and J. Meunier, "Wetting and spreading," *Reviews of Modern Physics*, vol. 81, no. 2, pp. 739–805, 2009.

[4] R. L. Baldwin, "Temperature dependence of the hydrophobic interaction in protein folding," *Proceedings of the National Academy of Sciences of the United States of America*, vol. 83, no. 21, pp. 8069–8072, 1986.

[5] R. Zhou, X. Huang, C. J. Margulis, and B. J. Berne, "Hydrophobic collapse in multidomain protein folding," *Science*, vol. 305, no. 5690, pp. 1605–1609, 2004.

[6] G. M. Whitesides, J. P. Mathias, and C. T. Seto, "Molecular self-assembly and nanochemistry: A chemical strategy for the synthesis of nanostructures," *Science*, vol. 254, no. 5036, pp. 1312–1319, 1991.

[7] D. Chandler, "Interfaces and the driving force of hydrophobic assembly," *Nature*, vol. 437, no. 7059, pp. 640–647, 2005.

[8] X. Huang, C. J. Margulis, and B. J. Berne, "Dewetting-induced collapse of hydrophobic particles," *Proceedings of the National Academy of Sciences of the United States of America*, vol. 100, no. 21, pp. 11953–11958, 2003.

[9] B. J. Berne, J. D. Weeks, and R. Zhou, "Dewetting and hydrophobic interaction in physical and biological systems," *Annual Review of Physical Chemistry*, vol. 60, no. 1, pp. 85–103, 2009.

[10] B. Samuel, H. Zhao, and K. Y. Law, "Study of wetting and adhesion interactions between water and various polymer and superhydrophobic surfaces," *Journal of Physical Chemistry C*, vol. 115, no. 30, pp. 14852–14861, 2011.

[11] B. Bhushan, Y. C. Jung, and K. Koch, "Self-cleaning efficiency of artificial superhydrophobic surfaces," *Langmuir*, vol. 25, no. 5, pp. 3240–3248, 2009.

[12] P. Eberle, M. K. Tiwari, T. Maitra, and D. Poulikakos, "Rational nanostructuring of surfaces for extraordinary icephobicity," *Nanoscale*, vol. 6, no. 9, pp. 4874–4881, 2014.

[13] K. Rykaczewski, "Microdroplet growth mechanism during water condensation on superhydrophobic surfaces," *Langmuir*, vol. 28, no. 20, pp. 7720–7729, 2012.

[14] T. Mouterde, P. S. Raux, C. Clanet, and D. Quéré, "Superhydrophobic frictions," *Proceedings of the National Academy of Sciences of the United States of America*, vol. 116, no. 17, pp. 8220–8223, 2019.

[15] Thomas Young, "III. An essay on the cohesion of fluids," *Philosophical Transactions of the Royal Society of London*, vol. 95, pp. 65–87, 1805.

[16] P.-G. de Gennes, F. Brochard-Wyart, and D. Quéré, *Capillarity and Wetting Phenomena*. New York: Springer New York, 2004.

[17] C. G. Furmidge, "Studies at phase interfaces. I. The sliding of liquid drops on solid surfaces and a theory for spray retention," *Journal of Colloid Science*, vol. 17, no. 4, pp. 309–324, 1962.

[18] P. R. Waghmare and S. K. Mitra, "Contact angle hysteresis of microbead suspensions," *Langmuir*, vol. 26, no. 22, pp. 17082–17089, 2010.

[19] C. W. Extrand and S. I. Moon, "Contact angles of liquid drops on super hydrophobic surfaces: Understanding the role of flattening of drops by gravity," *Langmuir*, vol. 26, no. 22, pp. 17090–17099, 2010.

[20] J. A. Kleingartner, S. Srinivasan, J. M. Mabry, R. E. Cohen, and G. H. McKinley, "Utilizing dynamic tensiometry to quantify contact angle hysteresis and wetting state transitions on nonwetting surfaces," *Langmuir*, vol. 29, no. 44, pp. 13396–13406, 2013.

[21] J. T. Korhonen, T. Huhtamäki, O. Ikkala, and R. H. Ras, "Reliable measurement of the receding contact angle," *Langmuir*, vol. 29, no. 12, pp. 3858–3863, 2013.

[22] M. G. Cabezas, A. Bateni, J. M. Montanero, and A. W. Neumann, "Determination of surface tension and contact angle from the shapes of axisymmetric fluid interfaces without use of apex coordinates," *Langmuir*, vol. 22, no. 24, pp. 10053–10060, 2006.

[23] A. Kalantarian, R. David, and A. W. Neumann, "Methodology for high accuracy contact angle measurement," *Langmuir*, vol. 25, no. 24, pp. 14146–14154, 2009.

[24] S. Srinivasan, G. H. McKinley, and R. E. Cohen, "Assessing the accuracy of contact angle measurements for sessile drops on liquid-repellent surfaces," *Langmuir*, vol. 27, no. 22, pp. 13582–13589, 2011.

[25] K. Liu, M. Vuckovac, M. Latikka, T. Huhtamäki, and R. H. Ras, "Improving surface-wetting characterization," *Science*, vol. 363, no. 6432, pp. 1147–1148, 2019.

[26] M. Backholm, D. Molpeceres, M. Vuckovac, H. Nurmi, M. J. Hokkanen, V. Jokinen, J. V. Timonen, and R. H. Ras, "Water droplet friction and rolling dynamics on superhydrophobic surfaces," *Communications Materials*, vol. 1, no. 1, p. 64, 2020.

[27] A. Rana, A. Patra, M. Annamalai, A. Srivastava, S. Ghosh, K. Stoerzinger, Y. L. Lee, S. Prakash, R. Y. Jueyuan, P. S. Goohpattader, N. Satyanarayana, K. Gopinadhan, M. M. Dykas, K. Poddar, S. Saha, T. Sarkar, B. Kumar, C. S. Bhatia, L. Giordano, S. H. Yang, and T. Venkatesan, "Correlation of nanoscale behaviour of forces and macroscale surface wettability," *Nanoscale*, vol. 8, no. 34, pp. 15597–15603, 2016.

[28] V. Dupres, D. Langevin, P. Guenoun, A. Checco, G. Luengo, and F. Leroy, "Wetting and electrical properties of the human hair surface: Delipidation observed at the nanoscale," *Journal of Colloid and Interface Science*, vol. 306, no. 1, pp. 34–40, 2007.

[29] M. Delmas, M. Monthioux, and T. Ondarçuhu, "Contact angle hysteresis at the nanometer scale," *Physical Review Letters*, vol. 106, no. 13, p. 136102, 2011.

[30] S. Peppou-Chapman and C. Neto, "Mapping Depletion of Lubricant Films on Antibiofouling Wrinkled Slippery Surfaces," *ACS Applied Materials and Interfaces*, vol. 10, no. 39, pp. 33669–33677, 2018.

[31] M. J. Hokkanen, M. Backholm, M. Vuckovac, Q. Zhou, and R. H. Ras, "Force-Based Wetting Characterization of Stochastic Superhydrophobic Coatings at Nanonewton Sensitivity," *Advanced Materials*, vol. 33, no. 42, p. 2105130, 2021.

[32] T. Eastman and D. M. Zhu, "Adhesion forces between surface-modified AFM tips and a mica surface," *Langmuir*, vol. 12, no. 11, pp. 2859–2862, 1996.

[33] Y. Sun, Y. Li, X. Dong, X. Bu, and J. W. Drelich, "Spreading and adhesion forces for water droplets on methylated glass surfaces," *Colloids and Surfaces A: Physicochemical and Engineering Aspects*, vol. 591, p. 124562, 2020.

[34] R. M. A. Sullan, A. B. Churnside, D. M. Nguyen, M. S. Bull, and T. T. Perkins, "Atomic force microscopy with sub-picoNewton force stability for biological applications," *Methods*, vol. 60, no. 2, pp. 131–141, 2013.

[35] B. J. R. Thio and J. C. Meredith, "Measurement of polyamide and polystyrene adhesion with coated-tip atomic force microscopy," *Journal of Colloid and Interface Science*, vol. 314, no. 1, pp. 52–62, 2007.

[36] X. Sheng, Y. P. Ting, and S. O. Pehkonen, "Force measurements of bacterial adhesion on metals using a cell probe atomic force microscope," *Journal of Colloid and Interface Science*, vol. 310, no. 2, pp. 661–669, 2007.

[37] H. J. Butt, B. Cappella, and M. Kappl, "Force measurements with the atomic force microscope: Technique, interpretation and applications," *Surface Science Reports*, vol. 59, no. 1-6, pp. 1–152, 2005.

[38] V. Liimatainen, M. Vuckovac, V. Jokinen, V. Sariola, M. J. Hokkanen, Q. Zhou, and R. H. Ras, "Mapping microscale wetting variations on biological and synthetic water-repellent surfaces," *Nature Communications*, vol. 8, no. 1, p. 1798, 2017.

[39] M. D. Peri and C. Cetinkaya, "Non-contact microsphere-surface adhesion measurement via acoustic base excitations," *Journal of Colloid and Interface Science*, vol. 288, no. 2, pp. 432–443, 2005.

[40] J. W. Nicholas, L. E. Dieker, E. D. Sloan, and C. A. Koh, "Assessing the feasibility of hydrate deposition on pipeline walls-Adhesion force measurements of clathrate hydrate particles on carbon steel," *Journal of Colloid and Interface Science*, vol. 331, no. 2, pp. 322–328, 2009.

[41] C. J. Taylor, L. E. Dieker, K. T. Miller, C. A. Koh, and E. D. Sloan, "Micromechanical adhesion force measurements between tetrahydrofuran hydrate particles," *Journal of Colloid and Interface Science*, vol. 306, no. 2, pp. 255–261, 2007.

[42] R. Ungai-Salánki, B. Csippa, T. Gerecsei, B. Péter, R. Horvath, and B. Szabó, "Nanonewton scale adhesion force measurements on biotinylated microbeads with a robotic micropipette," *Journal of Colloid and Interface Science*, vol. 602, pp. 291–299, 2021.

[43] T. Gerecsei, I. Erdődi, B. Peter, C. Hős, S. Kurunczi, I. Derényi, B. Szabó, and R. Horvath, "Adhesion force measurements on functionalized microbeads: An in-depth comparison of computer controlled micropipette and fluidic force microscopy," *Journal of Colloid and Interface Science*, vol. 555, pp. 245–253, 2019.

[44] N. Gao, F. Geyer, D. W. Pilat, S. Wooh, D. Vollmer, H. J. Butt, and R. Berger, "How drops start sliding over solid surfaces," *Nature Physics*, vol. 14, no. 2, pp. 191–196, 2018.

[45] D. Daniel, C. L. Lay, A. Sng, C. J. Jun Lee, D. C. Jin Neo, X. Y. Ling, and N. Tomczak, "Mapping micrometer-scale wetting properties of superhydrophobic surfaces," *Proceedings of the National Academy of Sciences*, vol. 116, no. 50, pp. 25008–25012, 2019.

[46] D. W. Pilat, P. Papadopoulos, D. Schäffel, D. Vollmer, R. Berger, and H. J. Butt, "Dynamic measurement of the force required to move a liquid drop on a solid surface," *Langmuir*, vol. 28, no. 49, pp. 16812–16820, 2012.

[47] D. Mannetje, A. Banpurkar, H. Koppelman, M. H. Duits, D. Van Den Ende, and F. Mugele, "Electrically tunable wetting defects characterized by a simple capillary force sensor," *Langmuir*, vol. 29, no. 31, pp. 9944–9949, 2013.

[48] D. Daniel, J. V. Timonen, R. Li, S. J. Velling, and J. Aizenberg, "Oleoplaning droplets on lubricated surfaces," *Nature Physics*, vol. 13, no. 10, pp. 1020–1025, 2017.

[49] D. Daniel, A. Y. T. Chia, L. C. H. Moh, R. Liu, X. Q. Koh, X. Zhang, and N. Tomczak, "Hydration lubrication of polyzwitterionic brushes leads to nearly friction- and adhesion-free droplet motion," *Communications Physics*, vol. 2, no. 1, pp. 1–7, 2019.

[50] D. Daniel, J. V. Timonen, R. Li, S. J. Velling, M. J. Kreder, A. Tetreault, and J. Aizenberg, "Origins of Extreme Liquid Repellency on Structured, Flat, and Lubricated Hydrophobic Surfaces," *Physical Review Letters*, vol. 120, no. 24, p. 244503, 2018.

[51] M. Yamada, S. Doi, H. Maenaka, M. Yasuda, and M. Seki, "Hydrodynamic control of droplet division in bifurcating microchannel and its application to particle synthesis," *Journal of Colloid and Interface Science*, vol. 321, no. 2, pp. 401–407, 2008.

[52] H. Suda and S. Yamada, "Force measurements for the movement of a water drop on a surface with a surface tension gradient," *Langmuir*, vol. 19, no. 3, pp. 529–531, 2003.

[53] K. Y. Law, "Definitions for hydrophilicity, hydrophobicity, and superhydrophobicity: Getting the basics right," *Journal of Physical Chemistry Letters*, vol. 5, no. 4, pp. 686–688, 2014.

[54] D. Feldmann and B. E. Pinchasik, "How Droplets Move on Surfaces with Directional Chemical Heterogeneities," *Journal of Physical Chemistry Letters*, vol. 12, no. 48, pp. 11703–11709, 2021.

[55] M. Kiran Raj, S. Misra, and S. K. Mitra, "Friction and Adhesion of Microparticle Suspensions on Repellent Surfaces," *Langmuir*, vol. 36, no. 45, pp. 13689–13697, 2020.

[56] S. Shyam, P. K. Mondal, and B. Mehta, "Field driven evaporation kinetics of a sessile ferrofluid droplet on a soft substrate," *Soft Matter*, vol. 16, no. 28, pp. 6619–6632, 2020.

[57] D. Van Krevelen and K. Te Nijenhuis, "Interfacial Energy Properties," in *Properties of Polymers*, pp. 229–244, Elsevier, 2009.

[58] L. Gao and T. J. McCarthy, "Teflon is hydrophilic. Comments on definitions of hydrophobic, shear versus tensile hydrophobicity, and wettability characterization," *Langmuir*, vol. 24, no. 17, pp. 9183–9188, 2008.

[59] L. Gao and T. J. McCarthy, "Wetting 101°," *Langmuir*, vol. 25, no. 24, pp. 14105–14115, 2009.

[60] H. J. Butt, I. V. Roisman, M. Brinkmann, P. Papadopoulos, D. Vollmer, and C. Semprebon, "Characterization of super liquid-repellent surfaces," *Current Opinion in Colloid and Interface Science*, vol. 19, no. 4, pp. 343–354, 2014.

Chapter 11

Microparticle Suspensions and Bacteria-Laden Droplets: Are They the Same in Terms of Wetting Signature? [1]

11.1 Overview

The adhesion behavior of microbial pathogens on commonly encountered surfaces is one of the most pertinent questions now. We present the characterization of bacteria-laden droplets and quantify the adhesion forces on highly repellent surfaces with the help of a simple experimental setup. Comparing the force signature measured directly using an in-house capillary deflection based droplet force apparatus, we report an anomalous adhesion behavior of live bacteria (*E. coli*) laden droplets on repellent surfaces, which stands in stark contrast to the observed adhesion signature when the doping agent is changed to inert microparticles or the same bacteria in an incapacitated state. We showed that the regular contact angle measurements using optical goniometry is unable to differentiate between the live bacteria and the dead ones (including microparticles) and thus delineate its

[1] Adapted with permission from M., Kiran Raj, **Misra, S**, Mitra, S.K., *Langmuir*, 2021, 37, 4, 1588–1595. Copyright ©2021, American Chemical Society.

limitations and the complementary nature of the adhesion measurements in understanding the fundamental interfacial interaction of living organisms on solid surfaces.

11.2 Introduction

Understanding the adhesion of microbial pathogens is of critical interest with implications in both personal and public health and has far-reaching consequences during pandemics like COVID-19. One of the serious questions that is still under scrutiny is the nature of adhesion and subsequent survival of these microbes on surfaces like glass and metals which are ubiquitous in our daily lives. A clear understanding of the mechanism of surface adhesion of these microbes will enable us to design and develop surfaces and surface-specific treatments as engineering strategies to mitigate the severe consequences of an impending pandemic and to address the larger issue of public health risks in community spaces.

The model candidates for lab scale studies of pathogens is *E. coli*, a gram-negative bacterium that is found in the human intestine, enjoying a symbiotic relationship [1]. It is an important candidate in the research community due to its ease of use and the availability of the literature, especially the vast amount of genetic data and detailed taxonomical management [2]. The colony formation and the biofilm development are of considerable interest in recent times that underpins the synergistic effects of bacterial growth with the host surface [3]. *E.coli* find significant applications in diverse areas of science and engineering [4–6] including microfluidics [7], carbon sequestration [8], superfluids [9] and as a pedagogical tool [1, 10]. Though there are many useful applications, it remains a public health hazard, posing danger as outbreaks and adversely affecting the community hygiene plans [6]. The severity of such events depends on the ease of transmission and one of the most effective ways is to utilize surfaces that do not promote bacterial growth by introducing antibacterial agents [11]. Another strategy is to deploy liquid-repellent surfaces which have gained considerable momentum in the last few decades in the context of 'superhydrophobic' or extremely water-repellent surfaces which typically show a static water contact angle in air greater than 150° [12, 13]. A plethora of fabrication techniques have been employed to

create superhydrophobic surfaces from artificially engineered coatings [14, 15] and more readily available soot particles [16–18] which rely on the Cassie-Baxter state of wetting to repel water droplets easily [12]. The conventional first step towards probing the interaction of microbe-laden droplets on superhydrophobic surfaces is to employ microparticles as surrogates [19, 20]. However, the interaction of microbial pathogens like *E.coli* with these surfaces is still not explored in detail [21] although there are a number of studies on bioactive components like vesicles [22], red blood cells [23]. From a theoretical perspective, there are two approaches to understanding bacterial adhesion: DLVO (Derjaguin–Landau–Verwey– Overbeek) theory [24, 25] and thermodynamics [26, 27]. In the former, the free energy is treated as a balance between the van der Waals forces and electrostatic forces whereas in the latter, the free energy is described in terms of the interfacial tensions between the bacteria, the solid substrate, and the surrounding fluid medium.

Traditionally, the wetting characterization for such microbes on typical surfaces is the contact angle-based measurements [28]. Advanced approaches, such as droplet-based adhesion measurement is an important tool in terms of modified substrates and underwater scenarios. In a recent study [29], a cantilever-based droplet system was utilized to directly quantify accurately the adhesion and friction forces between the microparticle-laden droplets and the solid substrate. In their experiments, they used surfaces with different degrees of superhydrophobicity and established that the force-based measurements (such as adhesion) often provide a better understanding of the interfacial interaction of microparticle-laden droplets on solid substrates.

Literature suggests that contact angle measurements have been the primary tool to characterize the repellency of *E.coli* on superhydrophobic surfaces [21, 30]. However, its direct signature on the adhesion force on such surfaces has never been reported. It is to be noted that the use of *E. coli* as a model microorganism still requires a certified Bio Safety Level II facility. Therefore, often a simplified approach [31, 32] is taken where colloidal microparticles are used as surrogates to mimic bacteria-surface interaction. This stems from the reports [24, 33] that a physicochemical description involving colloidal principles might suffice to provide a qualitative understanding of the ensuing dynamics in the initial stage of adhesion. However, this assumption does not account for the viability and motility of bacterial cells. In this study, through direct measurement of adhesion forces,

we attempt to critically evaluate the applicability of inert colloidal particles as suitable bacterial surrogates.

The present work combines the simplicity of an in-house developed adhesion measurement device with the complex interfacial dynamics of the bacterial movement within a droplet that interacts with a hydrophobic surface. The force-based approach is extended from inert microparticles [29] to motile bacteria, adding the complexity of a living organism within a fluidic environment of physiological relevance. In doing so, various fluids of biophysical interest have been explored as the suspending medium of the bacterial load. This study aims to provide a more accurate picture of the wetting signature for living microorganisms such as *E. coli* and look more closely at the validity of microparticle/microbeads as a surrogate model.

11.3 Experimental Section

For contact angle measurements (static and dynamic), sessile drop goniometry is employed (DSA 30, Krüss USA), following the standard protocols within the built-in processing software as shown in Figure 11.1(a) [34]. A sessile droplet of volume 3 μl is dispensed on the surface using a disposable stainless steel needle (needle diameter 0.5mm, NE44, Krüss USA) mounted on the automatic dispense unit of DSA 30 and the image is captured using a camera to measure the static contact angle (θ). For contact angle hysteresis measurement, the liquid is slowly pumped at a rate of 0.1 μl/min, increasing the volume of the droplet and the advancing contact angle (θ_a) is estimated once the contact line starts moving as shown in Figure 11.1(b)(i). Further, during the retraction of the fluid volume, the receding contact angle (θ_r) is estimated as shown in Figure 11.1(b)(ii) [34].

The adhesion measurement is based on the deflection of a polymeric cantilever, similar to the droplet force apparatus [35–37] and the one used recently in a separate work [29] by the authors for measuring the friction and adhesion forces of microparticle doped aqueous suspensions. An acrylic capillary tube (Paradigm Optics Inc, WA, USA) with length L = 72 mm and external diameter d = 360 μm is used as the cantilever sensor with a stiffness constant k = 27.6 mN/m, calibrated separately (see Appendix I, section I.1 for

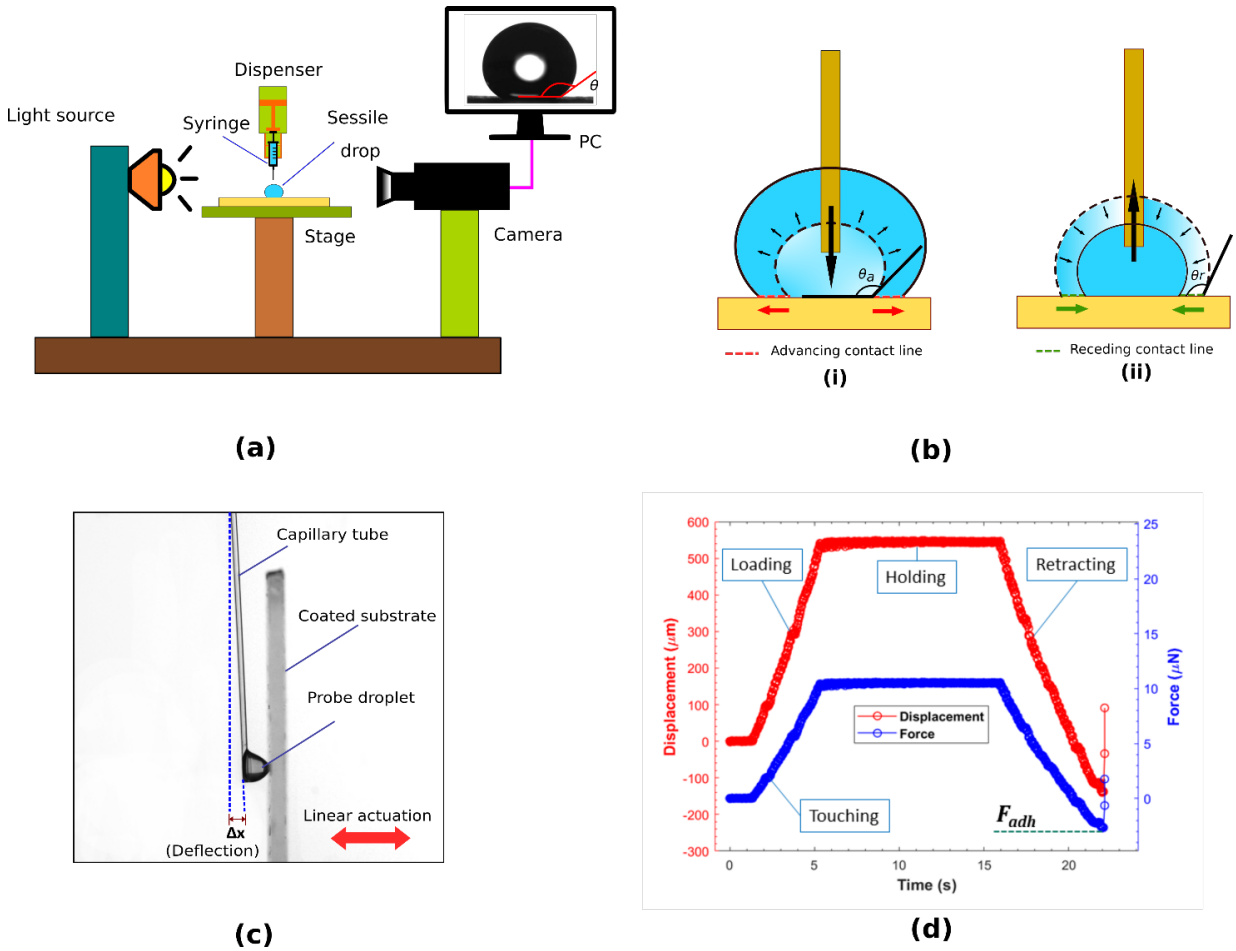

Figure 11.1: (a) The goniometry setup used for contact angle measurements, showing the sessile droplet and the static contact angle θ, (b)(i) Advancing contact angle (θ_a) (ii) Receding contact angle (θ_r), (c) The experimental setup for measuring adhesion force, showing the cantilever deflection Δx due to the adhesion of the probe droplet on the substrate, (d) Typical deflection profile over time and the estimated force showing the four steps involved in the procedure and the final value of adhesion F_{adh}.

calibration details). The probe droplet with a volume of 5 μl is dispensed at the tip of the cantilever using a micropipette. It is to be noted that a glass capillary tube of diameter 410 μm was used in our earlier work with microparticles [29], which resulted in $k = 305$ mN/m. However, no significant difference in adhesion force measurements is observed between the two sets of cantilevers, elucidating the universality of the probing technique. The target hydrophobic surfaces were attached vertically on a motorized linear stage (Zaber Technologies Inc., BC, Canada) and translated with a velocity of 500 μm/s. After smoothly touching the substrate and holding in the position for 10 s, the stage is moved in the opposite direction, thereby deflecting the cantilever as shown in Figure 11.1(c) due to the adhesion of the droplet on the substrate. The deflection of the cantilever tip from its mean position (Δx) is captured using a video camera (Photron FASTCAM Mini) at 60 frames per second with a strong backlight. Further, the video is analyzed using an open source video analysis program [38] from which the deflection with respect to time is extracted as shown in Figure 11.1(d). The entire measurement procedure can be segregated into four steps based on the typical displacement curve of the cantilever tip as shown in Figure 11.1(d). From this, the adhesion force is calculated as $F_{adh} = k\Delta x_{max}$ where Δx_{max} is the maximum deflection of the cantilever before the droplet is detached from the surface.

We have used *E. coli* (K-12 Strain SMG 123 (PTA-7555), ATCC, Cedarlane, Canada) as the model microbe in our experiments. An overnight culture was grown in Lauryl Tryptose (LT) Broth (Catalog No. DF0241170, Difco), diluted in deionized (DI) water (Milli-Q, 18.2 MΩ cm, MilliPore Sigma, Canada) with a concentration of 35.6 g/l. More details on the bacterial culture could be found in section I.2 of Appendix I. After culturing, the solution containing bacteria was centrifuged (VWR, Mississauga, Canada) at 5000rpm for 10 min and the supernatant was removed to get the *E. coli* in pellet form. Followed by washing in DI water twice, the pellet is then resuspended in three different base fluids which served as the stock solution for creating bacteria doped probe droplets. This ensured that any residue that might arise due to the presence of the culture media is completely removed during the adhesion experiments. We have used three different base liquid media in this study, namely, DI water, phosphate-buffered saline (PBS, 1X, pH 7.4, Catalog No. 10010-023, Gibco), and Lauryl Tryptose (LT) broth (with the same concentration as the one used for bacterial culture), to explore the dependency of the adhesion behavior on the

suspending medium. These three base liquids are routinely used in biological experiments. Starting with the full concentration stock solution, a serial dilution process (more details in the Appendix I, section I.3) was followed with a dilution factor of 1/10 at each step to generate samples of sequentially reducing bacterial concentration with the same base fluid. An agar plate counting reveals that the concentration of the bacteria in the undiluted (full concentration) stock solution is 8.2×10^6 CFU/ml (see Appendix I, section I.4). The dilution is limited to four steps in the present study as beyond this concentration, a negligible number of bacterial colonies are observed in agar plating.

In order to understand the physicochemical mechanisms inherent to a live bacterial strain in comparison to dead bacteria (akin to microparticle suspension), bacterial colonies were incapacitated where fresh sets of full concentration stock solutions with different base fluids containing *E. coli* were treated with 70% isopropyl alcohol (IPA, Fisher Scientific). A live/dead assay test (BacLight Kit, Invitrogen) was conducted on the samples to quantify the percentage of live and dead bacteria in the bacterial suspension (see section I.5 in Appendix I for detailed protocol). For non-IPA treated samples, an average of 72.3% bacteria were live. However, after IPA treatment, the percentage dropped down to 0, providing a visual confirmation that IPA solution indeed killed all the bacteria in the solution. This was also confirmed by agar plating, where no colony formation was observed in the IPA-treated sample after incubation. In the present work, the bacterial signature is compared against inert polystyrene latex microparticles with a nominal diameter of 1 μm (Magsphere Inc., Pasadena, CA, USA). These microparticles have a length scale comparable to that of *E. coli* [39] ($\sim$ few μm). The microparticle suspension is subsequently diluted in DI water in varying concentrations from 0 to 5% (w/v). Detailed physical and chemical characteristics and scanning electron microscopy (SEM) images of these microparticles are available at the manufacturer's website [40]. For *E.coli*, for both the live and dead state, the characteristics are well reported in the literature [41–44].

In this study we used two types of surfaces with two different repellent coatings, namely, S1 (Glaco, Soft99, Japan) and S2 (Glass Protect-SH, SiO2 International, Canada), both were coated on clean glass slides (Catalog No. 12-550-A3, Fisher Scientific, Canada). While S1 was spray coated, S2 was dip coated and both were heated thereafter at 60°C for 1 hour. Both coatings formed transparent hydrophobic surfaces with static contact

angle, θ measured as $126^\circ \pm 1.6^\circ$ and $151^\circ \pm 1.9^\circ$ for S1 and S2, respectively. Please refer to Appendix I, section I.6 for surface characterization data using SEM and atomic force microscopy (AFM).

11.4 Results & Discussion

Figure 11.2 shows the contact angle (CA) values for both microparticles as well as bacteria-doped droplets with varied concentrations for all three base liquids and two target surfaces. S2 showed a higher CA compared to S1 for all the cases, indicating a higher degree of hydrophobicity, which was also confirmed from the Attenuated Total Reflectance Fourier Transform Infrared (ATR-FTIR) spectra (see section I.7 in Appendix I for further details) of the surfaces. The FTIR spectra of S2 indicate the presence of C-F bonds on the surface, which contributes to lower surface energy and consequently, higher hydrophobicity [45].

As can be seen in Figure 11.2(b) and 11.2(c), probe droplets with DI water as a base medium showed a higher static contact angle followed by that of PBS and LT, on both the target surfaces. Also, the probe droplet with live bacteria as dopant always showed a lesser static contact angle than its dead counterpart for the same bacterial concentration, base medium, and target surface. Moreover, an overall decreasing trend of θ with increasing bacterial concentration is observed which bears qualitative similarity with the experimental observation for microparticle laden droplet reported in Figure 11.2(a). It gives a preliminary indication that the presence of more bacteria within the probe droplet enhances surface wetting.

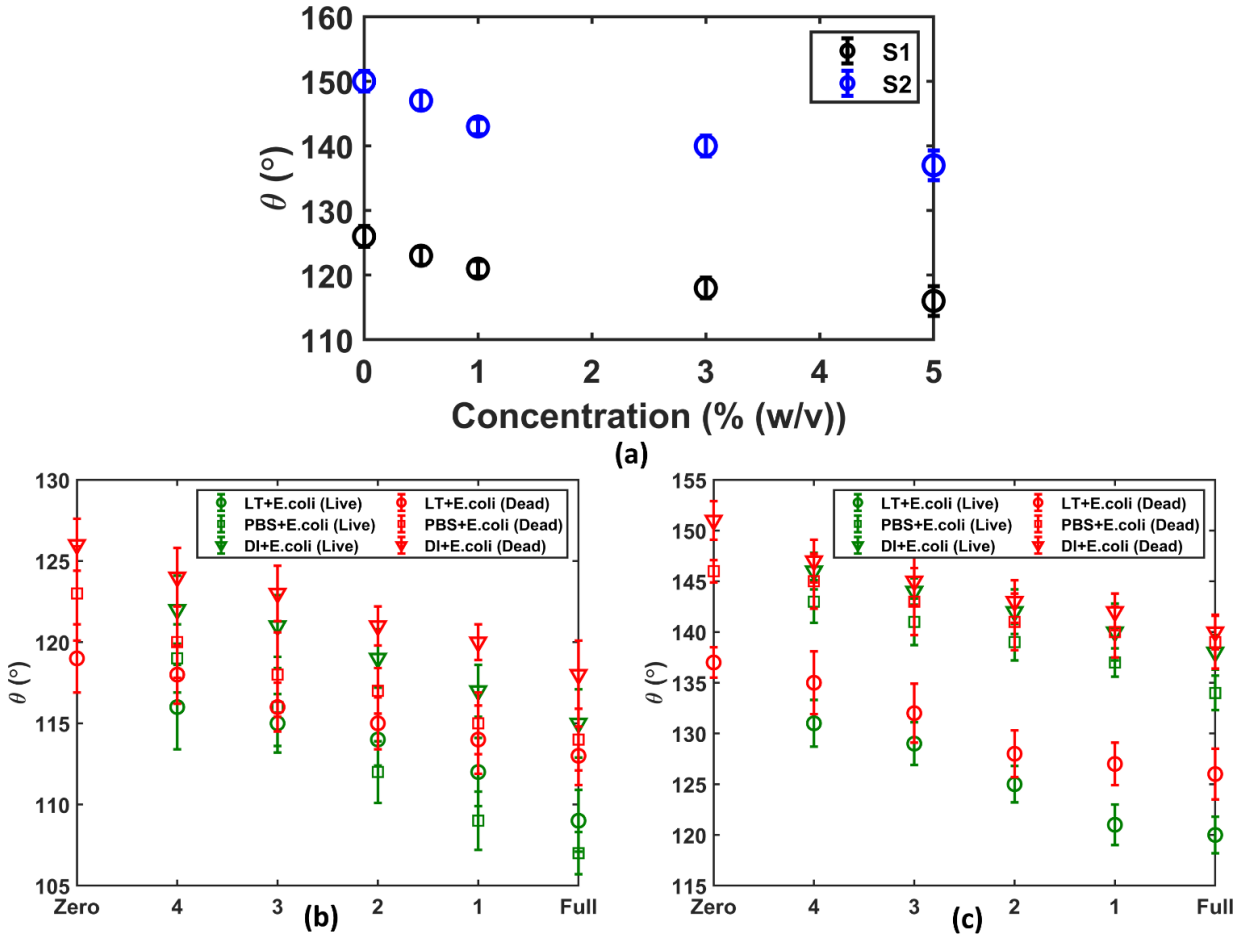

Figure 11.2: Static contact angle (θ) values for all probe-liquid and target surface combinations - (a) represents θ values on S1 and S2 for varying microparticle concentration in the probe droplet, with DI water as base medium while (b) & (c) report θ values with varied bacterial (*E. coli*) concentration in the probe droplet, for both dead and live bacterial cells as dopants and with three different base media, namely LT, PBS, and DI water. (b) represents the static contact angle data on surface S1 while (c) corresponds to surface S2. In both (b) and (c) Zero and Full on the X (concentration) axis correspond to the undoped base liquid and bacterial stock solution, while 4, 3, 2, 1 represent 10000, 1000, 100 & 10-fold dilution respectively from the stock solution i.e., increase in bacterial count from 8.2×10^2 CFU/ml to 8.2×10^5 CFU/ml in multiples of 10.

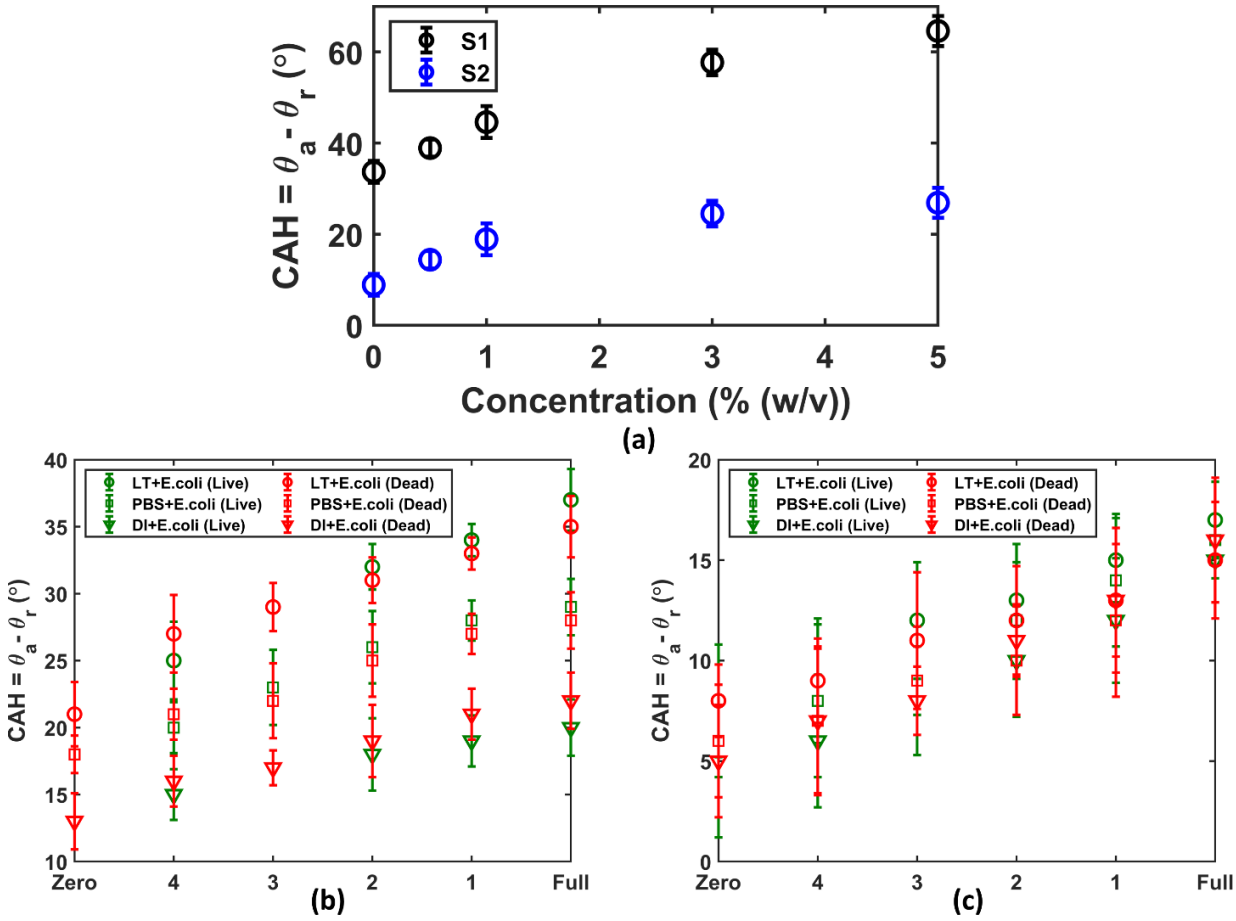

Figure 11.3: Contact angle hysteresis (CAH) values for all probe-liquid and target surface combinations - (a) represents CAH values on S1 and S2 for varying microparticle concentration in the probe droplet, with DI water as base medium while (b) & (c) report CAH values with varied bacterial (*E. coli*) concentration in the probe droplet, for both dead and live bacterial cells as dopants and with three different base media, namely LT, PBS and DI water. (b) contains the CAH data on surface S1 while (c) corresponds to surface S2. In both (b) and (c) Zero and Full on the X (concentration) axis correspond to the base liquid (with no doping) and the bacterial stock solution, while 4, 3, 2, 1 represent 10000, 1000, 100 & 10-fold dilution respectively from the stock solution, i.e., increase in bacterial count from 8.2×10^2 CFU/ml to 8.2×10^5 CFU/ml in multiples of 10.

Figure 11.3 shows the contact angle hysteresis values for all the studied cases. The general observation is that the CAH increases with an increase in doping concentration on all studied surface-probe liquid combinations. The increasing trend of CAH indicates a stickier droplet-surface contact with an increase in doping concentration, which is consistent with the wetting signature obtained from static contact angle measurements. The observed trend of contact angle hysteresis for microparticles is consistent with previously reported literature [19, 29]. It is to be noted here that there are several overlaps and crossovers between the experimentally observed trends for live and dead bacterial droplets. And unlike Figure 11.2, where probe droplet containing dead bacteria always showed a higher static contact angle than its live counterpart, no such generalizable criteria could be established for CAH, making CAH-based conclusive distinction between live and dead bacterial suspensions impossible.

Figure 11.4 reports the adhesion force measurements, and here interestingly, there is a stark contrast in the concentration dependence of adhesion force between dead and live bacterial suspension. As can be seen in Figure 11.4(a), for microparticle suspension, F_{adh} increased with increasing doping concentration, which is in line with our observation reported in a recent work [29]. However, a decrease in the adhesion force is observed as the bacterial concentration is increased when the probe droplet contains live bacterial cells, for all the studied base liquids and target surface combination, as could be seen in Figure 11.4(b) & 11.4(c). On the contrary, with dead bacteria as the dopant, we see an increase in adhesion force with increasing doping concentration, which is similar to the observed trend for microparticle suspension (as shown in Figure 11.4(a)). This is a direct indication that the viability and possible motility of bacterial cells are responsible for reduced adhesion. This happened despite the fact that around 30% of the bacteria within the stock solution were not active. As illustrated in Figures 2 & 3 through contact angle measurements, probe droplets showed a qualitatively similar dependence on doping concentration, where for all the studied droplet-surface combinations, an increase in concentration corresponds to a lower static contact angle and a higher contact angle hysteresis. This qualitative similarity in wetting signature might give a false indication that perhaps microparticle suspension is an appropriate surrogate for probing bacterial adhesion. However, our framework enables direct measurement of the adhesion response, which unambiguously indicates that despite

the resemblance in wetting signature, the adhesion behavior is indeed significantly different between live and dead bacteria. Although there is some qualitative resemblance between dead bacteria and microparticle suspension, probe droplets doped with live bacterial cells exhibit a completely different adhesion signature, owing to the bacterial viability and motility, which clearly can not be replicated using inert microspheres. Contextually, it is to be noted here that the presence of nutrient residue (from the culture medium) in the probe droplet can create a nutrient gradient, causing a chemotactic movement of bacteria inside the droplet. This movement can have unwanted implications on the ensuing adhesion behavior. However, we thoroughly washed the cultured bacteria with DI water twice before resuspending them in the base medium, which ensures the complete removal of nutrient residues before the preparation of the stock solutions. Further, the extremely low Reynolds number flow ($\sim 10^{-5}$) for the bacteria [10] makes any rapid chemotactic movement improbable unless there are strong advective currents within the droplet.

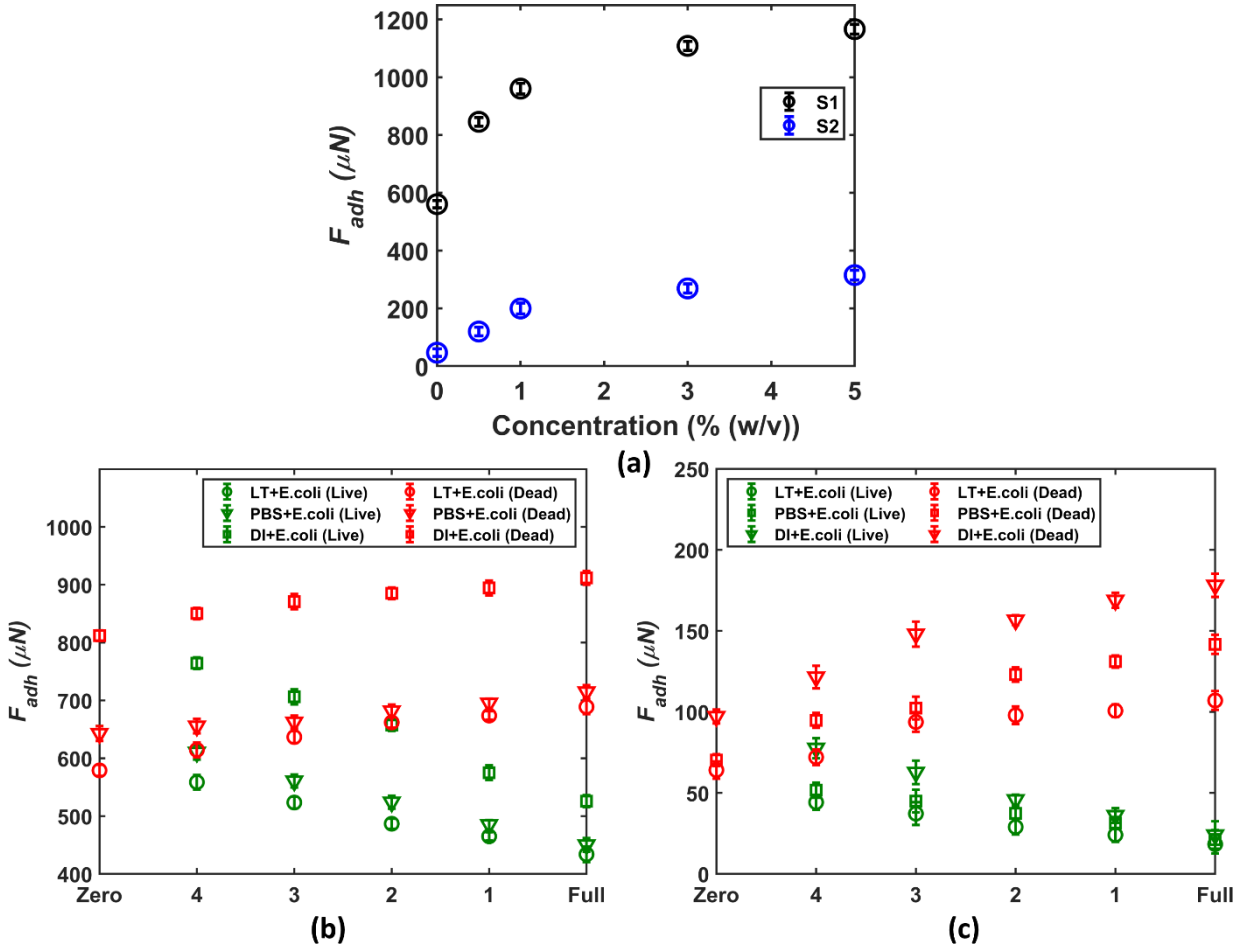

Figure 11.4: Adhesion force (F_{adh}) measurement for all probe-liquid and target surface combinations - (a) represents F_{adh} values on S1 and S2 for varying microparticle concentration in the probe droplet, with DI water as base medium while (b) & (c) report F_{adh} values with varied bacterial (E.coli) concentration in the probe droplet, for both dead and live bacterial cells as dopants and with three different base media, namely LT, PBS and DI water. (b) represents the static contact angle data on surface S1 while (c) corresponds to surface S2. In both (b) and (c) Zero and Full on the X (concentration) axis correspond to undoped base liquid and stock solution, while 4, 3, 2, and 1 represent 10000, 1000, 100 & 10-fold dilution respectively from the stock solution, i.e., increase in bacterial count from 8.2×10^2 CFU/ml to 8.2×10^5 CFU/ml in multiples of 10.

Based on the trend in the adhesion measurements, a mechanism is proposed here consisting of the motility-driven depinning of the *E. coli* from the surface, as shown in Figure 11.5. Due to the roughness-enabled hydrophobicity of the coated surfaces, which in turn is responsible for the Cassie-Baxter state of wetting, the pinning sites are already limited. The comparable size of the bacteria aids in augmenting this further, thereby leading to an early detachment of the droplet. Previous works have shown that for higher contact time with a given surface, the bacteria favor adhesion and growth [46, 47]. However, in the early stage of adhesion with short contact time (as in the present case), structural unfavorability of bacterial attachment on the surface becomes more important, leading to low adhesion force.

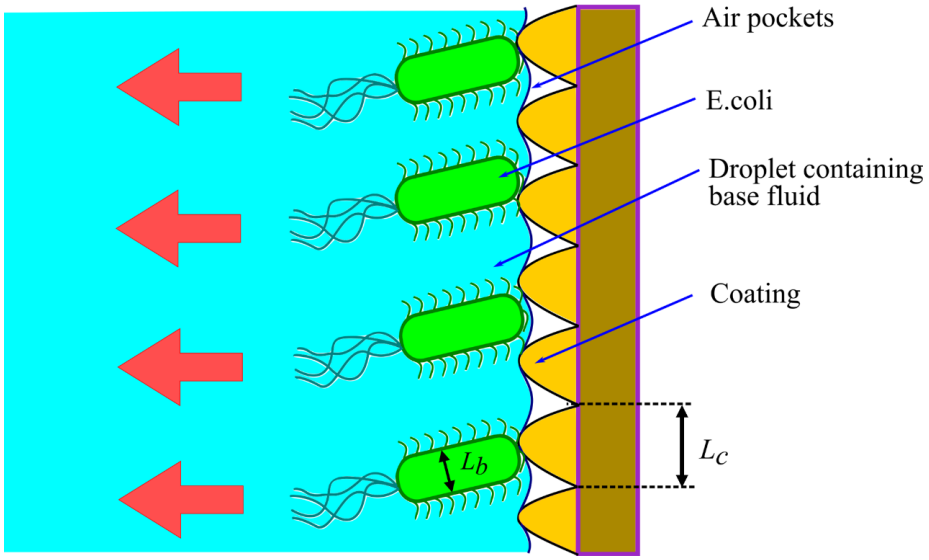

Figure 11.5: Proposed mechanism for depinning of the bacteria from a structured superhydrophobic surface. The diameter of the bacterial cells (L_b) is comparable with the roughness length scale (L_c). The arrows indicate the preferential direction of bacterial mobility in presence of a structured superhydrophobic surface.

A direct comparison of bacteria and microparticles in terms of concentration used in the solution for the respective measurements, be it the contact angle or the adhesion force, is not straightforward, however from an electrostatic perspective, both have negative charges on their surface and are expected to interact with the surface in a similar way. The

advantageous consequence is that we can now rule out that the surface charge is responsible for this enhanced depinning from the coated surface, then the microparticles should also have behaved in a similar way. As dead bacteria and the microparticles show a similar trend, the probable cause for this anomaly must be attributed to the motility of the live bacteria.

It is to be noted here that culture-to-culture variance can alter the adhesion signature as different cultures may have different initial viability (percentage of live and dead bacteria), which is a key contributor to the ensuing dynamics, as we have identified earlier. As a precaution, we have always compared results from the same stock solution, which ensures the same parental identity and thereby eliminates the possibility of culture-to-culture variation. However, in order to establish the generality of experimental observations, we have also monitored the key quantities of interest (namely, percentage of live/dead bacteria, static and dynamic contact angle, and adhesion force) across different cultures, where we maintained the same culture conditions but cultured them separately as different aliquots. Our investigation confirmed that there was no significant difference across different aliquots, which reaffirms the generality of the conclusions. Details are presented in section I.8 of Appendix I.

We emphasize that the results from the contact angle-based study should complement that of adhesion experiments. The present study aims to delineate the limitations of goniometry over direct adhesion signature while dealing with bioactive samples like bacteria. Especially with high values of contact angle for repellent surfaces, the image-based static angle measurements cannot be relied upon in their entirety [48, 49]. The next viable estimate is the dynamic contact angle measurements based on the hysteresis of the contact line, which again suffers the limitations from imaging artifacts while determining the incipient contact line movement [34]. Apart from reaffirming the non-unique interpretations of a regular goniometry, the adhesion-based approach opens up the possibility of sensing and detecting the presence of bacteria (i.e., live versus dead), without any biochemical agents and time-consuming plating or gene sequencing. Further, the adhesion signature using the current experimental set-up can be quantified with reasonable accuracy and confidence level, which, unlike AFM, does not demand sophisticated infrastructure and operational expertise.

11.5 Conclusion

We have presented the salient aspects of bacterial adhesion over highly repellent hydrophobic surfaces. We show that contact angle-based optical goniometry provides an incomplete (and consequently inconclusive) description of the ensuing interfacial interaction between bacterial droplets and repellent surfaces. Apart from the imaging uncertainties (typically arising at high contact angle), the wetting signature only captures the behavior of the three-phase contact line and does not reveal any information on the contact surface underneath the droplet which is directly responsible for the adhesion behavior. We report that despite the qualitative similarity in concentration dependence of static as well as dynamic contact angle between microparticle suspension and bacterial (both live and dead) loads, the adhesion behavior exhibits a completely contrasting dependence on doping concentration, where unlike dead bacteria and inert microparticles, motility of live bacteria contributes to a reduction in adhesion force with an increase in concentration. A simple force-based adhesion measurement, as illustrated here, can elaborate on the true nature of these interactions, which gives a clear indication that bacterial viability and motility play a crucial role in governing adhesion behavior. We test with the most common fluids in biochemical experiments with both dead and live conditions and compare the outcome with the inert microparticle suspension to conclude that despite similar length scale, inert microparticles are not suitable surrogates for living bacterial cells.

References

[1] R. Phillips, J. Kondev, J. Theriot, H. G. Garcia, and N. Orme, *Physical Biology of the Cell*. Garland Science, 2012.

[2] Z. D. Blount, "The natural history of model organisms: The unexhausted potential of *E. coli*," *eLife*, vol. 4, 2015.

[3] M. Hennes, J. Tailleur, G. Charron, and A. Daerr, "Active depinning of bacterial droplets: The collective surfing of bacillus subtilis," *Proceedings of the National*

Academy of Sciences of the United States of America, vol. 114, no. 23, pp. 5958–5963, 2017.

[4] R. Monds and G. O'Toole, "The developmental model of microbial biofilms: ten years of a paradigm up for review," *Trends in Microbiology*, vol. 17, no. 2, pp. 73–87, 2009.

[5] Y. Zhang, F. Buchholz, J. Muyrers, and A. Francis Stewart, "A new logic for dna engineering using recombination in escherichia coli," *Nature Genetics*, vol. 20, no. 2, pp. 123–128, 1998.

[6] J. Jang, H.-G. Hur, M. Sadowsky, M. Byappanahalli, T. Yan, and S. Ishii, "Environmental escherichia coli: ecology and public health implications—a review," *Journal of Applied Microbiology*, vol. 123, no. 3, pp. 570–581, 2017.

[7] S. Pajoumshariati, M. Azizi, S. Zhang, B. Dogan, K. Simpson, and A. Abbaspourrad, "A microfluidic-based model for spatially constrained culture of intestinal microbiota," *Advanced Functional Materials*, vol. 28, no. 48, 2018.

[8] B. Jo, I. Kim, J. Seo, D. Kang, and H. Cha, "Engineered escherichia coli with periplasmic carbonic anhydrase as a biocatalyst for co2 sequestration," *Applied and Environmental Microbiology*, vol. 79, no. 21, pp. 6697–6705, 2013.

[9] H. López, J. Gachelin, C. Douarche, H. Auradou, and E. Clément, "Turning bacteria suspensions into superfluids," *Physical Review Letters*, vol. 115, no. 2, 2015.

[10] E. Purcel, "Life at low reynolds number," *American Journal of Physics*, vol. 45, no. 1, pp. 3–11, 1977.

[11] J. Hasan, R. Crawford, and E. Ivanova, "Antibacterial surfaces: The quest for a new generation of biomaterials," *Trends in Biotechnology*, vol. 31, no. 5, pp. 295–304, 2013.

[12] M. Nosonovsky and B. Bhushan, "Superhydrophobic surfaces and emerging applications: Non-adhesion, energy, green engineering," *Current Opinion in Colloid and Interface Science*, vol. 14, no. 4, pp. 270–280, 2009.

[13] M. Palacio and B. Bhushan, "Research article: Bioadhesion: A review of concepts and applications," *Philosophical Transactions of the Royal Society A: Mathematical, Physical and Engineering Sciences*, vol. 370, no. 1967, pp. 2321–2347, 2012.

[14] X. Tian, S. Shaw, K. Lind, and L. Cademartiri, "Thermal processing of silicones for green, scalable, and healable superhydrophobic coatings," *Advanced Materials*, vol. 28, no. 19, pp. 3677–3682, 2016.

[15] J. Simpson, S. Hunter, and T. Aytug, "Superhydrophobic materials and coatings: A review," *Reports on Progress in Physics*, vol. 78, no. 8, 2015.

[16] X. Deng, L. Mammen, H.-J. Butt, and D. Vollmer, "Candle soot as a template for a transparent robust superamphiphobic coating," *Science*, vol. 335, no. 6064, pp. 67–70, 2012.

[17] B. Majhy, R. Iqbal, and A. Sen, "Facile fabrication and mechanistic understanding of a transparent reversible superhydrophobic – superhydrophilic surface," *Scientific Reports*, vol. 8, no. 1, 2018.

[18] R. Iqbal, B. Majhy, and A. Sen, "Facile fabrication and characterization of a pdms-derived candle soot coated stable biocompatible superhydrophobic and superhemophobic surface," *ACS Applied Materials and Interfaces*, vol. 9, no. 36, pp. 31170–31180, 2017.

[19] P. Waghmare and S. Mitra, "Contact angle hysteresis of microbead suspensions," *Langmuir*, vol. 26, no. 22, pp. 17082–17089, 2010.

[20] R. Iqbal, B. Majhy, A. Shen, and A. Sen, "Evaporation and morphological patterns of bi-dispersed colloidal droplets on hydrophilic and hydrophobic surfaces," *Soft Matter*, vol. 14, no. 48, pp. 9901–9909, 2018.

[21] X. Zhang, L. Wang, and E. Levänen, "Superhydrophobic surfaces for the reduction of bacterial adhesion," *RSC Advances*, vol. 3, no. 30, pp. 12003–12020, 2013.

[22] H. Li, Z. Liu, C. Li, Q. Feng, Y. Liu, Q. Li, Z. Dong, Y. Wang, and L. Jiang, "Efficient spreading and controllable penetration of high-speed drops on superhydrophobic surface by vesicles," *Journal of Materials Chemistry A*, vol. 8, no. 34, pp. 17392–17398, 2020.

[23] R. Iqbal, A. Shen, and A. Sen, "Understanding of the role of dilution on evaporative deposition patterns of blood droplets over hydrophilic and hydrophobic substrates," *Journal of Colloid and Interface Science*, vol. 579, pp. 541–550, 2020.

[24] M. van Loosdrecht, J. Lyklema, W. Norde, and A. Zehnder, "Bacterial adhesion: A physicochemical approach," *Microbial Ecology*, vol. 17, no. 1, pp. 1–15, 1989.

[25] M. Hermansson, "The dlvo theory in microbial adhesion," *Colloids and Surfaces B: Biointerfaces*, vol. 14, no. 1-4, pp. 105–119, 1999.

[26] H. Busscher, A. Weerkamp, H. van Der Mei, A. van Pelt, H. de Jong, and J. Arends, "Measurement of the surface free energy of bacterial cell surfaces and its relevance for adhesion," *Applied and Environmental Microbiology*, vol. 48, no. 5, pp. 980–983, 1984.

[27] D. Absolom, F. Lamberti, Z. Policova, W. Zingg, C. van Oss, and A. Neumann, "Surface thermodynamics of bacterial adhesion," *Applied and Environmental Microbiology*, vol. 46, no. 1, pp. 90–97, 1983.

[28] P.-G. De Gennes, F. Brochard-Wyart, and D. Quéré *Capillarity and Wetting Phenomena: Drops, Bubbles, Pearls, Waves*, 2004.

[29] M. Kiran Raj, S. Misra, and S. Mitra, "Friction and adhesion of microparticle suspensions on repellent surfaces," *Langmuir*, vol. 36, no. 45, pp. 13689–13697, 2020.

[30] Y. Yuan, M. Hays, P. Hardwidge, and J. Kim, "Surface characteristics influencing bacterial adhesion to polymeric substrates," *RSC Advances*, vol. 7, no. 23, pp. 14254–14261, 2017.

[31] J. Meinders, H. van der Mei, and H. Busscher, "Deposition efficiency and reversibility of bacterial adhesion under flow," *Journal of Colloid And Interface Science*, vol. 176, no. 2, pp. 329–341, 1995.

[32] C. Beloin, A. Houry, M. Froment, J.-M. Ghigo, and N. Henry, "A short-time scale colloidal system reveals early bacterial adhesion dynamics," *PLoS Biology*, vol. 6, no. 7, pp. 1549–1558, 2008.

[33] M. van Loosdrecht, W. Norde, J. Lyklema, and A. Zehnder, "Hydrophobic and electrostatic parameters in bacterial adhesion - dedicated to werner stumm for his 65th birthday," *Aquatic Sciences*, vol. 52, no. 1, pp. 103–114, 1990.

[34] T. Huhtamäki, X. Tian, J. Korhonen, and R. Ras, "Surface-wetting characterization using contact-angle measurements," *Nature Protocols*, vol. 13, no. 7, pp. 1521–1538, 2018.

[35] D. Daniel, J. Timonen, R. Li, S. Velling, M. Kreder, A. Tetreault, and J. Aizenberg, "Origins of extreme liquid repellency on structured, flat, and lubricated hydrophobic surfaces," *Physical Review Letters*, vol. 120, no. 24, 2018.

[36] D. Daniel, A. Chia, L. Moh, R. Liu, X. Koh, X. Zhang, and N. Tomczak, "Hydration lubrication of polyzwitterionic brushes leads to nearly friction- and adhesion-free droplet motion," *Communications Physics*, vol. 2, no. 1, 2019.

[37] D. Daniel, C. Lay, A. Sng, C. Lee, D. Neo, X. Ling, and N. Tomczak, "Mapping micrometer-scale wetting properties of superhydrophobic surfaces," *Proceedings of the National Academy of Sciences of the United States of America*, vol. 116, no. 50, pp. 25008–25012, 2019.

[38] D. Brown, "Tracker free video analysis and modeling tool for physics education," *Open Source Physics*, 2012.

[39] G. Reshes, S. Vanounou, I. Fishov, and M. Feingold, "Cell shape dynamics in escherichia coli," *Biophysical Journal*, vol. 94, no. 1, pp. 251–264, 2008.

[40] C. Pasadena *U.S.A. Uniform Polystyrene Latex Particles*, 0000.

[41] R. Li, U. Goswami, M. King, J. Chen, T. Cesario, and P. Rentzepis, "In situ detection of live-to-dead bacteria ratio after inactivation by means of synchronous fluorescence

and pca," *Proceedings of the National Academy of Sciences of the United States of America*, vol. 115, no. 4, pp. 668–673, 2018.

[42] X.-Y. Ni, H. Liu, C. Wang, W.-L. Wang, Z.-B. Xu, Z. Chen, Y.-H. Wu, and H.-Y. Hu, "Comparison of carbonized and graphitized carbon fiber electrodes under flow-through electrode system (fes) for high-efficiency bacterial inactivation," *Water Research*, vol. 168, 2020.

[43] V. Gopinath, S. Priyadarshini, M. Loke, J. Arunkumar, E. Marsili, D. MubarakAli, P. Velusamy, and J. Vadivelu, "Biogenic synthesis, characterization of antibacterial silver nanoparticles and its cell cytotoxicity," *Arabian Journal of Chemistry*, vol. 10, no. 8, pp. 1107–1117, 2017.

[44] Z.-Y. Huo, G.-Q. Li, T. Yu, C. Feng, Y. Lu, Y.-H. Wu, C. Yu, X. Xie, and H.-Y. Hu, "Cell transport prompts the performance of low-voltage electroporation for cell inactivation," *Scientific Reports*, vol. 8, no. 1, 2018.

[45] V. Dalvi and P. Rossky, "Molecular origins of fluorocarbon hydrophobicity," *Proceedings of the National Academy of Sciences of the United States of America*, vol. 107, no. 31, pp. 13603–13607, 2010.

[46] C. Crick, S. Ismail, J. Pratten, and I. Parkin, "An investigation into bacterial attachment to an elastomeric superhydrophobic surface prepared via aerosol assisted deposition," *Thin Solid Films*, vol. 519, no. 11, pp. 3722–3727, 2011.

[47] K. Ellinas, D. Kefallinou, K. Stamatakis, E. Gogolides, and A. Tserepi, "Is there a threshold in the antibacterial action of superhydrophobic surfaces?," *ACS Applied Materials and Interfaces*, vol. 9, no. 45, pp. 39781–39789, 2017.

[48] H.-J. Butt, I. Roisman, M. Brinkmann, P. Papadopoulos, D. Vollmer, and C. Semprebon, "Characterization of super liquid-repellent surfaces," *Current Opinion in Colloid and Interface Science*, vol. 19, no. 4, pp. 343–354, 2014.

[49] K. Liu, M. Vuckovac, M. Latikka, T. Huhtamäki, and R. Ras, "Improving surface-wetting characterization," *Science*, vol. 363, no. 6432, pp. 1147–1148, 2019.

Chapter 12

Conclusion

The central theme of the present thesis is wetting, capillarity & evolving interfaces. Here we attempt to address several unresolved challenges of pertinent practical and commercial relevance, which include liquid-liquid encapsulation, thin film dynamics, capillarity, and droplet-surface interaction. In brief, the major contributions of the thesis can be listed as follows :

- Development of a holistic platform for stable, robust & ultrafast liquid-liquid encapsulation. Two different approaches, impact-driven & magnet-assisted encapsulation, are explored in detail, and the practical applications are demonstrated.
- Development of an interferometric framework for spatiotemporal reconstruction of the topological evolution of ultrathin ($\sim$ nm - μm) liquid films. The framework is applied to probe the condensation dynamics of low-surface-tension, volatile test liquids on high energy surfaces where we unravel a previously unknown precursor film-mediated spontaneous thermocapillary motion.
- Development of lubricant depletion tolerant, long-term stable, large-scale slippery surfaces with remarkable outdoor durability using the fundamentals of capillarity-driven self-lubrication.

- Development and demonstration of a wettability invariant cantilever-deflection-based force measurement protocol for the accurate quantification of the surface interaction between a test droplet and a target substrate. We use the framework to probe how bacteria-laden droplets interact with (super)hydrophobic surfaces and in the process, detect an anomalous adhesion behavior of live bacterial load.

12.1 Key outcomes from the present thesis

Here we present a detailed summary of the key outcomes of this thesis. The discussion is organized according to the following four subtopics/objectives explored in this thesis -

12.1.1 Liquid-Liquid Encapsulation

Chapters 2 - 5 focus on the development and subsequent exploration of a novel liquid-liquid encapsulation framework. Two different approaches are adopted to achieve encapsulation, namely, impact-driven and magnet-assisted. Chapters 2-4 explore the impact-driven approach in detail, while Chapter 5 elaborates on the development of the magnet-assisted encapsulation framework.

In Chapter 2, we propose and demonstrate a first-of-its-kind impact-driven liquid-based encapsulation method. We choose an eligible liquid triplet and utilize gravity-driven impact to exploit its energetically favorable tendency towards wrapping ($\Delta G_{\text{formation}} < 0$) for achieving ultra-fast yet controllable and reproducible encapsulation of a core drop inside another thin liquid layer. The stability and integrity of the resulting encapsulated drops are confirmed experimentally. The fundamental theoretical criteria for the formation of such stable encapsulated drops are also derived from an equilibrium thermodynamic perspective. From the perspective of execution, the proposed method is extremely straightforward and can be conducted as a tabletop experiment with minimal infrastructural requirements. It offers more flexibility in the choice of core and shell materials as well. Additionally, this method allows us to obtain stably encapsulated drops even when the core and the host liquids are miscible. These operational advantages make the proposed method a simple

yet robust, efficient, and ultrafast alternative toward stable encapsulation. The promising scalability and the associated commercial prospects have prompted us (myself and my supervisor) to co-found a startup, SLE Enterprises B.V., on this invention which is now fully operational in Eindhoven, The Netherlands. We also worked with a supplier to design and develop a fully automated encapsulation station capable of performing programmable liquid handling (dispensation/dosing, aspiration/refill) of both core and shell fluids. The encapsulation station can perform 4 encapsulations at a time in a fully programmable manner. The setup is now fully operational in our lab (Micro & Nano-Scale Transport Laboratory, University of Waterloo). See Appendix J for the engineering drawing of the encapsulation station.

Chapter 3 expands the applicability of the liquid-liquid encapsulation method demonstrated in Chapter 2. The method demonstrated in Chapter 2 had three primary restrictions. First, the generation of practically utilizable encapsulated droplets is possible only after successful interfacial penetration of the core droplet. It puts a stringent restriction on both the minimum allowable size of the core drop and the height of impact. In other words, the success of the previous method was kinetic energy dependent. The insufficient kinetic energy of the impacting core droplet leads to the drop not being able to penetrate through the interfacial layer and instead getting trapped at the interface. Second, the participating liquid triplet (the core, the shell, and the host liquid) needs to adhere to a density criterion. The core liquid needs to be the heaviest as the encapsulated cargo needs to separate from the interfacial layer and settle down at the bottom of the host bath. Third, being an all-liquid system, the encapsulated droplet is only stable as long as it is inside the host bath. The cargo cannot be extracted from the host bath for further processing/handling, often desired in multiple practical applications. In the present work, we show a holistic platform for liquid-liquid encapsulation using PDMS as the shell-forming liquid, which resolves all three above issues while retaining the simplicity and robustness of our previous approach. We demonstrate that complete interfacial penetration is not a strict prerequisite for successfully encapsulating the impacting core. Depending on the kinetic energy of impact, $\boldsymbol{KE}_{impact}$ (manifested in the impact Weber number, We_i), stable encapsulation can be achieved either by interfacial penetration or via interfacial trapping. We present a non-dimensional experimental regime for the occurrence of both cases in

terms of We_i and the non-dimensional interfacial layer thickness (δ/R_c). We also identify a critical Weber number, We_{cr}, as a function of δ that demarcates the two outcomes. We establish via experimental evidence and thermodynamic argument that, in either case, the resulting configuration is an encapsulated state where the interfacial layer wholly encloses the core droplet. It eliminates the minimum size restriction, the impact height limitation, and the density criteria and renders the method universal in terms of kinetic energy requirement, despite the impact-driven nature of the technique. Further, the presented framework is minimally restrictive regarding thermophysical property requirements. Stable encapsulation can be achieved as long as the participating liquid triplet (core, shell, and host liquid) adheres to an identified interfacial energy criterion. We also show that successful wrapping can safeguard liquid cores despite their miscibility with the host bath. Further, we leverage the interfacial trapping mechanism to create multifunctional Janus capsules. Next, the extraction of the interfacially trapped capsules is also demonstrated via heat curing of the PDMS outer shell, where we confirm the robustness of the wrapping layer in the cured state. We show that the interfacially trapped capsule with $V_{core} = 150$ μl and $V_{PDMS} = 1000$ μl possesses a crushing strength value of $P_{cr} \sim 4.7$ MPa. We also demonstrate that increasing V_{core} with a fixed V_{PDMS} leads to a reduction in both crushing force, $\boldsymbol{F}_{cr}$, and crushing strength, P_{cr} owing to a decrease in shell thickness in the cured capsules. To the best of our knowledge, this is the first time the practical utility of the interfacially trapped encapsulated state is being demonstrated. We believe the present work builds the foundation of a robust and minimally restrictive liquid-liquid encapsulation technology well suited for both commercial production and exploratory endeavors toward novel encapsulated material synthesis.

In Chapter 4, we use the impact-driven method demonstrated in Chapters 2 & 3 to demonstrate the underwater generation of encapsulated droplets with a magnetoresponsive (ferrofluid) shell. We show that both single component (here laser oil) core droplets and compound droplets (ethylene glycol droplets inside laser oil droplets generated using Y-junction flow arrangement) can be successfully wrapped with a thin ferrofluid layer. The wrapping ferrofluid film renders the entire encapsulated cargo magnetoresponsive. In the presence of an external permanent magnet, the interaction between the magnetic nanoparticles with the magnetic field results in the migration of the ferrofluid shell layer from

the apex to the bottom of the droplet. We utilize this behavior of the wrapping layer to perform controlled non-contact manipulation of the encapsulated cargo using a permanent magnet. We explore the linear motion of the permanent magnet in both horizontal (along the length direction of the cuvette) and vertical (along the axis of the droplet) directions to achieve different characteristics. We move the permanent magnet in the horizontal direction (along the length of the cuvette) to study the transportation characteristics of the encapsulated droplet. We quantify the translational characteristics in terms of disengagement length (δ), magnet speed (v_m) and the magnetic Bond number (Bo_m). We found that at a fixed Bo_m, an increase in v_m results in a decrease in δ and at a fixed v_m, an increase in Bo_m results in the increment in δ. We also show that for every Bo_m, there is a threshold value of v_m below which the droplet travels all along the cuvette length, and disengagement is not observed. Next, we show the robustness of the impact-driven wrapping by moving the permanent magnet up and down along the vertical axis. Although the ferrofluid shell layer is seen to migrate up and down in response to the moving magnet, the wrapping remained intact even after multiple cycles of magnet motion along the vertical direction. Further, we utilize the motion of the permanent magnet in the vertical direction and the consequent change in the morphology of the shell layer to develop a platform for controlled underwater coalescence of the encapsulated compound droplets. To the best of our knowledge, this is a first-time demonstration of the controlled coalescence of the encapsulated compound droplets via magnetic manipulation. It allows us to achieve underwater mixing of the internal ethylene glycol cores despite their miscibility with the surrounding aqueous medium. Finally, we show that magnetic actuation can also be used to release the inner ethylene glycol cargo in the encapsulated compound droplets, thus paving the way for future research on targeted/controlled cargo delivery.

Chapter 5 demonstrates a magnet-assisted facile encapsulation technique in which ferrofluid (FF) core droplets are encapsulated inside polydimethylsiloxane (PDMS) floating on a water bath inside a cuvette. This approach serves as an alternative to the impact-driven liquid-liquid encapsulation method presented in Chapters 2 - 4. Underwater formation of an encapsulated droplet in the impact-driven approach requires the core droplet to possess a threshold kinetic energy, which poses a restriction on the minimal usable drop size and the height of impact. The approach presented in this chapter enables us to circumvent

this restriction when the core is magnetoresponsive. In this work, a magnetoresponsive (ferrofluid) core droplet is gently placed on top of the floating interfacial layer instead of impinging from a separation. The core drop is then pulled downward using a permanent magnet placed below the cuvette at a vertical separation. A complex interplay between the magnetic force $\boldsymbol{F_m}$ and the interfacial tension force $\boldsymbol{F_i}$ results in the formation of a thin PDMS layer around the FF droplet which efficiently protects the PEG-based FF droplet underwater despite its complete miscibility in water. Based on the experimental observations, three regimes are identified: stable encapsulation, unstable encapsulation, and no encapsulation, which depends on the magnetic Bond number and the thickness of the PDMS layer. The technique is exploited to demonstrate stable wrapping of multiple ferrofluid droplets inside a single PDMS shell and successful underwater manipulation of the encapsulated droplets. Further, we also show the generalizability of the approach by demonstrating successful encapsulation with canola oil, a less viscous, non-viscoelastic shell-forming liquid compared to PDMS.

12.1.2 Interferometric observation of nanometric thin film

In Chapters 2 - 5, although we could confirm successful encapsulation via indirect experimental evidence (e.g., wetting signature, colorimetric change upon encapsulation, or evidence of efficient protection of miscible cargo), direct visualization/thickness estimation of the thin (nm - μm scale) wrapping layer remains extremely challenging using conventional imaging techniques. Chapters 6 and 7 are dedicated towards the development and subsequent exploration of a non-invasive imaging framework that can detect & reconstruct the spatiotemporal dynamics of such ultrathin films using confocal mode reflected laser interferometry.

Chapter 6 discusses the development of the framework in detail. To demonstrate the framework's capability, we chose the model case of low surface tension microdroplet condensation. The condensed microdroplets exhibit very low contact angles ($< 5°$), and the height of the condensed microdroplets is often less than $\sim$1 μm. It makes optical visualization of condensation dynamics extremely challenging. However, using our in-house developed framework, we could obtain sufficiently sharp experimental interferograms by

appropriately controlling the confocal pinhole. An automated numerical framework has also been developed to dynamically reconstruct the complete three-dimensional topography of the droplets from the obtained interferograms. For the demonstrated test case, our proposed framework allows us to determine the droplet shape with a vertical resolution of ~ 90 nm. Although we have illustrated the framework for studying dropwise condensation, the protocol, in its present form, finds direct applicability in the study of a wide range of fundamental phenomena involving droplet dynamics, including wetting, spreading, droplet pinning and motion, contact angle hysteresis, droplet coalescence, etc.

In Chapter 7, we delve deeper into the study of the dynamics of dropwise condensation of low surface tension liquids (here ethanol) using the interferometric framework demonstrated in Chapter 6. In doing so, we discovered a novel motion during the condensation process where the small condensed microdroplets spontaneously moved to relatively large droplets in the vicinity. Through structured experimentation, we confirmed that this motion is exclusive to the event of condensation of low-surface tension test liquids (e.g., ethanol/acetone) on high-surface energy test substrates (e.g., glass). In addition, the moving droplets showed extremely low contact angle hysteresis. From these observations, we attributed this motion to two factors: the formation of an ultrathin precursor film and a gradient in local temperature inside the small microdroplet caused by the difference in the size of adjacent droplets. We argue that the local temperature gradient causes thermocapillary effect and thus makes the small microdroplets move towards the large droplet close to them. The presence of the ultrathin precursor film underneath the nucleated droplets facilitates the motion by reducing the resistive force to migration. The driving force for the migration and the temperature gradient inside a small microdroplet were quantitatively calculated from the force balance of the pinned microdroplets. The extremely small driving force and the onset of the movement of the microdroplets with a very small base radius were presented as incontrovertible evidence of the existence of precursor film and its role in the detected motion.

12.1.3 Application of thin films: Liquid-infused porous surfaces with remarkable durability

Chapter 8 discusses a direct application of thin film-mediated wetting in materials research where we succeeded in designing lubricant depletion tolerant, long-term stable, large-scale slippery surfaces by infusing silicone oil into a bicontinuous porous composite of ZnO and PDMS. Despite their promising prospects, depletion of the surface lubricant layer during outdoor operation and subsequent loss of functionality have been a serious bottleneck for slippery lubricant-infused surfaces. In this work, we demonstrate a paradigm where we utilize unassisted capillary transport through the interconnected pores of the base layer to allow the surface to recover the surface lubricant layer even after exposure to severe depleting stimuli. As a proof of concept, we prepared meter-scale "LuBiCs roof" which retained water-repellent behavior without any maintenance even after exposure to harsh outdoor conditions for over 9 months in the sub-tropical climate of Japan, which involved both elevated & near-freezing temperatures, UV irradiation, and most importantly, heavy rainfall. To the best of our knowledge, similar long-term practical durability of lubricant-infused surfaces has not been reported before in the literature. Owing to the white color of the ZnO microfillers, the porous elastomeric base layer of LuBiCs is white in appearance and therefore is highly reflective, making them well-suited as coating materials for energy-efficient cool-roofing. Further, due to the usage of non-toxic, biocompatible silicone materials both as the backbone of the base layer and the infused lubricant, the LuBiCs stand out as an environmentally friendlier and sustainable choice over slippery surfaces employing base solid/lubricants. With the aforementioned functional advantages, we envision this work will pave the way toward the market entry of sustainable LIS for outdoor applications.

12.1.4 Quantification of droplet-substrate interaction

Chapters 9 - 11 discusses the development of a direct force-based characterization framework for droplet-substrate interfacial interaction, which is applicable for a wide range of surface wettabilities and Chapter 11 applies the framework to investigate how bacteria-

laden droplets interact with (super)hydrophobic surfaces.

In Chapter 9, we demonstrate a simple cantilever deflection-based adhesion characterization framework to investigate the frictional and adhesion characteristics of microparticle-laden drops over repellent surfaces. The force signature is captured by probing the target surface with a droplet of the test liquid mounted at the tip of a flexible cantilever and then tracking the deflection of the tip of the cantilever as the target surface retracts from the probe droplet-cantilever assembly. We show that the direct force measurements thus obtained are more reliable than regular optical goniometry for surfaces having high contact angle values where the inherent difficulties in optically imaging the solid–liquid interface and the challenges associated with the dispensation of the probe liquid significantly compromise the accuracy of measurements. Three coatings with different physicochemical properties but similar static water contact angles were investigated using the cantilever-based framework. We demonstrate that the theoretically estimated friction forces using the contact angle values obtained from optical goniometry differ significantly from the directly measured force values. This substantiates the need for the direct quantification of interaction forces over indirect force estimates obtained from the wetting signature for accurate surface characterization.

Chapter 10 critically revisits, augments, and redefines the cantilever deflection-based direct force measurement framework towards a more accurate and wettability invariant characterization of droplet-surface adhesion interaction. The cantilever-based adhesion measurement technique, as described in Chapter 9, has been limited to characterizing low-energy substrates, mainly due to the inability of the probe droplet to fully retract from high-energy surfaces. The present study generalizes this methodology, in particular, toward characterizing maximum substrate adhesion force over a broad surface energy spectrum. In doing so, we raise and subsequently answer some fundamental questions regarding the cantilever-based adhesion measurement approach. We use three substrates with different characteristic wettabilities to demonstrate the wettability invariance of our adopted approach. We quantify the adhesive interaction between the probe droplet and the test substrates based on high-speed imaging and subsequent image processing. We provide direct experimental evidence of a time gap between the occurrence of maximum deflection of the cantilever ($x_{\min}$ in $x - t$ curve) and the event of pull-off of probe droplet.

Important to mention that literature to date attributes the pull-off stage (of the probe droplet from the test substrate) as the occurrence of maximum deflection of the cantilever. The observed time-gap pinpoints an involved inaccuracy in the conventional approach of characterizing adhesion ($\boldsymbol{F}_{adh}$) by pull-off of the probe droplet. The time gap becomes more prominent as the surface energy of the test substrate is increased. Following this, we further demonstrate that even the maximally deflected state of the cantilever does not correspond to $\boldsymbol{F}_{adh}$, as the depinning of the triple contact line (TCL), the sole physical criterion with direct correspondence to $\boldsymbol{F}_{adh,}$ precedes the onset of the retraction of the cantilever by a prominent time gap. This insight, in particular, expands the applicability of the cantilever-based approach to higher energy surfaces, where we show that $\boldsymbol{F}_{adh}$ could be estimated just by detecting the depinning initiation of the TCL. Further, with detailed mechanistic analysis of cantilever motion, we establish that the point of zero acceleration of the cantilever corresponds to the point of depinning of the TCL and, thus, to the point of occurrence of $\boldsymbol{F}_{adh.}$ It eliminates the need to optically track the TCL, which is often plagued by imaging challenges near the contact line. We have also demonstrated that the fate of the droplet after cantilever detachment, which is dictated primarily by an interplay between the surface energies of the test substrate-probe droplet- cantilever triad, does not influence the definition of $\boldsymbol{F}_{adh}$. The characteristic adhesion is defined at the point of depinning of the droplet's triple contact line, irrespective of whether the droplet splits into two or gets pulled off from the substrate by the cantilever as a whole. From the execution perspective, the present methodology is general and straightforward. Simple tracking of the motion of the cantilever and subsequent computation of its acceleration, which can be automated, enable the user to characterize the ensuing maximum adhesion between the probe droplet and the test substrate, as long as the contact line of the probe droplet depins from test substrate during the retraction stage of the substrate. We envision that the inferences of this fundamental study will be beneficial in the rational design of direct wetting characterization methods for a wide range of test substrates with varying wettabilities.

In Chapter 11, we probe the adhesion behavior of bacteria-laden droplets on highly repellent hydrophobic surfaces using the method outlined in Chapter 9. The objective of this work is to assess whether similarly sized microparticles can be used as proxies for live bacteria in wetting studies. We show that contact angle-based optical goniometry pro-

vides an incomplete (and consequently inconclusive) description of the ensuing interfacial interaction between bacterial droplets and repellent surfaces. Apart from the imaging uncertainties (typically arising at high contact angle), the wetting signature only captures the behavior of the three-phase contact line and does not reveal any information on the contact surface underneath the droplet, which is directly responsible for the adhesion behavior. We report that despite the qualitative similarity in concentration dependence of static as well as dynamic contact angles between microparticle suspension and bacterial (both live and dead) loads, the adhesion behavior of live bacterial load exhibits a completely contrasting dependence on doping concentration. Unlike dead bacteria and inert microparticles, the adhesion force reduces with increasing doping concentration in the case of probe droplets containing live bacterial loads. We attribute this contrasting adhesion signature of live bacteria to its viability and motility. We test three common biochemically relevant fluids as the suspension medium on two different repellent surfaces, and the conclusion remains the same. It confirms that despite similar length scales, inert microparticles are not suitable surrogates for living bacterial cells in wetting studies.

12.2 Directions for Future Work

The liquid-liquid encapsulation paradigm developed in this thesis presents a wealth of opportunities for both fundamental explorations and practical pursuits. In the present thesis, we explored only a small subset of these possible directions, and we tried to maintain a practical outlook while deciding the direction to pursue. There exist several alternate avenues of exploration that involve both rich fundamental physics and practical utility.

For example, the hydrodynamics of droplet impact at the three-fluid interface (host bath - interfacial layer - air) remains an open problem that will likely have its own physical understanding. Although the dynamics of droplet impact on both thin liquid films and deep liquid pools have been the subjects of extensive investigation, studies on the impact dynamics on thin liquid films floating on a deep pool are extremely rare. After we reported the liquid-liquid encapsulation framework [1], Kim *et al.* reported an impact study [2] on floating liquid film where the impacting droplet is of the same composition as the floating

interfacial layer. Impact study where the impacting droplet and the floating layer are dissimilar & immiscible (similar to the paradigm of liquid-liquid encapsulation) is almost nonexistent. Also, in Chapter 3, we briefly discussed the interesting role of the shell-forming liquid's viscoelasticity in the dynamics of encapsulation. A structured hydrodynamic study in this regard could generate new physical insights.

Moreover, a critical assessment of the practical utility of the liquid-liquid encapsulated drops would require a thorough understanding of the stability of the liquid wrapping film (the "shell"). Such thin liquid films (with thickness ranging between nm - μm) are dynamically evolving under the influence of the surrounding entities (here the host bath and bottom substrate). This is an ongoing research direction in our lab. The framework developed in Chapter 6 - 7 is being used to capture the dynamic evolution of the liquid wrapping layer of the encapsulated droplet while the droplet is still residing in the host bath.

Also, in Chapter 4, we demonstrated magnet-assisted release of the enclosed inner cargo in ferrofluid-wrapped droplets. However, the controllability of the release is yet to be optimized, which can be a rewarding research direction. In our lab, we are now exploring the possibility of combining alginate chemistry with the liquid-liquid encapsulation framework to achieve controlled release of the encased cargo.

Further, as noted in Chapter 8, the optimization of the mixing ratio of ZnO and PDMS during the fabrication of the base layer of LuBiCs is an interesting engineering pursuit toward finding the optimal balance between the lubricant storage capacity and the speed of capillarity driven self-healing.

We also believe that the attempt to extend the adhesion characterization framework discussed in Chapters 9 - 11 to probe underliquid droplet-surface adhesion will be a challenging yet practically rewarding research direction. A logical follow-up of this endeavor could be to use the liquid-liquid encapsulated droplet as the probe droplet and then characterize its adhesion with different target surfaces in the presence of the viscous surrounding medium (host bath).

Additionally, in Chapter 11, we reported an anomalous adhesion behavior of live bacteria on repellent surfaces. We are now probing the internal dynamics of motile bacteria in sessile droplets using micro-Particle Image Velocimetry (μ-PIV) to better explain this

anomaly.

References

[1] S. Misra, K. Trinavee, N. S. K. Gunda, and S. K. Mitra, "Encapsulation with an interfacial liquid layer: Robust and efficient liquid-liquid wrapping," *Journal of colloid and interface science*, vol. 558, pp. 334–344, 2020.

[2] D. Kim, J. Lee, A. Bose, I. Kim, and J. Lee, "The impact of an oil droplet on an oil layer on water," *Journal of Fluid Mechanics*, vol. 906, p. A5, 2021.

APPENDICES

Appendix A

Supporting Information for Chapter 2

A.1 Shape of the interfacial film layer

When the canola oil is dispensed dropwise on top of the water bath using a needle, the oil drops spread on top of the bath upon contact with water and ultimately attains a lens shape, where the bottom part of the lens is in contact with water while the top side faces air (see the schematic in Figure A.1A). However, from the experimental images (presented in Figure A.1B, A.1C) it might appear that the oil lens is completely submerged in water and there is an intermediate water film that prevents any direct contact of the lens with air. It resembles the pseudo-total wetting state as reported in [1]. Confirmation of the possibility of formation of any such intermediate water film is crucial for this work as the existence of such a film of the surrounding medium would require the core drop to come in direct contact with the host liquid before it can interact with the interfacial wrapping layer and any possible direct contact with the surrounding would violate one of the fundamental requirements of successful encapsulation, viz., the isolation of the core material from surrounding.

However, according to [1], for such a pseudo-total wetting state to form, the spreading parameter of the floating liquid (L2) on the bath (L3), S_{23} should be negative with the spreading parameter of the bath (L3) on the floating liquid (L2), S_{32} being positive. S_{23}

and S_{32} are defined as,

$$S_{23} = \gamma_3 - \gamma_2 - \gamma_{23} \quad \& \quad S_{32} = \gamma_2 - \gamma_3 - \gamma_{23}$$

In our experiments with canola oil (L2) layer on water (L3),

$$S_{23} = (72 - 31.3 - 18.01)\ \text{mN/m} \ = \ 22.69\ \text{mN/m} \ > \ 0$$
$$S_{32} = (31.3 - 72 - 18.01)\ \text{mN/m} = -\ 58.71\ \text{mN/m} < 0$$

Therefore, as both the theoretical requirements are unmet, existence of such a pseudo-total wetting state stands theoretically infeasible.

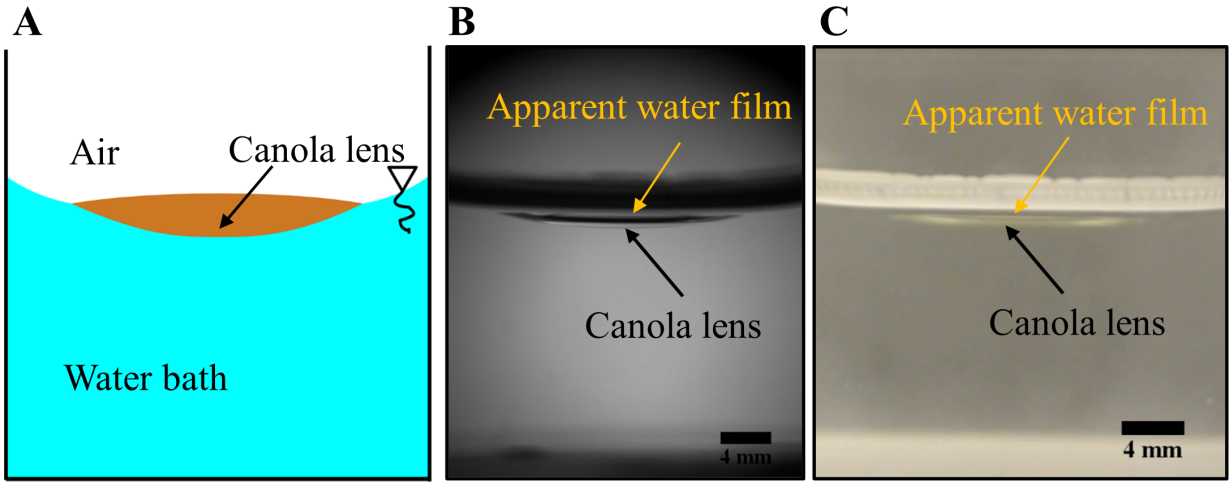

Figure A.1: Shape of interfacial layer – **(A)** Schematic representation (not to scale) of the canola lens floating on top of a water bath, **(B)** grayscale experimental image of the interfacial canola oil layer dispensed on top of the water bath, captured with a high-speed camera, **(C)** colored image of the interfacial layer in same experimental set up captured using a digital SLR camera from a plane perpendicular to that of the high-speed camera.

We would like to comment that this is merely an imaging artefact arising due to the curved concave meniscus shape of water in glass cuvette. To reaffirm this, we have conducted a simple experiment (see movie S2). After a canola film layer (with film volume of 220 μL) is formed on top of the water bath, a water drop is dispensed on top of the

film with a pipette. Had there been an intermediate water film on top of the canola layer, the dispensed water drop would have spread instantaneously due to direct contact between two similar liquid surfaces. However, the drop does not spread and is seen to retain itself. This serves as a practical confirmation that there is no intermediate water film between the canola lens and water.

A.2 Estimation of maximum thickness of the interfacial oil layer

The shape of the interfacial liquid (L2) layer is dependent on the values of surface and interfacial tensions and the volume of the dispensed liquid. In our experiments, upon being dispensed on the water (L3) - air interface, the canola oil (L2) film takes the shape of a bi-convex lens with one side in contact with water while the other side is exposed to air.

The lens can be approximated to be the intersection of two spheres of different radii at a common circular plane, the diameter of which is equal to the diameter of the contact line (l_c). The top portion (air side) and bottom portion (water side) of the lens therefore can be represented geometrically by caps of two spheres with radii R_A and R_B respectively. And the two aforementioned spherical caps subtend angles $2\theta_A$ and $2\theta_B$ at their respective center, where θ_A and θ_B are the air and water side contact angles of the liquid lens. See Figure A.2 for a schematic representation of the cross-sectional view of such a lens with relevant geometric parameters. δ_{max} is the maximum thickness of the entire lens and h_B is the maximum thickness of the spherical cap on the water side (bottom).

$$l_c = 2R_A \sin\theta_A \ = 2R_B \sin\theta_B$$

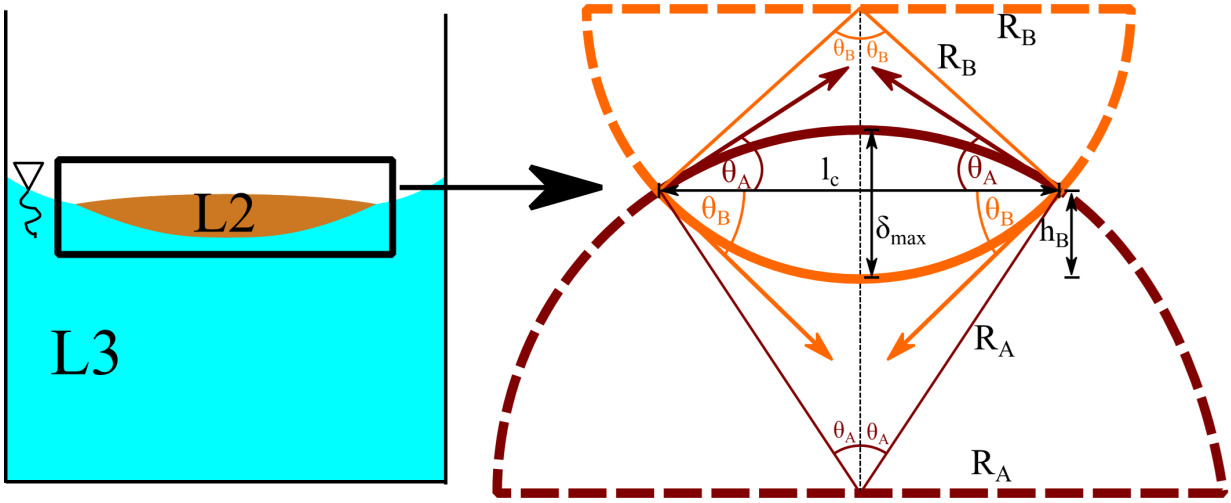

Figure A.2: Cross-sectional view of the geometric profile of the interfacial oil layer – Representation of the liquid lens as an intersection of two spheres with different radii at a common circular plane.

As mentioned earlier in section A.1, due to the concave shape of water-air meniscus, experimental visualization of the entire lens shape becomes difficult as the downward curved meniscus obscures the side view of the top part of the lens. However, as can be seen in Figure A.1C, the water side (bottom portion) of the lens can be imaged from the side-view. The diameter of the contact line l_c and the maximum thickness on the water side h_B can therefore be unambiguously determined from the image. Due to spherical geometry, θ_B can be obtained thereafter from l_c and h_B as, $\theta_B = 2\tan^{-1}\left(\frac{2h_B}{l_c}\right)$.

Now the total volume of the lens V_{film} (combining the individual volumes of the two spherical caps) can be expressed as a function of l_c , θ_A, and θ_B as

$$
\begin{aligned}
&V_{\text{film}}\left(l_c, \theta_A, \theta_B\right) \\
&\qquad = \frac{\pi {l_c}^3}{24}\left(2\csc\theta_A{}^3 + \cot\theta_A{}^3\right. \\
&\qquad \left. - 3\cot\theta_A\csc\theta_A{}^2 + 2\csc\theta_B{}^3 + \cot\theta_B{}^3 - 3\cot\theta_B\csc\theta_B{}^2\right)
\end{aligned}
\tag{A.S1}
$$

The volume of the dispensed liquid is known. Also, l_c and θ_B are determined from the

experimental image. Eq. (A.S1) can be solved now to obtain the value of θ_A which allows us to reconstruct the entire shape of the interfacial oil lens.

The maximum thickness of the lens, δ_{max} can be determined thereafter from

$$\delta_{\max} = \frac{l_c}{2}\left(\tan\frac{\theta_A}{2} + \tan\frac{\theta_B}{2}\right) \tag{A.S2}$$

A general observation is that both the diameter of contact line, l_c and maximum film thickness δ_{max} increase with increase in the volume of interfacial layer. The calculated values of l_c and δ_{max} are tabulated in Table A.1 for different values of interfacial film volume, V_{film} used in this work.

V_{film} (μL)	l_c (mm)	δ_{max} (mm)
30	8.15	1.14
80	10.82	1.73
100	12.06	1.74
120	12.22	2.02
160	14.14	2.02
220	15.60	2.28
270	17.09	2.33
320	17.72	2.56
370	18.72	2.65
420	19.26	2.84
470	19.88	2.99
500	20.17	3.08
550	20.67	3.23
600	21.21	3.34
650	21.71	3.45
850	22.72	4.13
900	23.31	4.15
1150	25.85	4.31
1200	26.31	4.34
1400	27.45	4.65

Table A.1: Dependence of contact line diameter, l_c and maximum layer thickness, δ_{max} on interfacial film volume,V_{film}

A.3 Estimation of volume and thickness of encapsulating layer using image processing

First the outlines of the drops have been extracted from the grey-scale experimental images (the 2D projection of the drops) employing a Sobel-Feldman edge detector algorithm before discretizing the obtained drop shapes to a pixel level precision. The volume, cross-sectional area and surface area of the drops have been calculated thereafter assuming axial symmetry of the drops around a central vertical axis. A theoretical framework to estimate the encapsulated film thickness has also been developed utilizing the extracted outline of the encapsulated drop under the assumption that the film is of uniform thickness.

Once the outline of the drop is determined using the edge detector algorithm, the local radius of the drop, r can be expressed as a function of z. Thereafter the volume of both the core drop as well as the encapsulated drop can be estimated by approximating the drops to be a vertical stack multiple cylindrical sections with radius r(z) and height 1 pixel. Figure A.3 provides a schematic representation of the axis-symmetric encapsulated drop shape that has been used to calculate the geometric properties of the drops.

$$V_{\text{core}} = \int_{z_{\text{apex}}}^{z_{\text{nose tip}}} \pi \left\{ r\left(z\right) \right\}^2 dz$$

$$V_{\text{core + shell}} = \int_{z_{\text{apex}}}^{z_{\text{nose tip}}} \pi \left\{ r\left(z\right) + \delta \right\}^2 dz$$

$$\therefore\ V_{\text{shell}} = \int_{z_{\text{apex}}}^{z_{\text{nose tip}}} \pi \left\{ \delta^2 + 2r\left(z\right)\delta \right\} dz = \pi\delta^2 L_{\text{drop}} + \ \pi\delta A_{\text{cs, core}} \tag{A.S3}$$

Here V_{core} is the volume of the core, V_{shell} is the volume of the shell layer, δ is the thickness (uniform) of the shell layer, L_{drop} is the vertical span of the drop expressed as $L_{\text{drop}} = z_{\text{nose tip}} - z_{\text{apex}}$ and $A_{\text{cs, core}}$ is the cross-sectional area of the core drop about a central vertical axis.

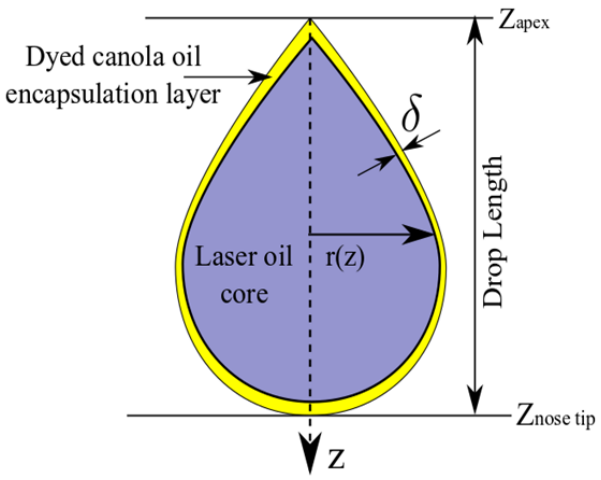

$$V_{core} = \int_{z_{apex}}^{z_{nosetip}} \pi \{r(z)\}^2 dz$$

$$V_{core+shell} = \int_{z_{apex}}^{z_{nosetip}} \pi \{r(z)+\delta\}^2 dz$$

$$\therefore V_{shell} = \pi \delta^2 L_{drop} + \pi \delta A_{cs,core}$$

Figure A.3: Schematic representation (not to scale) of the 2-D projection of an axis-symmetric encapsulated drop with uniform shell thickness.

As highlighted already in the main manuscript, if we consider the drop shape just before it reaches the bottom of the cuvette, the encapsulated drop can be assumed spherical with uniform shell thickness when the interfacial film volume is moderately low (< 500 μL). This simplifies the process for ballpark estimation of encapsulating layer thickness. In that case film thickness, δ can be estimated as $\delta = \left(\sqrt[3]{\frac{3V_{\text{core+shell}}}{4\pi}} - \sqrt[3]{\frac{3V_{\text{core}}}{4\pi}} \right)$.

A.4 Dye assisted visualization of encapsulation process

Although visible, the distinctive identification of the core-shell structure in Figure 2.2B-D still remains subjective in nature as both the core drop and the shell layer are optically translucent. To facilitate objective visualization, a partially oil soluble particle-based dye (Product Name: OrcoSolve Quinoline, Organic Dyes and Pigments, Rhode Island, RI, USA) is mixed with liquid L2 to prepare a suspension. This suspension is used to form the interfacial layer. Addition of this dye renders the interfacial layer optically opaque. To ensure homogeneity, the prepared suspension is thoroughly stirred using a vortex mixer (Product catalog No. 02-215-422, Fisherbrand^{TM} Pulsing Vortex Mixer, Fisher Scientific,

Ottawa, Ontario, Canada) at 2700 rpm for 1 minute before conducting the experiments.

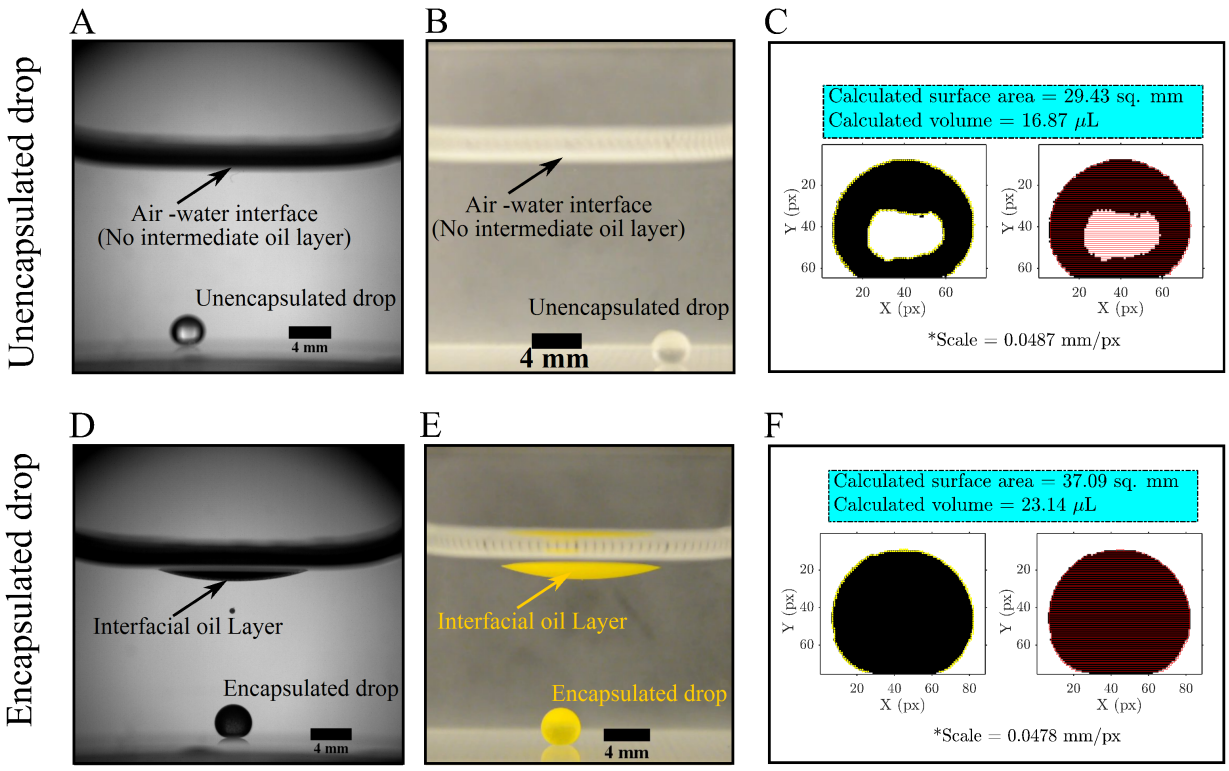

Figure A.4: Dye assisted visualization of encapsulation process: (A, D) represent of grayscale images of settled unencapsulated and encapsulated drops respectively captured using high speed camera. **(B, E)** provides colored visualization of the unencapsulated and encapsulated drops respectively captured using a digital SLR camera from a plane perpendicular to that of high-speed camera. **(C, F)** illustrates the extracted drop shape (using image processing) and results of volume and surface area calculation using vertical stack of axisymmetric cylinders with varying radius for the unencapsulated and encapsulated drops respectively.

Thereafter an encapsulation experiment is carried out for an impact height of 8 cm in the presence of an interfacial film of volume 150 μL consisting of the aforementioned optically opaque, homogeneously dyed suspension. The suspension is prepared by thoroughly mixing 2.5 gm of a yellow particle-based dye with 100 mL of canola oil. The surface tension of the

prepared suspension was measured using pendant drop tensiometry and found to remain practically invariant upon addition of the dye (the calculated value of surface tension of the dyed suspension was 32.36 mN/m while the undyed canola oil has a surface tension of 31.3 mN/m). However, it is to be noted that upon addition of dye, the density and viscosity of the interfacial liquid change in comparison to that of undyed canola oil. The density increases to 926 kg/m^3, which is still less than of the host liquid because of which the interfacial layer can remain stably suspended on the host water bath underneath. However, due to addition of the dye, the average viscosity increases to 71.82 mPa-s in comparison to 63 mPa-s in undyed canola oil. This increment corresponds to an increase in viscous resistance offered by the interfacial layer to the core drop in the penetration process. Consequently, necessary modification in the interfacial film volume and/or the impact height is needs to be incorporated to ensure successful encapsulation.

Successful encapsulation yields an encapsulated drop with a distinctively visible all-around yellow wrapping layer. While the unencapsulated drop (when there is no floating interfacial layer in the path of water entry of the core drop) remain translucent (see Figure A.4A, A.4B and movie S3), the encapsulated drop turns optically opaque (Figure A.4D, A.4E and movie S3), as can be seen from both the grayscale image captured with a high-speed camera and the colored image captured with a digital SLR camera. Additionally, assuming axisymmetric drop shape, the volumes of both the encapsulated as well as unencapsulated drops are calculated using the image processing protocol described in section A.3. The encapsulated drop registers 37% more volume in comparison to its unencapsulated counterpart (Figure A.4C and A.4F). This volume increment is a result of the formation of an encapsulating layer. These two aforementioned differences between the two drops serve as another conclusive evidence of encapsulation.

Contextually, it is to be noted that this post encapsulation volume increment does not require usage of dye in interfacial layer. Even in the absence of any dye, the encapsulated drop registers a higher volume than its unencapsulated counterpart (as can be confirmed from the side-by-side visual comparison of drop size in Figure 2.2B as well as from the reported values of encapsulated drop volume in Figure 2.6 in Chapter 2).

References

[1] J. Sebilleau, "Equilibrium thickness of large liquid lenses spreading over another liquid surface," *Langmuir*, vol. 29, no. 39, pp. 12118–12128, 2013.

Appendix B

Supporting Information for Chapter 4

B.1 Variation of magnetic field ($\boldsymbol{H}$) in the z-direction

As stated in Chapter 4, if the strength of the magnetic field at a particular magnet height is known, it can be used to calculate the magnetic Bond number Bo_m. For this, we performed simulations of the magnetic field (H, in A m^{-1}) using commercial finite element solver COMSOL Multiphysics 5.2a. We first create a geometry of the magnet that we used in the experiments. The magnet size is $a = b = c = 1.27$ cm, which is kept inside an air box with size $p = q = r = 12.7$ cm. The computational domain is meshed using tetrahedral elements of a maximum mesh size of 0.69 cm and minimum mesh size of 0.05 cm. The mesh growth rate is 3.55 cm. The input parameters used in the simulation are the relative permeability of air $\mu_r = 1$ and the relative permeability of the neodymium iron boron magnet $\mu_m = 1.05$. The following governing equations are used to solve the system.

$$\begin{aligned} \nabla \cdot \boldsymbol{B} &= 0 \\ \boldsymbol{B} &= \mu\mu_r \boldsymbol{H} + \boldsymbol{B_r} \\ \boldsymbol{H} &= -\nabla V_m \end{aligned} \tag{B.S1}$$

where, $\boldsymbol{B}$ is the magnetic flux density, $\boldsymbol{B_r}$ is the remnant flux density and V_m is the

magnetic scalar potential. The above equations are subject to the following boundary conditions.

$\boldsymbol{B_r} = 0$ in air and $\boldsymbol{B_r} = 1.32\ T$ inside the magnet.

At the air-box boundary, the insulation boundary condition is imposed $n \cdot \boldsymbol{B} = 0$. The results are presented in Figure B.1 in terms of variation of $\boldsymbol{H}$ vs z.

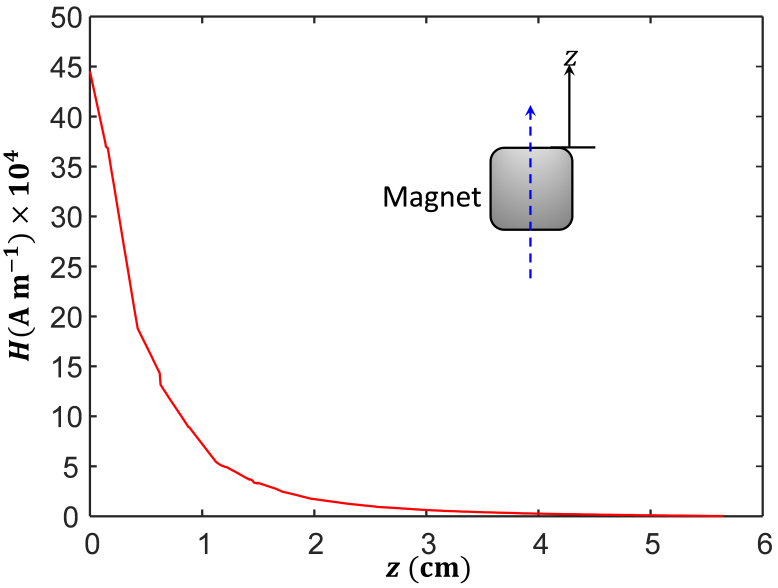

Figure B.1: Variation of the magnetic field $\boldsymbol{H}$ along the distance z from the surface of the neodymium iron boron magnet used in the experiments. The axis of magnetization is shown by the dashed blue line.

B.2 Image processing of ferrofluid excess layer

Here, we discuss the calculation scheme for excess ferrofluid layer width w_{ff} and its coverage area A_{ff} as discussed in Figure 4.4(b2)-4.4(b5) in the manuscript. w_{ff} is defined as the span of the excess ferrofluid layer along a vertical direction as shown in Figure B.2a. A_{ff} is defined as the spherical cap surface area of the excess layer as shown in Figure B.2b.

We identify the span of the excess layer using image processing in MATLAB. We first convert the color image to a grayscale image using the function 'rgb2gray()' as shown in Figure B.2c. For the grayscale image, the pixel intensity ranges from **0** to **255.** We convert the grayscale image to a binary image using a threshold grayscale intensity of **35** as shown in Figure B.2d. Any pixel with an intensity less than **35** is assigned a new intensity value of **0**. Conversely, the remaining pixels are assigned a new intensity of **255**. We then call the 'Sobel' edge detection function to locate the apex of the droplet. If the excess layer begins from the top, then the apex is taken as the starting pixel of the span having **0** grayscale intensity.

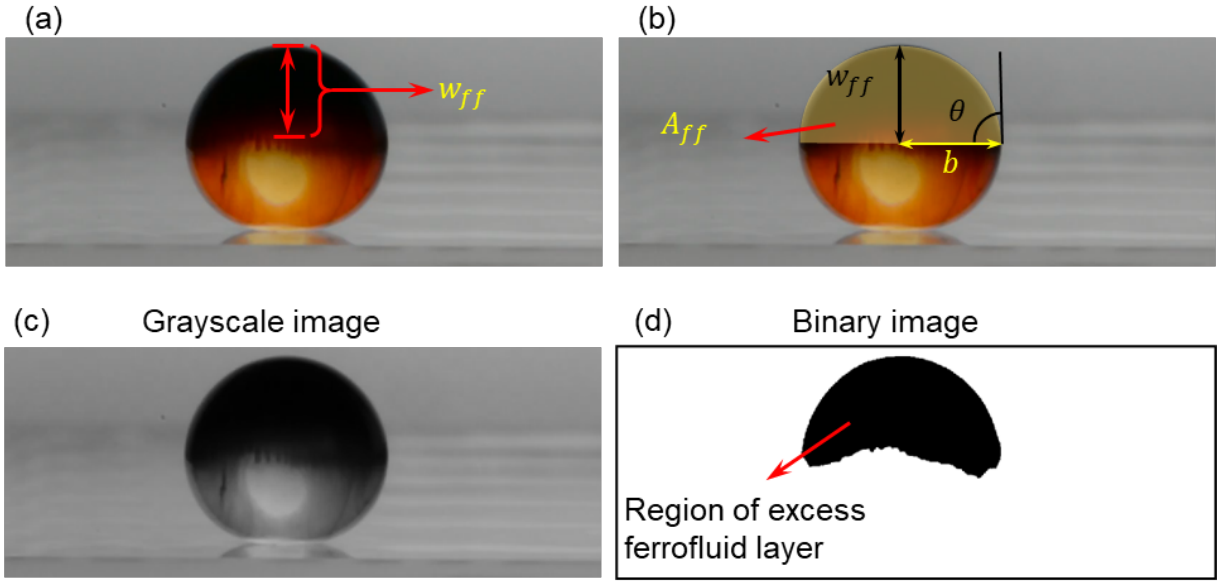

Figure B.2: Steps used for calculating excess layer width w_{ff} and its coverage area A_{ff}. (a) Color image of the ferrofluid encapsulated droplet. The dark appearance at the top hemisphere is visually identified as the region of excess ferrofluid layer. The vertical separation of the excess layer region is defined as the width w_{ff} of the ferrofluid layer across the droplet surface. (b) Illustration of excess layer coverage area A_{ff} assuming spherical cap geometry. b and θ represent the base radius and contact angle of the spherical cap, respectively. (c) Grayscale image of the droplet (shown in (a) and (b)). (d) Binary image with appropriate grayscale thresholding to identify the region of excess ferrofluid layer.

Next, we probe the grayscale intensity of each pixel vertically downward from the apex. Since, the binary image only has two values of pixel intensities, with **0** representing the excess ferrofluid layer and **255** the non-excess layer region, the pixel location at which the grayscale intensity changes from **0** to **255** is marked as the end point of the excess layer span. However, if due to magnetic force, the ferrofluid layer is pulled below the apex, then the starting pixel location of the span is identified according to whether the grayscale intensity changes from **255** to **0** when starting down from the apex. Thereafter the endpoint of the span is identified as discussed earlier. The pixel span is then converted to real scale, which gives us the width of the ferrofluid layer across the droplet surface. For the image shown in Figure B.2, the excess layer begins from the apex, hence apex pixel location is the starting pixel of the excess layer span. The apex pixel location is **12** for the image shown in Figure B.2d. MATLAB image processing environment counts pixel location from the top left corner of an image, hence the value of **12** here implies that the apex lies at the $\mathbf{12^{th}}$ row from the top. Similarly, the end location of the excess layer is found to be **142**. Thus, the width w_{ff} in pixels is $\mathbf{142 - 12 = 130}$. The pixel span is then converted to real scale values by multiplying with the length scale, which for Figure B.2 is **0.0131 mm** per pixel. This converts to a value of **1.7 mm** for w_{ff}.

Similarly, we calculate the coverage area A_{ff} using the spherical cap assumption. If the excess layer starts from the apex, then A_{ff} is simply given by the area of the corresponding spherical cap, otherwise, it is subtracted from the total surface area of the droplet. The spherical cap base radius b is calculated using $b = \sqrt{w_{ff}\,(D - w_{ff})}$ and the excess layer coverage area is calculated using $A_{ff} = \pi\left(b^2 + w_{ff}^2\right)$. Here, D is the droplet diameter and is equal to **3.7 mm** for the droplet image shown in Figure B.2. Using the value of $\boldsymbol{w_{ff} = 1.7}$ **mm** and $\boldsymbol{D = 3.7}$ **mm**, we calculate $\boldsymbol{b = 1.8}$ **mm**. Then using b and w_{ff}, we calculate $\boldsymbol{A_{ff} = 18.8}$ $\mathbf{mm^2}$ for the droplet image shown in Figure B.2.

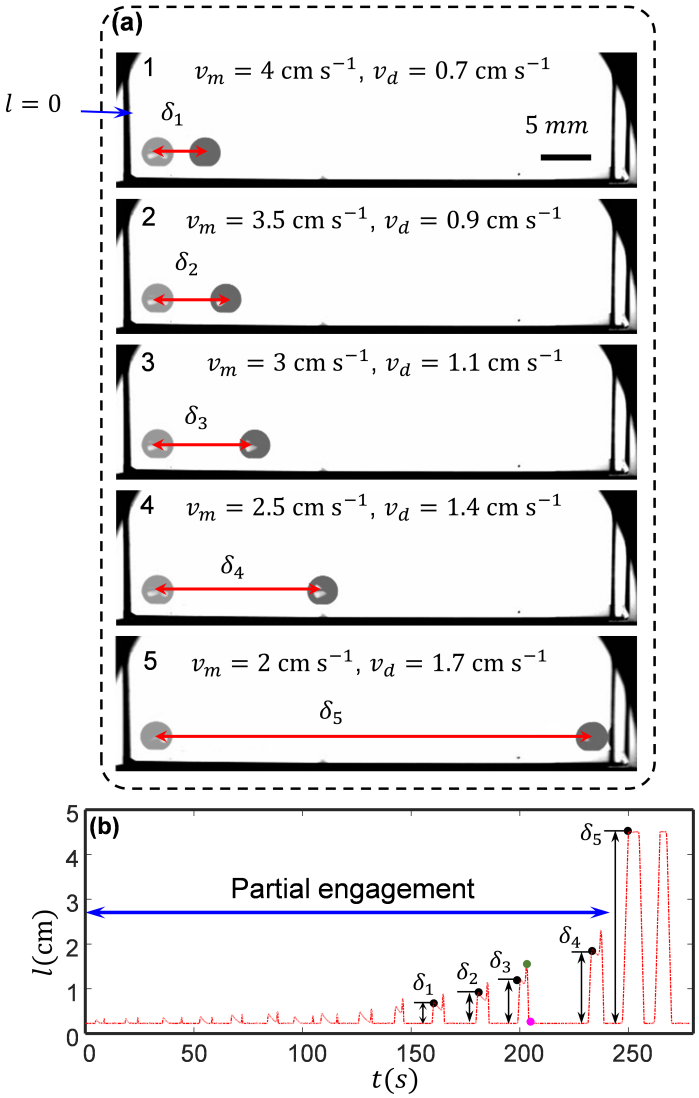

Figure B.3: (a) Sideview snapshots of the high-speed video for droplet disengagement length δ at different magnet speeds v_m. (b) The plot showing the temporal variation of the droplet displacement l. The peaks and valleys in the plot denote the translation and disengagement of the droplet with the moving magnet. The disengagement lengths δ corresponding to the snapshots in (a) are denoted by numeric $1-5$.

B.3 Experimental process adopted for obtaining the disengagement length.

For the results shown in Figure 4.5(a-d) in Chapter 4, we start from a high magnet speed and gradually decrease it in discrete steps using the linear translator. For clarity of discussion, we present Figures 4.5a and 4.5b from the manuscript here as Figure B.3. Let us consider an intermediate point on the plot in Figure B.3b denoted by numeric $\boldsymbol{\delta_3}$, which corresponds to the image number **3** in Figure B.3a, having a magnet speed of **3 cm/s**. Initially, the droplet is at the extreme left of the cuvette. As the magnet moves inward from the left-hand side, it actuates the droplet by a distance of $\sim$**1 cm**, beyond which the droplet disengages, and the magnet moves ahead. This event is marked by an abrupt upward jump in the plot of $\boldsymbol{l}$ vs $\boldsymbol{t}$ (Figure B.3b) at the location marked by the numeric 3.

The droplet remains stationary until it is actuated again when the magnet moves back from the right-hand side. Initially, the droplet is immediately pulled towards the right and engages with the magnet (shown by the green dot), after which it moves towards the left, eventually coming to a full stop due to the cuvette wall (shown by the pink dot). The above sequence of events repeats with now the droplet at point **4** and the magnet speed decreased to **2.5 cm/s**. Gradually, at a sufficiently low magnet speed of **2 cm/s**, the ferrofluid encapsulated droplet travels left and right, all along the cuvette length, denoted by numeric **5** in Figure B.3a. The corresponding point in Figure B.3b is shown by $\boldsymbol{\delta_5}$, which is the maximum length of travel for the given cuvette size. Here, it is to be noted that while the cuvette size is **5 cm**, the maximum displacement is less than **5 cm**. Since we track the droplet center in our calculations, the actual distance available for maximum translation is $\sim$**4.5 cm**, which is why the value of $\boldsymbol{\delta_5}$**<5 cm**. Another interesting feature is observed in the trend of $\boldsymbol{v_m}$ and $\boldsymbol{v_d}$ mentioned in Figure B.3a. Initially for the high value of $\boldsymbol{v_m}$, $\boldsymbol{v_d}$ is relatively low. Gradually, as $\boldsymbol{v_m}$ decreases, $\boldsymbol{v_d}$ increases such that at a sufficiently low $\boldsymbol{v_m}$**=2 cm/s**, $\boldsymbol{v_d}$**=1.7 cm/s** is high enough for complete translation along the cuvette. The above discussion pertains to a single value of $\boldsymbol{v_m}$ to illustrate the mechanism of drop translation.

B.4 Image processing of drop translation

We perform image processing of drop translation using MATLAB. The steps used in the implementation are shown in Figure B.4. First, we extract the raw image from the source video file and suitably crop the region of interest as shown in Figures B.4a and B.4b. The cropped image is then converted to a binary image using appropriate grayscale thresholding. For every pixel, the grayscale intensity can take a value between **0** to **255**, with **0** implying a pure black pixel and **255** implying a pure white pixel. For the image shown in Figure B.4a and Figure 4.5a in Chapter 4, we adopt a threshold intensity of **150** such that any pixel with intensity less than **150** is assigned a new grayscale intensity of **0** and any pixel with intensity greater than or equal to **150** is changed to **255**. We thus, convert the original grayscale image to a binary image with the droplet represented by pixels of **0** intensity, i.e., the droplet appears completely black as shown in Figure B.4c. Conversely, the ambient pixels have a grayscale intensity of **255** and hence, appear white. We then call the inbuilt 'Sobel' edge detection function in MATLAB to identify the droplet profile. 'Sobel' function scans every pixel and wherever it finds a change in the value of grayscale intensity, it identifies that pixel as a boundary point and assigns it a value of **1**. Since the binary image in Figure B.4c has only two grayscale intensity values of **0** and **255**, 'Sobel' function easily detects the boundary pixels and assigns them a value of **1**. The remaining pixels are assigned a value of **0**. This transformation gives us the droplet profile shown by the white contour in Figure B.4d. We next convert the pixel location of the droplet profile to real scale values and superimpose it onto the original image shown by the blue color profile in Figure B.4e. Assuming a circular droplet profile, we finally locate the center of the droplet shown by the red star. We repeat the above steps for all the video frames which give us a data array for drop displacement l and drop speed v_d with time.

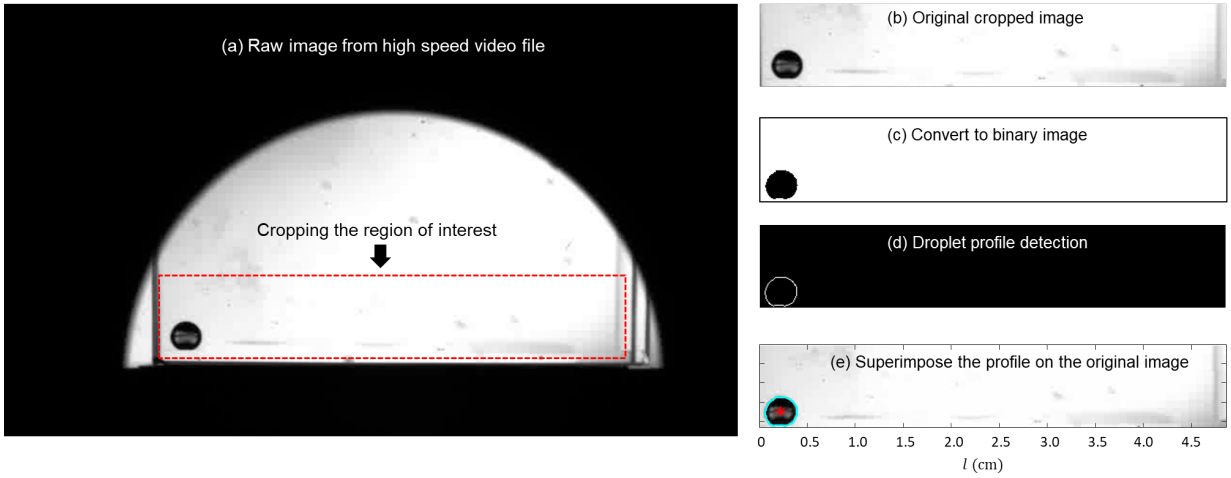

Figure B.4: Image processing steps for extracting the date for drop translation. (a) Raw grayscale image from the source video file. (b) Original Cropped image for image processing. (c) The cropped image was converted to a binary image with the droplet represented in black with 0 pixel intensity. (d) The droplet profile is shown by the white contour. (e) The droplet profile is superimposed on the original cropped image with the droplet center denoted by the red star.

B.5 Ethylene glycol-ferrofluid (EMG 900) incompatibility

As discussed in Chapter 4, the oil-based ferrofluid (EMG 900) used in the current work is found to be incompatible with ethylene glycol. We show incompatibility by performing an experiment in which the ethylene glycol is dispensed on the ferrofluid layer from close proximity as shown in the top view images in Figure B.5.

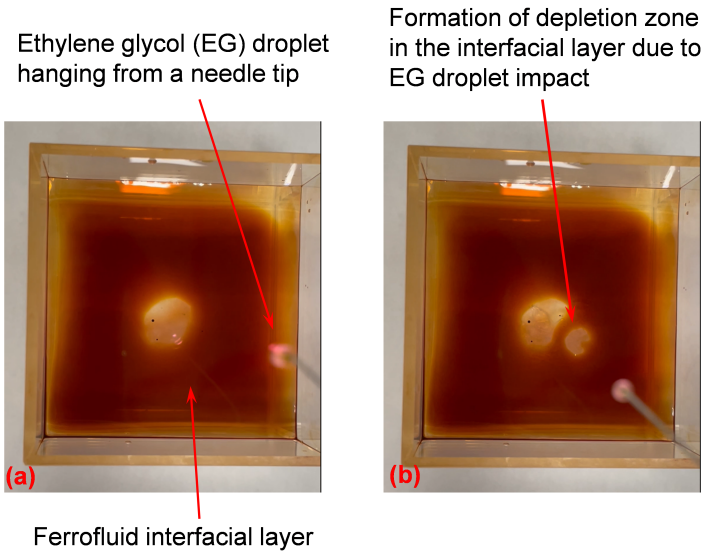

Figure B.5: (a) Top view image of the cuvette showing the ferrofluid interfacial layer and a dyed ethylene glycol droplet just about to detach from the needle tip. The central grey area is the ferrofluid depletion zone that formed due to the previous dispensation of an EG droplet. (b) Image showing the formation of a second depletion zone due to the impact of the EG droplet shown in (a).

It is clearly observed from Figure B.5 that the impact of the EG droplet on the ferrofluid interfacial layer leads to formation of circular depletion zones which are visibly devoid of ferrofluid. The images reveal that EG droplet itself cannot be encapsulated by the oil-based ferrofluid and hence, needs to be packaged inside laser oil in a compound droplet configuration.

Appendix C

Supporting Information for Chapter 5

C.1 Variation of H-field

The H-field ($\boldsymbol{H}$, in A m^{-1}) produced by the rectangular permanent magnet was estimated using the analytical expression [1]. The schematic of the rectangular permanent magnet is shown in Figure C.1, and the variation of the H-field is depicted in Figure C.2.

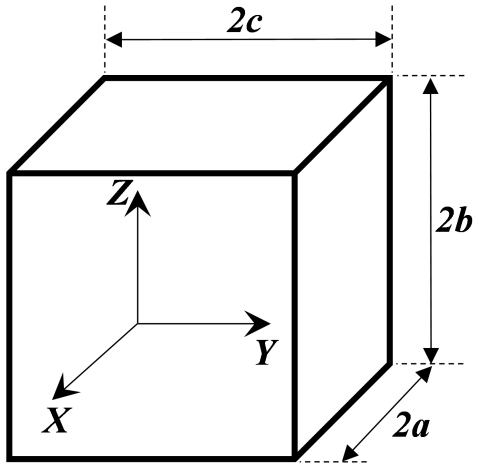

Figure C.1: Schematic of a magnet.

The H-field in the x-direction is given by

$$H_x = -\frac{B_r}{4\pi\mu_0}\Big[F_1\left(-x,\ y,\ z\right) + F_1\left(-x,\ y,\ -z\right) + F_1\left(-x,\ -y,\ z\right) + F_1\left(-x,-\ y,-\ z\right) + F_1\left(x,\ y,\ z\right) + F_1\left(x,\ y,\ -z\right) + F_1\left(x,\ -y,\ z\right) + F_1\left(x,-\ y,-\ z\right)\Big] \tag{C.S1}$$

The H-field in the y-direction is given by

$$H_y = \frac{B_r}{4\pi\mu_0}\left[\ln\left(\frac{F_2\left(-x,-y,z\right)F_2\left(x,y,z\right)}{F_2\left(-x,y,z\right)F_2\left(x,-y,z\right)}\right)\right] \tag{C.S2}$$

The H-field in the z-direction is given by

$$H_z = \frac{B_r}{4\pi\mu_0}\left[\ln\left(\frac{F_2\left(-x,-z,y\right)F_2\left(x,z,y\right)}{F_2\left(-x,z,y\right)F_2\left(x,-z,y\right)}\right)\right] \tag{C.S3}$$

where,

$$F_1\left(x,y,z\right) = \tan^{-1}\left[\frac{\left(c+y\right)\left(b+z\right)}{\left(a+x\right)\sqrt{\left(a+x\right)^2+\left(c+y\right)^2+\left(b+z\right)^2}}\right]$$

$$F_2\left(x,y,z\right) = \frac{\sqrt{\left(a+x\right)^2+\left(c+y\right)^2+\left(b-z\right)^2}+b-z}{\sqrt{\left(a+x\right)^2+\left(c+y\right)^2+\left(b+z\right)^2}-b-z}$$

$B_r = 1.48$ T is the residual magnetic field density of the permanent magnet. In the present case, $2a = 2b = 2c\ = 12.7$ mm.

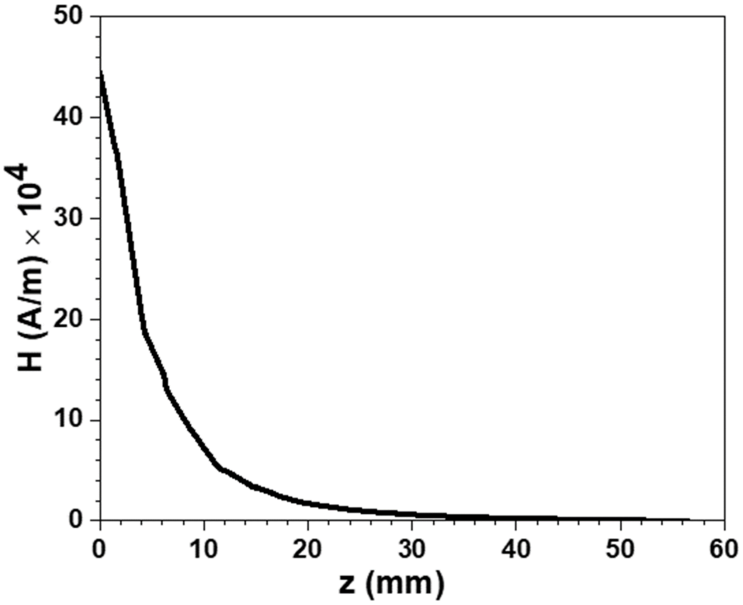

Figure C.2: Variation of H-field for the magnet used in the experiments.

References

[1] Z. Yang, T. Johansen, H. Bratsberg, G. Helgesen, and A. Skjeltorp, "Potential and force between a magnet and a bulk y1ba2cu3o7-δ superconductor studied by a mechanical pendulum," *Superconductor Science and Technology*, vol. 3, no. 12, p. 591, 1990.

Appendix D

Supporting Information for Chapter 6

D.1 Time evolution of a condensing acetone microdroplet on quartz surface – additional observation set (set #2)

In addition to the observation set #1 (Figure 6.3) reported in Chapter 6, we analyze another set of data from the same experiment where we target a different droplet and track its evolution as it grows and undergoes multiple coalescence due to condensation. The evolution of the droplet is represented in the form of a discrete timeseries in Figure D.1.

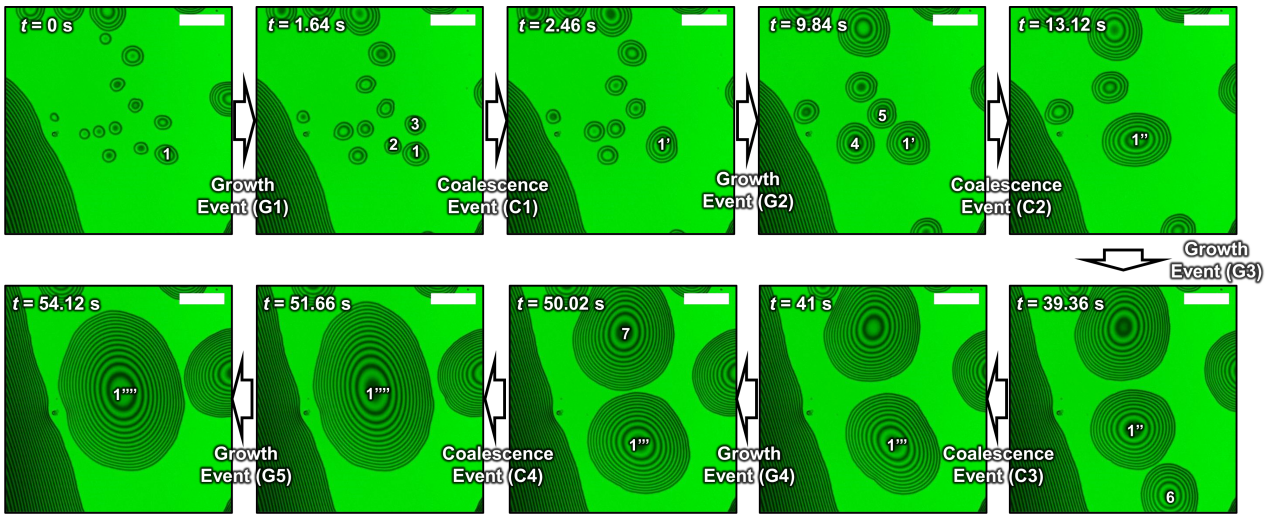

Figure D.1: Time evolution of a typical acetone microdroplet condensation event (observation set #2). During the observation period of 54.12 s, the droplet of interest (denoted by 1) underwent five such growth events (namely, G1, G2, G3, G4 and G5) and four coalescence events (namely, C1, C2, C3 and C4). The droplet number is kept the same during the pure growth phases while it has been updated after each coalescence. During C1, droplet numbered 1, merges with droplets numbered 2 and 3 to form droplet numbered 1'. Similarly, droplet 1' merges with droplets 4 and 5 to from droplet 1" during C2. Droplets numbered 1" and 6 undergo coalescence thereafter to form droplet 1"' during C3. Following this, droplets 1"' and 7 merge to form droplet 1"" during C4. The scale bar is 50 μm. The corresponding experimental dynamics is presented in the form of a time-series of simultaneously captured dual-wavelength interferograms in supporting video S2, with identically marked events.

D.2 Quantitative analysis of growth and coalescence of a condensed acetone microdroplet –observation set #2

To assess the consistency of our observed quantitative trend for observation set #1 (Figure 6.4), we carry out similar quantitative analysis of the experimental data for observation set #2 as well. The results are illustrated in Figure D.2. As can be seen in Figure D.2A, volume, V and liquid-vapor surface area, S_{lv} follow similar scaling relationship with mean base radius, r_{mean} as the ones reported in Figure 6.4A. For observation set #2, we obtain $S_{lv} \sim {r_{mean}}^{1.98}$ and $V \sim {r_{mean}}^{2.98}$ by carrying out a power-law fitting to the experimental data, which stand in excellent agreement with the analytical formulas[17] for an ideal spherical cap where $S_{lv} \sim {r_{mean}}^{2}$ and $V \sim {r_{mean}}^{3}$. It implies that the spherical cap approximation is consistent and can be applied for observation set #2 as well.

Further, the values of mean contact angle, θ, have also been plotted against r_{mean} in Figure D.2B. In observation set #2, the contact angle values remained almost constant (within 3.25°–4.75°) and the values were effectively invariant with respect to changes of the base radii, similar to the reported trend for observation set #1 (Figure 6.4B).

Additionally, we have also captured the experimentally observed trend of growth of mean base radius r_{mean} with time in Figure D.2C and compared it to the theoretical prediction of Rykaczewski for droplet growth in constant contact angle mode, given by Eq. (6.6) of Chapter 6. For observation set #2, ϕ is assumed to be 3.96° as the time averaged value of mean contact angle over the entire observation window of 54.12 s was 3.96°. As shown in Figure D.2C, we have obtained fitted values of ΔT in the range of (9.5–14 mK) for the observation set #2 which is comparable with that of the observation set #1 (7.5–25 mK).

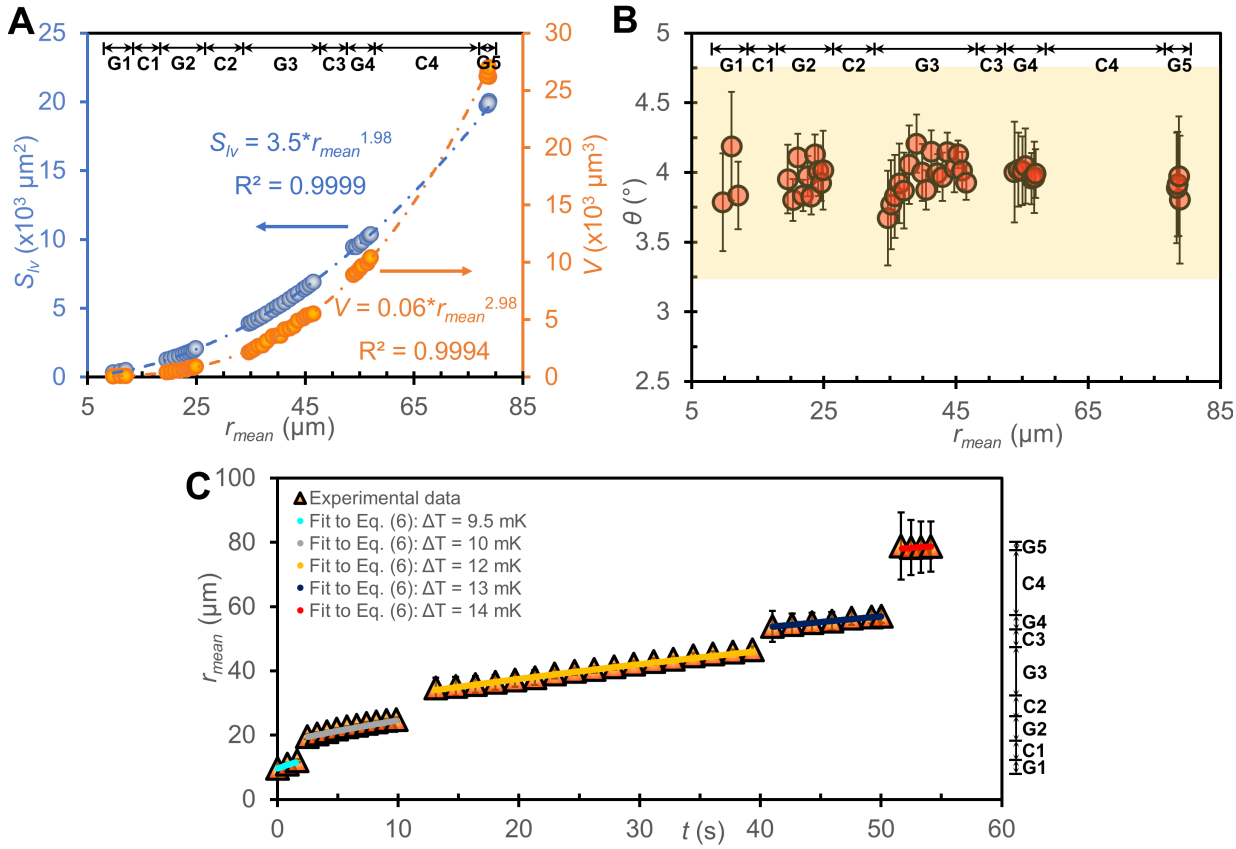

Figure D.2: Quantitative analysis of the dynamics of growth of a condensing acetone microdroplet corresponding to observation set #2. (A) Variation of droplet volume V and liquid-vapor surface area S_{lv} with mean base radius. (B) Dependence of the mean contact angle value on mean base radius. A total of 360 local contact angles were averaged across the contact line of the droplet at each instance. The error bars represent the standard deviation of these 360 local values. (C) The evolution of mean base radius r_{mean} with time during condensation. Similar to Figure D.2B, a total of 360 local values of base radii were considered along the 180 different slicing direction with 1° angular interval to evaluate the mean base radius. The error bars represent the standard deviation of these 360 local base radius values. The presented plots characterize the evolution of the droplet denoted by 1 in Figure D.1 and supporting video S2, with G1, G2, G3, G4 and G5 indicating the individual growth events and C1, C2, C3 and C4 denoting the coalescence events.

Appendix E

Supporting Information for Chapter 7

E.1 Lateral extension of precursor film

In order for small microdroplets to approach and merge with large microdroplets, the precursor films around them need to be connected. In fact, the precursor films are formed not only by the direct adsorption of vapor to the surface but also by the motion of the macroscopic three-phase contact line [1, 2]. In particular, when the microdroplets move towards the other droplets, the precursor film extends in the direction of the spontaneous movement. Moreover, even when the three-phase contact line is stationary, the precursor film continues to grow by surface diffusion. The time evolution of the length l of the diffusively grown precursor film is expressed as follows3,

$$l=\sqrt{\frac{A_{\mathrm{LL}}}{6\pi\eta h_c}t} \tag{E.S1}$$

where η is viscosity, h_c is a thickness of the precursor film and t is time. By assuming that the material parameters of ethanol are $\eta = 1.2 \times 10^{-3}$ Pa·s and $h_c = 20 \times 10^{-9}$ m, we can obtain the transient growth of the precursor film.

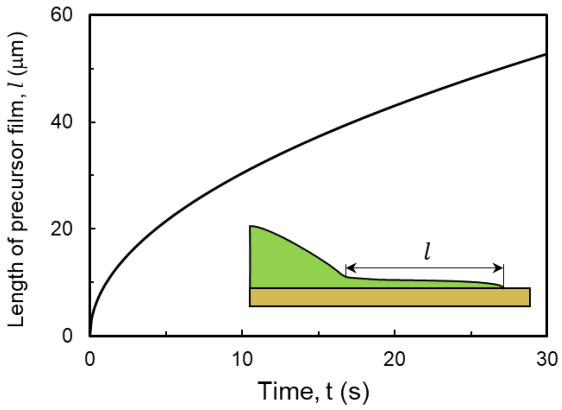

Figure E.1: Length of diffusive precursor film l as a function of time t.

Figure E.1 indicates that a diffusive precursor film with a length of about 10 μm is formed around the droplet within 1 second and grows to 50 μm in 30 seconds. Therefore, it can be considered that the precursor film entirely covers the observation area in Figure 3 and Figure 5 in the main manuscript.

E.2 Background noise of reflected light in RICM observation

In this section, we discuss why the precursor film could not be detected in RICM images. Here we consider the interference of the lights reflected from the interfaces between air and precursor film and between precursor film and quartz. The intensity of interfered light is described by the following equation [3],

$$I = I_1 + I_2 + 2\sqrt{I_1 I_2}\cos\left(\frac{4\pi n_1}{\lambda}h\right) \tag{E.S2}$$

where $I_1 = r_{01}^2 I_0$ and $I_2 = (1 - r_{01}^2) r_{12}^2 I_0$ are the intensities of the signals reflected at the air/precursor film interface and precursor film/quartz interface, respectively. I_0 is the intensity of incident light and $r_{ij} = \frac{n_i - n_j}{n_i + n_j} \quad (i,\ j = 0,\ 1,\ 2)$, where n is reflective index of

each materials. The values of reflective index used for our analysis are $n_0 = 1$, $n_1 = 1.37$, $n_2 = 1.55$ for air, ethanol, and quartz, respectively.

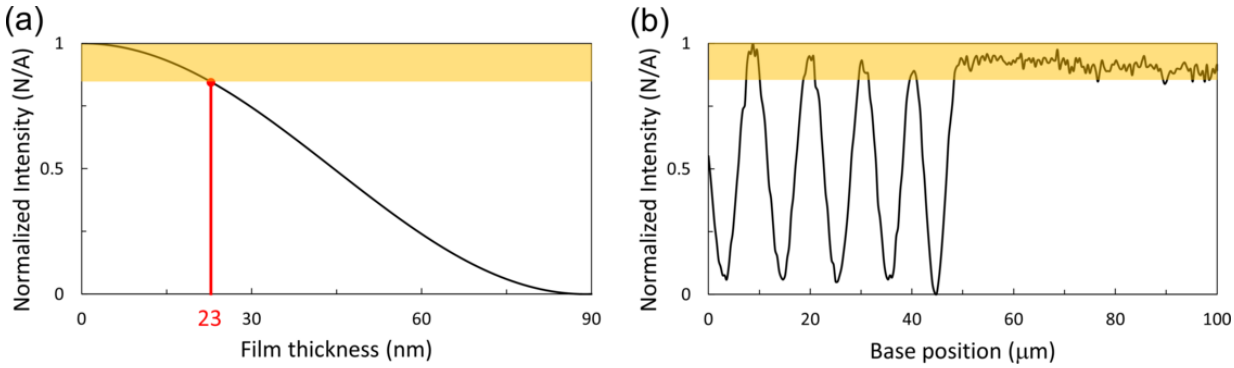

Figure E.2: (a) Relationship between normalized intensity vs film thickness obtained from Eq. S4. (b) Normalized intensity profile obtained from the position indicated by a white broken line shown in Figure 3(a) in the main paper. Yellow stripes indicate the range of the background noise.

Figure E.2(a) shows the relationship between normalized intensity vs film thickness obtained from Eq. S4. The intensity decreases as the thickness of liquid film increases from 0 nm and eventually becomes 0 (i.e., dark fringe) when the thickness is approximately 90 nm. Figure E.2(b) shows the normalized intensity profile obtained from the position indicated by a white broken line shown in Figure 3(a). In Figure E.2(b), the intensity profile where base position > 50 μm corresponds to a region where microdroplets do not exist. The intensity profile oscillates due to the background noise. Yellow stripes indicate the range of this background noise. When the change of the light intensity caused by the presence of a thin liquid film does not exceed the range of the background noise, the liquid film cannot be detected in RICM observation. From the intersection of the curve shown in Figure E.2(a) and the limit of background noise, in this experimental setup, it was found that the liquid film with a thickness of 23 nm or less cannot be visualized. It was experimentally reported that the precursor film of ethanol appearing on a glass surface during condensation is the thickness of approximately 8.3 nm [4]. Therefore, we cannot observe the precursor film in our RICM experiments.

References

[1] M. N. Popescu, G. Oshanin, S. Dietrich, and A. M. Cazabat, "Precursor films in wetting phenomena," *Journal of Physics Condensed Matter*, vol. 24, no. 243102, pp. 1–30, 2012.

[2] J. Joanny and P.-G. De Gennes, "Upward creep of a wetting fluid: a scaling analysis," *Journal de Physique*, vol. 47, no. 1, pp. 121–127, 1986.

[3] L. Limozin and K. Sengupta, "Quantitative reflection interference contrast microscopy (ricm) in soft matter and cell adhesion," *ChemPhysChem*, vol. 10, no. 16, pp. 2752–2768, 2009.

[4] S. J. Gokhale, J. L. Plawsky, P. C. Wayner, and S. DasGupta, "Inferred pressure gradient and fluid flow in a condensing sessile droplet based on the measured thickness profile," *Physics of Fluids*, vol. 16, no. 6, pp. 1942–1955, 2004.

Appendix F

Supporting Information for Chapter 8

F.1 Surface Characterization of LuBiCs

Energy Dispersive X-Ray (EDX) spectra of the base layer

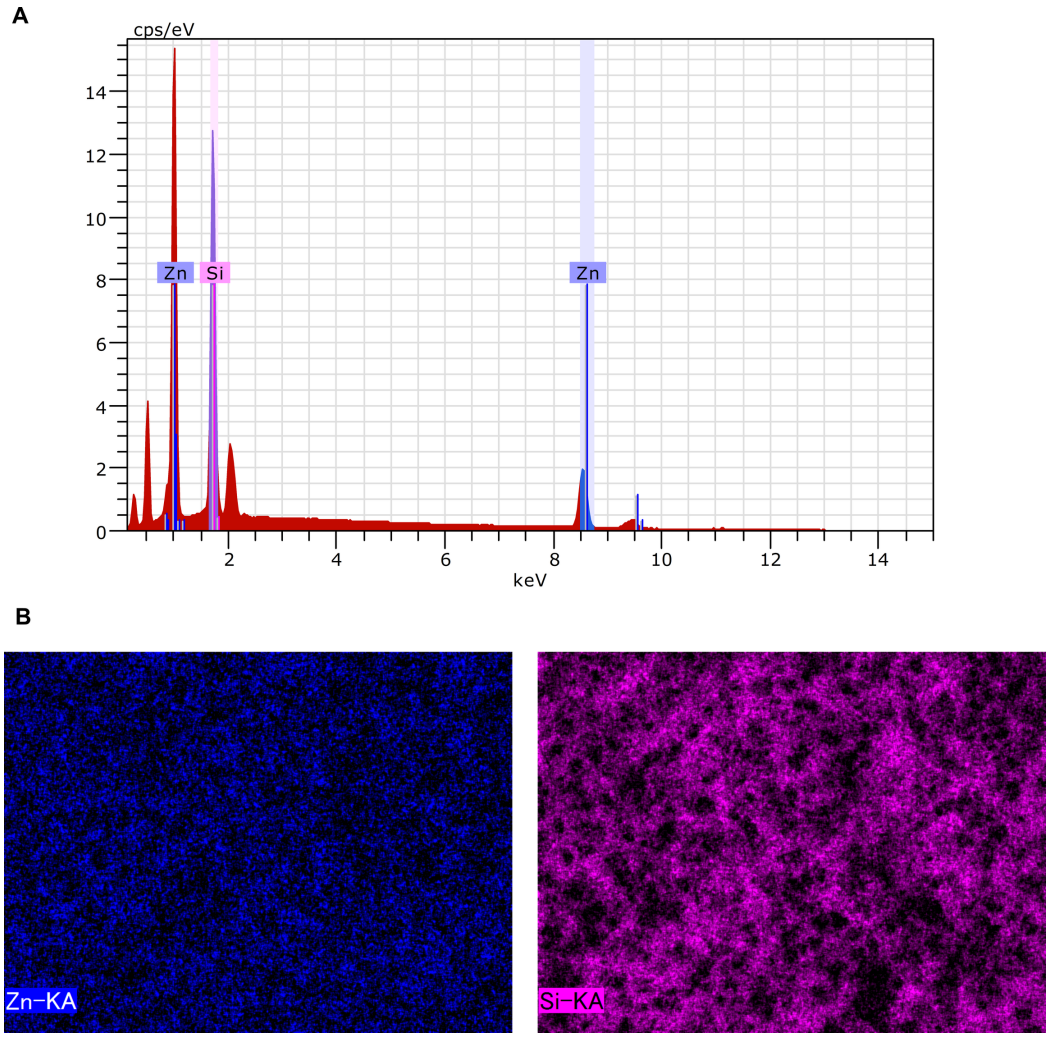

Figure F.1: (A) EDX spectra of the top surface the dry superhydrophobic base layer, (B) EDX elemental map for Zn and Si, respectively.

Raman spectroscopy of the top surface of the dry superhydrophobic base layer

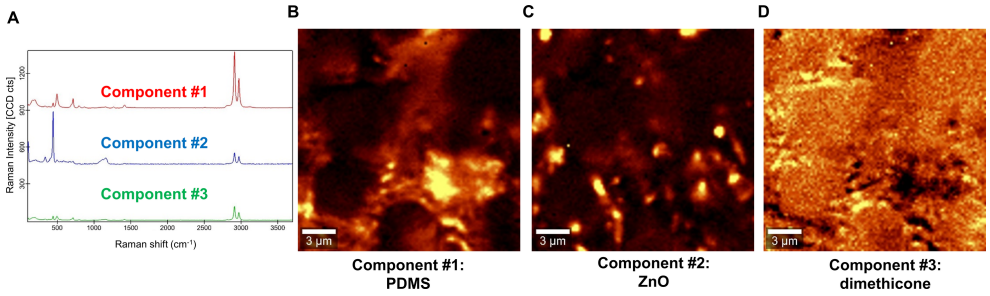

Figure F.2: Raman spectroscopy of the top surface of the dry superhydrophobic base layer:(A) Raman spectra of the three components identified by cluster analysis. (B-D) Individual Raman images of the three identified components. The measurement was performed over a 20 μm x 20 μm surface area. These images correspond to the composite Raman image presented in Figure 2E.

Raman spectroscopy of the top surface of the lubricated sample

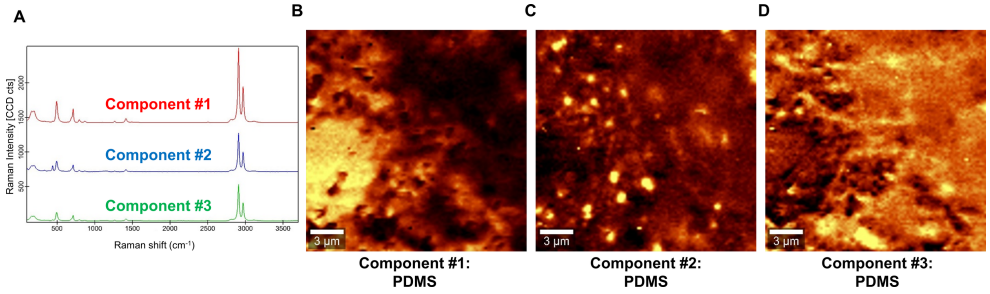

Figure F.3: Raman spectroscopy of the top surface of the lubricated sample: (A) Raman spectra of the three components identified by cluster analysis. (B-D) Individual Raman images of the three identified components. The measurement was performed over a 20 μm x 20 μm surface area. These images correspond to the composite Raman image presented in Figure 2F.

F.2 Pressure stability of LuBiCs

Figure F.4 summarizes a droplet impact experiment on a LuBiCs-coated surface that assesses the pressure stability of the infused lubricant layer. The coated surface was mounted on a 30° incline. Subsequently, we impacted a 6μl water droplet with Weber number We $= \rho_d V^2 D/\gamma_d$ (ρ_d: density, V: impact velocity normal to the surface, D: diameter, and γ_d: surface tension), giving a ratio of kinetic energy on impact to surface energy as 92. It corresponds to a dynamic pressure, $P_{\mathrm{d}} = \frac{1}{2}\rho_d V^2 \approx 1450$ Pa and water hammer pressure [1], $P_{\mathrm{wh}} = k\rho_d c V \approx 509.356$ kPa. where $c = 1497$ ms^{-1} is the speed of sound in water and k is a calibration factor assumed to be 0.2 for droplet impact on solid [2]. The impacting droplet spreads on the surface immediately upon collision and deforms in a pancake-like shape (see the timestamp corresponding to 3 ms). However, the slippery state of the droplet is restored very fast as the impact momentum is dissipated by the viscous lubricant layer, and the drop is subsequently seen to slide down the incline with minimal CAH. The droplet did not split during the impact, and no tiny droplets remained on the surface once the droplet slid off. In the absence of the lubricant layer, droplet impact with such a high We on rough/porous superhydrophobic surfaces leads to irreversible impalement [3] of the droplet due to Wenzel transition.

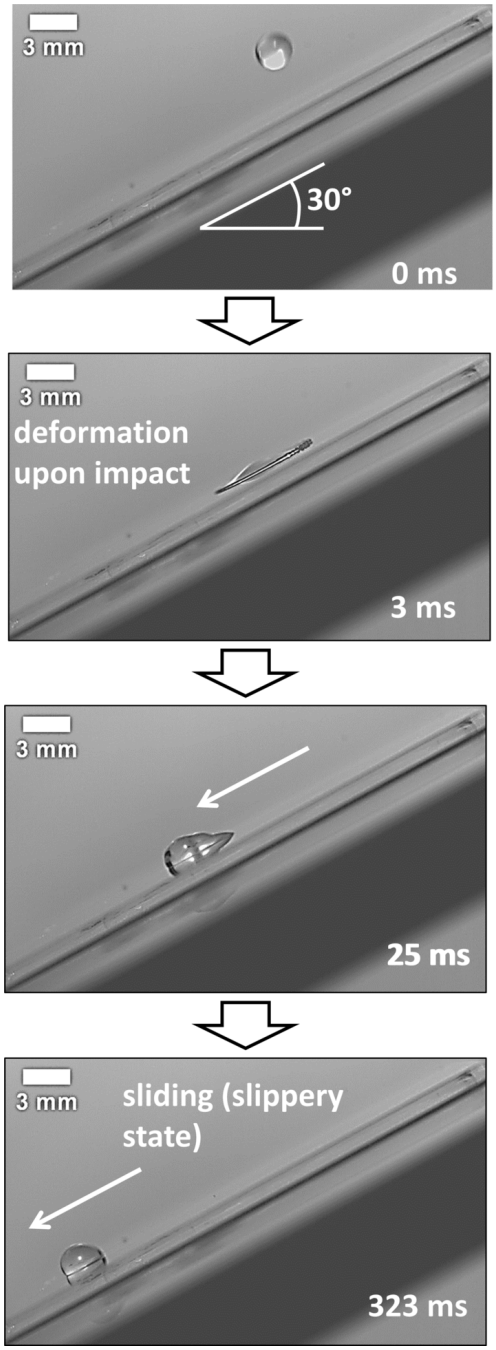

Figure F.4: Pressure stability of LuBiCs: High-speed dynamics of impact (presented in the form of a timeseries) of a 6 μl water droplet on a LuBiCs coated glass surface kept on a 30° incline.

F.3 UV stability of LuBiCs

Figure F.5 summarizes UV stability of the LuBiCs. A LuBiCs-coated glass slide was exposed to 25 W UV illumination for 48 h. Water contact angle readings were taken at different time intervals, and no noticeable change was observed in contact angle hysteresis and sliding angle values. The surface consistently demonstrated $< 3°$ CAH and SA values. Note that UV-stable superhydrophobic [4], as well as lubricant-infused surfaces [5] based on metal oxide-PDMS framework, has been reported in the literature. Here we confirm the UV stability of our ZnO-PDMS framework used to fabricate the LuBiCs. Even during the outdoor durability test (Figure 8), when a large-scale LuBiCs sample was exposed to UV from direct sunlight for more than a year, the surface maintained its water-repellent behavior.

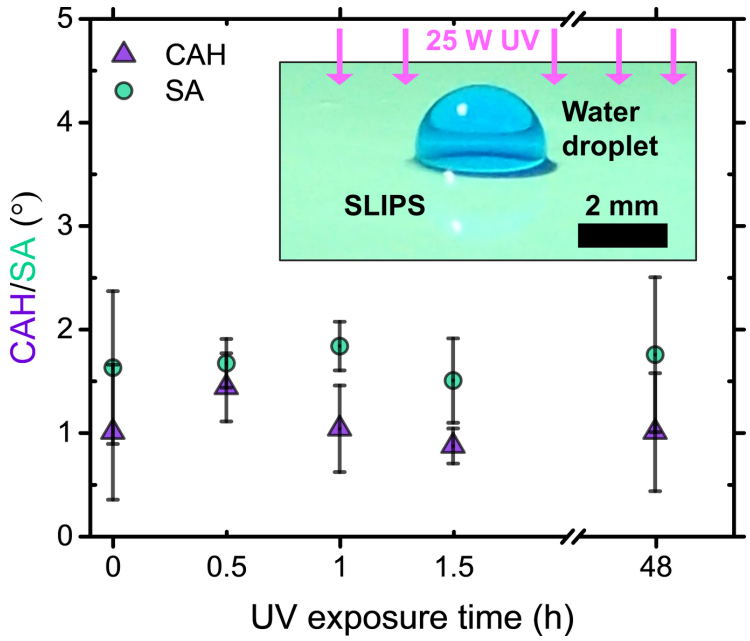

Figure F.5: UV stability of LuBiCs: Evolution of CAH and SA values of water on the LuBiCs coated surface upon UV exposure.

F.4 Theoretical formulation to describe the capillary transport through the base layer

The complete dynamic description of capillary transport [6] in a capillary tube can be obtained by considering a force balance between inertia, capillary force, viscosity, and gravity force.

$$\frac{d\left(Mv\right)}{dt} = F_{cap} - F_{visc} - F_g \tag{F.S1}$$

Assuming the capillary imbibition height at time t to be z_c,

$$F_{cap} = 2\pi R\gamma\cos\left(\theta\right); \quad F_{visc} = 8\pi\eta z_c\dot{z}_c; \quad F_g = Mg = \rho g\pi R^2 z_c.$$

$$\Rightarrow \underbrace{\frac{d\left(\rho\pi R^2 z_c\dot{z}_c\right)}{dt}}_{\text{Inertia}} = \underbrace{2\pi R\gamma\cos\left(\theta\right)}_{\text{Capillarity}} - \underbrace{8\pi\eta z_c\dot{z}_c}_{\text{Viscous effect}} - \underbrace{\rho g\pi R^2 z_c}_{\text{Gravity}} \tag{F.S2}$$

Here R is the pore radius, and θ is the contact angle between the rising liquid and the inner walls of the tube. M is the mass of the liquid column inside the capillary tube and v is the instantaneous velocity of rise of the liquid at time t, defined as $v = \dot{z}_c = \frac{dz_c}{dt}$.

We can represent Eq. (F.S2) in the dimensionless form [7, 8]. z_c can be normalized by Jurin height $z_0 = \frac{2\gamma}{\rho g r}$ which is the final static height of the rising liquid column obtained by balancing the capillary force with the weight of the column. Further, t can be normalized by $\tau_c = \frac{z_0}{c}$. Here $c = \left(\frac{2\gamma}{\rho r}\right)^{1/2}$ is the inertial celerity [7], a constant rising velocity obtained by balancing the inertia forces with capillary force during the early stage of the rise.

Non-dimensionalize z_c by z_0 and t by τ_c so that $\bar{z} = \dfrac{z_c}{z_0}$ and $\bar{t} = \dfrac{t}{\tau_c}$

$$\Rightarrow \frac{\pi R^2 \rho z_0^2}{\tau_c^2} \frac{d}{dt}\left(\bar{z}\dot{\bar{z}}\right) = 2\pi R\gamma \cos\left(\theta\right) - 8\pi\eta \frac{z_0^2}{\tau_c} \bar{z}\dot{\bar{z}} - \rho g \pi R^2 z_0 \bar{z}$$

Divide each side by $\dfrac{\pi R^2 \rho z_0^2}{\tau_c^2}$

$$\Rightarrow \frac{d}{dt}\left(\bar{z}\dot{\bar{z}}\right) = \frac{2\gamma \cos\left(\theta\right)\tau_c^2}{R\rho z_0^2} - \frac{8\eta\tau_c}{R^2\rho z_0^2}\bar{z}\dot{\bar{z}} - \frac{g\tau_c^2}{z_0}\bar{z}$$

$$\Rightarrow \frac{d}{dt}\left(\bar{z}\dot{\bar{z}}\right) = \frac{2\gamma \cos\left(\theta\right)}{R\rho}\left(\frac{R\rho}{2\gamma}\right) - \frac{8\eta}{R^2\rho}\left(\frac{\tau_c}{z_0}\right)\left(\frac{1}{z_0}\right)\bar{z}\dot{\bar{z}} - \left(\frac{g}{z_0}\right)\left(\frac{2\gamma}{R\rho g^2}\right)\bar{z}$$

$$\Rightarrow \frac{d}{dt}\left(\bar{z}\dot{\bar{z}}\right) = \cos\left(\theta\right) - \frac{8\eta}{R^2\rho}\left(\frac{R\rho}{2\gamma}\right)^{1/2}\left(\frac{2\gamma}{R\rho g}\right)\bar{z}\dot{\bar{z}} - \left(\frac{R\rho g^2}{2\gamma}\right)\left(\frac{2\gamma}{R\rho g^2}\right)\bar{z}$$

$$\Rightarrow \frac{d}{dt}\left(\bar{z}\dot{\bar{z}}\right) = \cos\left(\theta\right) - \frac{8\sqrt{2}\eta\gamma^{1/2}}{R^{5/2}\rho^{3/2}g}\bar{z}\dot{\bar{z}} - \bar{z}$$

$$\Rightarrow \frac{d}{dt}\left(\bar{z}\dot{\bar{z}}\right) = \cos\left(\theta\right) - 8\sqrt{2}\frac{\frac{\eta}{(\rho R\gamma)^{1/2}}}{\frac{\rho R^2 g}{\gamma}}\bar{z}\dot{\bar{z}} - \bar{z}$$

$$\therefore \bar{z}\ddot{\bar{z}} + \dot{\bar{z}}^2 = \cos\left(\theta\right) - 8\sqrt{2}\left(\frac{Oh}{Bo}\right)\bar{z}\dot{\bar{z}} - \bar{z}\,, \tag{F.S3}$$

where $Oh = \frac{\eta}{(\rho R\gamma)^{1/2}}$ is the Ohnesorge number and $Bo = \frac{\rho R^2 g}{\gamma}$ is the Bond number.

Due to the existence of a PDMS covering on the surface microstructures and the chemical conformity between the PDMS in the base layer and the infused silicone oil lubricant, θ can be assumed to be $0°$.

Therefore Eq. (F.S3) can be simplified as

$$\boxed{\bar{z}\ddot{\bar{z}} + \dot{\bar{z}}^2 = 1 - 8\sqrt{2}\left(\frac{Oh}{Bo}\right)\bar{z}\dot{\bar{z}} - \bar{z}} \tag{F.S4}$$

For capillary transport of a viscous liquid through a narrow tube or micro-pores, the movement of the liquid through the pores is essentially slow. In other words, due to the narrow constriction, the entire liquid column experiences the effect of the wall where a

no-slip boundary condition must exist. We have confirmed from SEM imaging (see Figure 8.2 of Chapter 8) that the base layer of LuBiCs is a bi-continuous porous matrix with microscale porosity where the majority of the pores have a pore diameter d_{pore} between 0.5 μm and 2.5 μm. During capillary wicking, the viscous silicone oil lubricant (kinematic viscosity 100 cSt) rises through the microporous base layer (0.5 μm $\leq d_{pore} \leq$ 2.5 μm) of LuBiCs. During the process of capillary wicking through the base layer of the LuBiCs, the viscous dissipation force is dominant due to the combined effect of the high viscosity of the lubricant and the narrow constriction, as evident from a very high value of $\frac{Oh}{Bo}$ $\left(1.4 \times 10^9 \geq \frac{Oh}{Bo} \geq 2.5 \times 10^7\right)$. Therefore, the inertia term (the left-hand side of Eq. (F.S4)) can be neglected, which leads to the following formulation -

$$\boxed{1 - 8\sqrt{2}\left(\frac{Oh}{Bo}\right)\bar{z}\dot{\bar{z}} - \bar{z} = 0} \tag{F.S5}$$

Note that the effect of inertia becomes prominent [7–10] during the early stage of capillary rise of low-viscosity liquids through wider channels (diameter $\sim$ mm). This situation corresponds to a low $\frac{Oh}{Bo}$ $\left(\frac{Oh}{Bo} \ll 1\right)$ where the fast-rising liquid undergoes an oscillation around the Jurin heightz_0 before equilibrating atz_0.

To further verify that the inertia term can indeed be ignored for our case, we numerically solve both Eq. (F.S4) and Eq. (F.S5) for different values $\frac{Oh}{Bo}$ and compare them side-by-side in **Figure F.6**. Figure F.6(A) compares the solution profiles for $\frac{Oh}{Bo} = 1 \times 10^{-2}$. Although both the profiles equilibrate around Jurin Height within about ~ 1 s, the complete numerical solution to Eq. (F.S4), which includes the inertial term, captures the early-stage oscillatory behavior which could not be captured using the inertia-free formulation of Eq. (F.S5). Note that a $\frac{Oh}{Bo}$ value as low as 1×10^{-2} is not achievable in our case. For our silicone oil lubricant, it would require d_{pore} to be $\sim$ 14.4 mm which is 4 orders of magnitude higher than the pore size observed in LuBiCs. Such low values of $\frac{Oh}{Bo}$ can only be attained during the capillary rise of low-viscosity liquids (e.g., ethers) through a capillary tube of much wider cross-section, as also shown in the work of Quéré *et al.* [8]. On the other hand, Figure F.6(B) computes and compares the z_c vs. t profiles from Eq. (F.S4) and Eq. (F.S5) when $\frac{Oh}{Bo}$ is large. Two different values of $\frac{Oh}{Bo}$ are chosen, $\frac{Oh}{Bo} = 2.5 \times 10^7$and $\frac{Oh}{Bo} = 1.4 \times 10^9$. These two values represent the two extremities of the pore diameter range observed in our

base layer. $\frac{Oh}{Bo} = 1.4 \times 10^9$ corresponds to $d_{pore} = 0.5$ μm while $\frac{Oh}{Bo} = 2.5 \times 10^7$ corresponds to $d_{pore} = 2.5$ μm. It is evident from Figure F.6(B) that the solutions are almost coincident for both cases. Therefore, the inertia-free formulation of Eq. (F.S5) is suitable for our case. Note that at high $\frac{Oh}{Bo}$, the order of magnitude of the inertia term becomes very small in comparison to the viscous term, rendering Eq. (F.S4) stiff. Therefore, a stiff solver is recommended to numerically solve the ordinary differential equation (ode) of Eq. (F.S4). We use the ode15s solver in MATLAB for this purpose.

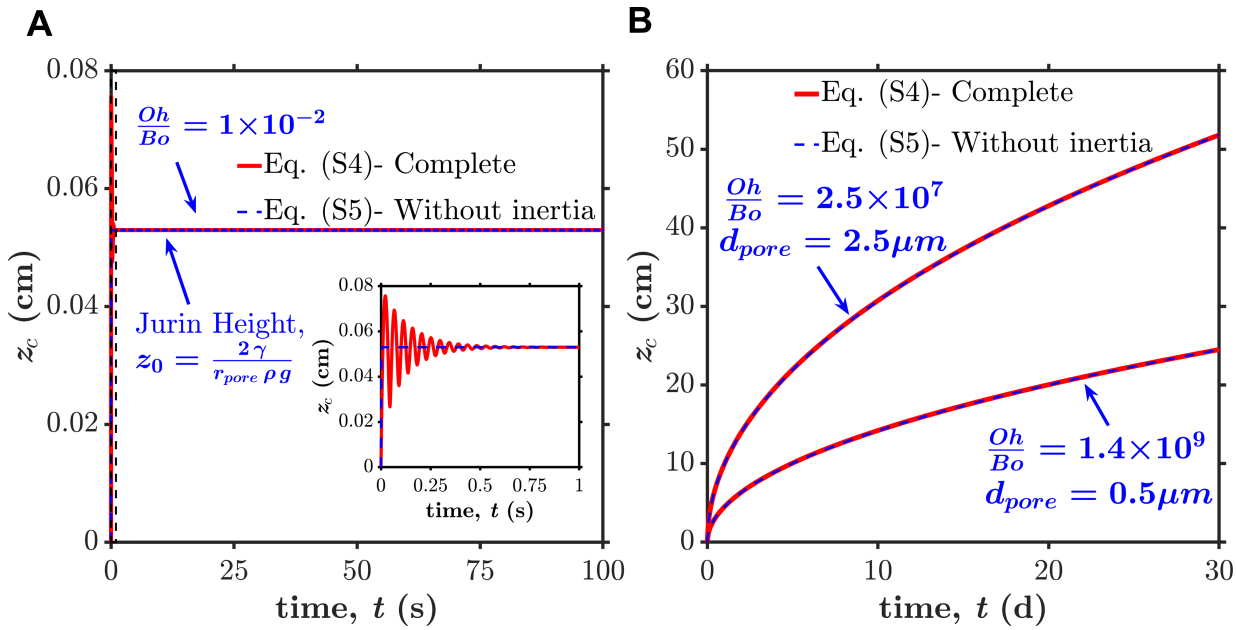

Figure F.6: Role of the inertia term in describing the capillary wicking process: (A) Comparison of the z_c vs. t profiles obtained from the numerical solutions of the complete formulation given by Eq. (F.S4) and the inertia-free formulation of Eq. (F.S5) for $\frac{Oh}{Bo} = 1 \times 10^{-2}$. The inset presents the zoomed-in view of the region indicated by the black dashed rectangle in the main figure. (B) Comparison of the z_c vs. t profiles obtained from the numerical solutions of Eq. (F.S4) and Eq. (F.S5) for $\frac{Oh}{Bo} = 2.5 \times 10^7$and $\frac{Oh}{Bo} = 1.4 \times 10^9$.

Eq. (F.S5) has a closed-form analytical solution, as shown below:

$$1 - 8\sqrt{2}\left(\frac{Oh}{Bo}\right)\dot{\bar{z}}\bar{z} - \bar{z} = 0$$
Assume $8\sqrt{2}\left(\frac{Oh}{Bo}\right) = \phi$
$\Rightarrow \phi\frac{\dot{\bar{z}}\bar{z}}{1-\bar{z}} = 1$
Integrating with respect to $\bar{t}$,
$\Rightarrow \phi(-\ln(1-\bar{z}) + 1 - \bar{z}) = \bar{t} + c$,
where c is the constant of integration
$\Rightarrow \bar{z} = W\left(-e^{-(\bar{t}+c)/\phi}\right) + 1$

W is the Lambert W function (Product Logarithm function) which is the inverse function of $f(W) = We^W$

Substituting the initial condition : $\bar{z}(0) = 0$
$W\left(-e^{-c/\phi}\right) = -1 \quad \Rightarrow c = \phi$

$$\therefore \boxed{\bar{z} = W\left(-e^{-1-\bar{t}/\phi}\right) + 1} \tag{F.S6}$$

Eq. (F.S6) can be expressed in dimensional form as follows,

$$\boxed{z_c = \frac{2\gamma\left(W\left(-\,\mathrm{e}^{-\frac{1}{16}\left(\frac{Bo}{Oh}\right)\frac{t}{\sqrt{\frac{\gamma}{Rg^2\rho}}} - 1}\right) + 1\right)}{Rg\rho}} \tag{F.S7}$$

If we ignore the gravity term in Eq. (F.S5), the resulting ODE, $8\sqrt{2}\left(\frac{Oh}{Bo}\right)\bar{z}\dot{\bar{z}} = 1$, can be solved with an initial condition $\bar{z}(0) = 0$ to obtain $\bar{z} = 2^{-5/4}\left(\frac{Bo}{Oh}\right)^{1/2}\sqrt{\bar{t}}$. In dimensional form, it reduces to

$$\boxed{z_c = \sqrt{\frac{\gamma R t}{2\eta}}} \tag{F.S8}$$

Eq. (F.S8) is the classical Washburn equation [11] of capillary rise.

As noted previously, the capillary wicking through LuBiCs base layer occurs at a high $\frac{Oh}{Bo} \sim O(10^7 - 10^9)$. In a previous work of our group [10], we have shown through scaling analysis that during vertical capillary filling, the ratio of the viscous force F_{visc} and the

gravitational force F_g scales as $\frac{Oh}{Bo}$. Therefore, at high $\frac{Oh}{Bo}$, viscous effects dominate the gravitational effects, and the interplay between the viscous force, F_{visc} and capillary force, F_{cap} dictates the rise profile till the late stage. The influence of gravity becomes relevant only at the late stage of the rise. Thus the classical Washburn profile of Eq. (F.S8) does a reasonably accurate job in providing a dynamic description of the capillary imbibition, at least till the late stage of the rise. To verify this, we compute the z_c vs. t profiles from the analytical formulations of Eq. (F.S7) and Eq. (F.S8) for different values of $\frac{Oh}{Bo}$ across a wide range with $O\left(10^{-2} - 10^{9}\right)$ and compare them side-by-side in **Figure F.7**. As can be concluded from Figure F.7, the deviation between the classical gravity-free formulation of the Washburn equation (Eq. (F.S8)) and the gravity-inclusive analytical formulation of Eq. (F.S7) is profound at lower $\frac{Oh}{Bo}$, and the former significantly overpredicts the imbibition height z_c. It is indicative that gravity, indeed, is a significant retarding force under these operating conditions. It opposes the capillary drive and influences the rise profile. However, as $\frac{Oh}{Bo}$ increases, the deviations start to become less and less pronounced. The profiles overlap in the initial stage of the rise before starting to deviate from each other, and the onset of deviation gets delayed with increasing $\frac{Oh}{Bo}$. It indicates that the applicable timespan of the classical Washburn model increases with increasing $\frac{Oh}{Bo}$, which can be as long as multiple weeks for the capillary rise of viscous lubricant through microporous geometries, as is the case with our LuBiCs base layer. In fact, as shown in Figure F.7(F), the profiles do overlap for $\frac{Oh}{Bo} = 1.4 \times 10^9$ (corresponding $d_{pore} = 0.5$ μm, the lower limit of pore diameter observed from SEM imaging of the base layer) over the entire 30-day observation window that we reported in Figure 8.7 for capillarity-driven self-lubrication in the large scale sample in Chapter 8. However, upon the onset of deviation, Eq. (F.S7) predicts a slower rate of rise which eventually saturates around the Jurin height (see Figure F.7(B)). On the other hand, the classical Washburn formulation of Eq. (F.S8) is a monotonically increasing function of time and therefore shows no saturation.

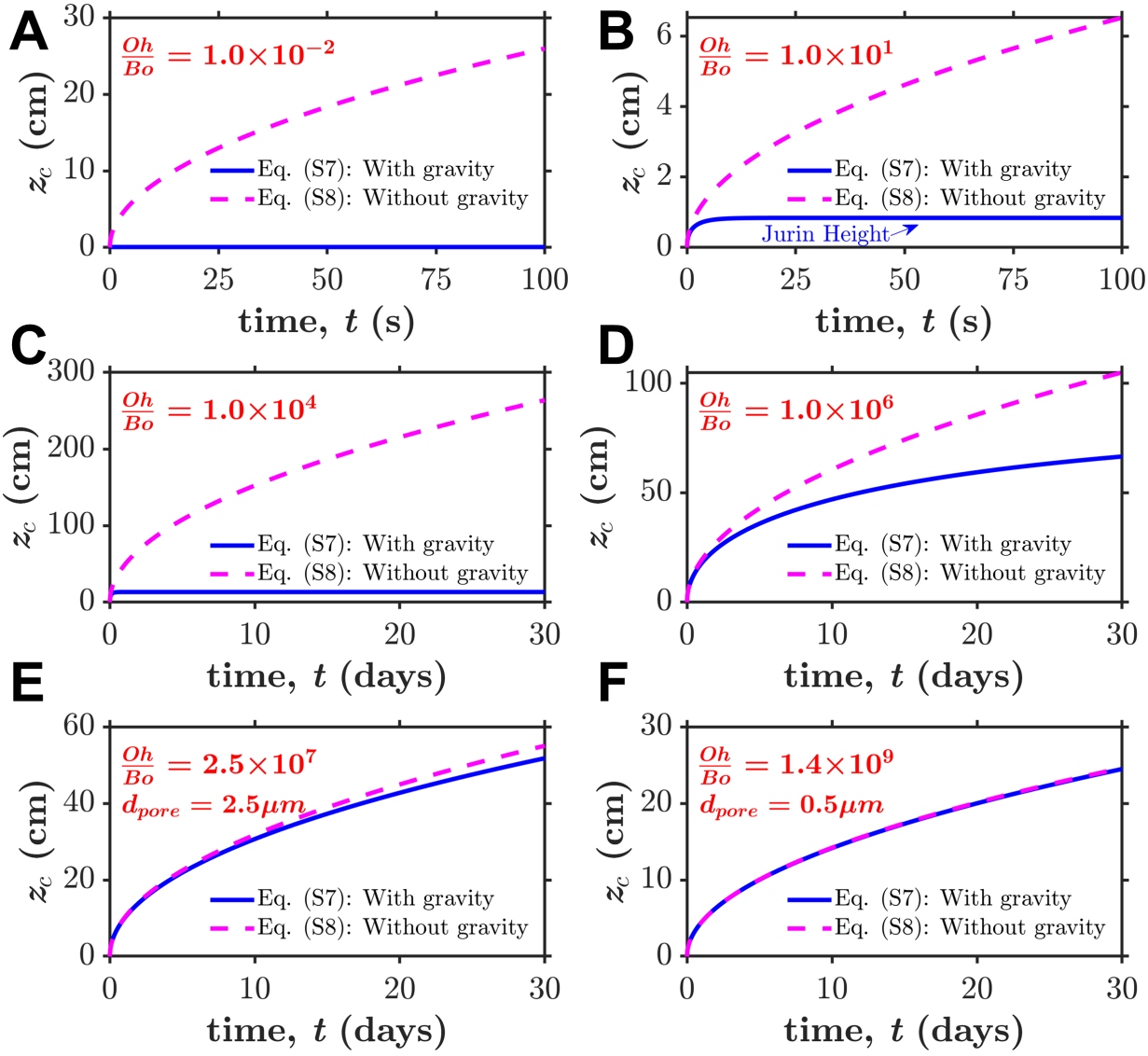

Figure F.7: Role of gravitational force in dictating the capillary imbibition profile: Comparison of the classical Washburn profile, Eq. (F.S8) and the analytical formulation of Eq. (F.S7) that includes gravity in addition to capillary and viscous forces for (A) $\frac{Oh}{Bo} = 1\times10^{-2}$, (B) $\frac{Oh}{Bo} = 10$, (C) $\frac{Oh}{Bo} = 1\times10^{4}$, (D) $\frac{Oh}{Bo} = 1\times10^{6}$, (E) $\frac{Oh}{Bo} = 2.5\times10^{7}$ and (F) $\frac{Oh}{Bo} = 1.4\times10^{9}$. The two $\frac{Oh}{Bo}$ values considered in (E) and (F) correspond to the two extremities of the observed distribution of pore diameter in the base layer of LuBiCs. (E) corresponds to $d_{pore} = 2.5$ μm , while (F) corresponds to $d_{pore} = 0.5$ μm.

In **Figure F.8**(A), we compare the profiles obtained from Eq. (F.S7) and (F.S8) in describing our large-scale experimental data. The experimental data are first fitted to Eq. (F.S7) (the blue line) which yields $d_{pore} = 0.79$ μm. The corresponding z_c vs. t profile (with the same d_{pore}) obtained from Eq. (F.S8) is then plotted in cyan. As we can confirm, the deviation between the two is minimal for the experimental time span of 1 month considered in our large-scale self-lubrication study. Both the classical Washburn formulation (Eq. (F.S8)) and the gravity-inclusive formulation of Eq. (F.S7) represent the experimental data with excellent accuracy (R-Square values 0.9906 and 0.99209, respectively). Although the gravity-inclusive formulation does a slightly better job, the difference is minimal. For $d_{pore} = 0.79$ μm, there is only $\sim$ 1% difference between the $z_c$values predicted by Eq. (F.S7) and Eq. (F.S8) at $t = 30$ days, which is of the same order as the reported standard deviation of the experimental data. The deviation becomes substantial after a long time, as shown in Figure F.8(B). In Figure F.8(B), we present and compare the solutions of Eq. (F.S7) and Eq. (F.S8) for $d_{pore} = 0.79$ μm over a very long timespan (of the order of several 100 years). As we can see in Figure F.8(B), Eq. (F.S7) indeed saturate and asymptotically converge to the theoretical Jurin height ($\sim$ 9.64 m for our case) while Eq. (F.S8) shows an unphysical continuously increasing trend with time due to the absence of gravitational damping. Note that the capillary transport of the viscous lubricant through such a narrow submicron-scale constriction is extremely slow at the late stage of the rise. As shown theoretically in Figure F.8(B), it takes an enormously long time ($\sim$ 575 years) to reach the steady state around Jurin height. Here the steady state is defined as the state where the wicking front reaches 99% of the Jurin height. Therefore, effectively, the one-month timespan that we report in this study is a small timespan with respect to the overall timescale of the problem. It explains why the gravity effects are insignificant for our purpose. However, it is fundamentally more accurate to use the gravity-inclusive formulation of Eq. (F.S7) to describe the capillary wicking process, as Eq. (F.S8) cannot account for a finite imbibition height. That is why we consistently employed Eq. (F.S7) to model our experimental data both at the small scale (Figure 8.4D) and large scale (Figure 8.7A) in Chapter 8 despite the apparent simplicity and reasonably large applicable timespan of the classical Washburn formulation in our context.

Also, note the difference between the theoretical limit for the capillary imbibition, $z_{\max}$

shown in Figure 8.7A and Figure F.8(A), and the Jurin height, z_0 for the same $d_{pore} = 0.79$ μm in Figure F.8(B). Jurin's law applies to capillary rise in a vertical capillary with a single continuous cross-section. This is not the case with porous media with a random arrangement of interconnected pores. A more accurate (and restrictive) estimate of the maximum attainable capillary imbibition height $z_{\max}$ can be obtained [6] from macroscopic energy balance as $z_{\max} = \frac{(1-\phi)(\gamma_S - \gamma_{SL})}{\phi \rho_L d_{pore} g} = \frac{(1-\phi)\gamma_L \cos(\theta)}{\phi \rho_L d_{pore} g} \approx \frac{(1-\phi)\gamma_L}{\phi \rho_L d_{pore} g} \approx 1.55$ m,which includes the volumetric porosity ϕ of the media. Here γ_S is the surface energy of the dry base layer and γ_{SL} is the interfacial energy between the dry base layer and the infused lubricant, which has a density ρ_L.

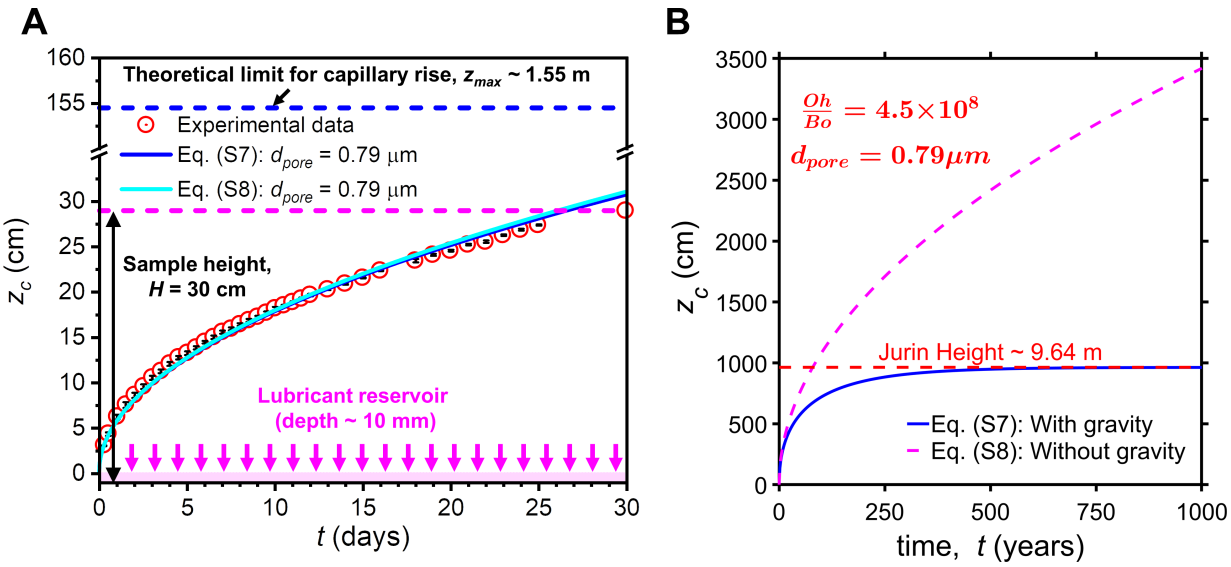

Figure F.8: **(A)** compares Eq. (F.S7) and Eq. (F.S8) in describing the experimentally obtained capillary imbibition data in the large-scale sample over 30 days, as reported in Figure 8.7 of Chapter 8. **(B)** provides a comparison between z_c vs. t profiles obtained from Eq. (F.S7) and Eq. (F.S8) over a very large time span of 1000 years.

F.5 Multi-surface applicability of LuBiCs

We confirmed that the LuBiCs coating could be formed on a wide range of substrates (**Figure F.9**), including metals, alloy, polymers, wood, cotton, and paper, using the same fabrication method demonstrated here (one-step wet process for base layer formation followed lubricant infusion by immersion). All these surfaces exhibit slippery functionality.

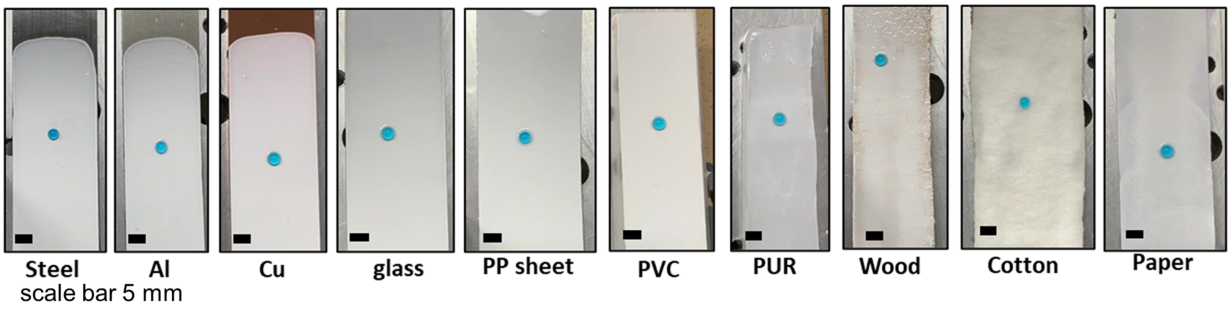

Figure F.9: LuBiCs coating applied on a wide variety of surfaces. Scale bar 5 mm.

F.6 Retention of slippery functionality of LuBiCs at high and low temperatures

Figure F.10 shows sustained slippery functionality of LuBiCs at very high and near freezing temperatures. As shown in Figure F.10A, a LuBiCs-coated glass slide was placed at a tilt angle of 10° on a hot plate. The temperature was set to $\sim$ 204° C (Leidenfrost point of water on flat solids [12]). Subsequently, boiled water droplets were dispensed on the surface using a transfer pipette. The droplets slid off the surface (see supporting video S7 for the experimental video). From the sliding velocities of the droplet, it appears that the successful water removal from the surface is due to the slippage of the oncoming droplets on the lubricating oil film. However, a detailed investigation of the dynamics of the interaction of water droplets with LuBiCs at such elevated temperature could be an interesting topic of separate investigation as other researchers have shown that different

regimes of interaction of water droplets could exist [13] on heated LIS including boiling, self-propulsion or Leidenfrost levitation.

Further, we checked the water repellence of LuBiCs at below freezing point and near the freezing point of water (see Figure F.10B) using iced water as the probe liquid. The LuBiCs sample was placed on a Peltier cooling stage to control its temperature. When the temperature was set below the freezing point, the oncoming water droplets were seen to get pinned on the surface. It could be due to the capillary migration [14] of the infused lubricant from the wetting ridge and from within the surface textures to the surface of frozen droplets at such freezing temperatures. However, when the temperature was slightly elevated so that it is just around the freezing point of water, we could see that the oncoming droplets slid off the surface with relative ease.

These results demonstrate that LuBiCs can maintain their slippery functionality over a broad range of operating temperatures.

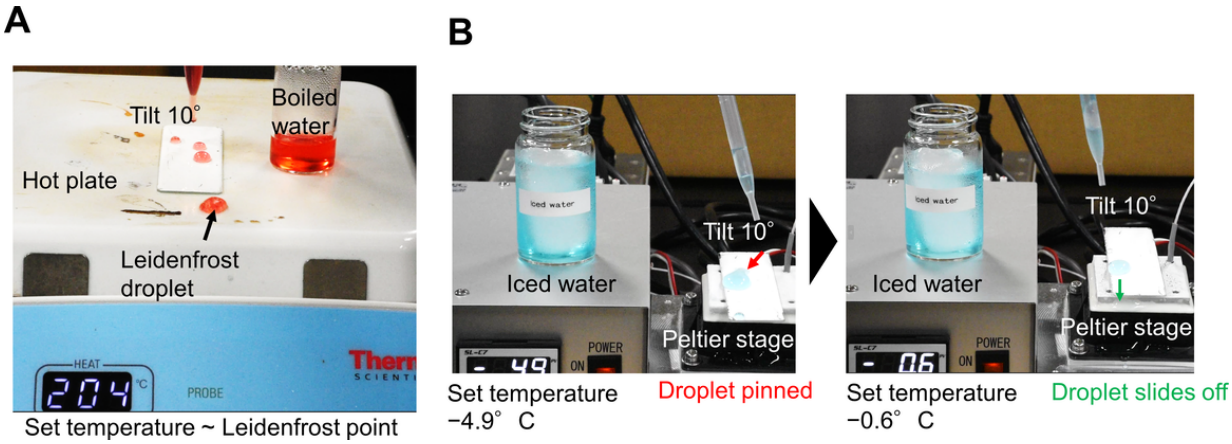

Figure F.10: (A) Water repellence of LuBiCs at elevated temperature (∼ Leidenfrost point), (B) Water repellence of LuBiCs at near freezing temperature.

References

[1] M. S. Ghidaoui, M. Zhao, D. A. McInnis, and D. H. Axworthy, "A Review of Water Hammer Theory and Practice," *Applied Mechanics Reviews*, vol. 58, no. 1, pp. 49–76,

2005.

[2] O. G. Engel, "Waterdrop collisions with solid surfaces," *Journal of Research of the National Bureau of Standards*, vol. 54, no. 5, p. 281, 1955.

[3] D. Bartolo, F. Bouamrirene, Verneuil, A. Buguin, P. Silberzan, and S. Moulinet, "Bouncing or sticky droplets: Impalement transitions on superhydrophobic micropatterned surfaces," *Europhysics Letters (EPL)*, vol. 74, no. 2, pp. 299–305, 2006.

[4] S. Wooh, N. Encinas, D. Vollmer, and H.-J. Butt, "Stable Hydrophobic Metal-Oxide Photocatalysts via Grafting Polydimethylsiloxane Brush," *Advanced Materials*, vol. 29, no. 16, p. 1604637, 2017.

[5] S. Wooh and H.-J. Butt, "A Photocatalytically Active Lubricant-Impregnated Surface," *Angewandte Chemie International Edition*, vol. 56, no. 18, pp. 4965–4969, 2017.

[6] P.-G. De Gennes, F. Brochard-Wyart, and D. Quéré, *Capillarity and wetting phenomena: drops, bubbles, pearls, waves*, vol. 336. Springer, 2004.

[7] D. Quéré, "Inertial capillarity," *Europhysics Letters (EPL)*, vol. 39, no. 5, pp. 533–538, 1997.

[8] D. Quéré, Raphaël, and J.-Y. Ollitrault, "Rebounds in a Capillary Tube," *Langmuir*, vol. 15, no. 10, pp. 3679–3682, 1999.

[9] B. V. Zhmud, F. Tiberg, and K. Hallstensson, "Dynamics of Capillary Rise," *Journal of Colloid and Interface Science*, vol. 228, no. 2, pp. 263–269, 2000.

[10] S. Das and S. K. Mitra, "Different regimes in vertical capillary filling," *Physical Review E*, vol. 87, no. 6, p. 063005, 2013.

[11] E. W. Washburn, "The Dynamics of Capillary Flow," *Physical Review*, vol. 17, no. 3, pp. 273–283, 1921.

[12] A. Bouillant, T. Mouterde, P. Bourrianne, A. Lagarde, C. Clanet, and D. Quéré, "Leidenfrost wheels," *Nature Physics*, vol. 14, no. 12, pp. 1188–1192, 2018.

[13] V. J. Leon and K. K. Varanasi, "Self-Propulsion of Boiling Droplets on Thin Heated Oil Films," *Physical Review Letters*, vol. 127, no. 7, p. 074502, 2021.

[14] K. Rykaczewski, S. Anand, S. B. Subramanyam, and K. K. Varanasi, "Mechanism of Frost Formation on Lubricant-Impregnated Surfaces," *Langmuir*, vol. 29, no. 17, pp. 5230–5238, 2013.

Appendix G

Supporting Information for Chapter 9

G.1 Calibration of the cantilever

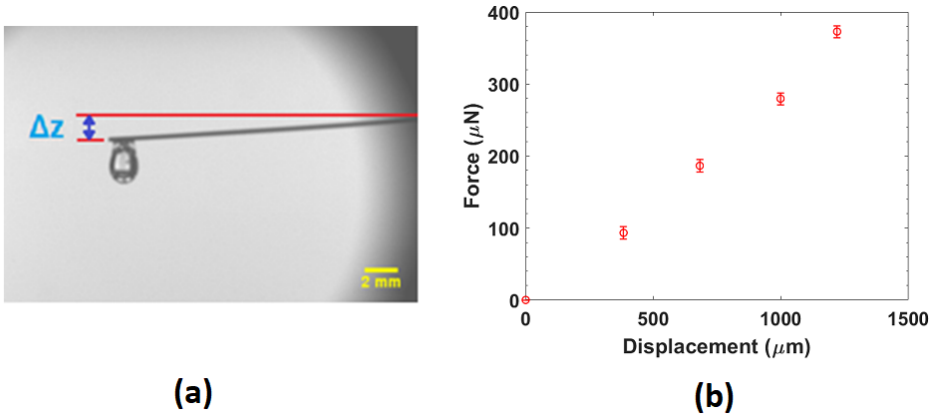

Figure G.1: Calibration of the cantilever. (a) An oil droplet placed on the cantilever tip. Δz is the deflection (b) The force vs. deflection curve.

Laser oil with density, $\rho = 1900\text{kg/m}^3$ is used for the calibration. Oil drops of varying volume (V) are dispensed to the tip of the cantilever as shown in Figure G.1(a) and the corresponding vertical deflection Δz is recorded. The weight of the droplet then gives the force acting on the cantilever tip as $F = mg$ where g is the acceleration due to gravity

Vol. of droplet, V (μl)	***Mass of droplet, $m = \rho V$ (μg)***	***Force, $F = mg$ (μN)***	***Δz (μm)***
0	0	0	0
5	9.5	93.195	383.643
10	19	186.39	682.137
15	28.5	279.585	998.698
20	38	372.78	1120.577

Table G.1: Estimation of force-displacement characteristics of the cantilever from calibration data

(9.81 m/s^2) and mass $m = \rho V$. The values obtained from the calibration experiment are tabulated in Table G.1 and the force-deflection curve is plotted in Figure G.1(b). The slope of this linear curve then gives the stiffness constant of the cantilever k from the spring equation given by $F = k\Delta$z. For each volume, the experiment was repeated three times to obtain a reliable value of the spring constant for the capillary tube used in this work.

G.2 Interfacial tension (IFT) of particle-laden droplet

IFT was measured using a pendant drop method based on the Young-Laplace equation given by

$$\Delta P = \gamma \left(\frac{1}{R_1} + \frac{1}{R_2} \right).$$

Here, ΔP is the pressure difference between either side of an interface having R_1, R_2 as the principal radii of curvature and γ is the IFT. In this method, the image of a small droplet that is dosed from a metallic needle and suspended in the open air is captured using a high magnification camera as shown in Figure G.2 (a). A custom-made image processing algorithm [1] is then employed to estimate the IFT which iteratively attempts to fit the

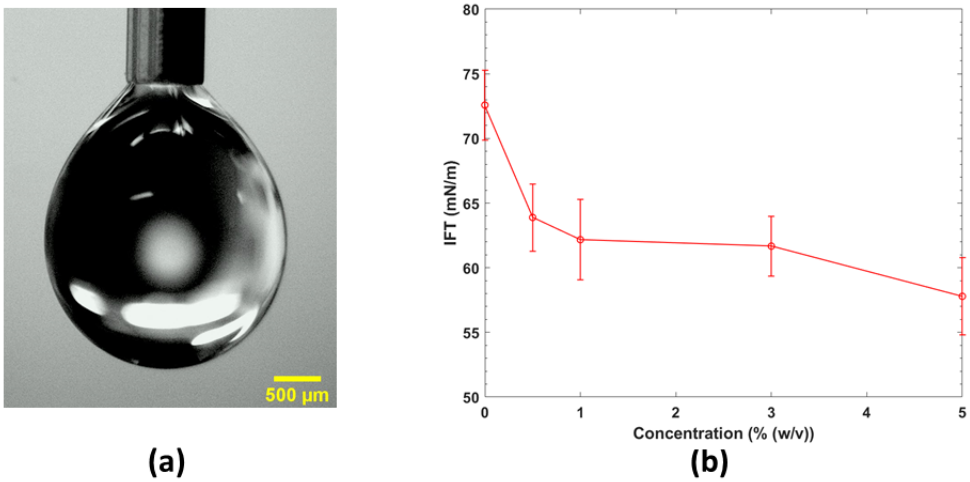

Figure G.2: IFT measured for different concentrations of microparticles in aqueous solutions used in the present experiment (a) Image of the pendant drop captured for image analysis (b) Variation of IFT with concentration (0 represents DI water (no particles)).

above equation on the identified interface on the captured image to yield γ and is plotted in Figure G.2 (b).

G.3 Tilt angle measurement for indirect estimation of friction force

First, a droplet of desired volume (here 10 μL) is placed on the target substrate and then the substrate is gradually tilted till the droplet starts sliding down the incline. The tilt angle when the droplet starts sliding is denoted as θ_{tilt}. Just when the drop starts sliding, the weight component of the droplet acting along the incline balances with the droplet-surface friction (F_{fric}), which yields

$$F_{fric} = V_d \rho_d g sin\theta_{\text{tilt}} \ ,$$

where V_d and ρ_d are the volume and density of the droplet, respectively, g is the acceleration due to gravity.

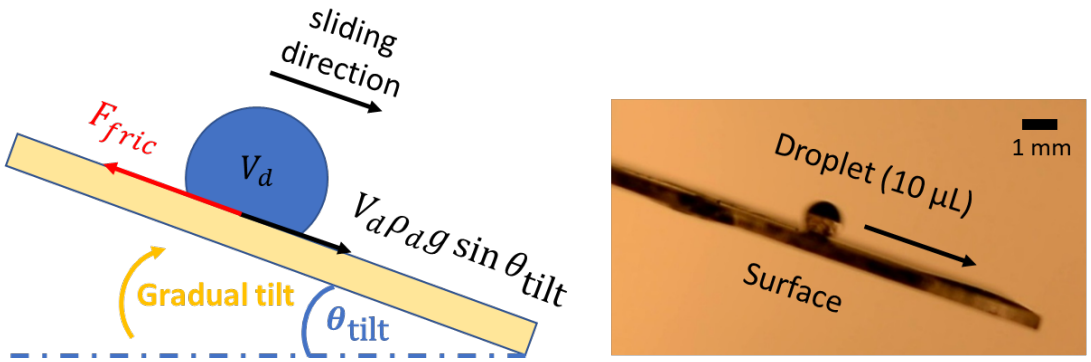

Figure G.3: (a) Schematic of the sliding experiment used to measure the tilt angle required for a droplet to start sliding down the surface, (b) an experimental snap showing a 10 μL droplet sliding down a tilted repellent surface.

The friction force thus estimated was then compared against the value directly measured using our capillary deflection force sensor. As an example, a 10 μL water droplet showed $\theta_{\text{tilt}} = 16.33° \pm 1.76°$ on S1 (soot) surface, which results in $F_{fric} = 27.55 \pm 2.36$ μN, while our force apparatus registered a friction value of 36.78 ± 9.65 μN.

G.4 Reflection interference contrast microscopy (RICM) with particle-laden droplet

In order to probe the capillary bridges formed at the droplet-solid interface we have carried out RICM using a confocal microscope (Zeiss). The sample with Glaco coating (S2) is placed on the microscope stage and a droplet laden with microparticles (concentration = 5 % w/v) is slowly dispensed on the coated surface using a micropipette. A monochromatic laser beam with a wavelength $\lambda = 532$nm is focused on the interface and raster scanned over an area of 500μm x 500μm with a 40x objective lens as shown in Figure G.3 (a). Due to the thin film interference at the curved capillary bridge, alternate dark and bright fringes are formed which are recorded on the camera attached to the microscope as shown in Figure G.3 (b).

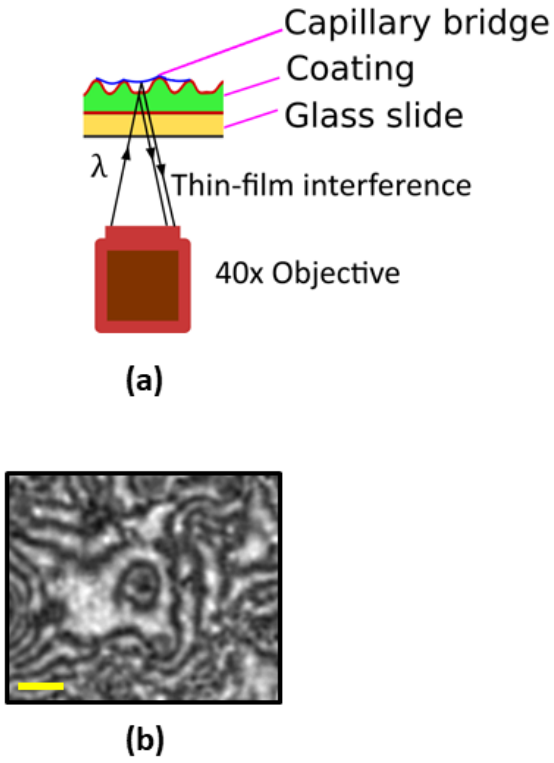

Figure G.4: (a) Schematic of the RICM showing the objective lens which focuses the laser beam to the sample and collects the reflected rays to form an image on the camera (b) The fringes formed due to interference at the capillary bridge. Scalebar represents 10μm.

G.5 Effect of substrate velocity (U) in friction measurement

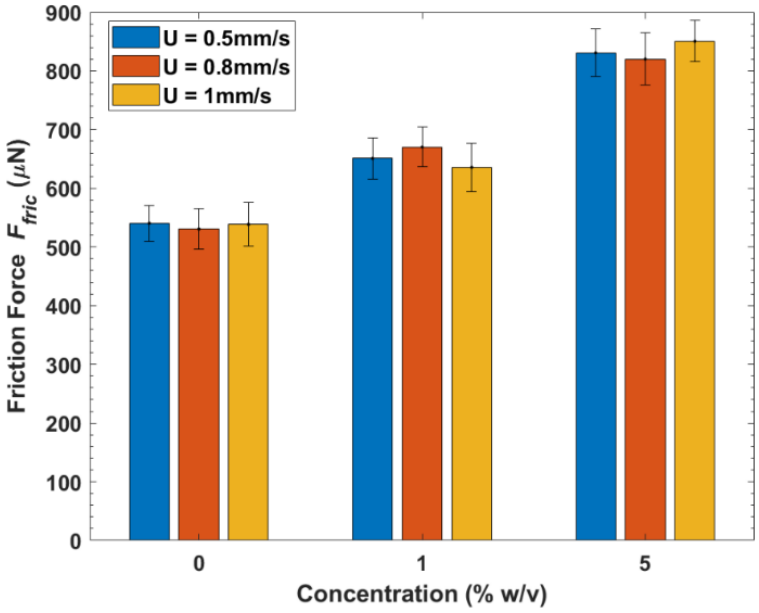

Figure G.5: Friction force (F_{fric}) measured for different U for the case of S2 for the range of concentration of the microparticles used in the present study. Error bars represent the standard deviation from three runs of experiments.

To investigate the effect of contact line velocity on the friction measurement, the velocity of translation of the substrate (S2) was varied in the range U = 0.5-1 mm/s and the corresponding friction force (F_{fric}) was measured using the method described in Chapter 9. For a given concentration, no significant variation of the F_{fric} was observed, as shown in Figure G.5. However, the increase in F_{fric} was observed with increase in the concentration of microparticles as shown in Figure 9.4(b) in Chapter 9.

G.6 FTIR (Fourier-transform infrared spectroscopy) of the coatings

ATR (Attenuated total reflectance) FTIR spectra were recorded at room temperature in the mid-IR range (400–4000 cm^{-1}) on a Bruker Vertex Series FTIR spectrometer using Platinum ATR accessory with a single reflection diamond crystal as shown in Figure G.6. Typical features of a silicone coating like Si-CH_3, Si-O-Si, C-F are visible for both S2 and S3 due to the constituent ingredients. These were absent in S1 (soot) as it is mostly carbon deposition. Probing at 4-5 random locations for each of the coatings showed similar spectra and thus we conclude that the coating is uniform, without any chemical inhomogeneities.

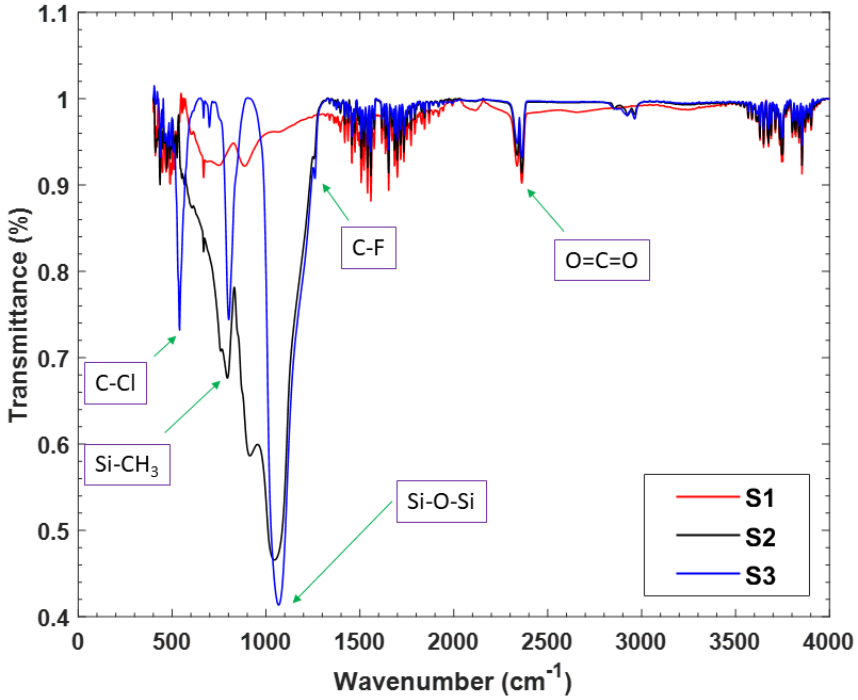

Figure G.6: Transmittance FTIR spectra of the three samples studied. The prominent peaks and corresponding functional groups are identified based on the available literature.

References

[1] J. Berry, M. Neeson, R. Dagastine, D. Chan, and R. Tabor, "Measurement of surface and interfacial tension using pendant drop tensiometry," *Journal of Colloid and Interface Science*, vol. 454, pp. 226–237, 2015.

Appendix H

Supporting Information for Chapter 10

H.1 Optimum polynomial fitting for motion analysis

For motion analysis, we use a polynomial function to fit the $X-t$ profile of the cantilever tip during stage C (substrate retraction phase). To ensure an optimal fitting, we analyzed the residue of the fitted polynomial using the following equation

$$sr = \frac{\text{Square of residue}}{n-(m+1)} \tag{H.S1}$$

where n is the number of data points and m is the order of the polynomial

As can be observed from Figure H.1, sr reduces upon increasing the order of the polynomial till $m = 5$. However, beyond $m = 5$, an increase in m does not lead to any significant improvement in sr. Therefore, in the present work, we use $m = 5$, as the order of the fitted polynomial.

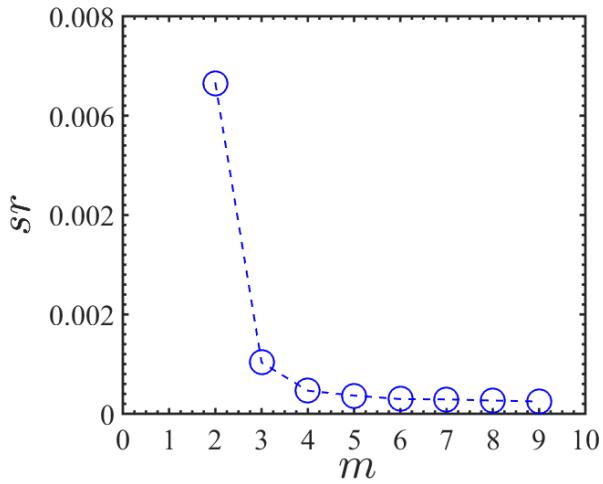

Figure H.1: Variation of sr for the various orders of the fitting polynomial (m).

H.2 Image analysis

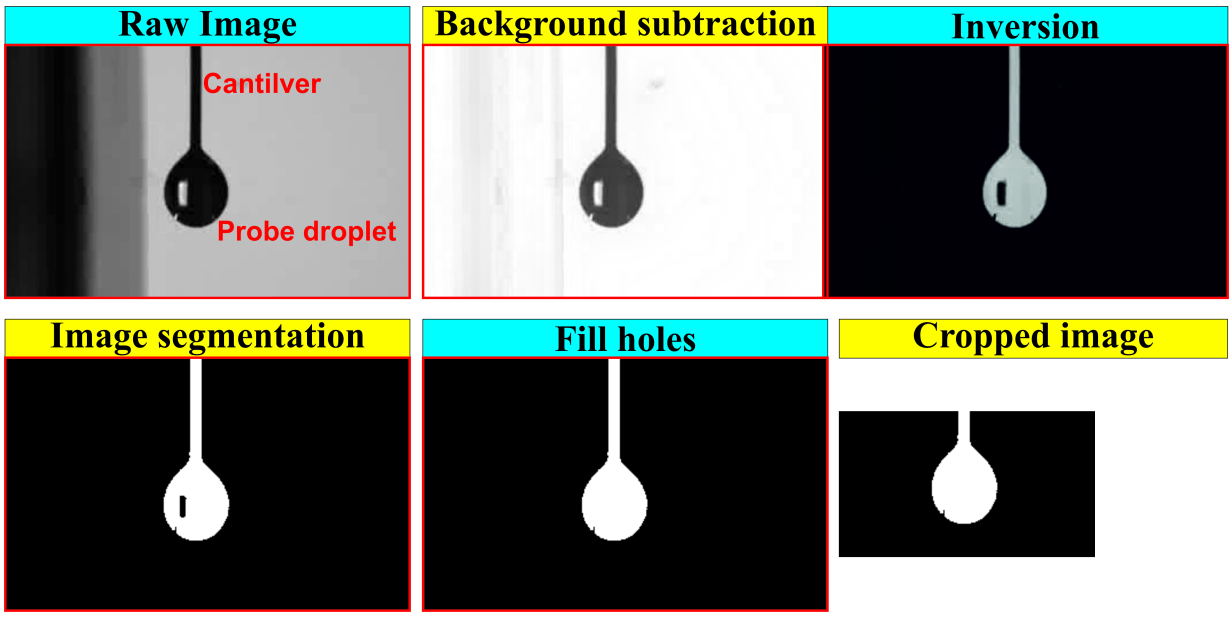

Figure H.2: Figure shows the various intermediate steps of the image processing methodology.

The image processing strategies involved in the present work are described below

1. **Background subtraction:** Background subtraction is one of the critical elements whereby we can differentiate between the moving object (e.g., the cantilever) and the static background. After the background subtraction, we are left with the cantilever and the probe droplet.

2. **Inversion:** After the background image is subtracted, inversion of the image is carried out. Inversion results in a grayscale image with light background.

3. **Edge detection/image segmentation:** In edge detection, we identify the boundaries of the cantilever and the droplet. For edge detection, we rely on the Sobel method, which computes the local maxima in intensity gradients and identifies edges as locations where the gradient exceeds a user-defined threshold between 0 and 1. The image segmentation converts the resulting grayscale image to a binary image.

4. **Cropping:** Once we attain proper segmentation, the images are cropped depending on the region of interest, i.e., the area encompassing the cantilever tip and the probe droplet.

5. **Tracking:** We now have the cropped binary image in which we track the deflection of the cantilever and convert it to the appropriate force by multiplying it with the spring constant of the cantilever.

We show in Figure H.2, the snapshots of the images undergoing the above-mentioned processing sequences.

H.3 Characterization of low-energy substrate

We carried out another set of similar experiments on a low-energy substrate to further check the validity of our hypothesis. In this regard, we prepared a superhydrophobic coating on a glass substrate using a commercially available single-part spray (Make: Glaco-Soft99,

Japan), which demonstrates a static water contact angle of $\sim 140^\circ$ [1] and characterized its adhesion signature. The nanoscale surface structure responsible for the superhydrophobicity of the substrate can be visualized in the scanning electron micrograph presented in Figure H.3(a). In Figure H.3(b), we show the $X - t$ curve during a typical adhesion measurement cycle on the test substrate. It can be easily observed from Figure H.3(b) that the deflection of the cantilever is significantly less when compared to a high-energy substrate, e.g., PMMA, (see Figure 10.4 of Chapter 10). We show in the inset of Figure H.3(b) the $\dot{X} - t$, and $\ddot{X} - t$ curves for the Glaco-water pair. As discussed in Chapter 10, at $\ddot{X} = 0$ the triple contact line of the probe droplet depins, while the cantilever begins its retraction from the test substrate at $\dot{X} = 0$. We argued that this temporal lag is due to the inertia of the cantilever in realizing the adhesion force. Figure 4 of Chapter 10 shows the temporal gap between $\dot{X} = 0$ and $\ddot{X} = 0$ for a relatively higher energy PMMA substrate to be $\sim$ 2.6 sec. However, this gap reduces to $\sim$0.15 sec for lower surface energy Glaco substrate (see inset of Figure H.3(b)). This further validates our arguments that for low surface energy substrates, the effect of inertia on the motion of the cantilever is also less due to reduced droplet-substrate adhesion force.

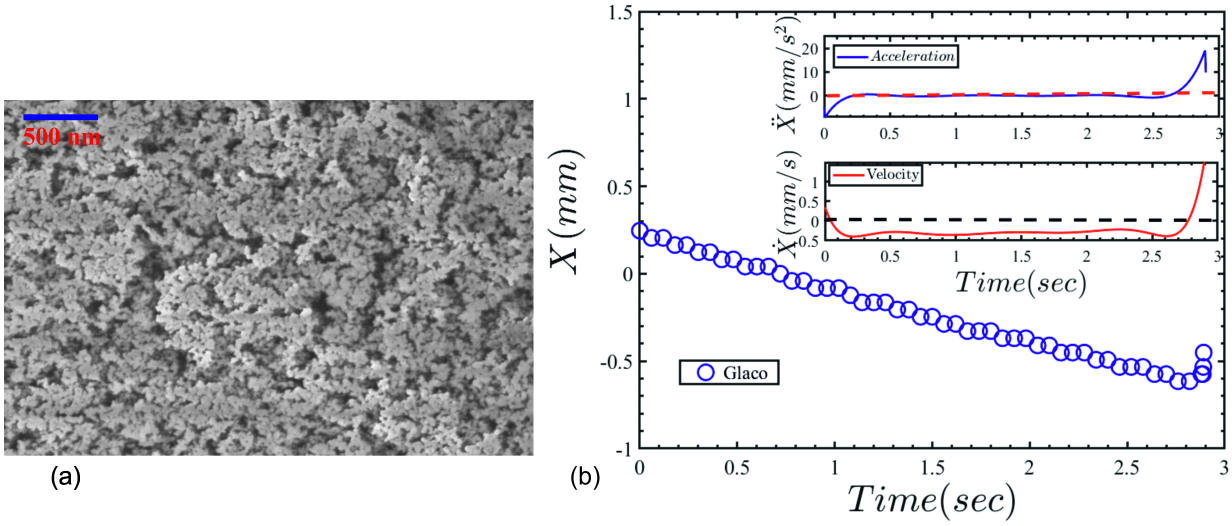

Figure H.3: (a) Snapshots shows the scanning electron microscopy images of Glaco coated surface. (b) Plot shows the temporal variation of the displacement (X) of the cantilever tip for a Glaco-water pair. The top-right inset shows the velocity ($\dot{X}$) and acceleration ($\ddot{X}$) variation of the cantilever. The black and red-dotted lines are the zero lines for velocity and acceleration, respectively. The volume of the probe droplet is 5μl.

H.4 Motion analysis for polypropylene (PP) substrate

Figure H.4(a) shows the $X-t$, $\dot{X}-t$, and $\ddot{X}-t$ curves respectively for a PP substrate. It can be clearly observed from Figure H.4(b) that for the PP substrate, the characteristic adhesion force corresponding to $\ddot{X} = 0$ is significantly low when compared to PMMA substrate. This observation is in line with what has already been reported in the literature, i.e., the surface energy of a PP substrate is low in comparison to that of PMMA [2].

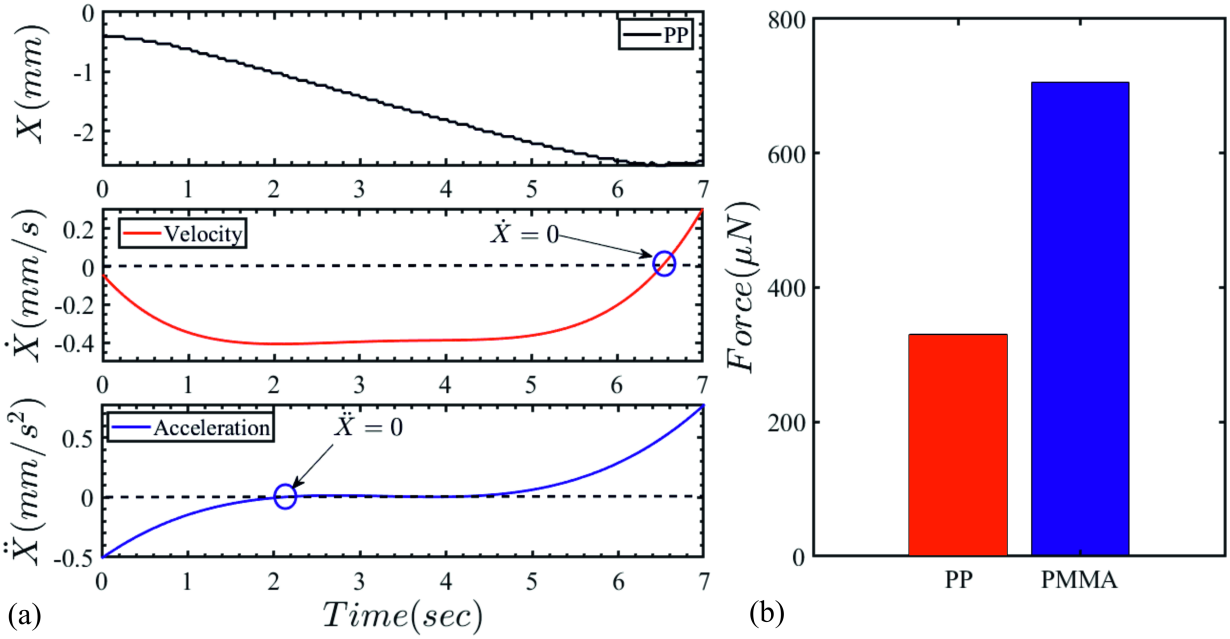

Figure H.4: (a) Plot shows the temporal variation of the displacement (X), velocity ($\dot{X}$) and acceleration ($\ddot{X}$) of the cantilever tip for a PP-water pair. The black-dotted line indicates the zero line. (b) The bar graph shows the adhesion forces for PP-water and PMMA-water pairs. The adhesion force is measured using the cantilever deflection corresponding to $\ddot{X} = 0$. The volume of the probe droplet is 5 μl.

H.5 Calibration of the cantilever

We show in Figure H.5 the calibration curve of the cantilever. Laser oil droplets (density 1900 kg/m^3) of different volumes (range: 0 - 20 μl) are sequentially dispensed at the tip of the cantilever, and the corresponding deflections are recorded. Figure S5 shows the applied force (the weight of the droplet in μN) on the Y-axis and the corresponding deflection of the cantilever on the X-axis. The slope of this calibration curve gives the stiffness of the cantilever. The calibration experiments are repeated four times. The stiffness value, K, is found to be k $\sim 305 \pm 6.1$ nN/μm.

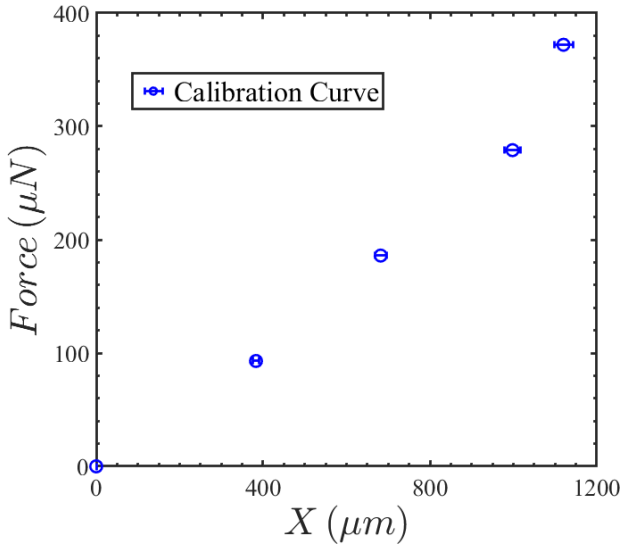

Figure H.5: Plot shows the calibration curve of the cantilever.

H.6 Variation of the left and right contact angle of the probe droplet

We show in Figure H.6, the left and the right contact angle variation of the probe droplet as it interacts with the substrate. No proper correlation between the contact angle and the adhesion force can be directly observed in Figure H.6. The correlation between

the adhesion force/the work of adhesion and the macroscopic wetting parameters remains a challenging task, and it is kept beyond the scope of the present work.

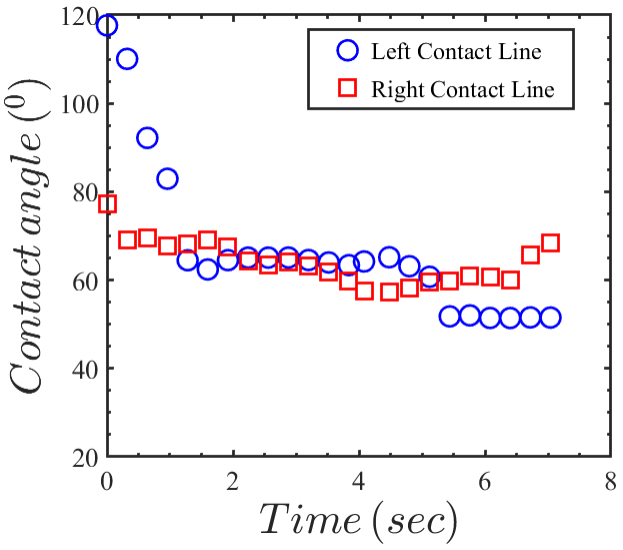

Figure H.6: Variation of the left and right contact angle of the probe droplet. The figure is a continuation of Figure 10.4 of Chapter 10. All experimental parameters are in accordance with Figure 10.4 of Chapter 10.

References

[1] M. Kiran Raj, S. Misra, and S. K. Mitra, "Friction and Adhesion of Microparticle Suspensions on Repellent Surfaces," *Langmuir*, vol. 36, no. 45, pp. 13689–13697, 2020.

[2] D. Van Krevelen and K. Te Nijenhuis, "Interfacial Energy Properties," in *Properties of Polymers*, pp. 229–244, Elsevier, 2009.

Appendix I

Supporting Information for Chapter 11

I.1 Calibration of the cantilever

The calibration is carried out by attaching known weights at the tip of the cantilever and then recording the corresponding deflection caused by the vertically acting weight. A broad range of force (0 - 840 μN) is considered for calibrating the cantilever. For smaller applied force ($\leq$ 100 μN), droplets of DI water (density, $\rho = 1000 \text{kg/m}^3$) are used as loads (Method 1). Water drops of varying volume (V) are dispensed to the tip of the cantilever as shown in Figure I.1(b) and the corresponding deflection from the horizontal plane, Δz_{tot} is recorded. However, this arrangement has an inherent restriction on the maximum usable droplet size (and consequently on the applied load) as the cantilever cannot support the weight of droplets beyond a certain volume. Therefore, for loads beyond 100 μN, known weights were prepared by folding appropriate sizes of aluminum foil (Method 2). Those were then attached to the tip of the cantilever with a string of known weight as shown in Figure I.1(c) and the resulting deflections were recorded thereafter.

It is to be noted here that in this arrangement, the cantilever deflects under its own weight even when there is no external applied force, as shown in Figure I.1(a). The corresponding deflection at no external load (Δz_0) needs to be subtracted from Δz_{tot} to obtain the deflection Δz only due to the applied external load, i.e., $\Delta z = \Delta z_{tot}$ - $\Delta z_{0.}$ The applied

load F can then be related to the deflection Δz by the spring equation $F = k\Delta z$, where k is the flexural spring constant. The corresponding deflection-force curve is plotted in Figure I.1(d). As can be seen from Figure I.1(d), a linear fit describes the deflection-force curve with excellent accuracy (with an R-Square value of 0.99545). The inverse of the slope of the fitted deflection-force curve gives the value of k as $k = 27.6$ mN/m.

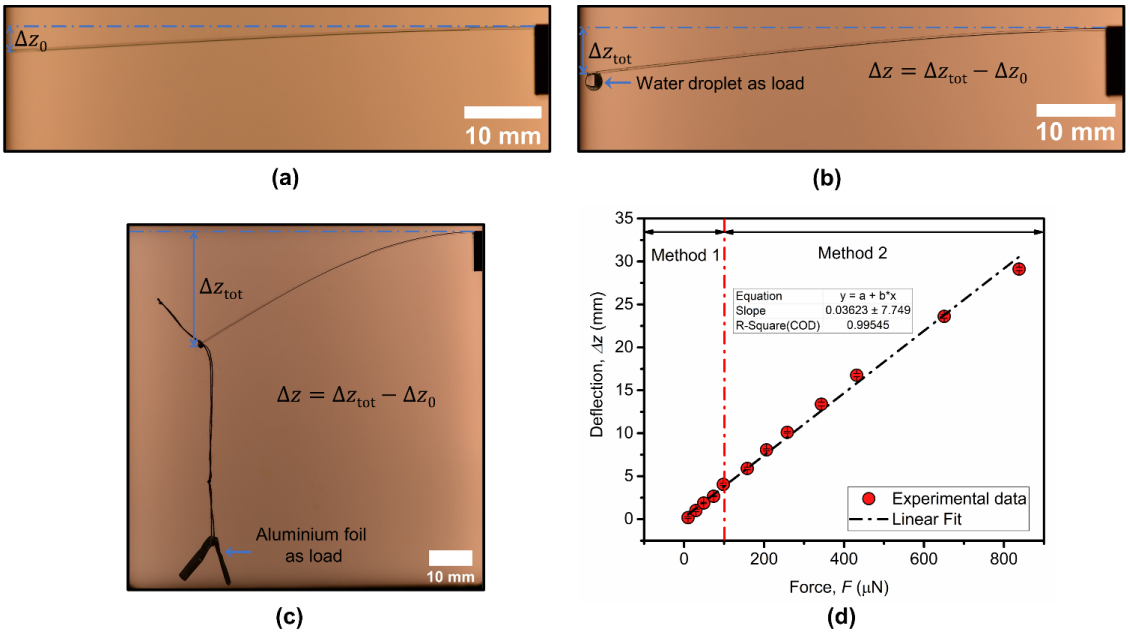

Figure I.1: Calibration of the cantilever. (a) Deflection of the cantilever (z_0) due to its own weight, (b) Method 1: calibration at lower loads - the deflecting force is applied by attaching a water droplet of predetermined volume at the cantilever tip. The volume of the attached droplet here is 7.5 μL. (c) Method 2: calibration for higher loads using folded aluminum foils as weights. The total load here (including the weight of the aluminum foil and the hanging thread) is 650.4 μN, (d) The deflection vs force curve and the linear fit.

I.2 Bacterial culture

The lyophilized *E. coli* was mixed with autoclaved Lauryl Tryptose (LT) broth and incubated in a shaker incubator (VWR, Mississauga, Canada) at 37°C as shown in Figure I.2(a-c). The growth is monitored via turbidity measurement (turbidity meter, HATCH) and the time evolution of turbidity is presented in Figure I.2(d).

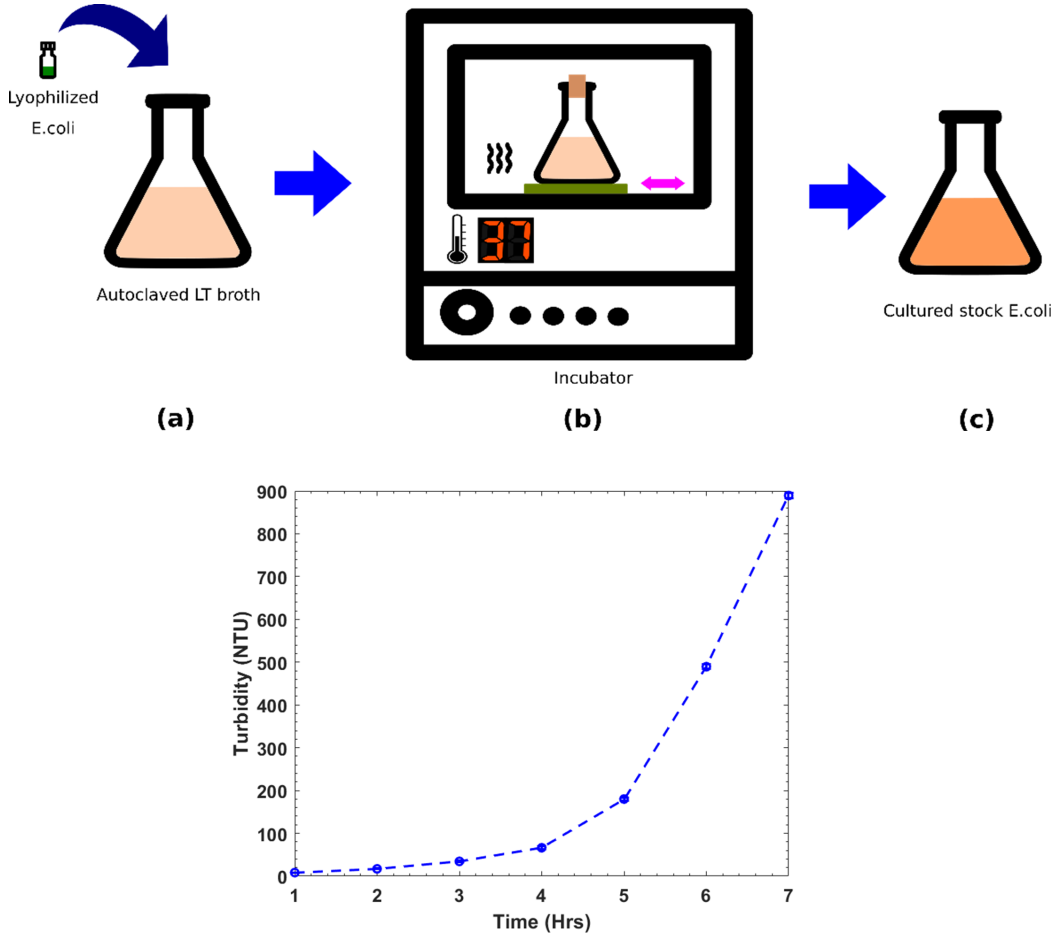

Figure I.2: The culturing method (a) Autoclaved LT broth in a conical flask (b) Incubation at 37°C with a cotton plug at the neck of the flask (c) Prepared stock in a flask, more turbid than the bare broth. (d) Turbidity measured over time in NTU.

I.3 Serial dilution of bacterial solution

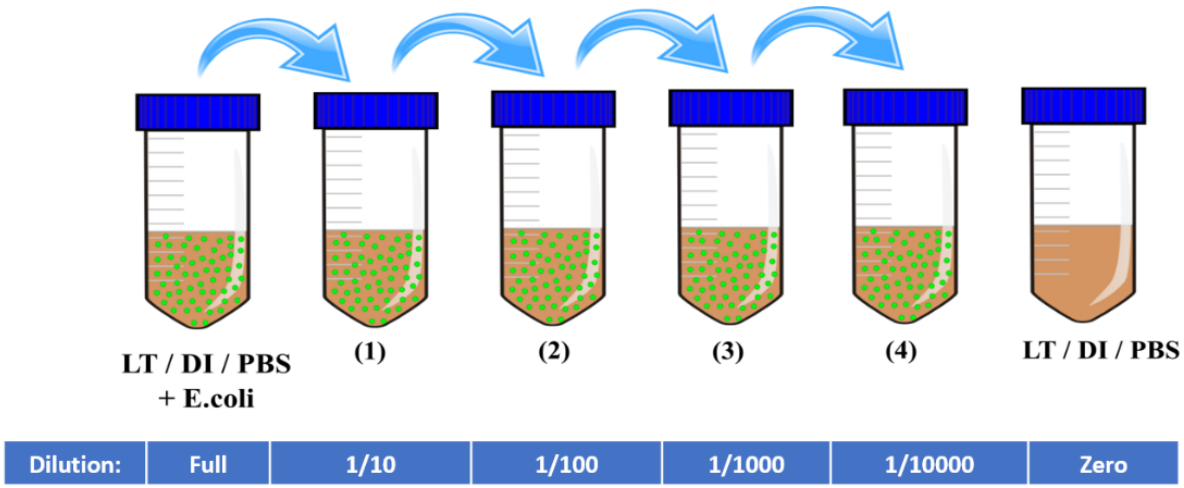

Figure I.3: The serial dilution of the stock bacterial solution to four concentrations, each diluted by $1/10^{\text{th}}$ of the previous concentration. A zero dilution refers to pure LT, DI, and PBS liquid (without any bacteria).

A serial dilution process is followed to prepare sample solutions with varying bacterial concentration. The dilution factor is kept at 1/10. At each step, 1 ml of sample solution is added to 9 ml of base liquid, which leads to a ten-fold dilution in sample concentration. The dilution is limited to four steps in the present study, where the fourth step corresponds to 10000-fold dilution in comparison to the stock solution, as a negligible number of bacterial colonies are observed in agar plating below this concentration.

I.4 Agar plate counting of bacterial colonies

Agar plates were prepared by pouring autoclaved Luria Bertani medium (10 g of Tryptone, 5 g of yeast extract, 10 g of NaCl, and 15 g of agar per 1 L of medium, BD Biosciences) into Petri dishes. As shown in Figure I.4(a), solutions with serially reducing

bacterial concentrations (with a reduction factor of 1/10) were prepared in separate falcon tubes according to the serial dilution protocol outlined in section I.3. A small amount of bacterial solution from each of the tubes was then streaked on separate agar plates using sterile inoculating loops as shown in Figure I.4(b) and then incubated in an incubator (VWR, Mississauga, Canada) overnight after inverting the plates. A decreasing amount of colony formation will be visible on the plates in the order of increasing dilution. After choosing a plate with a fairly readable count, the concentration is calculated by converting it into a power of 10 according to the dilution and finally expressing in CFU/ml of the original stock solution.

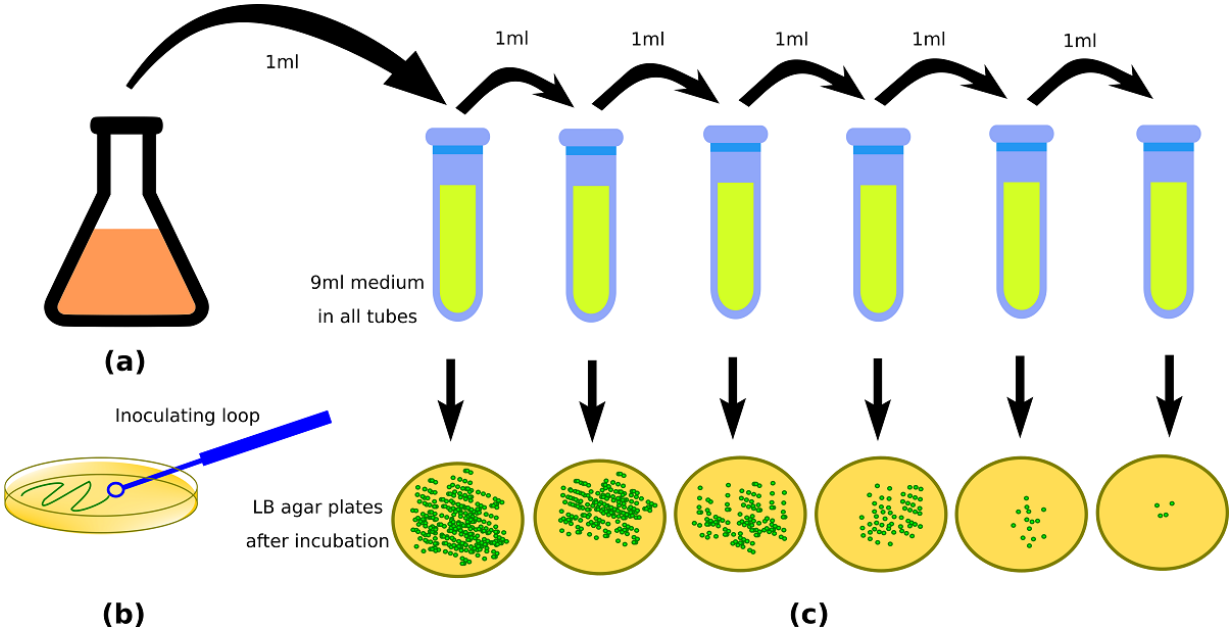

Figure I.4: Agar plating (a) Stock *E. coli* in LT medium. (b) *E. coli* streaked on agar plates (c) Growth of bacterial colonies from serial dilution.

I.5 Live/Dead Assay

The dead/live test was conducted using the ready-to-use bacterial viability kit from Invitrogen (BacLight™) [1]. The bacterial kit contains two fluorescent stains - SYTO9

green fluorophore and propidium iodide (PI) red fluorophore. These two were mixed in equal volumes in a microfuge to prepare the dye solution. A few drops of this dye solution were added to the *E. coli* stock and the dyed solution was then incubated for 30min in the dark after shaking in a vortex for 15 min. After incubation, few drops of the solution were spread over a coverslip and observed under a confocal microscope (Zeiss LSM 800). Fluorescein isothiocyanate (FITC) and Texas Red filter sets were used to detect the presence of SYTO 9 and PI fluorophores, respectively. Live bacteria with intact cell membranes fluoresce green while dead bacteria with disrupted/broken cell membranes emit red as shown in Figure I.5(a & b). The images were later processed in ImageJ and counted after thresholding to give the quantity of live bacteria in the stock solution given by:

$$\%\text{ of Live bacteria}(L_{\%}) = \frac{\text{No. of live bacteria}}{\text{No. of live bacteria} + \text{No. of dead bacteria}} \times 100.$$

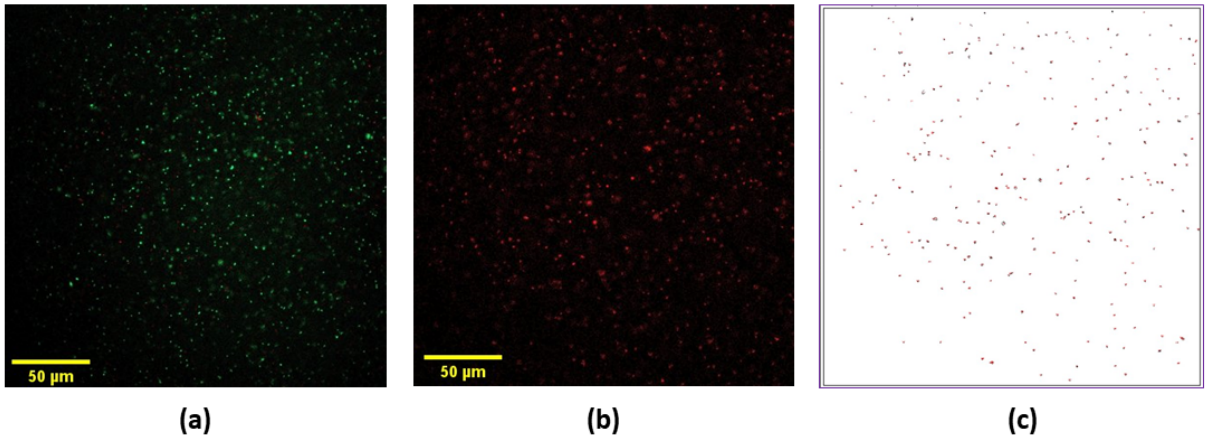

Figure I.5: (a) Live cell imaging using Fluorescein isothiocyanate (FITC) (b) Dead cell imaging using Texas Red (c) Counting of bacteria after thresholding individual channels.

I.6 Surface characterization

Surface characterization was carried out using scanning electron microscopy (SEM) and atomic force microscopy (AFM). For surface characterization, the samples are cut in 1 cm

$\times$ 1 cm substrates, and for SEM imaging, a conductive gold coating was deposited on the surface by sputtering. The respective average roughness, R_a from the AFM for S1 is 31.09 $\pm$ 4.37 nm and for S2, it is 76.86 $\pm$ 7.81 nm. Corresponding mean peak-to-peak distances (PPD) are 76.83 $\pm$ 7.6 nm and 187.49 $\pm$ 12.45 nm, respectively.

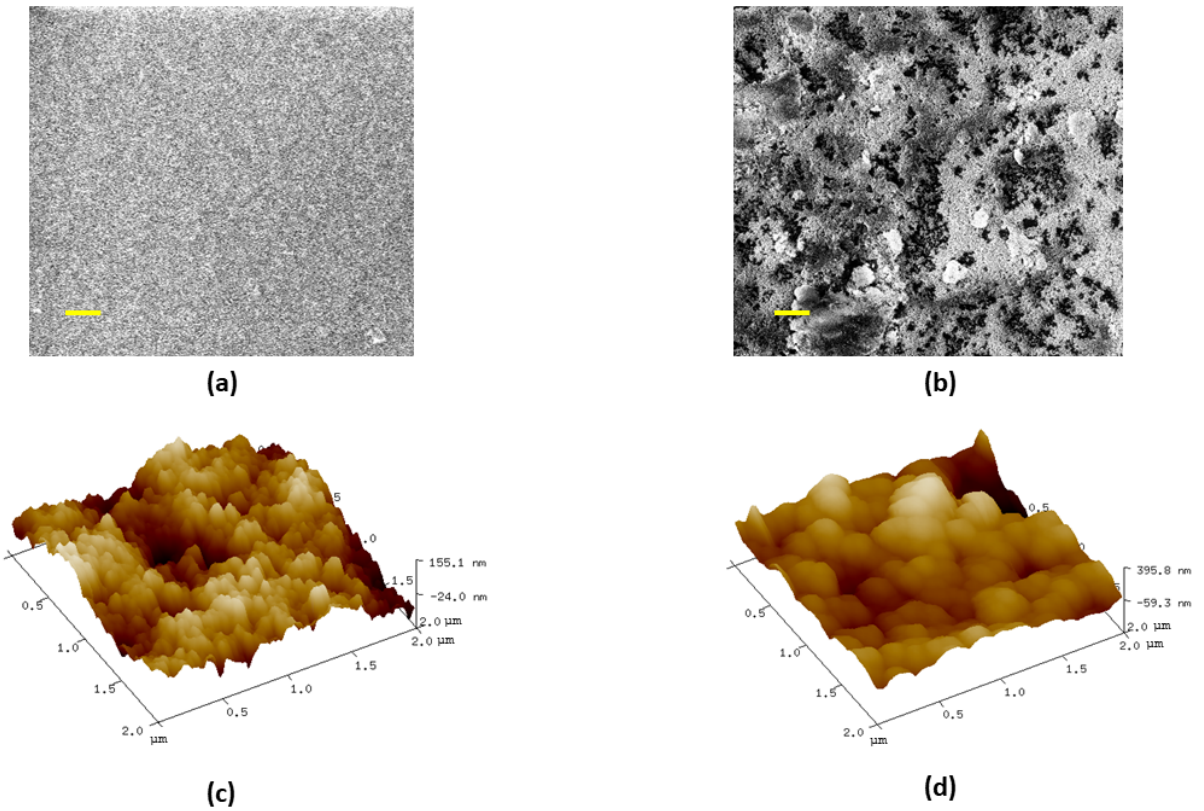

Figure I.6: Surface characterization using scanning electron microscopy (SEM) and atomic force microscopy (AFM) - (a) & (b) contain SEM microstructure images of surfaces S1 and S2, respectively. The scale bar here represents 10 μm. (c) & (d) represent the surface topology of S1 and S2, respectively, captured using AFM.

I.7 Fourier Transform Infrared (FTIR) spectroscopy of the coated surface

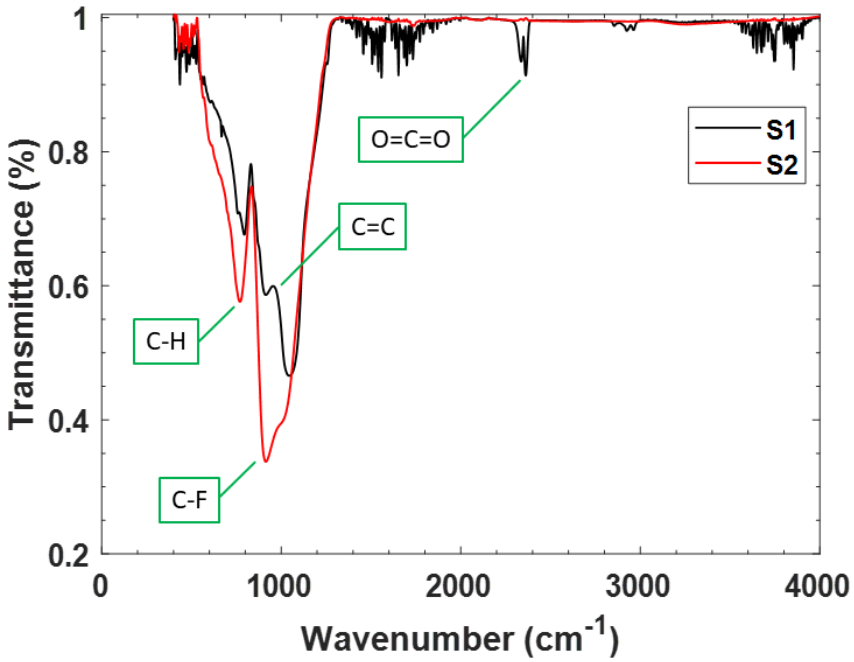

Figure I.7: Transmittance FTIR spectra of the S1 and S2. The prominent peaks and corresponding functional groups are identified based on the available literature.

ATR (Attenuated total reflectance) FTIR spectra were recorded at room temperature in the mid IR range (400-4000 cm^{-1}) on a Bruker Vertex Series FTIR spectrometer using Platinum ATR accessory with a single reflection diamond crystal at multiple points on 1 cm $\times$ 1 cm sample surfaces as shown in Figure I.7. Characteristic bonds in silicones like C=C, O=C=O are observed for S1, and the typical C-F bond due to fluorination is observed for S2 [2–4]. Probing at 4-5 random locations for both S1 and S2 showed similar spectra implying that the coating is uniform, without any chemical inhomogeneities.

I.8 Culture invariance of experimental observations

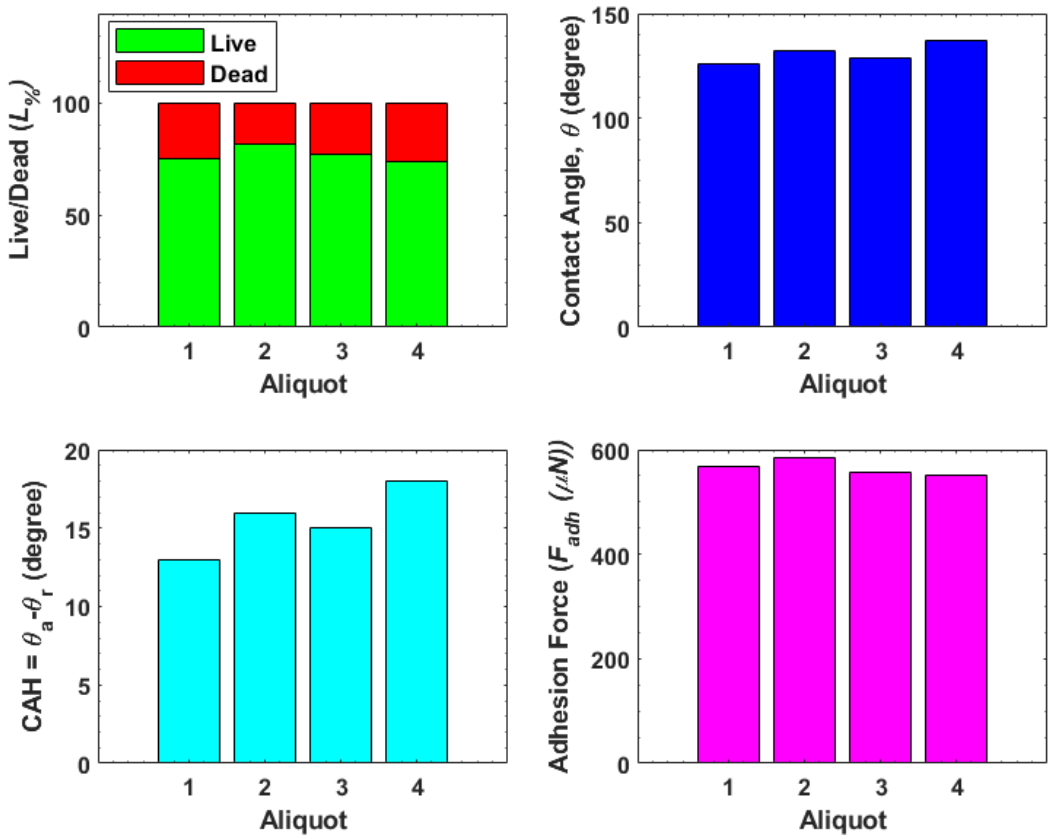

Figure I.8: Culture invariance across different aliquots - (a) Percentage of live and dead bacteria (b) Static contact angle, (c) Contact angle hysteresis, (d) Adhesion Force. All the reported results in (b), (c) & (d) correspond to experiments conducted with probe droplets of full concentration stock solution with DI water as the base medium and on surface S1.

One of the key concerns while dealing with bacterial cultures is the sample-to-sample variation as the cultures may differ in their percentage of live and dead cells based on the culture conditions. For the present experiments, we always drew the sample from the same stock and thus ensuring the same parental identity same. To ascertain the

difference in cultures, we have performed a series of experiments with different cultures, all of them sharing the same ancestral bacterial inoculum as the starting point of growth in the medium, cultured as separate aliquots. The live/dead percentages of bacteria in all the aliquots were then quantified. Contact angle (both static and dynamic) and adhesion signature were captured thereafter using probe droplets of full concentration stock solution (prepared from all four aliquots) with DI water as the base medium and S1 as the target surface. The results are illustrated in Figure I.8. It shows that there is no significant difference in experimental observations across the aliquots, which establishes the generality of the conclusions of the study.

References

[1] Invitrogen, "LIVE / DEAD® BacLight Bacterial Viability Kits," 2004.

[2] D. R. Anderson and A. L. Smith, "Analysis of silicones," *Wiley-Interscience, New York*, p. 247, 1974.

[3] L. J. Bellany, "The infrared spectra of complex molecules," *Chapman Hall, London*, vol. 1, 1975.

[4] A. L. Smith and J. M. Harnly, "Spectrochim," *Aeta*, vol. 16, p. 87, 1960.

Appendix J

Engineering drawing of the programmable 4-droplet encapsulation station

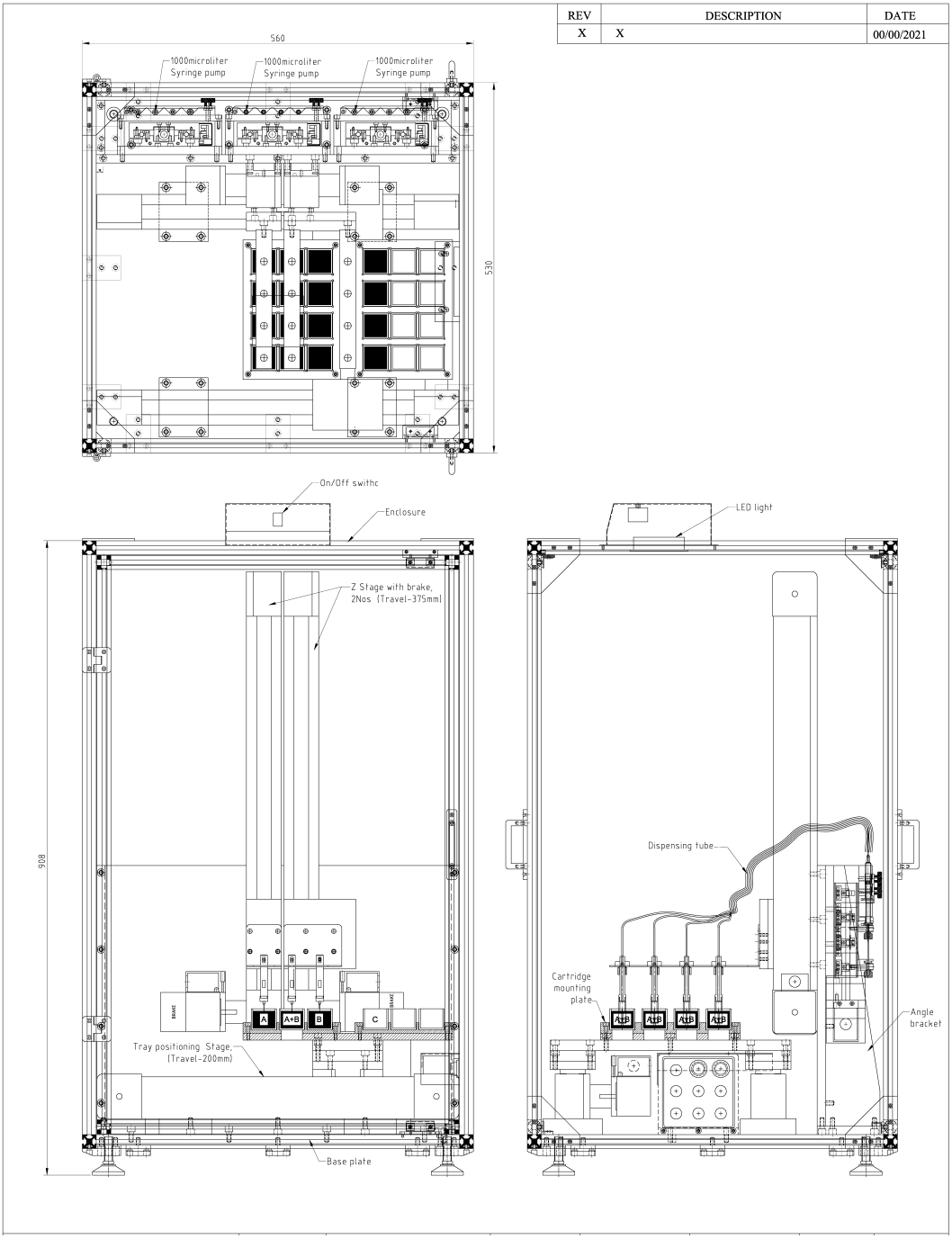

Figure J.1: Engineering drawing of the programmable & automated 4-droplet encapsulation station